

AD-A078 423

DAVID W TAYLOR NAVAL SHIP RESEARCH AND DEVELOPMENT CE--ETC F/G 20/4
AN INVENTORY OF SOME FORCE PRODUCERS FOR USE IN MARINE VEHICLE --ETC(U)
NOV 79 M B WILSON , C V KERCZEK
DTNSRDC-79/097

UNCLASSIFIED

NL

1 OF 5
AD-
A 078423



DTN8RDC-79/097

AN INVENTORY OF SOME FORCE PRODUCERS FOR USE IN MARINE VEHICLE CONTROL

ADA 078423

DDC FILE COPY

LEVEL *[Handwritten signature]*

[Handwritten initials]



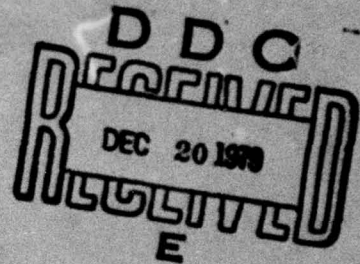
**DAVID W. TAYLOR NAVAL SHIP
RESEARCH AND DEVELOPMENT CENTER**

Bethesda, Maryland 20884

**AN INVENTORY OF SOME FORCE PRODUCERS
FOR USE IN MARINE VEHICLE CONTROL**

by

Michael B. Wilson
and
Christian von Kerczak



APPROVED FOR PUBLIC RELEASE: DISTRIBUTION UNLIMITED

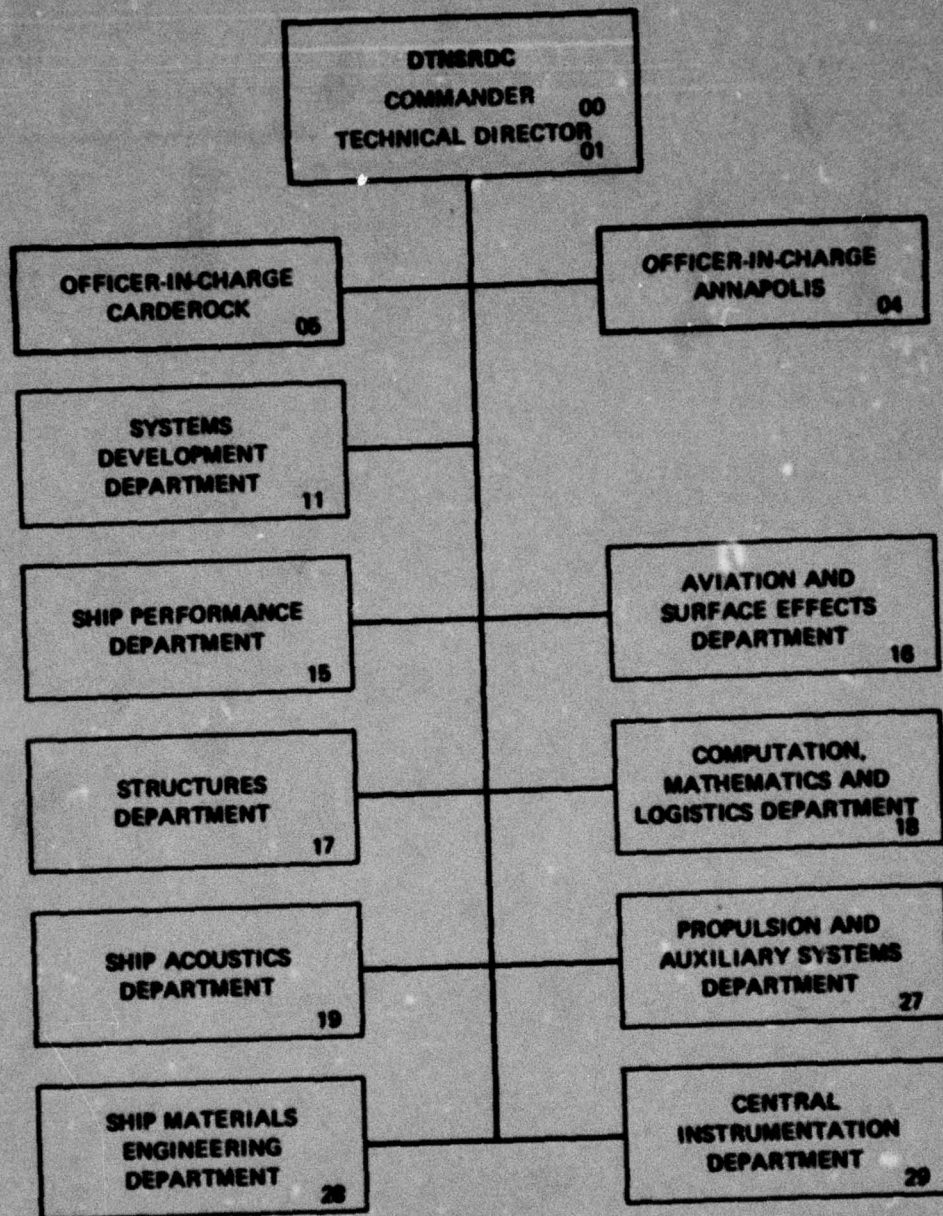
**SHIP PERFORMANCE DEPARTMENT
RESEARCH AND DEVELOPMENT REPORT**

79 12 18 014

November 1979

DTN8RDC-79/097

MAJOR DTNSRDC ORGANIZATIONAL COMPONENTS



UNCLASSIFIED

SECURITY CLASSIFICATION OF THIS PAGE (When Data Entered)

REPORT DOCUMENTATION PAGE		READ INSTRUCTIONS BEFORE COMPLETING FORM
1. REPORT NUMBER (14) DTNSRDC-79/097	2. GOVT ACCESSION NO.	3. RECIPIENT'S CATALOG NUMBER
4. TITLE (and Subtitle) (6) AN INVENTORY OF SOME FORCE PRODUCERS FOR USE IN MARINE VEHICLE CONTROL		5. TYPE OF REPORT & PERIOD COVERED
7. AUTHOR(s) (10) Michael B. Wilson Christian von Kerczek		6. PERFORMING ORG. REPORT NUMBER
9. PERFORMING ORGANIZATION NAME AND ADDRESS David W. Taylor Naval Ship Research and Development Center Bethesda, Md. 20084		8. CONTRACT OR GRANT NUMBER(s) (12) 410
11. CONTROLLING OFFICE NAME AND ADDRESS David W. Taylor Naval Ship Research and Development Center Bethesda, Md. 20084		10. PROGRAM ELEMENT, PROJECT, TASK AREA & WORK UNIT NUMBERS Program Element 6275N 6275N Task Area AF 43 423 001 ZF 43423001 Work Unit T-1563-001
14. MONITORING AGENCY NAME & ADDRESS (if different from Controlling Office)		12. REPORT DATE (11) Nov 79
		13. NUMBER OF PAGES 442
		15. SECURITY CLASS. (of this report) UNCLASSIFIED
		15a. DECLASSIFICATION/DOWNGRADING SCHEDULE
16. DISTRIBUTION STATEMENT (of this Report) APPROVED FOR PUBLIC RELEASE: DISTRIBUTION UNLIMITED		
17. DISTRIBUTION STATEMENT (of the abstract entered in Block 20, if different from Report) (16) F 43 423 (17) ZF 43 423 001		
18. SUPPLEMENTARY NOTES (9) Research and development repts		
19. KEY WORDS (Continue on reverse side if necessary and identify by block number) Survey of Force Producers Comparison of Lift Producers Submarine Control Lateral Thrusters and Jets Lift Augmentation Powered Lift Producers		
20. ABSTRACT (Continue on reverse side if necessary and identify by block number) This report is a collection of information about the force-producing capabilities and characteristics of some hydrodynamic devices that could possibly be used for the control of submarine or surface ships. Emphasis is on the variety of concepts available for this purpose, something about the physical nature of how each device operates, and descriptions of the forces attainable. Out of all the devices considered, a preliminary judgment is formed of those devices that seem most likely to be of use in the immediate future.		

DD FORM 1473

EDITION OF 1 NOV 65 IS OBSOLETE
S/N 0102-014-8601

387682 UNCLASSIFIED

SECURITY CLASSIFICATION OF THIS PAGE (When Data Entered)

TABLE OF CONTENTS

	Page
ABSTRACT	1
ADMINISTRATIVE INFORMATION.	1
INTRODUCTION	1
SCOPE OF THE STUDY	2
SUMMARY AND CONCLUSIONS	4
RANKING	4
SELECTED FORCE PRODUCERS	6
APPENDIX A - EVALUATION OUTLINES OF FORCE-PRODUCER CONCEPTS	15
TABLE OF CONTENTS	
CHAPTER 1 - CIRCULATORY LIFT DEVICES	19
CHAPTER 2 - REACTION DEVICES	251
CHAPTER 3 - EXTERNAL FORCE DEVICES	367
APPENDIX B - PATENT CATEGORIES SEARCHED	389
REFERENCES	397

Accession For	
NTIS Grant	<input checked="" type="checkbox"/>
DDC TAB	<input type="checkbox"/>
Unannounced	
Justification	
By _____	
Distribution/_____	
Availability Codes	
Dist	Avail and/or special
A	

LIST OF FIGURES

	Page
1 – Hydrodynamic Efficiency (Equivalent Lift-to-Drag Ratio) versus Section Lift Coefficient for 16 Representative Circulatory Lift-Producing and Lift-Augmenting Schemes	8
2 – Mechanics of Maximum Circulatory Lift	20
3 – Basic Flap Arrangements	24
4 – Flap Types	25
5 – Slotted Single Flap, Deflected by Angle δ Showing a Simultaneous Chord Extension	28
6 – Flap Effectiveness Factor $\lambda_1 (c_f/c')$, Applies to All Flaps	28
7 – Correction Factor to Flap Effectiveness with Respect to Flap Angle δ for Plain, Split, and Slotted Flaps	28
8 – External Foil Flap	29
9 – Example Lift Performance and Schematic Arrangement of Douglas Double-Slotted Flap	30
10 – Function $\lambda_3(b_f/b)$: Ratio of Lift Increment from Part-Span Flap to Full-Span Flap	32
11 – Function $\lambda_2(\delta)$ for Estimating Flap Lift Increment	33
12 – Function for Estimating Lift Increment of an Auxiliary Flap	34
13 – Variation of Lift-Curve Slope with Aspect Ratio for Finite-Span Lifting Surfaces	35
14 – Functions $\delta_1(c_f/c)$ and $\delta_2(\delta)$ for Estimating Drag Increment Due to Deflection of Plain and Split Flaps	37
15 – Function $\delta_3(b_f/b)$ for Estimating Drag Increment of Part-Span Flaps	38
16 – Factors for Estimating Flap Drag and Induced Drag	39
17 – Configuration and Sample Data from Tests on a Flapped Rudder	41
18 – Aerodynamic Characteristics of NACA 66(215)–216 Airfoil Section with 0.2c Sealed Plain Flap	44
19 – Slats and Leading Edge Flaps	45

	Page
20 – Effect of Leading-Edge Devices on Lift and Drag of NACA 64A210 Section with Double-Slotted Flap	48
21 – Main Types of Lift Spoilers	51
22 – Body Flaps from U.S. Patent 3,125,313	52
23 – Dive-Brake Flaps	53
24 – Trapped Vortex	55
25 – Flow Over a Flapped Control-Surface Foil	57
26 – Configurations of Blown Conventional Flaps, Flap Chord Greater Than 20 Percent of Total Foil-Flap Chord	59
27 – Lift Data on Effect of Blown Flaps, Showing Identification of Critical Attachment Momentum Coefficient $C_{\mu_{crit}}$	61
28 – Sample Blown Flap Test Results	61
29 – Curves of Lift Increments Normalized by the Theoretically Achievable Values ΔC_{ℓ}	62
30 – Theoretical Section Lift Increment Due to Flap Deflection at Zero Incidence $E = c_f/c$	62
31 – Effects of Rear Flap Blowing	63
32 – Two-Dimensional Data Showing Sample Comparison of ΔC_{ℓ} for Several High-Lift Concepts, Including Trailing-Edge Blown Flaps	64
33 – Theoretical Thin-Foil Derivative ($C_{\ell_{\alpha}}$) versus C_{μ} for a Jet- Augmented Flap	65
34 – Theoretical ($C_{\ell_{\delta}} \alpha=0$) for Thin Foil with a Blown Flap; Contours of c_f/c	65
35 – Polar Plots of Total Lift and Drag Coefficients C_L and C_D for Arrangement Shown in Figure 28a	67
36 – Variation of Aerodynamic Drag C_{DA} with Blowing Momentum Coefficient C_{μ} for Scheme of Figure 28a	68
37 – Effect of Flap Blowing upon Stall Incidence Angle	71
38 – Effect of Leading-Edge Flap Knee Blowing on Lift-versus- Incidence Curves for NPL 8-Percent Foil Shape	73

	Page
39 - Variation of $C_{\mu_{crit}}$ with Flap Angle, Two-Dimensional Results	74
40 - Graph for Estimating C_{μ_f} as a Function of Flap Angle and Aspect Ratio, where $C_{\mu_f} = (\dot{m}_T V_j / q_{\infty} S_f)_{crit}$	75
41 - Some Jet-Flap Arrangements	79
42 - Influence of the Arrangement of the Blowing Slot at the Trailing Edge for Two-Dimensional Flow	80
43 - Sample Two-Dimensional Lift Data for a Jet-Flapped 16-Percent- Thick Elliptical Section Shape	82
44 - Approximate Finite-Aspect-Ratio Factor for Jet-Flapped Wings, Large AR, for Elliptic Loading	83
45 - Comparison of Lift Derived by the Elementary Vortex Distribution Method and the Maskell and Spence Method for a Jet-Flapped Wing with an Elliptical Planform and an Elliptical Jet-Momentum Distribution	85
46 - Comparison of Theoretical and Experimental Lift for Jet Flapped Wings with a Rectangular Planform and Uniform Full Span Blowing, $C_{\mu} = 1.0$	85
47 - Total Lift-Curve Slope versus Total Jet-Momentum Coefficient, Rectangular Planform, Flat Plate Section, Contours of Aspect Ratio	86
48 - Total Lift-Curve Slope versus Total Jet Momentum Coefficient	87
49 - Total Lift-Curve Slope versus Total Jet Momentum Coefficient	88
50 - Sample Data for the Lift Variation on a Rectangular Planform Jet-Flapped Wing, AR = 2.75	90
51 - Total Lift Coefficient for a Jet Flapped Rectangular Lifting Surface, AR = 8.4	91
52 - Two-Dimensional Drag versus Jet Momentum Coefficient, Data for the Jet-Flapped 16-Percent-Thick Elliptical Shape of Figure 43	93
53 - Sample Total Thrust Data Corresponding to Jet-Flapped- Wing-Thrust Data of Figure 50	94

	Page
54 - Circulation-Control Foils with Tangential Blowing Slots	97
55 - Elliptic Foil Section	98
56 - Flow about an Elliptic Circulation-Control Foil with a Rounded Trailing Edge	100
57 - Model Geometry of a 15-Percent-Thick Elliptic Circulation-Control Foil with a Rounded Trailing Edge	100
58 - Lift Variation versus Angle of Attack	101
59 - Lift Variation versus Momentum Coefficient	102
60 - Lift Augmentation for Rounded Ellipse	103
61 - Variation of Pressure Coefficient versus Chordwise Position for a Rounded Ellipse 15-Percent-Thick Uncambered Circulation- Control Foil	104
62 - Variation in Drag Coefficient versus Momentum Coefficient	105
63 - Comparison of Measured and Equivalent Drag Coefficients, $\alpha_{geo} = 0$, $h_j = 0.01$ Inch	109
64 - Equivalent Lift-to-Drag Ratios versus Lift Coefficient	110
65 - Example Design of a Circulation-Control Wing for Application to the $AR = 0.908$ Stern Plane of a Submarine	112
66 - Ejector Thrust Augmentation	115
67 - An Ejector Flap	115
68 - Ejector Flapped-Wing Section	117
69 - Lift Characteristics of Suction Airfoil with Regular Blowing	117
70 - Linearized Theoretical Ejector Flap Analysis	118
71 - Linearized Theoretical Ejector Flap Performance	118
72 - Data and Calculations for an Aspect Ratio 8 Augmentor Wing	120
73 - Concept of an Augmentor Wing with Jet-Flap Diffusion	121
74 - Chordwise Combined Blowing Suction, Compared with Blowing Airfoils	124

	Page
75 – Combined Blowing and Suction, Using Ejector-Pump Geometry to Produce the Suction	124
76 – Circulation Control by Combined Suction and Blowing at the Trailing Edge of an Airfoil in Two-Dimensional Flow	125
77 – Recirculation Flap Proposed by H.B.Helmbold	125
78 – Configuration for Trailing-Edge Suction, Induced by Jet, and Blowing over Highly Deflected Midchord Split Flap	125
79 – Combined Suction and Blowing on Double-Flaps of SO 6020, Polar and Lift Curves	126
80 – Duct Thrust Augmentation and Side-Force Production by Combined Slot Blowing and Suction on a Kort Nozzle	127
81 – Wind Tunnel Model of a Trapped-Vortex-High-Lift Foil Section	129
82 – Sample Two-Dimensional Lift Data for the Trapped-Vortex Foil Pictured in Figure 82a	131
83 – Effect of Nose Blowing Variation on Total Drag for Trapped-Vortex Foil.	132
84 – Blowing Jet Power Coefficients versus Momentum Coefficients for Trapped-Vortex Foil	132
85 – Plot of Two-Dimensional Equivalent Lift-to-Drag Ratio versus Section Lift Coefficient for ATC Trapped-Vortex-High-Lift Foil	133
86 – Performance of High-Lift Systems for STOL-Tactical Fighter Configuration – $AR = 4$	135
87 – Free-Streamline-Flap with Blowing Control	136
88 – A Coanda Thrust Augmentor	138
89 – Possible Arrangement of Coanda Thrusters at Tips of Submarine Stern Planes	138
90 – Slot Blowing at Wing Tips	139
91 – Beating Jet-Flap Wing for Propulsion or Thrust Production	140
92 – External Blowing on Lower Surface of a Flapped Wing	142
93 – Upper Surface Blowing (USB) over a Flapped Wing	143
94 – Concept of Spanwise Blowing to Improve Lift	145
95 – Typical Pressure Distributions on Wing with Spanwise Blowing	146
96 – Lift Due to Spanwise Blowing, Optimum Nozzle Size and Position	148

	Page
97 - Comparison of Spanwise Blowing with Pure Jet Flap	149
98 - Flap-Blowing Effectiveness by Means of Spanwise Blowing	149
99 - Experiment on Spanwise Blowing over Knee of Flap on a Model Airplane with an Aspect Ratio 3.39 Wing	150
100 - Variation of Drag and Lift Coefficient Increments versus Flap Angle δ_f with Contours of C_{μ} for Model Flow Situation Pictured in Figure 99a	151
101 - Variation of Lift Increments with Blowing Momentum; Comparison between Spanwise Blowing and Chordwise Blowing	153
102 - Two Airfed Foils Tested in a Water Tunnel	156
103 - C_L versus C_Q for Hydrofoil A, $a/c = 0.30$, at Various Angles of Attack	157
104 - C_L versus α for Hydrofoil B with $a/c = 0.30$	158
105 - Ventilation Efficiency versus Angle of Attack for Hydrofoils A and B	158
106 - Airfeeding into the Waterflow Past a Body or Ring Wing for Control Purposes	160
107 - Ring Wing Assembly in Tunnel	161
108 - Force Coefficients versus Angle of Attack with Various Airflow Coefficients for Ring Wing of Figure 107 with Ventilation Hole Configuration 5	162
109 - Example of Sensitive BLC Control	164
110 - Flapped Airfoil with Single Suction Slot at Knee of Flap	166
111 - Flapped Airfoil as in Figure 110	166
112 - Foil-Flap Arrangement for Slot Suction-Lift Augmentation Scheme	168
113 - Minimum Slot Suction Flow-Rate Coefficient Required to Prevent Separation on the Flap as a Function of Flap Angle δ_f and Angle of Attack	168
114 - Variations of the Lift and Drag Coefficients C_L and C_D with the Slot Suction Flow Rate Coefficient C_Q , Contours of α , C_L , and of Flap Angle δ_f	169
115 - Specially Designed 8.5-Percent-Thick Nose-Slot Suction Airfoils	172
116 - Experimental Variations of Maximum Lift versus Suction Quantity for Specially Designed Thin Airfoils with Slots near Leading Edge	173
117 - Effect of Slot Width Variation on Nose-Suction Airfoils	173

	Page
118 - Flow Streamlines around an Unflapped Foil with a Suction Slot on the Upper Surface	174
119 - Circulation Control by Suction	174
120 - Sample Two-Dimensional Lift Characteristics of NACA 23015 Foil Shape Modified for Trailing-Edge Suction	175
121 - Sample Two-Dimensional Drag Characteristics of NACA 23015 Foil Modified for Trailing-Edge Suction	176
122 - Sample Two-Dimensional, Pressure-Loss Coefficient for Suction Flow about a NACA 23015 Foil, Modified for Trailing-Edge Suction	177
123 - Possible Arrangement of a Symmetric Trailing-Edge Slot Suction Foil (Modified)	179
124 - Low-Drag Slot Suction Airfoils	180
125 - Experimental Lift Curves for a NACA 63A009 Airfoil with Porous Nose	182
126 - Curves of $\Delta C_{L_{max}}$ (Due to Suction) versus $C_Q R_e^{\frac{1}{2}}$ for Four Different Nose Area Suction Configurations	183
127 - An Airplane Model, Equipped with Porous Area Suction Flaps on the Flaps and Ailerons	184
128 - Results for Airplane Model of Figure 127	185
129 - Setup of Circulatory Flow about a Thwaites-Flapped Porous Circular Cylinder	187
130 - Experimental Lift and Form Drag for a Totally Porous 3-Inch-Diameter Circular Cylinder Fitted with a Thwaites Flap	188
131 - Theoretical Velocity Distributions on Specially Designed Elongated Foil Shape for Lift at Zero Incidence	189
132 - Pressure Distribution of Suction-Vortex Profile	191
133 - Example of a Cusp-Suction Profile	192
134 - Variation of Lift Coefficient on an Aspect Ratio 10, Cusp-Suction Wing with Large Flap Deflections versus Flow-Rate Coefficient	192
135 - Lifting Foil Flow-Control Concepts, Using a Captured Vortex	193
136 - Magnus Lift Coefficient versus Velocity Ratio, for a Variety of Aspect Ratios b/d and End Conditions	196
137 - Variation of Lift and Drag Coefficients versus Velocity Ratio u/V for Rotating Cylinder Experiments	198

	Page
138 – Lift Coefficient as a Function of Velocity Ratio for Rotating Cylinder with and without End Disks	199
139 – Polar Plot of Lift and Drag Ratios for Rotating Cylinder with and without End Disks	199
140 – Effect of Reynolds Number on Aerodynamic Characteristics of a Lifting Cylinder, $c/d = 0.06$, $\delta = 90$ Degrees	202
141 – Effect of Flap Angular Position on Aerodynamic Characteristics of a Lifting Cylinder for Two Reynolds Numbers, $c/d = 0.06$	203
142 – Trailing-Edge Rotating Cylinder Foil, Circulation-Control Mode	205
143 – Smooth and Knurled Cylinders Used for Tests on a Foil with a Trailing-Edge Rotating Cylinder	205
144 – Variation of Lift Coefficient versus Velocity Ratio for Trailing-Edge Rotating Cylinder Foil, Circulation-Control Mode	205
145 – Variation of Drag Coefficient versus Velocity Ratio for a Trailing-Edge Rotating Cylinder Foil, Circulation-Control Mode	206
146 – Variation of Horsepower Required to Drive Trailing-Edge Cylinder versus RPM for a Trailing-Edge Rotating Cylinder Foil, Circulation-Control Mode	208
147 – Leading-Edge Rotating Cylinder Foil BLC Mode	211
148 – Rotating Cylinder Foil	211
149 – Variation of Lift Coefficient versus Velocity Ratio for an Aspect Ratio 1.67 Rudder with a Leading-Edge Rotating Cylinder	212
150 – Leading-Edge Rotating Cylinder Foil	213
151 – Variation of Lift Coefficient versus α	214
152 – Variation of Drag Coefficient versus α	214
153 – Variation of Section Lift and Uncorrected Drag Coefficients versus Velocity Ratio for the Rotating Cylinder Flap	215
154 – Rotating Foils	219
155 – Rotating-Flap Airfoil	220
156 – Variation of $C_{L_{max}}$ versus Velocity Ratio u/V for Aspect Ratio 2.67 Rotating-Flap Wing	222

	Page
157 - Variation of Lift Coefficient C_L versus α for the Aspect Ratio 2.67 Rotating Flap Wing of Figure 156	223
158 - Polar Curves of C_L versus C_D for Aspect Ratio 2.67 Rotating Flap Wing of Figure 156	224
159 - Variation of Power Coefficient K_{PR} versus u/V for an Aspect Ratio 2 Rotating Wing, Biconvex, Circular Arc Section Shape, $t/c = 0.167$	225
160 - A Possible Combination of External-Foil Flap and Rotating-Flap Foil for an Emergency High-Lift and Braking-Drag Device	227
161 - Moving-Belt Foil	229
162 - Moving-Belt Drag Data	231
163 - Variation of Total-Belt-Drag-per-Unit-Area versus Surface Speed	232
164 - Fluid Pressure Jumps, Arising on a Waving Flexible Plate Moving at a Speed U through a Fluid	234
165 - Variations of Swimming-Thrust Coefficients K_T versus Reduced Frequency σ	236
166 - Swimming Flexible Plate Studies	237
167 - Conceptual Flow Decomposition, Linearized, for Swimming, Flexible Plate Lifting Foils	238
168 - Traveling Wave Propulsion	240
169 - Forced Harmonic Wave, Flexible Plate Propulsion	241
170 - Rigid-Plate Swimming, Produced by Harmonic Pitching and Heaving Motions	241
171 - Thrust Coefficient k_T and Efficiency η , Predicted by Two-Dimensional Airfoil Theory	243
172 - Variation of Separate Ideal Thrust Efficiencies η_h , Heave Only, and η_p , Pitch Only, versus σ for Rigid-Plate Propulsion	243
173 - Conceptual Flow Decomposition, Linearized, for Swimming, Oscillating, Rigid-Plate Lifting Foil	245
174 - Hydrodynamic Efficiency C_q/C_{de} versus Section-Lift Coefficient C_q for 16 Representative Circulatory Lift-Producing or Lift-Augmenting Schemes	250

	Page
175 – Some Propeller-Driven Tunnel Thrusters	253
176 – Lateral Tunnel Thrusters on the Deep-Submergence Rescue Vehicle	253
177 – Idealized Hull Section and Propeller-Driven Lateral Tunnel Thruster	254
178 – Jet Deflections at Very Low, Intermediate, and High Forward Speed	256
179 – Variation of Body Side-Force and Body Moment with Velocity Ratio for the Deep-Submergence Rescue Vessel with a Tunnel Bow Thruster	256
180 – Curves of Thrust/Power Ratio versus Power/Area Ratio with Contours of Static Merit Coefficient C	259
181 – Data Points for Curves of Figure 180	260
182 – Two-Directional Ejector Thruster Designs	262
183 – Arrangement of Two-Stage Ejector System	262
184 – Low and High Specific Speed Pump-Driven Thruster Units	263
185 – Plot of C versus α_R , Contours of ξ_r , for Plain Nozzles in Figure 184	265
186 – Ejector Thruster	266
187 – Optimum C -Values versus α_R for Ejector System, Compared with Maximum C -Values for Plain Nozzles	266
188 – Possible Thruster Systems Augmented by Jet-Flap Diffusion	268
189 – Plain Jet, an Ejector, and an Ejector with Jet-Flap Diffusion	269
190 – Thrust Comparison of an Ejector with Jet-Flap Diffusion with a Plain Jet at <i>Fixed</i> Total Power	271
191 – Fan-In-Wing Vertical Takeoff and Landing Aircraft, Ryan XV-5A	274
192 – Definition of Flow Field and Terms Used for Induced Lift Computation	274
193 – Variation of Lift with Velocity Ratio for Several Fan-In-Wing Models, Flaps Up	274
194 – Induced Lift with Different Lift-Fan Arrangements	275

	Page
195 – Influence of Fan-To-Wing Area Ratio on Induced Lift	275
196 – Influence of Fan Chordwise Position on Induced Lift	277
197 – Effect of Spanwise Fan Distribution on Drag Due to Fan Operation	277
198 – An Experimental Fan-In-Wing Configuration	278
199 – Incremental Lift and Drag Coefficients versus Propeller Loading, for the Fan-In-Wing Scheme of Figure 198	278
200 – Vertical Takeoff and Landing Morphology	280
201 – Trainable Propeller Thrusters	281
202 – Variation of Available Thrust with Forward Speed at Constant Power	283
203 – Sample Characteristics of a B 4 Series Propeller (Wageningen)	285
204 – Results of Open Water Tests on Four-Bladed Propellers of the B 4-55 Type	287
205 – Example Performance of a Right-Angle Thruster as a Function of Inclination Angle to Free Stream	288
206 – General Form of Streamlines Enforced by Different Nozzle Types	290
207 – Efficiency Factor Due to Frictional Nozzle Drag as a Function of C_T and ℓ/D	292
208 – Optimum Ideal Efficiency and Efficiency Losses Due to Frictional Nozzle Drag of a Ducted-Propeller System	292
209 – Ducted Propeller with a Diffusing Shroud; Notation for Static Thrusting	294
210 – Sample Data for Wageningen B 4-55 Propeller as a Ducted Screw and as an Open Screw	296
211 – Results of Open-Water Tests with Ka 4-70 Screw Series in Nozzle 19a	297
212 – Ducted Propeller at an Angle of Incidence	298
213 – Ducted Propeller Performance at Various Incidence Angles	299
214 – Ducted Propeller Configurations with Rudders	300
215 – Ringpropellers	302

	Page
216 – Particulars of Multiple Nozzle-Ringpropeller System	302
217 – Efficiency Factor η_d of B 4-70 Screw Series, Ka 4-70 Screw Series in Nozzle 19A, and Different Ringpropeller Series	303
218 – Comparison between a Regular Ducted Propeller and One with Jet-Flap Diffusion	304
219 – Blown-Duct Shrouded Propeller	306
220 – Arrangement of Conventional Powered Rudder behind the Screw of a Surface Ship	307
221 – Flow and Geometry of the Active Rudder	307
222 – A Waterjet Propulsion Unit Having a Centrifugal Pump	311
223 – Cross Sectional View of Flush-Mounted Waterjet	311
224 – Energy Density Variation through a Plain Aligned Waterjet	312
225 – Contours of $T/\rho A_j$ versus V_j and V_0 for Plain Waterjet	314
226 – Jet Efficiency versus Jet-Velocity Ratio for Various Nondimensional Loss	316
227 – Aligned Waterjet Propulsors in Static Operation	318
228 – Comparison of Relative Thrust Values at Constant Power	321
229 – Ejector Cross Section and Details of Hypermixing Nozzle	321
230 – Bypass Systems Showing Two Combinations of Rotor and Jet	322
231 – Two Basic Types of Air-Augmented Waterjet Thrusters	325
232 – Air-Augmented Waterjet	326
233 – Variation of Thrust Augmentation with Pump-Outlet Pressure	326
234 – Variation of Thrust Augmentation with Mass Flow Ratio	327
235 – Variation of Thrust Augmentation with Air-Injection Temperature	327
236 – Hydroturbojet	327
237 – Principal Parts of a Water-Ramjet	329
238 – Nuclear Powered Water-Ramjet Adapted to a Hydrofoil Vessel	330

	Page
239 - Hydropulsejet	330
240 - Aerohydrotor Propulsion Concept	330
241 - Principle of the Foa Crypto-Steady Flow Eductor	331
242 - Bladeless Propeller	331
243 - Static Performance of a Bladeless Propeller for $\rho_2/\rho_1 = 1.0$	332
244 - Vortex Propeller	334
245 - Various Combinations of Thrust Vector Directions for Maneuvering, Using Four Vortex Propellers Mounted on Hull of a Surface Ship	334
246 - Optimum Propulsor Efficiencies as a Function of Power Parameter K	336
247 - Six-Bladed Vertical Axis Propeller	339
248 - Possible Applications of Vertical Axis Propellers for Submarine Control	339
249 - Blade Paths for Pure Cycloidal Motions at Zero Slip	340
250 - Propeller Efficiencies with Six Rectangular Blades at Zero Steering Angle	341
251 - Thrust Characteristics with Six Rectangular Blades at Zero Steering Angle	342
252 - Torque Characteristics with Six Rectangular Blades at Zero Steering Angle	343
253 - Full Circle Polar Diagram for Vertical Axis Propeller	345
254 - Haselton Configuration, Tandem Very Large Hub Propellers	348
255 - Thrust and Torque Coefficients and Efficiency versus A for a Front-Mounted Shrouded Very Large Hub Propeller with Collective Pitch Angle θ_0 as a Parameter	349
256 - Extrapolated Thrust Performance of Tandem Very Large Hub Propellers On a Body 269 Feet Long and 40 Feet in Diameter	351
257 - Transverse Force Coefficients K_y and K_z as a Function of A, for Very Large Hub Propellers	352
258 - Vectorial Representation of Transverse Force Developed by Very Large Hub Propeller	353
259 - Additional Thrust and Torque Due to Cyclic Pitch for Very Large Hub Propeller	355

	Page
260 – Representative Side-Force-to-Thrust Ratios as Function of Rake Angle α_0 and Cross Flow Condition	356
261 – Three-Bladed, 39-Degree, Raked Controllable Pitch Propeller, VARIVEC	358
262 – Thrust and Torque Coefficients for Entire Six-Bladed Propeller	359
263 – Efficiency Curves for Entire Six-Bladed Propeller	360
264 – Side-Force Coefficients for Rectangular-Bladed Propeller as a Function of Blade Rake and Cyclic Pitch at Zero Advance	361
265 – Two-Dimensional Lift Characteristics of Blown Elliptic Airfoil Shapes	364
266 – Various Methods of Electromagnetic Propulsion	368
267 – Six-Pole Static Field External Flow Electromagnetic Propulsion Arrangement	370
268 – Orientation of Static \vec{E} and \vec{B} Fields for One Pair of Magnetic Conductor/Electrode Coils Used in Scheme of Figure 267	370
269 – Field Configurations for an External Field Induction Propulsion System for a Submarine	372
270 – Classic Recovery System, Using a Deployable Parachute	374
271 – Drag Coefficients of Sheet-Metal Caps as a Function of Height-to-Diameter Ratio	375
272 – Aerodynamic Characteristics of Hemispherical Shells, Rigidly Suspended in Wind Tunnels	375
273 – Drag Coefficient, Based on Frontal Area, of Pervious Sheets and Parachutes, as a Function of the Velocity Ratio w_p/V	375
274 – Flat Circular Canopy with Its Triangular Gore	377
275 – Ribless Guide Surface Canopy	378
276 – Ribbon Canopy	378
277 – Average Performance Characteristics of Parachute Canopies	379
278 – Parachute and Deployment System Used for a Full-Scale, Emergency-Braking Experiment with a Large Tanker	380
279 – Examples of Drogues	381

	Page
280 - Maximum Lift-to-Drag Performance Spectrum as a Function of Wing Rigidity	383
281 - Variation of Longitudinal Aerodynamic Characteristics with Angle of Attack for a Single-Keel Flexible Wing Supporting a Lifting Body	384
282 - Effect of Control Line Shortening on Some Aerodynamic Characteristics of a Twin-Keel, All Flexible, Tension-Structure Parawing with Ram-Inflated Upper Surface Tubes	385
283 - System of Axes and Positive Directions of Forces and Moments Used in Presentation of Data	386
284 - Performance of Parawing with Inflated Cylindrical Tubes (Figure 283)	387
285 - Aerodynamics of a Parawing with Rounded Leading Edges	388
286 - Lift-to-Drag Values for Parawings with Conical and Cylindrical Surfaces	388

LIST OF TABLES

	Page
1 - Relative Ranking of Force-Producer Concepts	5
2 - Selected Force Producer	6
3 - Values of Horsepower-per-Unit Span Required in Actuating Six Selected Powered Lift-Augmentation Schemes	10
4 - Values of Lift Increment-per-Power for the Six Selected Powered Lift-Augmentation Schemes of Table 3	12
5 - Some Theoretical Estimates for K_L for Predicting Maximum Circulatory Lift	21
6 - Extremes of Lift and Drag for Flapped and Unflapped Slotted Clark Y Foils	49
7 - Geometry and References for Data about Circulatory Lift Devices Plotted in Figure 174	247
8 - Comparison of Loss Coefficient	315

NOTATION

A	Characteristic area
A_o	Disc area; for propellers
A_1	Actuator disk area for tunnel thruster
A_j (or A_{j1})	Cross section area of jet sheet or jet stream of a propeller or jet
$AR = b^2 / S$	Aspect ratio
a_0	Section (2D) lift-curve slope = $C_{l\alpha}$ (foil section)
\vec{B}	Magnetic induction vector
B_p	Dimensional power coefficient for propellers
BLC	Boundary layer control
b	Span of control surface or wing
b_f	Span of flap
C	Static merit coefficient
CC	Circulation control
$C_D = D/q_\infty S$	Drag coefficient of finite-space planform
C_{DA}	Aerodynamic drag coefficient, total C_D minus jet reaction part, also called C_{D_p} or pressure drag
C_{DB}	Jet power coefficient (see Equation (51))
C_{De}	Equivalent finite-aspect-ratio drag coefficient
C_{Di}	Induced drag coefficient
C_{D0}	Drag coefficient for parachute, based on total fabric area
C_{DN}	Nozzle drag coefficient, for ducted propellers
C_{Dp}	Drag coefficient for parachute, based on projected area
$C_{Dp} = D_p/q_\infty S$	Profile drag coefficient for finite aspect ratio, total viscous drag: friction + viscous pressure drag

C_{D_R}	Jet reaction force coefficient in drag direction; for blowing jet devices
$C_d = D_{(2D)}/q_{\infty} c$	Section drag coefficient
$C_{d_e} = D_{e(2D)}/q_{\infty} c$	Equivalent section drag coefficient; see Equation (103)
\bar{C}_d	Integrated average of C_d (across the span)
C_{d_p}	Section profile drag coefficient
C_{d_w}	Section wake or profile drag coefficient
C_F	Effective fluid friction coefficient for rotating cylinder torque
C_i	Ideal static merit coefficient, based on ideal power
$C_L = L/q_{\infty} S$	Lift coefficient of finite-span planform
C_{L_A}	Aerodynamic or pressure lift coefficient
C_{L_Γ} (or C_{L_p})	Lift coefficient due to circulation, i.e., pressure or aerodynamic lift coefficient
C_{L_R}	Jet reaction force coefficient in lift direction; for blowing jet devices
$C_\ell = L(2D)/q_{\infty} c$	Section lift coefficient
C_{ℓ_t}	Theoretically achievable section lift coefficient, with flap
C_{ℓ_α}	Slope of C_ℓ with respect to angle of attack α
C_{ℓ_δ}	Slope of C_ℓ with respect to flap deflection angle δ
$C_P = P/q_{\infty} U_{\infty} c$	Section power coefficient for a variety of 2D powered lift augmentation devices; here P is the applied power-per-unit span
$C_P = P/q_{\infty} U_{\infty} A_0$	Power-loading coefficient; for propellers
$C_{P_R} = P_R/q_{\infty} V S_R$	Rotating-flap power coefficient, based on area $S_R = b c_f$ $C_P = C_{P_R} (c_f/c)$
$C_{P_f} = P_f/q_{\infty} S U_{\infty}$	Fluid-power coefficient, or general fluid-control, pumping power
$C_{P_r} = P_r/q_{\infty} V S_r$	Rotating-cylinder fluid-torque power coefficient, based on area $S_r = b \cdot d$, where d = diameter, b = span

C_p	Pressure coefficient
$C_Q = Q/U_\infty c$	Section flow quantity coefficient
$C_{\bar{Q}} = Q_T/U_\infty S$	Total flow-quantity coefficient, finite-aspect ratio
$C_T = T/q_\infty A_o$	Thrust-loading coefficient; for propellers
$C_T = \bar{T}/q_\infty L$	Time-averaged 2D thrust coefficient; for swimming plates
$C_\mu = \dot{m} V_j / q_\infty c$	Section jet momentum coefficient
$C_{\mu_{crit}}$	Critical jet momentum coefficient required to achieve theoretically realizable lift increment with blown flaps
C_{μ_N}, C_{μ_R}	Jet momentum coefficient for nose and rear flap blowing, respectively
C_{μ_f}	Jet momentum coefficient for trailing edge flap blowing
$C_{\bar{\mu}} \text{ (or } C_j) = \dot{m}_T V_j / q_\infty S$	Total jet-momentum coefficient for finite-span planform
c	Chord length, usually
c	Wave speed for travelling deformation or magnetic field intensity
c'	Total effective chord length with flap extended
c_a	Average chord length for tapered planform
c_f	Flap chord length, in usual trailing edge location
c_N	Nose flap chord length
D	Drag force, usually refers to drag on finite-aspect-ratio planform; for lifting surfaces
D	Propeller diameter; for propellers
D_i	Induced drag on finite-span planform
D_N	Nozzle (or duct) drag force
D_p	Profile drag force for finite-aspect-ratio
D'_p	Profile drag force for finite-aspect-ratio, as modified by powered-augmentation device
d	Diameter of rotating cylinder

$E = c_f/c$	Flap chord ratio; for flapped lifting surfaces
\vec{E}	Electric-field vector
E_s	Ratio of semiperimeter-to-span
e	Factor for induced drag coefficient for non-elliptic planforms
$e_p = p/\rho$	Specific pressure energy
$e_v = \frac{1}{2} v^2$	Specific kinetic energy
e_f	Correction factor for flap lift increment
EVD	Elementary vortex distribution
$F_A(AR), F_A(AR, C_{\mu})$	Finite-span correction factor—without and with jet blowing, respectively
$F_S(AR) = a_0 F_A(AR)$	Finite-span correction on lift-curve slope, constant section wing
F_s	Side force; for propellers
g	Acceleration of gravity
H	Total head in units of length
H_L	Total system-head loss for waterjets
H_p	Pump-head loss
$H_{\infty} = \left(p_{\infty} + \frac{1}{2} \rho U_{\infty}^2 \right) / \rho g$	Ambient or free-stream total head
h_j	Average slot height for blowing or suction
$J = V_{\infty}/nD$	Advance coefficient
\vec{j}	Current density vector
K	Power parameter (see Equation (181))
K	Head loss coefficient for waterjets (see Equation (166))
K_{F_s}	Side force coefficient
K_L	Head loss coefficient for waterjets (see Equation (165))
$K_p = P/\rho n^3 D^5$	Propeller power coefficient, D = propeller diameter

$K_{P_R} = P_R / \frac{1}{2} \rho u^3 S_R$	Rotating-flap, power coefficient, based on peripheral velocity u and $S_R = b c_f$
$K_Q = Q_P / \rho n^2 D^5$	Propeller torque coefficient
K_S	Side force coefficient
$K_T = T / \rho n^2 D^4$	Propeller thrust coefficient
K_{T_N}	Thrust coefficient for nozzle (duct)
$K_{\bar{T}}$	Time averaged nondimensional thrust; for swimming plate thrusters
K_X, K_Y	Propeller X-force (thrust) and Y-force (side) coefficients
K_y, K_z	Propeller side and vertical force coefficients
K_α, K_δ	Partial span factors (see Equations (12) and (13))
K_J	Circulatory lift limit factor
$k = V_j / V_o$	Ratio of jet velocity to free-stream velocity; for waterjets
k	Dimensionless wave number; for swimming plates
k	Wave number
L	Lift force, usually on finite-span planform
L	Length of plate; for swimming plates
LE	Leading edge
\bar{L}_t	<i>Swimming plate time-averaged lift</i>
\dot{m}	Mass flow rate per unit span
\dot{m}_T	Total mass flow rate, finite-aspect ratio
n	Angular speed, usually, revolutions per second
n_s	Specific speed
P	Power, general
P/D	Pitch-to-diameter ratio; for propellers
P_f	Fluid power, the pumping power for fluid control

P_i	Ideal power
P_R	Rotating-foil or rotating-flap power
P_r	Rotating cylinder, fluid-friction power
p	Static pressure
p_v	Vapor pressure of water
Q	Flow rate quantity for blowing or suction flow control
Q or Q_p	Propeller torque
$q = \frac{1}{2} \rho v^2$	Dynamic pressure in flow of velocity v
$q_\infty = \frac{1}{2} \rho U_\infty^2$	Free-stream dynamic
$R_e = U_\infty \ell / \nu$	Characteristic Reynolds number; ν = kinematic viscosity; ℓ = characteristic length, usually a lifting surface chord length unless specified otherwise
r	Radius of rotating cylinder
S	Total planform area; for lifting surfaces
S_f	Planform area affected by flaps; for lifting surfaces
S_o	Total fabric area for parachute
S_p	Projected area of canopy for parachute
T	Thrust force or total lateral force for thrusters
TE	Trailing edge
t	Foil thickness, usually
t/c	Thickness-to-chord ratio
$U_\infty (V_\infty, V_0, V)$	Free-stream velocity
u	Peripheral velocity of rotating cylinder or rotating flap
V_b	Surface velocity of moving belt
V_j or V_j	Average jet velocity; for blowing jets, for waterjets, or for tunnel thrusters

V_t	Average tunnel or tube flow velocity
v	Local flow velocity
y_p	Lateral displacement of swimming plate
α	Angle of attack
α_o	Rake angle
α_R	Area ratio; for tunnel thrusters
β	Area ratio
Γ	Circulation strength
ΔC_ℓ	Increment in C_ℓ due to actuation of powered device
ΔC_{ℓ_t}	Theoretically realizable lift coefficient increment
ΔH	Change in total head in units of length
$\delta (\delta_f, \delta_R)$	Flap deflection angle for TE flapped foils
δ	Dimensional diameter coefficient for propellers
δ_1, δ_2	Flap deflection angles for compound flaps
δ_j or θ_j	Angle of jet sheet from chord line
δ_N	Nose flap deflection angle
δ_p	Planform correction factor for induced drag
$\bar{\delta}_1, \bar{\delta}_2, \bar{\delta}_3$	Universal empirical functions for incremental drag on foils with mechanical flaps
ζ'	Head loss coefficient for waterjets
ζ_j	Nozzle loss coefficient for waterjets
η or η_p	Efficiency for propellers, etc.
η_d	Static merit coefficient = C
η_j	Froude efficiency for waterjets
θ	Propeller blade pitch angle

θ_o	Collective pitch angle
$\Lambda = V_\infty/nD$	Advance coefficient; for propellers
Λ	Sweepback angle; for lifting surfaces
$\lambda_1, \lambda_2, \lambda_3$	Universal functions for incremental lift on foils with mechanical flaps
λ_{22}	Lift increment factor for auxiliary flap
$\mu = 1/k$	Ratio V_o/V_j ; for waterjets
ν	Kinematic viscosity
ν	Mass flow ratio (gas-to-water) for air-augmented waterjet
ξ_t, ξ_n	Loss coefficients; for thrusters
$\xi_o/2$	Nondimensional heave amplitude
ξ_1, ξ_2	Nondimensional pitch amplitudes
ξ_{ej}	Ejector loss factor
ρ	Mass density of water
ρ_a	Mass density of air
σ	Diffusion parameters; for ducted propellers and tunnel thruster
σ	Conductivity of seawater; for electromagnetic propulsion
σ	Reduced frequency parameter; for swimming plates
σ_v	Vapor cavitation number
τ	Ratio of propeller thrust to total thrust for ducted propeller
ϕ	Thrust augmentation ratio = total augmented thrust/thrust of primary jet; for ejectors
ϕ	Steering angle; for cycloidal propellers
ω	Angular speed in radians per second
2D	Two-dimensional

ABSTRACT

This report is a collection of information about the force-producing capabilities and characteristics of some hydrodynamic devices that could possibly be used for the control of submarines or surface ships. Emphasis is on the variety of concepts available for this purpose, something about the physical nature of how each device operates, and descriptions of the forces attainable. Out of all the devices considered, a preliminary judgment is formed of those devices that seem most likely to be of use in the immediate future.

ADMINISTRATIVE INFORMATION

The work reported herein was authorized and funded under a subtask of the Direct Laboratory Funded Project "Improved Control for Advanced Submarines," carried out under Program Element 6275N, Task Area AF 43 423 001, Work Unit 1-1563-001.

INTRODUCTION

Because of the increasing size and range of speed of submarines and many other types of marine vehicles, there is interest in improving the capabilities of control-force producers for maneuvering and course keeping. For advanced submarine designs, it will become more important to reduce or eliminate the incompatibility between high- and low-speed operations, curtail large motions, reduce the possibility of control-system casualties such as control plane jam and flooding, and explore ultraversatile controls for coordinated maneuvering. In many cases, the devices or concepts that might be candidates for achieving good control performance have been known for some time. This report presents a survey of such control devices and concepts. The list of concepts is not exhaustive; however, it does include all devices that the authors have been able to uncover that have met the requirement that the device be known, either by experiment or by sound theoretical or physical reasoning, to be capable of producing the promised force.

The purpose of this report, aside from cataloging these devices, is to provide (1) outlines of the force-producing characteristics of each device when available, and (2) preliminary judgments about the general feasibility of their use for submarine control. The outlines are based on whatever published nonclassified knowledge exists for each device. No attempt at new analysis is made in this report. Further work, both experimental and analytical, will be needed to cover the details of the selected devices.

This survey emphasizes the variety of potentially useful hydrodynamic force-producer concepts. The specific geometry appropriate to a submarine application is outside the scope of this effort. Certain characteristics which influence the usefulness of control concepts are not addressed in detail in this report. These include operational restrictions, durability,

complexity, sizing, noise production, weight, volume, and cavitation problems associated with individual flow-control techniques. However, whenever an item has an especially conspicuous disadvantage, this fact will be noted.

SCOPE OF THE STUDY

Most of the important known fluid mechanical devices for ship or aircraft control are considered here. The devices are divided into three broad categories according to the general character of the force produced.

1. Force due to circulation, i.e., hydrodynamic lift, where lift is used in a general sense
2. Hydrodynamic reaction force due to jet momentum
3. External forces created by electromagnetic fields or by a towed drag- or lift and drag producer.

All devices that seem appropriate for a marine vehicle can be fitted into one of these categories.

Appendix A presents summaries of information concerning each force-producer concept. The material is organized into three main chapters, corresponding to the physical character of the force production. A complete list of all the concept names is given at the beginning of Appendix A. Within the chapters, each concept is discussed in an outline format which contains the following items:

1. The name of the device or group of similar devices.
2. A description of the operation and configuration.
3. Estimates, when possible, of the magnitude of forces produced, i.e., the *lift* or usable force and the *drag* force penalty. Estimates of the *power* consumed and the effects of some gross geometric factors such as finite span are included as are short discussions of the mode of power input, possible application of the device and probable effectiveness, mechanical complexity, and any major disadvantages or limitations when these are known.

Each outline is somewhat self-contained. Some of them are more complete than others due to availability of information or because certain force-producer concepts seem to be intrinsically more practical and offer more meaningful prospects for marine applications.

Reference material for this study is taken from books, journal publications, and reports in the literature of hydro- and aerodynamics. Also, an extensive patent search for ideas was conducted by the authors at the U.S. Patent Office. The patent classification categories covered by this search are listed in Appendix B. It was found that most of the important and potentially useful ideas were not confined to patent files, if they ever originated there. Typically, many worthwhile concepts emerge in the open technical literature and are presented therein in a more convincing way than in a patent disclosure.

The scope of this study perforce does not include a quantitative discussion of the effects of *cavitation* on each individual concept. This is due mainly to the lack of test data in water for the vast majority of the items. However, some general observations can be made here as a framework for interpreting pertinent data whenever available. For many of the force-producer devices that have originated in the aeronautical technology, cavitation is not a problem and is rarely discussed. Of course, devices that are used on high-performance airplanes may be required to cope with compressibility effects at high subsonic Mach numbers. But these effects are qualitatively different from the problems encountered in an inherently two-phase situation such as cavitating flow. For applications in water, cavitation can pose definite limitations on performance. This could be especially true of the great variety of power-augmented circulatory lift devices—foils with slot blowing, slot suction, rotating cylinders, etc.—when suction pressure peaks at the foil nose and near the flow-control apparatus would be susceptible to cavitation inception at high speeds and shallow submergences. The elementary criterion for the cavitation inception is

$$C_{p_{min}} = -\sigma_v$$

where $C_{p_{min}} = (p_m - p_\infty)/q_\infty$ = pressure coefficient

$\sigma_v = (p_\infty - p_v)/q_\infty$ = vapor cavitation number

p_v = vapor pressure, $\cong 0.25$ psi for seawater at 60 F

p_m = local minimum static pressure along the foil.

To establish orders of magnitude at a submergence depth of 19 feet, the vapor cavitation numbers are $\sigma_v = 46.1, 11.5,$ and 2.9 at $U_\infty = 5, 10,$ and 20 knots, respectively. At a depth of 46 feet, the values of σ_v for the same speeds are $70.3, 17.5,$ and $4.37,$ respectively.

Some comments can be made about the implications of these numbers. Based on a review of the typical foil-surface pressure distributions measured or calculated for all of the various circulatory lift devices discussed in Appendix A, for thickness-to-chord ratio (t/c) nominally ≥ 12 percent, and for two-dimensional (2D) lift coefficients $C_L \leq 2.0$, the suction peak magnitudes are typically $C_p \geq -10.0$. For the low-speed range from 0 to 10 knots, where power-augmented devices on submarines are most appropriate, and for the large depths of expected submarine operation, the cavitation numbers quoted previously indicate that cavitation inception associated with foil-surface suction peaks will *not* be a problem for any of the force-producer devices noted in this survey. It is recognized that the two most important factors influencing the conditions for foil-surface cavitation are lift coefficient (circulation strength) and foil-thickness ratio. The magnitudes of the suction pressure peaks are made more extreme by increasing the foil circulation strength. On the other hand, the

peakedness of the suction pressure curve can be flattened, and the suction peak values can be reduced significantly by increasing the foil t/c, keeping the lift coefficient constant. Of course, increasing foil thickness carries the penalty of increasing the profile drag.

Aside from being an important general indicator, the simple criterion of foil-surface cavitation is not the complete story, and great caution must be exercised in this area. It is likely that cavitation in narrow gaps or in internal ducting will impose earlier inception boundaries than the external section-shape pressure peaks. This means that expected trouble spots will be in the gaps between rotating cylinders and the foil or between the hull and a deflected control plane and in the narrow slits of typical blowing or suction nozzles. This is because of the local very high fluid velocities anticipated at these locations. At this time there is a general lack of data about the effects of cavitation in these instances, especially for very high lift devices, and further research is required.

A second point indicated by the cavitation numbers quoted previously is that at higher speeds of ≥ 20 knots, actuation of a powered lift-augmenting device could very quickly produce a locally cavitating flow along the surface of the foil, either at the nose or near the flow control device. This means that certain powered devices are increasingly less appropriate at high speeds. While it may be possible that some amount of cavitation will not necessarily significantly degrade performance of many augmentation schemes, the accompanying hydrodynamic noise would definitely be undesirable for submarine applications. Again there is a lack of experimental data to use as a guide concerning this question.

SUMMARY AND CONCLUSIONS

RANKING

Each item in the entire collection of devices discussed in Appendix A can be ranked in three groups as to its possible usefulness. The ranking definitions are as follows:

Group 1 The device seems to have promise for practical application on submarines within the framework of present-day designs.

Group 2 The device or concept is interesting, perhaps useful; however, it is either not directly applicable to the present overall submarine configuration or there is insufficient information available to speculate about operation of the device in a marine environment.

Group 3 The device is not practical for submarine application.

The relative rankings presented as follows have been determined partly on the basis of a qualitative judgement and partly by direct quantitative comparison of hydrodynamic performance. Results of the ranking are given in Table 1. The order in which the items are arranged within each group is not based on preference but merely corresponds to the order of appearance in Appendix A.

TABLE 1 - RELATIVE RANKING OF FORCE-PRODUCER CONCEPTS

Item	Page Number
GROUP 1	
Mechanical Flaps	23
Mechanical Slats	43
Mechanical Spoilers	47
Internally Blown Mechanical Flaps, Leading and Trailing Edges	56
Ejector Flaps, Augmentor Wing	114
Jet Flaps	77
Circulation Control by Tangential Jet Blowing	95
Blowing-Stabilized Trapped Vortex Foil	128
Spanwise Blowing	144
Airfeeding to Alter Lift	155
Blowing to Kill Lift, Fluid Spoilers	163
Trailing Edge Slot Suction Foil	171
Rotating Cylinders, Leading and Trailing Edges and Flap Knee	195
Rotating Flap Foil	218
Lateral Tunnel Thruster-Propeller-Driven; Ejector; and Ejector with Jet-Flap Diffusion	252
GROUP 2	
Orientable Propeller Devices	279
Augmented Orientable Waterjets	320
Controllable Pitch Propellers	354
Propellers with Blowing	363
External Blowing, Upper and Lower Surface Deflected Slipstream	141
Combined Blowing and Suction Devices	122
Miscellaneous Slot-Blowing Concepts	134
Parachutes, Drogues, and Parawings	373
GROUP 3	
Suction Through Slots, Other Than Trailing Edge	165
Area-Suction Devices	181
Suction-Stabilized Trapped Vortex Foils	190
Moving Belts	228
Rotating Foils	218
Swimming Plate-Lifting Surfaces	233
Impeller in Wing	273
Orientable Plain Waterjets	310
Vertical Axis (Cycloidal) Propellers	338
Large Hub (Haselton) Propellers	347
Electromagnetic Devices	367

In the present interpretation, with one exception, the only devices that qualify for Group 1 are the best of the circulatory lift producers. These feature either improved mechanical flap performance or powered high-lift augmentation. They could conceivably be used directly on existing types of submarine control planes or on other winglike components such as the sail, dorsal rudders, and auxiliary control planes. Lateral tunnel thrusters are also included in Group 1 because they are already in use on a specialized submarine, the deep-submergence rescue vessel (DSRV), and could conceivably be employed in improved form on other slow speed submarines.

Group 2 devices are generally those that are judged to be capable of efficient control-force production; however, their use would require a change in the philosophy of submarine control—use of orientable propellers, tilt waterjets, deployable parachutes, etc. Also included are those devices with either more complex geometries or too little experimental or analytical information available. It should be noted that orientable propellers or any type of trainable thruster are interesting because they could be used for slow-speed propulsion as well as control; in general, these all suffer some deficiency at high speed—large drag and/or degraded transverse-force effectiveness. All these devices would require more selective development for application to submarines, e.g., retractability at high speed.

Concepts in Group 3 have some discernible deficiency as regards their use in water or on a submarine such as an obviously complex arrangement.

SELECTED FORCE PRODUCERS

From the items in Group 1, there are seven concepts that deserve special attention for possible immediate exploitation or near-future development for use on submarines. These are listed in Table 2.

TABLE 2 – SELECTED FORCE PRODUCERS

Item	Page Number
• Improved Mechanical Flap	23
• Blown Mechanical Flap	56
• Circulation Control by Tangential Jet Blowing	95
• Rotating Flap Foil	218
• Spanwise Blowing	144
• Rotating Cylinder Foils	195

The basis for these choices is a mixture of engineering judgement, guided in part by existing quantitative information. Each of the devices mentioned is capable of delivering a large or adequate force at modest power expenditure without unreasonable complexity.

It is felt that all the items indicated in Table 2 are simple enough to be mechanically feasible for use on control surfaces for marine applications; they could be resistant to marine fouling, and they have the fewest obvious disadvantages of all the devices listed in Group 1.

Of course the clearest set of alternatives would be shown by providing numerical indexes for everything: force and power performance, weight, volume, cost, vibration intensity, noise production, etc. Sufficient information for such extensive comparisons is not available. In the present work, the main interest is in quantitative comparisons of force and power. One such comparison is contained in Figure 1, which shows the relative hydrodynamic efficiency, or equivalent lift-to-drag ratio, versus section-lift coefficient (C_L) for 16 representative circulatory lift-producing schemes, including both unpowered and power-augmented devices. The equivalent lift-to-drag ratio is a useful universal parameter that contains a "power-drag" penalty for powered devices. Figure 1 pertains to two-dimensional foil performance, and the nondimensional equivalent drag is defined in general terms as

$$C_{d_e} = \left(\frac{\text{resultant}}{\text{profile drag}} \right) / \frac{1}{2} \rho U_\infty^2 c + \left(\frac{\text{total estimated}}{\text{actuation power}} \right) / \frac{1}{2} \rho U_\infty^3 c$$

where c = chord length

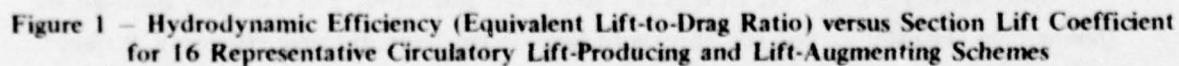
U_∞ = free-stream velocity

ρ = fluid density.

Discussions of the individual actuation power estimates for the various powered concepts are given throughout Chapter 1 of Appendix A.

The curves of Figure 1 show that the section hydrodynamic efficiencies of both the simple unflapped foil and the plain flapped foil, both "unpowered" devices, are superior in their regime of lift coefficient. The plain flapped-foil curve represents a *baseline* performance for submarine control surfaces. If large lift coefficients are desired such as for maneuvering at low forward speed, there are physical limits on the maximum lift coefficient that can be delivered by mechanical changes in angle of attack or camber. Most powered devices involve flow-control techniques aimed at extending the range of achievable lift coefficient. Figure 1 helps identify those powered devices capable of high lift coefficients with tolerable drag-and-power penalties by displaying which lift producers have performance curves exceeding C_L of the plain flapped foil. The plot is not to be construed as the final comparison because it does not contain optimized envelope curves for each concept. It does nevertheless show representative performance levels.

Other factors entering the choices in Table 2 are qualitative. For example, although the trailing-edge (TE) slot-suction foil appears to have decent hydrodynamic efficiency, it shares a common defect of all suction schemes of being vulnerable to marine fouling. There are no



8

ocean water data to verify this opinion. However, of all the suction devices, the TE slot-suction foil in particular would still function effectively if the flow control were *reversed* to purge the system; it could then perform as a jet flap. Then for this example, a desirable modified version might be a foil with a TE suction slot, formed with small deflectable flaps at the lips to act as jet-control flaps when the flow is reversed.

Once power-augmented lift concepts are included as candidates for a control surface, the usual problem of reaching a saturation level or maximum lift coefficient, by increasing angle of attack till stall, becomes considerably less important. This is because there is some powered arrangement that can be devised for the particular mode of operation that will deliver as much lift as is needed. The range of foil angle of attack for which this can be accomplished depends on the device under consideration. Some augmentation schemes, while increasing C_L at small to moderate angles of attack, tend to reduce the stall angle of the foil system, compared with the unpowered operation. An example of this is the simple internally blown TE flap. These kinds of devices could give stall problems if they were used in an application in which large incidence-angle excursions were anticipated. For such devices, the foil angle of attack would have to be carefully limited, and lift increases would be governed by increases in augmentation power and other geometry changes, e.g., heavier blowing over a larger flap angle. Other kinds of powered devices perform best at large angles of attack, e.g., leading-edge (LE) rotating cylinders and LE blown flaps, and could keep on delivering lift at angles exceeding the usual saturation boundaries, even for $\alpha \rightarrow 90$ degrees.

Of critical importance are (1) the amount of *power* needed to supply lift augmentation and (2) the *power-on drag penalty* to be paid for a special geometry, e.g., a blunt-based foil shape. Power is the most important factor. For example, with blown flaps or with a jet flap, the jet-reaction force generated by very strong blowing would produce "lift" far beyond what could be used. However, the power requirements would be large. The most desirable techniques are those that use minimal power to produce large changes in *circulation* lift.

As will be seen, there are great benefits to be derived from schemes for powered-lift augmentation. It would seem reasonable to propose that a separate power system be set up for lift-augmentation purposes, just as there is for the present day hydraulic system.

Sample horsepower requirements for the six powered types of selected concepts in Table 2 are given in Table 3, which gives the horsepower-per-unit span at $U_\infty = 5$ and 20 knots, needed to produce an increase in sectional 2D lift coefficient $\Delta C_L = 1.0$ on a foil of chord length $c = 15$ ft, $AR = \infty$. Here, the lift increment is defined as

$$\Delta C_L = C_L(\text{power on}) - C_L(\text{power off})$$

TABLE 3 - VALUES OF HORSEPOWER-PER-UNIT SPAN REQUIRED IN ACTUATING
SIX SELECTED POWERED LIFT-AUGMENTATION SCHEMES

Applies to a section (2D) lift increment $\Delta C_L = 1.0$ on $M = \infty$ foil.

$\Delta C_L = 1.0$

Item	Reference	Geometry	$\frac{\Delta C_L}{C_p}$	Blowing or Rotation Req's		Horsepower-per-Foot of Span; $c = 15$ ft		Power-Off Lift Coef- ficient C_{L_0}
				$U_\infty = 5$ kt	$U_\infty = 20$ kt	$U_\infty = 5$ kt	$U_\infty = 20$ kt	
Trailing Edge Blown Flap	Lawford and Foster (1970) 32	$\alpha = 0^\circ$, $\delta_{tr} = 40^\circ$ ($\delta_N = 0$, $C_{\mu N} = 0$)	33.2	$C_\mu = C_{\mu R} = 0.0174$ $V_f/U_\infty = 2.73$		0.491	31.5	1.3
Circulation Control by Tangential Jet Blowing	Englar (1971) **	$t/c = 15\%$, $\alpha = 0^\circ$	28.6	$C_\mu = 0.02$, $V_f/U_\infty = 2.77$		0.569	36.5	0.0
	Williams and Howe (1970) ***	$t/c = 20\%$, $\alpha = 0^\circ$ 5% camber	66.9	$C_\mu = 0.01$, $V_f/U_\infty = 1.98$		0.244	15.6	0.5
Rotating Flap Foil	Crabtree (1960) 110	$\alpha = 0^\circ$ $c_f/c = 0.25$ ΔC_L measured from autorotation	10.8	RPM = 75	RPM = 300	1.52	97.3	2.89
Spanwise Blowing	Dixon (1971) 77	$\alpha = 0^\circ$ $\delta_t = 40^\circ$	6.25	$C_\mu = 0.0255$ $V_f/U_\infty = 12.36$		2.61	167.0	1.62
Rotating Cylinders LE Cyl (camb'd) BLC mode	Wolff and Koning (1926) 107	$\alpha = 20^\circ$ $d/c = 0.2$	67.3*	RPM = 80.6	RPM = 323	0.242	15.5	0.81
Leading Edge Cyl (symm) BLC mode	Steele and Harding (1970) 102	$\alpha = 40^\circ$ $d/c = 0.174$	95.2*	RPM = 86.5	RPM = 346	0.171	11.0	1.5
Flap Knee BLC mode	Alvarez-Calderon and Arnold (1961) Ref. 108	$\alpha = 9^\circ$ $\delta_t = 40^\circ$ $d/c = 0.1143$	7.48*	RPM = 354	RPM = 1415	2.18	140.0	2.09
Trailing Edge Cyl CC mode	Brooks (1963) 103	$\alpha = 0^\circ$ $d/c = 0.1364$	52.6†	RPM = 101	RPM = 405	0.31	20.0	0.0
Trailing Edge Slot Suction Foil	Hazen, Sweeney, Lehnert, and Ringleb (1953) 91	$\alpha = 10^\circ$ (α taken at apparent min. of duct press. coeff.)	3.2	$C_Q = 0.05$ $C_{product} \approx 7.25$		5.1	326.0	1.3

* Assumes $C_F = 0.007$. † Uses Brooks' actual data for knurled cylinder.

**NSRDC Technical Note AL-211 (1971)

***NSRDC Technical Note AL-176 (1970)

where $C_L = L / \frac{1}{2} \rho U_\infty^2 c$

L = lift per unit span

c = chord.

The numbers in Table 3 are representative of typical good performance for devices in the vicinity of their individual best modes of operation, low or high α . The poweroff lift coefficients are therefore not all the same for all the devices, and these values are included in the last column of Table 3. Two-dimensional performance data are used to avoid the various complications of aspect ratio and planform shape from the comparison. Table 3 thus provides a rough estimate of the absolute magnitude of power involved with the various selected schemes.

Another performance parameter of interest is the lift-increment-per-power ratio $\Delta C_L / C_P$, where ΔC_L has been defined previously, and the two-dimensional power coefficient is $C_P = P / \frac{1}{2} \rho U_\infty^3 c$, where P = power per unit span. This parameter is occasionally used for direct comparisons of similar power-augmented devices in Appendix A. Values of $\Delta C_L / C_P$ for $\Delta C_L = 1.0$ are listed in Table 3 along with the blowing or rotation requirements pertaining to chord length = 15 feet, and $U_\infty = 5$ and 20 knots.

Table 4 contains lift-increment-per-unit-power values for the same types of powered devices as in Table 3; however, with $\Delta C_L = 0.5$. The corresponding poweroff lift coefficients are listed in the last column of the table.

It is interesting to note that the LE and T.E. rotating-cylinder devices have impressive performance, based on $\Delta C_L / C_P$, which means their *augmentation effectiveness* is very high, apparently better than the slot blowing devices, at least for $\Delta C_L = 0.5$ and 1.0. However, their overall hydrodynamic efficiency, based on equivalent lift-to-drag ratio, is either comparable or poorer. This is evident in Figure 1. The reason for this dramatic difference is that all rotating-cylinder or rotating-flap devices have inherently large drag, especially at high rotation rates, while slot-blowing devices invariably tend to *reduce* the foil profile drag. This tradeoff is an important feature to keep in mind when assessing these devices for a particular application.

In general, for large-sized, powered-lifting surfaces, having drag that is an important fraction of the total vehicle drag, slot-blowing devices are more appropriate; C_L / C_{d_e} indicates the better choice. For small-sized, powered-lifting surfaces producing a relatively small contribution to the overall vehicle drag, the rotating cylinder devices might be the optimum choice; $\Delta C_L / C_P$ is more important.

Concerning selected force producers (Table 2), improved mechanical flap systems might include gapped or single slotted flaps, spanwise-split flaps for separate actuation at low and

TABLE 4 - VALUES OF LIFT INCREMENT-PER-POWER FOR THE SIX SELECTED POWERED LIFT-AUGMENTATION SCHEMES OF TABLE 3

Applies to a section (2D) lift increment $\Delta C_L = 0.5$.

$\Delta C_L = 0.5$

Item	Reference	Geometry	$\frac{\Delta C_L}{C_P}$	Blowing or Rotation Required	Poweroff Lift Coefficient C_L
Blown Trailing Edge Flap	Lawford and Foster (1970) ³²	$\alpha = 0^\circ$ $\delta_f = 40^\circ$	42.6	$C_{\mu} = 0.008$ $V_j/U_\infty = 1.85$	1.30
Circulation Control by Tangential Jet Blowing	Englar (1971) [†]	$\alpha = 0^\circ$ $t/c = 0.15$ rounded ellipse	40.4	$C_{\mu} = 0.0085$ $V_j/U_\infty = 1.81$	0
Rotating Flap Foil	Crabtree (1960) ¹¹⁰	$\alpha = 0^\circ$ $c_f/c = 0.25$ ΔC_L measured from autorotation	60.3	$\frac{u}{V} = 0.872$	2.89
Spanwise Blowing	Dixon (1971) ⁷⁷	$\alpha = 0^\circ$ $\delta_f = 40^\circ$	25.2	$C_{\mu} = 0.00617$ $V_j/U_\infty = 6.072$	1.62
Rotating Cylinders Leading Edge Cylinder	Wolff and Koning (1926) ¹⁰⁷	$\alpha = 20^\circ$ $d/c = 0.2$	156.0*	$\frac{u}{V} = 0.9$	0.81
Flap Knee	Alvarez-Calderon and Arnold (1961) Ref. 108	$\alpha = 9^\circ$ $\delta_f = 40^\circ$ $d/c = 0.1143$	26.8*	$\frac{u}{V} = 1.95$	2.09
Trailing Edge Cylinder	Brooks (1963) ¹⁰³	$\alpha = 0^\circ$ $d/c = 0.1364$	93.2**	$\frac{u}{V} = 0.844$	0
Trailing Edge Slot Suction Foil	Hazen, Sweeney, Lehnert, and Ringleb (1953) ⁹¹	$\alpha = 10^\circ$	74.1	$C_Q = 0.015$	1.3
<p>*Assumes $C_F = 0.007$ (average values). **Uses actual data from Brooks for knurled cylinder.</p>					
†NSRDC Technical Note AL-211 (1971)					

high speeds, differentially deflected port and starboard sailplanes, or dorsal flaps fixed to the sail or on the rudders. Another provocative possibility is the combination of an "external foil flap," with a "rotating flap foil." Versions of any one or all of these concepts are plausible steps toward improved control.

Mechanical leading-edge devices would find application when a large angle of attack requires attention to the problem of leading-edge separation. Otherwise they would be less interesting than improved trailing-edge flaps. Mechanical or jet spoilers could be used quite effectively to reduce unwanted lift in some circumstances; however, they seem to be less desirable than a positive lift producer for an active control surface.

Internally blown mechanical flap arrangements offer excellent possibilities for versatile submarine control purposes. The main reason is that they provide control redundancy. Substantial force production is achievable at high speed from the deflection of flaps alone. At low or moderate speeds, slot-blowing augmented lift can be achieved efficiently, especially in the boundary layer control (BLC) range. If necessary, further lift augmentation is possible from supercirculation, provided sufficient blowing capability is supplied. At present, the simple TE blown flap is the most straightforward application of this idea. However, the "ejector flap," or augmentor wing, is a related flapped device that could provide even more impressive low speed effectiveness and could conceivably be retracted into a folded simple flap arrangement for high-speed operation. The latter concept requires further specialized development of a very robust version to be seriously considered for use in a marine environment.

For small amounts of blowing and for certain incidence angles, circulation control (CC) by tangential jet blowing is a flapless device that displays efficient high lift augmentation and has the interesting property of producing augmented lift nearly independent of forward speed. This property is definitely observed in two-dimensional tests at low C_{μ} ; however, it is more difficult to achieve with small aspect ratio wings and heavier blowing rates.

Because CC foil shapes must have rounded trailing edges, continuous symmetric blowing through the upper and lower slots should be used to keep low values of profile drag. There are experiments that indicate that this may be feasible, using merely ram pressure to supply a weak bleeding slot flow necessary for such "artificial streamlining" in the poweroff mode. It may be noted that the well-known jet-flap concept is also a flapless lift augmentation device in the present use of the term. It is by comparison considerably less desirable than other simple powered schemes because of its lack of redundancy and, more importantly, because its lift-augmentation efficiency is inferior to the proved performance of blown flaps, TE slot suction, or CC foils using tangential blowing. This can be shown on the basis of both C_l/C_{d_e} and $\Delta C_l/C_p$. It is felt that the jet flap does not qualify for the selected items of Table 2.

The rotating flap foil is potentially capable of very high lift forces accompanied by large drag and could be used as an emergency control device, even with an autorotating flap.

Spanwise blowing is placed in Table 2 because it has the distinct virtue of being extremely simple, although its lift augmentation characteristics are inferior to internally blown flaps, CC foils, and TE slot suction. This concept should be explored in applications where high angles of attack or large flap angles are anticipated.

The use of rotating cylinders for ship control is a proved success, e.g., the National Physical Laboratory "super-rudder." All similar devices should be studied carefully for submarine applications. Leading-edge cylinders are appropriate for foils at large deflection angles, while trailing-edge cylinders should be used when the foil angle of attack is always fairly small. Flap-knee cylinder devices require large flap deflection angles.

A real case for powered-lift systems can be made for the submarine operating in a near-surface hovering mode, when large forces are needed to hold a constant depth course. The correct choice of a power-augmentation scheme could provide nearly unsaturable control planes.

APPENDIX A

EVALUATION OUTLINES OF FORCE-PRODUCER CONCEPTS

TABLE OF CONTENTS OF APPENDIX A

	Page
CHAPTER 1. CIRCULATORY LIFT DEVICES	19
INTRODUCTION	19
SECTION A UNPOWERED CIRCULATORY LIFT DEVICES	23
Flaps	23
Lift: Two Dimensional	27
Lift: Finite-Aspect Ratio	31
Drag: Finite-Aspect Ratio	36
Slats and Leading-Edge Flaps	43
Flaps and Slots	47
Spoilers	47
Others	54
SECTION B: POWERED CIRCULATORY LIFT DEVICES	56
Fluid Control: <i>Blowing and Suction Devices</i>	56
Internal Blowing Systems for Boundary Layer Control and Circulation Control	56
External Blowing (Deflected Slipstream)	141
Spanwise Blowing Over a Lifting Surface	144
Airfeeding to Alter Lift	155
Blowing to Kill Lift (Jet Spoiler)	163
Suction Through Slots	165
Area Suction	181
Suction-Stabilized Trapped Vortex Foil	190
Flow Control by Moving Surfaces	194
Rotating Cylinders, Circulation- and Boundary Layer-Control Modes	195
Rotating Foils and Flaps	218
Moving Belts	228
Swimming Plates	233
SUMMARY FOR CHAPTER 1	246
CHAPTER 2. REACTION DEVICES	251
SECTION A THRUSTERS AND JETS	251
Tunnel Thrusters, Fixed Ducts	251
Propeller-Driven Lateral Tunnel Thruster	252
Ejector Lateral Tunnel Thruster	261
Ejector Lateral Tunnel Thruster with Jet-Flap Diffusion	267
Impeller-in-Wing	273
Directional Thrusters	279
Directional Propeller Devices	279
Directional Plain Waterjet	310
Directional Augmented Waterjet	320
SECTION B MAIN PROPELLERS	335
Vertical Axis, Cycloidal, Propellers	338

	Page
Controllable Pitch Propellers	347
Very Large Hub, Haselton, Propellers	347
Controllable Pitch Propellers with Rake	354
Propellers with Flow Control	363
CHAPTER 3. EXTERNAL FORCE DEVICES	367
SECTION A ELECTROMAGNETIC DEVICES	367
External Flow, Static Field Thruster	369
External Flow, Induction Thruster	371
SECTION B DEPLOYABLE DRAG PRODUCERS AND GLIDERS	373
Parachutes and Drogues	373
Parawings	382

CHAPTER 1. CIRCULATORY LIFT DEVICES

INTRODUCTION

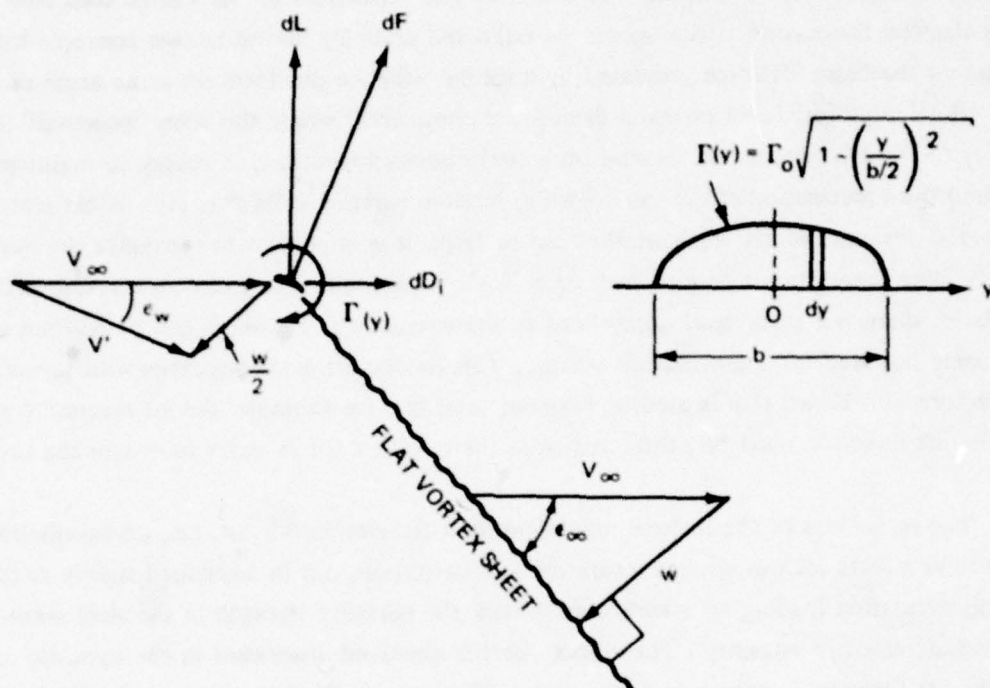
Circulatory lift-force producers are very important to the control of marine vehicles. The dive planes, control planes, and rudders on submarines are typical examples. They are important because of their simplicity of actuation and effectiveness. As will be seen later in this chapter, these same attributes can be improved upon by several known concepts that augment the basic lift force generated by a simple winglike planform set at an angle of attack.

Both unpowered and powered devices are considered, where the term "powered" devices refers to those concepts that depend on a continuous expenditure of energy to maintain the desired fluid mechanical effect—jet blowing, suction, rotating cylinders, etc. While with powered devices, the lift augmentation can be large, it is important to recognize that an indefinitely large force cannot be obtained, even in the ideal limit. For *finite-aspect-ratio* lifting surfaces, there is a theoretical upper limit to the circulatory lift, which can be reached only by some powered lift-augmentation scheme. Circulatory lift is synonymous with pressure lift. Therefore, if a blown flap is used to augment total lift, for example, the jet reaction force in the lift direction must be subtracted from the resultant lift in order to obtain the pressure lift.

The mechanics of the inviscid maximum limit for circulatory lift, i.e., disregarding entirely real fluid effects such as viscous separation and cavitation, can be explained simply as follows: If the circulation loading on a wing is increased, the vorticity strength in the shed wake sheet is also increased in intensity. The vortex sheet is displaced downward in the opposite direction to the lift force by a larger and larger angle. The magnitude of the downwash velocity induced by the vortex sheet becomes greater and may eventually grow to the same order of magnitude as the free stream velocity. The inclination of the wake gives rise to an induced velocity component opposing the free stream velocity V_∞ . Hence, the effective velocity onto the wing V' decreases in magnitude, in addition to being rotated farther downward as the circulation is increased. This gives rise to nonlinear dependence between the total resultant lift and the circulation strength. Figure 2 shows how a strong circulation loading affects the resultant flow geometry.

A second effect not indicated in the figure is that the rollup process of the flat vortex sheet wake into two concentrated vortex cores is accelerated by increasing the circulation intensity about the wing. The heavier the planform loading, the sooner complete rollup occurs. However, this effect alters the one described previously because the downward progression of the rolled-up vortices is slower than that of a flat sheet. Details of these phenomena are given, for example, by Cone,¹ Sato and Matsuoka,² and McCormick.³

*A complete listing of references is given on pages 397 to 409.



w = INDUCED DOWNWASH VELOCITY AT ∞
 V' = EFFECTIVE VELOCITY ONTO THE FOIL
 $\sin \epsilon_{\infty} = w/V_{\infty} = \Gamma_0/V_{\infty} b$
 $\sin \epsilon_w = (w/2V') \cos \epsilon_{\infty}$
 ϵ_w = DOWNWASH ANGLE AT THE WING
 $dF = \rho V T(y) dy$
 $\Gamma(y)$ = BOUND VORTICITY DISTRIBUTION

Figure 2 — Mechanics of Maximum Circulatory Lift

Spanwise elemental section dy of a finite-aspect-ratio wing loaded by an elliptic distribution of bound vorticity. Sketch shows flow velocities induced by a flat vortex sheet, deflected through a large angle ϵ_{∞} by a strong bound circulation strength. The resulting nonlinear dependence of lift upon Γ_0 gives rise to a maximum attainable circulatory lift; from Sato and Matsuoka.²

The end results of the various theoretical predictions indicate that $(C_{L\Gamma})_{\max}$ is linear with respect to aspect ratio $AR = b^2/S$ for small aspect ratios; it approaches a constant for large aspect ratios.

$$\text{Small and Moderate Aspect Ratio: } (C_{L\Gamma})_{\max} = (K_{\Gamma}) \cdot AR$$

Large Aspect Ratio:

$$(\text{i.e., } 6.5 \leq AR \rightarrow \infty, \text{ Cone}^1) \quad (C_{L\Gamma})_{\max} \rightarrow 2\pi(1 + t/c)$$

where K_{Γ} is a constant, and t/c is the foil section-thickness-to-chord ratio. Some results of estimates of K_{Γ} are presented in Table 5 for various theoretical attempts at analyzing the wake deformation and the induced forces.

TABLE 5 – SOME THEORETICAL ESTIMATES FOR K_{Γ} FOR PREDICTING MAXIMUM CIRCULATORY LIFT

$(C_{L\Gamma})_{\max} = (K_{\Gamma}) \cdot AR$		
	Source	K_{Γ}
Trailing Vortex Sheet Remains Flat	Sato and Matsuoka ²	0.855
Vortex Sheet Rolls Up Completely	Sato and Matsuoka ²	1.897
Small Aspect Ratio	McCormick ³	0.855
	Cone ¹ ($AR < 6.5$)	1.94
Moderate Aspect Ratio	McCormick ³	1.21

It should be noted that these estimates apply to lifting planforms, having typical elongated foillike section shapes. Unless some rotating motion is imparted to such shapes, the fluid stagnation points are always on the surface. If front and rear stagnation points coincide, the ideal lift coefficient of any section can reach 4π , e.g., Cone.¹ If the lifting device in question is an isolated rotating cylinder, it is possible to spin it fast enough for the single stagnation point in the fluid to be displaced completely away from the solid surface; the ideal infinite-aspect-ratio limit of 4π can then be exceeded; see e.g. Swanson.⁴

Experimental support for the existence and magnitude of maximum circulatory lift is presented for example by Sato and Matsuoka² and in data from Lowry and Vogler reproduced in McCormick.³ In Reference 2, the experimental value of K_{Γ} obtained with slot-blowing

suction-side boundary layer control seems to be independent of aspect ratio, reaching the predicted value of about 1.9 noted in Table 5. However, the results of Lowry and Vogler obtained with jet-flapped 16.7 percent thick foils show that the value of K_F does change slightly with aspect ratio, varying from about 1.0 at low aspect ratios to about 1.25 for aspect ratios larger than 6.

In general, the inviscid limit is never reached by ordinary foils or even by sophisticated versions of mechanically flapped foils because of flow separation. However as mentioned previously, a lifting foil employing a boundary layer control or circulation control device such as some form of jet blowing could reach its maximum C_{L_F} . The required intense circulation usually means heavy blowing rates, so that in a typical case, the jet reaction thrust alone is at least as large as the circulatory lift. This amount of blowing is not of practical interest because of the pumping power required.

Although the $C_{L_F}(AR)$ upper bound is seldom a practical issue except for heavily augmented lifting-surface arrangements, it is useful to keep in mind throughout this chapter that such an ideal limit does exist.

SECTION A UNPOWERED CIRCULATORY LIFT DEVICES

NAME: Unpowered Mechanical Devices

DEFINITION: The basic device under consideration is a lifting surface to which are attached auxiliary flaps, slats, or other appendages that can be deflected and which are controllable in their setting. Fully movable lifting surfaces are also included. Continuous expenditure of energy is not essential to their function, hence the term "unpowered." Although power is required to actuate these types of devices, it is possible to lock them in their deflected position and to maintain the desired lift force.

This section gives a brief illustration of various schemes that can be used and for which information exists. The body of literature about these devices is vast. There is no attempt to be exhaustive either here in the coverage of all variations or in the bibliography.

Lift, force normal to the oncoming stream, is the result of inducing circulation about the lifting surface. The basic purpose of unpowered auxiliary devices is to achieve changes in circulation and, hence, in lift at fixed angle of attack of the lifting surface by modifying the effective geometry of the surfaces. This is accomplished by changing the *camber* of the lifting surface or by changing circulation by gross alteration of the flow over the lifting surface, e.g., inducing boundary layer separation. The devices can be used individually or in combination. In this section a brief outline of the operation and effects of the following arrangements is given:

1. Flaps
2. Slats and Leading-Edge Flaps
3. Flaps and Slots
4. Spoilers
5. Others

DESCRIPTION AND FORCE ESTIMATES

Flaps

A flap is attached to a lifting surface at its trailing edge. Usually the flap system is an integral part of the lifting surface, essentially being only the trailing portion that is hinged to the fixed leading part. However, sometimes the flap takes the form of a completely separate and movable airfoil, called an external airfoil flap, positioned near the trailing edge of the fixed lifting surface. Figure 3 shows the basic flap arrangements.

Many variations of these basic arrangements exist as illustrated in Figure 4 but they cannot all be discussed herein. For fuller discussion of the subject and pertinent source material, see References 5 and 6.

The basic motion of a flap is a rotation about a hinge, which deflects the flap relative to the chord line of the lifting surface. It is advantageous to arrange the flap so that the

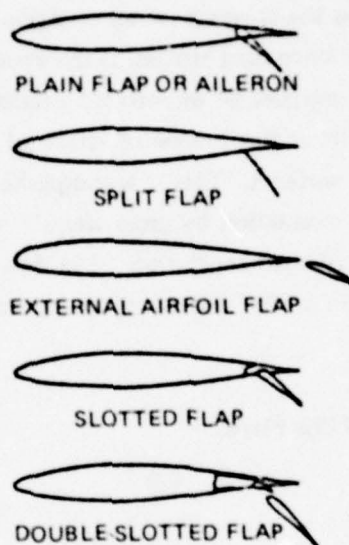


Figure 3 – Basic Flap Arrangements

Figure 4 - Flap Types

Young⁶

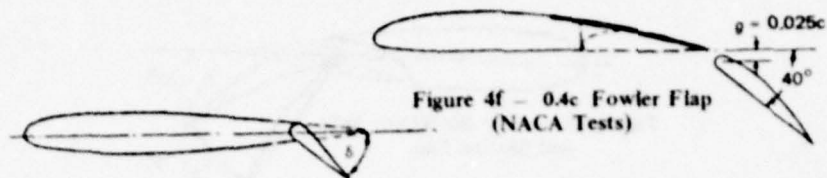


Figure 4a - 0.2c Plain Flap



Figure 4f - 0.4c Fowler Flap (NACA Tests)



Figure 4g - 0.4c Fowler Flap (RAE Tests)

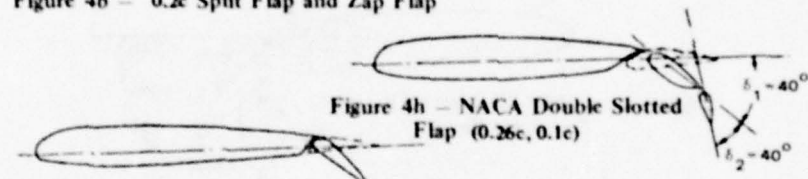


Figure 4b - 0.2c Split Flap and Zap Flap

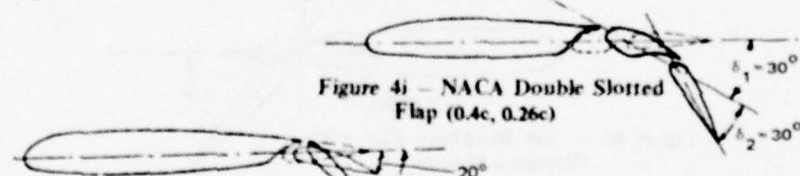


Figure 4h - NACA Double Slotted Flap (0.26c, 0.1c)

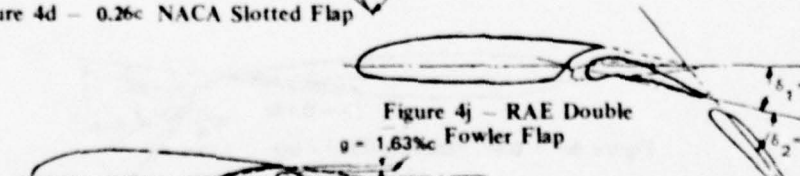


Figure 4c - 0.2c Slotted Flap (Handley-Page Type)

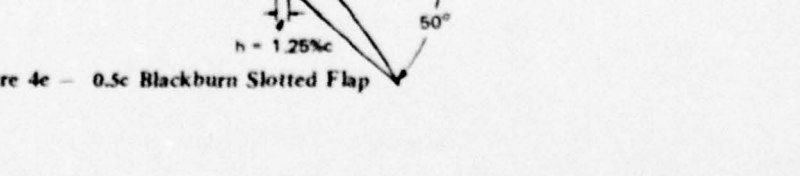


Figure 4i - NACA Double Slotted Flap (0.4c, 0.26c)

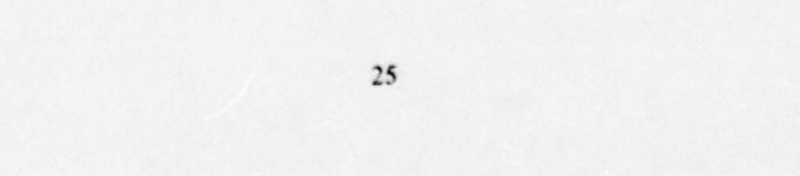


Figure 4j - RAE Double Fowler Flap



Figure 4e - 0.5c Blackburn Slotted Flap



Figure 4k — 0.5c Blackburn Split and Slotted Flap

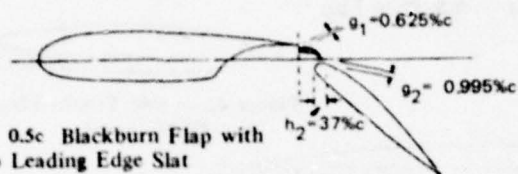


Figure 4l — 0.5c Blackburn Flap with Flap Leading Edge Slat

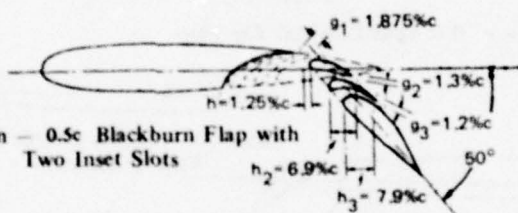


Figure 4m — 0.5c Blackburn Flap with Two Inset Slots

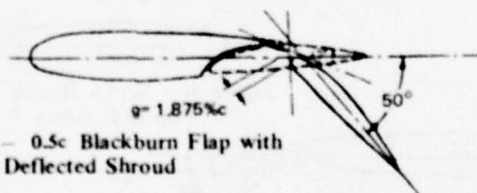


Figure 4n — 0.5c Blackburn Flap with Deflected Shroud

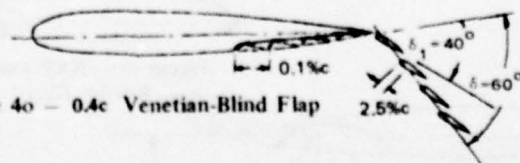


Figure 4o — 0.4c Venetian-Blind Flap

hinge simultaneously translates rearward as the flap deflects, thereby increasing the effective chord of the lifting-surface-flap combination.

Lift: Two Dimensional. For a two-dimensional, single, flapped foil section at an angle of attack α and flap angle δ (Figure 5), the section lift coefficient based on chord length c is

$$C_l = (C_{l_\alpha}) \alpha + 2\pi \cdot \lambda_1 \left(\frac{c_f}{c'} \right) \cdot e_f \cdot \delta \quad (1)$$

where C_{l_α} is the lift-curve slope $= a_0$, and $2\pi \cdot \lambda_1 (c_f/c')$ is the flap derivative $= C_{l_\delta}$, which correctly contains the variation of lift with respect to c_f/c' but which must be modified by an empirical factor $e_f(\delta)$ for its actual variation with respect to flap angle δ . Data originally compiled by Young⁶ have been presented by McCormick³ in terms of curves for two-dimensional flapped foils. Figure 6 gives the flap effectiveness factor $\lambda_1 (c_f/c')$, where c' is the extended chord length of the foil-flap section. The correction factor $e_f(\delta)$ for plain, split, and slotted single flaps is reproduced in Figure 7.

Usually the lift performance of flaps is measured in terms of the lift increment

$$\Delta C_l = 2\pi \lambda_1 (c_f/c') \cdot e_f \cdot \delta \quad (2)$$

with δ in radians.

A special case of the single-slotted flap is an external airfoil flap, an example of which is pictured in Figure 8a along with a curve of its maximum lift coefficients at various flap angles. A symmetric foil-flap version of this arrangement could conceivably provide positive lift, even if the incoming flow is at a negative angle of attack to the foil; see Figure 8b. To accomplish this without excessive flap angles, the flap chord must be comparable to the foil chord. Such an arrangement could be used to good effect for submarine maneuvering.

Double-slotted flaps are obviously more complex than single flaps; however, they do provide very large values of lift. An example of the section-lift performance of a 15-percent-thick airfoil with a 40-percent-chord, Douglas double-slotted flap is reproduced in Figure 9, taken from Reference 7. The graph shows a value $C_{l_{\max}} \approx 4.4$, C_l based on the original retracted chord length, at an angle of attack of 14 degrees. As far as is known, there is no good scheme reported in the literature for using double-slotted flaps on *symmetric* foil shapes in order to obtain symmetric lift increments, both plus and minus lift.

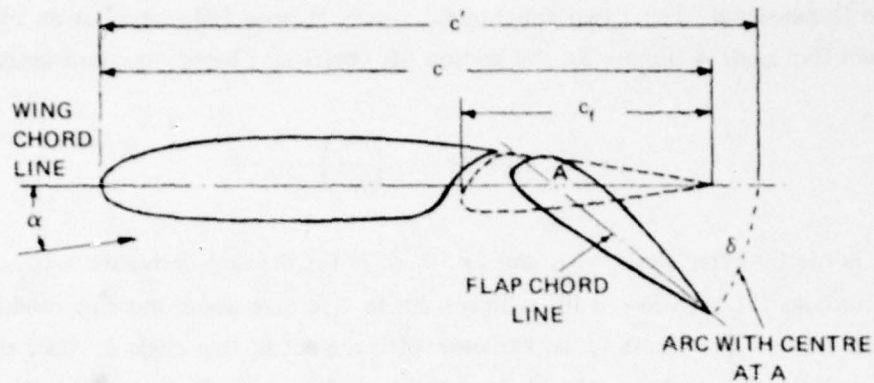


Figure 5 – Slotted Single Flap, Deflected by Angle δ Showing a Simultaneous Chord Extension

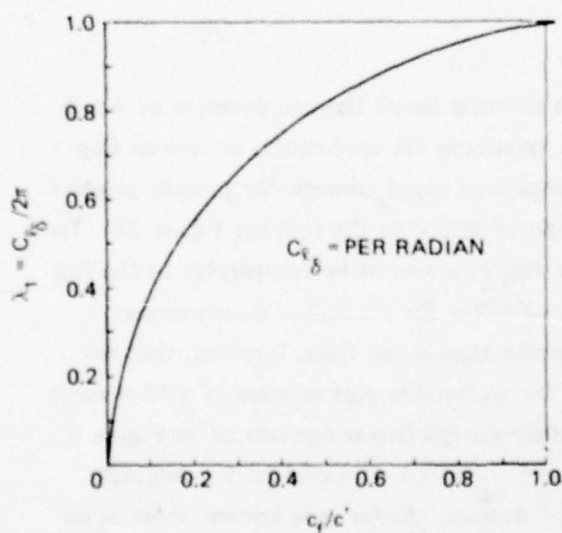


Figure 6 – Flap Effectiveness Factor $\lambda_1 (c_f / c')$, Applies to All Flaps
Young⁶ and McCormick.³

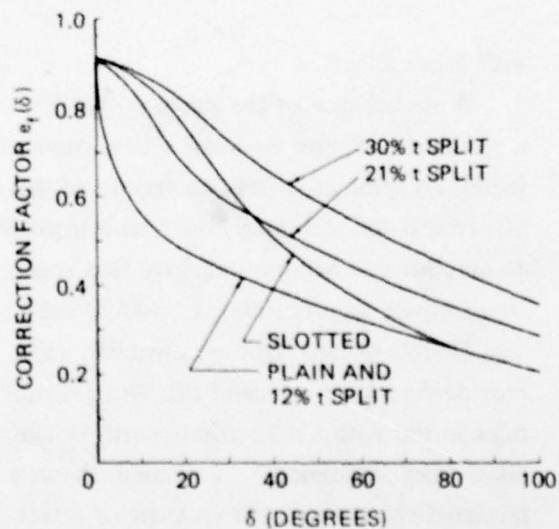


Figure 7 – Correction Factor to Flap Effectiveness with Respect to Flap Angle δ for Plain, Split, and Slotted Flaps
Young⁶ and McCormick.³

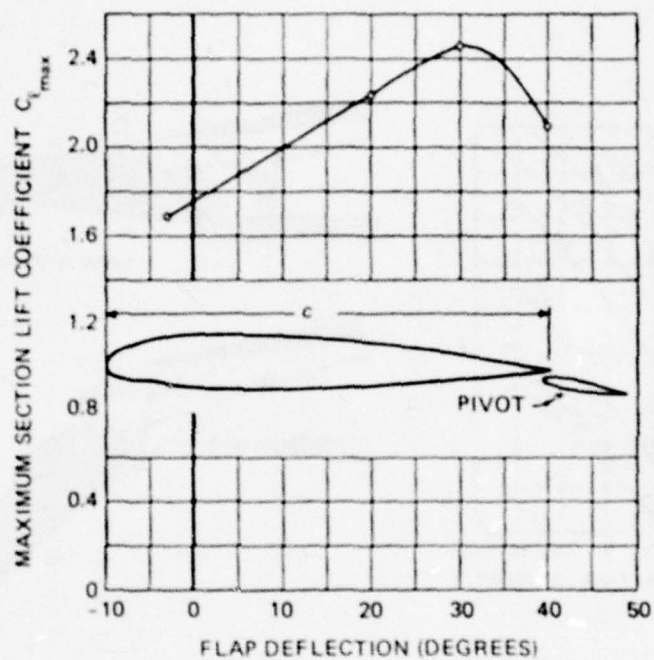


Figure 8a - Variation of Maximum Section Lift Coefficient, Based on Chord of Wing Section Plus Flap with Flap Deflection for NACA 23012 Wing Section with 0.20 c External-Airfoil Flap

Abbott and Doenhoff.⁵



Figure 8b - Symmetric Foil/External Foil Flap That Could Provide a Positive Lift, Despite a Negative Flow Angle of Attack

Figure 8 - External Foil Flap

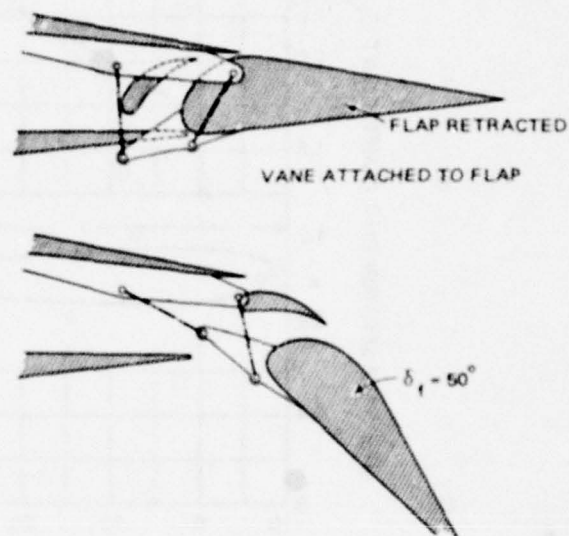
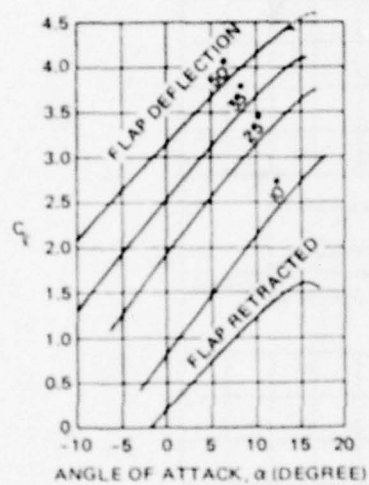


Figure 9 – Example Lift Performance and Schematic Arrangement of Douglas Double-Slotted Flap

Kuhlman⁷

Lift: Finite-Aspect Ratio. A full discussion of the prediction of the lift increments for general finite-aspect-ratio, flapped lifting surfaces is complicated and is beyond the scope of this survey. However, some crude estimates are possible. Using the data from Young,⁶ McCormick³ presents a formula for predicting the wing lift increment for an untwisted lifting surface with partial span flaps

$$\Delta C_L = F_S(AR) \cdot \lambda_1(c_f/c') \cdot c_f \cdot \delta \cdot \lambda_3(b_f/b) \quad (3)$$

where λ_1 , c_f , and δ have been discussed previously, and $F_S(AR)$ is the variation of lift-curve slope with respect to the aspect ratio AR , represented approximately by

$$\begin{aligned} F_S(AR) &= \frac{a_0}{E_s + 2/AR}, \quad \text{for } AR \geq 1 \\ &= \frac{a_0 AR}{2(1 + AR)}, \quad \text{for } AR < 1 \end{aligned} \quad (4)$$

where a_0 = section lift-curve slope, and E_s = ratio of semiperimeter to span. The function $\lambda_3(b_f/b)$ is a universal partial span correction factor reproduced in Figure 10, applicable for all flaps. The span of the flap is b_f , and b is the span of the lifting surface.

For double or compound flap systems, Young⁶ presents estimating curves based on a reference aspect ratio equal to 6. For example, for a foil-flap arrangement similar to Figure 9, the total lift increment $\Delta C'_L$, based on the final extended chord c' , is composed of two parts, $\Delta C'_{L_1}$ and C'_{L_2} , which depend on the flap chord ratios and angles of the first and second flap, respectively. For aspect ratio 6 lifting surfaces

$$\Delta C'_L = \lambda_1(c_{f_1}/c') \cdot \lambda_2(\delta_1) + \lambda_1(c_{f_2}/c') \cdot \lambda_{22}(\delta_2) \quad (5)$$

where $\lambda_1(c_f/c')$ is the flap effectiveness ratio shown in Figure 6, and the empirical functions $\lambda_2(\delta)$ and $\lambda_{22}(\delta)$ are reproduced in Figures 11 and 12. Note that Figure 11 presents the single flap curves of Figure 7 in a different form.

To estimate the lift increment for an aspect ratio different from $AR = 6$, the correction factor $F_S(AR)/F_S(6)$ displayed in Figure 13 is multiplied times the $\Delta C'_L$ of Equation (5). As before, the factor $\lambda_3(b_f/b)$ is used to predict the effect on lift of partial span flaps.

$$\Delta C_L(AR) = \frac{F_S(AR)}{F_S(6)} \cdot \Delta C'_L \cdot \lambda_3(b_f/b) \quad (6)$$

The spots in the graph of Figure 13 are computed, using Equations (4).

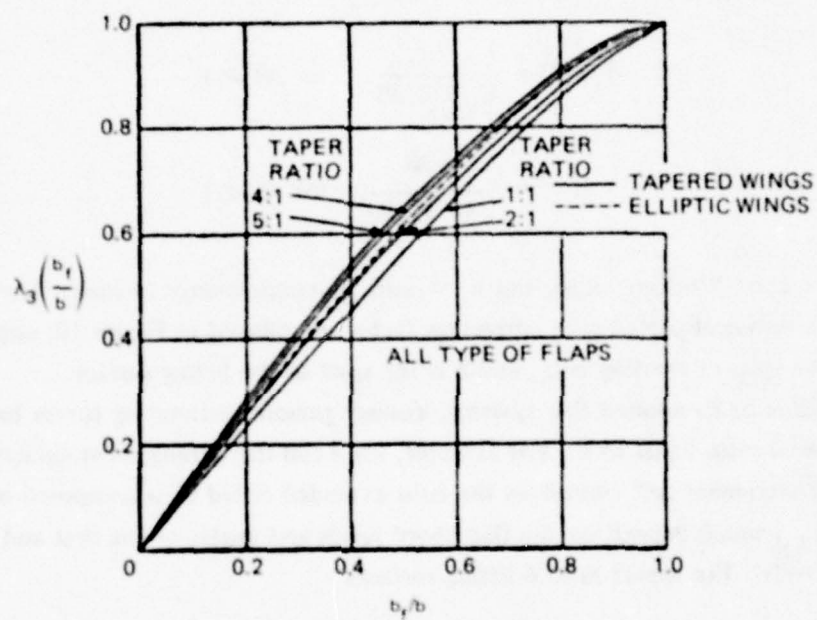


Figure 10 - Function $\lambda_3\left(\frac{b_f}{b}\right)$: Ratio of Lift Increment
from Part-Span Flap to Full-Span Flap
Young⁶

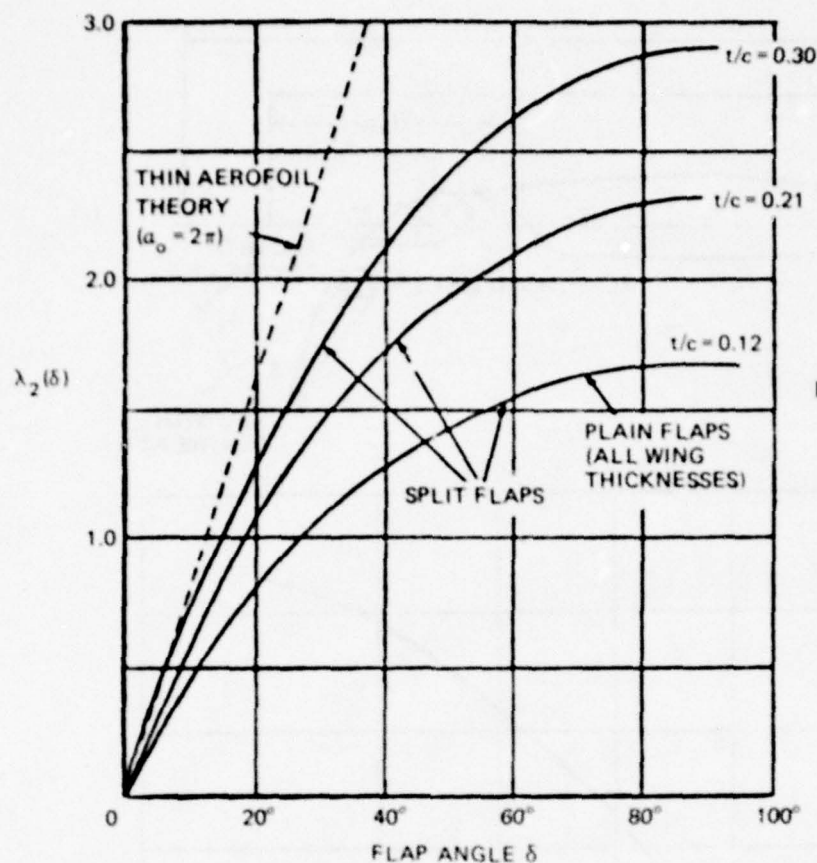


Figure 11a - Plain and Split Flaps, for $AR = 6$

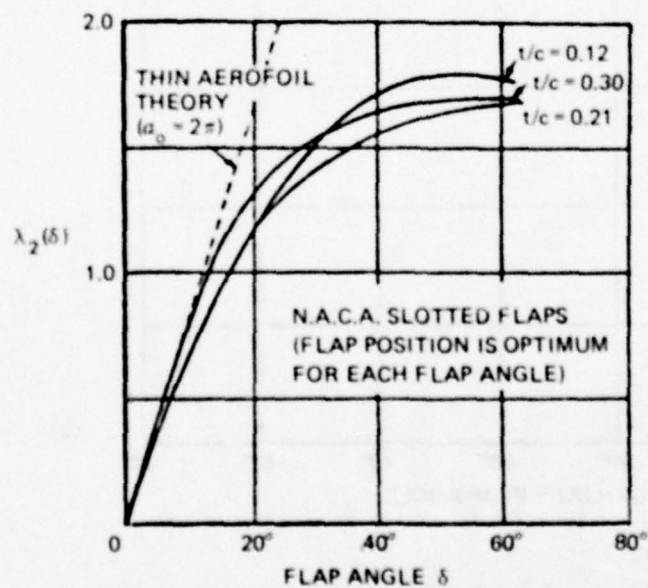


Figure 11b - NACA Slotted Flaps, for $AR = 6$

Figure 11 - Function $\lambda_2(\delta)$ for Estimating Flap Lift Increment
Young⁶

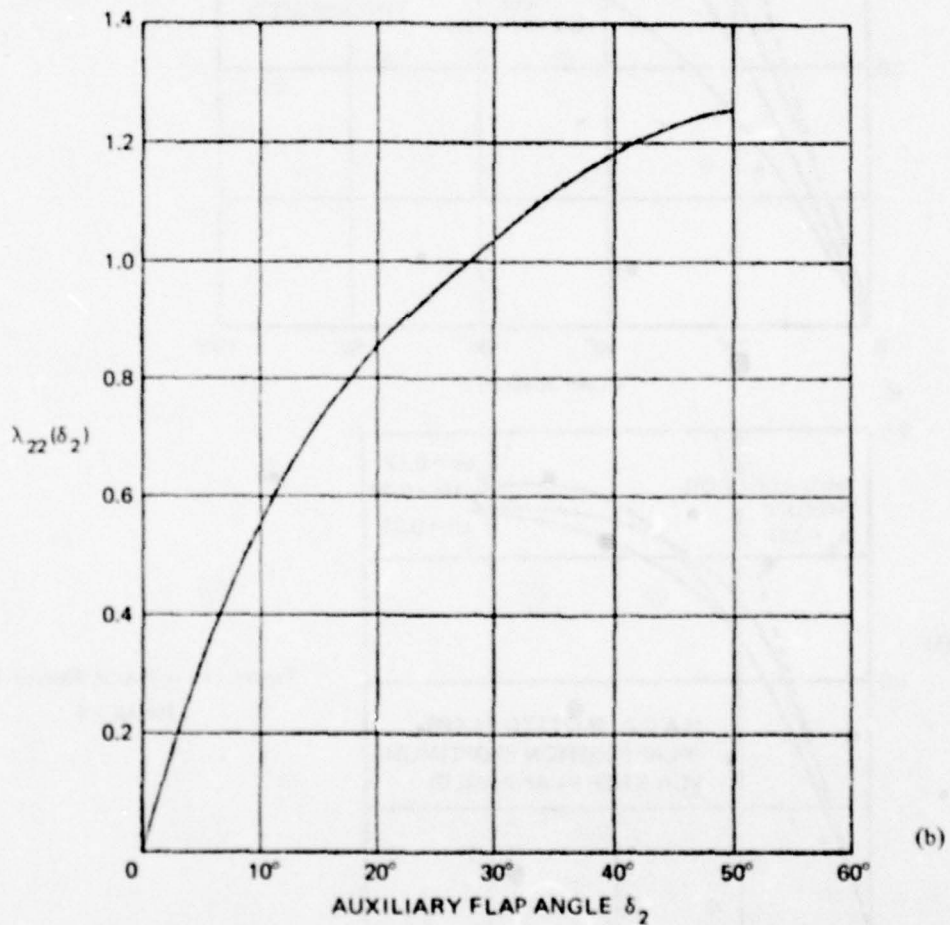
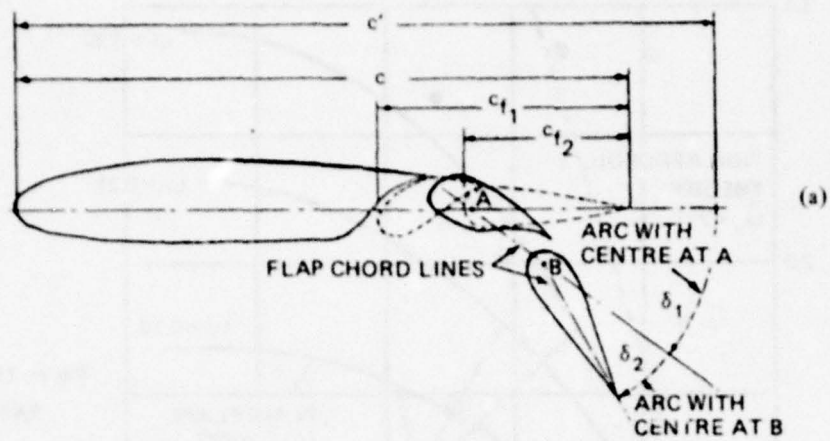


Figure 12 – Function for Estimating Lift Increment of an Auxiliary Flap
See (a), Young⁶

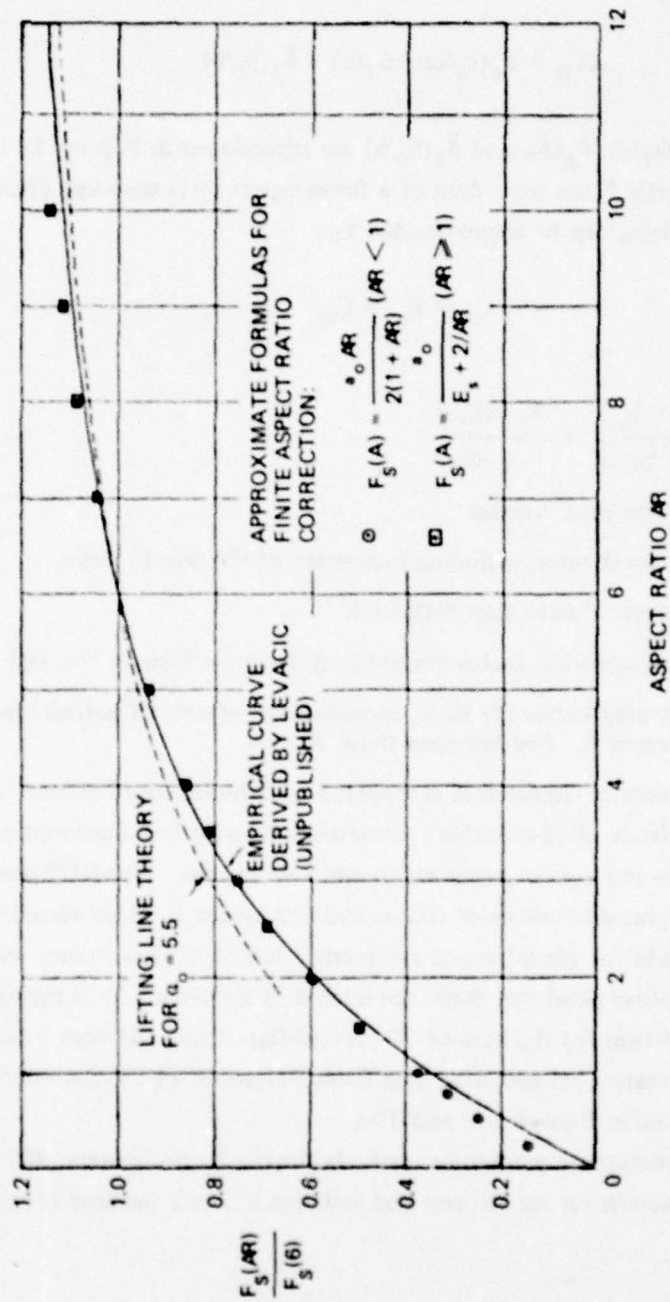


Figure 13 — Variation of Lift-Curve Slope with Aspect Ratio for Finite-Span Lifting Surfaces
 Based on Reference Aspect Ratio 6 of Young⁶

Drag: Finite-Aspect Ratio. The increment in profile drag due to the actuation of various flap systems is also discussed by Young⁶ and is presented in the form of multiplicative factors dependent on flap-chord ratio, flap angle, and flap- to wing-span ratio

$$\Delta C_D = \bar{\delta}_1(c_f/c) \cdot \bar{\delta}_2(\delta) \cdot \bar{\delta}_3(b_f/b) \quad (7)$$

where the curves for $\bar{\delta}_1(c_f/c)$, $\bar{\delta}_2(\delta)$, and $\bar{\delta}_3(b_f/b)$ are reproduced in Figures 14 through 16.

As indicated by Martin,⁸ the total drag of a finite-aspect ratio unswept lifting surface, including the effect of flaps, can be approximated by

$$C_D = \bar{C}_d + C_{D_i} \quad (8)$$

$$\text{where } C_{D_i} = C_L^2 \left[\frac{1 + \delta_p}{\pi AR} \right] + \frac{K_f(\Delta C_L)^2}{\pi AR}$$

\bar{C}_d = total section drag, average

C_L = total lift coefficient, including increment of lift due to flaps

ΔC_L = lift increment due to flap deflection

δ_p = planform correction factor for induced drag; see Figures 16c and 16d

K_f = planform drag factor for flaps, including the effects of partial span flaps; see Reference 6. For full span flaps, $K_f = 0$.

A considerable amount of useful data is reported by Whicker and Fehlner⁹ about the hydrodynamic characteristics of all-movable symmetric foils with low-aspect-ratio planforms featuring squared-off tips and various taper ratios and sweepbacks. Mandel¹⁰ provides a summary of these data plus discussions of simple foil-flap systems. More recently, Kerwin et al.¹¹ have provided data for plain-flapped symmetric NACA 66 foil shapes with squared-off tips. The flapped-rudder planform shape considered in Reference 11 is indicated in Figure 17a, and the root section for the case of 30-percent-flap chord and zero balance is shown in Figure 17b. Representative lift and drag data from Reference 11 for the configuration of Figure 17b are reproduced in Figures 17c and 17d.

An extensive compilation of prediction methods for the hydrodynamic lift, drag, and other performance characteristics for flapped and unflapped lifting surfaces is presented by Martin.⁸

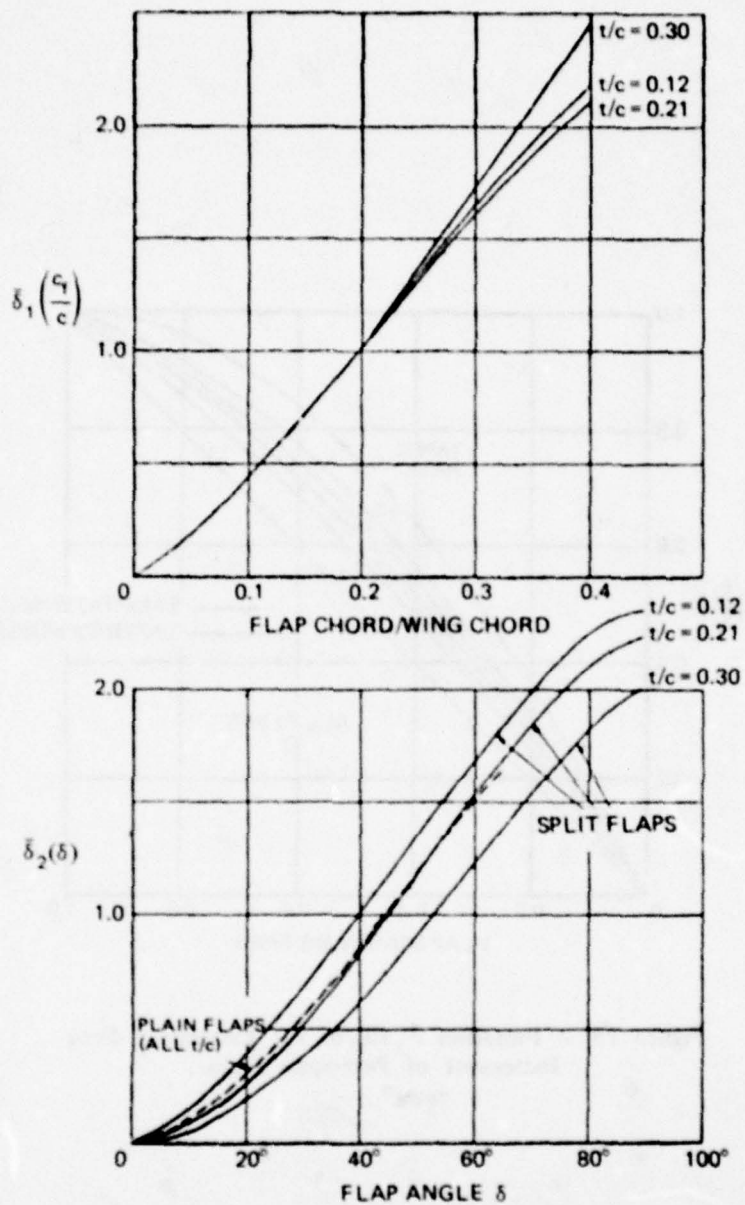


Figure 14 — Functions $\delta_1(c_f/c)$ and $\delta_2(\delta)$ for Estimating Drag Increment Due to Deflection of Plain and Split Flaps
Young⁶

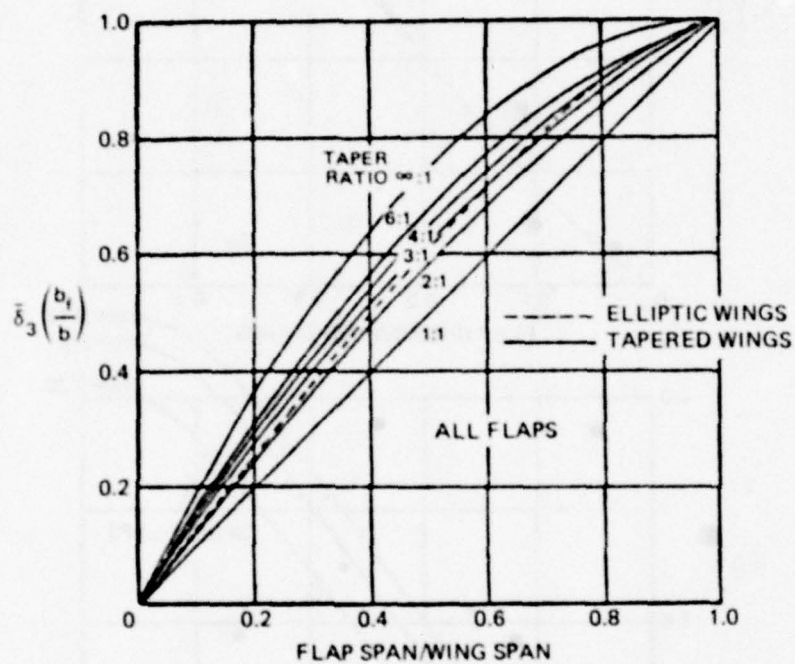


Figure 15 - Function $\delta_3(b_f/b)$ for Estimating Drag Increment of Part-Span Flaps
Young⁶

Figure 16 – Factors for Estimating Flap Drag and Induced Drag

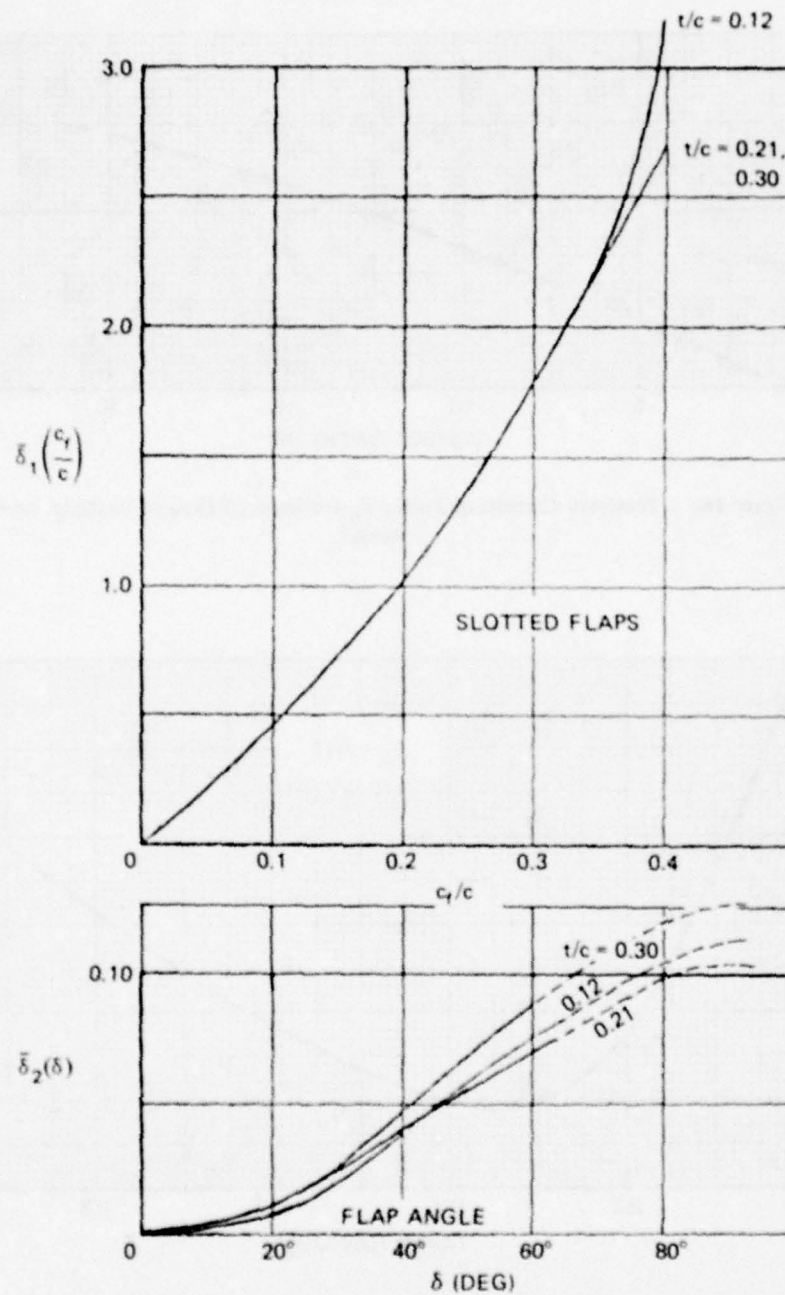


Figure 16 a,b – Functions $\delta_1(c_f/c)$ and $\delta_2(\delta)$ for Estimating Drag Increment for Slotted Flaps
Young⁶

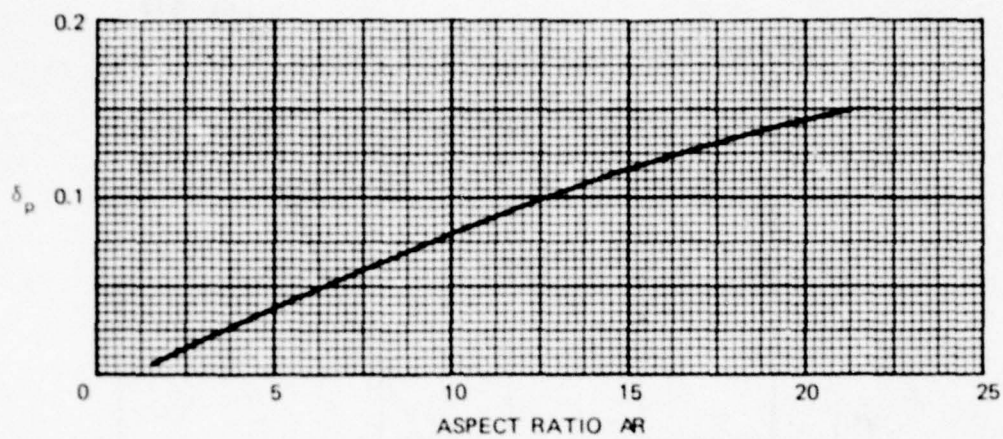


Figure 16c – Planform Correction Factor δ_p for Induced Drag of Rectangular Wings
Martin⁸

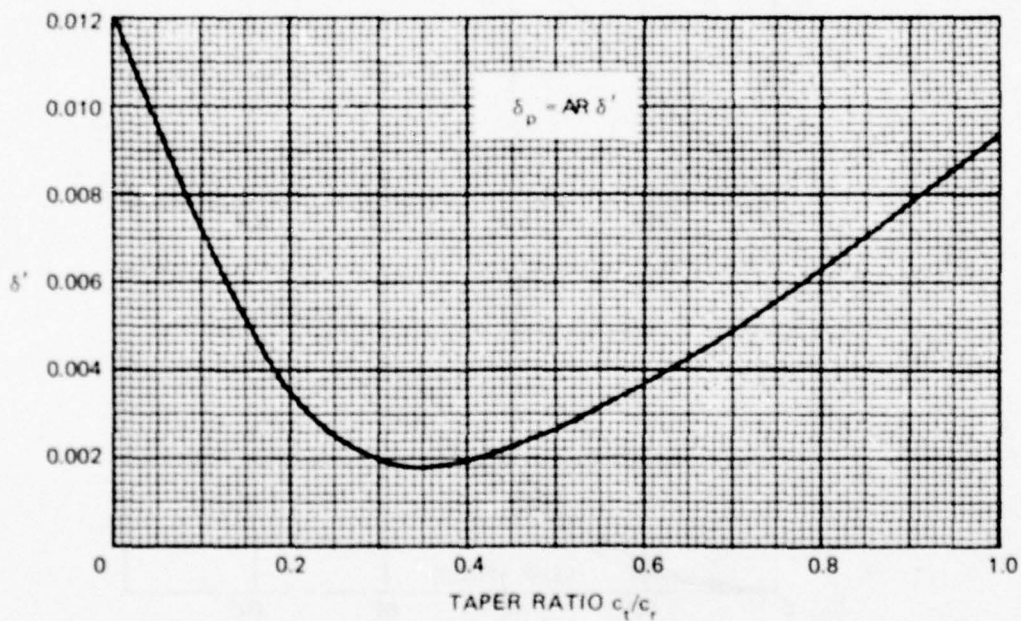


Figure 16d – Planform Correction Factor δ_p for Induced Drag of Tapered Wings
Martin⁸

Figure 17 - Configuration and Sample Data from Tests on a Flapped Rudder

Taper ratio equals 0.6, aspect ratio equals 1.4, root section NACA 66 t/c equals 0.2
tip section NACA 66 t/c equals 0.1, sweep of quarter chord equals 11 degrees aft.
Kerwin et al. 11

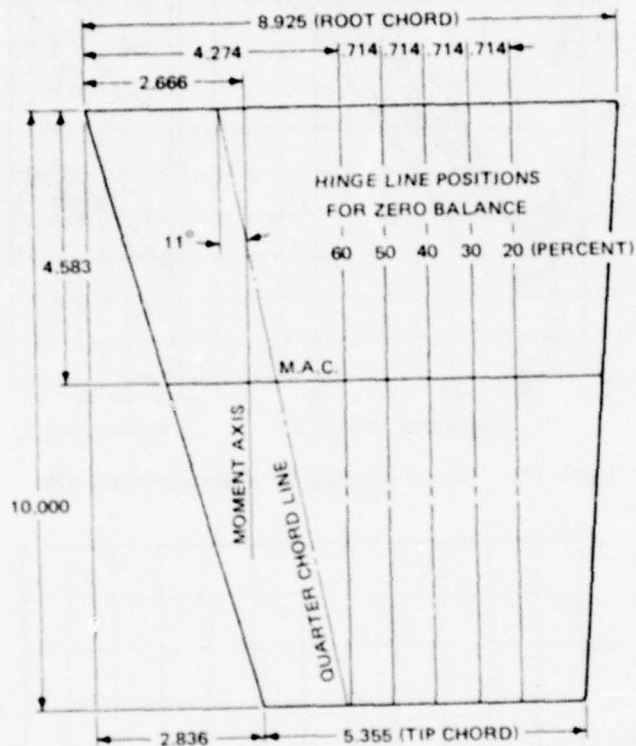


Figure 17a - Basic Outline for Rudder Model Series in Inches

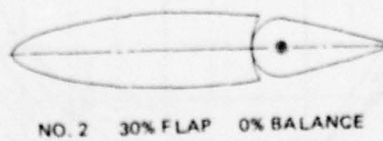


Figure 17b - Root Section of One of the Flapped Rudder Series

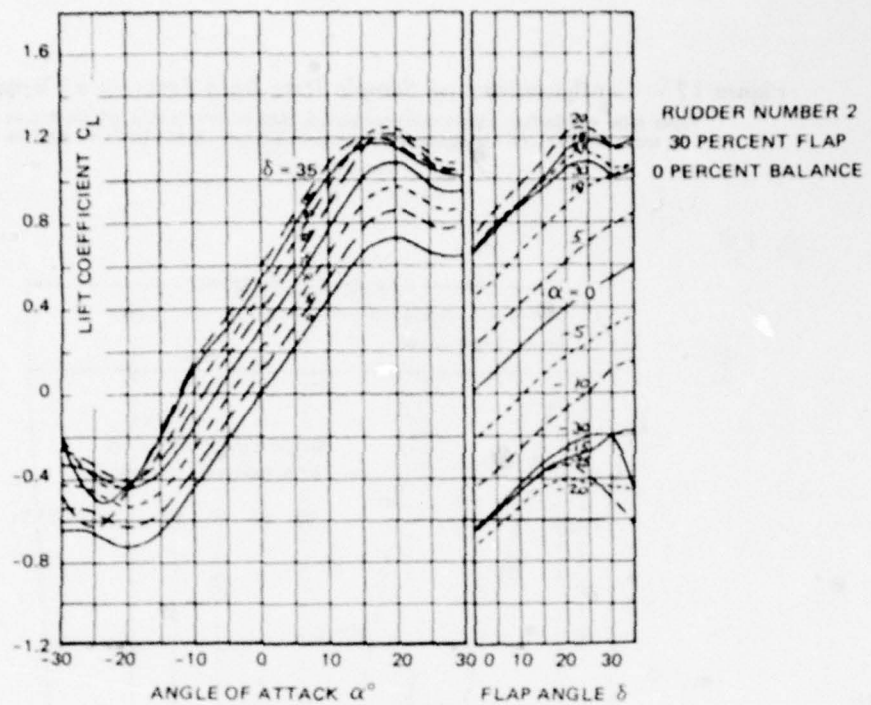


Figure 17c - Sample Lift Data for Rudder in Figure 17b

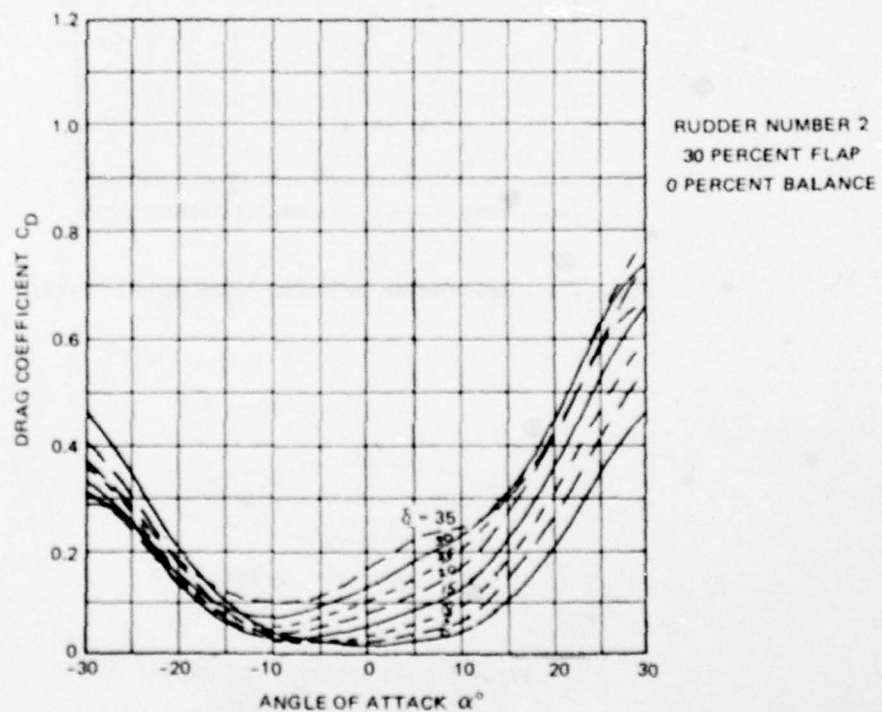


Figure 17d - Sample Drag Data for Rudder in Figure 17b

MAXIMUM LIFT AND STALL ANGLE

Deflection of any trailing-edge flap creates a desirable lift increment but also tends to aggravate the adverse pressure gradients near the nose of the foil, which in turn brings on stall at a smaller angle of attack. This is illustrated in Figure 18 for a plain flapped 16-percent-thick cambered airfoil. As will be discussed shortly, the use of a leading-edge device can extend the useful range of angle of attack and also allow greater values of maximum lift coefficient. The general problems of optimizing the lift performance of flapped lifting surfaces and the detailed problems of flap and slot shapes and sizes are complex. Some information and recommendations for design can be found in References 3, 5, 6, and 8 as well as in the source material cited by these references.

SPANWISE ARRANGEMENT OF FLAPS

Even with the simplest flap type, e.g., a "plain" flap, the spanwise distribution of a flap chord can increase the effectiveness of a lifting surface for control purposes. For example, differentially actuated port and starboard flaps with paired control surfaces can be used to develop roll moments for submarine maneuvering. A partial span arrangement of two different flap chords could be used for low- and high-speed operation—with the smaller c_f/c flaps being placed inboard for high speed, while the larger c_f/c flap would be placed outboard for low-speed operation. Small, separately actuated tabs mounted on the main flaps would accomplish a similar result. A partial span arrangement with various c_f/c flaps could be used on a dorsal rudder-flap system mounted on a submarine sail to help reduce roll moments in turns at various speeds.

Slats and Leading-Edge Flaps

Airfoils placed near and ahead of the leading edge of a wing can be beneficial to the lift performance by helping to suppress leading-edge separation and also by creating an increase in the effective camber and/or chord length of the foil. Slats and LE flaps are similar in appearance, the difference being that slats are separate foils that allow flow of pressure-side fluid to pass into the suction-side region. Slats are effective in increasing the maximum lift coefficient when used alone or in combination with trailing-edge flaps. Figure 19a illustrates three slat configurations. Incremental force data for the slat of Figure 19a(2), installed on a NACA 23012 section, is reproduced in Figure 19c. The corresponding increase in the angle of attack at which $\Delta C_{l_{max}}$ occurs is in the range from 8 to 14 degrees.

Leading-edge flaps are formed either by bending down the forward portion of the wing section, plain nose flaps, or by extending a surface forward and downward near the leading edge, Krueger type. These types are illustrated in Figure 19b. Typical incremental force

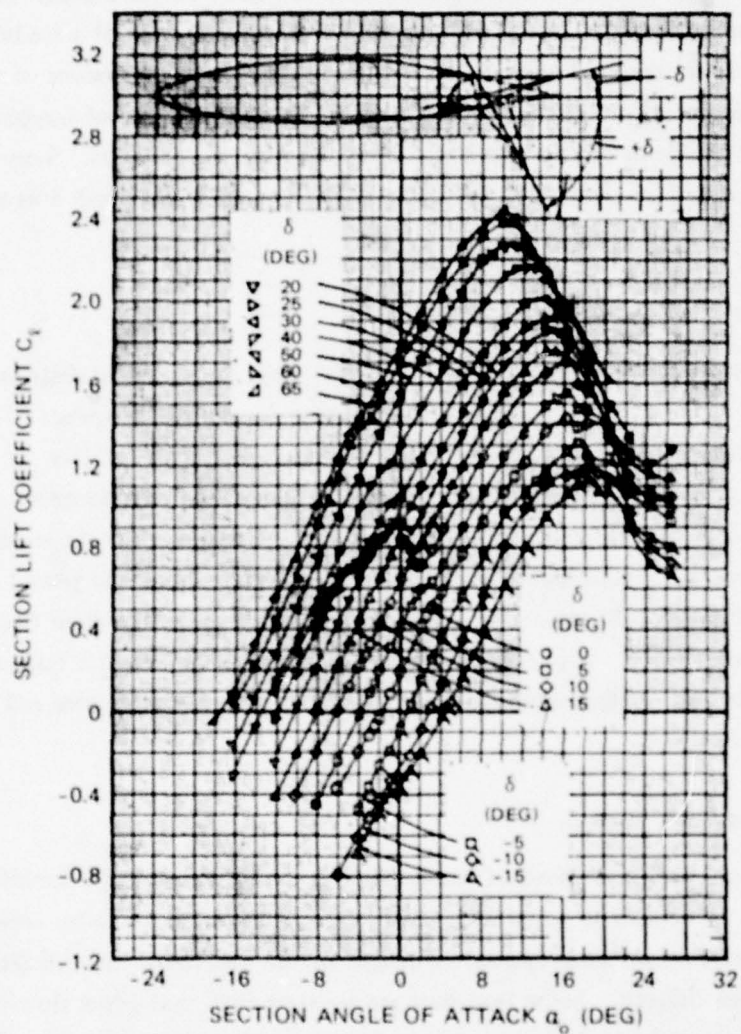


Figure 18 — Aerodynamic Characteristics of NACA 66(215)-216 Airfoil
Section with 0.20c Sealed Plain Flap

Decrease in stall angle with increasing flap angle and increasing $C_{L_{max}}$.
Abbott and Doenhoff⁵

Figure 19 - Slats and Leading Edge Flaps
 Abbot and Doenhoff⁵

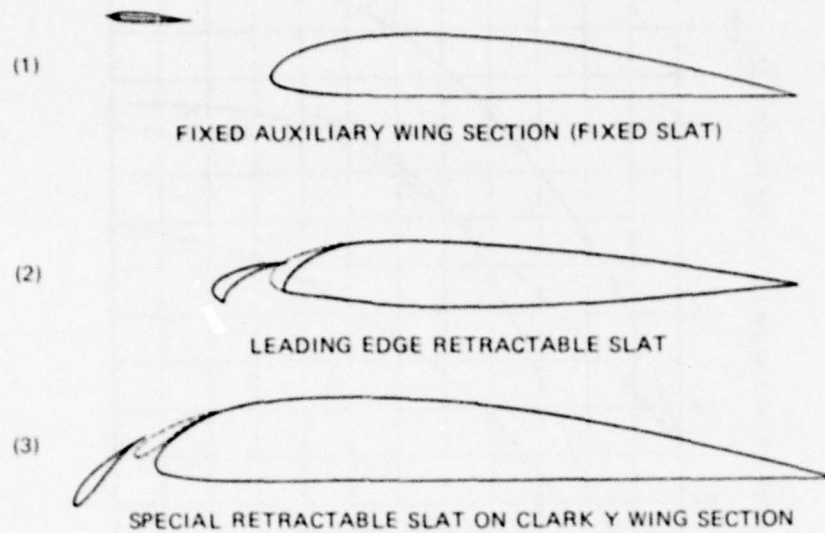


Figure 19a - Selected Slat Configurations

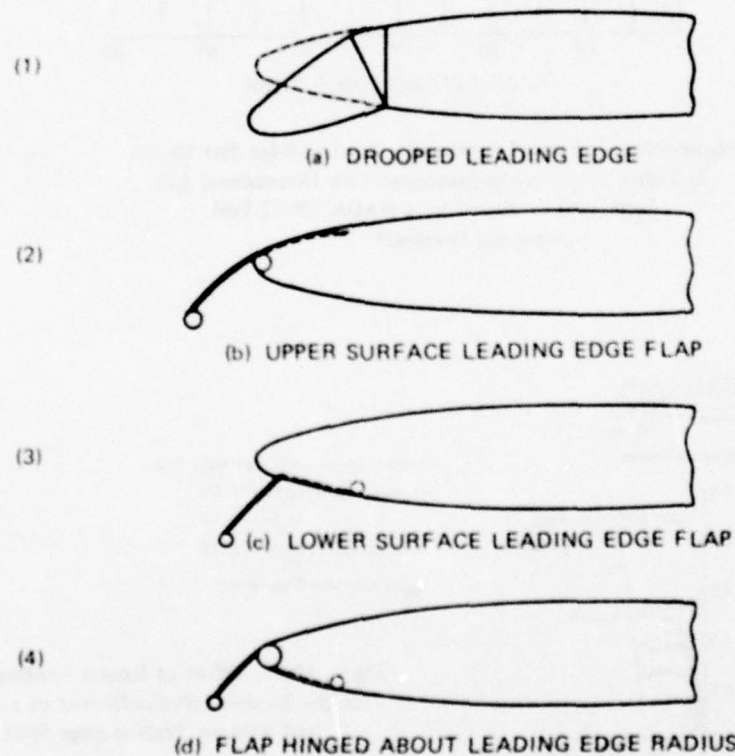


Figure 19b - Leading Edge Flap Arrangements

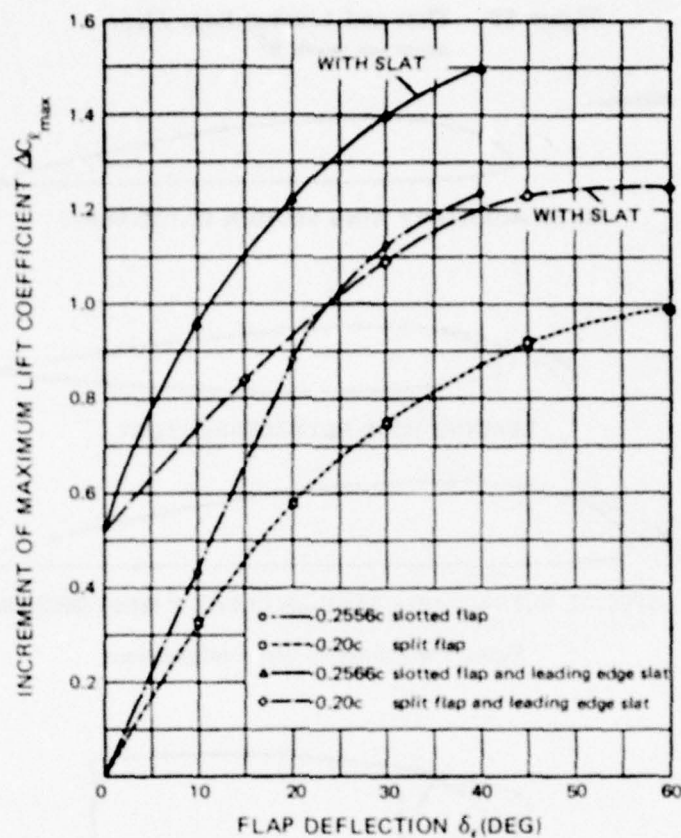


Figure 19c – Effect of Retractable Leading-Edge Slat Shown in Figure 19a(2) upon Maximum Two-Dimensional Lift Increment Produced by a NACA 23012 Foil
Abbott and Doenhoff⁵

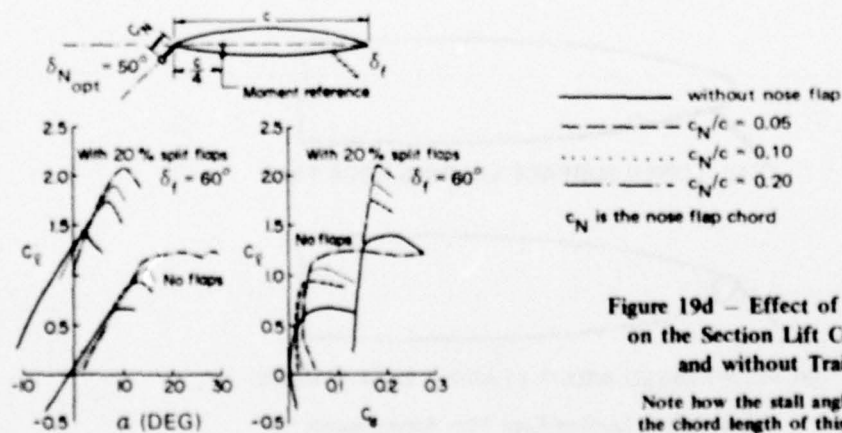


Figure 19d – Effect of Kruger Leading-Edge Flap on the Section Lift Coefficient of a Foil with and without Trailing-Edge Split Flap

Note how the stall angle is delayed by increasing the chord length of this leading-edge flap, Young.⁶

data for these devices fitted to foil sections can be found in Reference 5. Some sample data from Young⁶ on the effect of Krueger flaps at $\delta_N = 50^\circ$ are shown in Figure 19d, reproduced from McCormick.³ The most remarkable case of extending the useful range of α is seen for $\delta_f = 0$, $c_N/c = 0.20$.

Flaps and Slots

Slots are contoured passageways that allow the flow of high-energy fluid from the pressure side to help control the boundary layer on the suction side of a foil. The use of flaps and slots in combination can result in high lift coefficients. Possible arrangements are numerous, and the technology of high-performance multiple element foils is still unfolding, e.g., Callaghan and Beatty.¹² Some examples are included here. Figures 20a and 20b, reproduced from Mavriplis,¹³ illustrate the magnitude of gains that can be achieved with careful designs of foils with flaps and slots—in this case a double-slotted flap. Table 6, reproduced from Abbot and Doenhoff,⁵ provides a summary of lift and drag values for a number of combinations of flapped and unflapped, slotted, Clark Y-airfoil sections. Unfortunately, there are no known comparable data for slotted *symmetric* foil sections.

Spoilers

Spoilers are movable surfaces that can be deflected into the streamflow past a lifting foil. They are used extensively on aircraft for stability and control. When deflected asymmetrically, a loss of lift is caused by the separated region created behind them. When they are deflected symmetrically, the resulting wide wake-type flow is accompanied by large drag. A short, unpublished survey of some general features of lift diminution by spoilers, made by D.G. Lee, shows the main types of mechanical spoilers used for killing lift. Figure 21 is taken from the survey.

Hoerner¹⁴ presents data about incremental drag experienced by foils equipped with: spoilers or dive brakes.

Analyses of the effects of spoilers on lifting surfaces are presented, for example, by Woods¹⁵ and by Brown and Parkinson.¹⁶

Spoilers do not necessarily have to be used on lifting surfaces. They may be used directly on bodies and, for example, might find application for emergency, high-speed submarine control or maneuvering. In this case their effect is to alter the pressure distribution on the body, thus creating a force or moment on the hull. An example of "body flaps," reproduced from the patent of Soderberg,¹⁷ is shown in Figure 22. Two examples of the drag coefficient created by dive-brake flaps are reproduced from Hoerner¹⁴ in Figure 23. In the second scheme (Figure 23b) the dive brake consists of cascades of guide vanes which act to turn the flow out away from the body very efficiently. Hoerner¹⁴ also points out that by

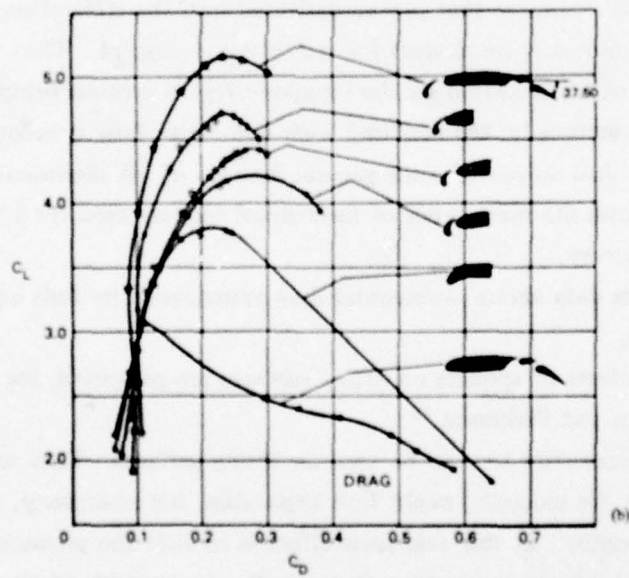
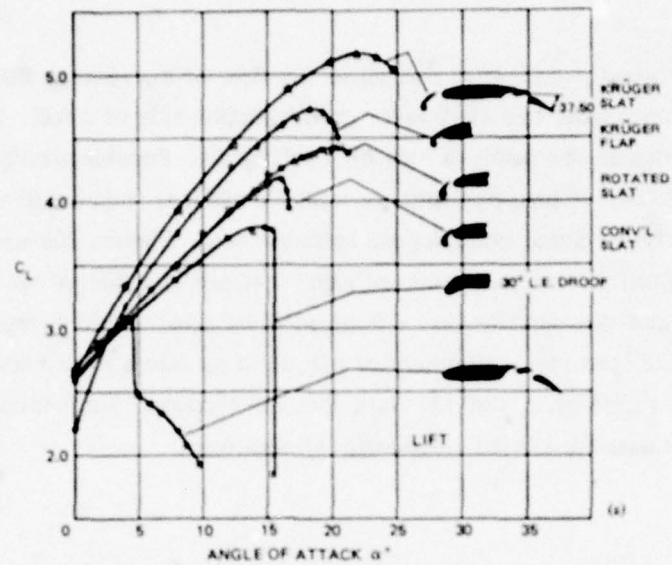



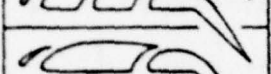
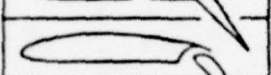
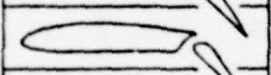
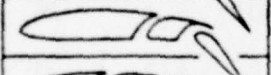



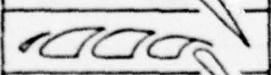
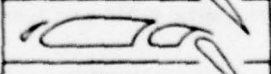
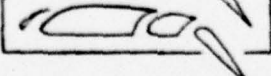
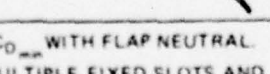
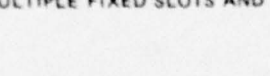


Figure 20 – Effect of Leading-Edge Devices on Lift and Drag of NACA 64A210 Section with Double-Slotted Flap

Mavriplix¹³

TABLE 6 - EXTREMES OF LIFT AND DRAG FOR FLAPPED AND UNFLAPPED
SLOTTED CLARK Y-FOILS

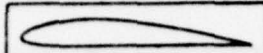
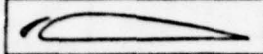
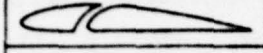
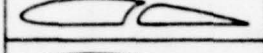
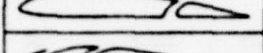
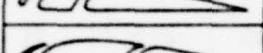
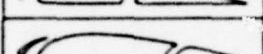
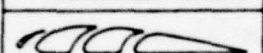
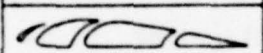
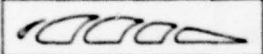
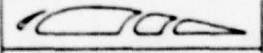
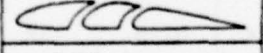
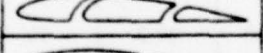
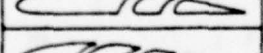
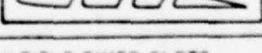
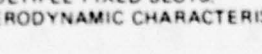
Reference: Abbot and Doenhoff⁵

SLOT COMBINATION	$C_{L_{max}}$	$C_{D_{min}}^*$	$\frac{C_{L_{max}}}{C_{D_{min}}}$	$\alpha_{C_{L_{max}}}$ DEGREES
	1.950	0.0152	128.2	12
	2.182	0.0240	91.0	19
	2.235	0.0278	80.3	20
	2.200	0.0340	64.7	21
	2.210	0.0270	81.8	20
	1.980	0.0164	120.5	12
	1.770	0.0164	108.0	14
	2.442	0.0208	117.5	16
	2.500	0.0258	96.8	18
	2.185	0.0214	102.0	18
	2.261	0.0243	93.2	19
	2.320	0.0319	72.7	20
	2.535	0.0363	69.8	20
	2.600	0.0298	87.3	20
	2.035	0.0298	68.3	21

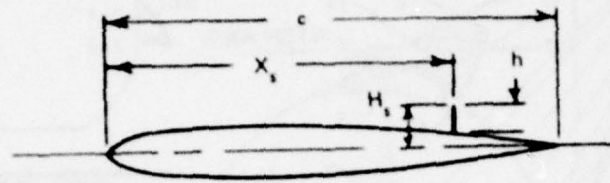
* $C_{D_{min}}$ WITH FLAP NEUTRAL.

MULTIPLE FIXED SLOTS AND A SLOTTED FLAP DEFLECTED 45 DEGREES.

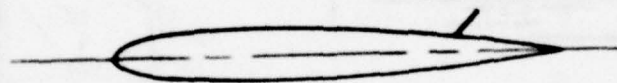
TABLE 6 (Continued)

SLOT COMBINATION	$C_{L_{max}}$	$C_{D_{min}}$	$\frac{C_{L_{max}}}{C_{D_{min}}}$	$\alpha_{C_{L_{max}}}$ DEGREES
	1.291	0.0152	85.0	15
	1.772	0.0240	73.8	24
	1.596	0.0199	80.3	21
	1.548	0.0188	82.3	19
	1.440	0.0164	87.8	17
	1.902	0.0278	68.3	24
	1.881	0.0270	69.7	24
	1.813	0.0243	74.6	23
	1.930	0.0340	56.8	25
	1.885	0.0319	59.2	24
	1.885	0.0363	51.9	25
	1.850	0.0298	62.1	24
	1.692	0.0228	74.1	22
	1.672	0.0214	78.2	22
	1.510	0.0208	72.6	19
	1.662	0.0258	64.4	22

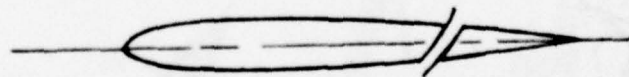
MULTIPLE FIXED SLOTS.
AERODYNAMIC CHARACTERISTICS OF A CLARK Y WING WITH SLOTS AND FLAPS.



(1) PLUG



(2) FLAP



(3) SLOTTED

Figure 21 – Main Types of Lift Spoilers
D.G. Lee

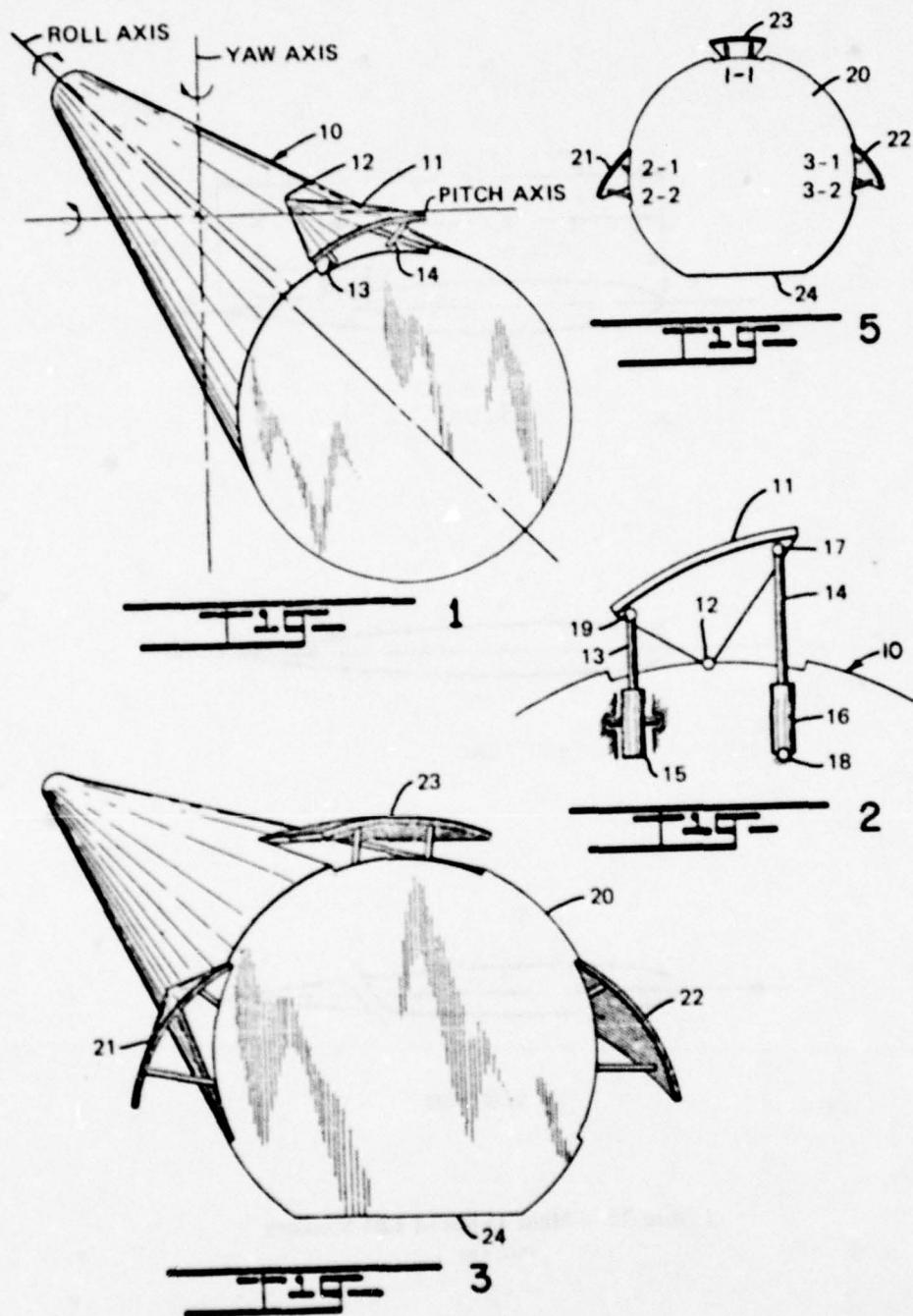


Figure 22 – Body Flaps from U.S. Patent 3,125,313
Soderberg¹⁷

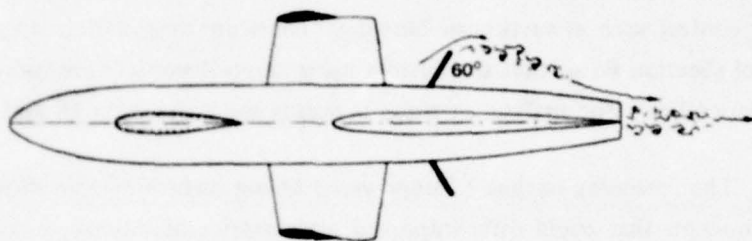


Figure 23a – Paired Plates Projecting into Flow Past Fuselage

$C_{D_{\square}} = 0.97$, where $C_{D_{\square}}$ is based on circumscribed area of plates.

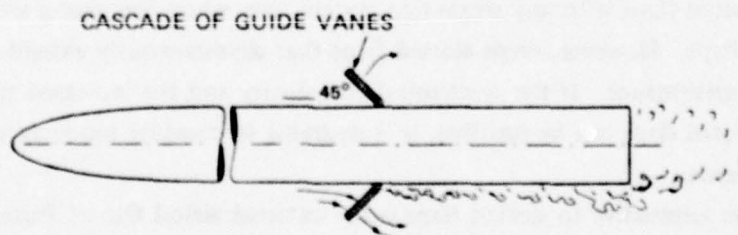


Figure 23b – Pair of Cascade Guide Vanes Set to Turn the Flow Outward

$C_{D_{\square}} = 1.48$

Figure 23 – Dive-Brake Flaps

Hoerner¹⁴

deflecting only one of the guide vane flaps pictured in Figure 23b, a lateral control force can be produced with a lift coefficient $C_{L\Omega} \approx 1.26$, based on the circumscribed area of the flap.

Others

Various other devices may be included in the category of unpowered mechanical devices. One example is the use of trapped vortices for the production or maintenance of lift. The snow cornice effect, or trapped vortex, is shown in Figure 24a. The flow separates cleanly at F and reattaches at S, trapping a lift-producing vortex within the region of the free streamline (FS) and the body. Figure 24b shows a conceivable arrangement of a cusped slot for passive control of leading-edge separation by a trapped vortex.

A variety of such flows can be imagined; however, in practice they require some form of boundary layer control such as suction or blowing. There are more efficient uses of boundary layer control (Section B) so that the devices using trapped vortices are more in the realm of interesting curiosities. For analysis of these concepts see References 18 and 19.

DISCUSSION: The foregoing outline of unpowered lifting surface devices shows that there are numerous concepts that could offer improved performance of submarine control surfaces. The accompanying force estimates for lift and drag on these devices provide some measure of comparison between the various types. Implementation of any one of these ideas is a design problem and is not part of the intent of this survey. Nevertheless, some general remarks can be made.

With regard to flaps, there is a more marked improvement of lift performance when comparing double-slotted flaps with any single-flap system than when comparing slotted single flaps with plain flaps. However, single-slotted flaps that simultaneously extend the chord also have good performance. If the mechanical complexity and the increased structural difficulties of slotted flaps can be justified, it is desirable to consider seriously the double-slotted arrangements.

An attractive alternative to slotted flaps is the external airfoil flap of Figure 8b, which may find useful applications on marine control surfaces.

Although flap performance can be greatly improved using a variety of leading-edge devices such as slats and leading-edge flaps, it is doubtful whether the added complexity of these arrangements can be justified for marine applications.

Differentially controlled body flaps (Figure 22) or, better yet, guide vane dive-brake flaps (Figure 23b) could be used for emergency high-speed deployment to generate a corrective turning moment on a submarine hull.

Use of lift-spoiling devices seems more appropriate on the submarine sail than on control planes, since it is the lift exerted on the sail during a turn that causes an undesirable inward roll moment. Also, spoilers have the virtue of being simple in geometry and in method of actuation.

The use of a passively captured vortex is impractical, considering the schemes devised to date. One main problem is that even if a foil with a cusped-slot arrangement could be designed for one speed and one large angle of attack, the off-design performance would probably be very poor.

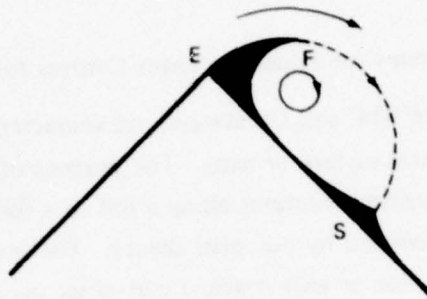


Figure 24a — Snow Cornice Trapped Vortex

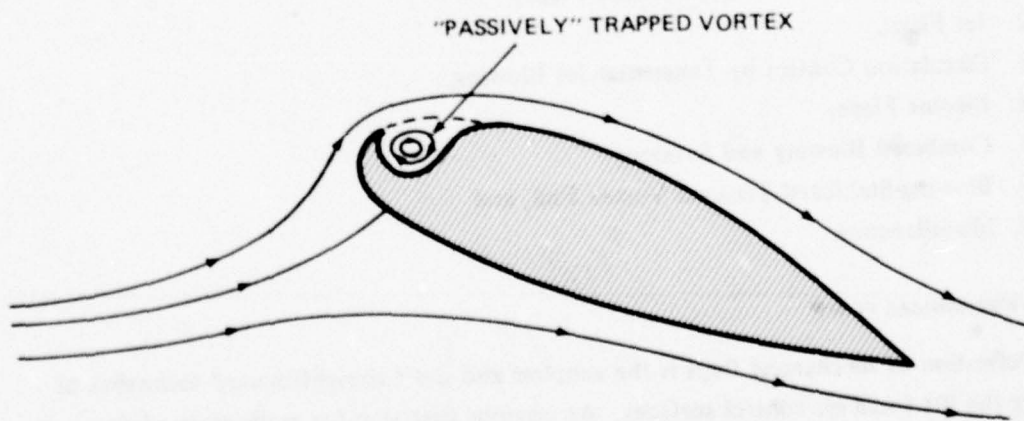


Figure 24b — Possible Arrangement of Cusped Slot for Passive (Unpowered) Boundary-Layer Control Near the Nose of a Foil

Figure 24 — Trapped Vortex

SECTION B POWERED CIRCULATORY LIFT DEVICES

Fluid Control: Blowing and Suction Devices

The principles of boundary layer and flow control have been widely applied to problems of lift-production and lift-augmentation, especially for use with aircraft. Many of these ideas can be applied directly in the hydrodynamic context as well. Unless otherwise stated, the fluid-control concepts outlined as follows are to be interpreted for water-in-water application.

NAME: Internal Blowing Systems for Boundary Layer Control and Circulation Control

DEFINITION: Internally blown BLC and CC systems are characterized by the use of fluid jets ducted from *within* the control surface or wing. The purpose of BLC is to use injected fluid to overcome separation at critical locations along a foil or a foil-flap arrangement and, thereby, to achieve lift forces predicted by potential theory. The purpose of blowing CC is to exploit the effects of either a free or wall-attached curved jet upon the overall circulation about a lifting surface.

DESCRIPTION AND FORCE ESTIMATES: This section is divided into seven general parts corresponding to the various types of internal blowing arrangements —

1. Blown Mechanical Flaps, Powered Flaps,
2. Jet Flaps,
3. Circulation Control by Tangential Jet Blowing,
4. Ejector Flaps,
5. Combined Blowing and Suction,
6. Blowing-Stabilized Trapped Vortex Foil, and
7. Miscellaneous.

BLOWN MECHANICAL FLAPS

Deflection of mechanical flaps is the simplest and most straightforward technique of altering the lift force on control surfaces. An obvious first step for application of flow control on force producers is to augment the performance of ordinary flaps.

Without some form of boundary layer control, when a trailing edge flap is deflected more than 10 to 15 degrees, the lift increase obtained is less than the value predicted by potential theory. This happens because of boundary layer separation over portions of the suction surface where severe adverse pressure gradients are occurring; see Figure 25. The nose-separation bubble is known to be aggravated by very large flap angles and by thin profile shapes.

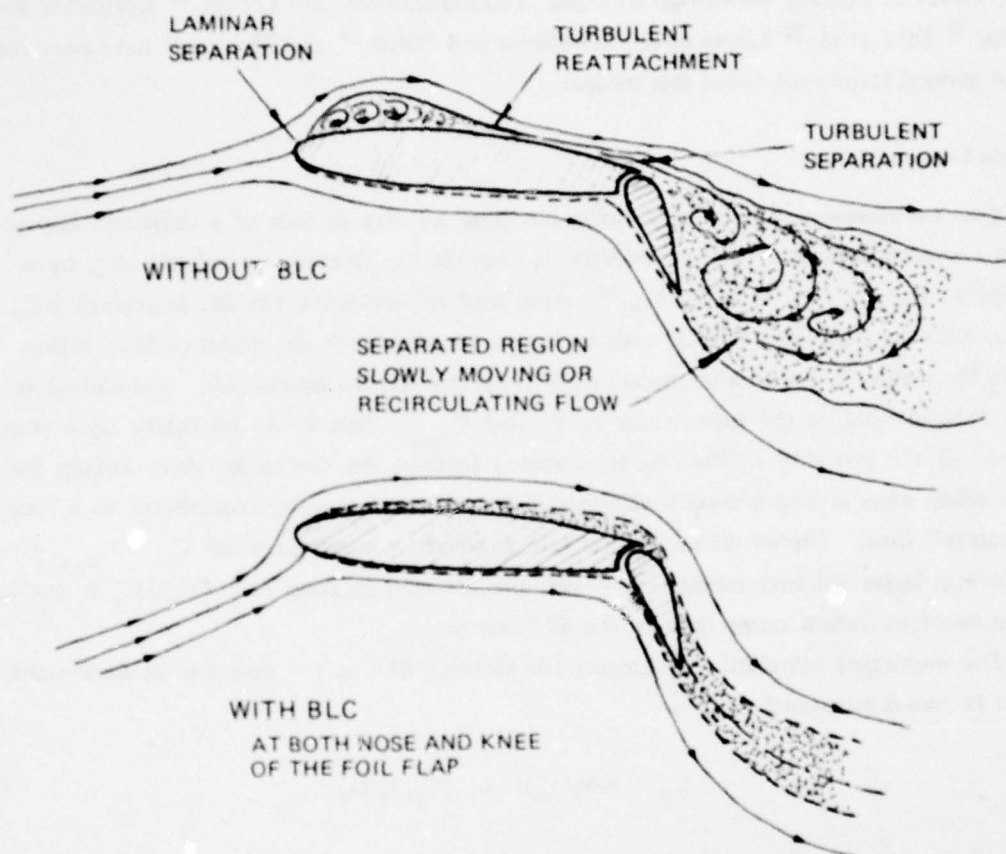


Figure 25 – Flow Over a Flapped Control-Surface Foil

Effect is shown of idealized boundary-layer control at the two most troublesome regions: at the knee of the flap and just aft of the foil nose.

The basic idea of blowing BLC is to force a plane jet sheet into a region of decelerating or separating flow, thereby inducing a flow which is energetic enough to negotiate the turn over the upper surface of the deflected flap. Usually, large flap angles are the most interesting because large lift increments can be realized.

The definition of conventional flap is restricted to those designs for which the flap chord is greater than or equal to 20 percent of the overall wing chord. Figure 26 includes the general features of existing blown-flap schemes. Poisson-Quinton and Lepage,²⁰ Korbacher and Sridhar,²¹ Dike et al.,²² Lopez et al.,²³ Williams and Butler,²⁴ and Thomas²⁵ have provided useful general references about this subject.

Force Estimates

Lift: Two-Dimensional. In tests, blowing out over the top surface of a deflected flap produces a small effect until the jet velocity V_j exceeds the free stream velocity U_∞ by a reasonable margin, e.g., $V_j > 1.2 U_\infty$.²⁴ At higher jet velocities, the lift increment ΔC_l , due to blowing, increases rapidly with increased blowing until the attached flow region covers the entire flap, and the theoretically realizable lift increment ΔC_{l_t} is obtained at some critical value of the momentum coefficient $C_{\mu_{crit}}$. This is the boundary layer control regime. If the intensity of blowing is increased further, the curved jet sheet leaving the flap trailing edge attains a certain stiffness of its own and thereby contributes to a "super-circulation" flow. The so called jet-flap effect, which commences when $C_\mu > C_{\mu_{crit}}$, gives rise to still larger lift increments. However, the lift-augmentation rate $\Delta C_l / \Delta C_\mu$ is smaller in the supercirculation range than in the BLC range.

The important correlation parameter for blowing BLC is the momentum coefficient, which in two-dimensional flow is

$$C_\mu = \dot{m} V_j / q_\infty c = 2 C_Q V_j / U_\infty \quad (9)$$

where \dot{m} = mass flow rate per unit span

V_j = jet velocity

c = chord

$C_Q = Q / c U_\infty$

$$q_\infty = \frac{1}{2} \rho U_\infty^2$$

Q = volume flow rate per unit span.

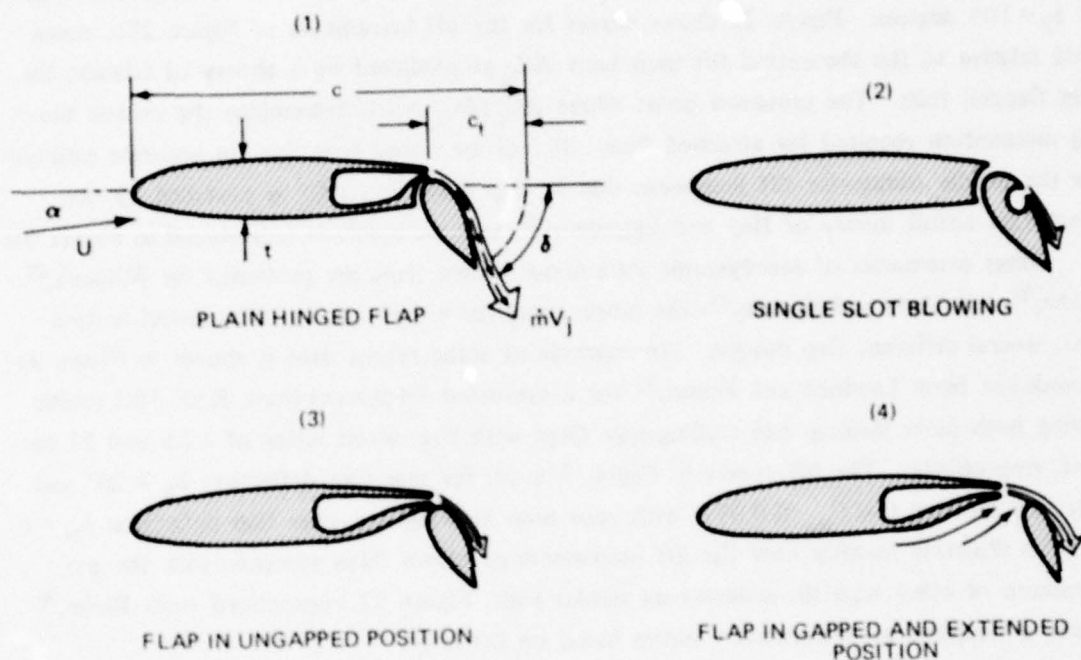


Figure 26a - Single Slot Blowing



Figure 26b - Multiple Slot Blowing

Figure 26 - Configurations of Blown Conventional Flaps, Flap Chord Greater Than 20 Percent of Total Foil-Flap Chord

Figure 27 shows a result²⁶ that displays the typical characteristics of section-lift coefficient C_l versus C_{μ} for a 20-percent-flap chord, 15-percent-thick NACA foil shape with slot blowing over the flap upper surface. It can be seen that the rate of increase of C_l decreases markedly once C_{μ} exceeds the value $C_{\mu_{crit}}$ required for completely attached flow.

For the plain flapped NACA 0010 profile of Figure 28a, a series of curves of lift increments due to blowing and flap deflection is shown in Figure 28b, taken from Thomas.²⁷ These are especially interesting because data are included for the unusually large flap angle of $\delta_f = 105$ degrees. Figure 29 shows curves for the lift increments of Figure 28b, measured relative to the theoretical lift increment ΔC_{l_t} as predicted by a theory of Glauert for thin flapped foils. The crossover point where $\Delta C_{l_t}/\Delta C_{l_t} = 1.0$ determines the critical blowing momentum required for attached flow. It may be noted here that an accurate estimate for the ideally obtainable lift increment due to flap deflection ΔC_{l_t} is provided by the exact thin airfoil theory of Hay and Eggington,²⁸ and the result is reproduced in Figure 30.

Other summaries of aerodynamic data about blown flaps are presented by Williams,²⁹ Riebe,³⁰ and Dods and Watson,³¹—the latter being for a thin NACA 0006 airfoil section with several different flap designs. An example of some recent data is shown in Figure 31, reproduced from Lawford and Foster,³² for a cambered 13-percent-thick RAE 102 profile having both plain leading- and trailing-edge flaps with flap chord ratios of 12.5 and 25 percent, respectively. The lift curves in Figure 31a are for rear flap deflection $\delta_R = 20^\circ$ and rear flap blowing $0 < C_{\mu_R} < 0.047$, with zero nose blowing and nose flap deflection $\delta_N = 0$.

To illustrate roughly how the lift increments of blown flaps compare with the performance of other high lift schemes on similar foils, Figure 32, reproduced from Riebe,³⁰ shows a sampling of performance curves based on lift only.

In general, for the geometry and notation shown in Figure 26a(1), the section-lift coefficient, with an approximate correction for foil thickness from Spence,³³ is expressed as

$$C_l = [(C_{l_\alpha}) \alpha + (C_{l_\delta}) \cdot \delta] (1 + t/c) \quad (10)$$

where the thin foil derivative $(C_{l_\alpha}) = (\partial C_l / \partial \alpha)_{\delta=0}$ is a function of C_{μ} only and is plotted in Figure 33. The derivative $(C_{l_\delta}) = (\partial C_l / \partial \delta)_{\alpha=0}$ is a function of both C_{μ} and the flap chord ratio c_f/c . These derivatives have been determined theoretically by Spence.^{33,34} Figure 34 shows a plot of the flap angle derivative (C_{l_δ}) versus C_{μ} for contours of c_f/c .

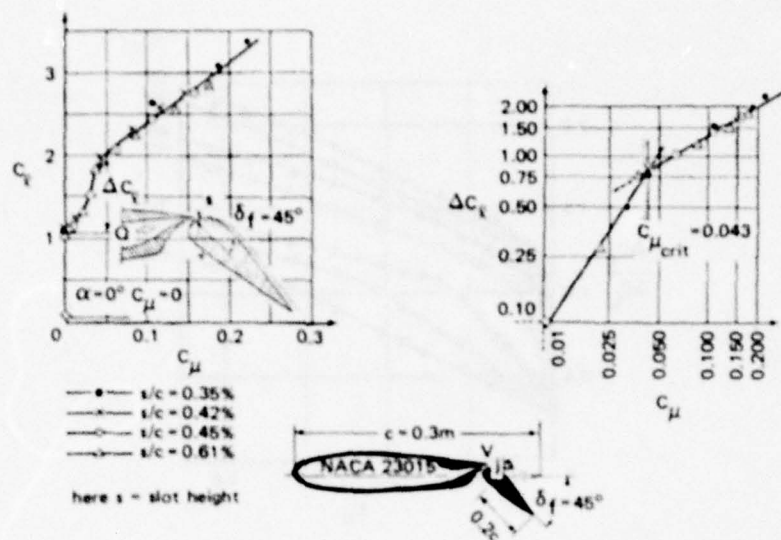


Figure 27 – Lift Data on Effect of Blown Flaps, Showing Identification of Critical Attachment Momentum Coefficient $C_{\mu, crit}$
 Attinello²⁶

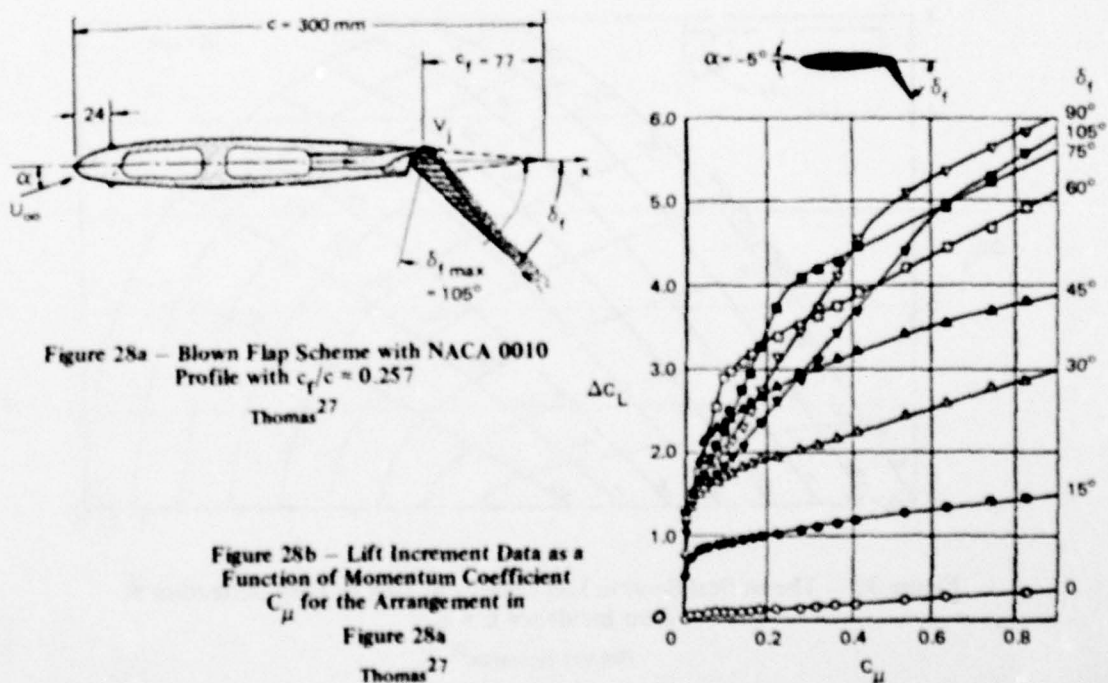


Figure 28 – Sample Blown Flap Test Results

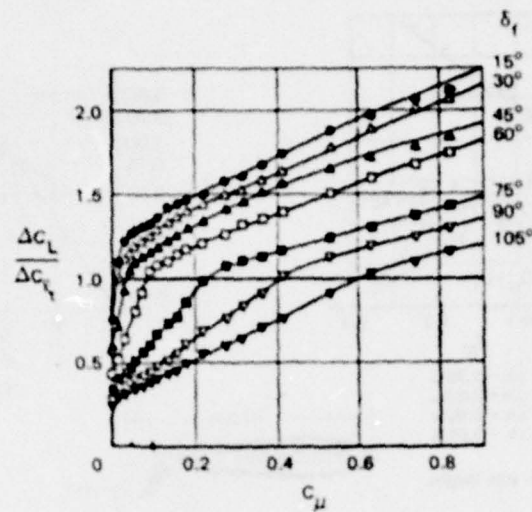


Figure 29 – Curves of Lift Increments Normalized by the Theoretically Achievable Values ΔC_{L_t}

Thomas²⁷

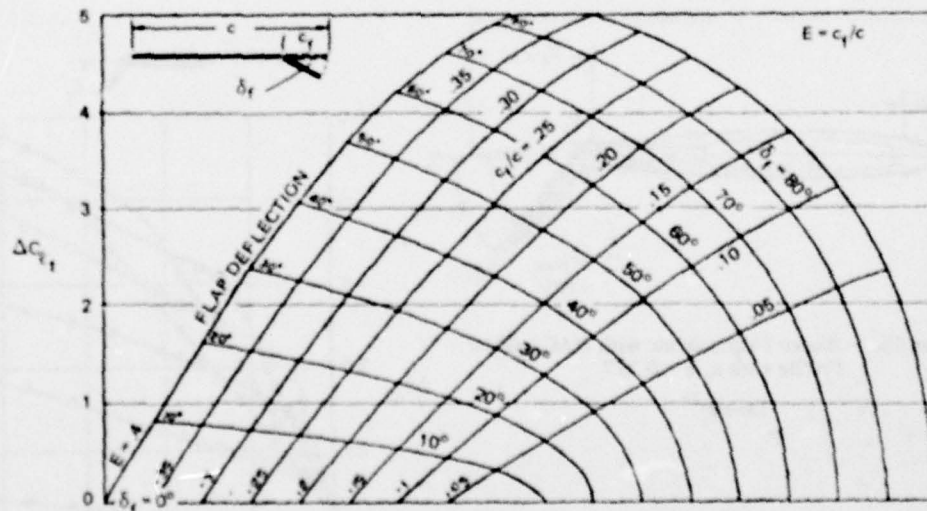


Figure 30 – Theoretical Section Lift Increment Due to Flap Deflection at Zero Incidence $E = c_f / c$

Hay and Eggington²⁸

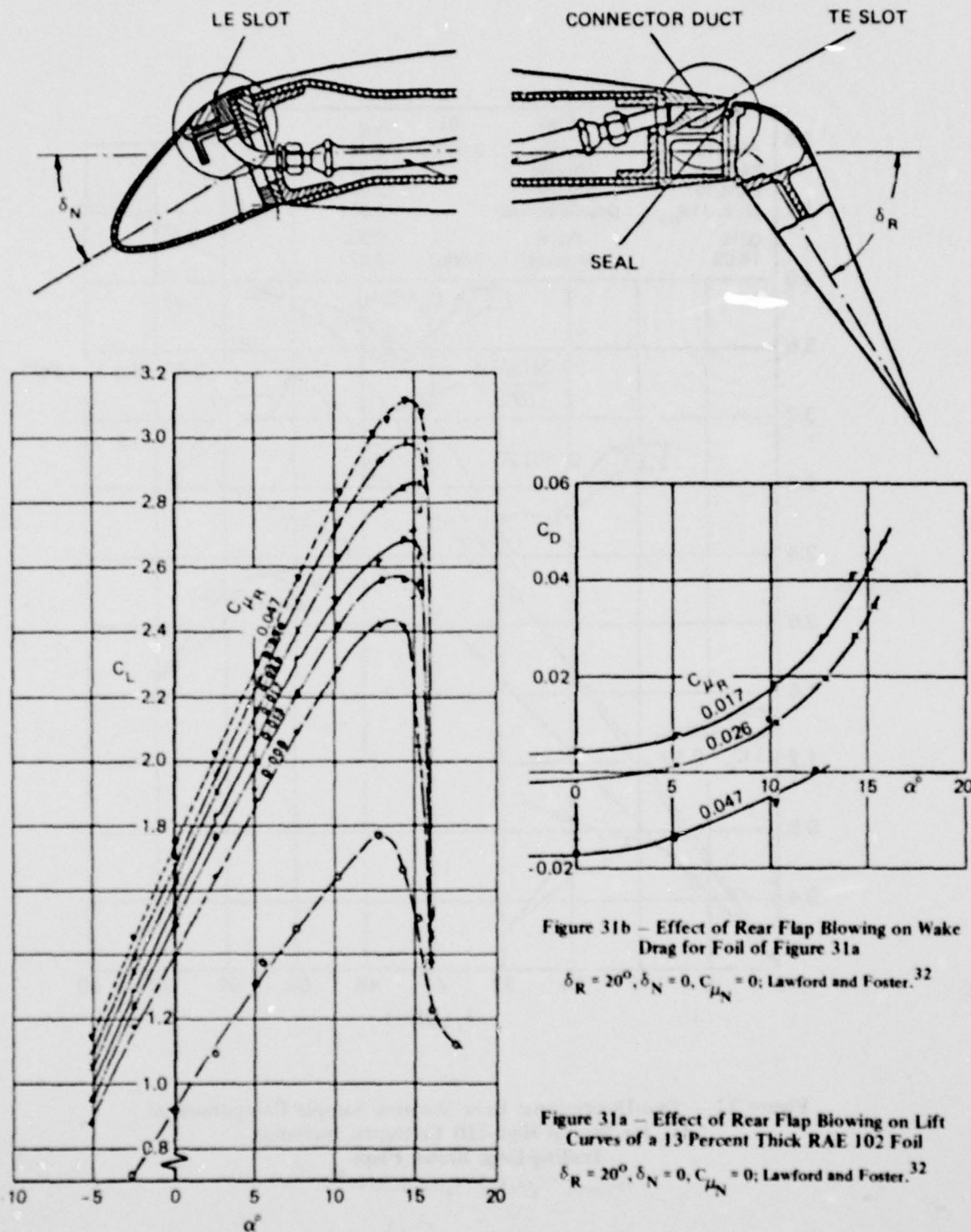


Figure 31b - Effect of Rear Flap Blowing on Wake Drag for Foil of Figure 31a

$\delta_R = 20^\circ, \delta_N = 0, C_{\mu N} = 0$; Lawford and Foster.³²

Figure 31a - Effect of Rear Flap Blowing on Lift Curves of a 13 Percent Thick RAE 102 Foil

$\delta_R = 20^\circ, \delta_N = 0, C_{\mu N} = 0$; Lawford and Foster.³²

Figure 31 - Effects of Rear Flap Blowing

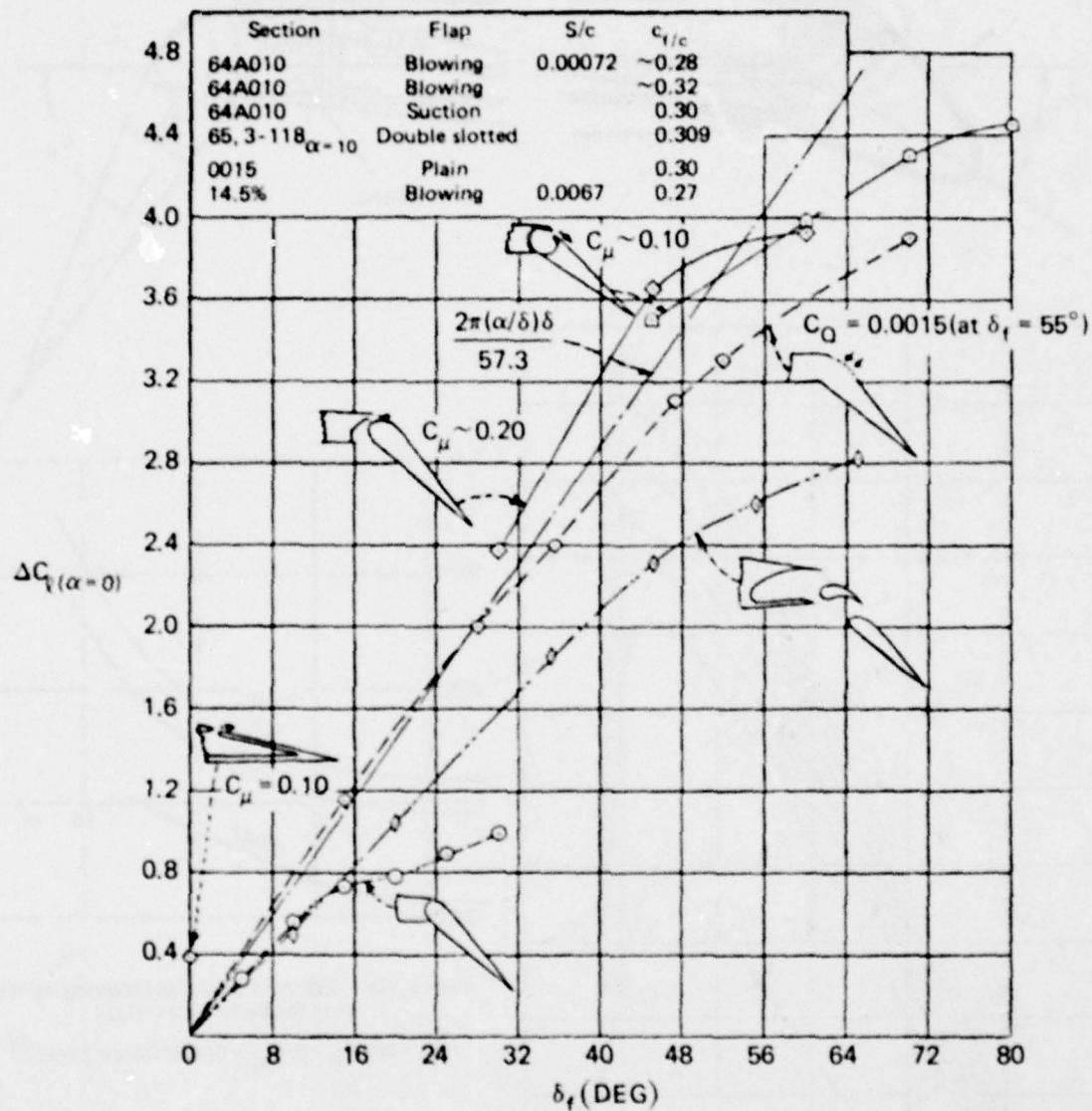


Figure 32 - Two-Dimensional Data Showing Sample Comparison of ΔC_l for Several High-Lift Concepts, Including Trailing-Edge Blown Flaps

$$\Delta C_{l(\alpha=0)} = C_{l(\delta_f, C_{\mu})} - C_{l(0, C_{\mu})}, \text{ Riebe}^{30}$$

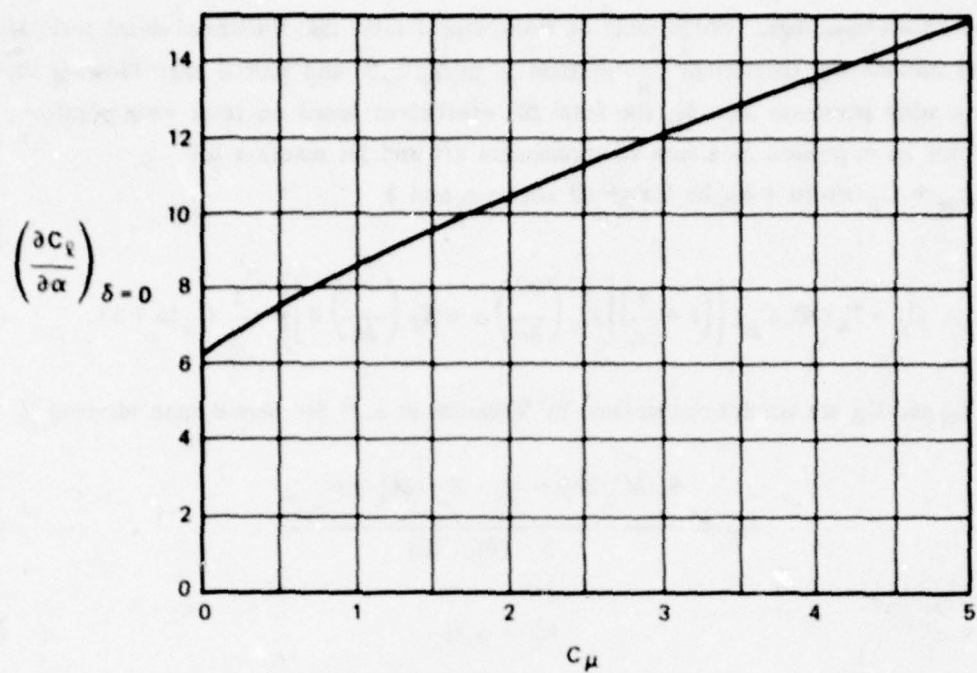


Figure 33 – Theoretical Thin-Foil Derivative (C_{ℓ_a}) versus C_{μ} for a Jet-Augmented Flap
Spence³³

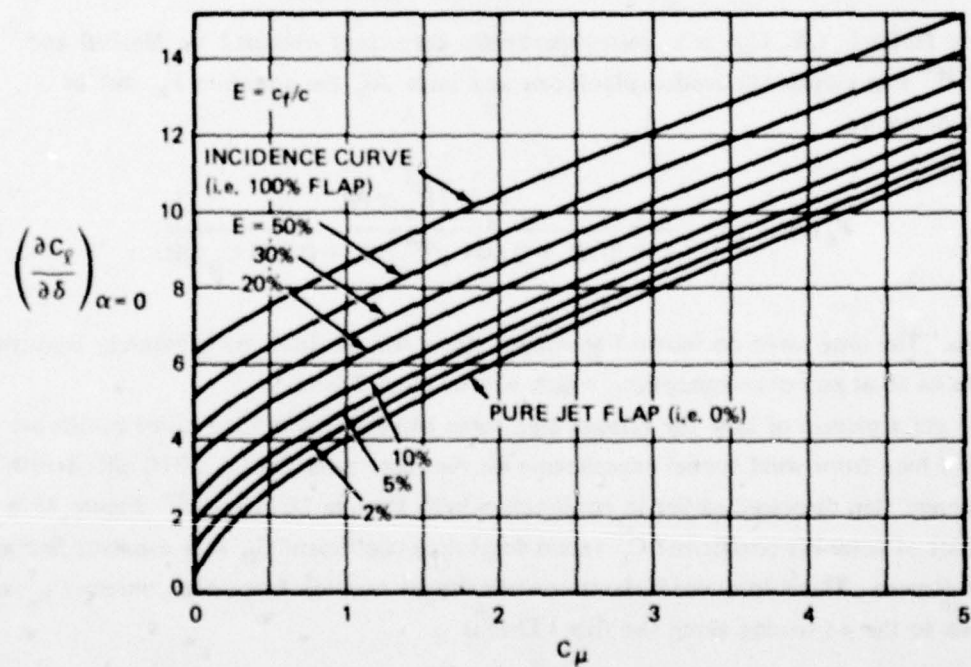


Figure 34 – Theoretical (C_{ℓ_h}) _{$\alpha=0$} for Thin Foil with a Blown Flap; Contours of c_f/c
Spence³⁴

Lift: Finite-Aspect Ratio. For a wing of finite-aspect ratio AR ; thickness chord ratio t/c ; total jet momentum coefficient $C_{\bar{\mu}}$, defined as $m_T V_j / q_{\infty} S$; and partial span blowing that affects a wing planform area S_f , the total lift coefficient based on total wing planform area S can be expressed as a sum of circulation lift and jet reaction lift $C_L = C_{L\Gamma} + C_{\bar{\mu}} \sin(\alpha + \delta)$, or for small angles α and δ

$$C_L = F_A(AR, C_{\bar{\mu}}) \left\{ \left(1 + \frac{t}{c} \right) \left[K_{\alpha} \left(\frac{\partial C_{\bar{\mu}}}{\partial \alpha} \right) \alpha + K_{\delta} \left(\frac{\partial C_{\bar{\mu}}}{\partial \delta} \right) \delta \right] \right\} - \frac{t}{c} C_{\bar{\mu}} (\alpha + \delta) \quad (11)$$

where K_{α} and K_{δ} are corrections devised by Williams, et al.³⁵ for partial span blowing

$$K_{\alpha} = \frac{S_f (\partial C_{\bar{\mu}} / \partial \alpha) + (S - S_f) (\partial C_{\bar{\mu}} / \partial \alpha)_{C_{\bar{\mu}}=0}}{S \cdot (\partial C_{\bar{\mu}} / \partial \alpha)} \quad (12)$$

$$K_{\delta} = S_f / S \quad (13)$$

The derivative $(\partial C_{\bar{\mu}} / \partial \alpha)$ refers to the thin wing derivative evaluated at the mean sectional momentum coefficient $C_{\bar{\mu}} = C_{\bar{\mu}} S / S_f$; see McCormick³ for details.

The factor $F_A(AR, C_{\bar{\mu}})$ is a finite-aspect-ratio correction obtained by Maskell and Spence.³⁶ For elliptically loaded planforms and large AR , the function F_A can be approximated by

$$F_A(AR, C_{\bar{\mu}}) = \frac{1 + 2C_{\bar{\mu}}/\pi AR}{1 + 2/AR + 0.604 \sqrt{C_{\bar{\mu}}}/AR + 0.876 C_{\bar{\mu}}/AR} \quad (14)$$

Drag. The *drag force* on blown flap-wing systems will be discussed separately from the problem of total *power* consumption, which will be treated later.

To get a picture of how the various drag force components behave, some results are reproduced here from wind tunnel experiments on the rectangular NACA 0010 airfoil with a 25.7-percent flap discussed earlier in conjunction with Figures 28 and 29.²⁷ Figure 35 is a polar plot of total lift coefficient C_L versus total drag coefficient C_D at a constant flap angle $\delta_f = 60$ degrees. These total coefficients contain the jet reaction force components C_{L_R} and C_{D_R} due to the jet issuing along the flap. That is

$$\begin{aligned} C_L &= C_{L_A} + C_{L_R} \\ C_D &= C_{D_A} + C_{D_R} \end{aligned} \quad (15)$$

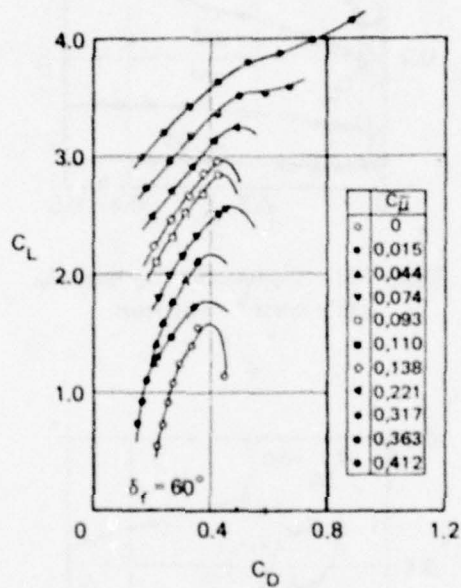


Figure 35 — Polar Plots for Total Lift and Drag Coefficients C_L and C_D for Arrangement Shown in Figure 28a

Jet reaction forces are included. C_μ is the total jet blowing momentum coefficient for planform area S , Thomas.²⁷

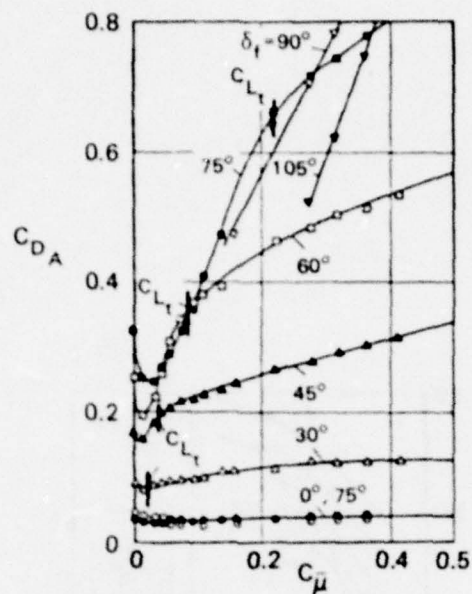


Figure 36a — Contours of Flap Angle δ_f
($\alpha = \text{const} = -5$ degrees)

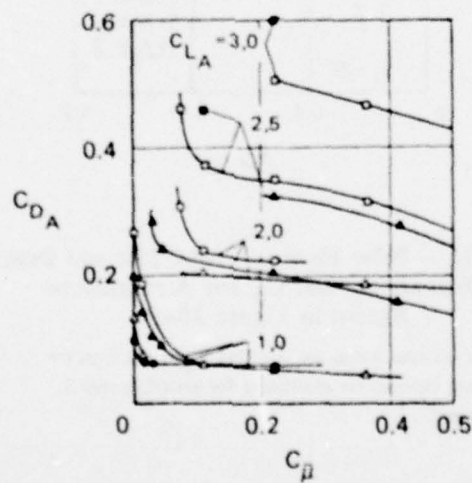


Figure 36b — Contours of Constant Aerodynamic Lift

Figure 36 — Variation of Aerodynamic Drag C_{DA} with Blowing Momentum Coefficient C_μ for Scheme of Figure 28a

Thomas²⁷

The jet reaction forces, neglecting losses in jet viscous effects are

$$\begin{aligned} C_{L_R} &= C_{\mu}^- \sin(\delta_f + \alpha) \approx C_{\mu}^- (\delta_f + \alpha) \\ C_{D_R} &= -C_{\mu}^- \cos(\delta_f + \alpha) \approx -C_{\mu}^- \end{aligned} \quad (16)$$

where δ_f = flap angle, and α = angle of attack. Here, $C_{\mu}^- = \dot{m}_T V_j / q_{\infty} S$, based on the total flow rate \dot{m}_T and total planform area S . It should be noted that the jet reaction forces are significant only for blowing in the supercirculation range because the C_{μ} values required for BLC are modest; see Figure 27.

The components C_{L_A} and C_{D_A} are aerodynamic contributions that represent, respectively, the pressure lift and drag as they are modified by the pressure peaks caused by blowing. The drag coefficient C_{D_A} is made up of profile drag C_{D_p}' as modified by blowing and induced drag as modified by blowing and induced drag C_{D_i} , which Thomas²⁷ writes as

$$C_{D_A} = C_{D_p}' + \frac{C_L^2}{\pi AR^*} \quad (17)$$

where in Thomas' experiments, the effective aspect ratio is $AR^* = 6$. Figures 36a and 36b show the variation of the aerodynamic drag coefficient C_{D_A} with momentum coefficient C_{μ}^- for the foil-flap scheme of Figure 28a. In Figure 36b the curves of drag at constant C_{L_A} values indicate that the profile drag is *reduced* by the effects of blowing, a feature displayed by most slot-blowing devices. It should be noted that a preferable formula for estimating the induced drag of a jet-augmented flapped wing with an elliptical circulation distribution is³⁶

$$C_{D_i} = \frac{C_L^2}{\pi AR + 2 C_{\mu}^-} \quad (17a)$$

Equation (17) would be increasingly poorer for correlation purposes as C_{μ}^- grows large.

For the flapped RAE 102 foil pictured in Figure 31, the measured wake-drag curves corresponding to $\delta_R = 20^\circ$, $\delta_N = 0^\circ$, and $C_{\mu_N} = 0$ are reproduced in Figure 31b.

A brief discussion of complete wing-drag coefficients, including the influence of partial span flaps and sweep is given by Williams and Butler.²⁴

An equivalent "kinetic energy" drag coefficient can be defined which contains a penalty for the power required for blowing systems. With this definition, it is possible to make direct comparisons of equivalent lift-to-drag ratios between various flap arrangements, blown-flap schemes, jet flaps, etc. The equivalent drag is defined as

$$D_e = D'_p + D_i + D_{\text{pump}} + D_{\text{ram}} \quad (18)$$

where D'_p = profile drag, modified by blowing, and includes effects of partial span flaps, etc.

D_i = induced drag, estimated from Equation (17a)

D_{pump} = pump power/ U_∞

D_{ram} = $\rho Q U_\infty$ = momentum drag force required to ingest the blowing flow rate.

Q = blowing volume flow rate = \dot{m}_T / ρ .

The pumping power supplies the jet flow rate and is approximated by

$$\text{Pump Power} = \rho g (\Delta H) \cdot Q \approx \frac{1}{2} \rho V_j^2 Q \quad (19)$$

The resulting equivalent drag coefficient based on wing planform, area S is

$$C_{D_e} = C'_{D_p} + C_{D_i} + \frac{1}{2} C_\mu \frac{V_j}{U_\infty} + C_\mu \frac{U_\infty}{V_j} \quad (20)$$

and the equivalent lift-to-drag is C_L / C_{D_e} . This points up the importance of the ratio V_j / U_∞ as well as the momentum coefficient C_μ in describing blown-flap systems or any other blowing technique for that matter.

Nose Flap Blowing. When the lift effectiveness of a foil is increased by trailing-edge flap blowing, there is an accompanying reduction in stalling incidence unless the foil section is thick and heavily cambered. A typical example of this is shown in Figure 37 where data are plotted for the NPL 8-percent-thick foil.³⁷ The stall angle is reduced from 15° at $\delta_f = 0$, $C_\mu = 0$ to approximately 5° at $\delta_f = 45^\circ$, $C_\mu = 0.053$. Especially for thin wing sections, the increased loading caused by a more effective trailing-edge device tends to promote early boundary layer separation near the foil leading edge.

Purely mechanical devices such as a leading-edge slat or a drooped-nose flap can be used successfully to control the LE separation and to extend the range of angle of attack below stall.

AD-A078 423

DAVID W TAYLOR NAVAL SHIP RESEARCH AND DEVELOPMENT CE--ETC F/G 20/4
AN INVENTORY OF SOME FORCE PRODUCERS FOR USE IN MARINE VEHICLE --ETC(U)
NOV 79 M B WILSON , C V KERCZEK
DTNSRDC-79/097

UNCLASSIFIED

NL

2 of 5
AD-
A 078423



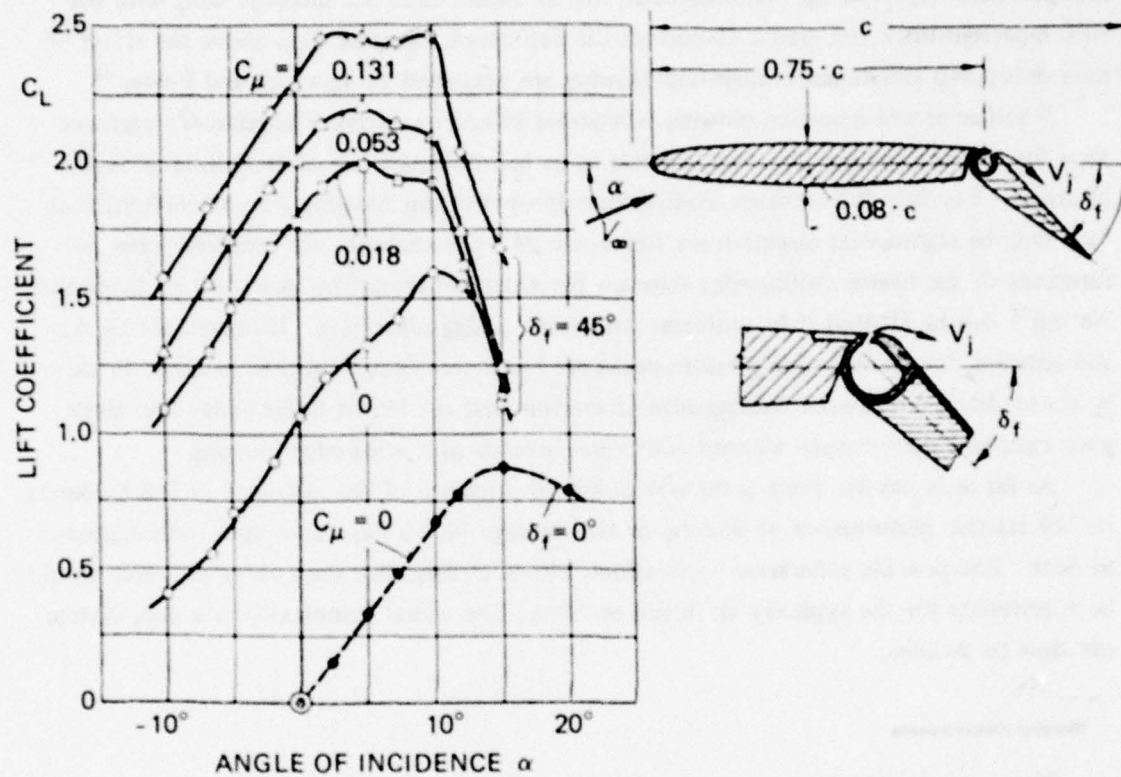


Figure 37 - Effect of Flap Blowing upon Stall Incidence Angle

Data for NPL 8 percent thick foil shape with $\delta_f = 45$ degrees
and $c_f/c = 0.25$, Williams³⁷

Boundary layer control by slot blowing can be used to supplement the effects of mechanical leading-edge devices. A good discussion of the problems of a blowing slot on a fixed leading edge, no droop, is presented by Williams and Butler.³⁴ One of the more attractive techniques is BLC slot blowing at the knee of a plain leading-edge flap. Large LE flap angles are used to guarantee that the locations of the strong adverse pressure gradients are moved back from the nose to the flap knee. Figure 38 shows the typical benefit derived from drooped nose-flap blowing. The curves are for an aspect ratio 3.3 unswept wing with the NPL 8-percent-thick foil, and a 10-percent-LE flap chord. Further data about the effect of nose droop and simultaneous nose-flap blowing are presented by Lawford and Foster.³²

Whether or not nose-flap blowing is required in order to achieve satisfactory performance for a blown trailing-edge flap depends upon foil thickness and desired range of angle of attack. For thin foil sections, leading-edge droop and slot blowing are so beneficial that they may be regarded as essential; see Reference 24. For example, the relatively poor performance of the blown trailing-edge flaps on the 6-percent-thick foils described by Dods and Watson³¹ can be attributed to problems with leading-edge separation. However, for thicker foil sections, the leading-edge pressure peaks are less severe than with thin sections, so there is less tendency for massive leading-edge separation, and the blown trailing-edge flap alone gives excellent performance without additional benefits of leading-edge blowing.

As far as is known, there is no systematic investigation of the influence of foil thickness on the relative performance of leading- or trailing-edge blown flaps or proper combinations of both. For possible submarine applications, blown trailing-edge flaps alone probably would be appropriate for the typically thick foil sections. The added complexity of a dual system can thus be avoided.

Blowing Requirements

The amount of blowing required to achieve the theoretically achievable two-dimensional lift increment ΔC_{l_t} is determinable by experiment, although there is an attempt by Thomas³⁸ at a two-dimensional prediction of $C_{\mu_{crit}}$. Figure 39 shows the range of experimental values of $C_{\mu_{crit}}$ versus δ_t from a number of references. The original references should be consulted for the details of foil shapes, Reynolds numbers, etc.

For finite-aspect-ratio wings, the magnitude of blowing required to achieve theoretical flap effectiveness is difficult to estimate theoretically. However, a correlation of data from experiments for $C_{\mu_{crit}}$ was made by H. R. Chaplin and is given here in Figure 40.

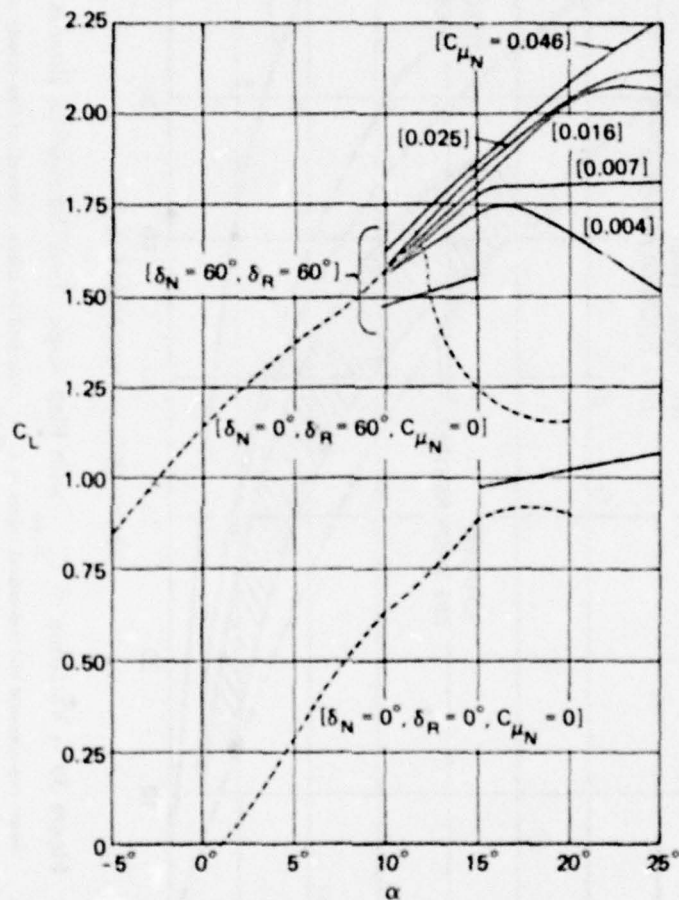
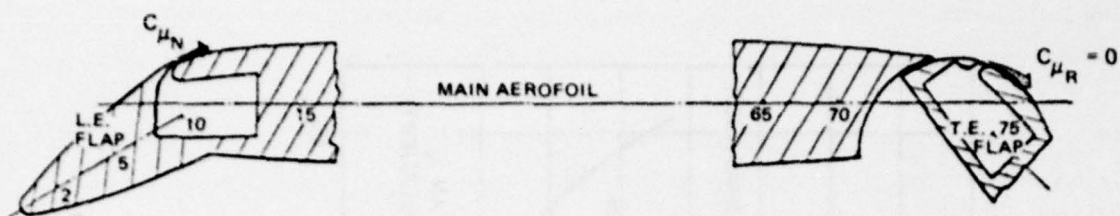


Figure 38 — Effect of Leading-Edge Flap Knee Blowing on Lift-versus-Incidence Curves for NPL 8 Percent Foil Shape

δ_N = nose flap angle, C_{μ_N} = nose slot-blowing momentum coefficient based on affected wing area, and δ_R = trailing edge flap angle, Williams and Butler.²⁴

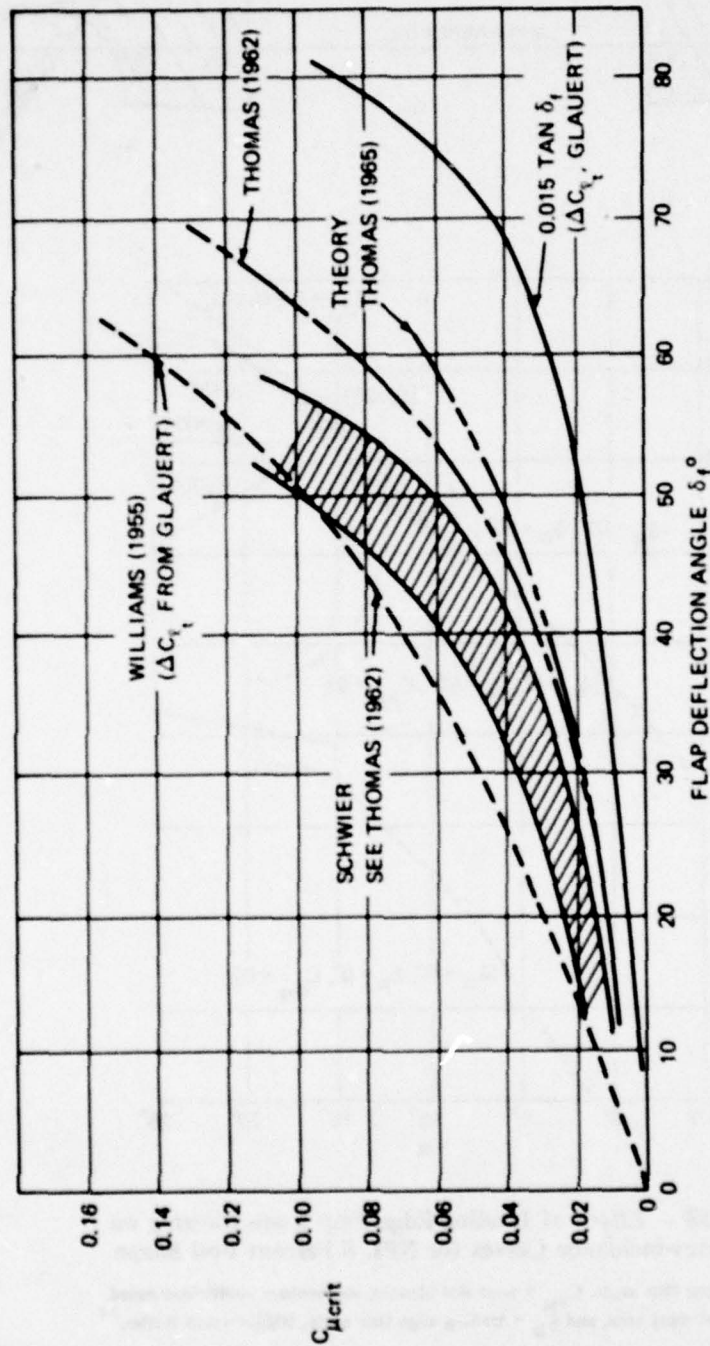


Figure 39 - Variation of $C_{\mu \text{ crit}}$ with Flap Angle, Two-Dimensional Results
Some experimental and theoretical values of $C_{\mu \text{ crit}}$, required to achieve theoretical flap effectiveness.

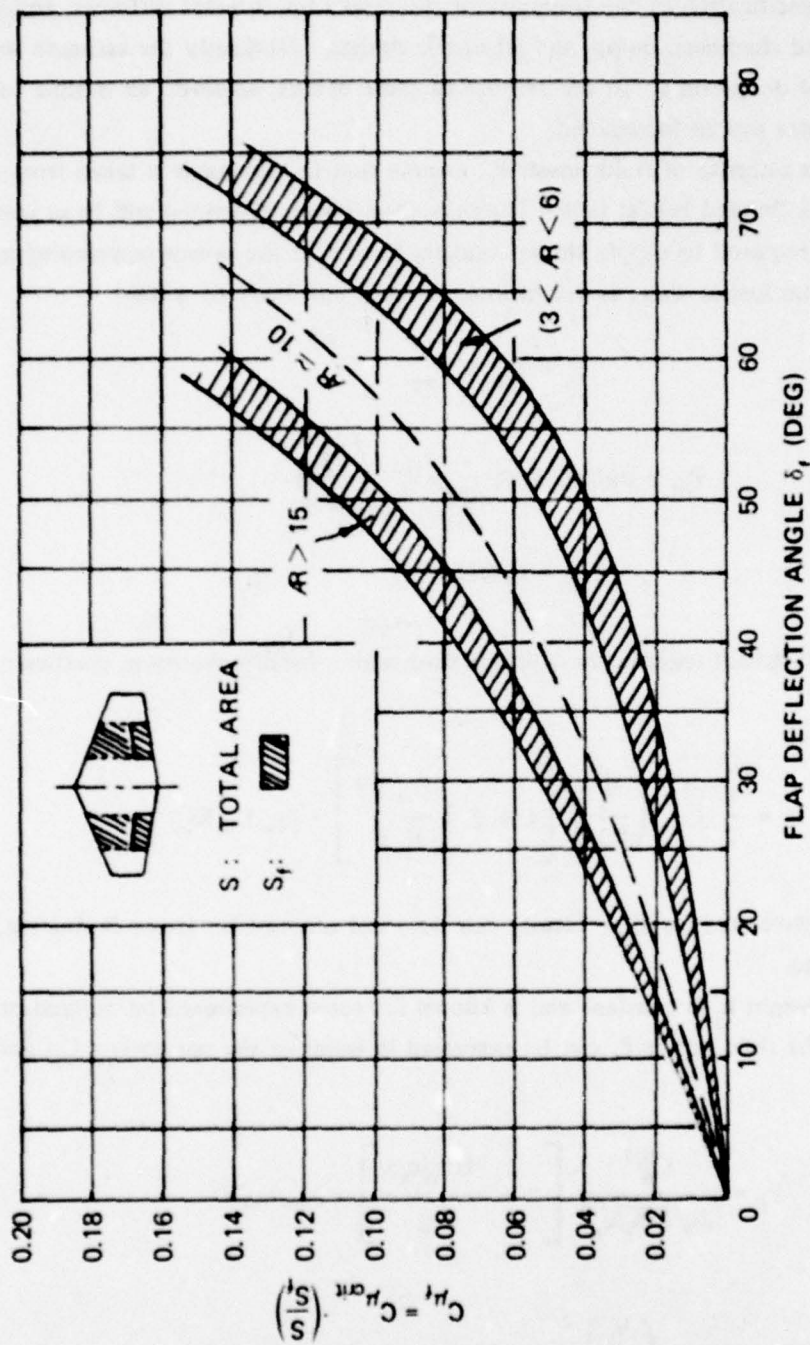


Figure 40 — Graph for Estimating C_{μ_f} as a Function of Flap Angle and Aspect Ratio,

Where $C_{\mu_f} = (\dot{m}_T V_f / q_{\infty} S_f)_{crit}$

H.R. Chaplin (DTMB Aero Rep 916, 1957)

Powering Requirements

An accurate estimate of power requirements for a particular blown-flap system would involve a detailed specification of the geometry of the intake lip, internal diffusers, and/or ducting from flooded chambers, pump, and jet-nozzle designs. Obviously the estimate would be applicable to that design only. In the absence of these details, however, an outline for some general estimates can be formulated.

For the crudest estimate of fluid power P_f , assume that the jet water is taken from a large reservoir, like a flooded ballast tank. Then the total power expended will be at least equal to the power required to supply the jet velocity head plus the power represented in the intake momentum loss as water is drawn into the large still body of water

$$P_f = P_{jet} + P_{ram}$$

where

$$P_{jet} = \rho g (\Delta H) Q \cong \frac{1}{2} \rho V_j^2 \left(\frac{\dot{m}_T}{\rho} \right) \quad (22)$$

$$P_{ram} = (\rho Q U_\infty) U_\infty$$

Hence, the power (ft-lb/sec) required to supply a flow with a total momentum coefficient $C_{\bar{\mu}}$ is

$$P_f = \frac{1}{2} C_{\bar{\mu}} \left(\frac{V_j}{U_\infty} \right) \left[1 + 2 \left(\frac{U_\infty}{V_j} \right)^2 \right] \cdot (q_\infty U_\infty S) \quad (23)$$

where S is the reference area for $C_{\bar{\mu}}$. Clearly this does not account for losses in ducting, diffusers, nozzles, etc.

If the jet slot height h_j is constant and is known for some experiment on tapered or rectangular wings, the fluid power P_f can be expressed in terms of the parameters $C_{\bar{\mu}}$ and h_j/c_a

$$P_f = \frac{C_{\bar{\mu}}^{3/2}}{2\sqrt{2}(h_j/c_a)} \left[1 + \frac{4(h_j/c_a)}{C_{\bar{\mu}}} \right] \cdot (q_\infty U_\infty S) \quad (24)$$

using the relation $C_{\bar{\mu}} = 2(h/c_a) \left(\frac{V_j}{U_\infty} \right)^2$, where c_a = average chord = $(c_{root} + c_{tip})/2$.

Sample values of lift-augmentation horsepower-per-foot in Table 3 were obtained for the various slot-blowing devices using Equations (23) or (24).

DISCUSSION: For application to submarine control, the general concept of a blown flap has several advantages when compared to other powered devices. It is mechanically relatively simple, requiring only ducting and valve-actuation for its operation. The flap size could be chosen to provide adequate performance without blowing at high forward speed; powered operation at low submarine speeds could provide a very wide range of available control force depending on the amount of blowing. The blown flap would offer a type of control-system redundancy; if there is a fluid pumping system failure, the flap could be used as a plain unpowered device, and vice versa. Water normally exhausted from the ship could be ducted into a high-pressure plenum that would act as a supply for blowing. Owing to the usual thick sections of submarine control planes, it is reasonable to predict that blowing over a trailing-edge flap alone would be sufficient to obtain significant lift improvement. Of course, leading-edge devices always improve performance and should not be totally ruled out.

The physical effect of boundary layer control by slot blowing over a deflected flap dictates that the jet sheet must be issued into a region of *adverse* pressure gradient; see Figure 25. This means, for example, that blowing at the underside of a flap knee into a favorable pressure gradient is useless at best and may degrade the overall performance. For submarine applications, lift is required in either direction, so a valving system is necessary to coordinate proper slot blowing with flap deflection.

One measure of purely hydrodynamic performance is the equivalent lift-to-drag ratio, where the equivalent drag is defined in Equation (18). Based on curves of two-dimensional equivalent lift-to-drag ratio versus lift coefficient assembled in Figure 1, the blown flap is one of the most attractive high-lift schemes of all those considered. The performance of blown flaps on the basis of lift augmentation $\Delta C_l / \Delta C_{\mu}$ is impressive. For example, from the results with the 13-percent blown-flap foil in Figure 31a, for the case when ΔC_l is measured from $C_{\mu} = 0$ and $\delta_R = 20$ degrees, $\Delta C_l / \Delta C_{\mu} = 62$ in the BLC regime and $\Delta C_l / \Delta C_{\mu} \approx 17$ to 5 in the supercirculation regime. For the case when ΔC_l is measured from $C_{\mu} = 0$ and $\delta_R = 0$, $\Delta C_l / \Delta C_{\mu} = 146$ in the BLC regime, for $\Delta C_l = 1.17$.

Some problem areas include: possible fouling of the narrow slits, possible noise from the high-speed jet sheets, the need for a practical valving system, and limitations due to cavitation—about which little is known.

JET FLAPS

The term jet flap is sometimes used to describe a wide variety of powered trailing-edge devices, including the blown flap discussed in the previous section; see Reference 21. However, as used here, jet flap refers specifically to a blowing lifting surface where a high-momentum

jet sheet issues out of or near the trailing edge at an angle to the foil chord. Because of its high momentum, the curved jet sheet achieves a stiffness which enables it to cause an asymmetrical flow pattern that provides an additional pressure lift, called supercirculation, on the wing. This jet-induced circulation lift magnifies the direct lift produced by the vertical component of the jet momentum. One way to view the effect of the jet flap is in terms of the movements of the fluid stagnation points on the foil surface. The trailing edge stagnation point is fixed near the jet nozzle position, but the total flow asymmetry created by the curved jet sheet causes the forward stagnation point to migrate further and further aft along the underside of the foil with increasing jet momentum. This, in turn, causes an augmented pressure jump across the foil and greater lift.

There are various ways to direct the jet sheet flow: blowing through fixed or variable slots, blowing out over variable angle control flaps, or blowing out through a Coanda-type nozzle. The mechanical flaps or nozzles included in this category are jet-control devices with small-flap chord ratios, less than 20 percent. The effect of flow control in this case is principally supercirculation. Figure 41 shows some of the schemes for jet-flap blowing. The references by Poisson-Quinton and Lepage,²⁰ Korbacher and Sridhar,²¹ Lopez et al.,²³ McCormick,³ and Lissaman³⁹ have been useful for general discussions about jet flaps.

Force Estimates

Lift: Two-Dimensional. A jet-flap geometry, employing slot blowing over a jet-control flap, ($c_f/c < 0.2$) is pictured in Figure 26a. The same definition for C_μ in Equation (9) applies here. The section lift coefficient C_{l_α} as given by Equation (10) can be estimated using the interpolation formulas³³

$$C_{l_\alpha} = 2\pi (1 + 0.151 \sqrt{C_\mu} + 0.219 C_\mu) \quad (25)$$

$$C_{l_\delta} = 2 \sqrt{\pi} C_\mu^{1/2} [1 + 0.151 \sqrt{C_\mu} + 0.139 C_\mu]^{1/2} \quad (26)$$

where δ (or δ_j) is the jet angle measured from foil chord line. Note that for small C_μ and at zero angle of attack, the theoretical section lift coefficient is

$$C_{l_\alpha} \cong 3.54 \sqrt{C_\mu} (1 + t/c) \delta \quad (27)$$

so that the usual lift increment ΔC_{l_α} (at fixed α) is also given by the same expression. As indicated in Figure 42, the slot geometry of jet flaps is important. In this comparison, the largest ΔC_{l_α} is achieved when the jet sheet is blown out through a Coanda nozzle-control flap, especially for the case of blowing over the upper surface.

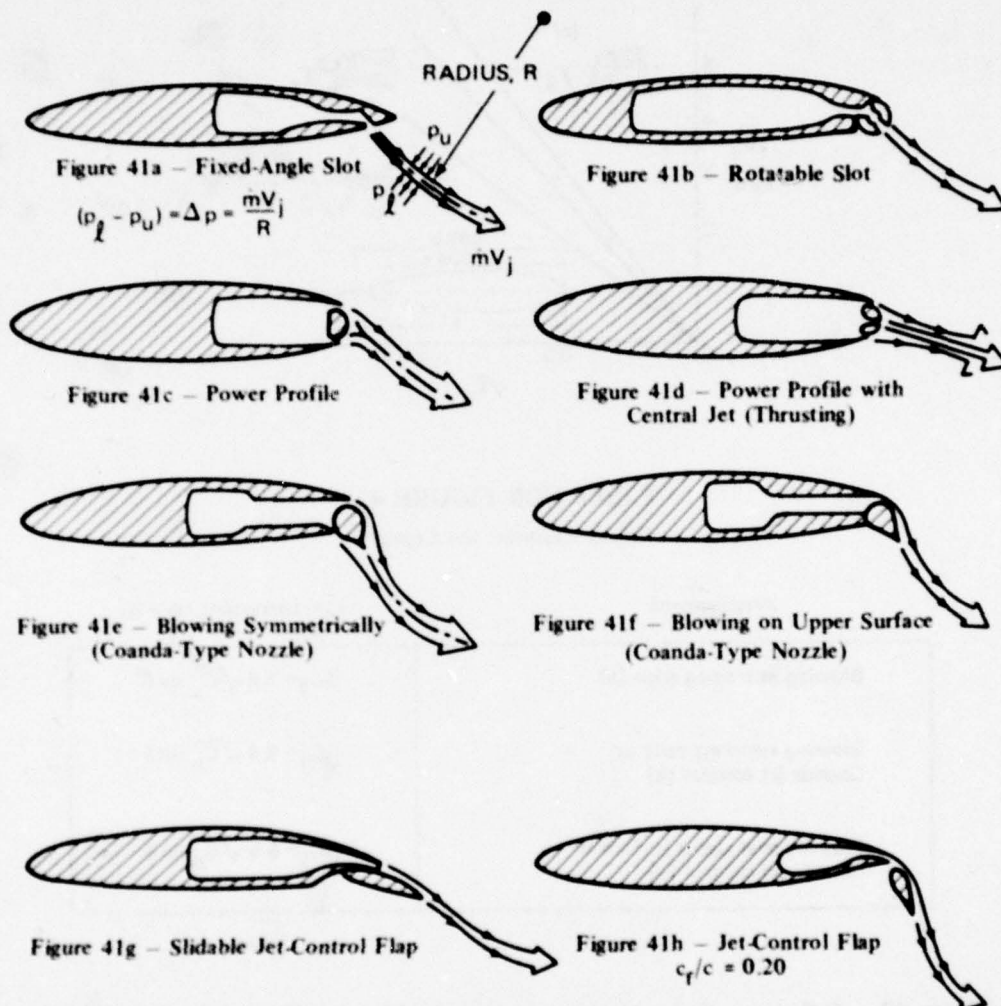


Figure 41 – Some Jet-Flap Arrangements

The curving jet boundary shape is determined by a balance between pressure and centrifugal forces. The pressure jump across the thin jet is given in Figure 41a. Fluid mechanically, the jet has the same effect as a curved vortex sheet extending far downstream.

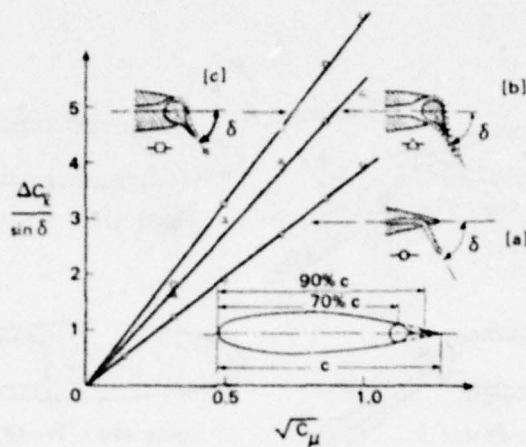


TABLE FOR FIGURE 42

Poisson-Quinton and Lepage²⁰

Arrangement	Lift Increment ($\alpha = 0$)
Blowing at trailing edge [a]	$\Delta C_L = 3.9 \sqrt{C_\mu} \sin \delta$
Blowing symmetrically on Coanda jet control [b]	$\Delta C_L = 5.4 \sqrt{C_\mu} \sin \delta$
Blowing over upper surface of Coanda jet control [c]	$\Delta C_L = 6.5 \sqrt{C_\mu} \sin \delta$

Figure 42 – Influence of the Arrangement of the Blowing Slot at the Trailing Edge for Two-Dimensional Flow

Data for NACA 0018 section shape with trailing-edge slot, truncated to accommodate Coanda-nozzle for cases [b] and [c].

The "power profile" shown in Figures 41c and 41d is a recent jet-flap foil developed by Smith and Thelander.⁴⁰ The plug in the blunt trailing edge is used to adjust the relative sizes of the upper and lower blowing slots. The resulting jet sheet can be aimed as desired, with the jet momentum directed either downward for high lift or aftward for propulsion thrust. Test results in Reference 40 on a 22.5-percent-thick, two-jet foil at zero incidence indicate that when the lower slot is completely closed, for high-lift operation, the two-dimensional lift coefficient increases linearly with $\sqrt{C_{\mu}}$, with a slope $\Delta C_l / \sqrt{C_{\mu}} \approx 7.8$.

Some sample two-dimensional jet-flap data from water tunnel tests described by Franklin and Bailey⁴¹ are shown in Figure 43 for a 16-percent-thick elliptic foil section with jet angle $\delta_j = 90$ degrees. As indicated in the plot, the results of Franklin and Bailey agree well with earlier wind tunnel experimental results reported by N.A. Dimmock for a 12.5-percent thick elliptic section jet-flapped foil, also with $\delta_j = 90$ degrees.

Lift: Finite-Aspect Ratio. For a finite-aspect-ratio lifting surface, the total lift is also given by Equation (11) as the sum of circulatory lift plus jet-reaction lift, for small δ and α , as $C_L \approx C_{L\Gamma} + C_{\mu}(\alpha + \delta)$, where the circulatory lift is

$$C_{L\Gamma} = \left(1 + \frac{t}{c}\right) \left\{ F_A [K_{\alpha} \cdot C_{\alpha} \cdot \alpha + K_{\delta} C_{\delta} \delta] - C_{\mu}(\alpha + \delta) \right\} \quad (28)$$

where K_{α} and K_{δ} are partial span factors given in Equations (12) and (13). Again, from Equation (11), the factor $F_A(AR, C_{\mu})$ corrects for finite-aspect ratio, and a plot from McCormick³ is reproduced in Figure 44. Kerney⁴² has presented a lifting-line theory for F_A , valid for large AR , and gives a comparison with several other theories at selected AR values. For an elliptical planform with a full-span, elliptical, jet-momentum distribution the C_{μ} and C_{μ} are equal

$$C_{\mu}(s) = \frac{J(s)}{q_{\infty} c(s)} = \frac{\bar{J}}{q_{\infty} S} = C_{\mu} \quad (29)$$

where, in general, $C_{\mu} = (q_{\infty} S)^{-1} \int_{-b/2}^{b/2} J(s) ds$, and $J(s) = \dot{m}(s) V_j(s)$ is the jet-momentum distribution, and $c(s)$ is the spanwise chord variation.

The aspect-ratio factor $F_A(AR, C_{\mu})$ for untwisted rectangular planforms with large aspect ratio is found by Tokuda⁴³ to be

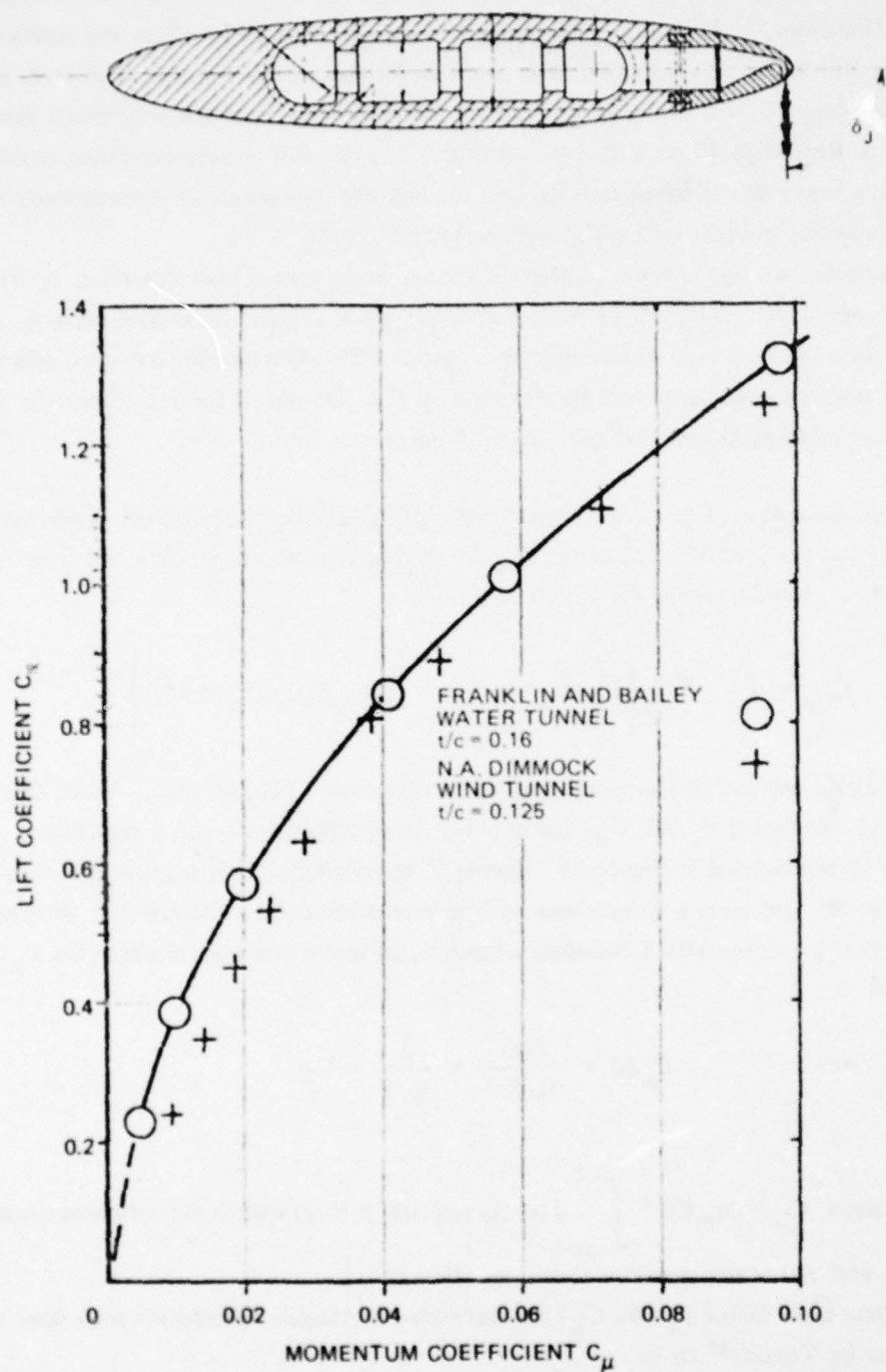


Figure 43 — Sample Two-Dimensional Lift Data for a Jet-Flapped 16-Percent-Thick Elliptical Section Shape

Incidence angle $\alpha \approx -0.15^\circ$, jet angle $\delta_J = 90^\circ$; these data are for noncavitating flow. Franklin and Bailey.⁴¹

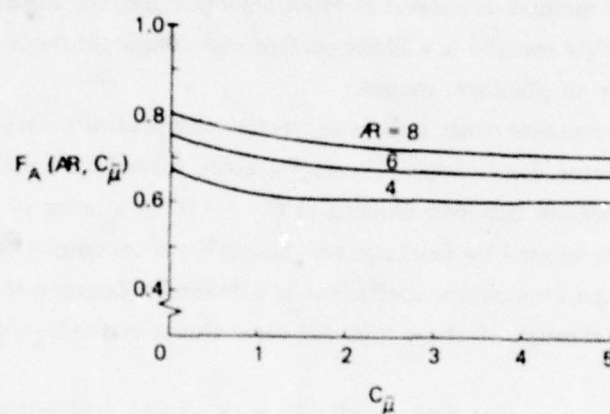


Figure 44 — Approximate Finite-Aspect-Ratio
Factor for Jet-Flapped Wings, Large AR
for Elliptic Loading
McCormick³

$$F_A(AR, C_{\mu}) = \frac{1}{1 + \left[\log_{10} \frac{8AR}{(C_{\mu})} + 1.577 \right] \frac{(C_{\mu})}{4\pi AR}} \quad (30)$$

where the lift curve slope C_{μ} is given in Equation 25.

Lissaman³⁹ presents a method for treating arbitrary geometry, high-aspect-ratio, jet-flapped wings, including thickness effects.

Figure 45, taken from Reference 44 shows curves of the total derivatives $(\partial C_L / \partial \alpha)$ and $(\partial C_L / \partial \delta_j)$ versus C_{μ} for an elliptical planform wing with $AR = 6.8$. The plots also show that there is good agreement between the theories of Maskell and Spence³⁷ and the elementary vortex distribution (EVD) method developed at McDonnell-Douglas; see Lopez and Shen⁴⁴ and Lopez et al.²³ The EVD method is a lifting-surface computational model which can be extended to a great variety of planform shapes.

For application to submarine control surfaces, rectangular planform shapes are typical. To predict their performances, for example, Figure 46, taken from Lopez and Shen,⁴⁴ shows total lift derivatives for uniform full-span blowing at $C_{\mu} = 1.0$ for a range of aspect ratios.

The jet-flap theory developed by Erickson and Kaskel⁴⁵ for rectangular planforms with an elliptic distribution of jet-momentum coefficient is specifically designed to include low aspect ratios. Figures 47 through 49 show total lift-curve slopes versus C_{μ} for a range of interesting aspect ratios.

There are several references that deal specifically with jet-flap applications in water. Franklin and Bailey⁴¹ show results for a 16-percent-thick jet-flapped elliptical section obtained in a water tunnel. Experiments were conducted under both noncavitating and cavitating conditions, so that some preliminary idea of the variation of the lift and drag of slot-blown foil performance versus cavitation number can be gained from their work.

Kaplan and Lehman⁴⁶ present data from water tunnel experiments with jet-flapped, rectangular foils with both steady and oscillating jet angle δ_j . The V_j/U_{∞} ratios considered in Reference 46 are low compared to the usual values found in experiments with air.

Verhagen⁴⁷ presents lift, drag, and moment data from experiments with a rectangular planform jet-flapped rudder tested in a towing tank. The foil is equipped with a Coanda-nozzle jet-control flap with $c_f/c = 0.0776$, and it is shown that for fixed α and δ_f , the lift increment due to blowing is $\Delta C_L = 2.5 \sqrt{C_{\mu}} \sin \delta_f$, so that $\partial C_L / \partial \delta_f = 2.5 \sqrt{C_{\mu}}$.

Williams and Alexander⁴⁸ present some wind tunnel data for a rectangular planform, aspect ratio 2.75, jet-flapped wing with an uncambered 12.5-percent-thick elliptic section. The overall lift coefficient for arbitrary δ_j and α is

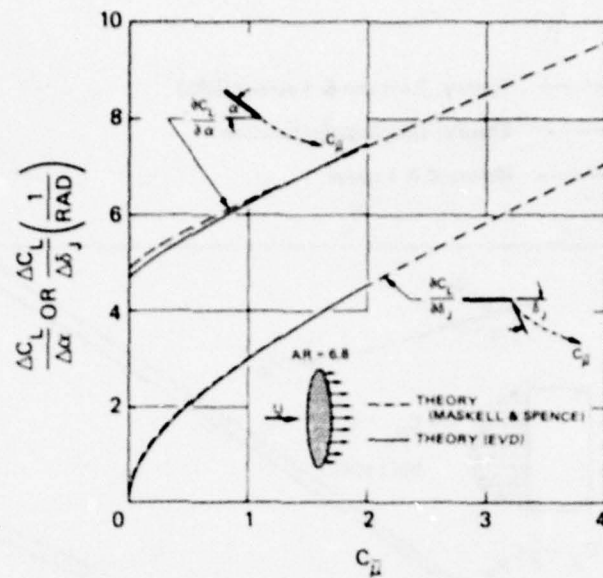


Figure 45 - Comparison of Lift Derived by the Elementary Vortex Distribution Method and the Maskell and Spence Method for a Jet-Flapped Wing with an Elliptical Planform and an Elliptical Jet-Momentum Distribution

Lopez and Shen⁴⁴

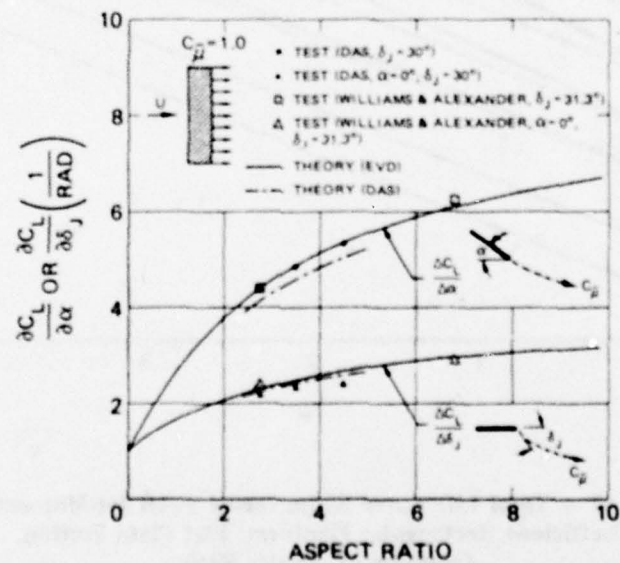


Figure 46 - Comparison of Theoretical and Experimental Lift for Jet Flapped Wings with a Rectangular Planform and Uniform Full Span Blowing, $C_{\mu} = 1.0$

Lopez and Shen⁴⁴

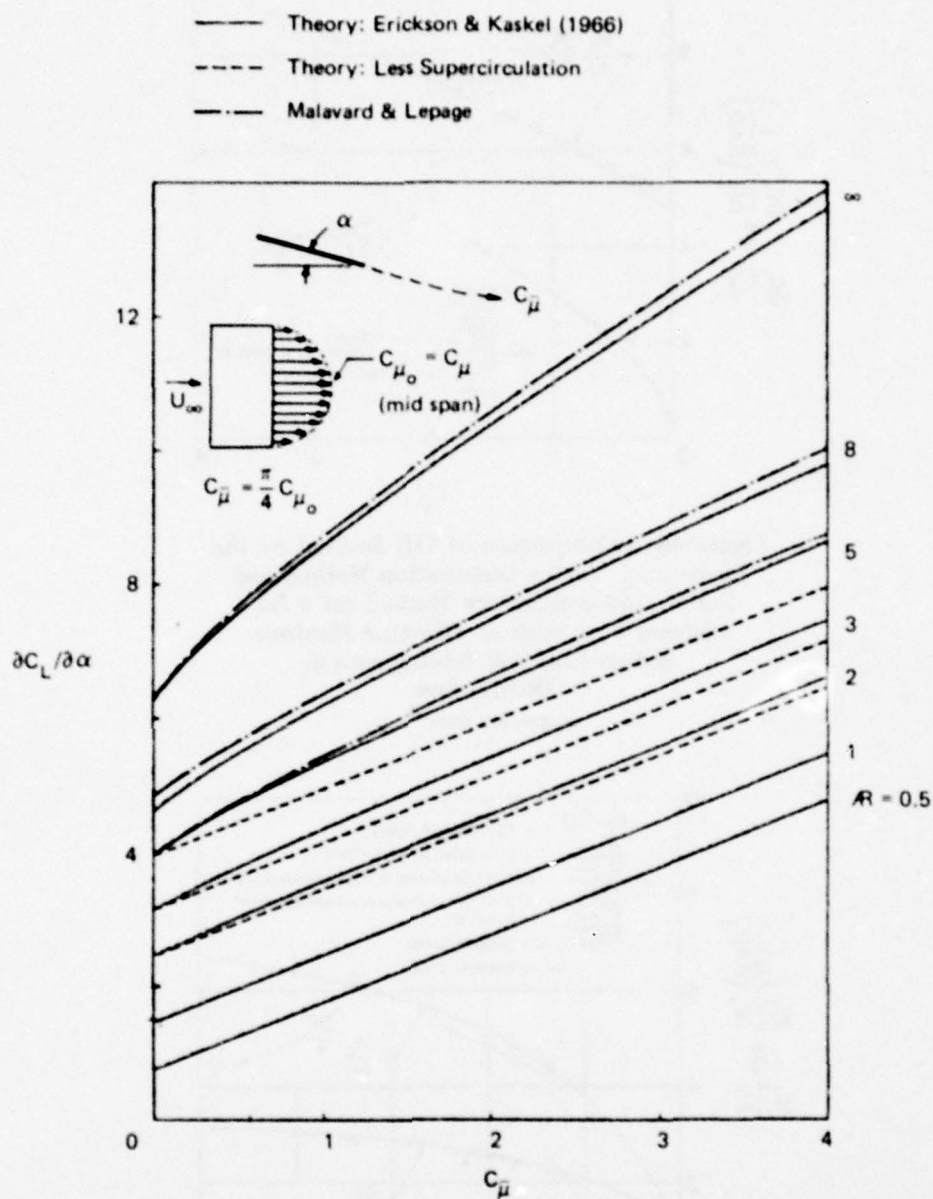


Figure 47 – Total Lift Curve Slope versus Total Jet-Momentum
 Coefficient Rectangular Planform, Flat Plate Section,
 Contours of Aspect Ratio
 Erickson and Kaskel⁴⁵

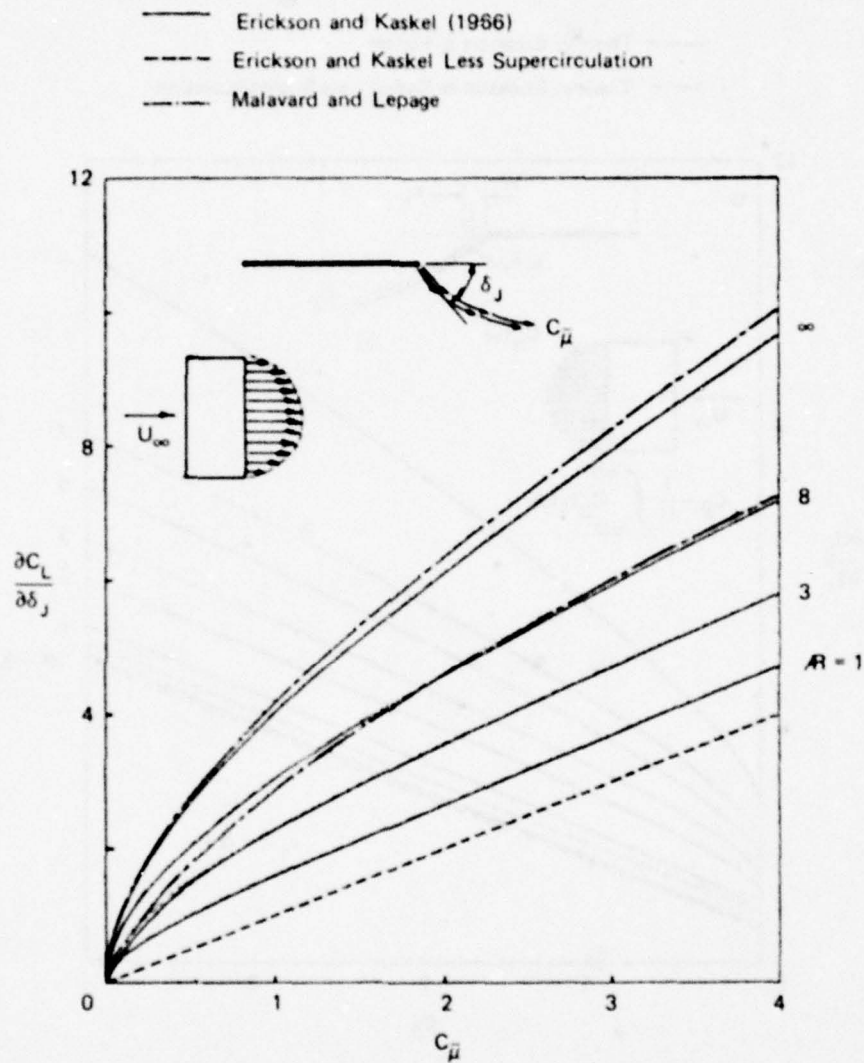


Figure 48 – Total Lift-Curve Slope versus Total Jet Momentum Coefficient
 Rectangular planform, flat plate, with jet blowing at trailing edge at angle δ_J to free stream
 contours of aspect ratio, Erickson and Kaskel.⁴⁵

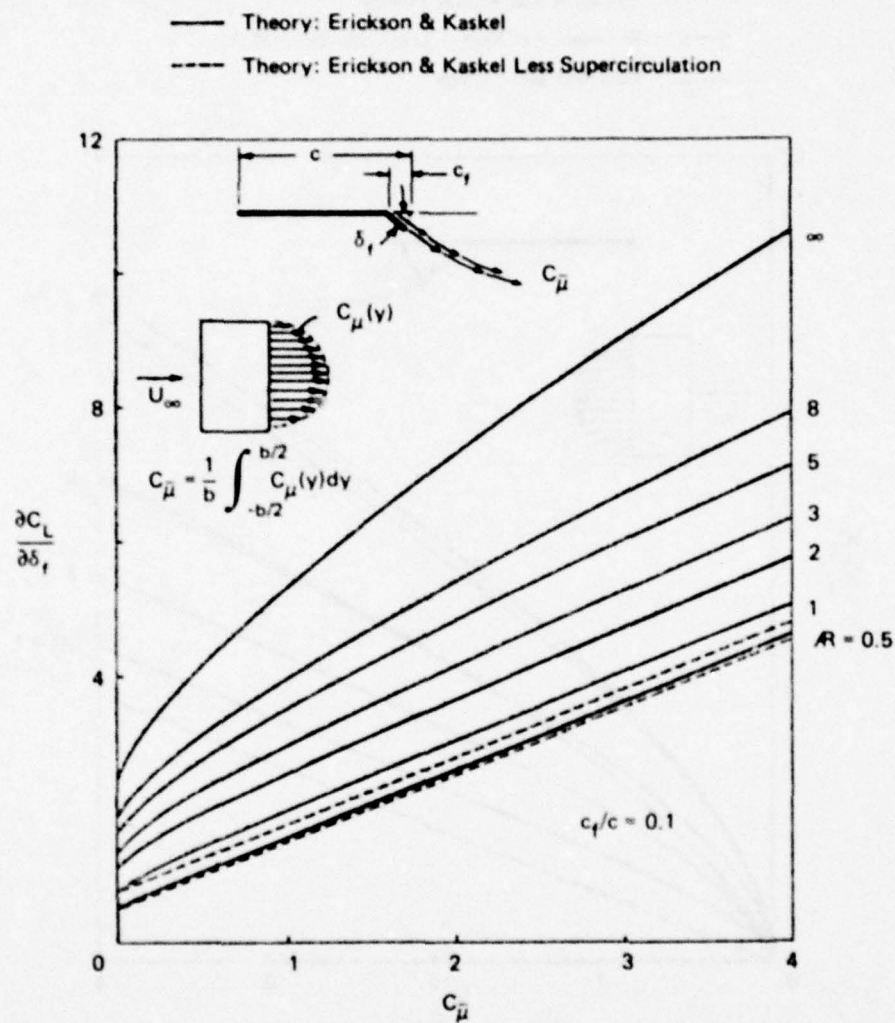


Figure 49 – Total Lift-Curve Slope versus Total Jet Momentum Coefficient
 Rectangular planform, flat plate, with deflected jet control flap ($c_f/c = 0.1$), contours of aspect ratio, Erickson and Kaskel.⁴⁵

$$C_L = C_{L_p} + C_J \sin(\delta_J + \alpha) \quad (31)$$

where C_{L_p} is the pressure lift, also called circulatory lift, denoted $C_{L\Gamma}$ elsewhere; $C_J = C_{\bar{\mu}}$ is the total jet-momentum coefficient; $\delta_J = \text{jet angle} = 31.3^\circ$ for the results shown. A plot of total lift coefficient versus $\sqrt{C_J}$ is reproduced in Figure 50, showing the pressure and jet-reaction components.

English et al.⁴⁹ present extensive data from water tunnel experiments with an aspect ratio 1.42, rectangular planform, 18-percent-thick rudder. Tests were made with both a jet-flap arrangement and a blown trailing-edge-cylinder scheme.

Kaplan and Goodman⁵⁰ have considered the use of jet-flapped fins for ship pitch control, and they present some preliminary estimates on how to estimate the performance limited by cavitation.

Experiments and theoretical work by Das⁵¹⁻⁵³ have included jet-flap wings with rectangular straight and sweptback planforms having full and partial span blowing.

Lift: Limit on Circulatory Lift. As noted at the outset of this chapter on circulatory lift, for finite-aspect-ratio wings, there is a limit to the lift coefficient $C_{L\Gamma}$ due to circulation. The theoretically predicted maximum usually takes the form

$$\text{Small and Moderate AR:} \quad \left(C_{L\Gamma}\right)_{\max} = (K_\Gamma) \cdot \text{AR} \quad (32)$$

$$\text{Large AR (2D limit):} \quad \left(C_{L\Gamma}\right)_{\max} \rightarrow 2\pi(1 + t/c) \quad (33)$$

where K_Γ is a constant, depending in part on the planform loading, and t/c is the thickness-to-chord ratio. Estimates of the constant factor K_Γ range from 0.855 for a flat-trailing vortex sheet² to 1.94 for a rolled-up trailing vortex sheet.¹

The maximum is seldom realized in practice; however, the subject of $\left(C_{L\Gamma}\right)_{\max}$ is mentioned specifically in this section about *jet flaps* because extremely large circulations can, in fact, be achieved by very strenuous jet-flap blowing. Also, practical experimental evidence for highly loaded planforms is particularly available for jet-flap arrangements.

Of course, with jet-flap blowing, the jet-reaction lift can produce total lift coefficients much higher than the circulatory maximum. It is interesting that in actual experiments, the $C_{L\Gamma}$ value does reach an obvious plateau. For example, Figure 51 from Lowry and Vogler⁵⁴ shows how the $C_{L\Gamma}$ appears to have an experimental maximum of 10.5 for an aspect ratio 8.4, jet-flapped wing. This gives a value of the constant $K_\Gamma = 1.25$.

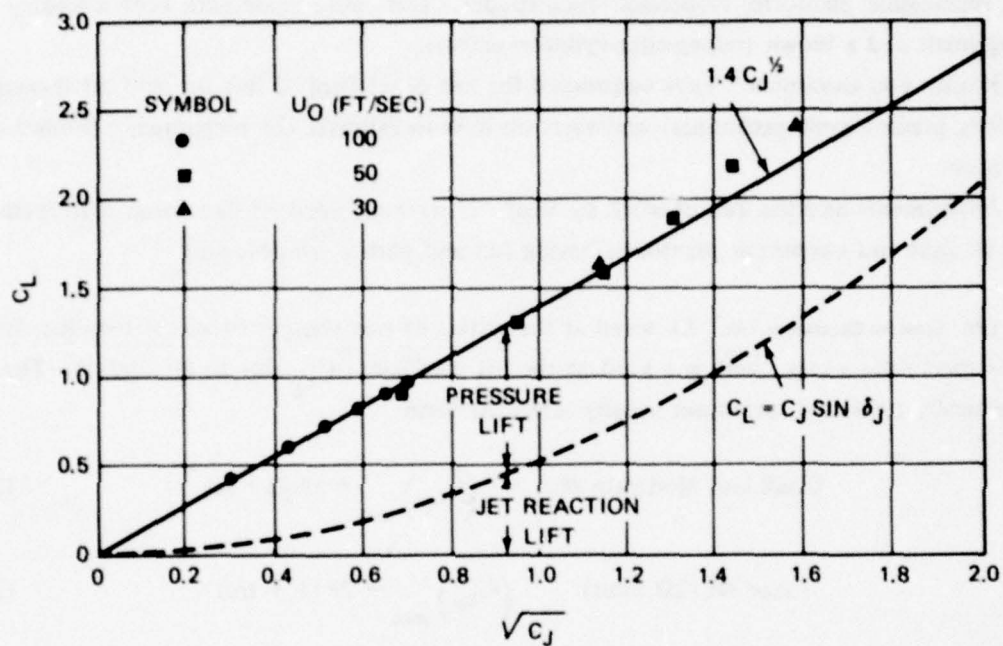


Figure 50 - Sample Data for the Lift Variation on a Rectangular Planform Jet-Flapped Wing, $AR \approx 2.75$

$\delta_J = 31.3$ degrees, 12-percent-thick elliptic section, at $\alpha = 0$, Williams and Alexander.⁴⁸

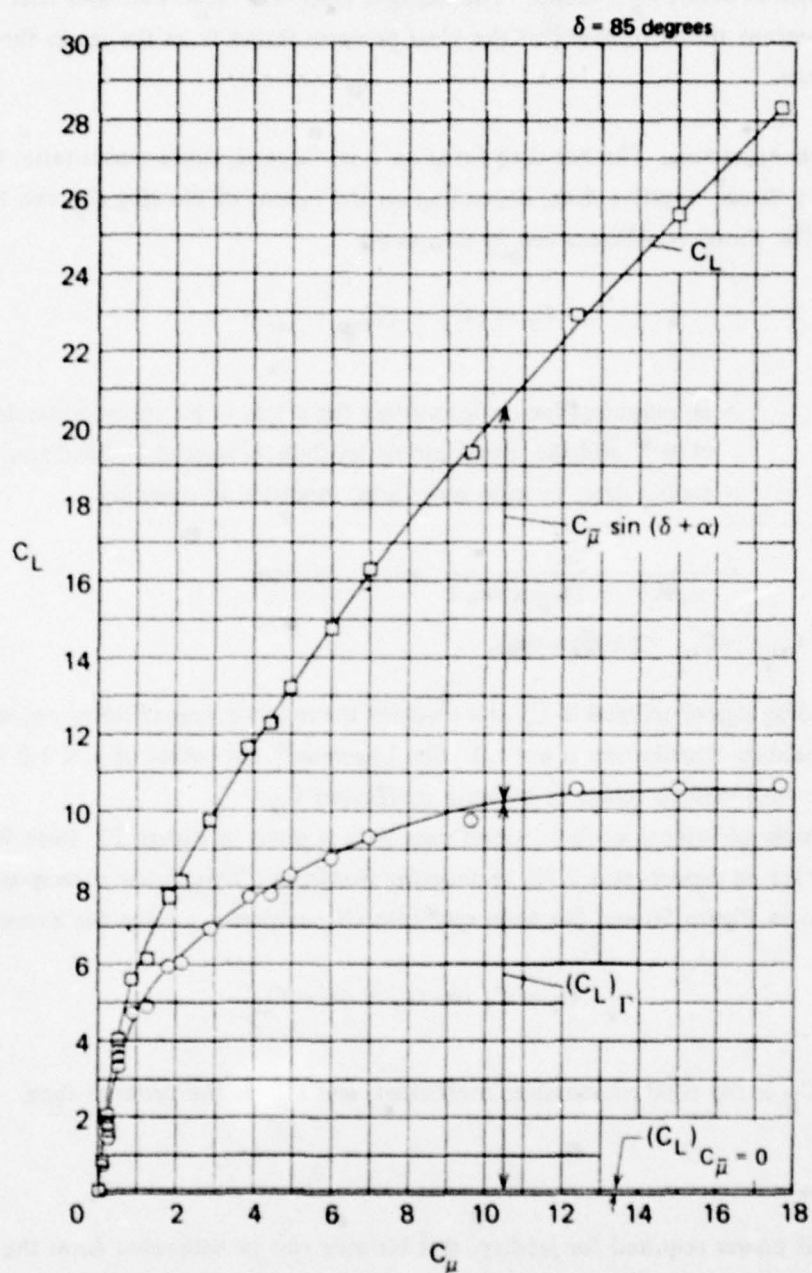
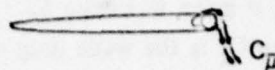


Figure 51 - Total Lift Coefficient for a Jet-Flapped Rectangular Lifting Surface, $AR = 8.4$

Tested at $\alpha = 0$, $\delta = 85$ degrees, maximum circulatory lift $(C_{L_\Gamma})_{\max} = 10.5$, Lowry and Vogler.⁵⁴

Drag: Two-Dimensional. An example of the variation of jet-flap section drag C_d versus blowing momentum coefficient C_{μ} is given in Figure 52. These data apply to the same 16-percent elliptic foil of Figure 43. Here C_d is the wake drag determined from a pitot survey, so that it includes the jet thrust. It can be seen that this two-dimensional jet-flap foil becomes a thrusting device at about $C_{\mu} = 0.035$. The negative slope of -0.40 indicates that there is about a 40 percent thrust recovery of the ideal pressure thrust from the jet in the case of $\delta_j = 90$ degrees.

Drag: Finite-Aspect Ratio. The net drag force on a jet-flapped, finite-aspect-ratio, lifting surface may be a thrust, negative drag, depending on the extent of blowing C_{μ} and the magnitude of the lift. The thrust coefficient can be expressed

$$C_T = r C_{\mu} - (C'_{D_p} + C_{D_i}) \quad (34)$$

where r = an empirical factor accounting for a loss in jet thrust; refer to Williams et al.³⁵ and the discussion of jet flaps presented by McCormick³

C'_{D_p} = profile drag, friction plus form, modified by blowing

$$C_{D_i} = \frac{C_L^2}{\pi AR [1 + 2C_{\mu}/\pi AR] e} = \text{induced drag} \quad (35)$$

$(C'_{D_p} + C_{D_i}) = C_{D_p}$ = pressure drag.

The induced drag is proportional to C_L^2 and contains the induced-drag efficiency e , which for elliptical circulation distribution is $e = 1.0$. See Lissaman³⁹ for values of $e < 1.0$ for rectangular planforms with various values of blowing coefficient C_{μ} .

An example of typical jet-flap-wing-thrust data is given in Figure 53, from Williams and Alexander,⁴⁸ for an aspect-ratio 2.75, rectangular planform. This thrust corresponds to the lift data given in Figure 50 and has been split into its components using the expression

$$C_T = C_J \cos(\delta_j + \alpha) - C_{D_p} \quad (36)$$

where $C_J = C_{\mu}$ is the total momentum coefficient, and C_{D_p} is the pressure drag.

Powering Requirements

The fluid power required for jet-flap, slot blowing can be estimated from the same expressions given in the discussion on slot blowing over mechanical flaps, i.e., Equations (23) and (24).

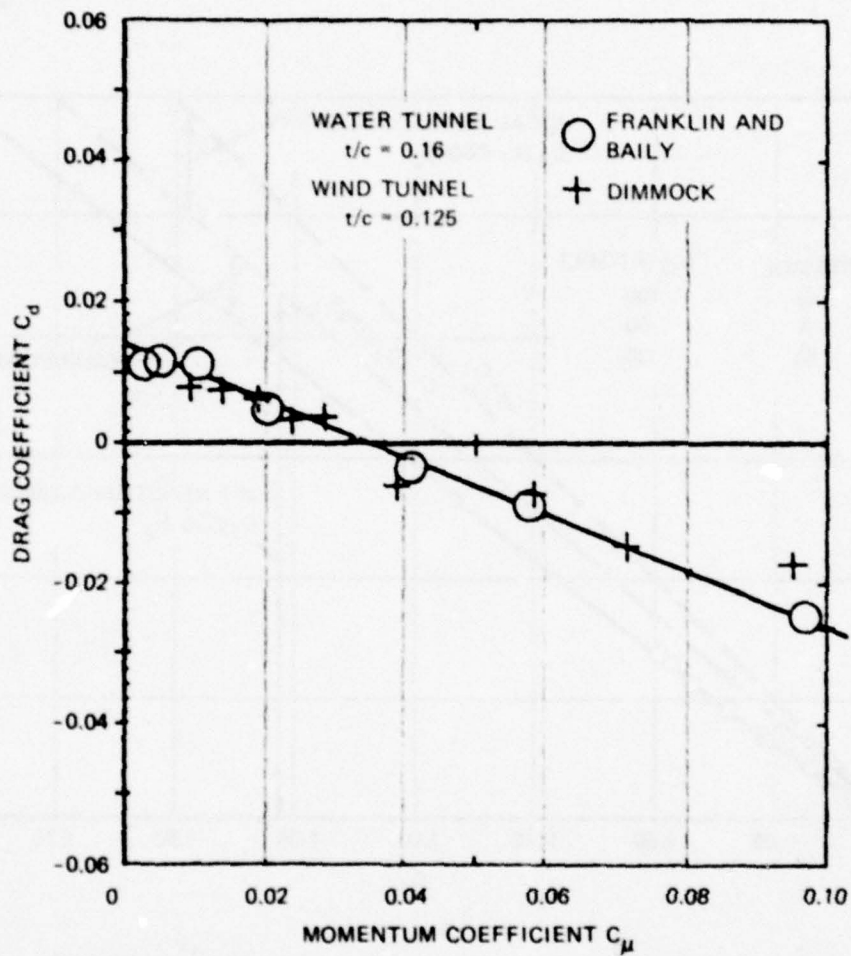


Figure 52 - Two-Dimensional Drag versus Jet Momentum Coefficient, Data for the Jet-Flapped 16-Percent-Thick Elliptical Shape of Figure 43
Incidence angle $\alpha = -0.15$ degrees jet angle $\delta_j = 90$ degrees, Franklin and Bailey.⁴¹

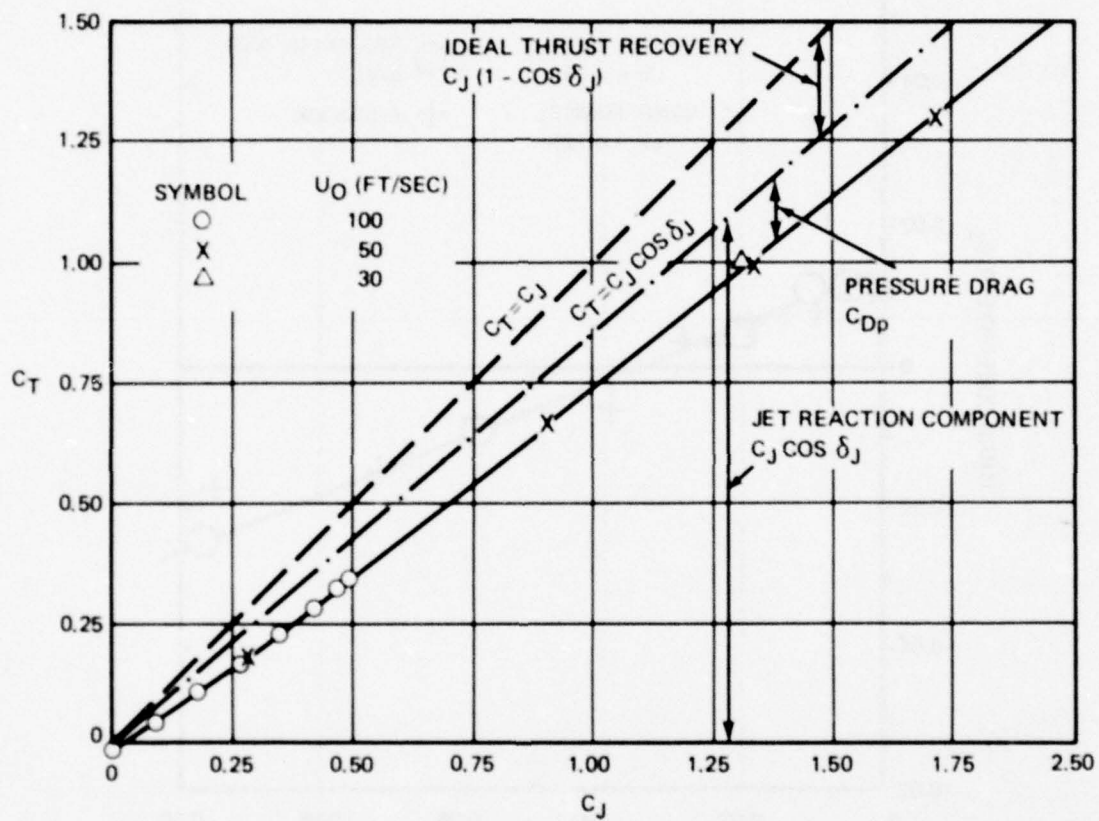


Figure 53 – Sample Total Thrust Data Corresponding to Jet-Flapped-Wing-Thrust Data of Figure 50

Variation of total thrust C_T versus C_J for rectangular planform $AR = 2.75$, $\alpha = 0^\circ$, $\delta_J = 31.3^\circ$, 12.5-percent-thick elliptic foil, Williams and Alexander.⁴⁸

DISCUSSION: General features of the jet-flap concept are that—

1. Lift can be produced independently of foil incidence. This could be of value for fine control purposes, where fluid valving would give a vernier adjustment of the force.
2. Lift falls off proportionally to $\sqrt{\dot{m}V_j} U_\infty$, instead of U_∞^2 , as it does with conventional flapped foils.
3. The relative hydrodynamic performance of jet flaps, based on equivalent lift-to-drag ratio is relatively poor as is seen in Figure 1. Also, the lift augmentation $\Delta C_l / \Delta C_{\mu}$ is low, e.g., ranging from ~ 5 to 0.3 for two-dimensional values deduced from the data of Williams and Alexander⁴⁸ for $\delta_j = 31.3$ degrees. For the jet-flapped foil data of Franklin and Bailey⁴¹ with $\delta_j = 90$ degrees, the lift augmentation is better, ranging from 28.5 to 7.8 at $C_{\mu} = 0.02$ and 0.1, respectively. The power profile described by Smith and Thelander⁴⁰ displays a range of two-dimensional lift augmentations in the high lift mode of $\Delta C_l / \Delta C_{\mu} \approx 8.3$ to 4 at $C_{\mu} = 0.16$ and 1.0, respectively.
4. The jet-flap wing typically has fairly good thrusting capability, compared to most other slot blowing schemes, since a good percentage of the blowing momentum $\dot{m}V_j$ is recovered as thrust. This would represent a significant force only for very heavy blowing $C_{\mu} \gtrsim 1.0$, which in turn could be achieved only with large power expenditure. Even though jet flaps are better thrusters than most other slot blowing concepts, their absolute thrust performance is inefficient; see Smith and Thelander.⁴⁰
5. From test results by Smith and Thelander,⁴⁰ the profile drag of blunt-based, two-slot foils such as the power profile can be significantly reduced by bleeding fluid out of the TE slots under ram pressure alone. This type of artificial streamlining is important for slot-blown CC foils too; see the next subsection.

For application to vehicle control, the jet flap would be relatively simple mechanically, provided that no incidence-angle capability were required for the foil. Then, failure of the jet-pumping system would render the control useless. If the foils could rotate, too, the structural problems would be more complex; however, there would be a redundancy in the force-producing capability.

Valving schemes for jet flaps for producing lift in either direction have been studied to some extent by English et al.⁴⁹

CIRCULATION CONTROL BY TANGENTIAL SLOT BLOWING

Circulation control (CC) by tangential slot blowing is a technique for obtaining high-efficiency-high-lift performance by manipulation of the separation point of the flow near the rear of a foil shape having a rounded trailing edge.

For typical airfoil shapes, the *sharp trailing edge* is the critical feature that positions the aft stagnation point. In potential flow analysis of airfoil flows, the Kutta-Joukowski condition is always applied at the trailing edge. However, if the foil shape has a bluff trailing edge, there is ambiguity in the 2D potential flow model as to the location of the rear stagnation point as well as the circulation strength. The basic method of circulation control is to eject a thin sheet of fluid tangentially over the end of a thick foil section. Owing to the Coanda effect, the jet sheet tends to adhere to the rounded surface until it reaches around to the underside. The angular extent of the jet turning is governed mainly by the jet momentum; jet-sheet detachment corresponds to the rear stagnation point. Thus, the effective trailing edge and the circulation strength of a CC foil are determined by blowing momentum instead of the location of a physical sharp edge. One of the appealing features of this technique of flow control is that large lift coefficients can be achieved with relatively little blowing.

Figure 54 shows several variations of lifting sections that have been used for CC foils.

Useful source material on this concept can be found, for example, in the references by Kind and Maull,⁵⁵ Dunham,⁵⁶ Williams,⁵⁷ and Williams and Rogers,⁵⁸ and Englar.*

Force Estimates

Lift: Two-Dimensional. An elliptical foil section is shown in Figure 55 with a specified angle of attack α and specified position of the rear stagnation point given by an angle γ . If t/c is the thickness-to-chord ratio, then it can be shown that the potential flow section lift coefficient is

$$C_L = 2\pi(1 + t/c) \sin \left(\alpha + \frac{c}{t} \gamma \right) \quad (37)$$

and thus the lift derivatives are

$$\partial C_L / \partial \alpha = 2\pi(1 + t/c) \cos \left(\alpha + \frac{c}{t} \gamma \right) \quad (38)$$

$$\partial C_L / \partial \gamma = 2\pi \left(\frac{c}{t} \right) (1 + t/c) \cos \left(\alpha + \frac{c}{t} \gamma \right) \quad (39)$$

For a 25-percent-thick section, the lift curve slopes at small α and γ are $(\partial C_L / \partial \alpha) = 10\pi/4 = 7.86$, and $(\partial C_L / \partial \gamma) = 10\pi = 31.4$. This shows that to achieve increased lift, changing the rear stagnation angle γ is four times as effective per degree as changing the angle of attack in this case. For the 25-percent-thick foil at zero incidence ($\alpha = 0$), if the stagnation point is deflected by the amount, $\gamma = 5^\circ$, a theoretical section lift coefficient of 2.69 is produced.

*NSRDC Technical Note AL-182 (1970).

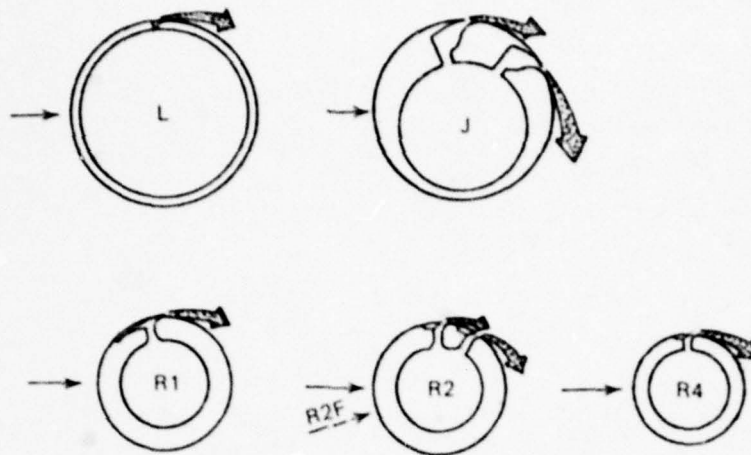


Figure 54a - Blown Slot(s) on Circular Cylinders

Dunham⁵⁶ and Cheeseman and Seed.⁶⁰

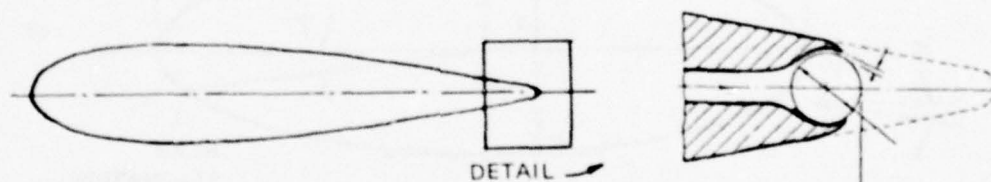


Figure 54b - Blown Trailing-Edge Cylinder on a Rudder

English et al.⁴⁹

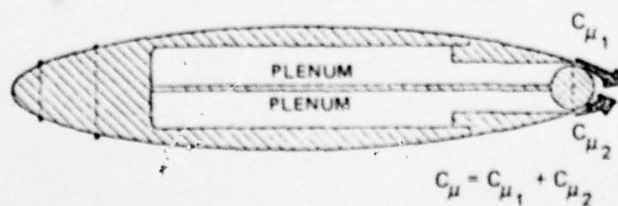


Figure 54c - Two Blown Slots on an Elliptical Foil Shape with a Rounded Trailing Edge

Kind and Maull.⁵⁵

Figure 54 - Circulation-Control Foils with Tangential Blowing Slots

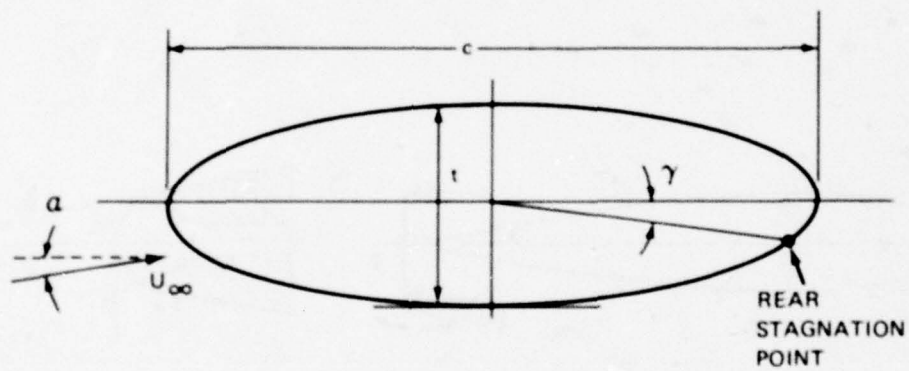


Figure 55 – Elliptic Foil Section

Of course this simple analysis neglects completely any real fluid effects such as leading-edge or suction-face separation. In general these effects degrade the lift performance. A schematic of the real flow is shown in Figure 56.

The jet sheet is issued from the aft-aimed slot with the momentum flux $\dot{m}V_j$ and the section momentum coefficient is defined in the usual way

$$C_\mu = \dot{m}V_j/q_\infty c \quad (40)$$

Unfortunately, the relationship between the amount of blowing C_μ and the effective angle γ involves a boundary layer problem of great complexity. It is too difficult for reliable prediction by present methods. Hence the variation of C_ℓ and $(\partial C_\ell / \partial C_\mu)$ versus C_μ must be determined by experiment.

The range of C_μ -values normally required for effective results by tangential jet blowing are mostly in the range of $(0 \leq C_\mu \leq 0.25)$. For example, Kind and Maull⁵⁵ restrict their interest to the range $0 \leq C_\mu \leq 0.1$. This means that the jet flows typical of this form of CC are almost never strong enough to provide a jet-flap effect of the type discussed in the previous section.

For reference, some example data for the section lift characteristics of the particular CC foil shown in Figure 57 are given here. Figures 58 through 62 are reproduced from Englar* and show the lift performance of a 15-percent elliptical section with a round trailing edge, having a radius-to-chord ratio of 0.0403 and a tangential blowing slot of thickness h_j/c of 0.0013, located at $x/c = 0.96$. In Figure 59, it is seen that there is a steeply rising relationship between C_ℓ and C_μ . This is revealed further in the curves of lift augmentation $\Delta C_\ell / \Delta C_\mu$ versus C_μ given in Figure 60. For example, at zero incidence $\alpha = 0$, the lift augmentation starts out at approximately $\Delta C_\ell / \Delta C_\mu \approx 60$ and decreases to about 40 at $C_\ell = 2$.

It is interesting to note that the maximum values of lift augmentation occur at certain *negative* angles of attack. A distinctive property of CC foils is the ability to generate high positive lift efficiently at negative incidence. Thicker CC foils also show this effect; see R.J. Englar.**

Detailed section lift data for elliptical sections can be found for example in the references by Osborn and Kettly⁵⁹ and in work at the Center by R.J. Englar,**,*** and by

*NSRDC Technical Note AL-211 (1971).

**NSRDC Technical Note AL-201 (1972).

***NSRDC Technical Note AL-182 (1970).

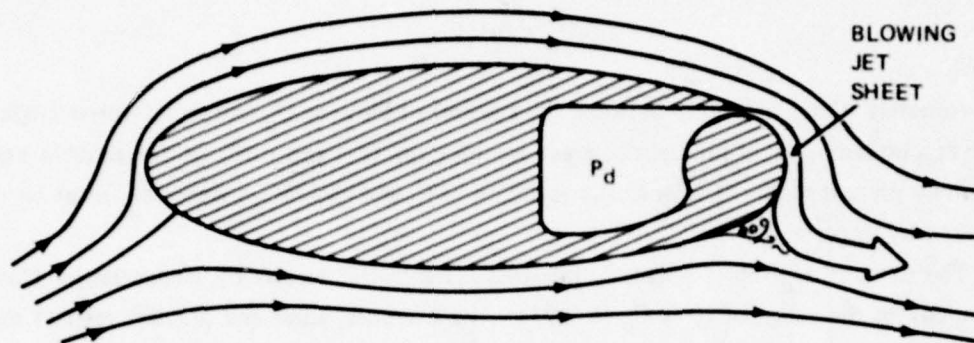


Figure 56 - Flow about an Elliptic Circulation-Control Foil with a Rounded Trailing Edge

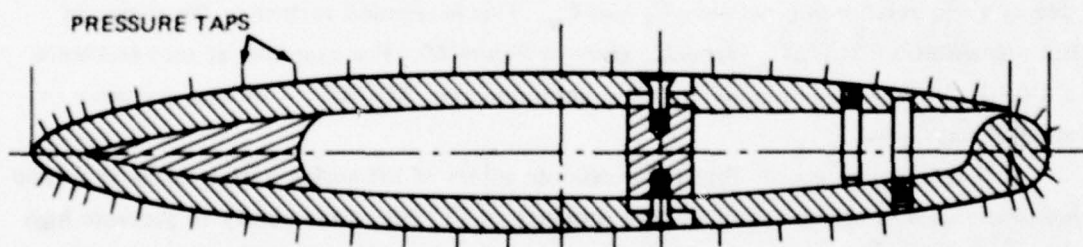


Figure 57 - Model Geometry of a 15-Percent-Thick Elliptic Circulation-Control Foil with a Rounded Trailing Edge

Data from tests with this foil are reproduced in Figures 58 through 60.

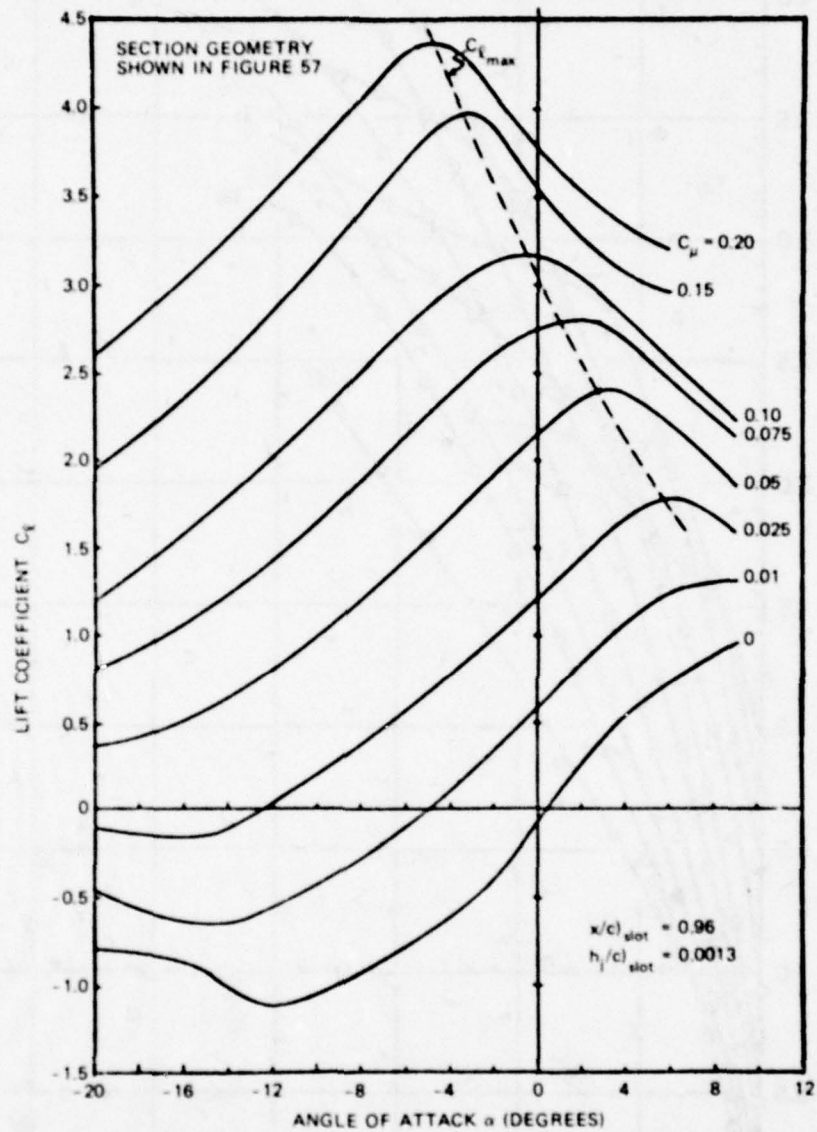


Figure 58 — Lift Variation versus Angle of Attack

Data for a rounded ellipse 15-percent-thick uncambered circulation-control foil, R.J. Englar.

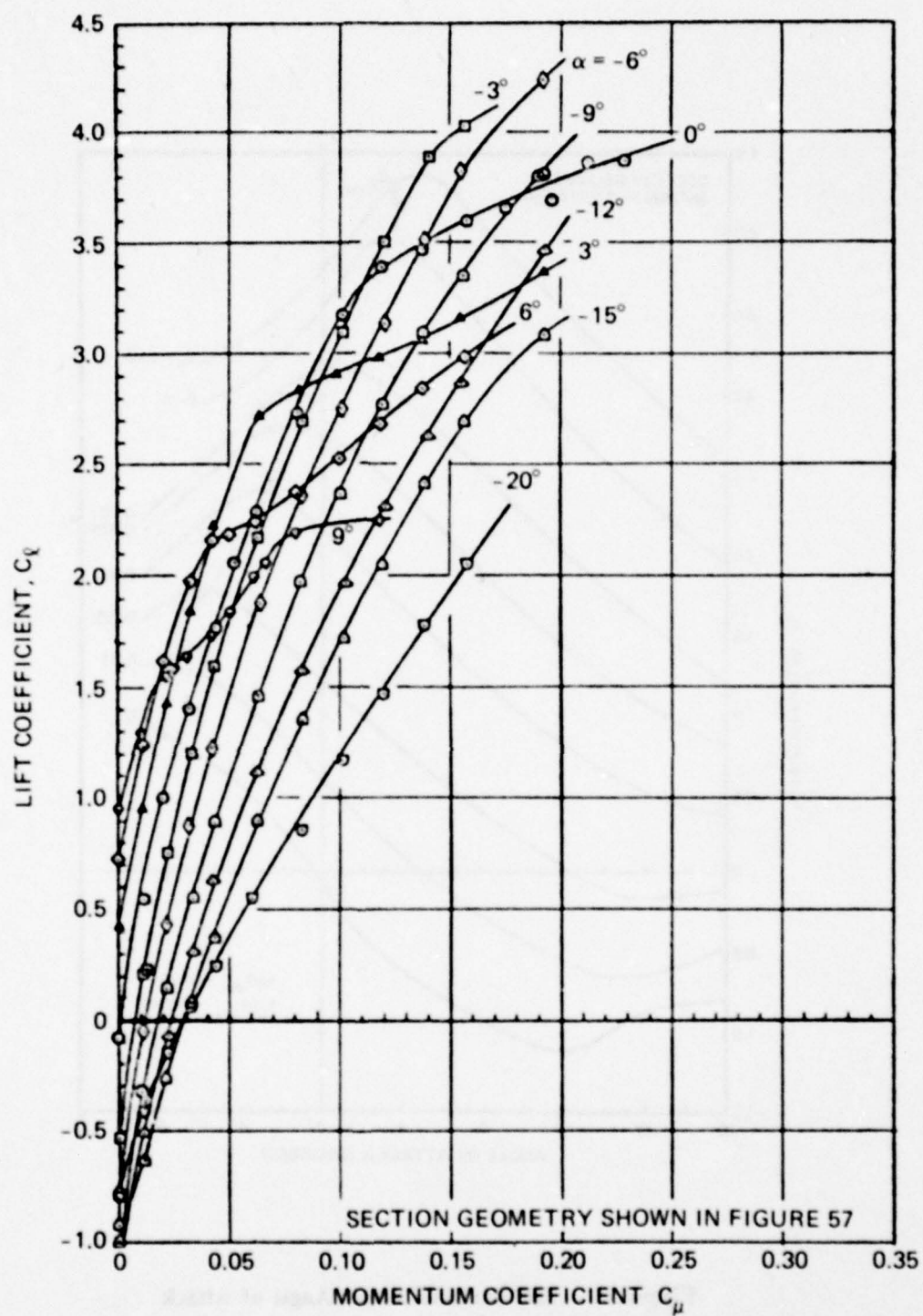


Figure 59 – Lift Variation versus Momentum Coefficient

Data for a rounded ellipse 15-percent-thick uncambered circulation-control foil: $h_j = 0.01$ inch, $h_j/c = 0.0013$, R.J. Englar.

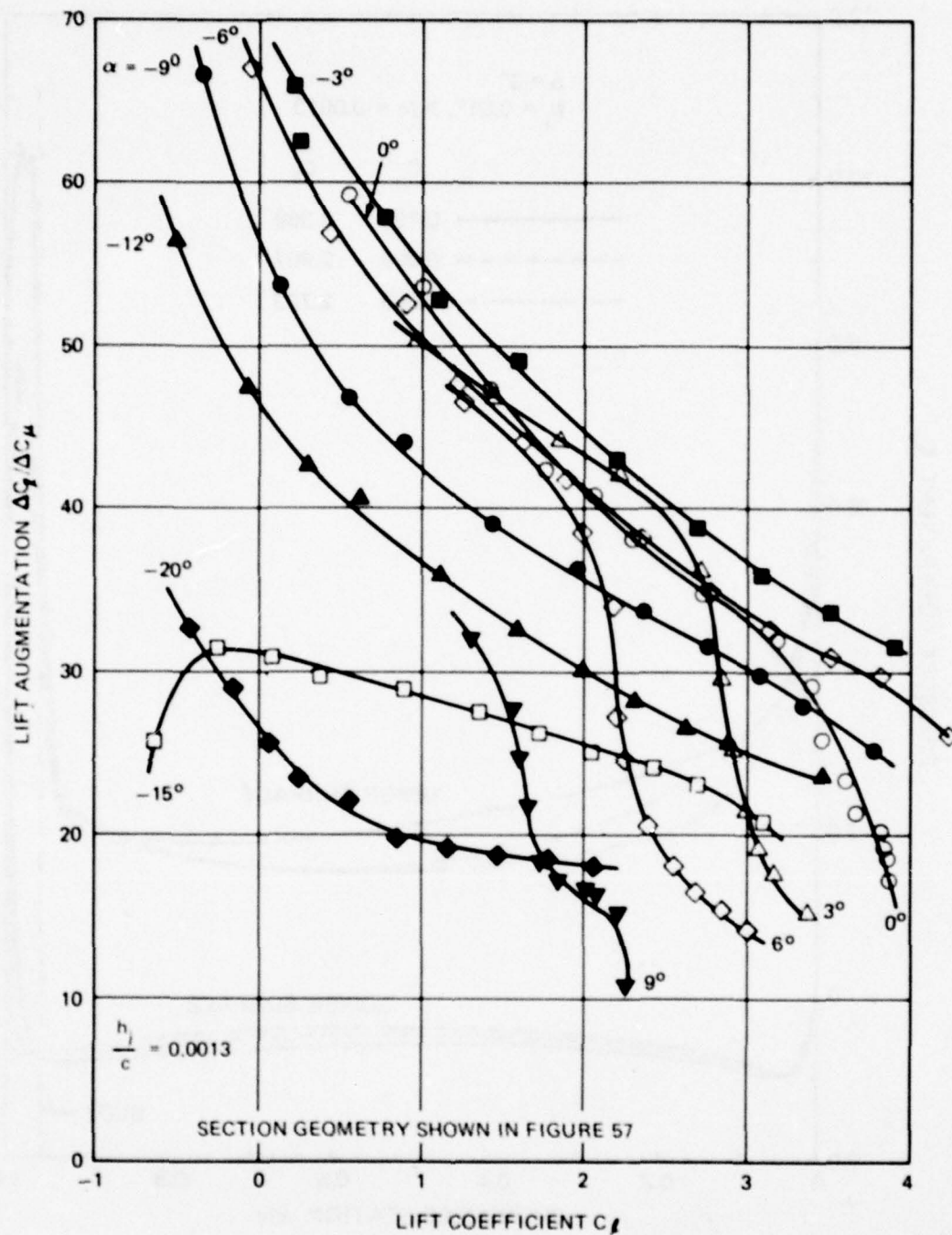


Figure 60 – Lift Augmentation for Rounded Ellipse
Data for a 15-percent-thick uncambered circulation-control foil, R.J. Englar.

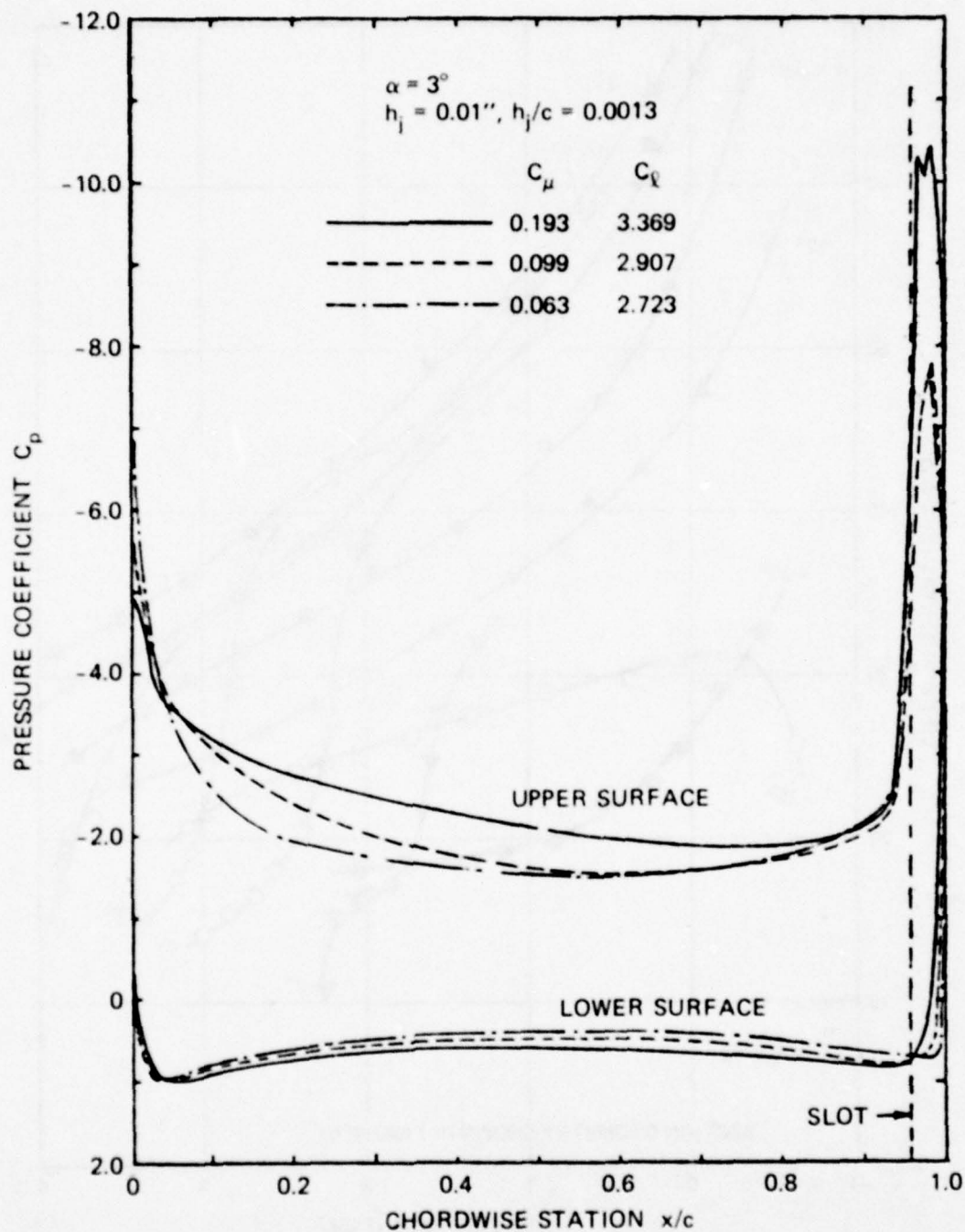


Figure 61 — Variation of Pressure Coefficient versus Chordwise Position for a Rounded Ellipse 15-Percent-Thick Uncambered Circulation-Control Foil

Corresponds to $\alpha = 3$ degrees curve in Figure 59. This shows leading edge suction loss at $C_\mu = 0.193$; and also shows location and relative size of Leading Edge and Trailing Edge suction pressure peaks at representative values of C_ℓ , R.J. Englar.

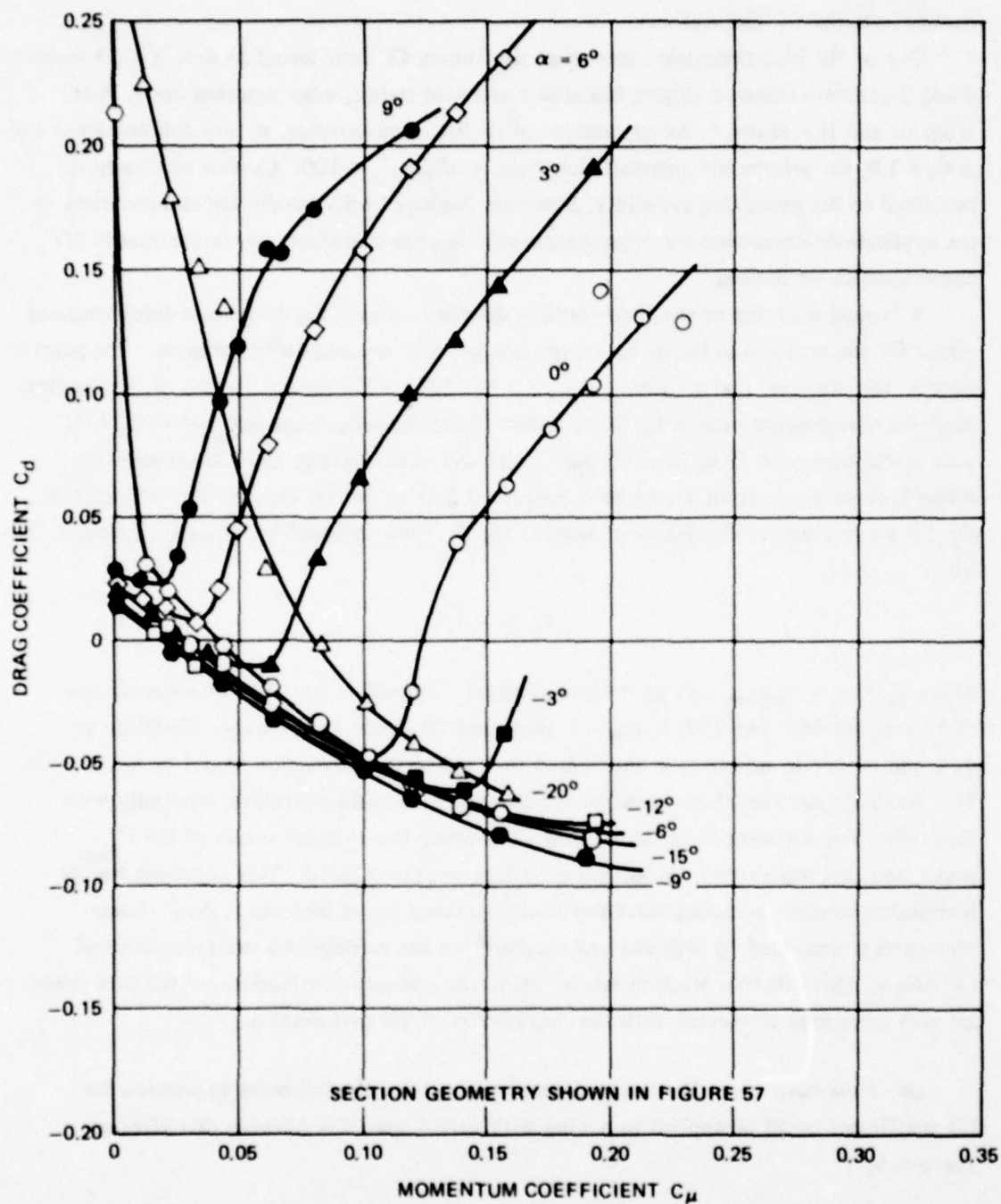


Figure 62 - Variation in Drag Coefficient versus Momentum Coefficient

Data for a 15-percent-thick rounded ellipse uncambered circulation-control foil;
 $h/c = 0.0013$, R.J. Englar.

R.M. Williams and H.J. Howe.* Dunham⁵⁶ and Cheeseman and Seed⁶⁰ present results on circular cylinder CC foil sections.

One of the best performers among all the known CC foils tested to date is a 20-percent-thick, 5-percent-cambered elliptic foil with a rounded trailing edge reported on by R.M. Williams and H.J. Howe.* As an example of its lift characteristics, at zero foil incidence and $\Delta C_\ell = 1.0$, the section lift augmentation ratio is $\Delta C_\ell / \Delta C_\mu = 100$. Camber obviously is beneficial to lift producing capability; however, cambered foils usually are inappropriate to the applications envisioned for most marine vehicle-control surfaces where symmetric lift characteristics are desired.

A typical variation of the fluid-pressure distribution over the 15-percent-thick rounded ellipse CC foil is shown in Figure 61 for the case of incidence angle $\alpha = +3$ degrees. The point to note is, for example, that to achieve a $C_\ell = 3.369$ ($\Delta C_\ell = 2.969$) at $C_\mu = 0.193$, the leading-edge-suction-pressure peak is $C_p \approx -5.0$, and the trailing-edge peak is $C_p \approx -10.25$. If such a foil were used at sufficiently high speed and at sufficiently shallow submergence, difficulties with cavitation would be encountered first at the TE blowing slot and next at the LE suction peak. The simplest criterion for the limit imposed by vapor cavitation is when

$$C_p = -\sigma_v$$

where $\sigma_v = (p - p_v)/q_\infty$, and p_v = vapor pressure. Typical values of σ_v at submergence of 19 feet are 46.1 and 2.88 at $U_\infty = 5$ knots and 20 knots, respectively. Certainly at slow and moderate speeds, it is anticipated that foil-surface cavitation would be no problem. This also indicates that there could be problems at high-speed operation, especially with thin foils. For the same C_ℓ , a thicker foil will display less extreme values of the $C_{p_{min}}$ peaks, and this will extend the surface cavitation-inception speed. This approach has its limitations because increasing thickness is accompanied by an increase in drag. Some discussion is presented by Williams and Rogers⁵⁸ on the aerodynamic characteristics of CC foils at high subsonic Mach numbers, where the pressure distribution and suction peaks are also intimately connected with the degradation of lift performance.

Lift: Finite Aspect Ratio. For crude estimating purposes, the following expression for lift coefficient could be applied to a wing with partial span slot blowing that effects the area S_f .

*NSRDC Technical Note AL-176 (1970)

$$C_L = F_A (AR) \left[\left(\frac{\partial C_\ell}{\partial \alpha} \right) \alpha + K_\mu^- \left(\frac{\partial C_\ell}{\partial C_\mu^-} \right) C_\mu^- \right] \quad (41)$$

where $(\partial C_\ell / \partial \alpha) = 2\pi(1 + t/c)$

$(\partial C_\ell / \partial C_\mu^-) \cong \Delta C_\ell / C_\mu^-$ from experimental 2D data and averaged over the blowing portion of the span; C_μ^- = total jet-momentum coefficient assumed = C_μ for convenience (see Equation (29))

$$K_\mu^- = S_f / S$$

$$F_A (AR) = \begin{cases} \frac{1}{E_s + 2/R} & \text{for } AR \text{ large or moderate } (AR \geq 1) \\ \frac{AR}{2(1 + AR)} & \text{for } AR < 1 \end{cases}$$

E_s = ratio of semiperimeter to span.

Drag: Two-Dimensional. Some examples of section data on drag characteristics of CC foils are given. Figure 62 from R.J. Englar* shows the drag coefficient C_d as a function of the momentum coefficient C_μ for the same 15-percent-thick rounded elliptical section used for obtaining the lift data of Figures 58 through 60. As is obvious from the curves, the section drag C_d for a CC foil can sometimes be drastically reduced by blowing. Especially at large negative values of angle of attack, the C_d is quickly reduced to minus values with increasing C_μ . When the angle of attack is positive, the drag advantage disappears and, in fact, for large $+\alpha$, the C_d begins to rise steeply with C_μ .

In the case of no blowing, the drag on the typical blunt shapes of CC foils could constitute an undesirable penalty, especially at high speeds. This is also a problem with the blunt foils using trailing-edge rotating cylinders for CC. However, for tangentially blown CC foils, the pressure drag over the rounded rear end can be reduced by *symmetrical* blowing from slots on the upper and lower surfaces, e.g., foil of Figure 54c. In this case, of course, the reduction of drag is accomplished by the expenditure of fluid pumping power.

Equivalent Section Drag - The equivalent drag coefficient C_{de} is defined to contain a penalty for the power required for blowing systems; (see Englar** and Williams⁵⁷).

*NSRDC Technical Note AL-211 (1971)

**NSRDC Technical Note AL-182 (1970).

$$C_{d_e} = C_d + C_{d_{\text{pump}}} + C_{d_{\text{ram}}} \quad (42)$$

where C_d = section profile drag = wake drag corrected for added mass efflux of jet
 $C_{d_{\text{pump}}} = (\text{Pump Power}/U_\infty)/cq_\infty$; where Pump Power $\simeq \frac{1}{2} \rho V_j^2 Q$
 $C_{d_{\text{ram}}} = [\rho Q U_\infty]/q_\infty c$; where $\rho Q U_\infty$ is the momentum drag force caused by ingesting the flow rate Q .

The final expression for C_{d_e} contains C_μ and the jet-velocity ratio

$$C_{d_e} = C_d + \frac{1}{2} C_\mu \left(\frac{V_j}{U_\infty} \right) + C_\mu \left(\frac{U_\infty}{V_j} \right) \quad (43)$$

Figure 63 shows a plot of section drag versus C_μ with typical variations of the components making up the equivalent drag C_{d_e} . This plot, reproduced from Englar,* is for a 30-percent-thick elliptical CC foil with a 1.5-percent, circular arc camber, tested at zero geometric incidence.

Section Efficiency – A good measure of the section-lift efficiency is the equivalent lift-to-drag ratio. Figure 64 shows the variation of C_l/C_{d_e} versus C_l for the same 15-percent-thick rounded elliptical CC foil, described in previous plots; see Figures 58 through 62.

Drag: Finite-Aspect Ratio. The drag coefficient for a finite-aspect-ratio lifting surface can be estimated using the expression

$$C_D = \bar{C}_d + C_{D_i} \quad (44)$$

where \bar{C}_d = an average over the span of the section-drag coefficient, as modified by blowing, and C_{D_i} = induced drag, estimated from Equation (8).

Submarine Application

The CC concept has already been explored to some extent for use in submarine control. For example, a design method for the typical small-aspect-ratio, tapered-stern-plane control surface has been developed by R.J. Englar and R.M. Williams** at the Center.

*NSRDC Technical Note AL-201 (1972).

**NSRDC Technical Note AL-200 (1971).

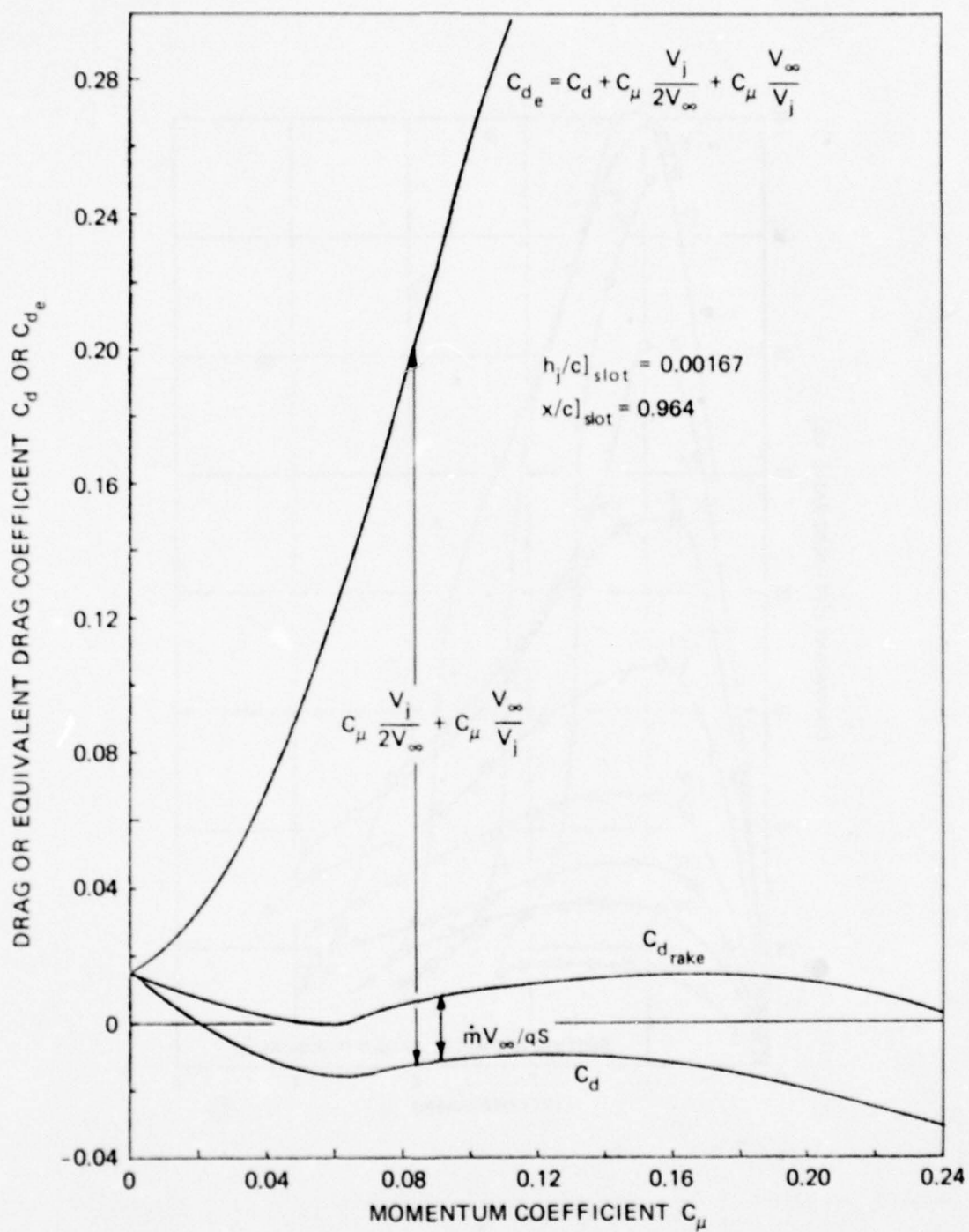


Figure 63 - Comparison of Measured and Equivalent Drag Coefficients,
 $\alpha_{geo} = 0$, $h_j = 0.01$ Inch
 Sample data for a 30-percent-thick elliptical circulation-control foil with 1.5 percent camber,
 R.J. Engler.

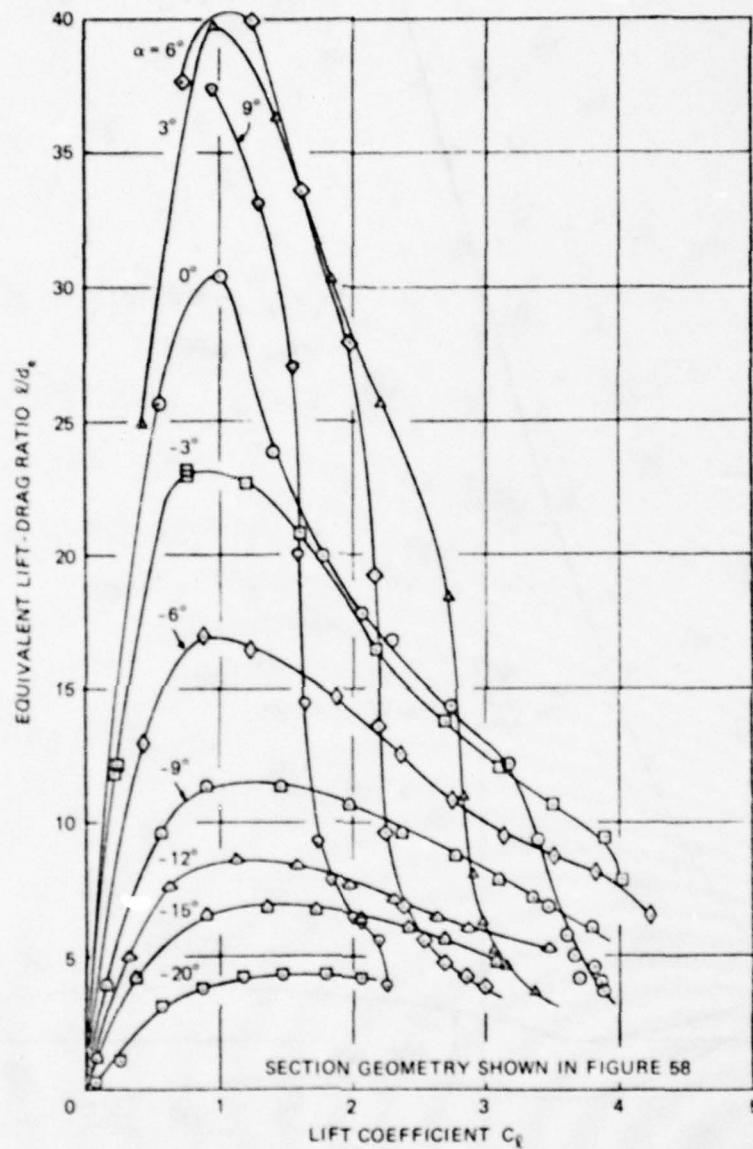


Figure 64 — Equivalent Lift-to-Drag Ratios versus Lift Coefficient
 Data for a 15-percent-thick rounded ellipse circulation-control foil, $h_f/c = 0.0013$,
 R.J. Englar.

Figure 65a shows the geometry of the submarine stern planes. Figure 65b shows the design of an aspect ratio 0.908, tapered CC wing for which there is a linear variation of t/c from the root to the tip. This wing will produce a lift coefficient of $C_L = 0.95$ at a geometric incidence $\alpha_{geo} = 0$, a jet-velocity ratio $V_j/U_\infty = 8$, and a total jet-momentum coefficient $C_{\bar{\mu}} \cong 0.1$.

Powering Estimates

The expressions for estimating the fluid power required for slot blowing given in Equations (23) and (24) apply here as well.

DISCUSSION: Several important features of this CC concept are summarized as follows:

1. Lift may be produced without imposing foil incidence, merely by changing the slot-blowing flow rate. Of course lift can be generated by both incidence and tangential jet blowing; however, the latter is apparently very efficient.
2. From two-dimensional experiments, sectional lift can be developed nearly independent of free-stream velocity. For example, as seen in Figure 59, there is a nearly linear relationship between C_l and $C_{\bar{\mu}}$ in the range of small $C_{\bar{\mu}}$. This means that over a fairly large range of parameters, section lift is proportional to mV_j , which can be kept constant by maintaining constant plenum pressure p_d . For low-aspect-ratio lifting surfaces, using CC by tangential blowing, the lift-induced flow can alter the net angle of attack at each section across the span of the wing; this in turn can introduce a variation of the net wing-lift coefficient C_L versus $C_{\bar{\mu}}$ that is different, not necessarily linear, from the simple two-dimensional variation.
3. Lift can be developed very efficiently at high lift coefficients. This can be seen from typical curves of hydrodynamic efficiency C_l/C_{d_e} . For example, Figure 64 shows the variation of equivalent lift-to-drag ratio for the uncambered 15-percent-thick CC foil discussed in this subsection.

Relative to other high lift concepts, the hydrodynamic performance of CC foils is good. The very best performers among the slot-blowing CC foils are evident in the plots of effective lift-to-drag ratio in Figure 1. The two standouts are (1) the 20-percent-thick, 5-percent-cambered, rounded TE elliptic foil tested by R.M. Williams and H.J. Howe at the Center. Data for this foil show that the maximum C_l/C_{d_e} value is ~ 93 at zero incidence with $C_l = 1.3$. Data from further tests indicate even better performance:

$(C_l/C_{d_e})_{max} = 115$ at $C_l = 1.3$. The same foil displays a C_l/C_{d_e} value of 10 at a

section lift coefficient $C_l \cong 6.0$. (2) The second example is a 50-percent-thick elliptic

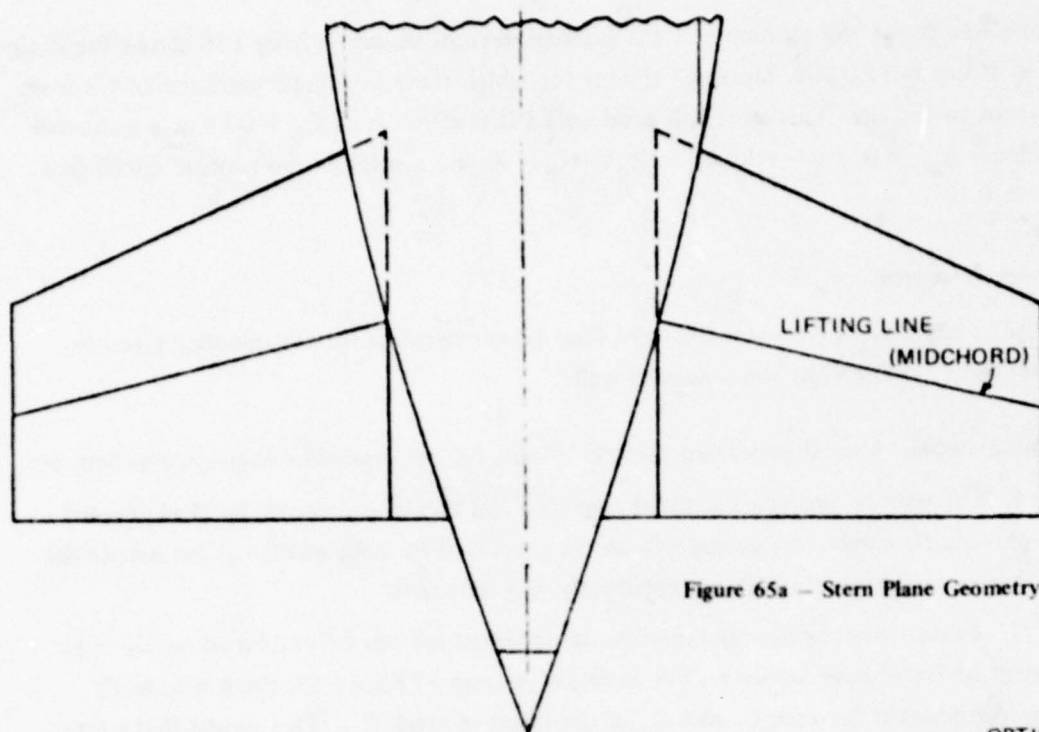


Figure 65a - Stern Plane Geometry

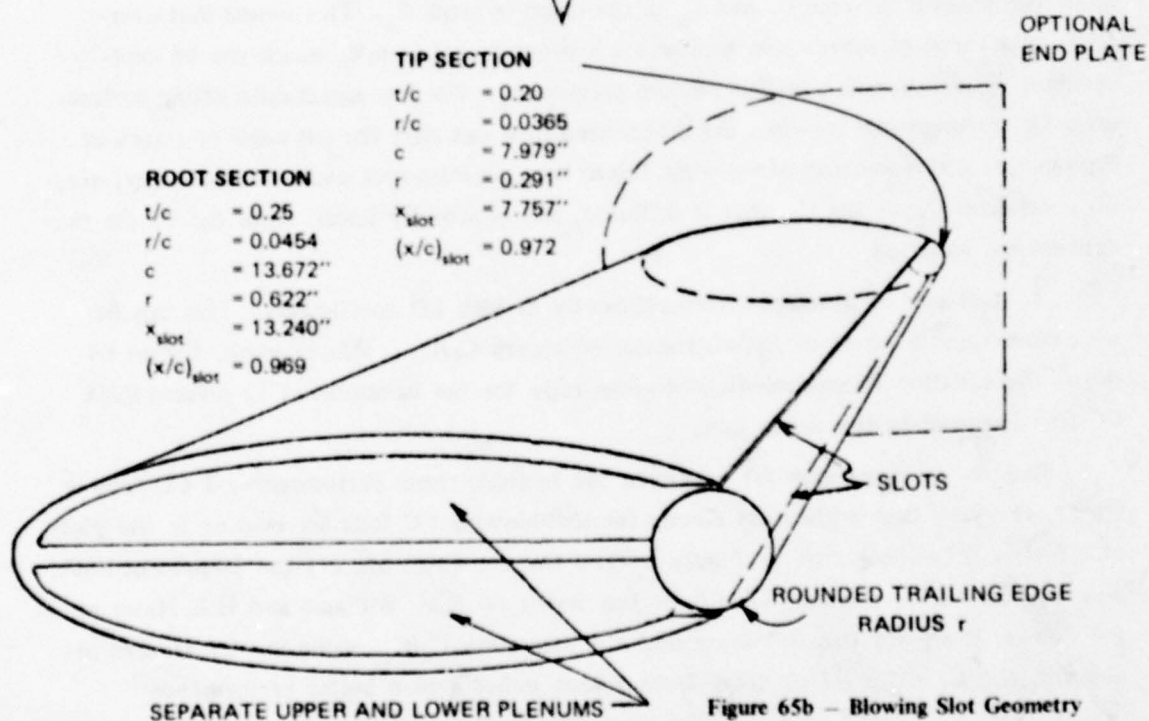


Figure 65b - Blowing Slot Geometry

Figure 65 -- Example Design of Circulation-Control Wing for Application to the $AR = 0.908$ Stern Plane of a Submarine

R.J. Englar and R.M. Williams.

foil with two blowing slots, the performance of which is mentioned in Williams and Rogers.⁵⁸ This foil achieves a $\left(C_l/C_{d_e}\right)_{\max} = 37$ at $C_l = 4.7$ and maintains a respectable $C_l/C_{d_e} = 23$, even at a section lift coefficient greater than 7.0.

4. Typical values of lift augmentation are impressive. For example, at zero incidence, the 15-percent-thick uncambered foil shown in Figure 58 has $\Delta C_l/\Delta C_\mu = 60$ at $C_l = 0.5$. Even at high lift, rather thin foils can maintain good efficiency. For example, the previously mentioned 20-percent-thick, 5-percent-cambered foil, developed by Williams and Howe displays a $\Delta C_l/\Delta C_\mu \approx 27$ at $C_l = 6.2$.

5. With CC foils it is possible to achieve experimental values of section-lift coefficient close to the theoretical maximum $C_l = 2\pi(1 + t/c)$; see Reference 57.

6. There is an obvious kinship between slot-blowing circulation control and the use of rotating cylinders at the TE of a foil. The latter is discussed in the moving surfaces subsection on powered-lift devices. In the case of slot-blowing, the rear stagnation point is determined by the jet-momentum coefficient C_μ . In the case of TE rotating cylinders, the separation point is determined by the ratio of cylinder peripheral velocity-to-free stream velocity u/V . One way to compare the relative efficiencies of the two techniques of circulation control is on the basis of the equivalent lift-to-drag ratio. Using available information, collected in Figure 1, it appears that the two CC techniques are quite comparable, at least for uncambered foils, considering a 20-percent-thick slot-blown CC foil, compared with an 18.2-percent-thick, TE, rotating-cylinder foil.

Another way to compare performance of the two CC concepts is the lift increment-to-power ratio. As an example, from the data of Figure 59 for the 15-percent-thick CC foil tested by R.J. Englar* at zero foil incidence, the blowing momentum coefficient is $C_\mu \approx 0.028$ to achieve a section lift $C_l \approx 1.12$. Then the two-dimensional, lift increment-to-power ratio is

$$\frac{\Delta C_l}{C_{p_f}} \approx 20.56$$

which is about 0.45 of the value achieved by an 18.2-percent-thick, TE rotating-cylinder foil also producing $C_l \approx 1.12$. For comparison, the 20-percent-thick, 5-percent-cambered, slot-blowing CC foil tested by Williams and Howe** achieves a more impressive value of $\Delta C_l/C_{p_f} \approx 66.9$ at $C_l = 1.5$.

For application to submarine control, the slot-blowing CC concept would be relatively simple mechanically. Because it is capable of lift without foil incidence, a CC control surface could provide a force either up or down by proper valving through the lower or

*NSRDC Technical Note AL-211 (1971)

**NSRDC Technical Note AL-176 (1970)

upper slot; see Figure 65. A failure of the jet pumping system would mean no control-force capability—unless the foil incidence could also be changed.

As with blown flaps, problem areas include: fouling of the slots by marine growth, possible noise generated by the jet sheet, limitations imposed by cavitation, and small-aspect-ratio end effects interfering with good Coanda flow, especially at the juncture of the control surface with the hull. With a submarine, there are intervals when no control force is demanded from a control surface. During these times, it should be feasible to bleed water continuously out of symmetric slots at a rate sufficient to prevent fouling, and at the same time reduce the profile drag on the blunt-end foil shapes. As mentioned previously, and in the discussion of jet flaps, Smith and Thelander⁴⁰ have shown that ram pressure is apparently sufficient to provide enough weak slot blowing to reduce significantly the profile drag on similar shaped blunt based foils, e.g., on the so-called power profile.

EJECTOR FLAPS, AUGMENTOR WING

If ejector augmentation is applied to the jet sheet blown over a flapped lifting surface, the resulting device is often referred to as an augmentor wing. The mode of operation of an ejector resembles that of a jet pump. That is, when a jet is issued out of a nozzle into a mixing chamber formed by shrouds, there is a strong secondary flow induced by entrainment of the surrounding fluid. The induced flow gives rise to a thrust augmentation of the original jet-reaction force.

The elements of simple ejector augmentation are presented for example by McCormick.³ A schematic drawing of a simple ejector geometry—a nozzle blowing inside a shroud—is shown in Figure 66a. The thrust-augmentation factor is defined as $\phi = (\text{thrust of jet} + \text{shroud})/(\text{thrust from plain jet})$. Then, it can be shown that

$$\phi = \rho u_2^2 A / \rho V_j^2 A_j = (u_2/V_j)/(A_j/A) \quad (45)$$

which is plotted in Figure 66b.

Large viscous shearing and turbulent mixing at the expanding boundary of the primary jet are responsible for the entrainment of the induced flow. To achieve the ideal ϕ -value, complete lossless mixing within the shroud is required.

Further information on thrust augmentors is discussed by McCormick³ and in an encyclopedic work by Payne⁶¹ which contains an extensive bibliography.

In the case of the augmentor wing, it is not only the thrust augmentation that is interesting but also the presence of the secondary flow. The shrouds can be shaped and oriented so that the entrained flow is turned efficiently through some desired angle. This is useful for the flow over a flapped wing. Figure 67 shows a sketch of a typical recent design of an ejector-flap wing.⁶² The shroud-flap passage provides the mixing chamber

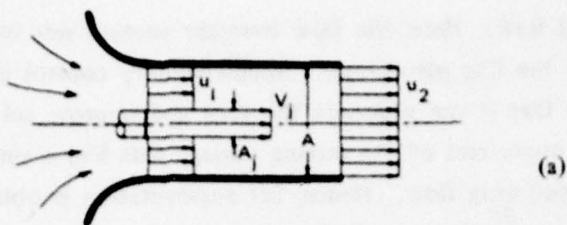


Figure 66a - Schematic of an Ejector

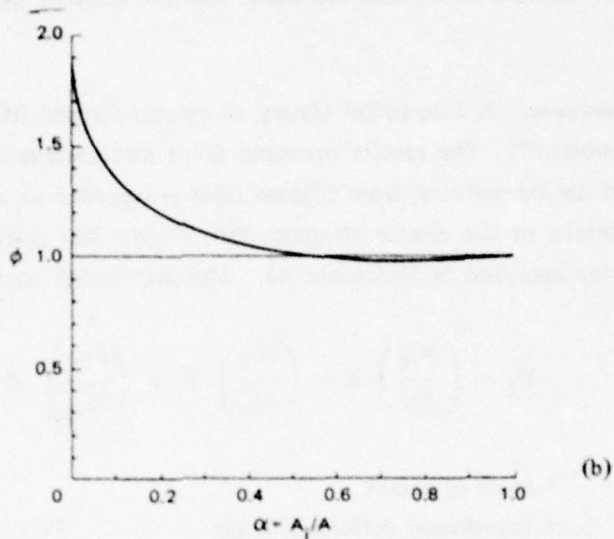


Figure 66b - Theoretical Augmentation Ratio versus Jet-Area Ratio for a Simple Ejector
McCormick³

Figure 66 - Ejector Thrust Augmentation

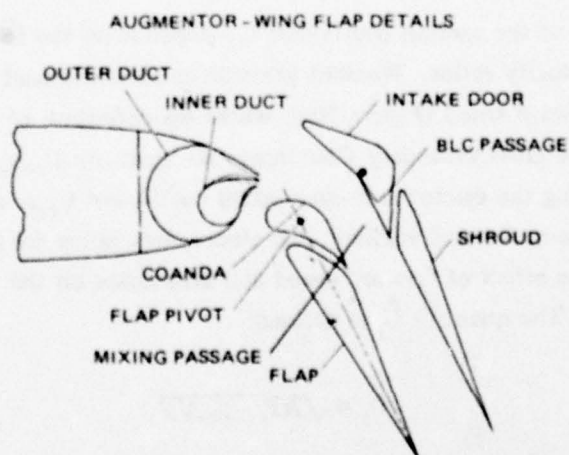


Figure 67 - An Ejector Flap
Quigley and Vomaske,⁶²

for the jet-induced flow. Here, the flow over the suction side of the wing is turned down, over, and through the flap mechanism. Supplementary control jets help energize the boundary layer so that it can negotiate the turn and improve mixing. Also, the entrained flow entering the upper end of the mixing passage acts like a sink, which has a beneficial effect on the flapped-wing flow. Hence, lift augmentation is obtained simultaneously from three different physical effects: a deflected mechanical flap system; an ejector-augmented jet-flap, jet sheet directed down and rearward; and the induced sink flow at the flap knee.

Force Estimates

Lift: Two-Dimensional. A thin-airfoil theory of ejector-flapped lifting section has been presented by Woolard.⁶³ The results resemble those discussed earlier for the jet-augmented flap. If the net ejector-induced flow (Figure 68a) is regarded as a sink flow of strength Q , located at the intake of the ejector shrouds, then Figure 68b is a definition sketch for the idealized geometry analyzed in Reference 63. The section-lift coefficient is expressed as

$$C_{\ell} = \left(\frac{\partial C_{\ell}}{\partial \alpha} \right) \alpha + \left(\frac{\partial C_{\ell}}{\partial \delta_f} \right) \delta_f + \left(\frac{\partial C_{\ell}}{\partial C_Q} \right) C_Q \quad (46)$$

where α = angle of attack
 δ_f = flap-shroud deflection angle
 $C_Q = Q/cU_{\infty}$ = suction flow coefficient

The thin foil derivative $(\partial C_{\ell}/\partial \alpha)$ is a function of the final ejector exit-momentum coefficient C_j and is plotted in Figure 33, where $C_{\mu} = C_j$. Curves for the derivative $(\partial C_{\ell}/\partial \delta_f)$ are given in Figure 34. The remaining derivative $(\partial C_{\ell}/\partial C_Q)$ is obtained by Woolard⁶³ and is reproduced in Figure 69.

The magnitude of the suction coefficient C_Q depends on the geometry of the ejector and upon various velocity ratios. Woolard presents an idealized analysis of the ejector operating with a forward speed (Figure 70a), where his definition of the net suction flow rate Q is taken as the gross secondary flow minus the quantity $U_{\infty} \bar{h}_s$; see Figure 70b. Details on determining the ejector exit-momentum coefficient C_j as a function of the primary jet momentum, forward velocity, and ejector-area ratios are given in Reference 63. Figure 71a shows the effect of forward speed and area ratios on the magnitude of the net suction coefficient. The quantity \hat{U}_j is defined

$$\hat{U}_j \equiv \sqrt{2(P_j - p_{\infty})/\rho} \quad (47)$$

where P_j is the total pressure of the primary jet, and p_{∞} is the free-stream static pressure.

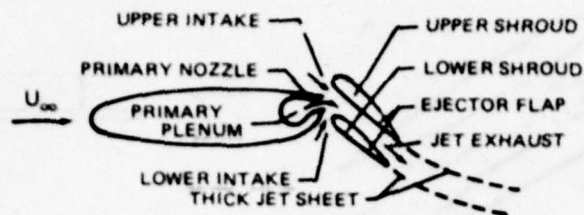


Figure 68a - Ejector Flapped-Wing Section

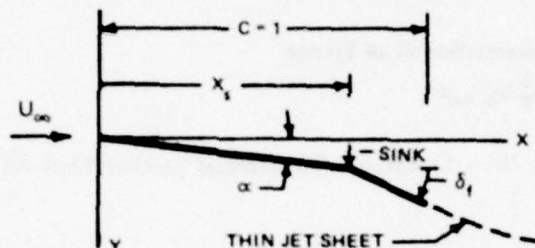


Figure 68b - Thin-Airfoil Representation of an Ejector-Flapped Wing Section with an Upper Surface Intake Only

Figure 68 - Ejector Flapped-Wing Section
Sketches from Woolard⁶³

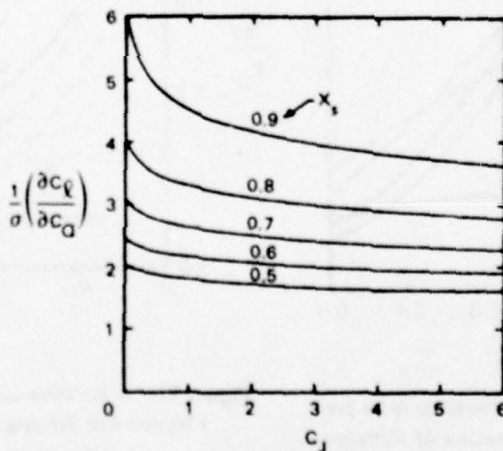


Figure 69 - Lift Characteristics of Suction Airfoil with Regular Blowing
 $\sigma = 1$ for sink on upper surface
 $\sigma = -1$ for sink on lower surface
Woolard⁶³

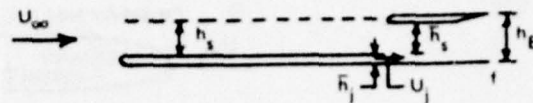
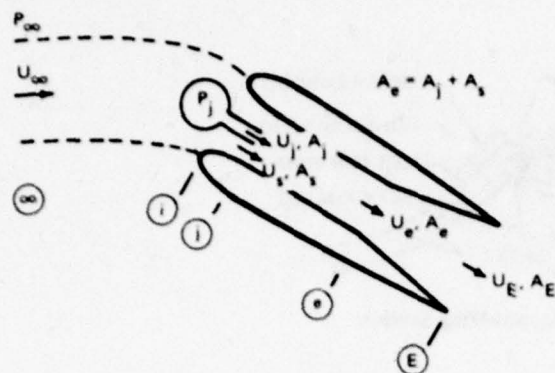


Figure 70b - Sketch Defining $c_Q = 0$
Woolard⁶³

Figure 70a - Schematic Representation of an Ejector
Flap, $C_J = \rho U_E^2 h_E / q_\infty c$

Figure 70 - Linearized Theoretical Ejector Flap Analysis

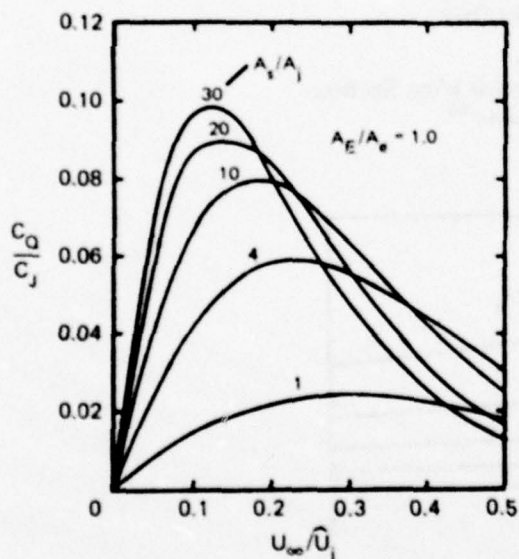


Figure 71a - Ratio of Suction Coefficient to Jet-Momentum Coefficient as a Function of Forward-Speed and Injection-Area Ratios
Woolard⁶³

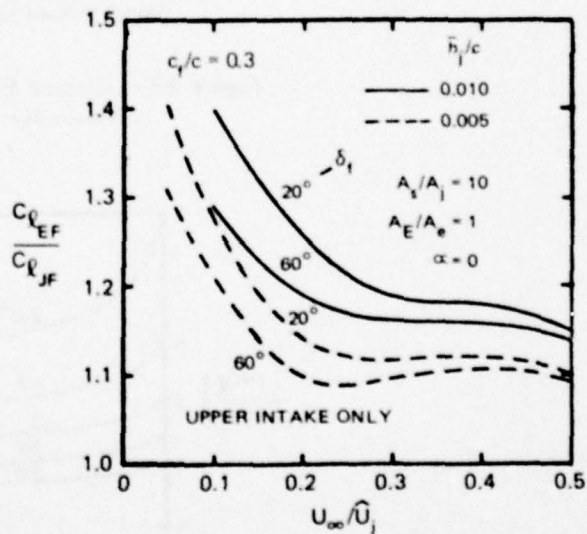


Figure 71b - Relative Lift Performance of Ejector-Flapped and Jet-Augmented-Flapped Wings
 $C_{L_{EF}}$ = ejector flap lift; $C_{L_{JF}}$ = jet-augmented flap lift;
Woolard⁶³

Figure 71 - Linearized Theoretical Ejector Flap Performance

Of course it is interesting to compare the ideal performance of an ejector-flapped foil with a similar jet-augmented-flapped foil. Figure 71b, reproduced from Woolard⁶³ shows the ratio of ejector-flap-lift $C_{L_{EF}}$ to jet-augmented, flap-lift $C_{L_{FF}}$ with contours of constant flap angle δ_f and two different primary jet-slot heights \bar{h}_j/c . This graph shows that the ejector-flap is superior, especially for jet velocity-to-forward speed ratios $\hat{U}_j/U_\infty > 4.0$. Also, the relative performance of the ejector-flap is better at smaller values of flap-deflection angle δ_f . This is because the relative suction contribution to the lift is larger at lower flap angles.

Finite-Aspect Ratio. To give some idea of the magnitudes of measured lift and drag coefficients obtained with such devices, Figure 72 shows data from Koenig and Corsiglia⁶⁴ for a large-scale-model, aspect ratio 8 wing with a partial span augmentor-flap blowing at $C_{\mu} = 1.15$. The theory curves on the graph are calculated by Lopez and Shen,⁴⁴ using the Douglas EVD method.

Powering Requirement. Given certain geometry and jet-momentum values, the fluid power required by the primary jet of an ejector wing can be estimated, using the formulas already mentioned in a previous outline; see Equations (23) and (24).

DISCUSSION: The augmentor wing is being considered seriously for use with vertical/short takeoff and landing (V/STOL) aircraft. For example, the integrated lift-propulsion scheme of the North American XFV-12A is a form of ejector-flap jet-wing. The main appeal of this type of device is in its static and near-static performance for use in hovering and transition flight.

It is possible to improve upon the simple ejector augmentation by use of diffusion of the flow downstream of the well-mixed region; see McCormick.³ Morel and Lissaman⁶⁵ have shown that by using a jet-flap diffuser at the exit of the mixing chamber, the secondary flow can be amplified further. This fact can be exploited in designing an augmentor wing. For example, Figure 73 shows a sketch from the U.S. patent by Harris⁶⁶ that uses jet-flap diffusion.

For application to marine vehicles, this device as presently developed has some disadvantages. It would probably be prone to fouling, and there would be problems making the shrouds, guide vanes, etc., robust enough for use in a marine environment. The complex flap shrouds would have large drag at high speeds.

Aside from the mechanical complexity of the ejector shrouds, the augmentor wing concept resembles the blown flap. Therefore the main points of discussion regarding blown flaps apply here as well.

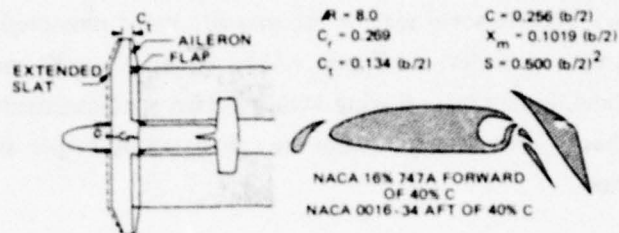


Figure 72a – Configuration of the Augmentor Wing Aircraft Used in the Experiment by Koenig et al.

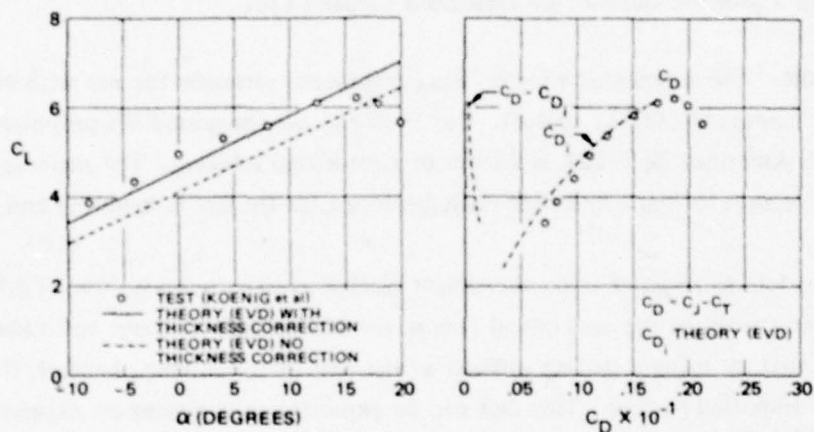


Figure 72 – Data and Calculations for an Aspect-Ratio 8 Augmentor Wing

$$C_{\bar{\mu}} = 1.15, \delta_{\text{flap}} = 52^\circ, \delta_{\text{jet}} = 0, \text{Lopez and Shen.}^{44}$$

May 23, 1972

G. L. HARRIS

U.S. Patent No.
3,664,611

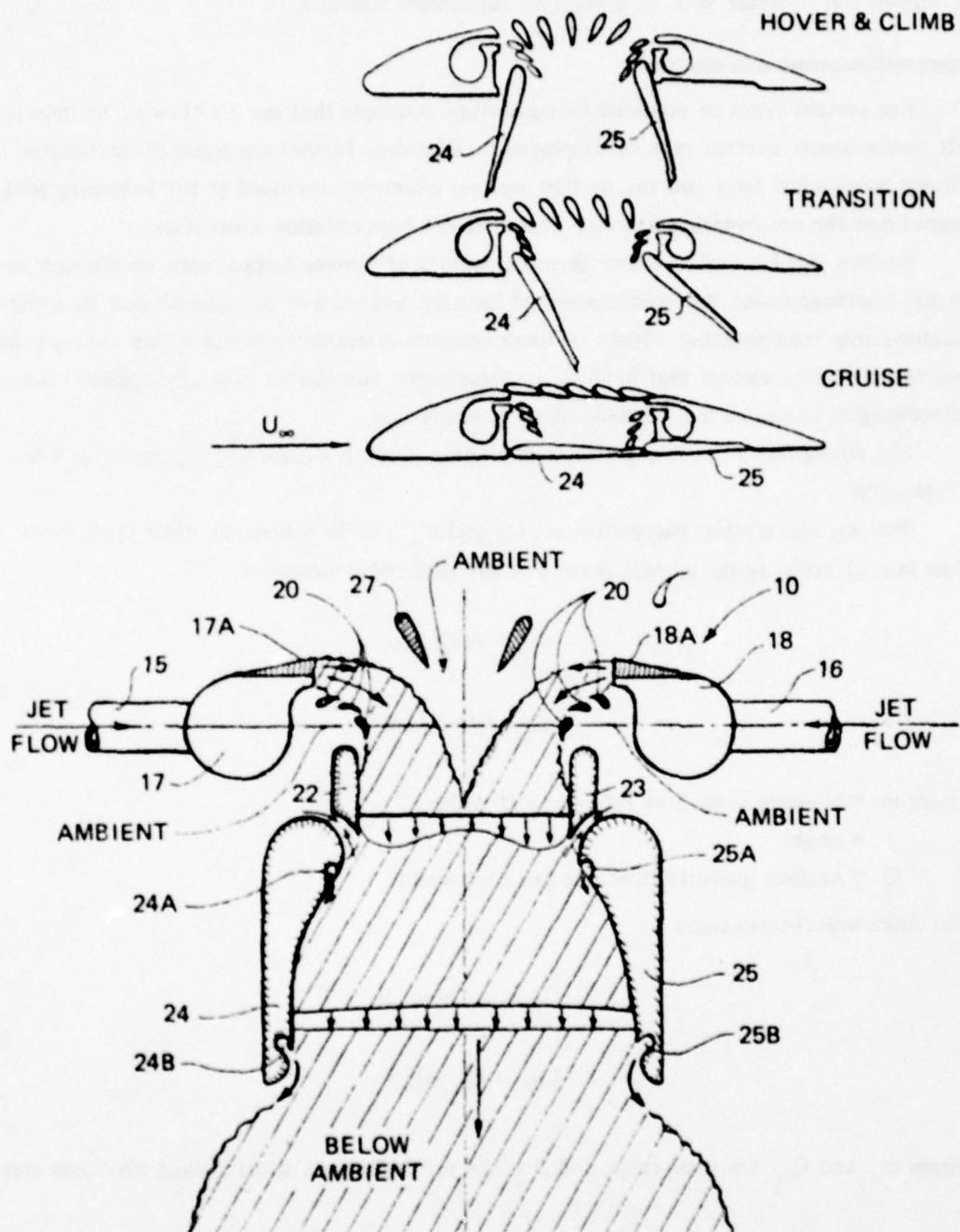


Figure 73 - Concept of an Augmentor Wing with Jet-Flap Diffusion

Harris⁶⁶

From its intrinsic performance characteristics, the ejector flap would be most useful at low speeds. If the flap-shroud system could be developed to fold up or could be retractable at high speed, a symmetric version of this device could be an excellent technique of integrating a flapped foil together with an orientable augmented waterjet.

COMBINED BLOWING AND SUCTION

For certain types of powered lifting-surface concepts that use jet blowing to improve the lift performance, suction may be employed to stimulate further the induced circulation. Blown mechanical flaps and the jet-flap are two examples discussed in the following text. Sometimes the combination has very attractive lift-augmentation properties.

Suction can be applied either through patches of porous surface area, or through slots. In some arrangements, the combination of blowing and suction is accomplished by using an ejector-pump configuration. Some of these schemes resemble the ejector flap concept discussed previously, except that in these configurations, the ejector typically appears to be an afterthought, buried in the top face of an ordinary flap.

The circulation-augmenting effects of suction alone are discussed separately in later subsections.

Blowing and suction parameters are C_μ and C_Q , defined as usual. Here the volume flow rate, Q , refers to the suction flow. For two-dimensional cases

$$\begin{aligned} C_\mu &= \dot{m} V_j / q_\infty c \\ C_Q &= Q / U_\infty c \end{aligned} \quad (48)$$

where \dot{m} = blowing mass flow rate per unit width

c = chord

Q = suction quantity-flow rate per unit width.

For finite-aspect-ratio cases

$$\begin{aligned} C_{\bar{\mu}} &= \dot{m}_T V_j / q_\infty S \\ C_{\bar{Q}} &= Q_T / U_\infty S \end{aligned} \quad (49)$$

where \dot{m}_T and Q_T are total rates, and S is the reference area, usually wing planform area.

Lift Force Estimates

Figure 74 shows some two-dimensional test results reported by Malavard et al.⁶⁷ on a 30-percent-flapped aerofoil with both flap suction and jet flap trailing-edge blowing. The upper curve shows the effect of distributed suction through a perforated surface just aft of the knee of the 45° deflected flap. The blowing jet is angled at 31° to the flap chord. The amount of suction is sufficient to maintain attached boundary layer flow over most of the flap surface. The lowest curve shows the pure jet-flap performance with no flap deflection, no suction, and jet angle $\delta_j = 76^\circ$. When the flap is deflected at 45° but with no suction, the middle curve shows the C_L versus C_{μ} variation.

In Figure 75 two possible design solutions are sketched which exploit the results of Figure 74. The first case uses a flapped airfoil; the second uses a jet-control-flap application. Both these arrangements are such that the suction flow is induced by the action of ejector-pump nozzles.

Figure 76, reproduced from Poisson-Quinton and Lepage,²⁰ shows the lift variation for combined slot-suction and slot-blowing at the slightly rounded trailing edge of a two-dimensional airfoil. This plot illustrates the separate linear increase of C_L with $\sqrt{C_{\mu}}$ and with C_Q .

Two other suggestions for combined blowing and ejector-induced suction are sketched in Figures 77 and 78, reproduced from Wagner.⁶⁸

Lift and Drag Force

Finite-Aspect Ratio. In Figure 79, results are plotted for wind tunnel tests of a 10-percent-thick, aspect ratio 4 wing with combined blowing and suction. The polar plot of C_L versus C_D indicates the large increase in induced drag for the high C_L values. With the 30° drooped-nose flap, $C_{L_{\max}} = 2.4$ at a total $C_{\mu} = 0.086$.

Blowing and Suction on a Kort Nozzle. A novel application of combined blowing and suction has been proposed by Oosterveld⁶⁹ in a U.S. patent; see Figure 80. The idea is to use slot-suction and slot-blowing to alter the strength and direction of circulation about the cylindrical shroud surrounding a propeller. Peripheral slots around the inner and outer sides of a Kort nozzle allow water to be selectively drawn into the inner slots and to be ejected from the outer slots, or vice versa, in order to augment the action of the nozzle as either an accelerating or a decelerating duct. The flow arrangement in Figure 80 is for an accelerating duct.

If water is selectively drawn in and ejected out of certain arc sections of the peripheral slots, a lateral steering force can be generated on the nozzle system without turning the nozzle about its vertical axis. This could provide maneuvering forces actuated by valves rather than by rudders, flaps or trainable ducts.

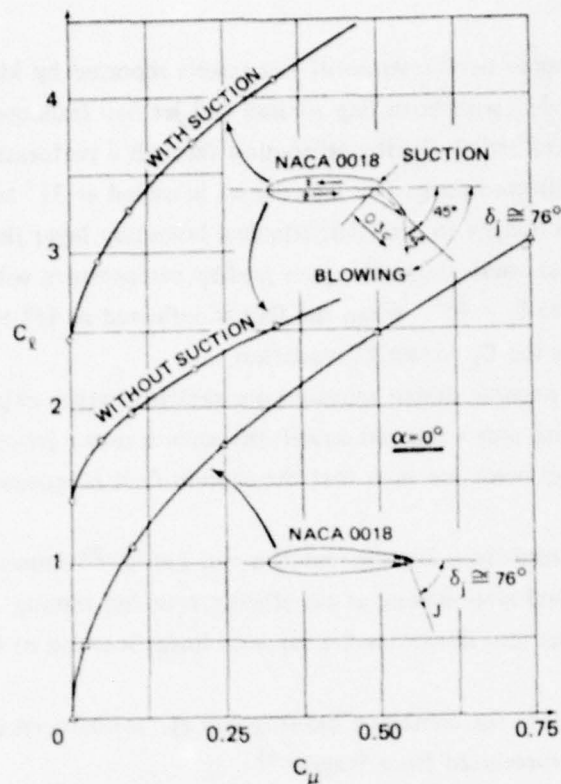


Figure 74 - Chordwise Combined Blowing Suction,
Compared with Blowing Airfoils

Malavard et al.⁶⁷

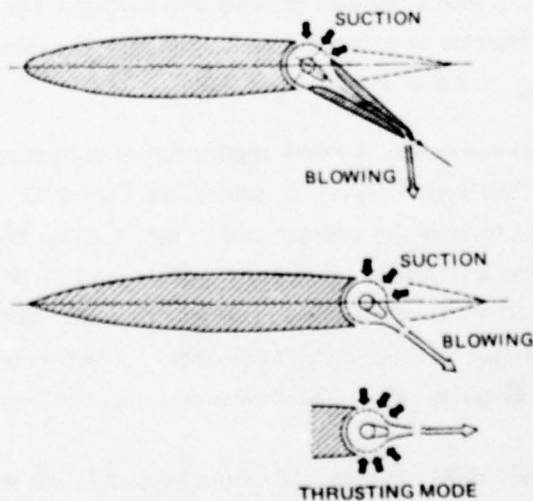


Figure 75 - Combined Blowing and Suction, Using Ejector-Pump
Geometry to Produce the Suction

Malavard et al.⁶⁷

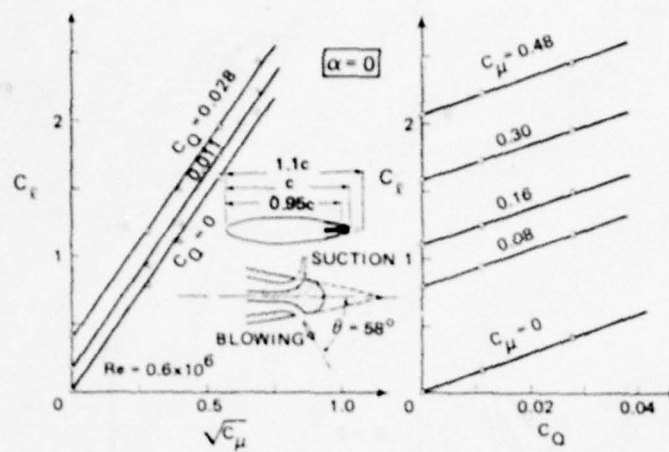


Figure 76 – Circulation Control by Combined Suction and Blowing at the Trailing Edge of an Airfoil in Two-Dimensional Flow

Poisson-Quinton and Lepage.²⁰

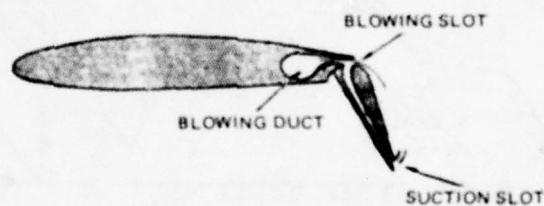


Figure 77 – Recirculation Flap Proposed by H. B. Helmbold

Wagner⁶⁸

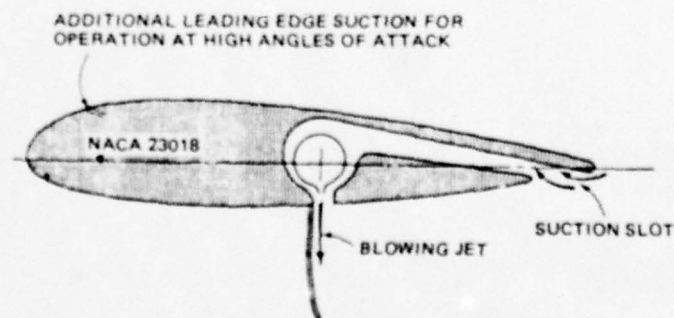
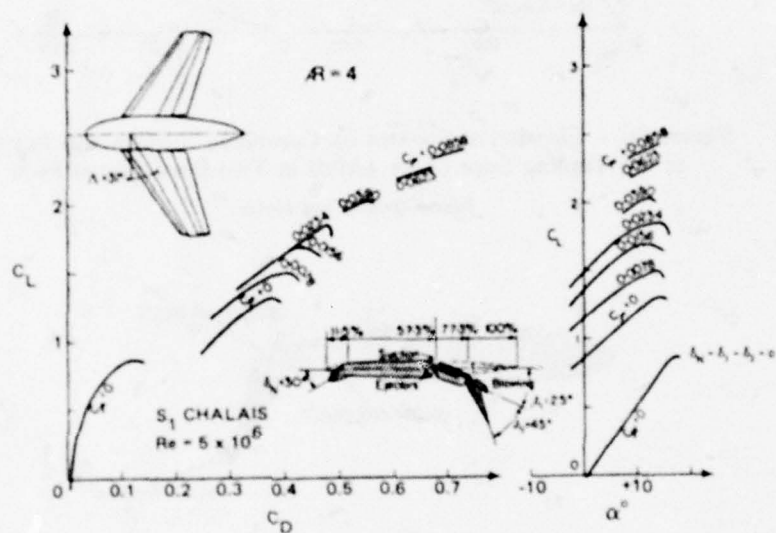


Figure 78 – Configuration for Trailing-Edge Suction, Induced by Jet, and Blowing over Highly Deflected Midchord Split Flap

Wagner⁶⁸



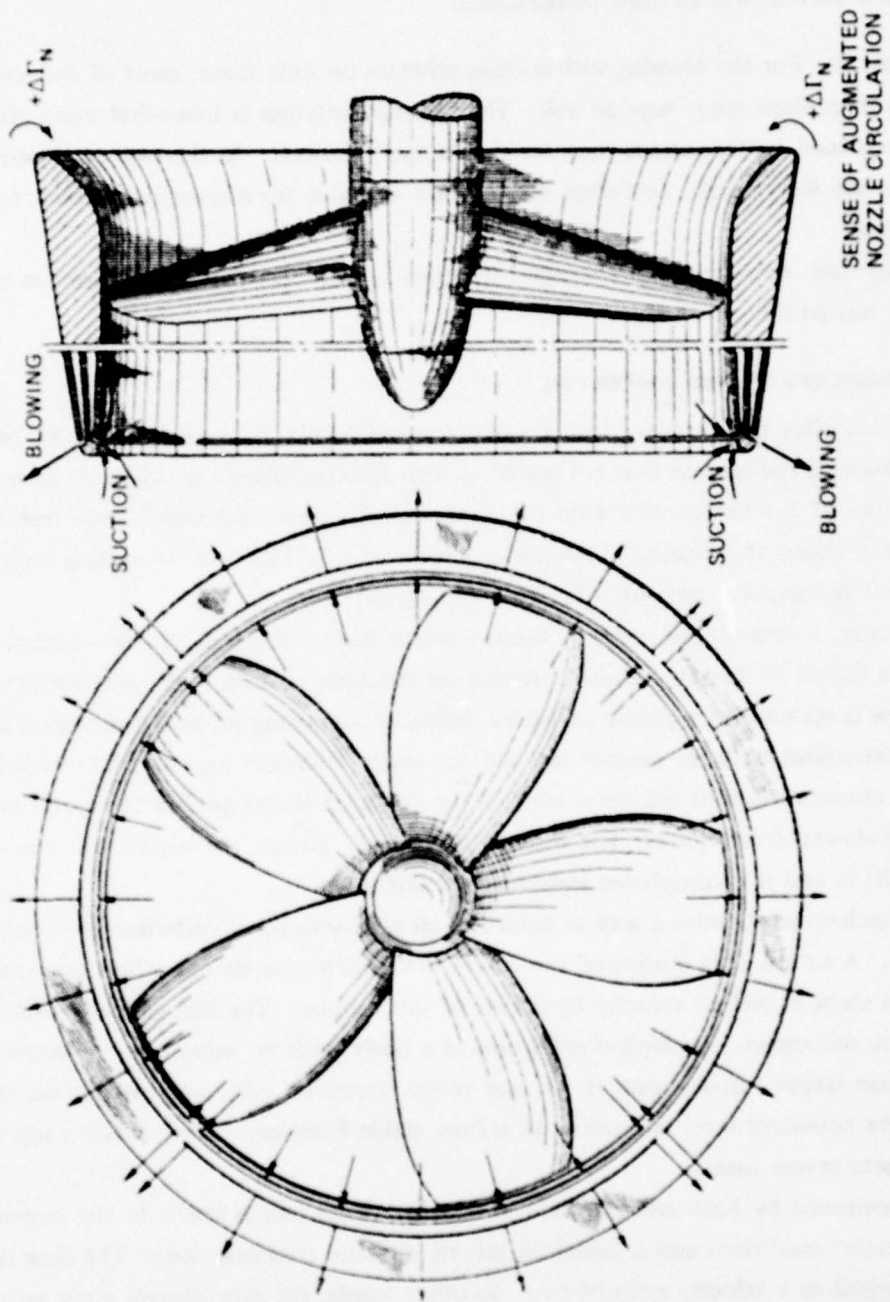


Figure 80 — Duct Thrust Augmentation and Side-Force Production by Combined Slot Blowing and Suction on a Kort Nozzle

Oosterveld⁶⁹

No experimental data are known to exist for the duct thrust augmentation or for the lateral force magnitudes possible with this concept. It would be possible to make crude estimates using the data of Figure 74. However, the flow through an entire duct with blowing and suction will be quite complicated.

DISCUSSION: For the blowing-with-suction schemes on foils alone, most of the remarks made about jet flaps apply here as well. The lift augmentation is somewhat more efficient for the combined configurations than for the jet flap, however. In the case of blowing and suction on the Kort nozzle, sufficient data are not available for a conclusion about force effectiveness.

In any case, *any* suction arrangement in seawater will have the special problem of being fouled by marine life.

BLOWING-STABILIZED TRAPPED VORTEX FOIL

The boundary layer control features of a trapped vortex can be exploited for the design of a flapped foil section that is capable of high lift coefficients at moderate blowing rates. Figure 81 is a sketch of a wind tunnel model of a nose- and rear-flapped foil shape, designed and tested at Advanced Technology Center, Inc. (ATC). An interesting discussion of this high-lift technique is presented by Krall and Haight.⁷⁰

Typically, a cusp-shaped cavity is located where BLC is required. In the configuration pictured in Figure 81 two of them are needed—at the knee of each flap. A recirculating vortex flow is maintained within a cavity by means of a blowing jet at the upstream lip. This jet reenergizes both the mainstream and the cavity boundary layers. The efficient entrainment characteristics of the outer edge of the captured vortex permit the local outer flow to be slowed down quickly but without separation. Hence, the vortex serves as a means of BLC, and it accomplishes low-loss flow diffusion.

This technique provides a way to achieve a stepped-velocity distribution over the top of the foil. A similar idea motivated the design of Griffith-type airfoils which accomplish the sudden steps in surface velocity by means of slot suction. The high velocity over the nose section undergoes a controlled reduction to a fairly uniform value over the midsection, which is then stepped down again at the rear vortex location. After each step-down in velocity, the boundary layer is restored to a thin, stable form capable of resisting separation until the next severe turn.

As mentioned by Krall and Haight,⁷⁰ the vortex cavity size is scaled to the incoming boundary layer conditions and is based on mixing distance considerations. The flow deceleration is limited to a velocity ratio of two. In other words, the downstream ramp velocity is most efficiently reduced to one-half the value of the incoming mainstream velocity at the lip of the vortex cavity.

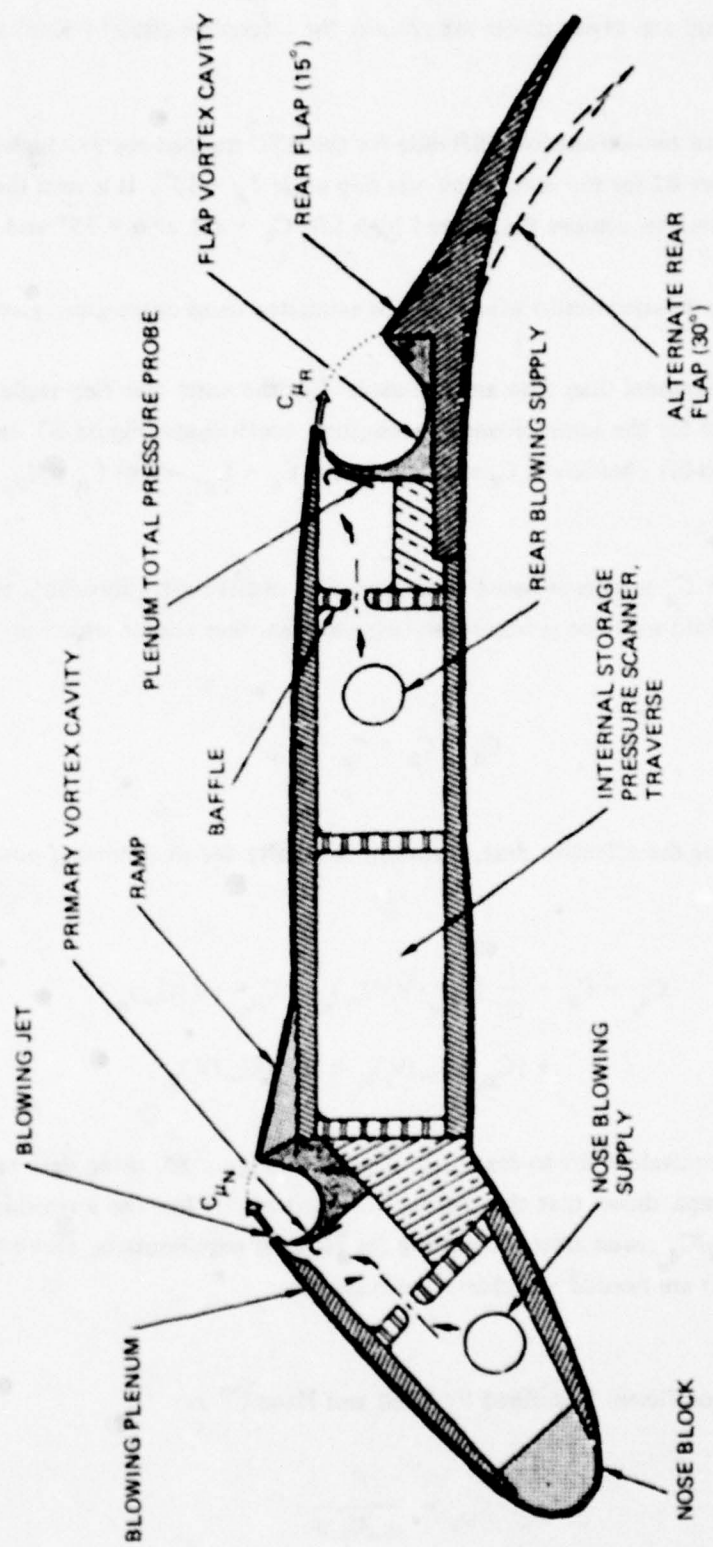


Figure 81 — Wind Tunnel Model of a Trapped-Vortex—High-Lift Foil Section
Krall and Haight.⁷⁰

Details of the foil and cavity design are given in the references cited by Krall and Haight.⁷⁰

Force Estimates

Example plots of two-dimensional lift data for the ATC trapped-vortex-high-lift foil are reproduced in Figure 82 for the case of the rear flap angle $\delta_R = 15^\circ$. It is seen that high angles of attack are required to achieve the desired high lift; $C_l \sim 6.1$ at $\alpha = 35^\circ$ and for $C_{\mu_N} + C_{\mu_R} = 0.244$.

The lift on a finite-aspect-ratio wing could be estimated using expressions given earlier; see Equations (41).

Some two-dimensional drag data are included. For the same rear flap angle as in Figure 82 ($\delta_R = 15^\circ$), and for the same blowing momentum coefficients, Figure 83 shows polar plots of the section-lift coefficient C_l versus the sum $C_d + C_\mu$, where $C_\mu = C_{\mu_N} + C_{\mu_R}$.

Equivalent Drag Ratio

The sum $C_d + C_\mu$ is a force-based equivalent-drag coefficient. Since in a real application the pumped fluid must be continuously ingested, another choice which includes an intake penalty is

$$C_d + C_\mu + C_\mu \frac{U_\infty}{V_j}$$

A better estimate of the effective drag, including a penalty for slot-blowing power, is given by

$$C_{d_e} = C_d + \frac{1}{2} [C_{\mu_N} (V_j/U_\infty)_N + C_{\mu_R} (V_j/U_\infty)_R] + [C_{\mu_N} (U_\infty/V_j)_N + C_{\mu_R} (U_\infty/V_j)_R] \quad (50)$$

A plot of section equivalent lift-to-drag ratio is given in Figure 85, using data taken from Figure 83. This graph shows that the trapped-vortex-high-lift foil has a reasonably large value of section C_l/C_{d_e} , even after accounting for blowing requirements. However, large angles of attack ($\alpha > 20^\circ$) are needed to achieve the high lift.

Power Estimates

A jet power coefficient is defined by Krall and Haight⁷⁰ as

$$C_{D_B} = \frac{P_j}{q_\infty U_\infty S} \quad (51)$$

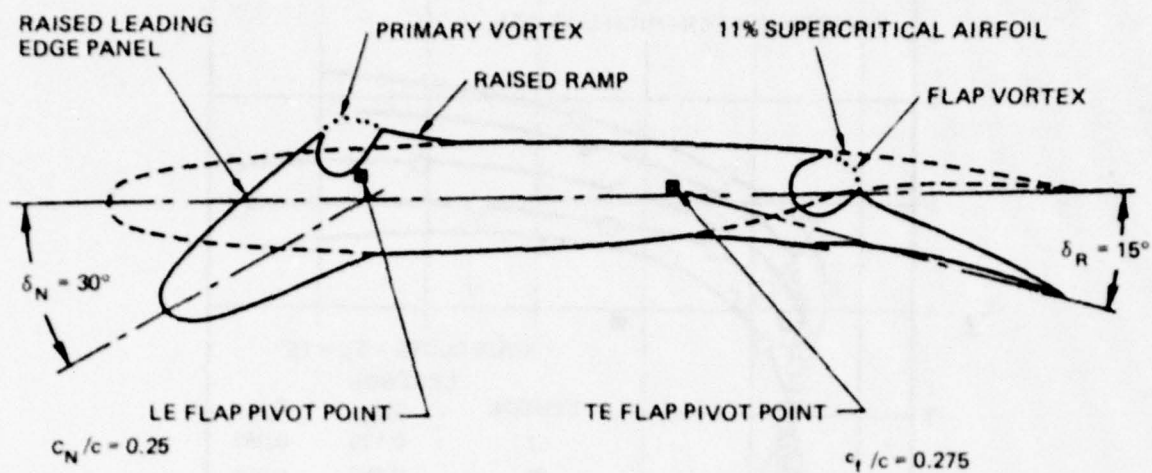


Figure 82a - Trapped-Vortex Foil

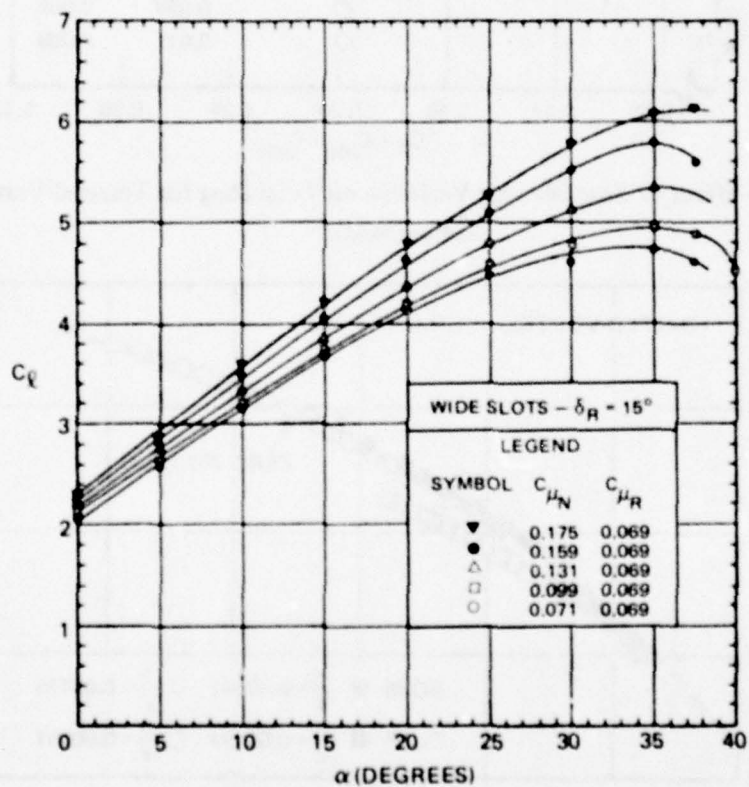


Figure 82b - Data for Lift versus Angle of Attack

Figure 82 - Sample Two-Dimensional Lift Data for the Trapped-Vortex Foil Pictured in Figure 82a

This shows the effect of nose blowing holding C_{μ_R} constant, Krall and Haight.⁷⁰

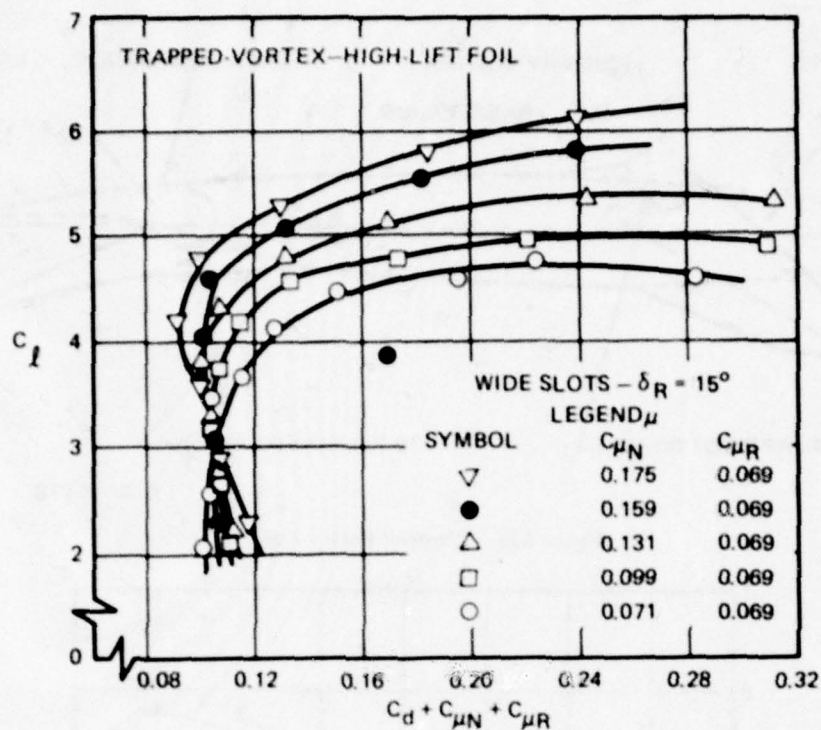


Figure 83 - Effect of Nose Blowing Variation on Total Drag for Trapped-Vortex Foil
Krall and Haight.⁷⁰

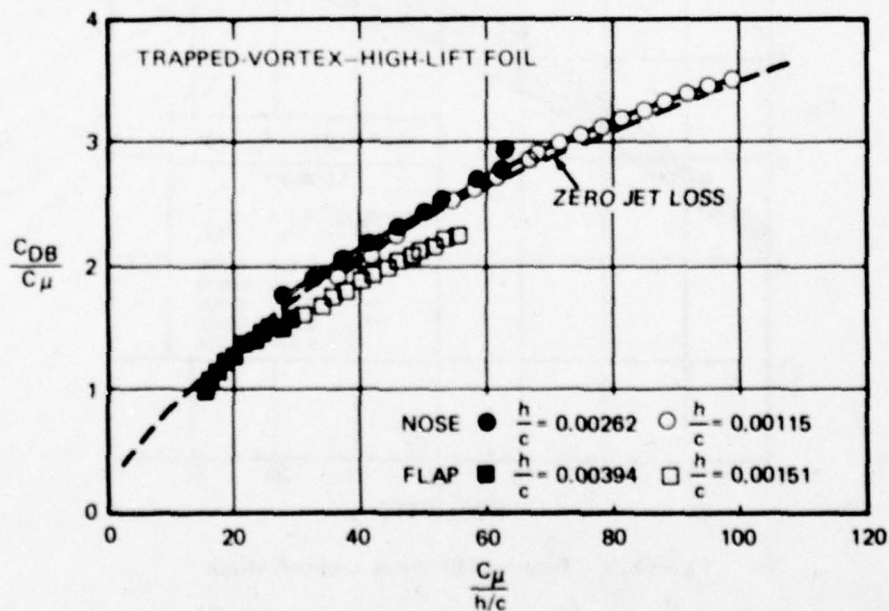


Figure 84 - Blowing Jet Power Coefficients versus Momentum Coefficients for Trapped-Vortex Foil

Here h = slot height, Krall and Haight.⁷⁰

$$C_{de} = C_d + \frac{1}{2} \left[C_{\mu N} \left(\frac{V_i}{U_{\infty}} \right)_N + C_{\mu R} \left(\frac{V_i}{U_{\infty}} \right)_R \right] + \left[C_{\mu N} \left(\frac{U_{\infty}}{V_i} \right)_N + C_{\mu R} \left(\frac{U_{\infty}}{V_i} \right)_R \right]$$

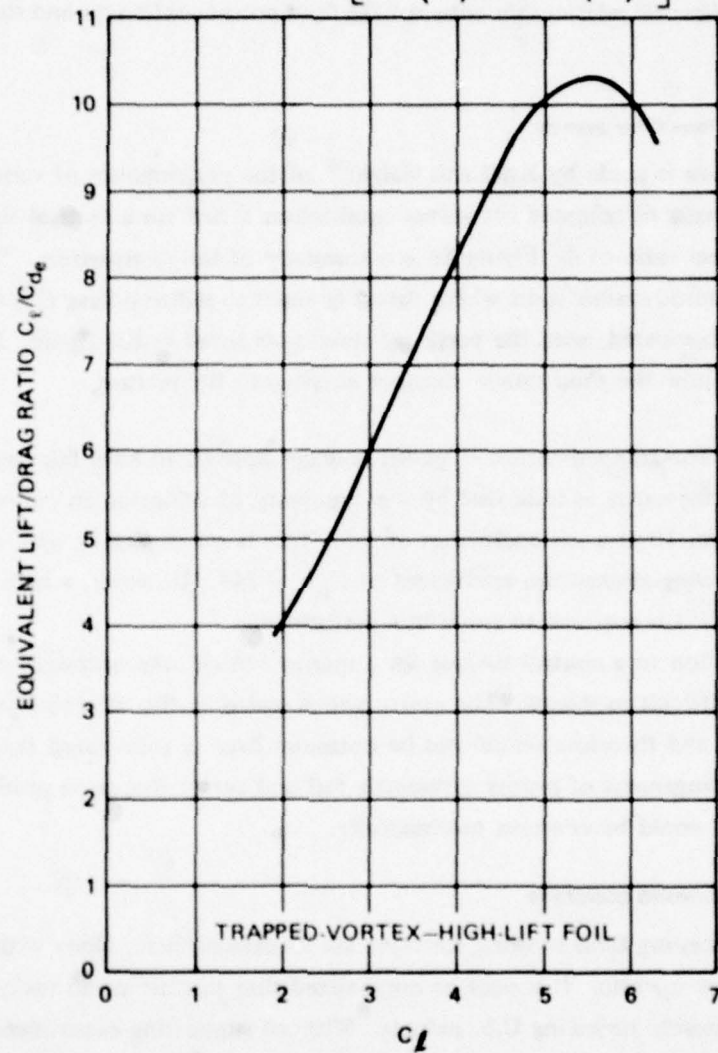


Figure 85 — Plot of Two-Dimensional Equivalent Lift-to-Drage Ratio versus Section Lift Coefficient for ATC Trapped-Vortex-High-Lift Foil

Data for the case: $\delta_R = 15^\circ$, wide slots, $C_{\mu N} = 0.175$, $C_{\mu R} = 0.069$, angle of attack range $0 \leq \alpha \leq 38^\circ$.

where P_j = jet-blowing power

$$q_{\infty} = \frac{1}{2} \rho U_{\infty}^2$$

$$S = b \cdot c$$

$$b = \text{span}$$

$$c = \text{chord.}$$

With the assumption of an incompressible fluid and no jet-nozzle losses, the curve in Figure 84 shows the experimental relationship between the fluid power coefficient and the momentum coefficient.

Comparison with Some Other Systems

A comparison is made by Krall and Haight⁷⁰ of the performance of various high-lift systems on the basis of trimmed lift versus equilibrium thrust for a tactical fighter airplane with a wing aspect ratio of 4. Figure 86 is a summary of the comparison. The crosshatched line denotes an aerodynamic limit where thrust is equal to induced drag $C_L^2 / \pi A Re$. Six high-lift systems are compared, with the pertinent references listed in the figure. It is not clear in this comparison how the *fluid power required* enters into the picture.

DISCUSSION: The trapped-vortex-high-lift concept appears to have fair two-dimensional aerodynamic performance as indicated by the capability of achieving an equivalent lift-to-drag ratio of more than 10 at a lift coefficient of 5.5. This is accomplished with a total two-dimensional, blowing-momentum coefficient of $C_{\mu} = 0.244$. However, a high angle of incidence ($\alpha \sim 35^\circ$) is required to reach this performance.

For application to a control surface for a marine vehicle, the necessary cusped cavities would present difficult problems. The cavity size is scaled to the incoming boundary layer flow conditions, and therefore would not be optimum over a wide speed range without adjustment. Arrangement of proper symmetric foil and cavity shapes to produce both positive and negative lift would be complex mechanically.

MISCELLANEOUS BLOWING CONCEPTS

Several interesting fluid blowing concepts are mentioned here, along with sketches showing how they operate. It should be emphasized that this list could easily be expanded indefinitely by merely reviewing U.S. patents. Without supporting experiments or analysis, however, many patent ideas are more like curiosities than serious force-producer concepts. The following are intended as provocative examples.

Free-Streamline Flap

Hurley¹⁹ has presented analysis and test data for a winglike lift producer; see Figure 87a. The free-streamline flow is created by angle of attack and by slot blowing as indicated. Lift and drag variations versus blowing coefficient C_{μ} are shown in Figures 87b and 87c with

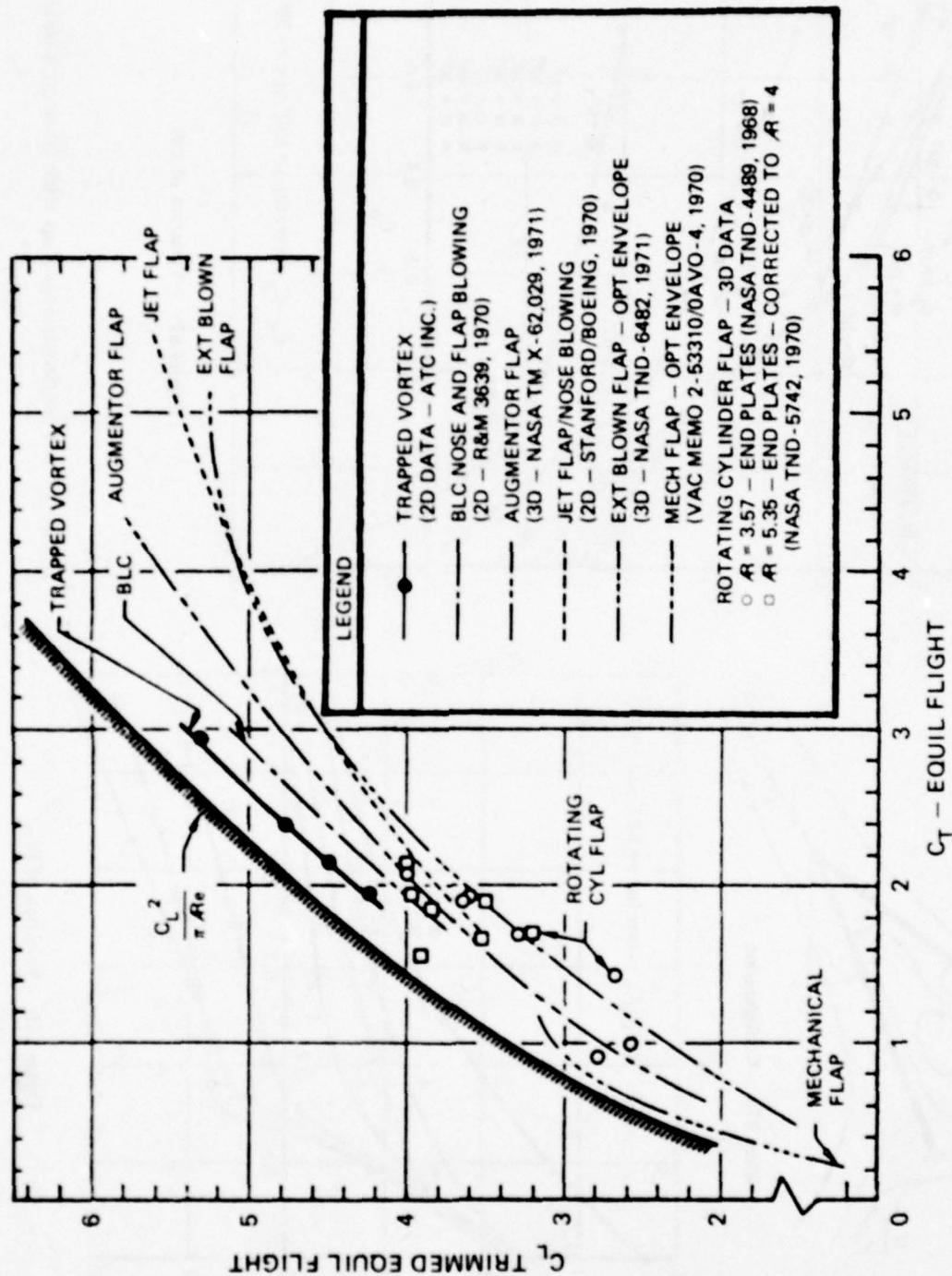


Figure 86 - Performance of High-Lift Systems for STOL-Tactical Fighter Configuration - $AR = 4$

Krall and Haight,⁷⁰

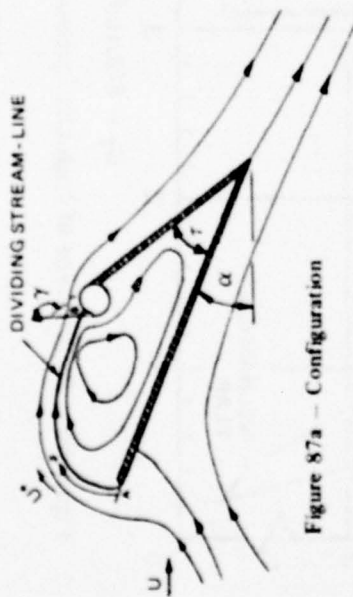


Figure 87a - Configuration

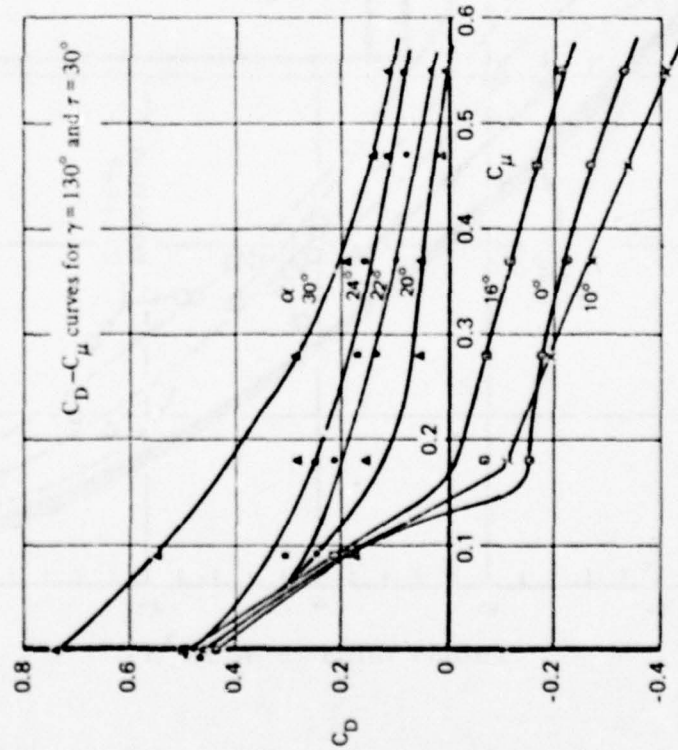


Figure 87b - Variation of Drag

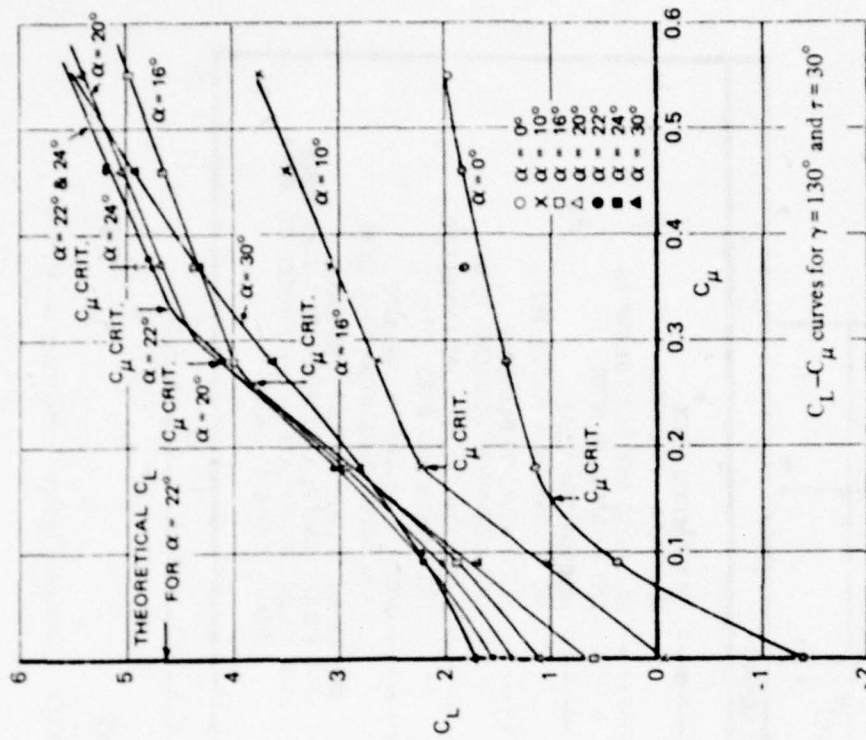


Figure 87c - Variation of Lift

Figure 87 - Free-Streamline-Flap with Blowing Control
Hurley¹⁹

contours of angle of attack. At some angles of attack and for sufficiently hard blowing ($C_{\mu} < 0.15$), the slot flow apparently adheres to the angled surface and is turned in the rearward direction to give a thrust ($C_D < 0$).

Coanda Thrust Augmentor

Figure 88 shows an arrangement of a blown slot and body shape that exploits the Coanda effect. A low pressure region exists around the *top* side near where the high-velocity jet is issued. As the flow is turned and begins to slow down, the pressure on the shaped bottom side is increased. A possible application of such a blown-slot thruster is shown in Figure 89.

Slot Blowing at Wing Tips

The concept of blowing out laterally from the wing tips is given in a U.S. patent by Kücheman et al.⁷¹; see Figure 90. The idea is to cause a virtual enlargement of the aspect ratio of the wing in order to give greater lift and smaller drag. Supporting wind tunnel data given in the patent indicate that the lift augmentation and drag reduction at $C_{\mu} = 0.138$ are

$$\Delta C_L / C_{\mu} \cong 1.0$$

$$\Delta C_D / C_{\mu} \cong -0.29$$

These are not impressive augmentations, when compared to blown flaps or CC by tangential jet blowing.

Beating Jet-Flap Thrust Wing

Saunders⁷² has prepared an idea in a U.S. patent to exploit the interaction between a waving jet sheet and a solid wing or between two waving jet sheets as shown in Figure 91. No firm predictions are given in the patent for the predicted time-averaged thrust versus C_{μ} and frequency for this gadget.

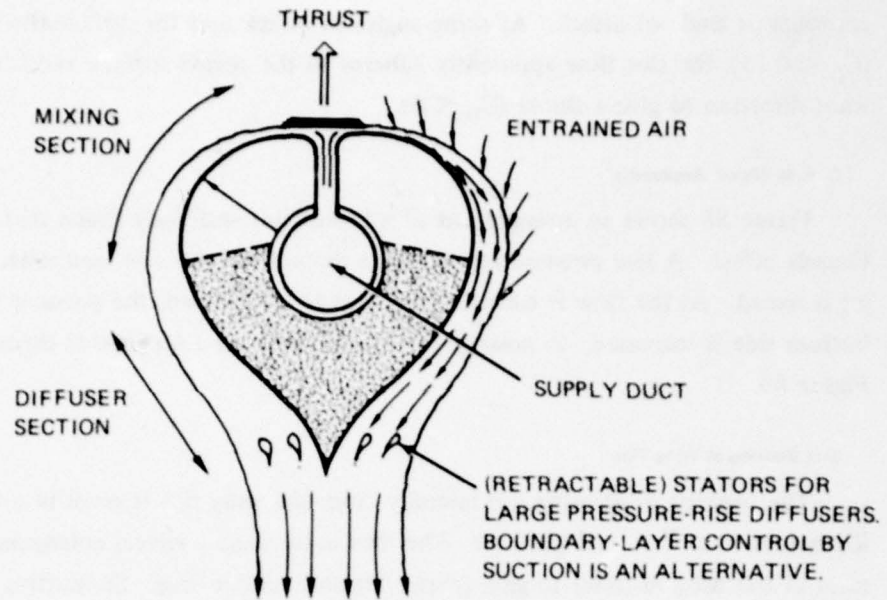


Figure 88 - A Coanda Thrust Augmentor

See discussion in Payne.⁶¹

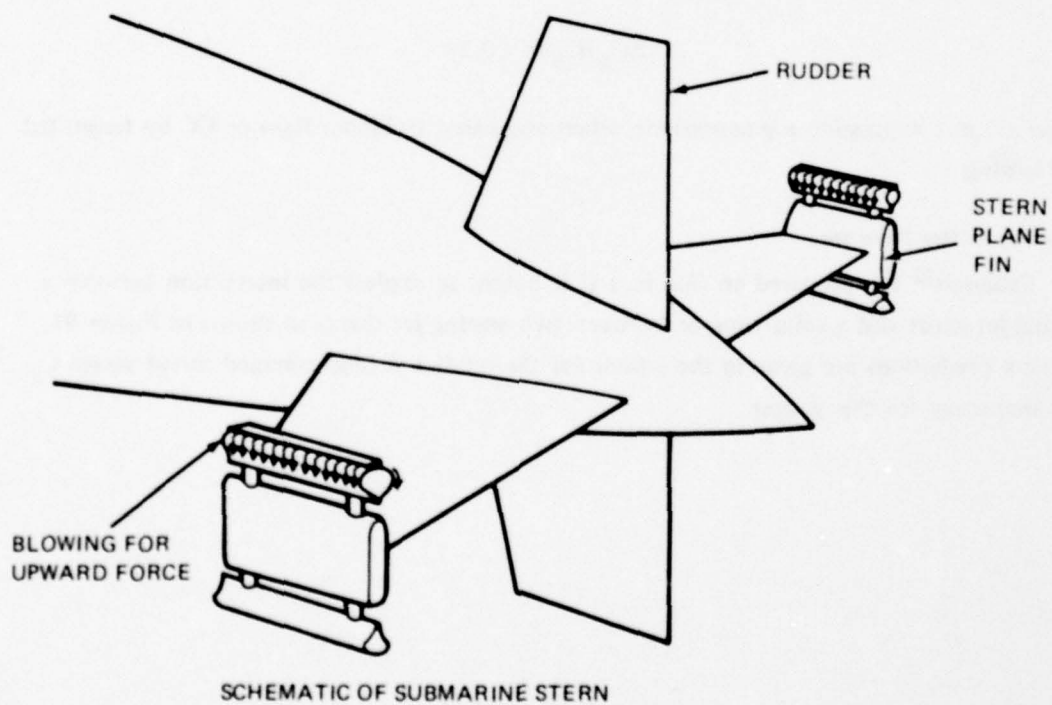
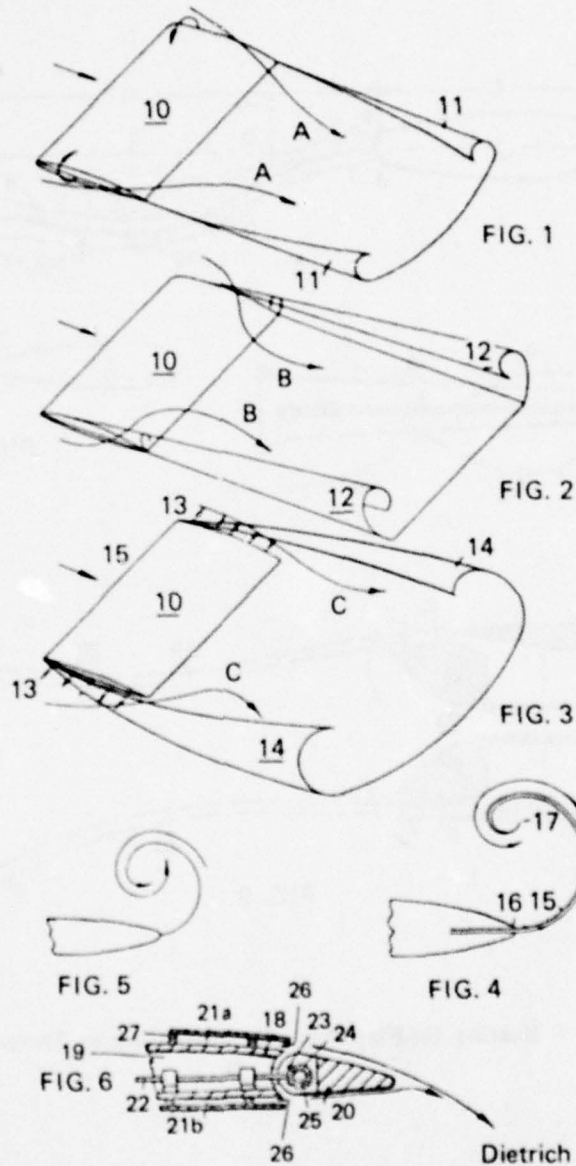


Figure 89 - Possible Arrangement of Coanda Thrusters at Tips of Submarine Stern Planes

May 21, 1963

D. KÜCHEMANN ET AL
AIRCRAFT

U.S. Patent No.
3,090,584



Inventors
Dietrich Küchemann,
Geoffrey M. Lilley & Eric C. Maskell

Figure 90 - Slot Blowing at Wing Tips

Kuechemann et al. 71

Feb. 9, 1965

W. S. SAUNDERS
BEATING JET-WING AIRCRAFT

U.S. Patent No.
3,168,997

FIG. 6

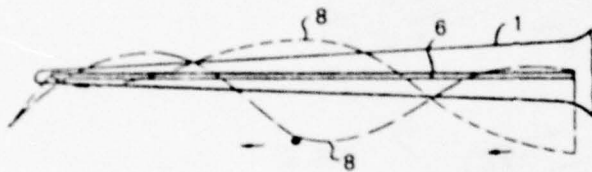
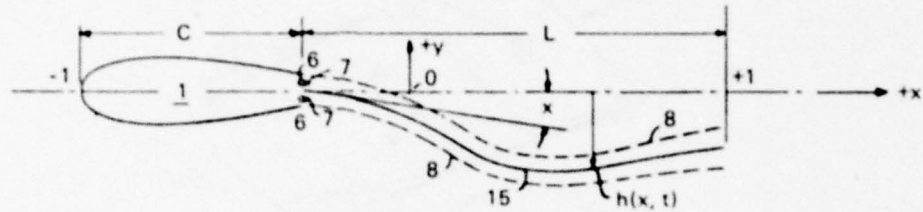


FIG. 7

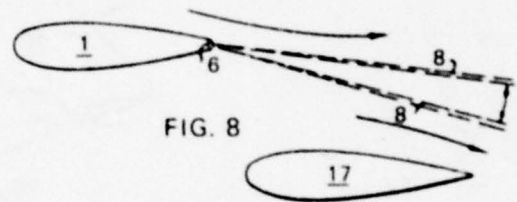


FIG. 8

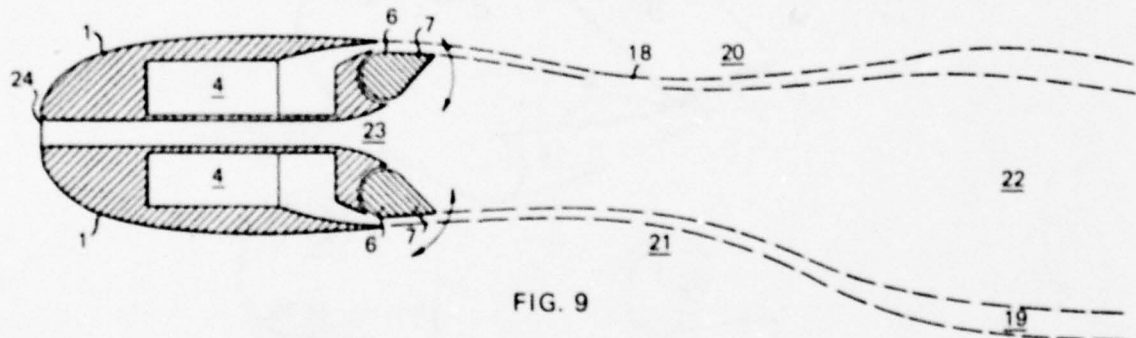


FIG. 9

Figure 91 - Beating Jet-Flap Wing for Propulsion or Thrust Production
Saunders⁷²

NAME: External Blowing, Deflected Slipstream

DEFINITION AND OPERATION: Deflecting either the exhaust stream of a thrusting jet or the slipstream of a propeller by means of flaps and vanes on lifting surfaces has been explored for STOL application, e.g. Goodmanson and Gratzner⁷³ and McCormick³. These types of force producers are all similar in that a fluid jet is turned either through some desired angle over the upper surface of the wing or under the lower surface of the wing, or the wing is immersed in the jet stream. The jet flow originates somewhere separate from the wing, hence the term "external blowing." In the aerodynamic literature, externally blown flap (EBF) refers strictly to the case of directing the exhaust of an external jet along the bottom surface of a slotted-flap arrangement. Upper surface blowing (USB) refers to the case where the jet exhaust is issued over the suction side of the wing-flap arrangement.

In a marine application, the slipstream flow could be produced by small auxiliary water jets or by ducted propellers located near flapped control surfaces.

An example of lift force augmentation and control by external blowing on the *lower surface* is shown in Figure 92 for a jet aircraft application. The swept wing has an aspect ratio of 3.14, with the propulsion jets located underneath, operating at a total jet-momentum coefficient $C_{\mu} = 1.1$. The graphs are for C_L versus C_D and C_L versus α for a constant value of flap deflection ($\delta_v = 45^\circ$) and various deflections of the jet exhaust. It is interesting to note that when the jet flow is directed up against the deflected flap ($\theta_d < 0$), not only is the lift performance very good, due to the local supercirculation, but the drag is remarkably low too.

External blowing over the *upper surface* is shown in Figure 93. The use of a deflector on the exhaust of the jet helps smear out the influence of the jet stream over the knee of the flap.⁷⁴

LIFT-FORCE ESTIMATES

For the case when the wing/flap arrangement is immersed in a slipstream, e.g. from a propeller, McCormick³ gives an outline of how to estimate the lift force. The main idea is that the jet stream is turned through an angle and is usually assumed to leave tangent to the flap trailing edge so that the overall flow resembles a jet-flap. The equivalent jet-momentum coefficient is

$$C_{\mu} = N_s T / q_{\infty} S_s \quad (52)$$

where N_s = number of propellers

T = thrust of the propeller producing the slipstream

S_s is the wing area immersed in the stream.

POWERING ESTIMATE

In the case of external blowing, power is consumed by the device producing the jet flow, a propeller or jet pump, etc. Power estimates for these devices are discussed elsewhere in this report. For example, ducted and unducted propellers and jet devices are covered in Chapter 2, Section B.

DISCUSSION: At first glance, the external blowing concepts seem somewhat far fetched for marine vehicle application. Since a submarine does not require hydrodynamic lift to keep it aloft, this type of integrated thrust-augmented lift does not seem necessary. However, if auxiliary orientable propellers or jets are ever seriously considered for slow-speed control, the range of flow turning of the slipstream could be greatly extended by use of flaps and vanes modeled after the devices described previously. The need for a mechanism to tilt a jet nacelle or ducted propeller could conceivably be eliminated if sufficient slipstream could be provided by flaps.

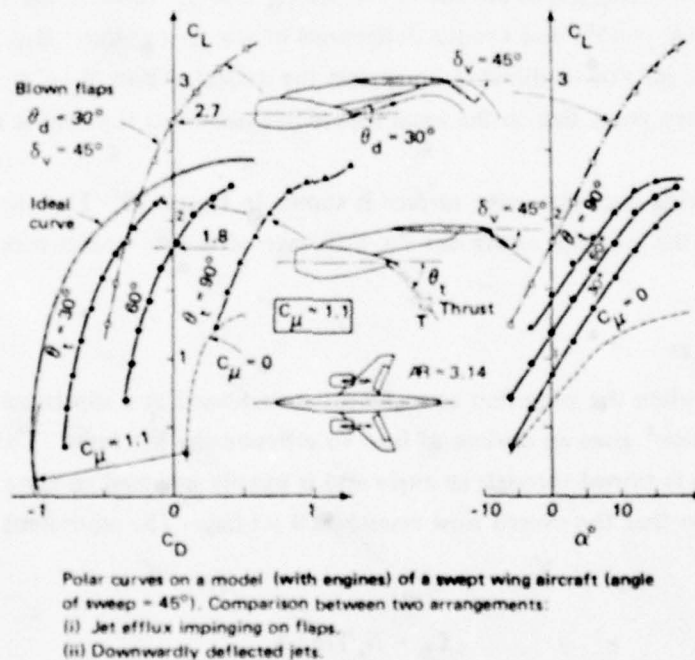


Figure 92 – External Blowing on Lower Surface of a Flapped Wing

Poisson-Quinton and Lepage.²⁰

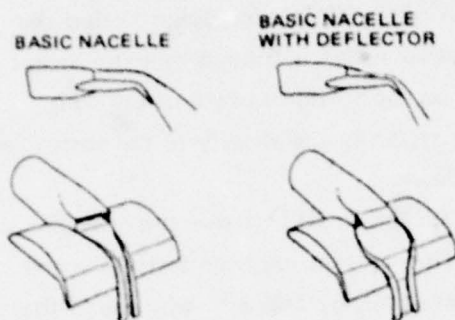


Figure 93a — Effect of Nacelle Exit

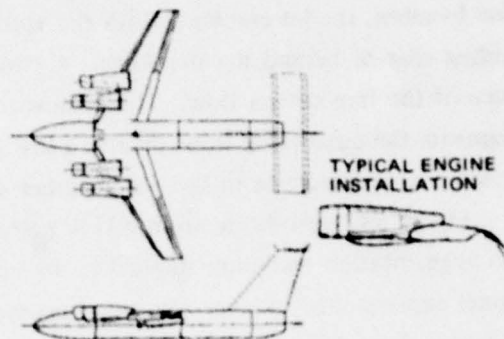


Figure 93b — Full-Span Upper Surface Blown Jet-Flap Model

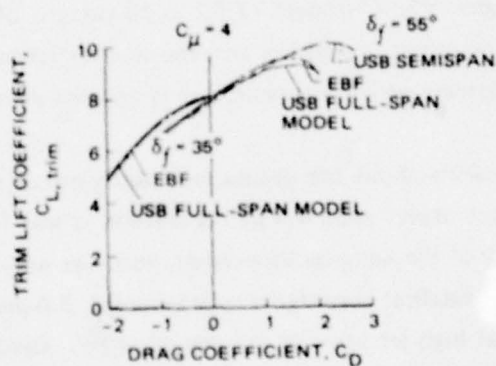


Figure 93c — Comparison of Lift-Drag Characteristics

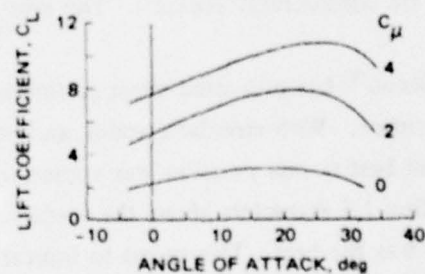


Figure 93d — Lift Characteristics of Semispan Model

Figure 93 — Upper Surface Blowing (USB) over a Flapped Wing

Phelps⁷⁴

NAME: Spanwise Blowing over a Lifting Surface.

DEFINITION AND OPERATION: Spanwise blowing is a unique form of lift augmentation by blowing. It combines the effects of both boundary layer and circulation control. A high-momentum jet is ejected from the hull over the suction side of a lifting surface in a direction *transverse* to the free stream. All the mass flow, \dot{m} , is blown out through the single round jet, and the total momentum coefficient C_{μ} is based on planform area S . Depending on its chordwise location, the jet combines with the vortical flow of the separation region behind the leading edge or behind the flap knee. A strong captured vortex is formed by entrainment of some of the free stream flow. This spanwise vortex on the suction surface of the wing augments the circulation flow, creates a low pressure region in the vicinity of the vortex, and causes a virtual increase in the wing camber and thickness.

Figure 94, reproduced from a U.S. patent by J.J. Cornish III,⁷⁵ shows the operation of this augmentation technique applied to an aircraft. This concept has been tested in wind tunnel experiments; some results were reported, for example, by Dixon,⁷⁶ who found that the jet-vortex flow does not remain concentrated over the entire span but grows rapidly in size and is reduced in its effectiveness far from the jet nozzle. Near the jet exit, at the wing root, the entrainment of free stream fluid causes the jet to roll up and form a vortex, which in turn creates large, suction peaks pictured in Figure 95. Outboard of 30 to 40 percent of the span of the tested wing, the vortex begins to smear out chordwise, and the suction pressure peaks are considerably reduced. The rate of increase of lift augmentation is greatest near the root.

Dixon⁷⁶ has presented some preliminary results about the optimum blowing nozzle size and location. With circular nozzles, and with the aspect ratio 4.4 lifting surface, it was found that the best nozzle position was approximately at the wing quarter-chord, with the nozzle centerline 1.5 diameters above the surface. The smallest convergent nozzle tested, 3.6-percent chord, was the best. This seems to indicate that high jet velocity is more effective. Dixon also discusses the entrainment capability of a higher V_j/U_∞ jet. For the flat-plate wing, a beveled, sharp leading edge gave slightly higher lift force values, compared with a rounded leading edge. However, a sharp LE would be less practical with the blowing turned off.

FORCE ESTIMATE - LIFT: FINITE ASPECT RATIO

At this time, there are few comprehensive test results that permit firm general statements about the effects of foil-section shape, thickness, planform shape, sweep, aspect ratio, etc. There is apparently no theory yet for describing the complicated rotational flow and the fluid forces. Such a theory would entail very difficult problems in the fluid mechanics of turbulent flows.

Nov. 25, 1969

J. J. CORNISH III

U.S. Patent No.
3,480,234

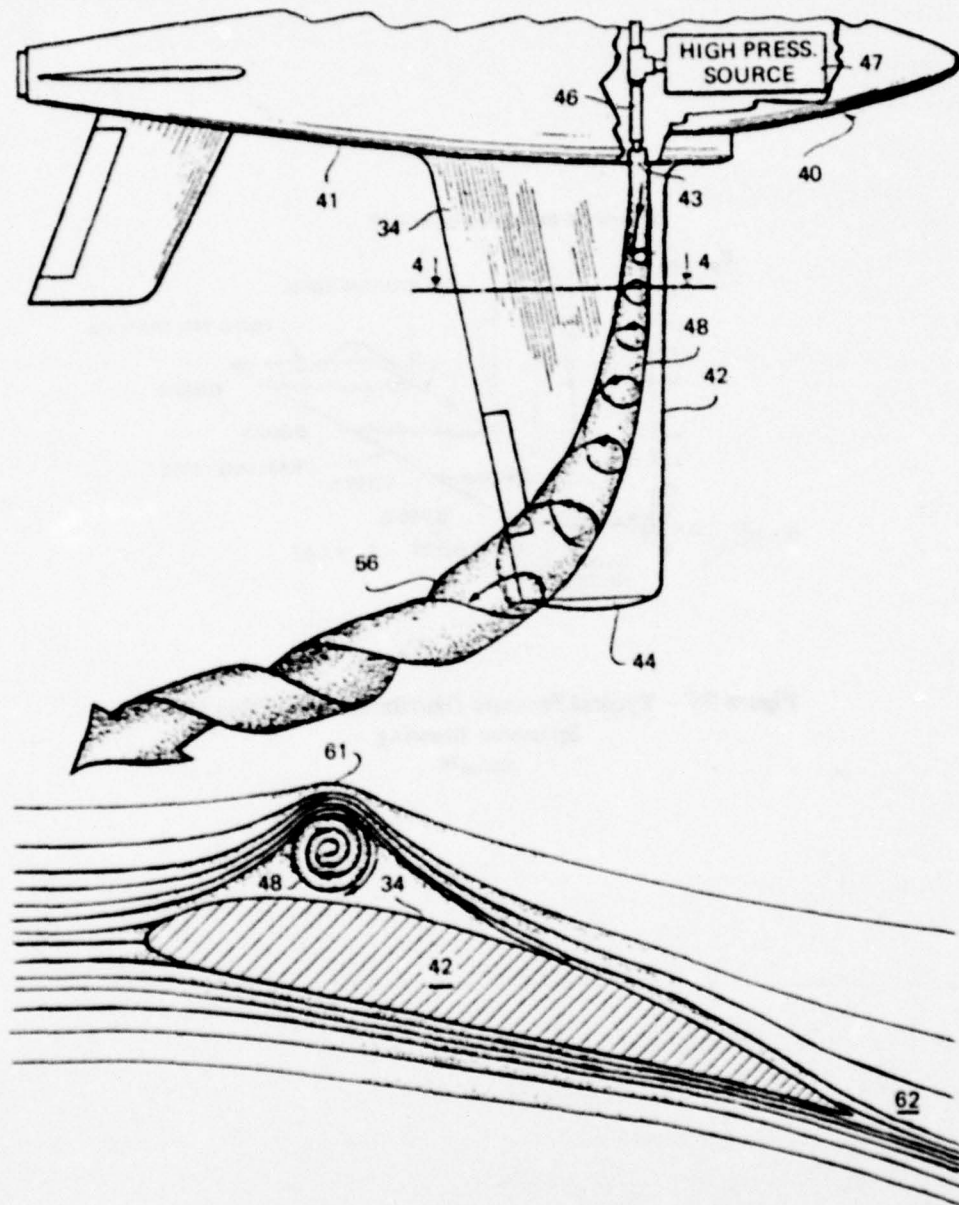


Figure 94 - Concept of Spanwise Blowing to Improve Lift
Cornish⁷⁵

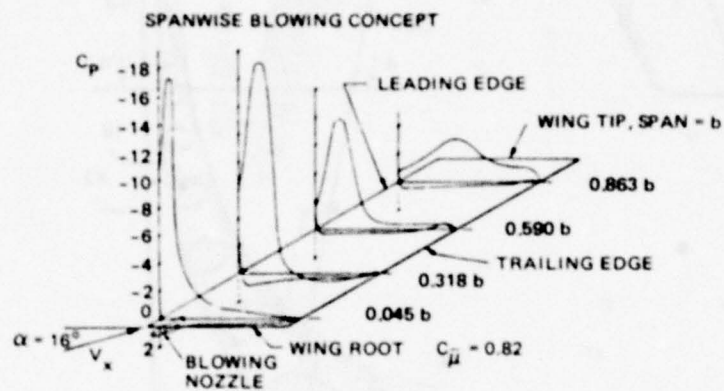


Figure 95 – Typical Pressure Distributions on Wing with Spanwise Blowing
 Dixon⁷⁶

Some experimental results are available for the forces. Figure 96 shows curves of the lift coefficient versus angle of attack for an aspect ratio 4.4 rectangular planform, flat-plate wing with a sharp leading edge and thickness ratio t/c of 2.5 percent. It is interesting to note that these lift curves are nonlinear with respect to angle of attack, especially at the larger angles of $12 \leq \alpha \leq 24$ degrees.

Figure 97 shows a comparison between a pure jet-flap wing of aspect ratio 2.75 and a laterally blown wing of aspect ratio 4.4. The lift efficiency of these two systems is of the same order. What is also interesting is that the curve of C_L versus $C_{\bar{\mu}}$ for spanwise blowing is essentially a straight line with a slope or lift augmentation of $\Delta C_L / C_{\bar{\mu}} \approx 2.3$ at an angle of attack of $\alpha = 20$ degrees. Of course, for the pure jet flap, the lift increase is $C_L \propto \sqrt{C_{\bar{\mu}}}$.

Spanwise blowing is also effective in controlling separation at the knee of trailing edge flaps. Figure 98 shows the lift coefficients obtained with the same flat-plate wing mentioned previously, but with a 25-percent-chord trailing-edge flap deflected 70 degrees, and a 7.5-percent-chord leading edge flap deflected 25 degrees. To control separation from the two flaps, there was lateral blowing across the knee location of each. The momentum coefficient $C_{\bar{\mu}_T}$ refers to blowing across the TE flap, and $C_{\bar{\mu}_N}$ refers to blowing across the nose flap. For a constant value of $C_{\bar{\mu}_N} = 0.176$, the initial lift augmentation slope is $\Delta C_L / \Delta C_{\bar{\mu}_T} \approx 4.2$.

With this particular high-lift concept, the effects of aspect ratio are difficult to predict accurately. This is particularly true for small-aspect-ratio wings $AR \leq 1$, where we should not expect to see the marked spanwise diminuation of the influence of the captured vortex as is shown in Figure 95.

To estimate the C_L value for aspect ratios not too far from 4.4, the data from Dixon⁷⁶ can be modified as follows

$$C_L(AR, C_{\bar{\mu}}) = \frac{F_A(AR)}{F_A(4.4)} \left[C_L(4.4, C_{\bar{\mu}}) + \left(\frac{\Delta C_L}{\Delta C_{\bar{\mu}}} \right) \frac{C_{\bar{\mu}}}{C_{\bar{\mu}_T}} \right] \quad (53)$$

where $F_A(AR)$ is given in Equation (41)

$C_{\bar{\mu}_T}$ = test value of $C_{\bar{\mu}}$ at $AR \approx 4.4$

$\frac{\Delta C_L}{\Delta C_{\bar{\mu}}}$ = lift augmentation at $AR \approx 4.4$.

In a more recent report, Dixon⁷⁷ has presented wind tunnel data for spanwise blowing on a 4.65-percent scale model of the F-8E(FN) French Crusader fighter aircraft. The wing had an aspect ratio = 3.39, NACA 65A006 profile, tapered to 5-percent thick at the tips. The jet was ejected from a simple circular nozzle mounted in the fuselage. Figure 99a shows the flow geometry and the characteristic jet rollup. Figure 99b indicates the arrangement of wing, flap, and nozzle. Figure 100 contains drag and lift data and its variation with flap angle and

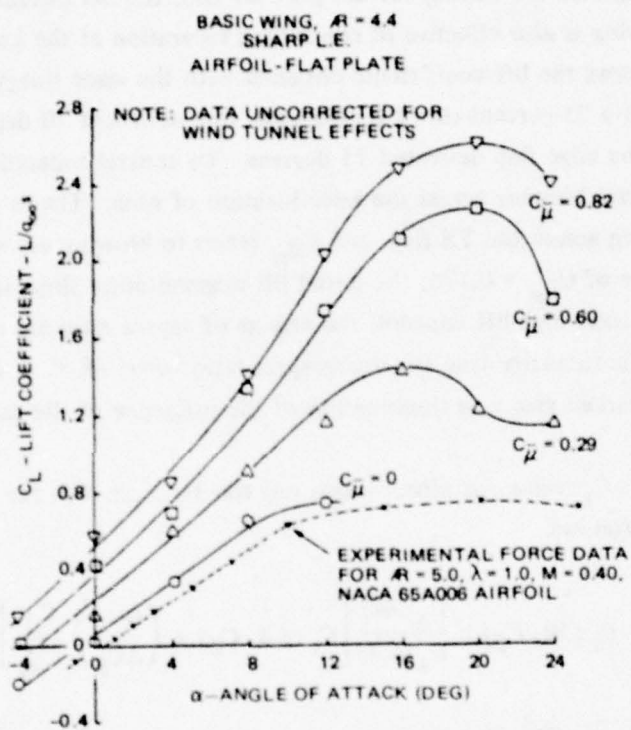


Figure 96 - Lift Due to Spanwise Blowing, Optimum
Nozzle Size and Position

Dixon⁷⁶

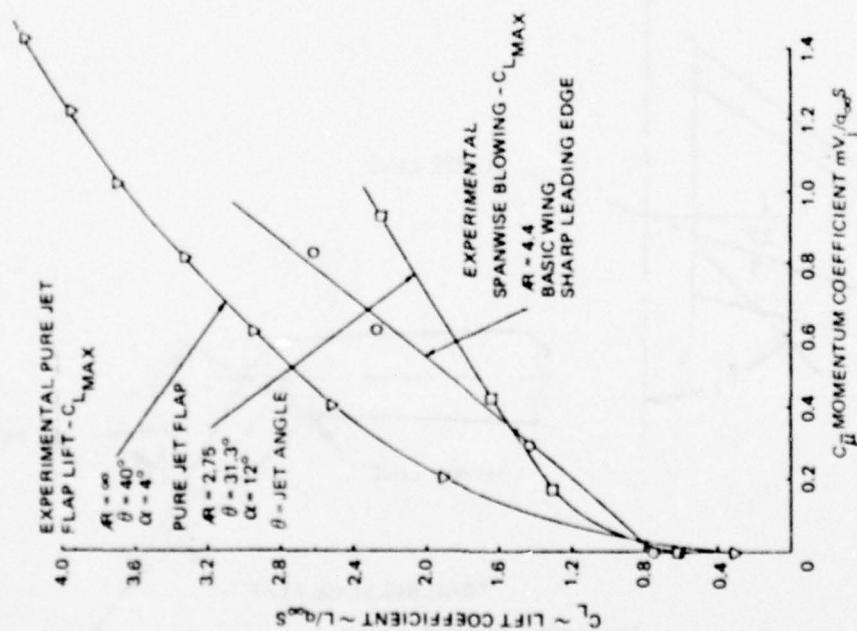


Figure 97 - Comparison of Spanwise Blowing
with Pure Jet Flap

Dixon 76

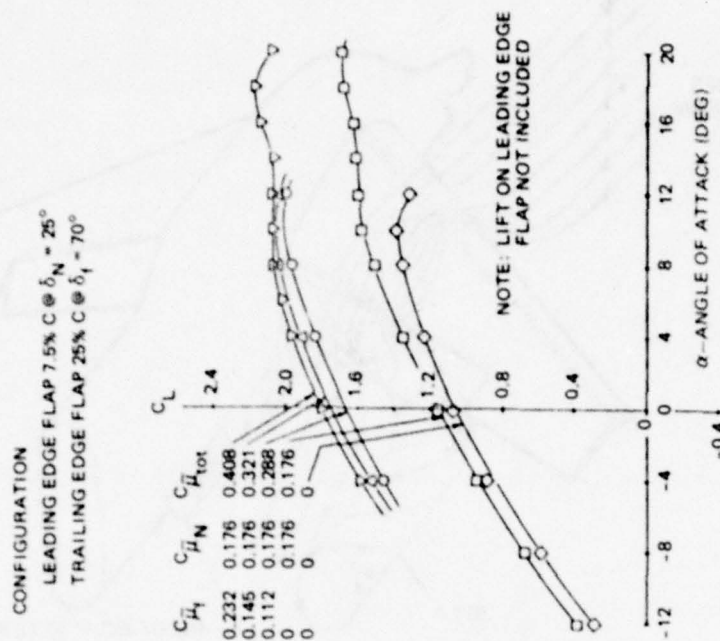


Figure 98 - Flap Blowing Effectiveness by
Means of Spanwise Blowing

Dixon 76

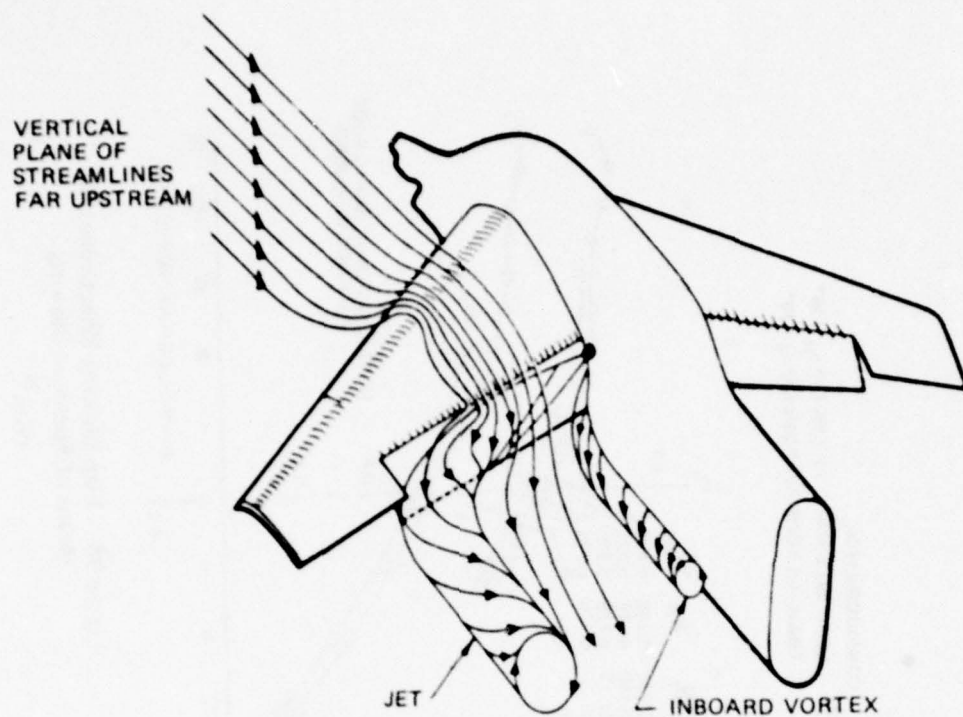


Figure 99a - Jet Roll Up and Free-Stream Entrainment

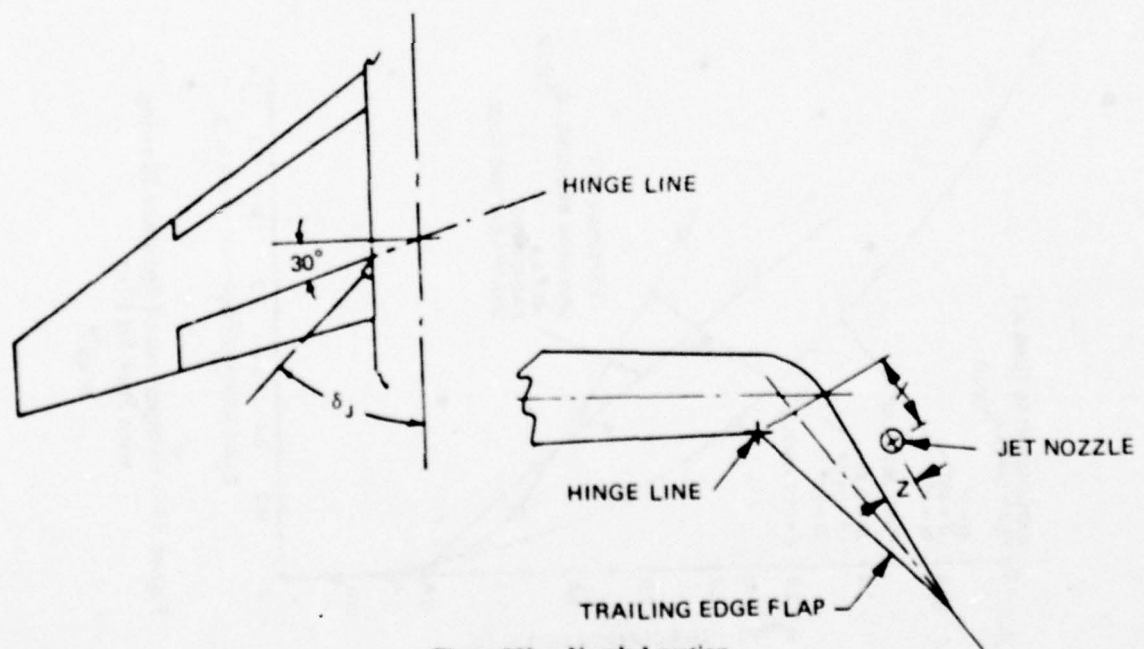


Figure 99b - Nozzle Location

Figure 99 - Experiment on Spanwise Blowing over Knee of Flap on a Model Airplane with an Aspect Ratio 3.39 Wing

Dixon⁷⁷

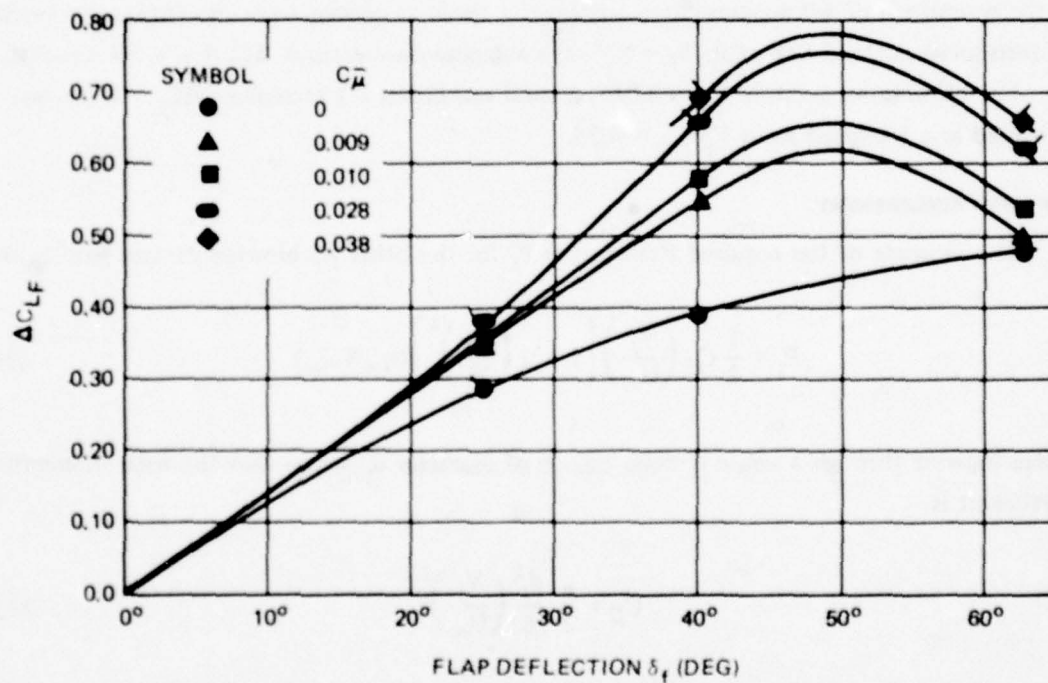
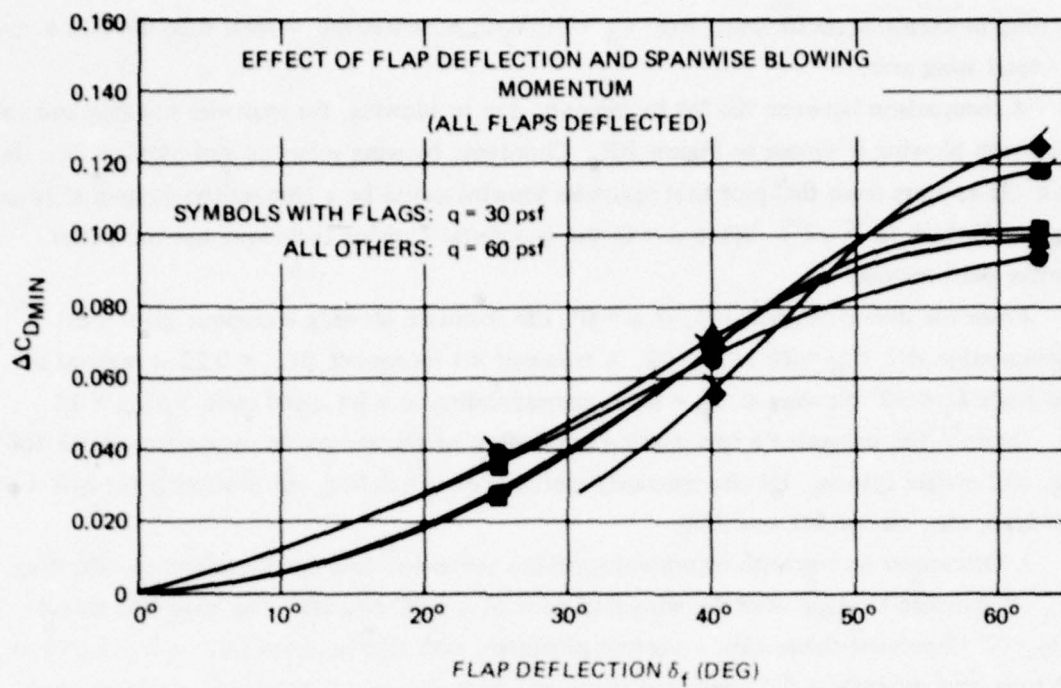


Figure 100 – Variation of Drag and Lift Coefficient Increments versus Flap Angle δ_f with Contours of $C_{\bar{\mu}}$ for Model Flow Situation Pictured in Figure 99a

Dixon⁷⁷

blowing momentum coefficient. Here $C_{\bar{\mu}} = \dot{m}_T V_j / q_{\infty} S$, where \dot{m}_T = total mass flow rate, and S = total wing area.

A comparison between the lift increments, due to blowing, for spanwise blowing and for chordwise blowing is shown in Figure 101. Chordwise blowing refers to slot-blowing at a flap knee. It appears from this plot that spanwise blowing could be a competitive system at large angles of attack ($\alpha \gtrsim 12^\circ$). When $\alpha = 0$, the chordwise blowing technique has the better relative performance.

From the data of Figure 101, at $\alpha = 0^\circ$, the spanwise blowing technique gives a lift augmentation $\Delta C_L / C_{\bar{\mu}} = 10$ as $C_{\bar{\mu}} \rightarrow 0$. A trimmed lift increment $\Delta C_L = 0.22$ is reached at flap angle $\delta_f = 50^\circ$ blowing at $C_{\bar{\mu}} = 0.28$, corresponding to a jet speed ratio $V_j / U_{\infty} = 13$.

Dixon⁷⁷ has presented a systematic examination of the geometric parameters of the foil, flap, and nozzle system. He also discusses methods of correlating and predicting the effect of flap span, etc., on the lift and drag.

J. Ottensoser in a private communication has presented data for the effect on lift, drag, etc., of spanwise blowing over the wing-flap knee of a T-2C aircraft. The wing had aspect ratio = 5, 12-percent thick foils, a tapered planform, with flap-to-chord ratio $c_f / c = 0.346$ at the root, and jet angle = 50° measured rearwards from the lateral direction. As an example of the magnitude of lift augmentation achieved, a result is quoted from the Ottensoser work. At zero incidence and flap angle $\delta_f = 53^\circ$, the augmentation ratio is $\Delta C_L / C_{\bar{\mu}} = 10$ for small $C_{\bar{\mu}}$. For blowing momentum $C_{\bar{\mu}} = 0.035$, a total maximum lift increment $\Delta C_L = 0.18$ was measured at a jet speed ratio $V_j / U_{\infty} = 9.25$.

POWERING REQUIREMENT

The estimate of the required fluid power P_f for the other jet blowing devices here as well

$$P_f = \frac{1}{2} C_{\bar{\mu}} \left(\frac{V_j}{U_{\infty}} \right) \left[1 + 2 \left(\frac{U_{\infty}}{V_j} \right)^2 \right] (q_{\infty} S U_{\infty}) \quad (54)$$

where blowing through a single circular nozzle of diameter d_j means that the total momentum coefficient is

$$C_{\bar{\mu}} = \frac{\pi}{2} \frac{d_j^2}{S} \left(\frac{V_j}{U_{\infty}} \right)^2 \quad (55)$$

DISCUSSION: Some pertinent features of spanwise blowing are summarized as follows.

1. Although lift cannot be produced independent of incidence angle or flap deflection, the lift augmentation $\Delta C_L / \Delta C_{\bar{\mu}}$ is nearly a constant at small values of $C_{\bar{\mu}}$ and at some

MOMENTUM EFFECT ON TRIMMED LIFT INCREMENTS
DUE TO BLOWING

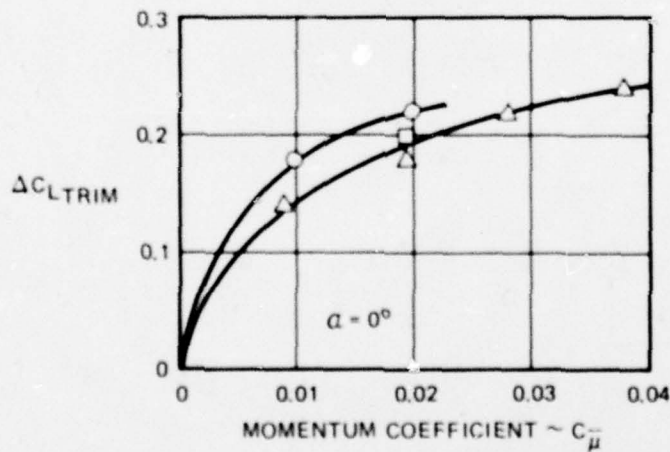
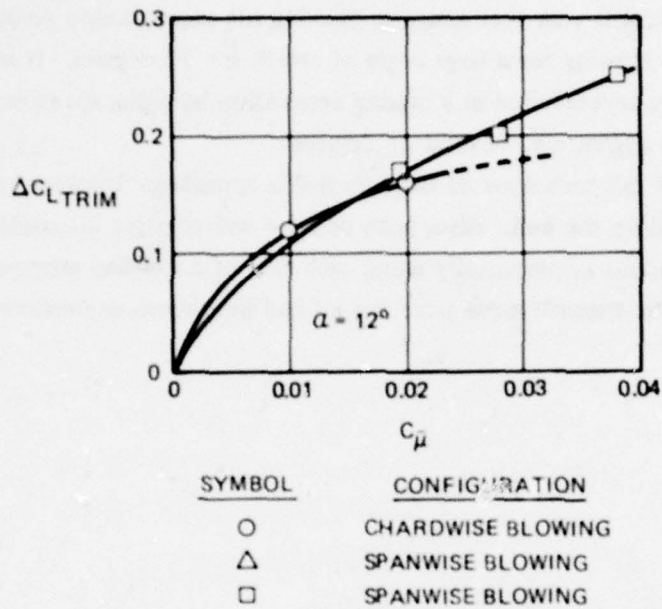


Figure 101 - Variation of Lift Increments with Blowing Momentum;
Comparison between Spanwise Blowing and Chordwise Blowing

Dixon⁷⁷

conditions of angle of attack and/or flap angle; see Figure 97. This means that the lift force is nearly independent of speed U_∞ , being proportional to $\dot{m}V_j$. More typical, however, are the ΔC_L vs $C_{\bar{p}}$ curves displayed in Figure 101 for spanwise blowing at the flap knee. There, the slope is not constant, and the ΔL would depend roughly linearly upon U_∞ as with a jet flap. Similar curves to those in Figure 101 were obtained by Ottensmeyer.

2. From Figure 101, it is seen that spanwise blowing lift-augmentation compares favorably with chordwise blowing for a large angle of attack $\alpha = 12$ degrees. It is poorer at $\alpha = 0$. This property may be exploited in a marine application by using spanwise blowing on *rudders* deflected at large angles, e.g., beyond 25 degrees.

3. The simplicity of this technique of flow control is appealing. Ducting for jet water need only be provided within the hull. Also, both positive and negative lift could be achieved by having jet nozzles arranged symmetrically along each face of a foil-flap arrangement.

Problem areas include: possible noise from the jet and limitations in performance due to cavitation.

NAME: Airfeeding to Alter Lift.

DEFINITION AND OPERATION: When a stream of air is injected into the water flow over the suction side or pressure side of a lifting foil, the hydrodynamic lift and drag can be markedly altered. In the case of air bleeding into the suction side, the lift is reduced; when air is fed into the pressure side, lift is increased. Usually the air is blown out through a line of closely spaced holes strung spanwise across a planform, or through a single hole.

This technique of airfeeding has been considered for lift control for hydrofoil boats, e.g., von Schertel⁷⁸ and, for maneuvering control forces on torpedoes, Smith.⁷⁹

For a range of the airflow coefficient C_Q between zero and some critical value $C_{Q_{cr}}$, the hydrodynamic force variations $\Delta C_L / \Delta C_Q$ and $\Delta C_D / \Delta C_Q$ are fairly steep and are often nearly linear, or at least monotonous. As usual, the flow-rate coefficient is defined as $C_Q = Q / U_\infty S$, where Q = *airflow* quantity.

The critical air quantity coefficient $C_{Q_{cr}}$ is defined as the ventilation quantity at which the flow becomes fully vented. At this airflow rate, the injected air coalesces into a cavity, which then extends downstream from the injection holes and beyond the TE of the foil. In the fully vented regime, the force coefficients change far less rapidly with increasing C_Q , and supercavitating foil theory can be used to model the flow situation.

For control of the lift force, the most interesting range is $0 \leq C_Q \leq C_{Q_{cr}}$, and all of the useful information about this regime is obtained experimentally.

FORCE ESTIMATES

Lang and Daybell⁸⁰ have presented results from water tunnel tests on foils with air vented into the suction side only. Two of their three foil sections are shown in Figure 102. In the experiments, air was exhausted through 55 holes, diameter = 0.012 inch. The foil chord length was $c = 4$ inches and span $b = 2.9$ inches. In Figure 103, curves of C_L versus C_Q for foil A show the typical rapid reduction of lift with increased air bleeding until $C_{Q_{cr}}$ is reached. Once the fully vented condition is achieved, the decline of C_L with C_Q tapers off significantly. For foil B, plots of C_L versus angle of attack α in Figure 104 indicate how the loss of lift ΔC_L changes with different α at a constant airflow rate.

A measure of the lift-reduction effectiveness of air feeding is given by the ventilation efficiency, based on $C_{Q_{cr}}$

$$\frac{\Delta C_L}{C_{Q_{cr}}} = \frac{C_L(\alpha, 0) - C_L(\alpha, C_{Q_{cr}})}{C_{Q_{cr}}} \quad (56)$$

Figure 105 shows curves of this ratio versus angle of attack for foils A and B. For example, foil B at $\alpha = 0^\circ$, and airhole location $a/c = 0.3$ has a lift-reduction effectiveness $\Delta C_L / C_{Q_{cr}} = 92$.

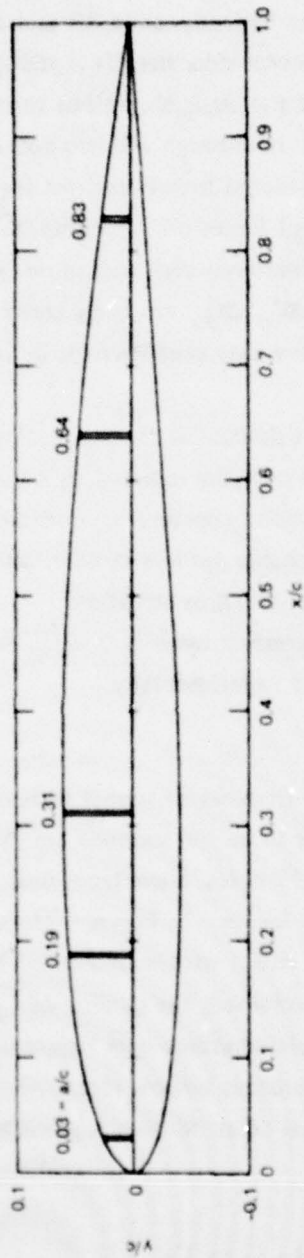


Figure 102a - Hydrofoil A, NACA 0010

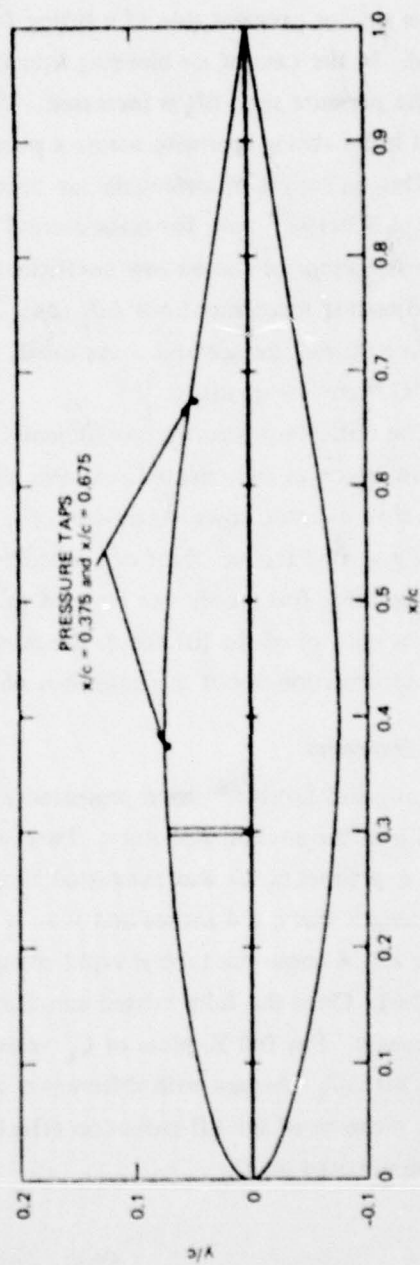


Figure 102b - Hydrofoil B, Modified 65₂-015

Figure 102 - Two Airfoils Tested in a Water Tunnel
Lang and Daybell, 80

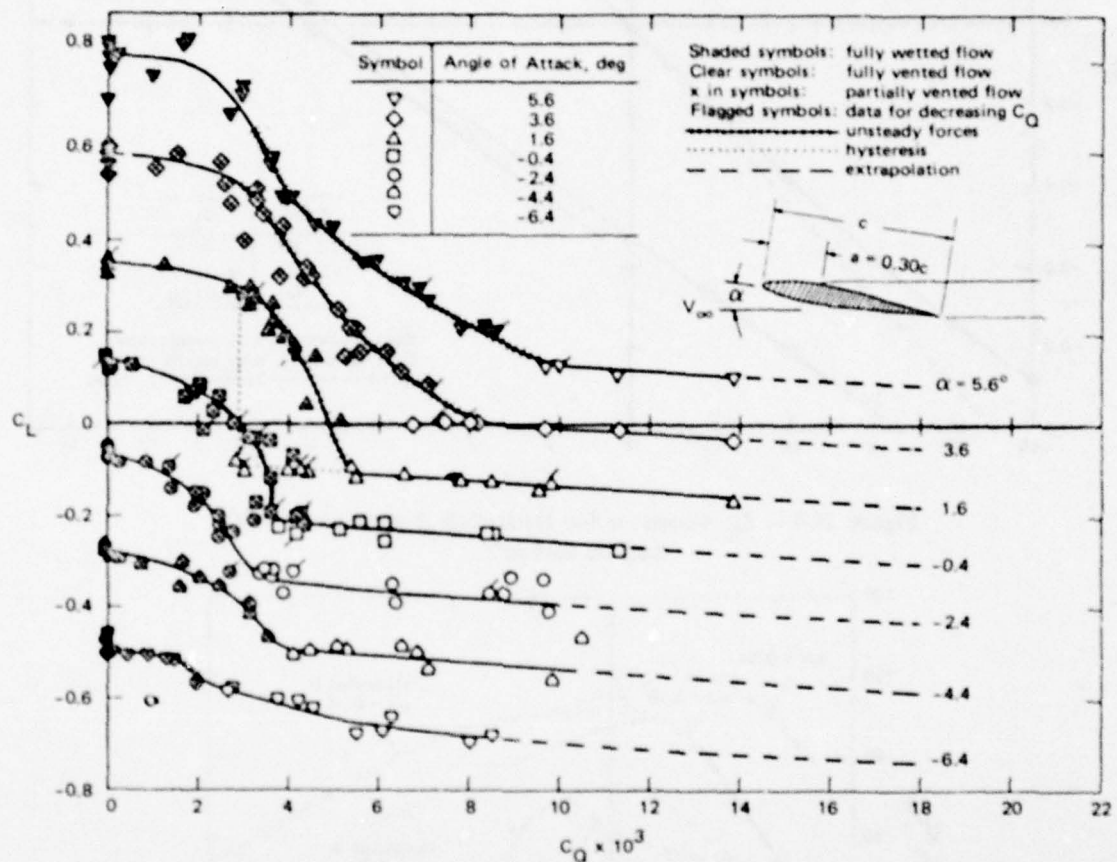


Figure 103 - C_L versus C_D for Hydrofoil A, $a/c = 0.30$, at Various Angles of Attack
 Lang and Daybell.⁸⁰

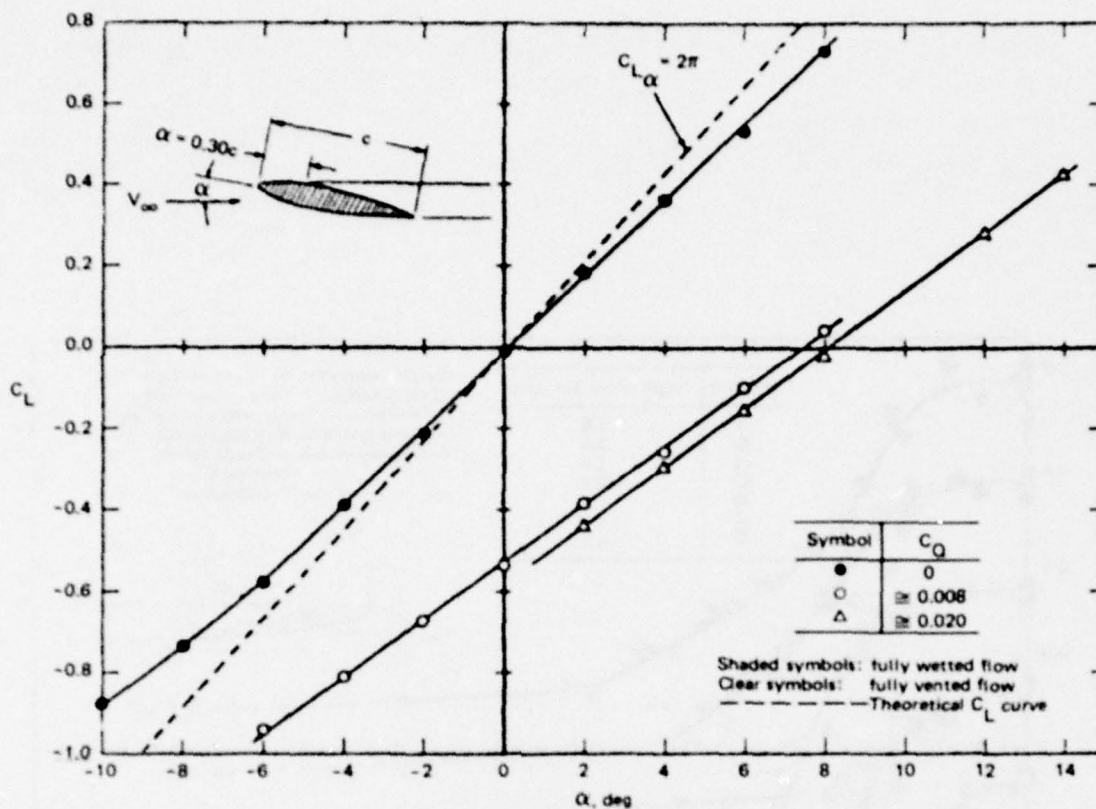


Figure 104 - C_L versus α for Hydrofoil B with $a/c = 0.30$
Lang and Daybell.⁸⁰

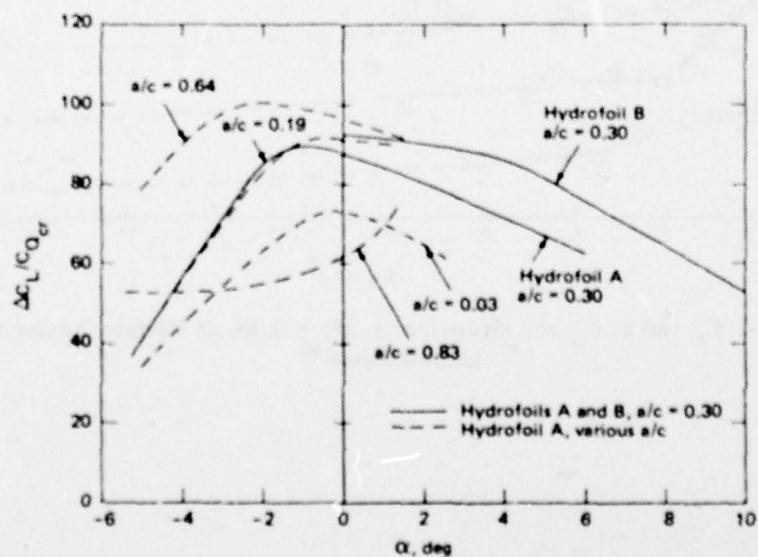


Figure 105 - Ventilation Efficiency versus Angle of Attack
for Hydrofoils A and B
Lang and Daybell.⁸⁰

Test data for air-fed foils of finite-aspect-ratio wings are not readily available, but is expected that the usual finite-aspect-ratio corrections can be applied to the section lift characteristics described herein.

For the sections tested by Lang and Daybell,⁸⁰ the drag increases as the air-venting rate C_Q is increased toward $C_{Q_{cr}}$. The maximum drag increase usually occurs before $C_{Q_{cr}}$ is reached. Near and beyond the critical air quantity, the drag increases become smaller. As an example, the drag-increase effectiveness for foil B at $\alpha = 0$ is $\Delta C_D / C_{Q_{cr}} \sim 1$ for air venting at $a/c = 0.30$.

VENTILATED RING WING

Air venting has been proposed as a method for steering a torpedo, or for producing control forces on a ring hydrofoil wing. These concepts are shown in Figure 106, reproduced from the U.S. patent by K.E. Smith.⁷⁹ Some experimental data for the lift, drag, and moment on a selectively ventilated, ring-wing hydrofoil are presented by Acosta and Wade.⁸¹ Figures 107 and 108 reproduced from Reference 81, show the test setup and typical increase in lift that can be achieved by exhausting air from a hole at the bottom of the ring. Acosta, et al.⁸² give test results on a slightly different configuration of ventilated ring wing.

POWERING REQUIREMENT

For air bleeding, the fluid power P_{air} required to supply an air quantity coefficient C_Q is estimated by

$$P_{air} = \rho_a g (\Delta H) Q \quad (57)$$

where $\rho_a g \Delta H \approx \frac{1}{2} \rho_a V_j^2$. Here ρ_a = density of air, and V_j is the average air-exhaust velocity through the venting holes. In terms of the coefficient C_Q

$$P_{air} = \frac{q_j}{q_{\infty}} C_Q \cdot (q_{\infty} U_{\infty} S) \quad (58)$$

where $q_j = \frac{1}{2} \rho_a V_j^2$, and $q_{\infty} = \frac{1}{2} \rho U_{\infty}^2$ with ρ = density of the water, and U_{∞} = free stream velocity. The exhaust velocity can be determined from

$$V_j = U_{\infty} C_Q \frac{S}{A_j} \quad (59)$$

where A_j = (total area of N_h venting holes, each d_j in diameter) = $N_h \pi d_j^2 / 4$, and S = planform area.

DISCUSSION: Some pertinent features of the airfeeding technique are:

1. Lift-force reduction can be produced without changes in foil incidence.
2. The time rate of change of hydrodynamic forces upon introduction of air is very rapid.
3. As the free-stream velocity is reduced, lift-force-changes on airfed foils fall off proportional to QU_{∞} .

An airfeeding system might well find application as an emergency measure to kill or reverse undesired lift on a jammed control surface. However, continuous operation of such a system would require a large supply of air. On a submarine this would be impractical and, moreover, would constitute a problem of concealment. Hence, for submarine application, airfed controls might conceivably be useful only intermittently.

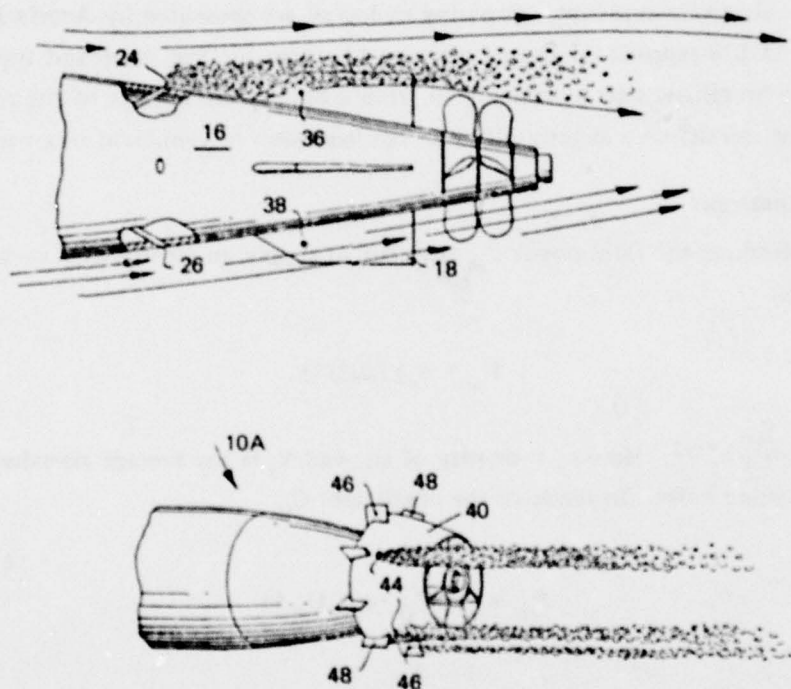


Figure 106 — Airfeeding into the Waterflow Past a Body or Ring Wing for Control Purposes

Smith⁷⁹

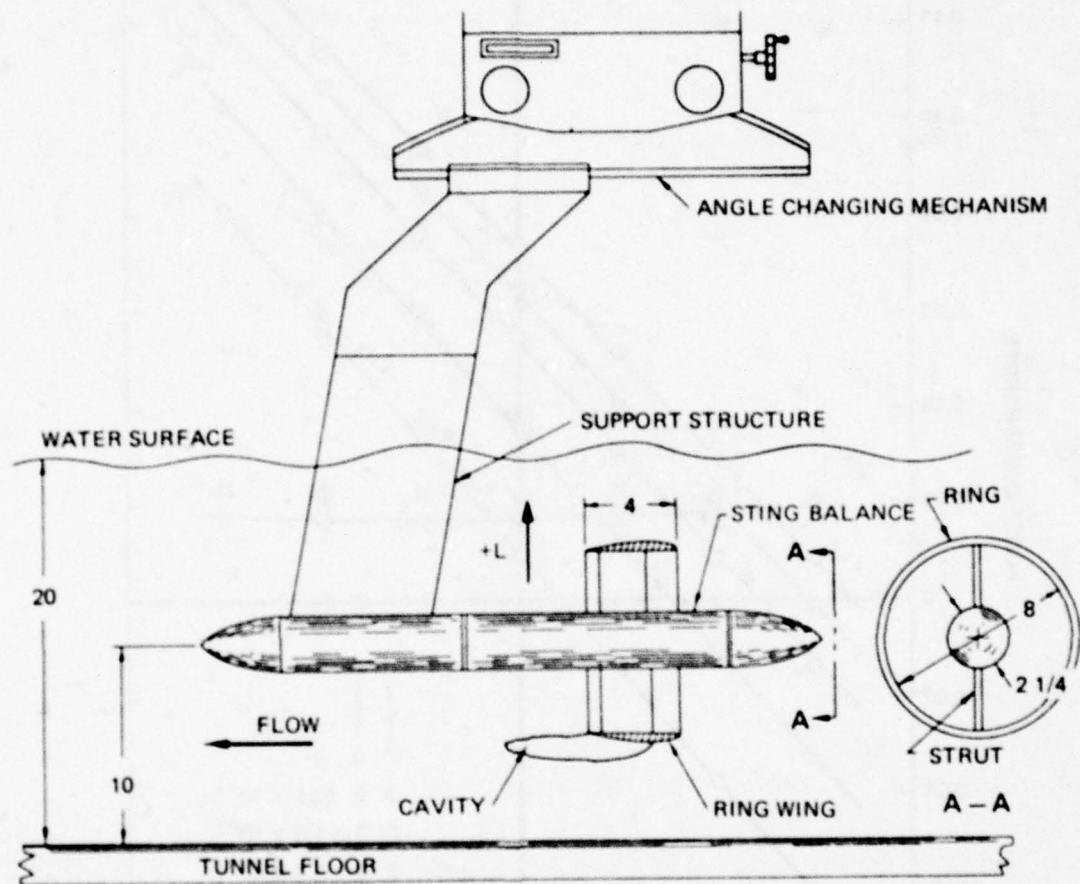


Figure 107 - Ring Wing Assembly in Tunnel

Selective airfeeding provides lateral control forces,
Acosta and Wade.⁸¹

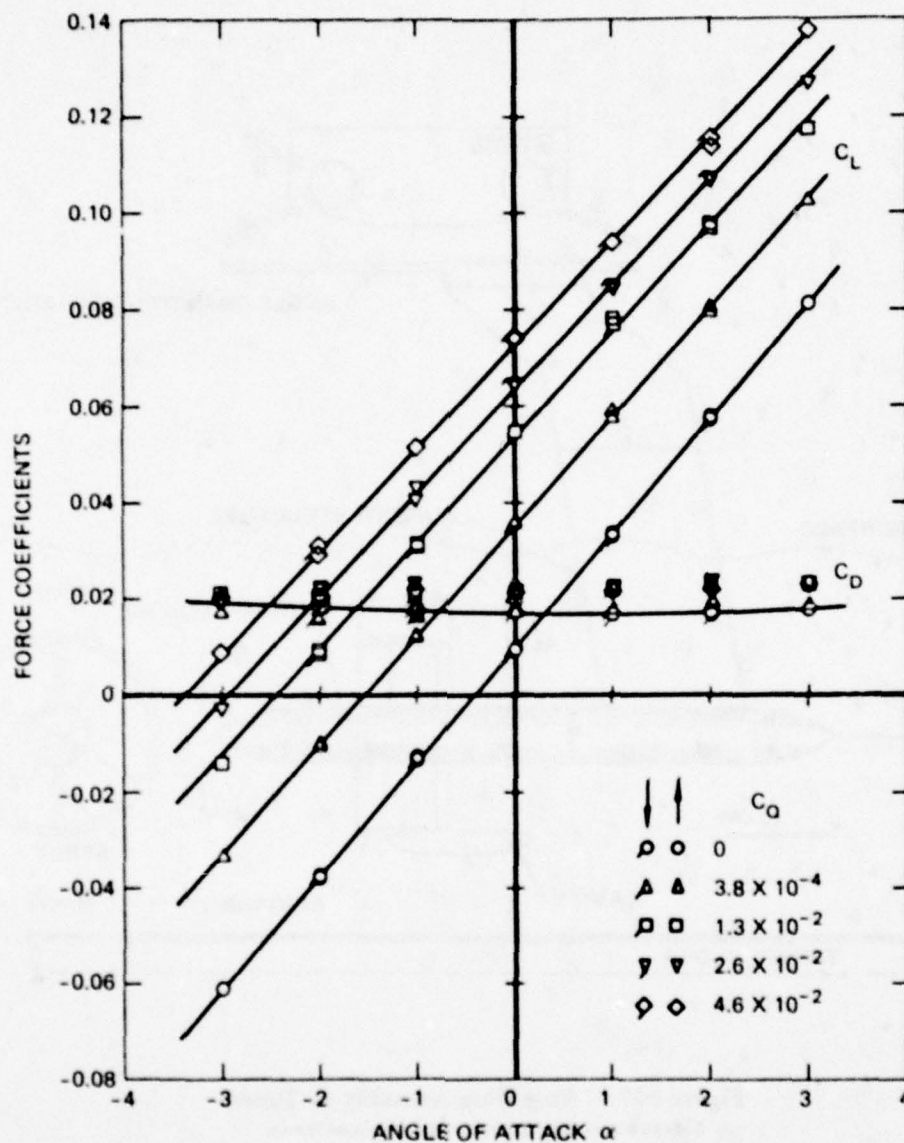


Figure 108 – Force Coefficients versus Angle of Attack with Various Airflow Coefficients for Ring Wing of Figure 107 with Ventilation Hole Configuration 5

Here $C_D = D / \frac{1}{2} \rho U_\infty^2 \pi d c$, $C_L = L / \frac{1}{2} \rho U_\infty^2 \pi d c$, $C_Q = \frac{\pi}{4} d^2 U_\infty$; where d = diameter of ring wing, c = chord; Acosta and Wade.⁸¹

NAME: Blowing to Kill Lift, Jet Spoiler.

DEFINITION AND OPERATION: A jet sheet can be used to spoil lift as well as augment it as in the case of the jet flap. By blowing fluid out through angled slots on the suction side of a lifting surface, the lift coefficient can be significantly reduced. At the same time, the drag force is increased, particularly when the jet velocity is directed back against the free stream.

LIFT-FORCE ESTIMATE

Very little data about or analysis of this concept are available in the literature. However, sufficient information has been generated to use for an aircraft design, e.g., Sweeney.⁸³ Also, some work on jet spoilers in supersonic flow is presented by Poisson-Quinton and Lepage.²⁰

Figure 109, reproduced from Wagner,⁶⁸ shows results for the effect of an angled jet spoiler on the 2D lift coefficient of an aerofoil versus angle of attack, for different values of flow-quantity coefficient $C_Q = Q/U_\infty S$. The jet sheet issues out at an angle of 40° back into the free stream. For this particular geometry, the 2D lift-reduction effectiveness is

$$\frac{\Delta C_l}{\Delta C_Q} = -45 \quad (60)$$

Note that by blowing out the bottom, the scheme in Figure 109 is a jet flap with a jet angle $\delta_j = 150$ degrees.

POWERING ESTIMATE

As in the discussion of blown flaps, the fluid power expended will be the sum of the ram drag power plus the power supplied to the jet velocity head. Here, in terms of the total flow quantity coefficient C_Q , the fluid power is expressed as

$$P_f = C_Q \left(\frac{V_j}{U_\infty} \right)^2 \left[1 + 2 \left(\frac{U_\infty}{V_j} \right)^2 \right] \cdot (q_\infty U_\infty S) \quad (61)$$

or if the average slot height \bar{h}_j is known, then $(V_j/U_\infty) = C_Q/(\bar{h}_j/c)$, and

$$P_f = \frac{C_Q^3}{(\bar{h}_j/c)^2} \left[1 + \frac{2(\bar{h}_j/c)^2}{C_Q^2} \right] \cdot (q_\infty U_\infty S) \quad (62)$$

DISCUSSION: Jet spoilers could be considered for application as an emergency device to counteract the lift on a jammed control surface, e.g., on a flapped foil at some angle of attack, or perhaps to reduce the lift developed by the sail during a turn. However, considerably more data would be needed than is available concerning how much blowing would be required at what angle and at what location along the chord.

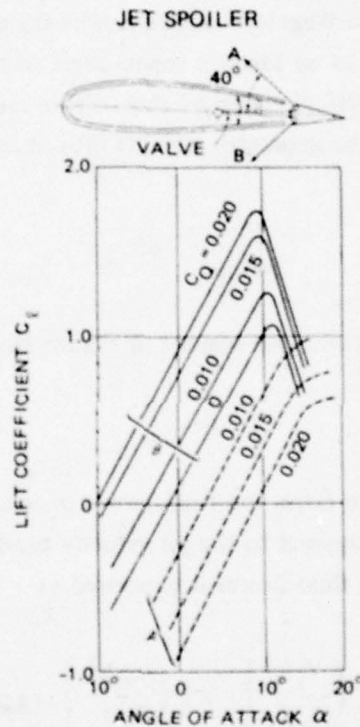


Figure 109 – Example of Sensitive BLC Control

This system of blowing on the upper or the lower side of the aerofoil was suggested by A. BETZ. Wind tunnel tests were performed in Gottingen before the end of World War II. The system operates on very small pumping power, Wagner.⁶⁸

NAME: Suction Through Slots.

DEFINITION: Slot suction can be used for boundary layer control and/or circulation control on lifting surfaces. The purpose of suction BLC is to remove a sufficient amount of boundary layer fluid in order to prevent separation at critical points along a foil surface or on a foil-flap configuration. For circulation control by suction, the action of a strong sinklike flow concentrated at certain locations has the effect of producing asymmetry or exaggerating existing asymmetry in the overall flow, thereby augmenting the circulation and the lift.

OPERATION AND FORCE ESTIMATES: Four general concepts will be discussed.

1. Slot Suction with Mechanical Flaps
2. Leading-Edge Suction Slot
3. Trailing-Edge Suction Slot
4. Slot-Suction Aerofoils with Low Drag

SLOT SUCTION WITH MECHANICAL FLAPS

Slot suction on the upper surface of a foil at the knee of the foil-flap arrangement appears to have a dual function. First, it has a boundary layer control effect because it helps guide the flow over the knee. It also has a circulation control influence because it distorts the flow and generates circulation augmentation even over an unflapped flat plate at some angle of attack; see Ringleb.⁸⁴

Force Estimates

The problem of a concentrated sink at the bend of a two-dimensional, flapped, flat plate has been studied theoretically, for example, by Ringleb.⁸⁴ The strength of the 2D sink, or slot-suction flow per unit width, is measured by the flow-rate coefficient $C_Q = Q/U_\infty c$, where Q is the suction-flow rate quantity per unit span, and c = chord. Figures 110 and 111 show the lift augmentation due to suction $\Delta C_L/C_Q$ as a function of flap angle δ_f and chord ratio c_f/c , respectively. The angle of attack on the flat plate foil in these curves is $\alpha = 0$.

The total drag of an actual two-dimensional flapped foil with suction would depend on the profile drag D_p as well as the momentum drag of the fluid removed by suction D_s , plus the equivalent drag components caused by losses in the suction system; see Pankhurst and Thwaites.⁸⁵ The momentum drag is

$$D_s = \rho Q U_\infty, \quad (63)$$

so that

$$C_{D_s} = D_s / \frac{1}{2} \rho U_\infty^2 c = 2C_Q \quad (64)$$

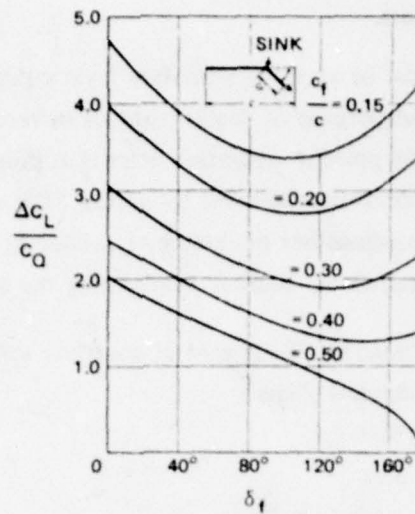


Figure 110 – Flapped Airfoil with Single Suction Slot at Knee of Flap

Theoretical sink lift for various flap chords, Wagner.⁶⁸

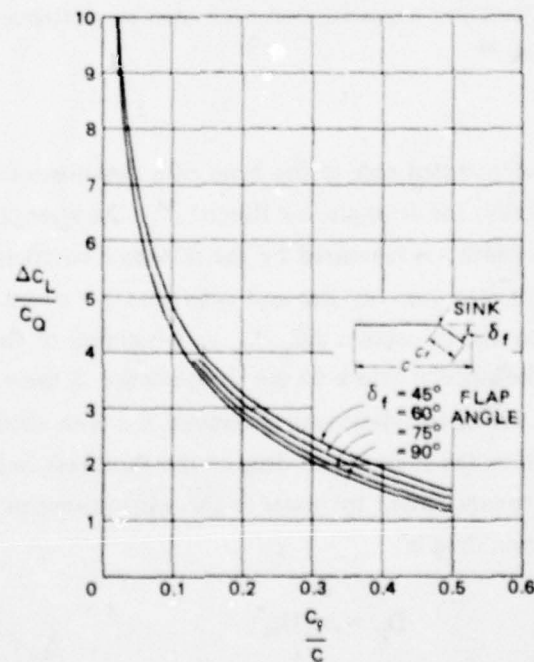


Figure 111 – Flapped Airfoil as in Figure 110

Effect of sink location from midchord to 98 percent of the chord, Wagner.⁶⁸

AD-A078 423

DAVID W TAYLOR NAVAL SHIP RESEARCH AND DEVELOPMENT CE--ETC F/G 20/4
AN INVENTORY OF SOME FORCE PRODUCERS FOR USE IN MARINE VEHICLE --ETC(U)
NOV 79 M B WILSON , C V KERCZEK
DTNSRDC-79/097

UNCLASSIFIED

NL

3 OF 5
AD-
A 078423



The remaining drag components depend, of course, on the details of the foil-section shape and internal ducting.

As an example of what the force coefficients look like for a slot-suction augmented-flap, some experimental results obtained by Arnold⁸⁶ are reproduced here. Figure 112 shows a NACA 66₄A421 profile shape with a 16.8-percent-flap chord and a suction slot just downstream of the flap knee. In wind tunnel tests, the foil spanned the width of the tunnel, and from the data it was determined that the effective aspect ratio was 7.5. All the data were acquired at a Reynolds number $U_{\infty}c/\nu = 3.3 \times 10^5$. With the total flow-rate coefficient defined as $C_{\bar{Q}} = Q/U_{\infty}S$, the minimum value necessary to maintain attached flow over the flap is denoted $C_{\bar{Q}_{crit}}$ and is shown in Figure 113 as a function of flap angle δ_f and angle of attack α . Figure 114 gives measured lift and drag coefficients versus the suction flow-rate coefficient $C_{\bar{Q}}$. The lift curve shows a nonlinear increase with $C_{\bar{Q}}$, which levels off abruptly when $C_{\bar{Q}_{crit}}$ is reached.

Power Requirements

To obtain an accurate estimate of power requirements for a fluid suction system, the particular details of the slot and ducting should be known. The fluid power necessary is expressed as

$$P_f = \rho g(H_{\infty} - H_d)Q \quad (65)$$

where $H_{\infty} = U_{\infty}^2/2g + p_{\infty}/\rho g$ and $H_d = U_d^2/2g + p_d/\rho g$ are the total heads in the free stream and in the duct, respectively. The change of head could be written in two parts

$$\Delta H = (H_{\infty} - H_{BL}) + (H_{BL} - H_d) \quad (66)$$

where the first part refers to the boundary layer loss up to the slot entry, and the second term depends on the details of the slot and internal ducting. In general these are difficult to estimate crudely as is done with blowing systems. For example, the analysis by Preston et al.⁸⁷ shows that the head-loss term $(H_{\infty} - H_{BL})$ depends on the velocity profiles within the boundary layer, and is thus a complicated function of the foil shape. Unless there are specific head-loss data available for a class of geometric arrangements, a good estimate of fluid power cannot be made.

Wagner⁶⁸ presents a discussion of various types of slot-suction, high-lift foils as well as an extensive outline about how to calculate BLC pumping power, using hydraulic-loss coefficients.

DISCUSSION: As a possible technique for lift augmentation on submarine control surfaces, slot suction at the flap knee is a poor contender. As will be seen in later sections, the purely

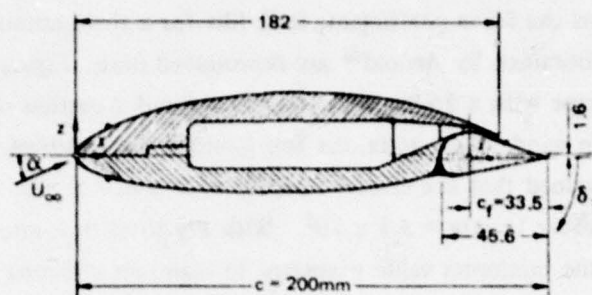


Figure 112 – Foil-Flap Arrangement for Slot Suction—
Lift Augmentation Scheme

Arnold⁸⁶

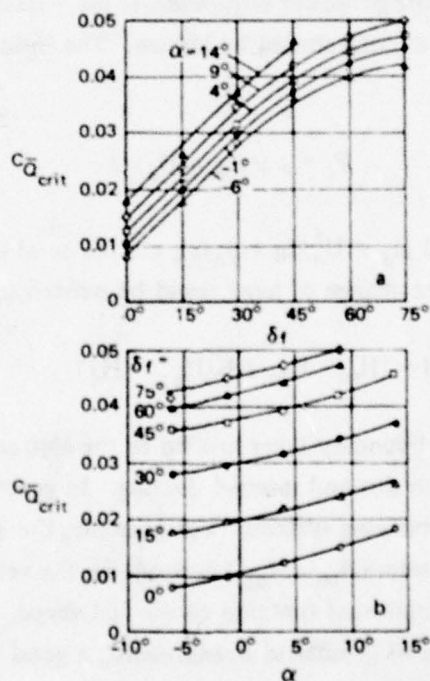


Figure 113 – Minimum Slot Suction Flow-Rate Coefficient
Required to Prevent Separation on the Flap as a Function
of Flap Angle δ_f and Angle of Attack

Data for the foil-flap geometry of Figure 112, Arnold.⁸⁶

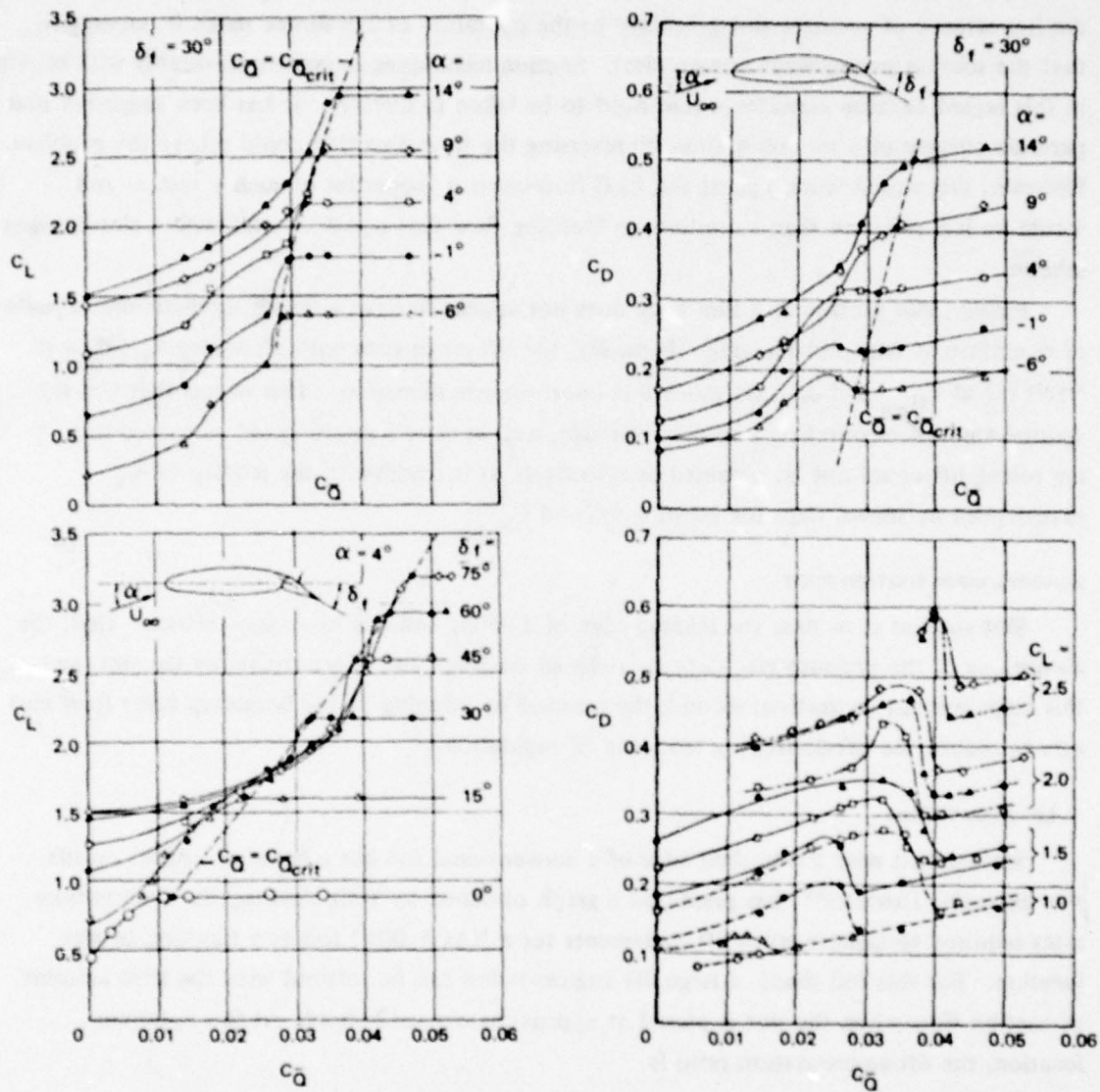


Figure 114 – Variations of the Lift and Drag Coefficients C_L and C_D with Slot Suction Flow Rate Coefficient C_Q , Contours of α , C_L , and of Flap Angle δ_f

Data for the foil-flap geometry of Figure 112, Arnold.⁸⁶

hydrodynamic performance of this concept as measured by effective lift-to-drag ratio is very low, even compared with other suction arrangements; see Figure 1.

Another disadvantage, common to all suction flow-control schemes, is the likelihood that the suction slots will be easily clogged with marine growth. The small size of the slots and the importance of accurate slot geometry to the operation of the device make it imperative that the suction passageways remain clear. Suction techniques compare unfavorably with blowing in this regard because seawater would need to be taken in directly. It has been suggested that periodic purging of a suction system by reversing the flow direction could relieve the problem. However, this would work against the BLC flow-control properties of such a system and would be less effective than a continuous bleeding flow that could be used with a slot-blowing scheme.

Finally, slot suction at a flap knee does not appear to have a strong supercirculation mode of operation as does slot blowing. Typically, the lift curve rises with increasing C_Q ; then it levels off at $C_{Q_{crit}}$ and displays much less improvement thereafter. This means that if a substantial amount of pumping power is available, e.g., at slow forward speed, continuously improving lift could not be obtained as effectively as it could with the jet-flap effect experienced by blown flaps for blowing beyond $C_{\mu_{crit}}$.

LEADING-EDGE SUCTION SLOT

Slot suction at or near the leading edge of a lifting foil has two major effects: first, the abruptness of the pressure gradients are reduced both up- and down-stream of the slot, and this helps prevent separation; second, the removal or thinning of the boundary layer flow also acts to reduce the lift-destroying tendency of separation.

Lift-Force Estimate

Slot suction near the leading edge of a conventional foil has a beneficial effect on lift. For example, Thwaites⁸⁸ has presented a graph obtained by Walz showing the suction-flow rates required to achieve given lift increments for a NACA 0012 foil as a function of slot location. For this foil shape, a large lift augmentation can be realized with the least amount of suction flow when the slot is placed at approximately 0.12 chord. At this optimum location, the lift-augmentation ratio is

$$\frac{\Delta C_{L_{max}}}{C_Q} \cong 100 \quad (67)$$

This optimum depends, however, upon the type of flow at stall, and would vary with section shape, thickness-to-chord ratio, leading-edge radius, and to some extent on the width of the slot.

Thin foil shapes designed especially for nose-slot suction have been obtained by Lighthill, Glauert, and Williams using methods developed by Goldstein⁸⁹ and others. Three shapes are shown in Figure 115, and the comparisons of maximum lift coefficients versus C_Q are displayed on Figure 116. Figure 117 shows the maximum lift coefficient versus flow-rate coefficient C_Q or suction-momentum coefficient C_μ for the Williams foil design NPL 434.⁹⁰ Data from three different slot widths have been included.

TRAILING-EDGE SLOT SUCTION

Slot suction at or near the trailing edge of a foil can be used to control the circulatory lift because the sink-flow into the slot causes an asymmetrical distortion of the overall flow about the foil shape. This is shown in Figure 118.

Force Estimates

Figure 119, from Poisson-Quinton and Lepage,²⁰ contains plots of the increments in section lift and drag coefficients due to slot suction. Note that the ΔC_D is nearly identical to the coefficient of the momentum drag of the fluid removed by suction, Equation (64).

An extensive theoretical and experimental treatment of circulation control by slot suction at the trailing edge is presented by Hazen et al.⁹¹ As an example of experimental lift-augmentation data obtained in Reference 91, some results are reproduced here for the particular TE slot-suction foil shown in Figure 120a. The section lift coefficient versus angle of attack is given in Figure 120b with contours of C_Q . Lift effectiveness here is $\Delta C_L / C_Q \approx 20$, using the values at $\alpha = 10^\circ$.

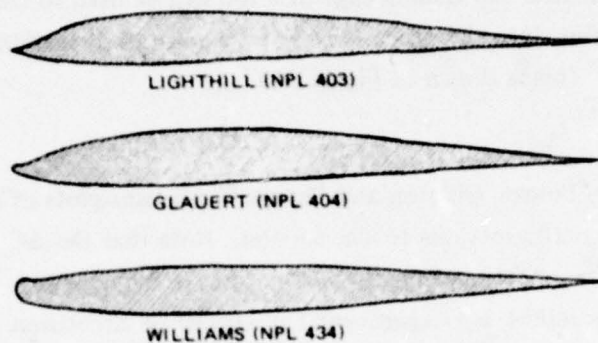
Section drag data for the same foil pictured in Figure 120a are shown in Figure 121, where C_{d_w} = wake drag or profile drag; the sum $(C_{d_w} + 2C_Q)$ is a modified drag coefficient, corrected for the momentum drag of the fluid removed by suction.

Power Estimate

Fluid power required by the slot-suction system is given by Equation (65). The formula requires data for both the duct static pressure p_d and the average velocity head $\frac{1}{2} \rho U_d^2$ within the duct. An approximate form of this expression, which neglects the part $\frac{1}{2} \rho U_d^2$, is quoted in Hazen et al.⁹¹ in terms of an equivalent fluid power

$$P_f = C_Q (C_p - 1) (q_\infty U_\infty S) \quad (68)$$

where $C_p = (p_\infty - p_d)/q_\infty$ is a pressure coefficient based on the duct pressure p_d within the foil and the ambient pressure p_∞ . In general C_p must be determined experimentally. Figure 122 gives data for C_p for the same foil configuration, trailing edge version I-b, shown in Figure 120.



NOSE SHAPES SCALE: - (5 x ABOVE)

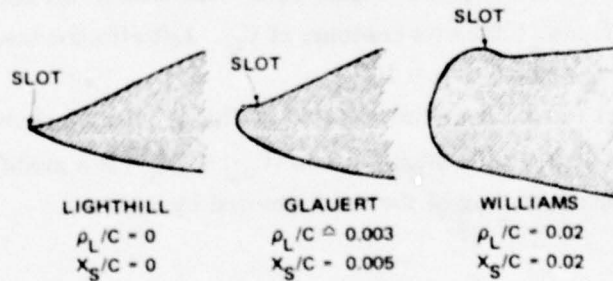


Figure 115 - Specially Designed 8.5-Percent-Thick Nose-Slot Suction Airfoils

Here ρ_L is the nose radius
 Williams⁹⁰

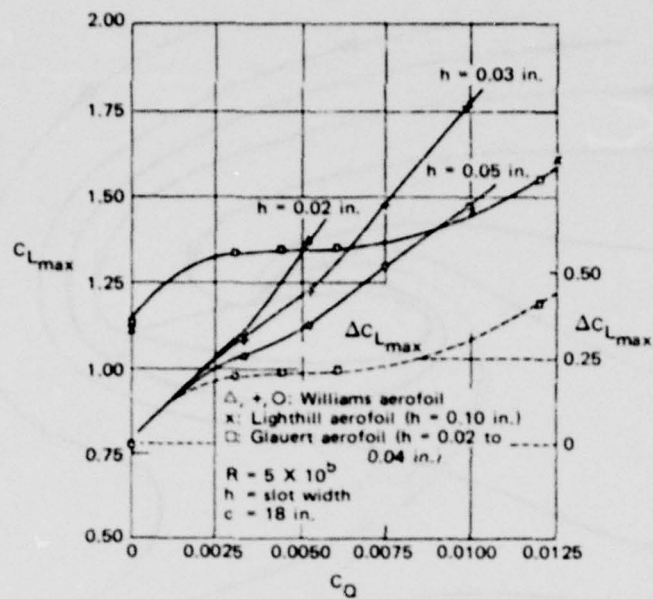


Figure 116 – Experimental Variations of Maximum Lift versus Suction Quantity for Specially Designed Thin Airfoils with Slots Near Leading Edge

Thwaites⁸⁸

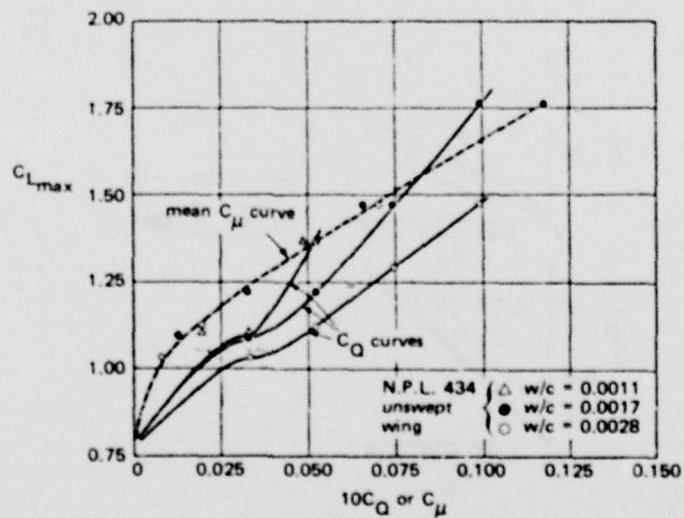


Figure 117 – Effect of Slot Width Variation on Nose-Suction Airfoils

Here w = slot width, Williams.⁹⁰

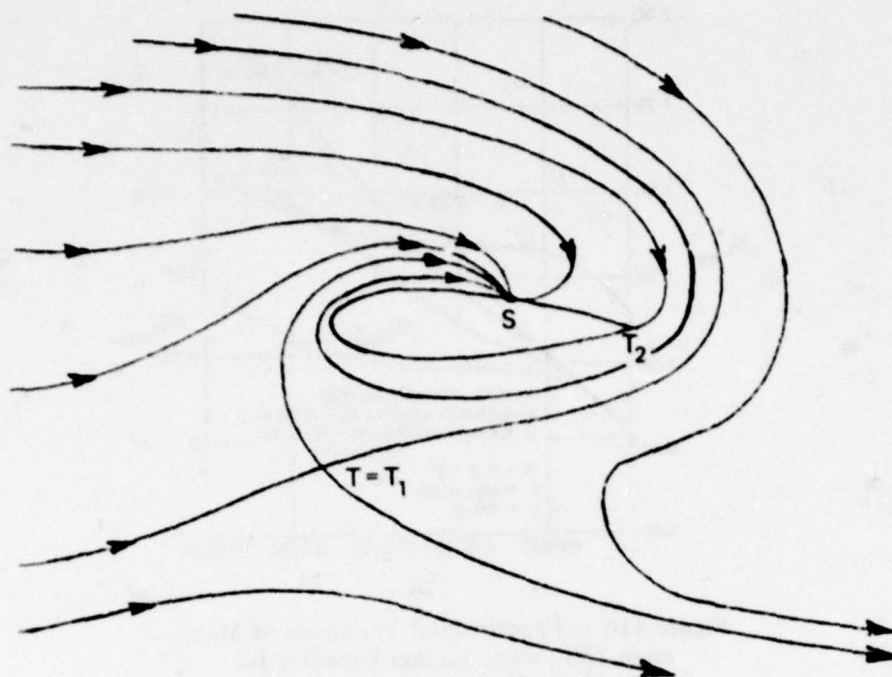


Figure 118 – Flow Streamlines around an Unflapped Foil with a Suction Slot on the Upper Surface

Hazen et al.⁹¹

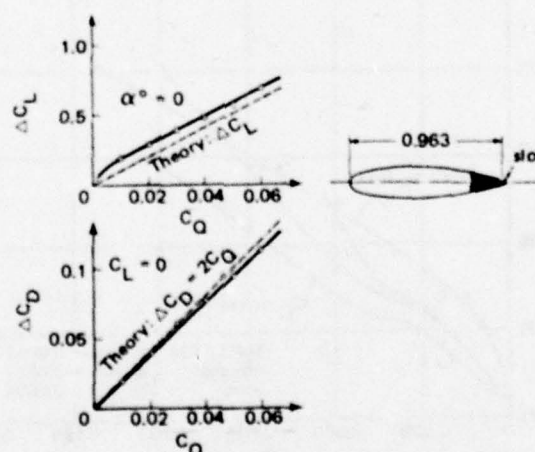


Figure 119 – Circulation Control by Suction

Variation of lift- and drag-coefficient increments versus flow-rate coefficient. Comparison between experiment and theory in two-dimensional flow, Poisson-Quinton and Lepage.²⁰

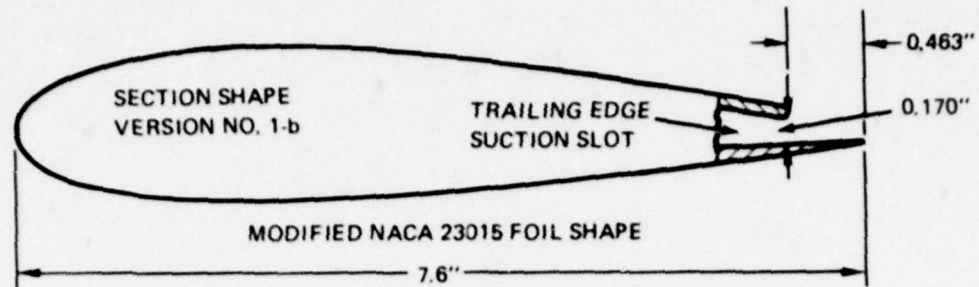


Figure 120a - Modified NACA 23015 Foil Shape

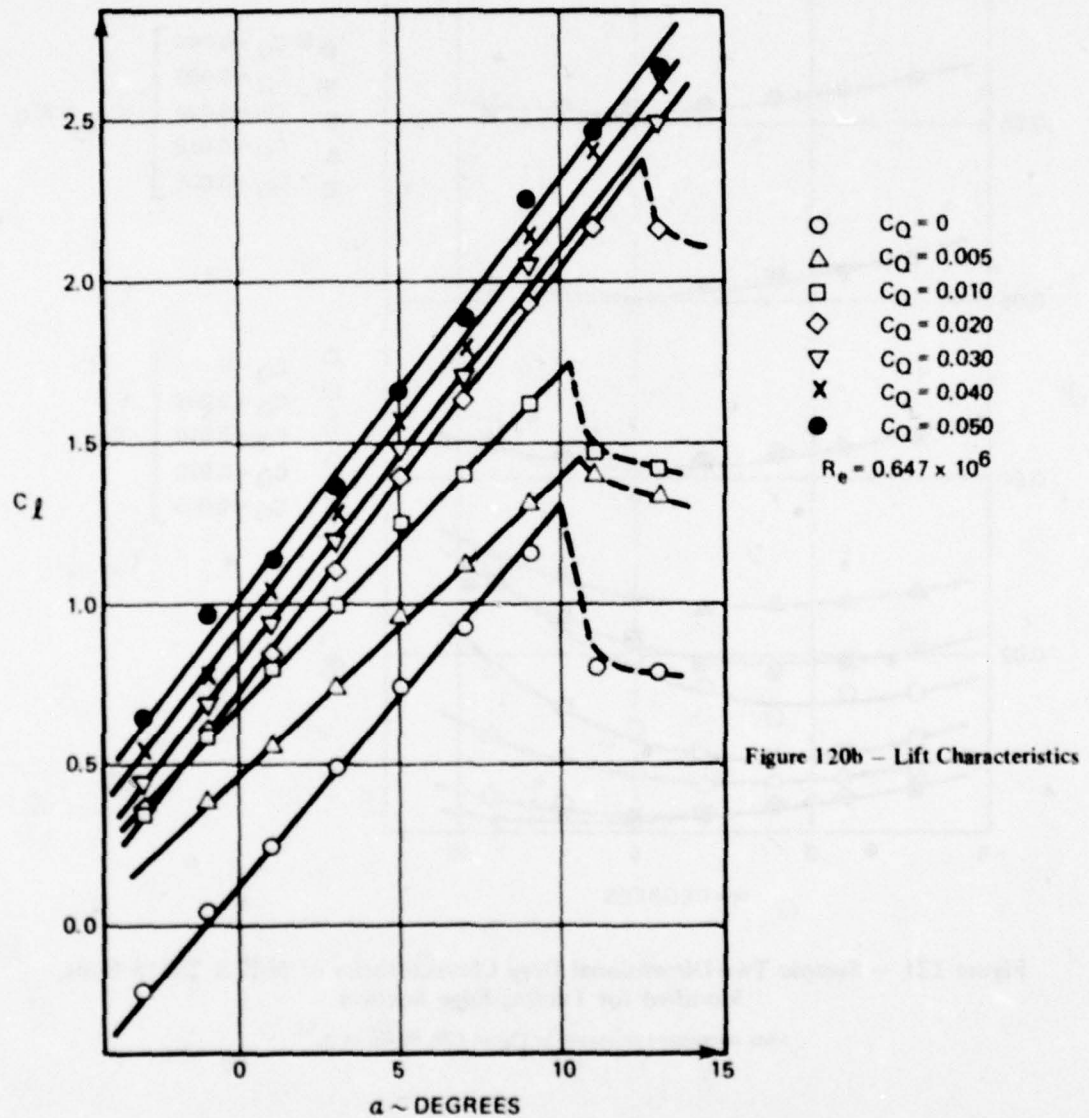


Figure 120b - Lift Characteristics

Figure 120 - Sample Two-Dimensional Lift Characteristics of NACA 23015 Foil Shape
Modified for Trailing-Edge Suction
Trailing-edge version 1-b, Hazen et al.⁹¹

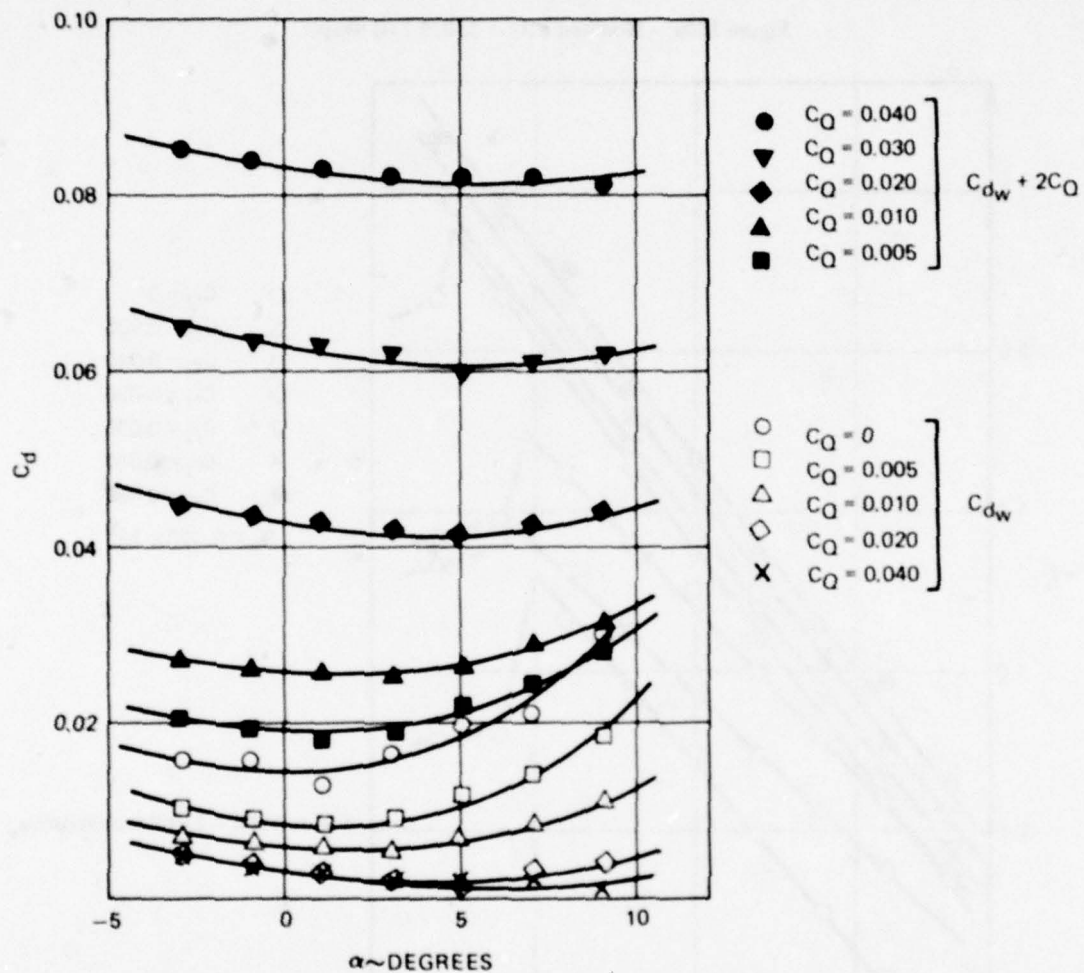


Figure 121 - Sample Two-Dimensional Drag Characteristics of NACA 23015 Foils, Modified for Trailing-Edge Suction

Data correspond to results in Figure 120, Hazen et al.⁹¹

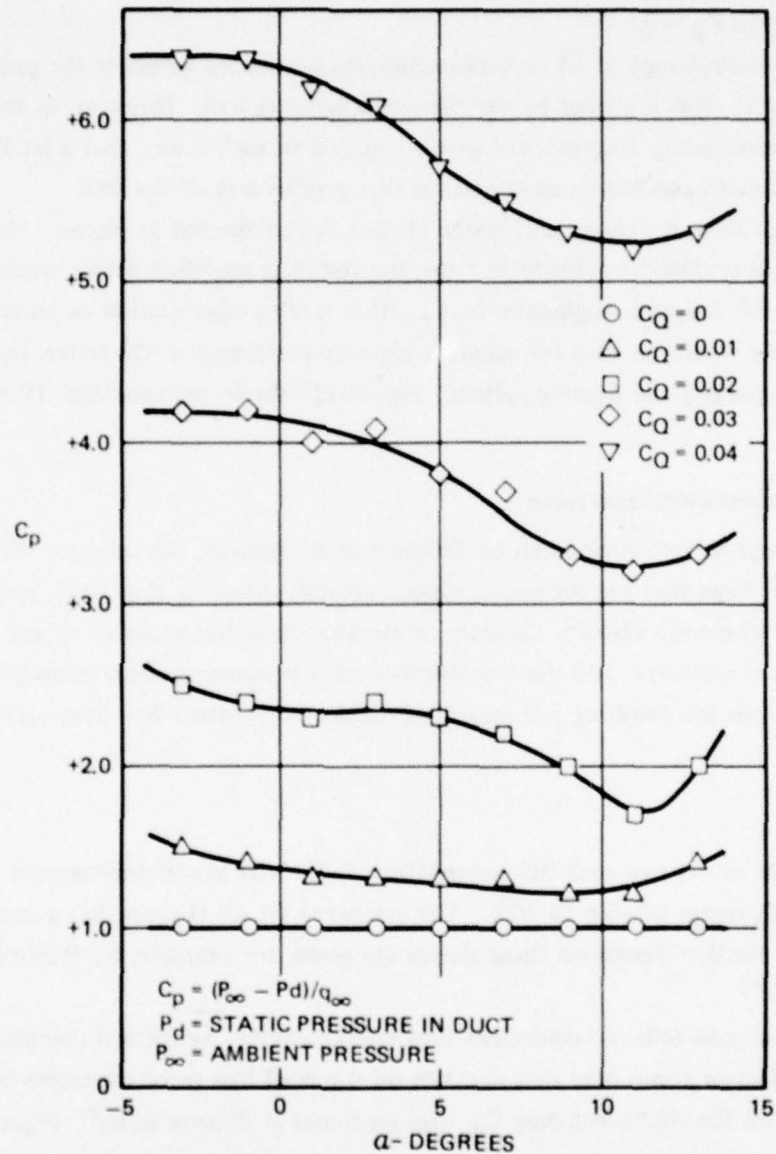


Figure 122 — Sample Two-Dimensional, Pressure-Loss Coefficient for Suction Flow about a NACA 23015 Foil, Modified for Trailing-Edge Suction

Corresponds to data in Figures 120 and 121, Hazen et al.⁹¹

DISCUSSION: From a hydrodynamic performance point of view, the technique of lift augmentation by trailing-edge suction is a moderately good scheme, as judged on the basis of equivalent lift-to-drag ratio using data for the cambered, 15-percent-thick foil of Figure 120. The lift-augmentation ratio at $\alpha = 5^\circ$, calculated from the data of Figure 120, is $\Delta C_\ell / \Delta C_Q = 80$ as $C_Q \rightarrow 0$. With an equivalent inflow jet speed to compute C_μ , the augmentation ratio is $\Delta C_\ell / \Delta C_\mu = 180$ as $C_\mu \rightarrow 0$.

The main disadvantage of all suction techniques mentioned earlier is the probable fouling by marine growth. This is shared by the present scheme as well. However, in this case, should the flow be intermittently reversed, the slot is oriented in such a way that a jet flow out of the same slot would have beneficial effects on the profile drag of the foil.

Moreover, if both the upper and lower TE slot lips of the foil in Figure 120a were replaced by small symmetric deflectable flaps, the resulting modified device would be a symmetric high-lift foil with augmentation by either trailing-edge suction or jet-augmented flap. The former would be used for efficient high-lift performance; the latter, for occasional actuation while purging the ducting system. Figure 123 shows the modified TE slot-suction foil concept.

SLOT SUCTION AIRFOILS WITH LOW DRAG

Another type of foil section can be designed to incorporate slot suction. The idea is to create a section shape that has increasing surface velocity all along the chord, except at the slot location(s) where the velocity abruptly drops, then increases again aft of the slot. In this way, separation is inhibited, and the stepwise favorable pressure gradient helps preserve laminar flow. Even though the resulting foil shapes are thick, they feature low drag over the design range of C_L .

Force Estimates

Figure 124a shows two such 30-percent-thick foils. The symmetric two-slot Griffith-foil has a low-drag C_L -range of -0.6 to $+0.6$. The cambered GLAS II shape has a design range of $0 < C_L < 2.0$. Further details on these shapes are given, for example, by Preston et al.⁸⁷ and by Glauert et al.⁹²

For these suction foils, an equivalent drag coefficient can be formed composed of profile drag plus an effective pump drag that depends on the head loss to be overcome by the suction pump. Details on the equivalent drag C_{D_e} can be found in Preston et al.⁸⁷ Figure 124b shows a comparison between the drag coefficients of the Griffith foil and those of an ordinary foil section. Figure 124c is a plot of the computed equivalent drag C_{D_e} for the GLAS II section pictured in Figure 124a.

DISCUSSION: All of the known data for the low-drag suction foils have been taken in a wind tunnel under more or less ideal conditions. A foil designed specifically for laminar flow to achieve low drag might not function properly in an ocean environment because of high ambient turbulence⁹³ and roughness effects aggravated by marine fouling. Aside from fouling on the foil surfaces, the problem of slot fouling would be severe. If a purging flow were to be used to clear the suction duct and slots, the fluid mechanical effect of blowing out the suction slots for these thick foils should be known. At this time, there are no data available to determine this effect on these foil shapes.

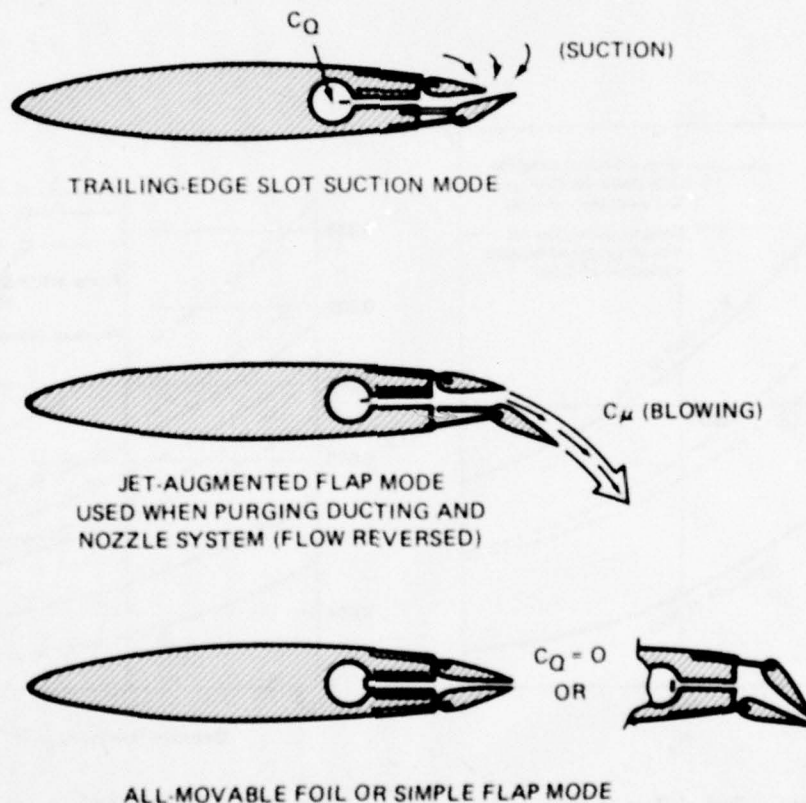


Figure 123 — Possible Arrangement of a Symmetric Trailing-Edge Slot Suction Foil (Modified)

Combination of trailing edge slot suction/jet-augmented flap/plain flapped foil.

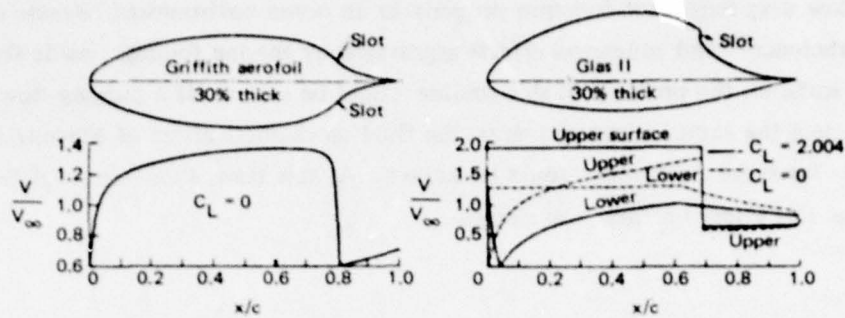


Figure 124a – Thick Low-Drag Airfoils with Suction Slots
Thwaites⁸⁸

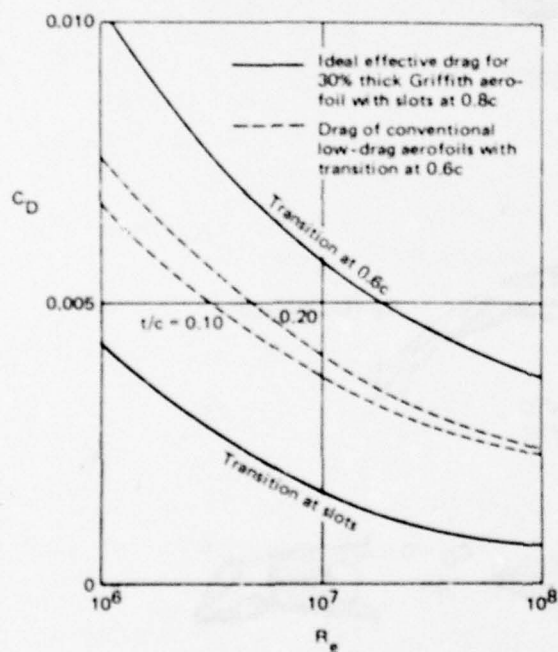


Figure 124b – Scale Effect of Drag Coefficients of Conventional and Suction Airfoils
Thwaites⁸⁸

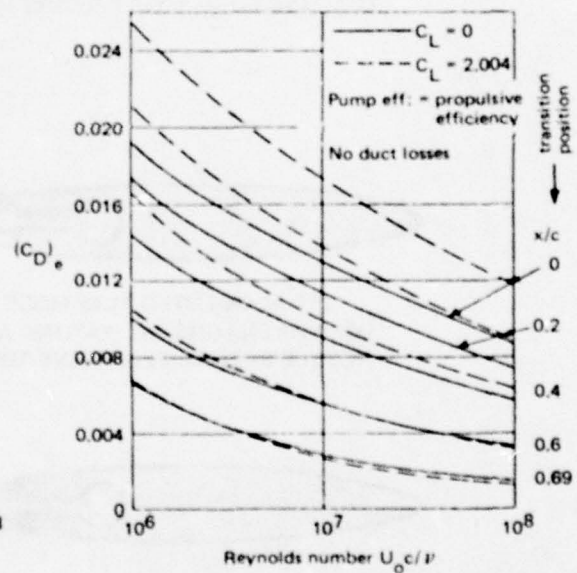


Figure 124c – Ideal Effective Drag Coefficient for GLAS II
Preston et al.⁸⁷

Figure 124 – Low-Drag Slot Suction Airfoils

NAME: Area Suction

DEFINITION: Distributed suction through a porous area can be used for boundary layer control and circulation control on lifting surfaces. The concepts are similar to the slot suction devices discussed earlier.

OPERATION AND FORCE ESTIMATES: Two types of lift-producing concepts are included here:

1. Area Suction on Conventional Foils, and 2. Lift Independent of Incidence, Thwaites Flap.

AREA SUCTION ON CONVENTIONAL FOILS

Area suction at the *nose* of a conventional foil shape has the same effect that slot suction does, except that the too-steep pressure gradients can be suppressed perhaps more smoothly. In this way an entire separation region at the nose of a thin airfoil at high incidence can be dealt with.

Area suction at the *knee* of a foil-flap arrangement also has basically the same effect that slot suction does at the same location; see previous discussion.

Lift Force Estimates

Figure 125 from Thwaites⁸⁸ shows the lift augmentation on a NACA 63A009 foil with a porous patch at the nose extending from $0 \leq x/c \leq 0.0275$. The inward suction velocity is denoted by w_w . Although the increase of C_L is not a linear function of C_Q , the lift-augmentation ratio at $\alpha = 16^\circ$ and for $C_Q = 0.002$ is of the order $\Delta C_L / C_Q = 250$.

Thomas²⁵ has presented curves of incremental lift coefficient varying with flow quantity coefficient C_Q and Reynolds number R_e for 8-percent-thick foils at a 15° angle of attack; see Figure 126.

Area suction at a flap knee has been explored, for example, in the airplane model experiments of Weiberg et al.⁹⁴ Figure 127 is a sketch of the aspect ratio 10 wing system, with a detail of the flap arrangement. In Figure 128, some curves are plotted for the overall lift coefficient versus the flap suction coefficient, C_{Q_f} . In this figure, the total thrust coefficient $T'_c = \text{thrust} / \frac{1}{2} \rho U_\infty^2 S$ may contribute slightly to the increase of the overall lift coefficient C_L . However, the lift-augmentation trend with the flap suction C_{Q_f} properly reflects the aerodynamic effect.

Details of the duct pressure losses necessary for power calculations are also presented by Weiberg et al.⁹⁴

General Trends

In general, area suction devices, either at the nose or on the flaps, are capable of producing respectable lift increments by increasing C_Q to a certain limit. Usually this limit is

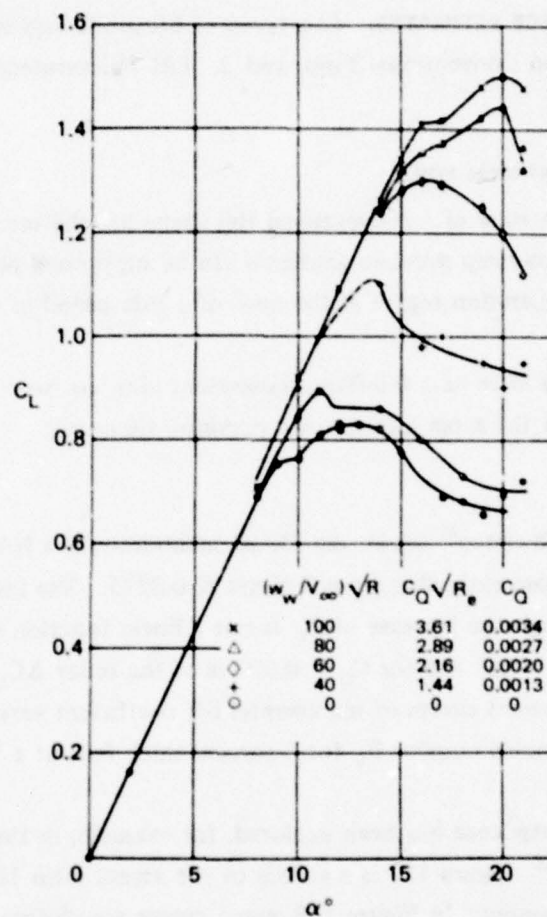


Figure 125 – Experimental Lift Curves for
a NACA 63A009 Airfoil with Porous Nose
Thwaites⁸⁸

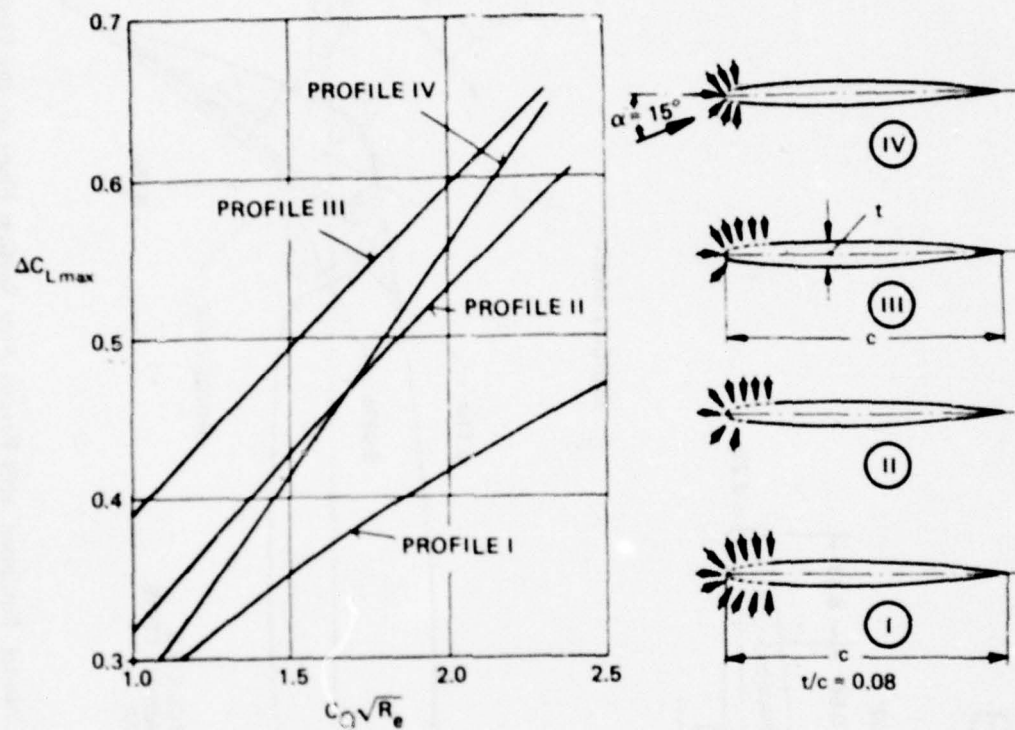


Figure 126 - Curves of $\Delta C_{L \max}$ (Due to Suction) versus $C_Q R_e^{1/2}$ for Four Different Nose Area Suction Configurations
 R_e = Reynolds number based on the chord, Thomas.²⁵

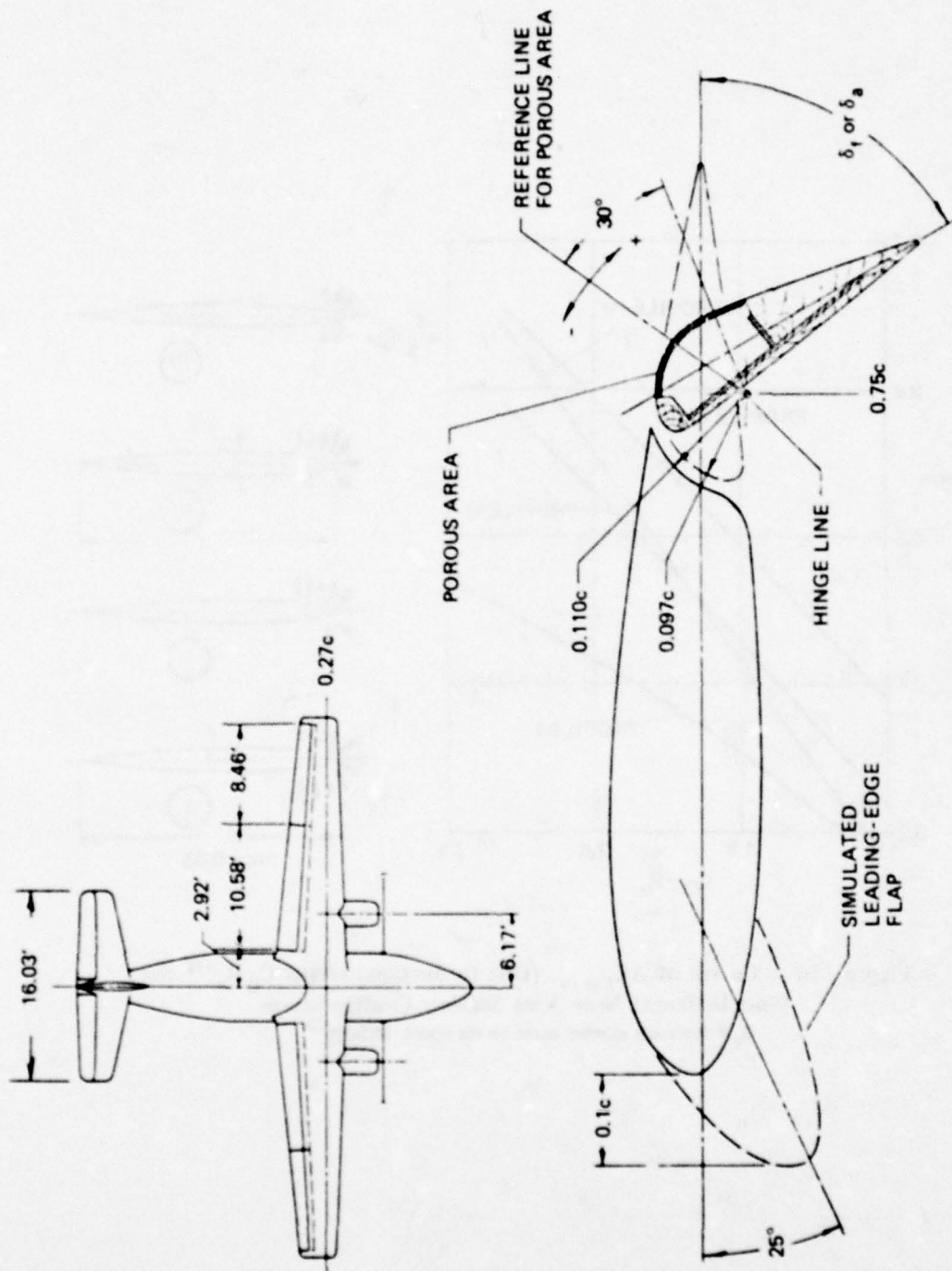


Figure 127 - An Airplane Model, Equipped with Porous Area Suction Flaps on the Flaps and Ailerons
Weiberg et al.⁹⁴

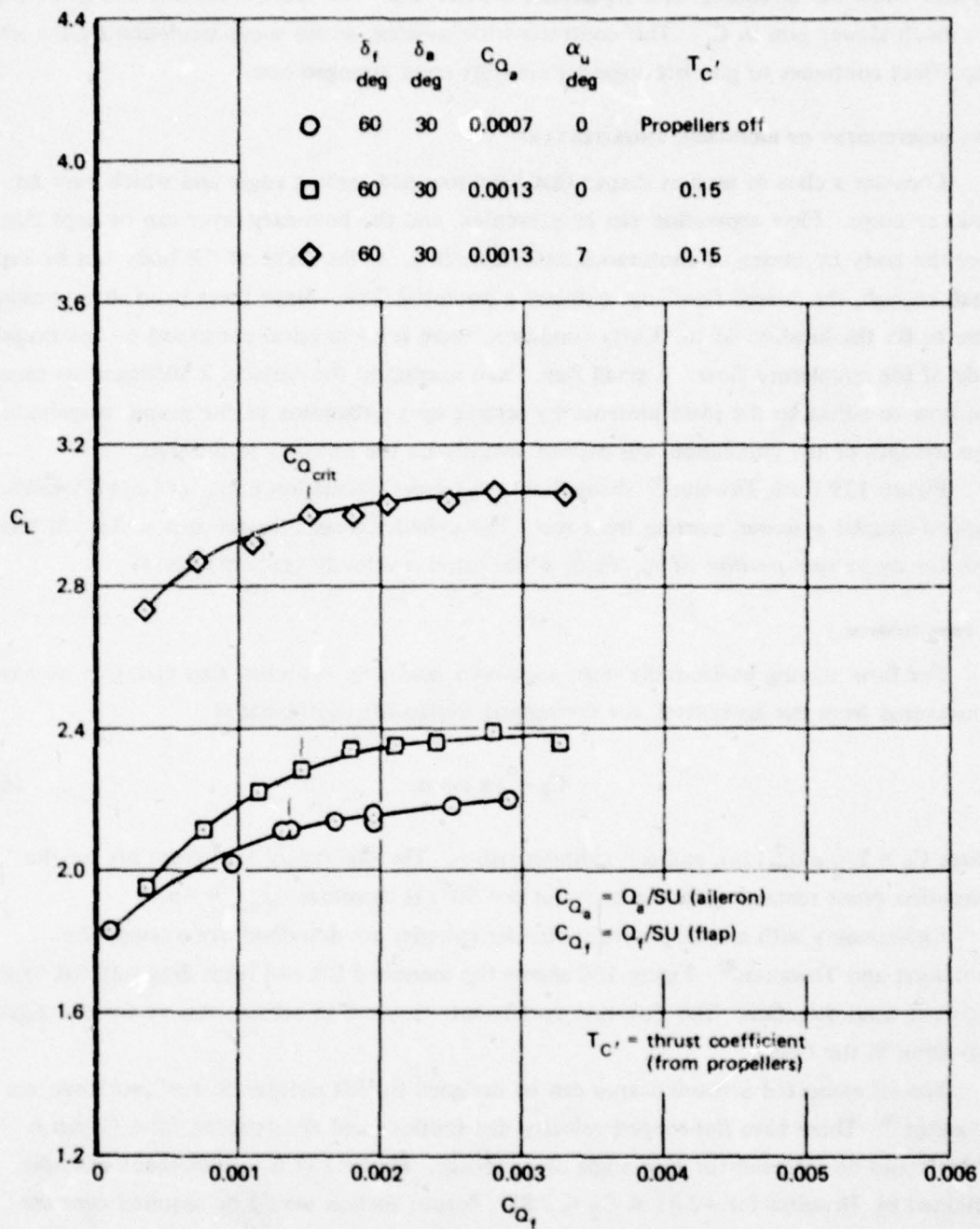


Figure 128 – Results for Airplane Model of Figure 127

Effect of angle of attack and aileron deflection on the overall lift coefficient C_L plotted versus flap suction flow rate coefficient C_{Q_f}

Weiberg et al.⁹⁴

reached when the offending flow separation is overcome. For suction beyond this limit, there is a much slower gain in C_L . This contrasts with blowing, where supercirculation by the jet-flap effect continues to give lift augmentation for most arrangements.

LIFT INDEPENDENT OF INCIDENCE, THWAITES FLAP

Consider a class of section shapes that have rounded trailing edges and which have no kinks or cusps. Flow separation can be prevented, and the boundary layer can be kept thin over the body by means of continuous surface suction. If the wake of the body can be kept small enough, the overall flow approximates a potential flow. Since there is no sharp trailing edge to fix the location of the Kutta condition, there is no physical constraint on the magnitude of the circulatory flow. A small flap, fixed normal to the surface, is sufficient to cause the flow to adjust to the plate presence by setting up a circulation of the proper magnitude. The strength of the circulation will depend entirely on the position of the flap.

Figure 129 from Thwaites⁹⁵ shows how the proper circulation is set up for a Thwaites flapped circular cylinder, starting from rest. The cylinder would require area suction at least over the *entire rear portion* of the circle where adverse velocity gradients occur.

Force Estimates

For flow moving horizontally onto a cylinder, and with the small flap placed at an angle α measured from the horizontal, the theoretical section-lift coefficient is

$$C_\ell = 4\pi \sin \alpha \quad (69)$$

where $C_\ell = L / \frac{1}{2} \rho U_\infty^2 (2a)$, and α = cylinder radius. The theoretical maximum lift for the stagnation point remaining on the body (at $\alpha = 90^\circ$) is therefore $C_{\ell_{\max}} = 4\pi$.

Experiments with a totally porous circular cylinder are described, for example by Pankhurst and Thwaites.⁸⁵ Figure 130 shows the measured lift and form drag referred to the apparent wind direction. The flow-rate coefficients required to achieve this performance are also given in the figure.

Special elongated aerofoil shapes can be designed for lift independent of incidence; see Thwaites.⁹⁶ These have flat-topped velocity distributions and are designed for a C_ℓ -range which could be achieved for zero angle of incidence. Figure 131 is a thick-shape example, obtained by Thwaites for $-2.81 \leq C_\ell \leq 2.81$. Porous suction would be required over the *rear portion* of the foil where decreasing velocities would occur. The small plate, not shown, would be placed at various positions around the rear of the foil to fix the desired circulation.

DISCUSSION: The previous discussion about slot-suction lift augmentation is applicable here as well. Hydrodynamically, the area suction types of lift-augmenting devices are not impressive.

For example, using data for the Thwaites flap, the resulting equivalent lift-to-drag curve shows a poorer performance than most of the other devices considered; see Figure 1. Also, marine fouling of *porous areas* is liable to be an even more severe problem than with suction-slot systems because of the typically smaller holes involved.

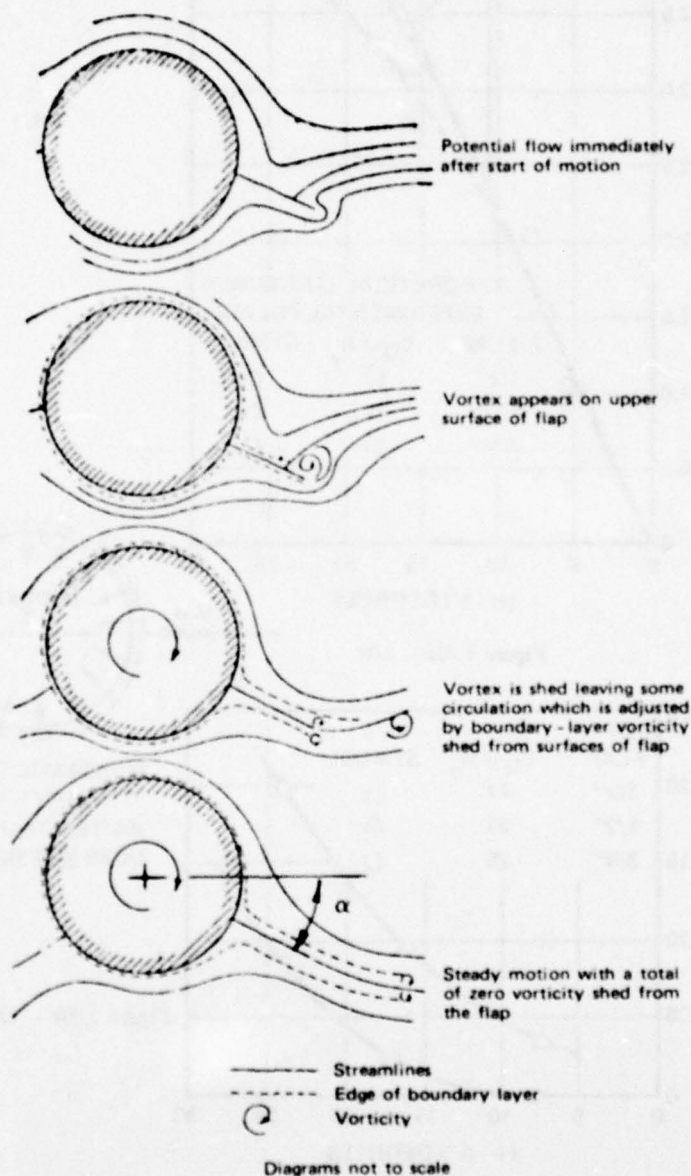


Figure 129 – Setup of Circulatory Flow about a Thwaites-Flapped Porous Circular Cylinder
Thwaites⁹⁵

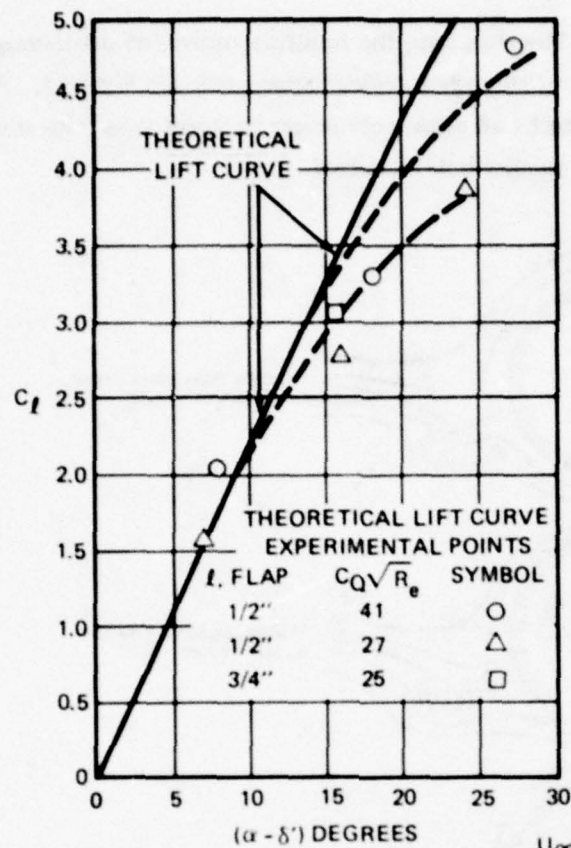
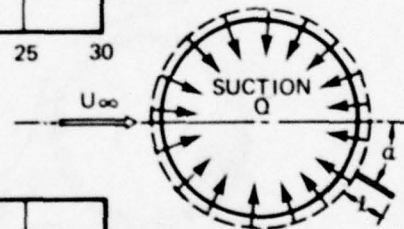


Figure 130a - Lift



SCHEMATIC OF
"THWAITES FLAP"
(NOTE: CYLINDER
DOES NOT ROTATE)

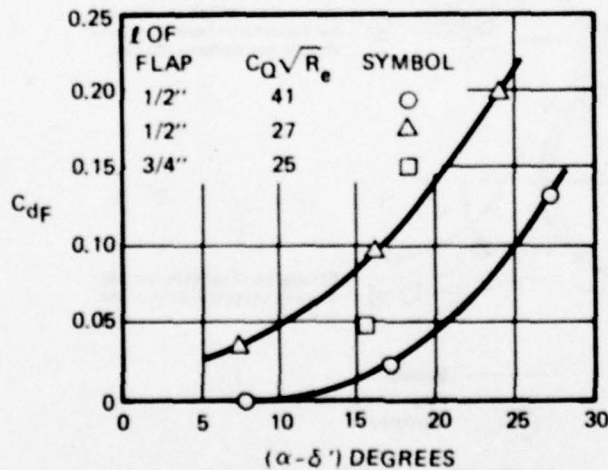


Figure 130b - Drag

Figure 130 - Experimental Lift and Form Drag for a Totally Porous
3-Inch-Diameter Circular Cylinder Fitted with a Thwaites Flap
Pankhurst and Thwaites.⁸⁵

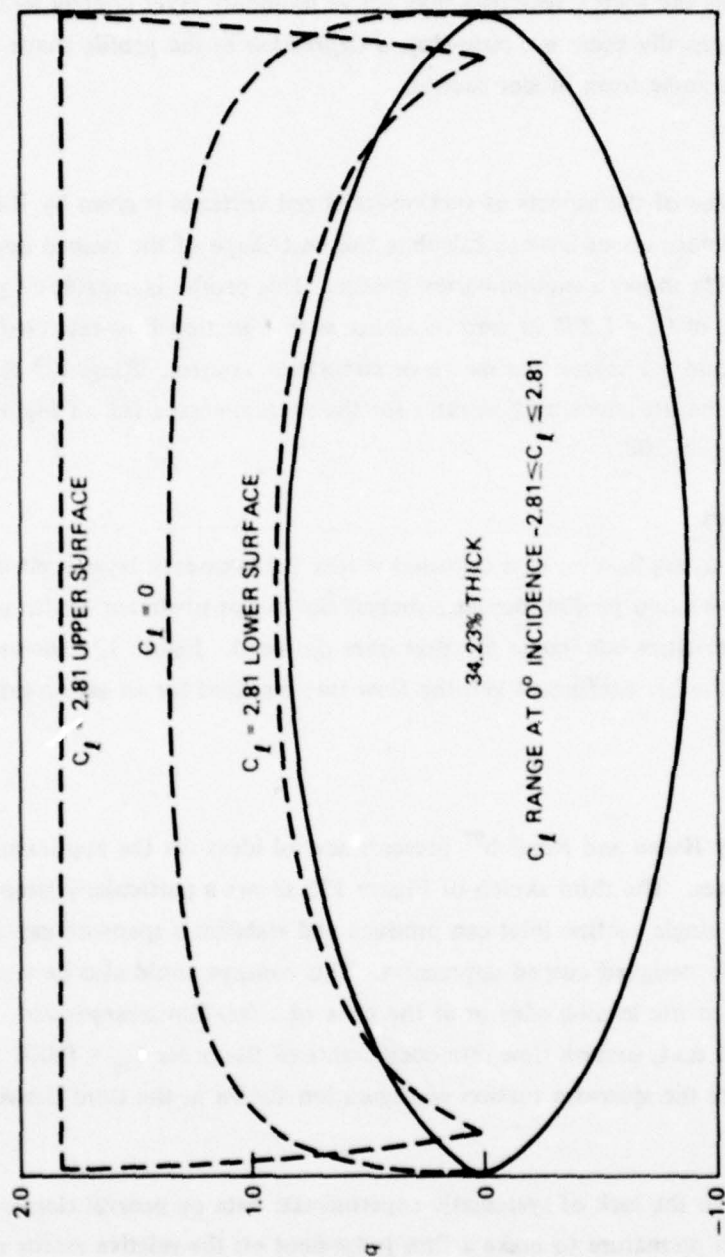


Figure 131 — Theoretical Velocity Distributions on Specially Designed Elongated Foil Shape for Lift at Zero Incidence

Location of small control plate is not shown; porous suction area would be required over the entire rear half of the body, Thwaites.⁹⁶

NAME: Suction-Stabilized Trapped Vortex Foil.

DEFINITION AND OPERATION: The presence of a captured vortex on or near a foil can improve its lift capability. In some cases this is due to induced velocities that can augment the circulation; in others the vortex velocities may act as boundary layer control to help suppress separation. Typically there is a *cusped depression* in the profile shape where the vortex is maintained by some form of slot suction.

CIRCULATION CONTROL

A discussion of some of the aspects of suction-stabilized vortices is given by Ringleb,¹⁸ which includes useful details about how to calculate the best shape of the cusped depressions. For example, Figure 132a shows a suction-vortex profile. This profile is capable of producing a section-lift coefficient of $C_l = 1.275$ at zero incidence with a suction flow-rate coefficient $C_Q = 0.0364$. In this case the vortex is a means of circulation control. Ringleb¹⁸ gives test data that indicate that the lift augmentation ratio for the suction-vortex foil of Figure 132a is of the order $\Delta C_l / \Delta C_Q \approx 208$.

BOUNDARY LAYER CONTROL

Figure 133 shows an application of a captured vortex for boundary layer control. With this version of the cusp-suction profile, the cusp-shaped slot is just upstream of the knee of the flap. The vortex velocities help guide the flow over the bend. Figure 134 shows the order of magnitude of the lift coefficient and the flow rate required for an aspect-ratio 10 wing at large flap angles.

SPANWISE SUCTION

The U.S. patent by Hazen and Ringleb⁹⁷ presents several ideas for the application of suction-stabilized vortices. The third sketch of Figure 135 shows a particularly simple arrangement whereby a single suction inlet can produce and stabilize a spanwise captured vortex within a correctly designed cusped depression. This concept could also be used for boundary layer control at the leading edge or at the knee of a foil-flap arrangement. According to the patent text, suction flow-rate coefficients of the order $C_Q = 0.002$ to 0.01 are sufficient to stabilize the spanwise suction configuration shown in the third drawing of Figure 135.

DISCUSSION: Owing to the lack of systematic experimental data on general classes of suction-vortex foils, it is premature to make a firm judgement on the relative merits of the hydrodynamic performance of these devices. Certain objections applicable to the other types of suction devices may not be as critical here. For example, the slot size may be permitted to be larger and potentially less likely to foul. Also, because of foil geometry, using



SUCTION-VORTEX PROFILE

Figure 132a - Suction-Vortex Profile

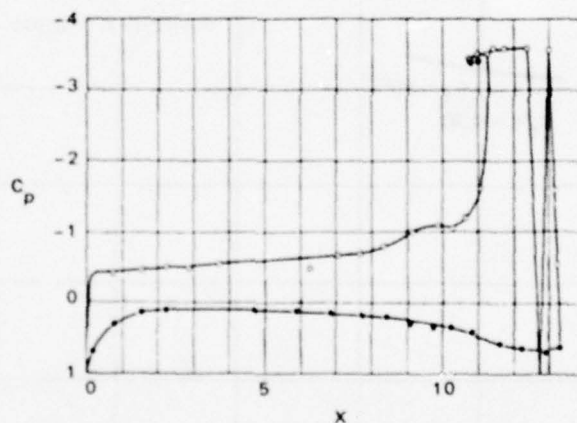


Figure 132b - Pressure Distribution

Figure 132 - Pressure Distribution of Suction Vortex Profile

$\alpha = 0$, $C_{L_i} = 1.275$, and $C_{D_i} = 0.0364$; foil has a lift coefficient of only $C_{L_i} = 0.096$ at $C_Q = 0.0307$; Ringleb.¹⁸

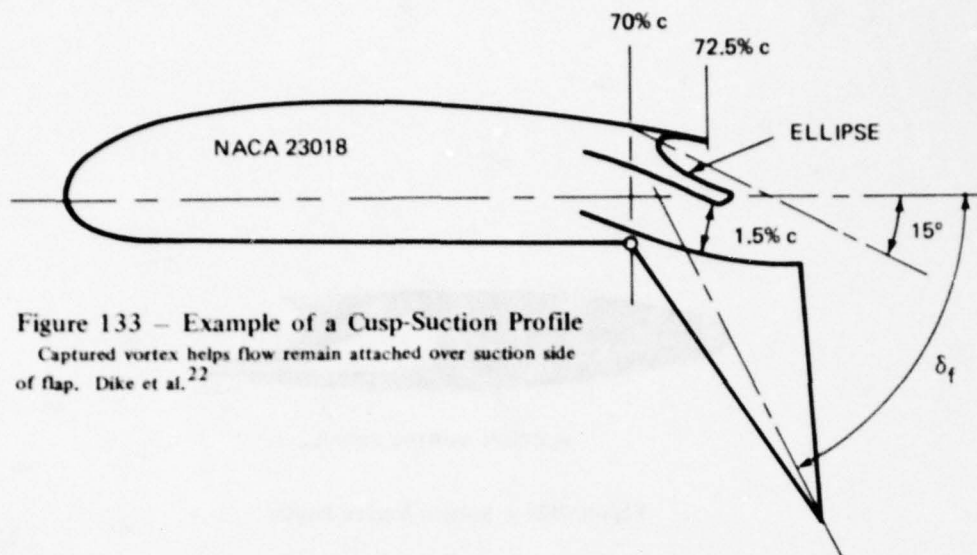


Figure 133 – Example of a Cusp-Suction Profile
 Captured vortex helps flow remain attached over suction side of flap. Dike et al.²²

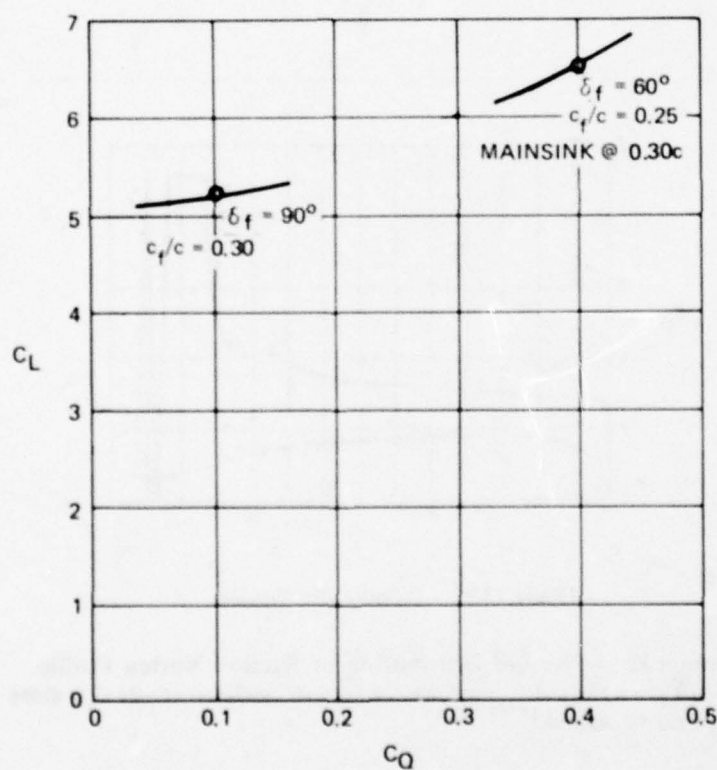


Figure 134 – Variation of Lift Coefficient on an Aspect Ratio 10, Cusp-Suction Wing with Large Flap Deflections versus Flow-Rate Coefficient
 Dike et al.²²

July 14, 1959

D. C. HAZEN ET AL
BOUNDARY LAYER CONTROL SYSTEM

U.S. Patent No.
2,894,703

Filed May 27, 1954

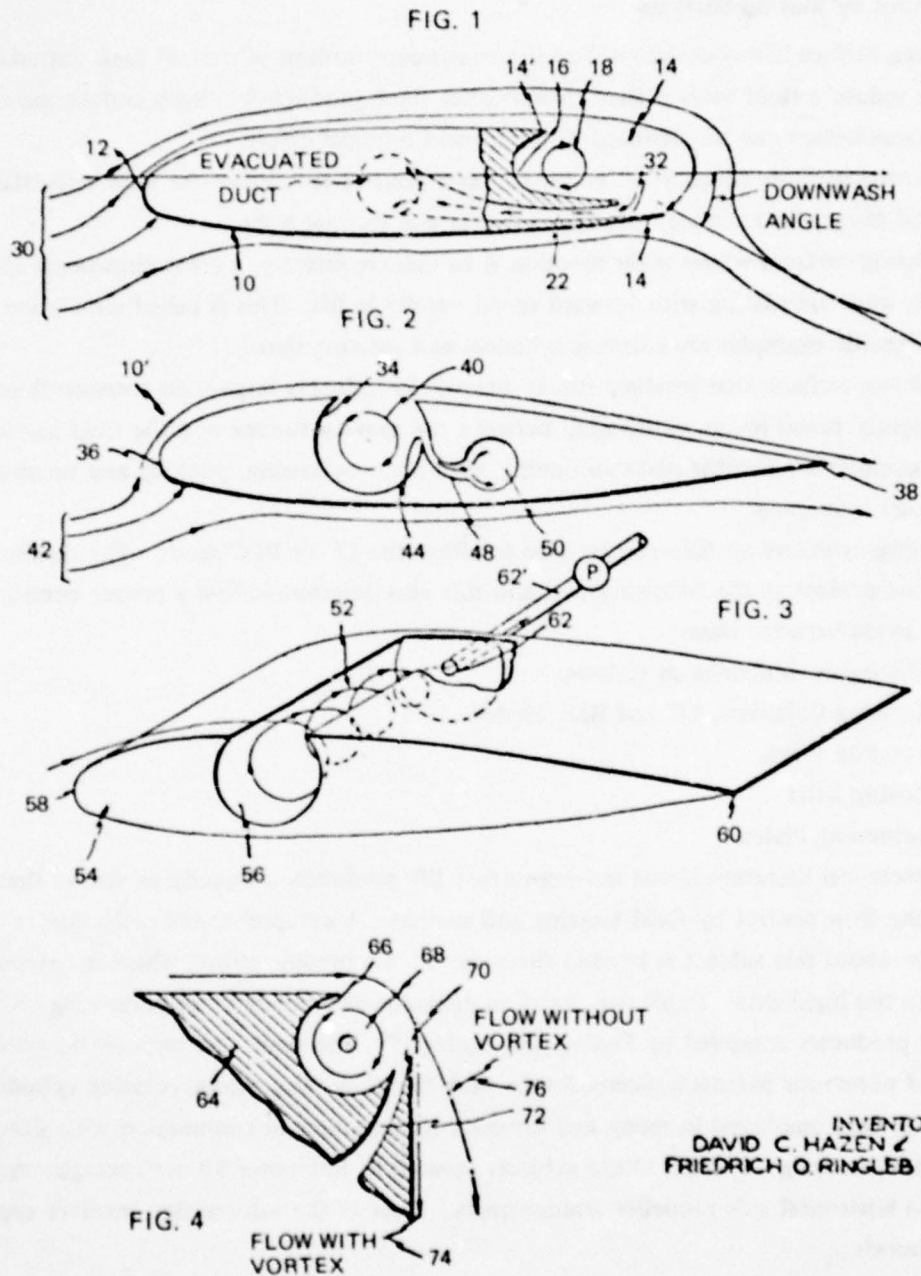


Figure 135 - Lifting Foil Flow-Control Concepts, Using a Captured Vortex
Figure 3 is a particularly simple version, Hazen and Ringleb.⁹⁷

intermittent flow reversal to purge the duct and slot systems may result in a foil with acceptable hydrodynamic characteristics. This would be necessary to reduce the profile drag and possible cavitation problems on such a blunt-based foil as that pictured in Figure 132a.

Flow Control by Moving Surfaces

Moving surface lifting-devices utilize the continuous motion of part of their material surface to induce a fluid motion that enhances the force production. Such surface movements for lift augmentation can be classified by their main physical effect:

- Moving surfaces which yield boundary layer control to achieve the ideal potential flow about a foil shape, for example, rotating cylinders and moving belts.
- Moving surfaces whose main function is to induce, directly, a gross circulation about a foil, which when translating with forward speed, results in lift. This is called circulation control. Specific examples are rotating cylinders and rotating flaps.
- Moving surfaces that produce forces directly by inducing large-scale pressure fluctuations with a properly tuned phase relationship between the moving surface and the fluid motion. Specific examples are flexible plate swimming; rigid-plate swimming, pitching and heaving; and flexible body swimming.

Rotating cylinders on foils can be used in either the CC or BLC mode. The distinction will be made evident in the following text and this also determines how a proper comparison should be made between them.

The discussion is divided as follows:

1. Rotating Cylinders, CC and BLC Modes
2. Rotating Flaps
3. Moving Belts
4. Swimming Plates.

The technical literature about moving-surface lift producers is equally as vast as that on devices using flow control by fluid blowing and suction. A comprehensive collection of information about this subject is beyond the scope of the present effort, which is necessarily confined to the highlights. There does exist an encyclopedic survey of rotating-wing—lift-and-thrust producers compiled by Foshag and Boshler.⁹⁸ The work concentrates on published reports and numerous patents concerned with such things as wing rotors; rotating cylinders; and rotating flaps employed in many and diverse configurations in conjunction with slats, flaps, and imbedded in wing sections. Other subjects covered in Reference 98 are cyclogiro systems and various horizontal axis propeller arrangements. Most of the information involves applications to aircraft.

NAME: Rotating Cylinders, Circulation- and Boundary Layer-Control Modes.

DESCRIPTION AND FORCE ESTIMATES:

ISOLATED ROTATING CYLINDERS, CIRCULATION-CONTROL MODE

The so-called Magnus effect is responsible for the lift force experienced by a circular cylinder spinning about its axis. As the moving surface sweeps through the fluid, it induces a vortical flow, circulation, which interacts with an oncoming stream to produce a force perpendicular to both the free stream velocity and the spin axis.

Force Estimates

If V is the free stream velocity, and Γ is the induced circulation strength produced by the spinning cylinder, then the lift force L per unit span is

$$L = \rho V \Gamma \quad (70)$$

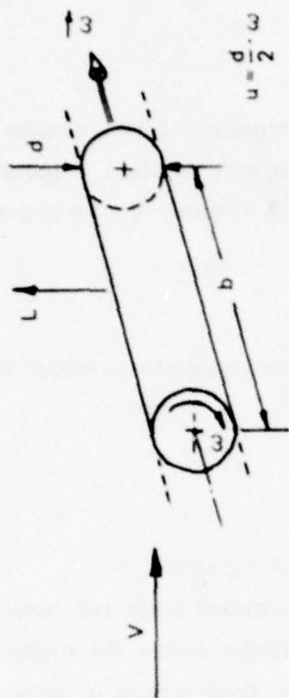
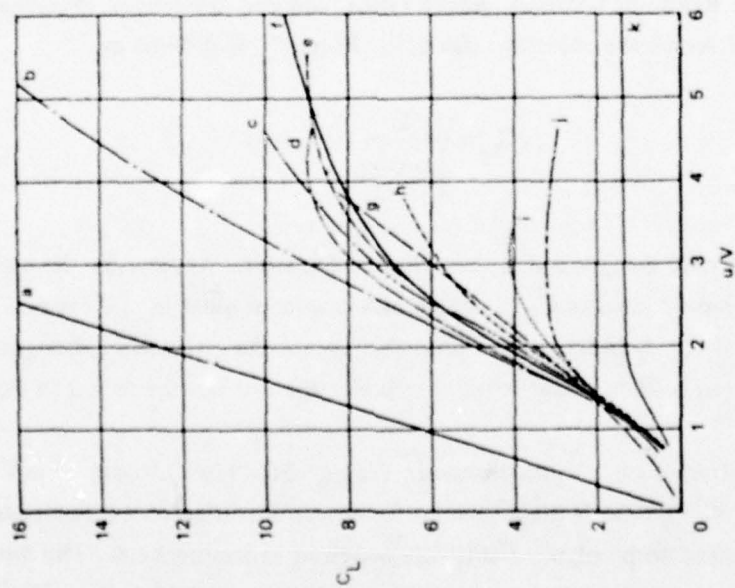
where ρ is the fluid density. This is the simplest form of circulation control.

It would appear that the only thing to be established by experiment is the relationship between the circulation Γ and the peripheral velocity u of the cylinder, hence, the rotation rate ω . As is expected, $\Gamma(u/V)$ is very sensitive to the aspect ratio (b/d) and to differences in cylinder end conditions. Moreover, even for an apparently two-dimensional geometry, the relationship between Γ and u/V changes character at some fairly moderate value of u/V . Figure 136, reproduced from Swanson,⁴ shows a large collection of data for isolated rotating cylinders with various Reynolds numbers, aspect ratios, and end conditions, showing lift coefficient C_L plotted versus the velocity ratio u/V . Here, C_L is defined as

$$C_L = \frac{L}{\frac{1}{2} \rho V^2 d} \quad (71)$$

where L is the lift per unit span, and d is the cylinder diameter. Apparently the smaller aspect ratio cylinders have a smaller C_{Lmax} which also occurs at smaller u/V ratios. End plates and roughness of the cylinder surface tend to increase the circulation strength, and thus lift. A large compilation of data about rotating-cylinder lift can also be found in Foshag and Boshler.⁹⁸

There are two extremes of u/V not shown in Figure 136, "large" values of $u/V > 7$ and "small" values of $u/V \leq 1.0$. Both these regimes have been investigated experimentally, for example, by Swanson, and some of the results are reviewed in Reference 4. The Swanson experiments are the closest to two-dimensional ($AR = b/d \rightarrow \infty$) available. For $u/V \gtrsim 1$, the



Curve	Investigator	Aspect ratio	Reynolds no.	Remarks
a	(Ideal fluid)	∞	∞	
b	Thom	12.5 and 26	$5.3 - 8.8 \times 10^4$	$3 \times$ cyl-dia end disks
c	Meid	13.3	$3.9 - 11.6 \times 10^4$	
d	(Göttingen)	4.7	5.2×10^4	$1.7 \times$ cyl-dia end disks
e	Thom	8	1.6×10^4	
f	Swanson	∞	$3.5 \times 10^4 - 3 \times 10^5$	
g	Thom	5.7	$3 - 9 \times 10^4$	Rough ("sanded") surface
h	Thom	5.7	$3 - 9 \times 10^4$	Smooth surface
i	(Göttingen)	4.7	5.2×10^4	
j	Schwartzberg	4.5	$5.4, 18.6 \times 10^4$	Unpublished (Case Int.)
k	Swanson	2	5×10^4	Continuous end sections

Figure 136 — Magnus Lift Coefficient versus Velocity Ratio, for a Variety of Aspect Ratios b/d and End Conditions

Swanson⁴

lift coefficient rises very slowly with u/V , and in the regime $u/V < 0.5$ the lift may be slightly negative or zero depending very sensitively on Reynolds number R_e , based on cylinder diameter. Some curves are given in Reference 4, for the low-velocity-ratio regime for $3.5 \times 10^4 < R_e < 50.1 \times 10^4$.

For a large range of u/V , Figures 137a and 137b reproduced from Swanson,⁴ show the variation of two-dimensional lift and drag coefficients plotted versus the velocity ratio u/V . The Reynolds number range for these data is $3 \times 10^4 < R_e < 3 \times 10^5$. There are two interesting features displayed here. First, although the lift curve changes steepness in the vicinity of $u/V = 3$, there seems to be no indication that there is a *peak* value of C_L (2D) as predicted by a potential theory model; see Swanson.⁴ Note also that the measured C_L (2D) curve exceeds the value 4π for $u/V > 12.5$. This means that the outer flow effective stagnation point has been moved completely away from the surface. The trend observed from the C_L curve obtained by Swanson is that lift can continue to increase by simply spinning the cylinder faster. Lift performance of a two-dimensional rotating cylinder can be approximated in two separate ranges of u/V by the following

$$1 < \frac{u}{V} < 3, \quad \frac{\Delta C_L}{\Delta(u/V)} \approx 3.5 \quad (72)$$

$$5 < \frac{u}{V} < 17 + \quad \frac{\Delta C_L}{\Delta(u/V)} = 0.47 \quad (73)$$

A second main feature of rotating-cylinder performance is that the two-dimensional drag coefficient does reach a maximum value of $C_{Dmax} = 2.85$ at $u/V \approx 4.2$, then it gradually decreases toward a constant value with further increases in u/V .

More data about lift and drag forces created by isolated rotating cylinders can be found in the numerous references cited by Swanson.⁴

Finite-aspect effects and end disks can have a great influence on the lift performance as indicated from the curves in Figures 138 and 139, adopted from Küchemann.⁹⁹ The lift coefficient for a finite-length, spinning cylinder rotating at a given u/V can be estimated from the formula

$$C_L = \frac{C_L(2D)}{1 + \kappa 2/AR} \quad (74)$$

where C_L (2D) is the two-dimensional lift coefficient at the given u/V , and κ is a correction factor dependent on the ratio between end plate height and the cylinder span that could be estimated, using the ideas presented by Mangler.¹⁰⁰

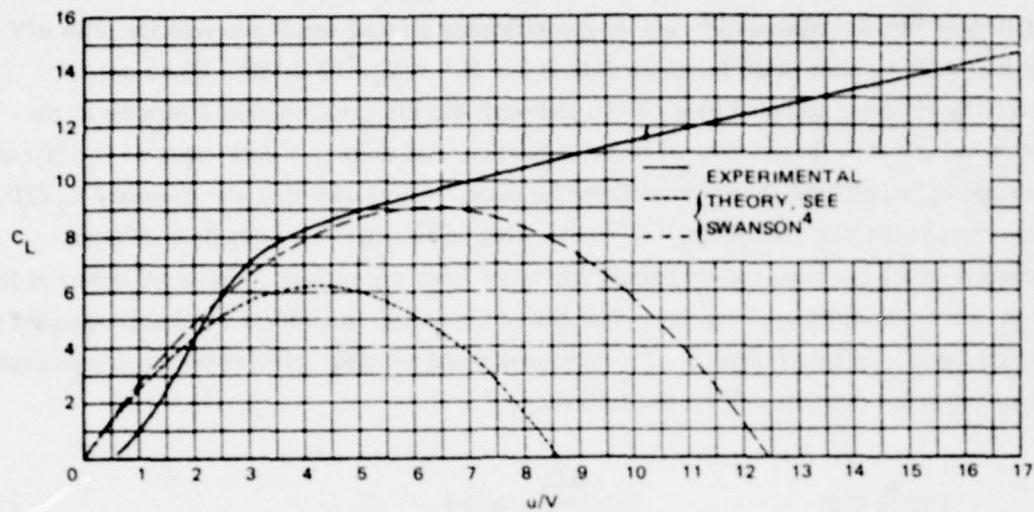


Figure 137a - Lift Coefficient C_L versus Velocity Ratio

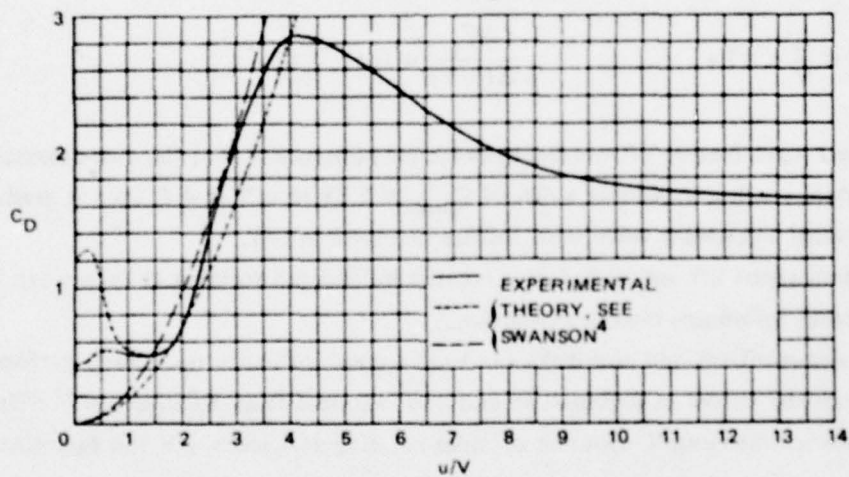


Figure 137b - Drag Coefficient C_D versus Velocity Ratio

Figure 137 - Variation of Lift and Drag Coefficients versus Velocity Ratio u/V for Rotating Cylinder Experiments

These are the best two-dimensional data available, Swanson.⁴

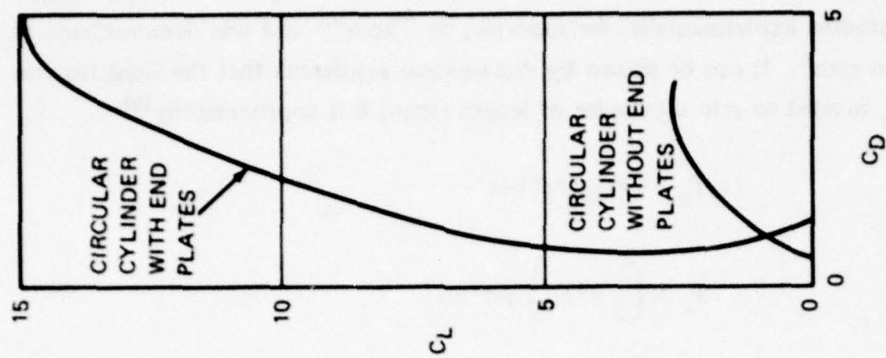


Figure 139 – Polar Plot of Lift and Drag Ratios for Rotating Cylinder with and without End Disks

Küchemann⁹⁹

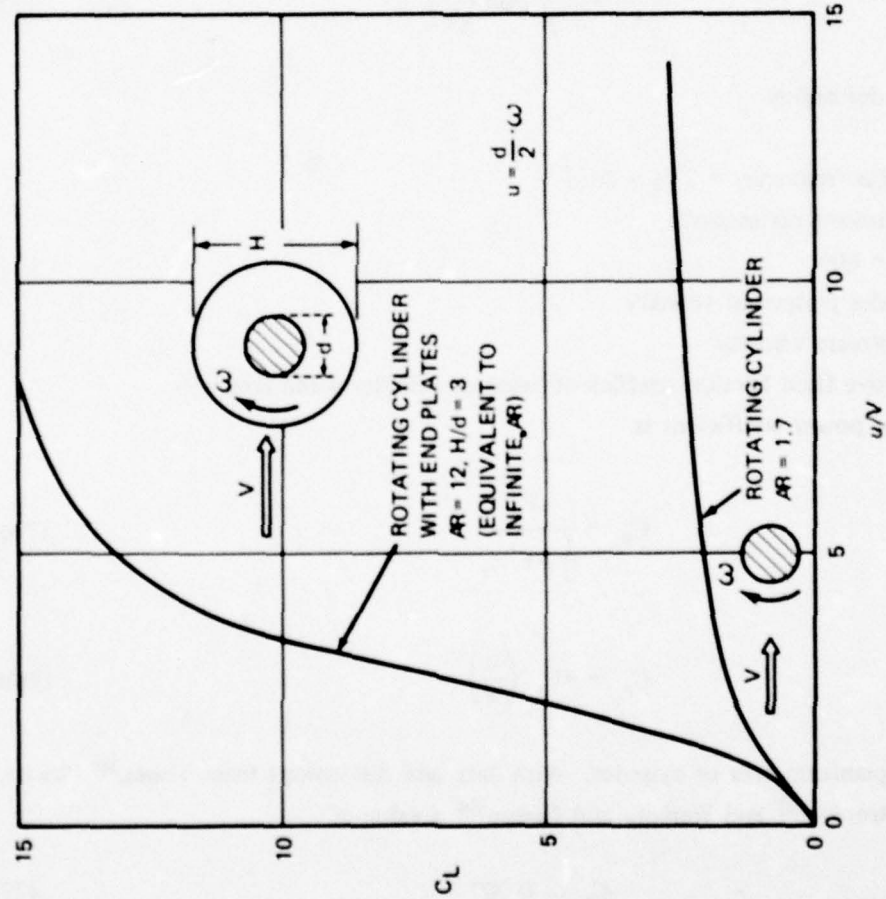


Figure 138 – Lift Coefficient as a Function of Velocity Ratio for Rotating Cylinder with and without End Disks

Küchemann⁹⁹

Powering Estimate

The power per unit span required to rotate a circular cylinder against the fluid friction torque has been studied experimentally, for example, by Thom¹⁰¹ and was demonstrated to be proportional to rpm^3 . It can be shown by dimensional arguments that the fluid friction rotation power P_r needed to spin a cylinder of length (span) b is approximately¹⁰²

$$P_r = (\pi C_F) \rho r^4 b \omega^3$$

thus

$$\begin{aligned} P_r &= \left(\frac{1}{2} \pi^4 C_F \right) \rho d^4 b n^3 \\ &= \left(\frac{1}{2} \pi^4 C_F (60)^{-3} \right) \rho d^4 b N^3 \\ &= \left(\frac{1}{2} \pi C_F \right) \rho db \left(\frac{u}{V} \right)^3 V^3 \end{aligned} \quad (75)$$

where r = cylinder radius

$d = 2r$

ω = circular frequency = $2\pi n = 2u/d$

n = revolutions per second

N = rpm = $60n$

u = cylinder peripheral velocity

V = free-stream velocity

C_F = effective fluid friction coefficient based on velocity u and area πdb

Then, the rotation power coefficient is

$$C_{P_r} = \frac{P_r}{\frac{1}{2} \rho V^3 S_r} \quad (76a)$$

or

$$C_{P_r} = \pi C_F \left(\frac{u}{V} \right)^3 \quad (76b)$$

where $S_r = db$ = planform area of cylinder. With data and discussions from Thom,¹⁰¹ Steele, and Harding,¹⁰² Brooks,¹⁰³ and Weiberg and Gamse¹⁰⁴ a value of

$$C_F \approx 0.007 \quad (77)$$

seems to fit the appropriate circumferential Reynolds number range ($> 10^6$) and applies to a moderate surface roughness; see H. Schlichting, "Boundary Layer Theory."

The same relationships hold true for the power required when the cylinder is partially imbedded in the leading or trailing edge of a hydrofoil or flap. That is, the exposed area of the rotating cylinder to the free stream has little influence on the power required to spin it.

Equivalent Section Drag

Parallel to the analysis of slot-blowing devices, it is convenient to define an equivalent drag for the case of rotating-cylinder devices, which contains a penalty for the power required to spin the cylinder. Here, the equivalent two-dimensional drag is defined as

$$D_{e(2D)} = D_{p(2D)} + \frac{P_r/b}{V}$$

where $D_{p(2D)}$ is the section profile drag force, experienced by the cylinder, with rotation, and P_r/b is the fluid friction-rotation power per unit span estimated from Equation (75). Then, an equivalent section-drag coefficient based on the cylinder diameter is

$$C'_{d_e} = C'_{d_p} + C_{P_r} \quad (78)$$

where $C'_{d_e} = D_{e(2D)} / \frac{1}{2} \rho V^2 d$, C'_{d_p} is the section profile drag coefficient, and C_{P_r} is defined in Equation (76a).

Forces on a Flapped, Nonrotating Cylinder

It is possible to generate lift forces on a cylinder even when there is no spin, by placing a small tab or flap, of length c , on the underside surface of the cylinder. However there is a large drag penalty. Figures 140 and 141, reproduced from Lockwood and McKinney¹⁰⁵ contain lift and drag data for the performance of a nonrotating lifting cylinder, fitted with a small flap of chord ratio $c/d = 0.06$. The effect of Reynolds number, based on cylinder diameter, is shown in Figure 140 for the case when the tab is positioned at 90° to the free stream. Variations of the force coefficients with the angular position δ of the flap are shown in Figure 141.

DISCUSSION: Use of a rotating cylinder alone for control-force production has several disadvantages. Even though large lift coefficients are possible, there is also a severe drag penalty. The overall hydrodynamic performance of the isolated spinning cylinder is low, as indicated by its equivalent lift-to-drag ratio curve plotted in Figure 1. To reverse the lift-force direction, the cylinder must be stopped and spun to the proper speed in the opposite direction. This would require a braking system and time. It is possible to generate a small

LIFT AND DRAG ON NONROTATING CYLINDER

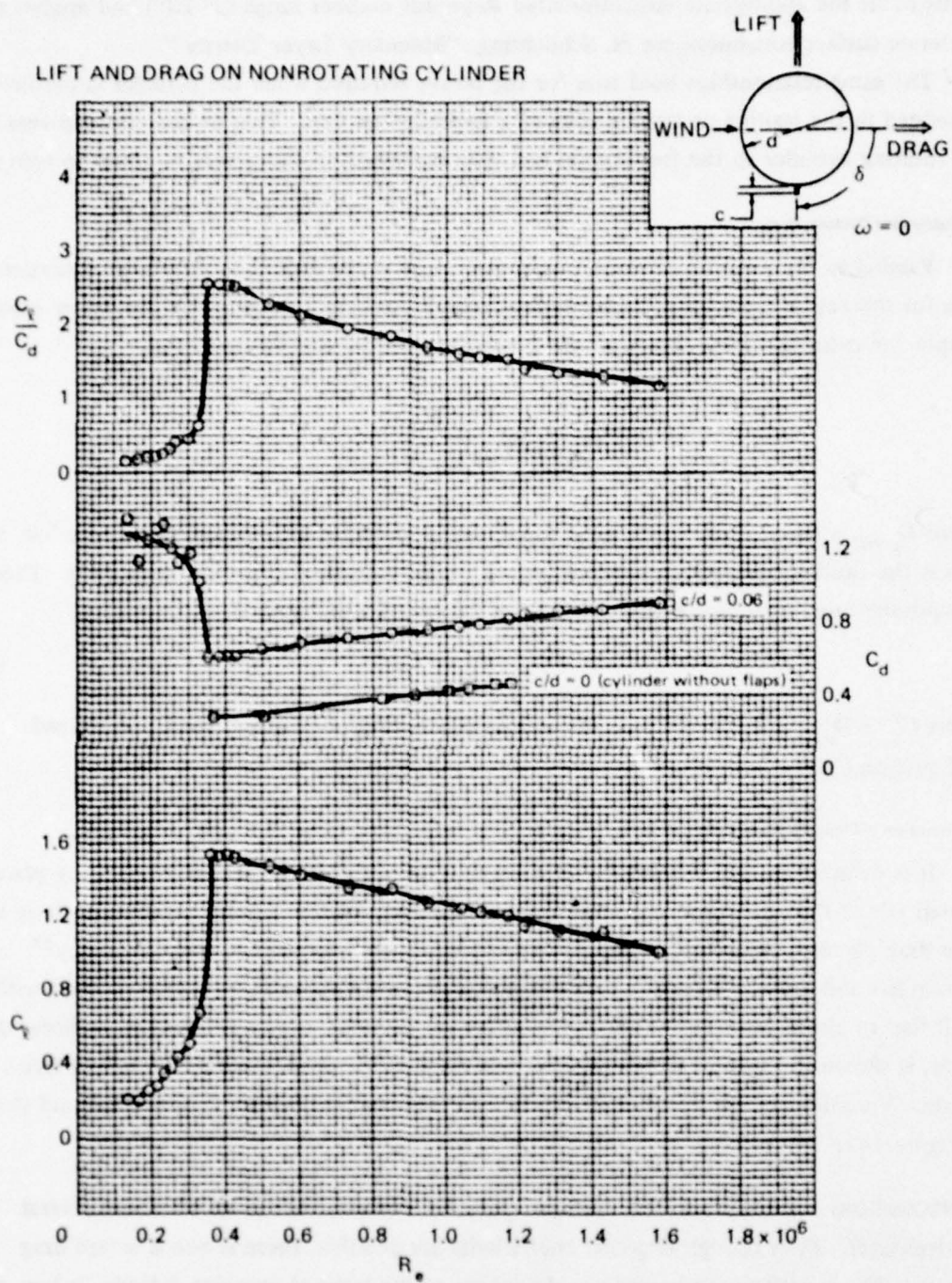


Figure 140 – Effect of Reynolds Number on Aerodynamic Characteristics of a Lifting Cylinder, $c/d = 0.06$, $\delta = 90$ Degrees

Lockwood and McKinney,¹⁰⁵

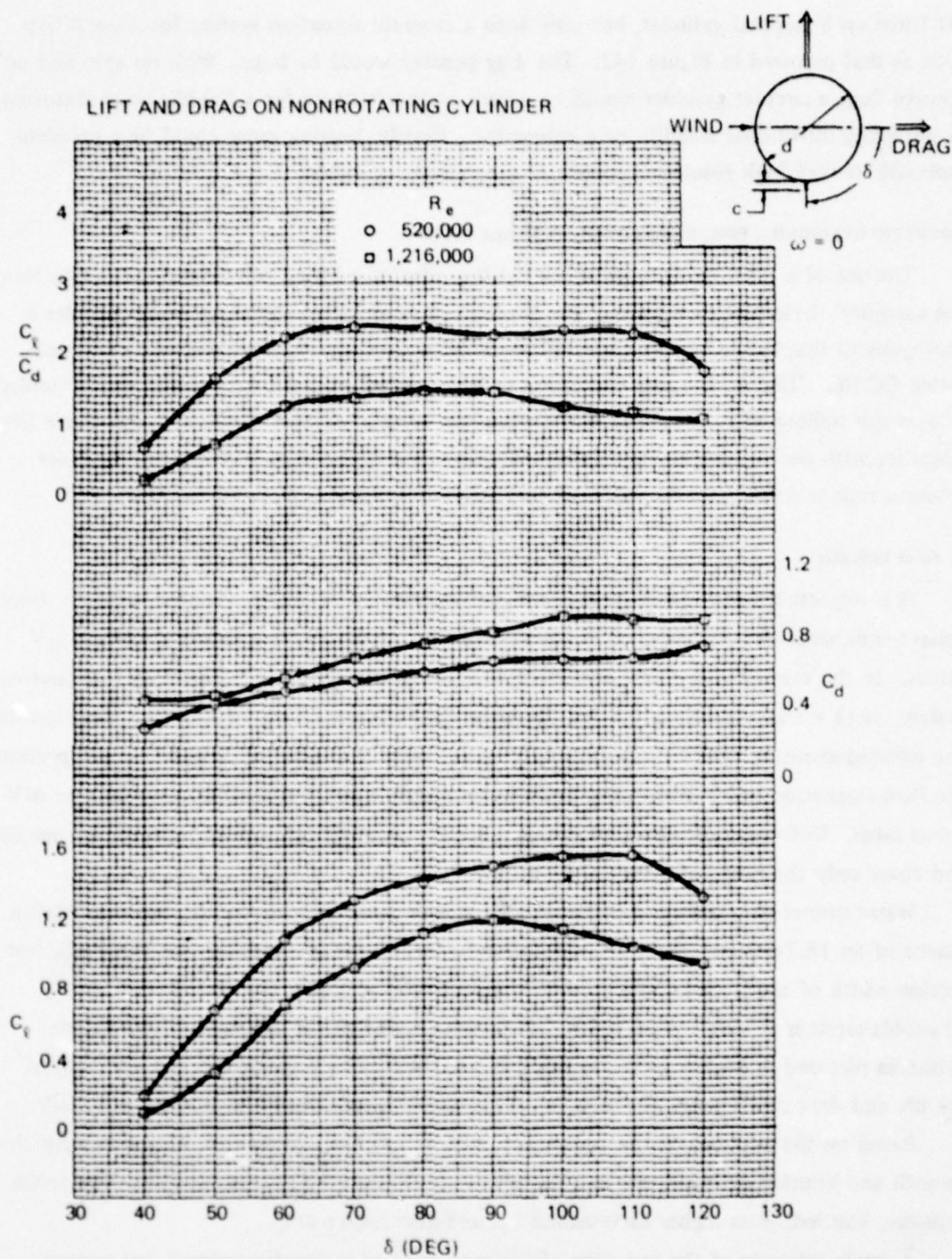


Figure 141 — Effect of Flap Angular Position on Aerodynamic Characteristics of a Lifting Cylinder for Two Reynolds Numbers, $c/d = 0.06$

Lockwood and McKinney,¹⁰⁵

lift force on a stopped cylinder, but only with a separate actuation system for a small flap such as that pictured in Figure 141. The drag penalty would be large. With no spin and no control flap, a circular cylinder would be a very poor substitute for a foil-like control surface in providing directional stability of a submarine. Finally, bearing noise could be a problem, especially if very high rotational speeds of the cylinder are used.

ROTATING CYLINDER - FOIL, CIRCULATION-CONTROL MODE

The use of a rotating cylinder at the *trailing edge* of a lifting foil (Figure 142) falls into the category of circulation control. The fluid mechanical effect of the spinning cylinder is analogous to that created by a tangential jet blowing over the rounded rear end of the so-called CC foil. That is, the rear stagnation point is pulled around to a position on the under-side of the trailing edge, causing a flow asymmetry associated with circulation and hence lift. Together with the foil-section thickness, foil shape, and free stream speed V , the cylinder rotation rate ω determines the effective rear stagnation point S pictured in Figure 142.

Force Estimates

It is expected that the two-dimensional lift augmentation due to cylinder rotation should behave somewhat like the curve shown in Figure 136, at least for small and moderate u/V values. In the present case, there is a theoretical maximum section-lift coefficient of approximately $2\pi(1 + t/c)$, where t is the foil thickness, and c is the chord. Unlike the situation with the isolated spinning cylinder, the geometry of the imbedded rotating cylinder would prevent the flow-stagnation point from being pushed completely away from the body surface as u/V grows large. Unfortunately the available data for the rotating cylinder CC concept are meager and cover only the range of small values of u/V .

Water tunnel data obtained by Brooks¹⁰³ provide some idea of the lift and drag performance of an 18.2-percent-thick, TE, rotating-cylinder-foil model spanning the 2.25-inch, test-section width of the tunnel. The geometric aspect ratio is 0.409, and the chord-length Reynolds number is $Vc/\nu = 1.33 \times 10^6$. Data were collected for the smooth and knurled cylinders pictured in Figure 143. Figures 144 and 145 show, respectively, the variation of the lift and drag coefficients, for zero foil incidence, plotted versus the velocity ratio u/V .

Based on the portions of the curves near $u/V \approx 1.4$, the lift-augmentation ratios for the smooth and knurled cylinders are $\Delta C_L / \Delta(u/V) \approx 0.162$ and 0.317, respectively. The rough cylinder, knurled, gives higher incremental lift and also higher drag.

A crude estimate of the variation of lift increment of a two-dimensional foil section having a TE rotating cylinder can be made using the inviscid analysis of Neumark¹⁰⁶ for a rotating flap airfoil. In the limit of a rotating cylinder replacing a rotating flap, the approximate estimate for lift becomes

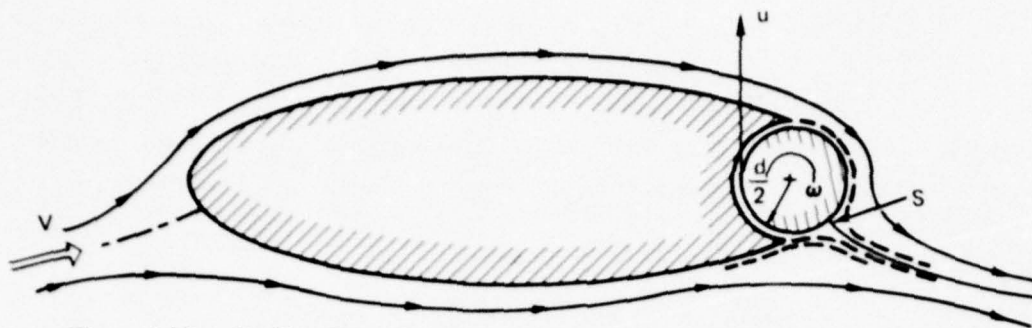


Figure 142 – Trailing-Edge Rotating Cylinder-Foil, Circulation-Control Mode

u is the cylinder peripheral velocity.

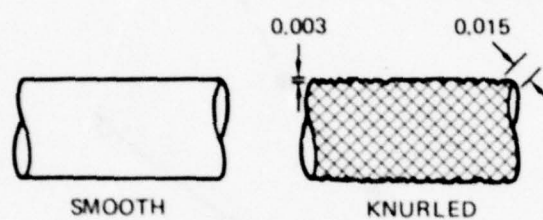


Figure 143 – Smooth and Knurled Cylinders Used for Tests on a Foil with a Trailing-Edge Rotating Cylinder

Brooks¹⁰³

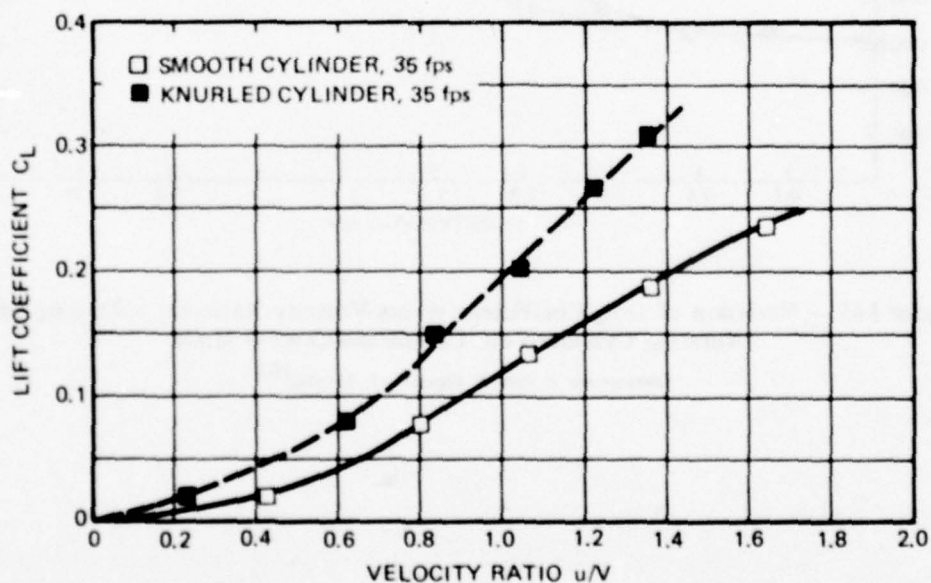


Figure 144 – Variation of Lift Coefficient versus Velocity Ratio for Trailing-Edge Rotating Cylinder Foil, Circulation-Control Mode

Brooks¹⁰³

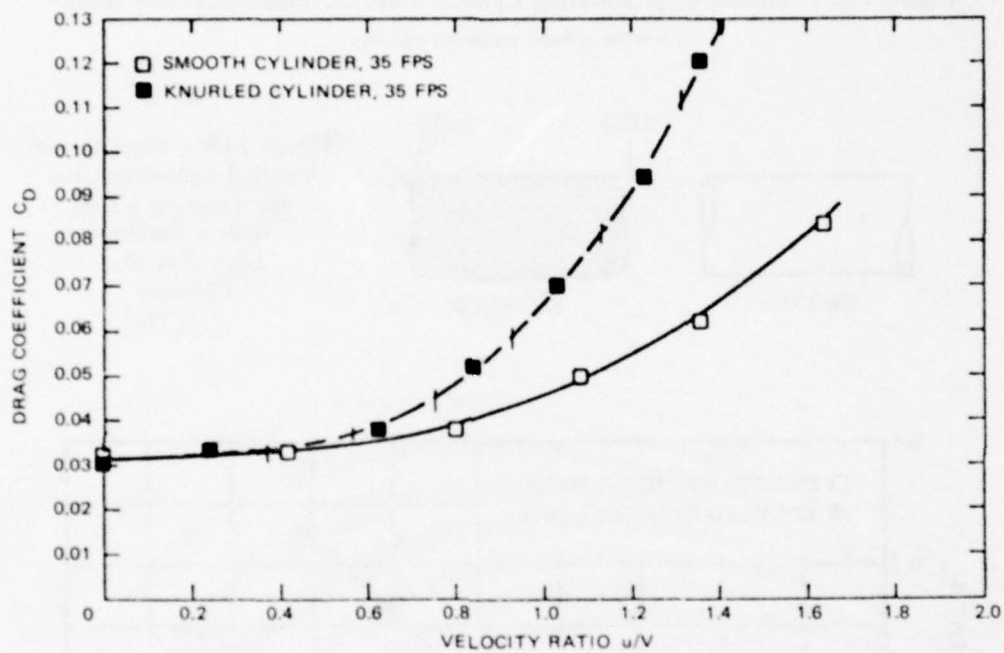


Figure 145 — Variation of Drag Coefficient versus Velocity Ratio for a Trailing-Edge Rotating Cylinder-Foil, Circulation-Control Mode

Corresponds to data of Figure 144, Brooks,¹⁰³

$$\Delta C_i \approx \sqrt{2 \frac{d}{c} \left(1 + \frac{d}{2c}\right)} \left(\frac{u}{V}\right)$$

at zero foil incidence. If the data of Brooks¹⁰³ are corrected to infinite-aspect ratio, using an effective aspect ratio of 1.208, the empirical variation for the Brooks case ($d/c = 0.136$) in the neighborhood of $u/V = 1.4$ is

$$\Delta C_i \approx \sqrt{6.88 \frac{d}{c} \left(1 + \frac{d}{2c}\right)} \left(\frac{u}{V}\right) \quad (79)$$

where d is the cylinder diameter, and c is the chord.

Effects of finite-aspect ratio on lift and drag can be accounted for crudely in the usual way. That is, the lift coefficient of the finite-aspect ratio foil can be expressed in terms of the section values as

$$C_L \left(\frac{u}{V}\right) = F_A(AR) \cdot C_{i_s} \left(\frac{u}{V}\right) \quad (80)$$

where C_{i_s} is the section-lift coefficient, and $F_A(AR)$ is the approximate aspect ratio correction factor given in Equation (41). The three-dimensional drag coefficient is written as

$$C_D = C_{D_p} + C_{D_i} \quad (81)$$

where C_{D_p} is the profile drag with cylinder rotation, and the induced-drag term C_{D_i} is obtained from Equation (8).

Numerous other TE rotating-cylinder-foil arrangements are discussed by Foshag and Boshler⁹⁸ for a variety of aspect ratios and wingbody configurations.

Powering Estimate

The fluid friction power required to spin the cylinder has the parameter variation expressed in Equation (75). Figure 146, reproduced from Brooks,¹⁰³ shows the horsepower required to spin the 3/4-inch-diameter cylinder fitted at the rear end of the 5.5-inch-chord foil shape. From these data, the effective friction coefficients (Equation (75)) applicable to the Brooks results are

$$\text{Knurled Cylinder} \quad C_{F_{\text{eff}}} \approx 0.0208 \quad (82a)$$

$$\text{Smooth Cylinder} \quad C_{F_{\text{eff}}} \approx 0.006 \quad (82b)$$

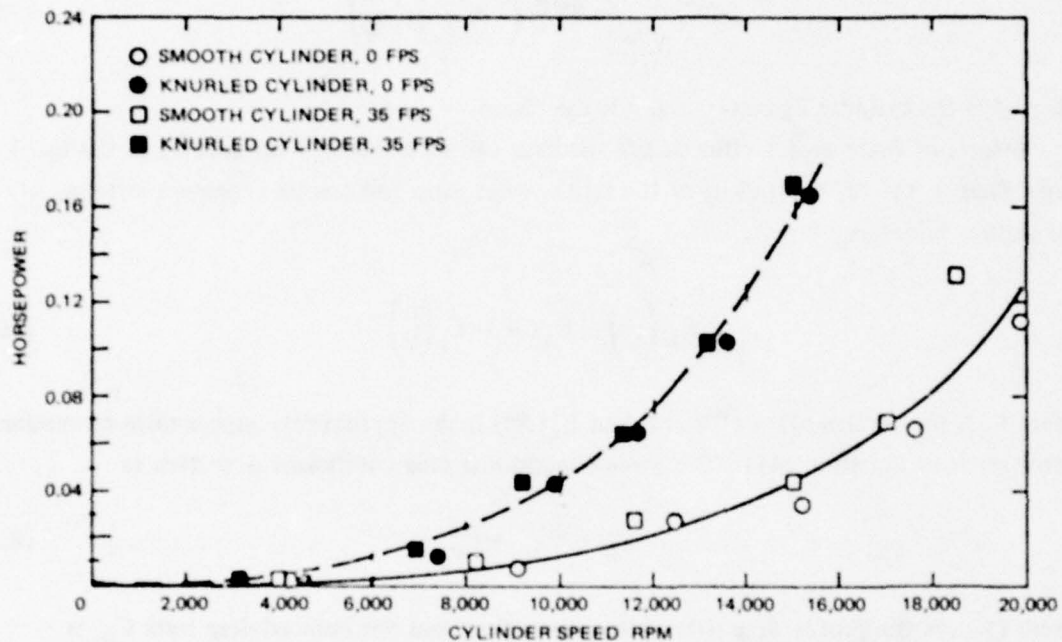


Figure 146 - Variation of Horsepower Required to Drive Trailing-Edge Cylinder versus RPM for a Trailing-Edge Rotating Cylinder Foil, Circulation-Control Mode

Corresponds to data of Figure 144, Brooks.¹⁰³

at a cylinder circumference Reynolds number $R_{\text{circum}} \approx 5.7 \times 10^5$. So the value of $C_F = 0.007$ chosen for general estimates (Equation (77)) has a reasonable intermediate value for a roughened surface.

A lift-to-power ratio can be formed, using the expressions for both lift increment and for power; see Equation (79). Using values from the Brooks¹⁰³ data, the lift coefficient increment per unit power coefficient is

$$\frac{\Delta C_l}{C_P} \sim \frac{\left[\Delta C_l / \left(\frac{u}{V} \right) \right]_{\text{meas}}}{\pi C_F (d/c) (u/V)^2} \quad (83)$$

where the C_F -values are given in Equations (82); the power coefficient based on total foil planform area is $C_P = C_{P_t} (S_t/S) = C_{P_t} (d/c)$; and $\left[\Delta C_l / \left(\frac{u}{V} \right) \right]_{\text{meas}}$ is the measured lift increment ratio.

DISCUSSION: Because of the fluid mechanical similarity between rotating-cylinder CC foils and foils using tangential blowing, there are certain similarities in overall characteristics. The main advantages are: (1) Lift may be produced independent of foil incidence and (2) substantial lift may be generated at low forward speed merely by increasing the velocity ratio u/V .

The principle disadvantages are:

1. There will be a relatively larger drag penalty at all velocity ratios u/V , compared with the tangential jet blowing technique. This is because of the inherent high drag characteristics of rotating cylinders. For zero foil incidences, at zero rotation (zero lift), the drag will be large because of the rounded trailing edge. On the basis of equivalent lift-to-drag ratio, the rotating cylinder form of CC is no better than CC by tangential jet blowing.

2. The power consumption grows very large at high speed, being proportional to rpm^3 or V^3 for constant (u/V) ; see Equation (75). However, at small values of u/V the lift increment-to-power ratio is actually superior to that achieved by tangential blowing. For example from the Brooks¹⁰³ data corrected to infinite-aspect ratio, the section-lift coefficient is $C_l \approx 1.12$ at $u/V = 1.4$ for the knurled cylinder. This gives a lift increment-to-power ratio from Equation (83)

$$\frac{\Delta C_l}{C_P} \approx 45.6 \quad (84)$$

which is about 2.2 times larger than the value for the 15-percent-thick tangential blowing CC foil performance achieved for $C_l = 1.12$ at $C_{\mu} = 0.028$ (Englar at the Center). However, a cambered 20-percent-thick slot blowing CC foil (Williams and Howe at the Center) delivers

$\Delta C_k/C_p \approx 67$ at $C_k = 1.5$.

3. To reverse the lift force direction, the cylinder will have to be stopped and reversed. This will add complexity.

4. Other problem areas will include: noise and cavitation at the sharp lips of the foil adjacent to the cylinder.

ROTATING CYLINDER FOIL, BOUNDARY LAYER CONTROL MODE

Figures 147 and 148a show the two different schemes for the use of rotating circular cylinders as boundary layer control devices. In both cases, the gains to be achieved by the BLC effect of a spinning cylinder are greatest at *large* deflection angles of the trailing foil or flap. Unlike the TE rotating cylinder foil, the BLC version *must* be operated at high angles of attack. The fluid mechanical effect of the rotating cylinder at those locations where the boundary layer is likely to separate, the moving surface energizes the flow so that it can negotiate the turn over the foil or over the trailing-edge flap. This is shown in Figure 148b. The role of the rotating cylinder is to force the flow to remain attached over the foil or flap, and thereby to achieve the ideal predicted lift coefficient. Because of the sharp trailing edge, the maximum section circulation is fixed by the flap deflection angle.

Force Estimates

Some sample existing data are presented for lifting foils, having either the leading-edge or the flap-knee location of a spinning cylinder.

Leading-Edge Cylinder. Figure 149 shows data obtained in a water tunnel by Steele and Harding¹⁰² for the variation of lift coefficient versus velocity ratio for a rudder ($AR \approx 1.67$) equipped with a leading-edge cylinder. The sketch shows this augmented control surface in one of the possible applications on a surface ship rudder. Note that for a given angle of deflection α (angle of attack), there is a value of u/V beyond which the lift does not increase further. This velocity ratio is identified as the $(u/V)_{crit}$ required to obtain the ideal potential flow C_L .

Wolff and Koning¹⁰⁷ have presented wind tunnel data for an aspect ratio 5.4 rectangular wing, having the foil section shape indicated in Figure 150a. The variation of lift coefficient versus angle of attack for various velocity ratios is shown in Figure 150b. Figures 151 and 152 show, respectively, the variation of lift coefficient and drag coefficient versus α for $u/V = 3.2$. All the data of Figures 151 and 152 were obtained at a Reynolds number, based on chord length, of $\sim 6 \times 10^4$.

Flap-Knee Cylinder. Example two-dimensional lift and drag data for a foil with a 45-inch-diameter rotating cylinder at the flap knee are shown in Figure 153, reproduced from

Figure 147 – Leading-Edge Rotating Cylinder
Foil, BLC Mode

u is the cylinder peripheral velocity.

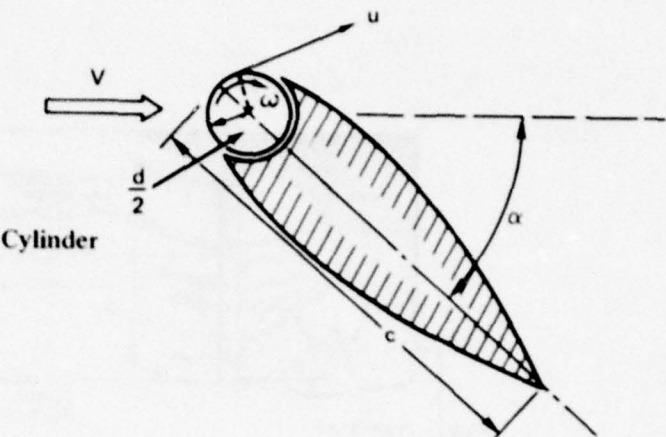
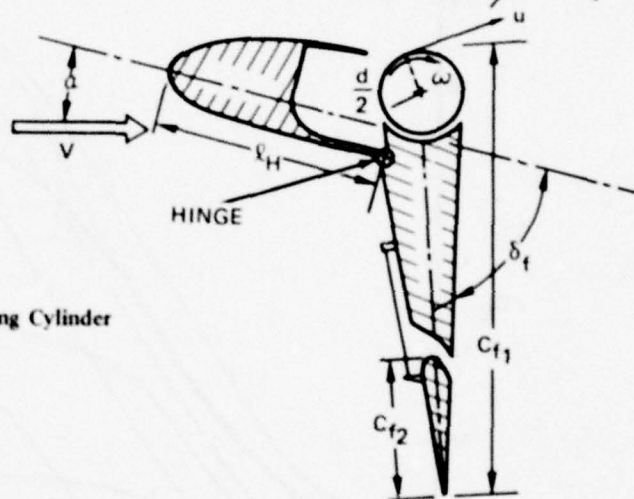


Figure 148a – Flap-Knee Rotating Cylinder
Foil, BLC Mode



WEAK BOUNDARY LAYER

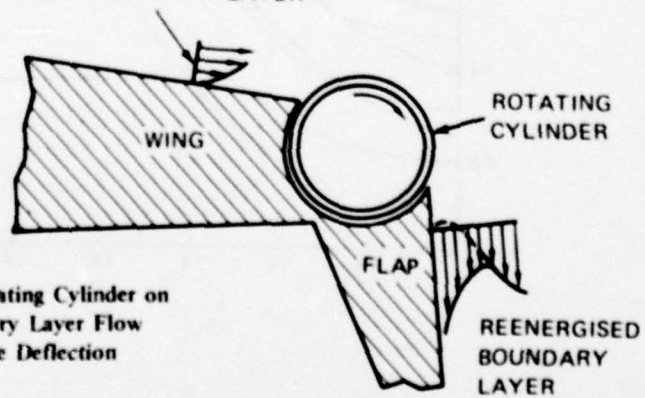


Figure 148b – Effect of a Rotating Cylinder on
Otherwise Separated Boundary Layer Flow
near a Flap Knee When the Deflection
Angle is Large

Figure 148 – Rotating Cylinder Foil

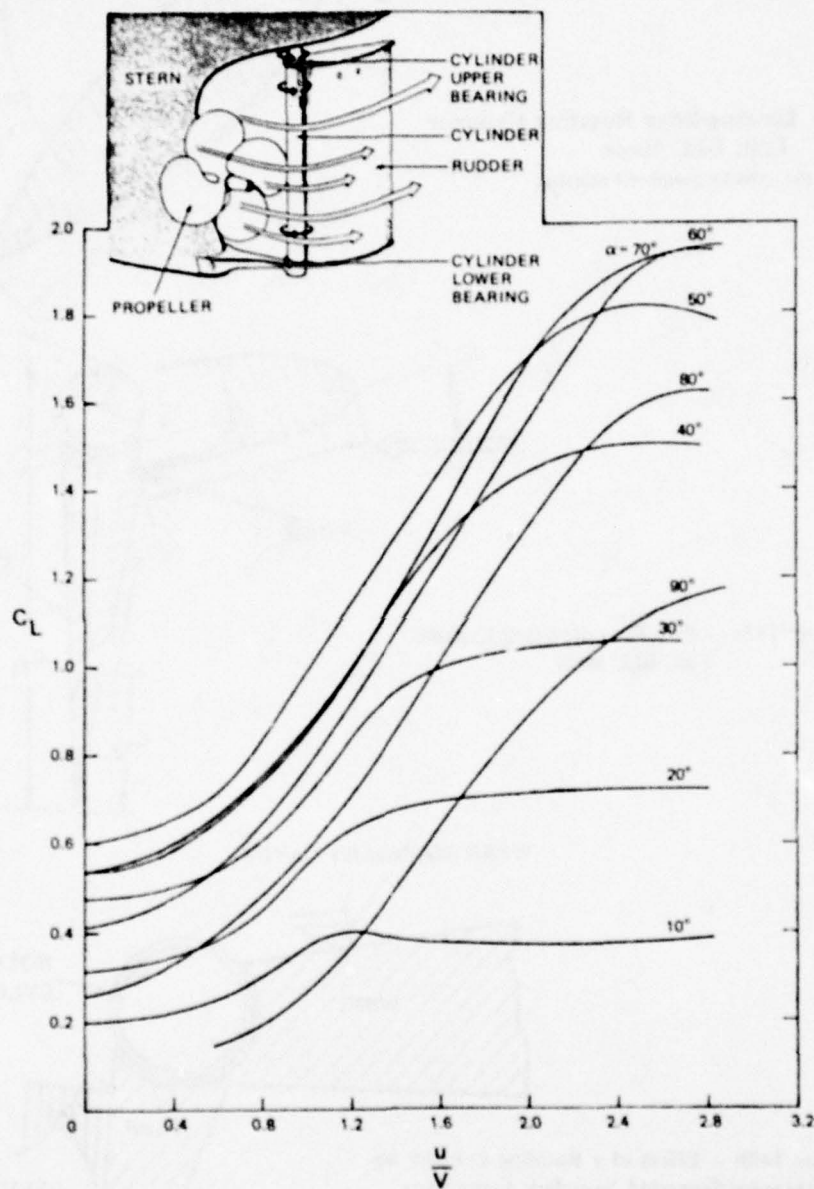


Figure 149 – Variation of Lift Coefficient versus Velocity Ratio for an Aspect Ratio 1.67 Rudder with a Leading-Edge Rotating Cylinder
Steele and Harding.¹⁰²

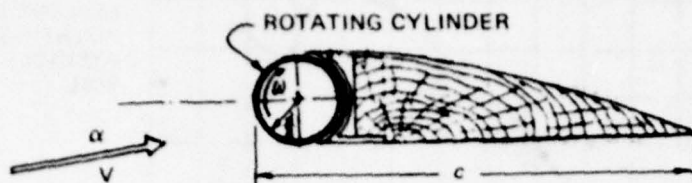


Figure 150a - Foil Cross Section with a Leading-Edge Rotating Cylinder

Tested by Wolff and Koning;¹⁰⁷ $t/c = 0.2$, u - peripheral velocity $= \omega d/2$
 Model: $d = 1.46$ Inches, $c = 7.28$ Inches.

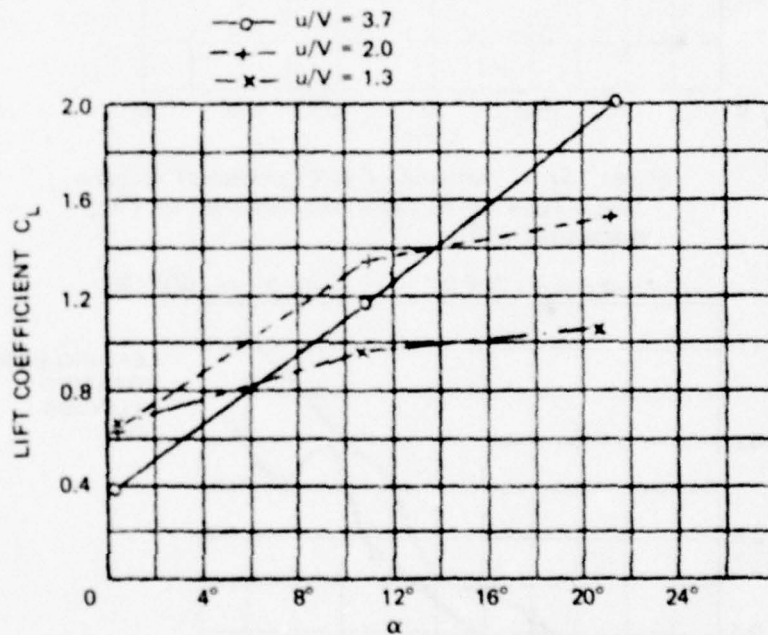


Figure 150b - Variation of Lift Coefficient versus Angle of Attack for the Leading Edge Rotating Cylinder Foil of Figure 150a
 Contours of velocity ratio u/V , Wolff and Koning.¹⁰⁷

Figure 150 - Leading Edge Rotating Cylinder Foil

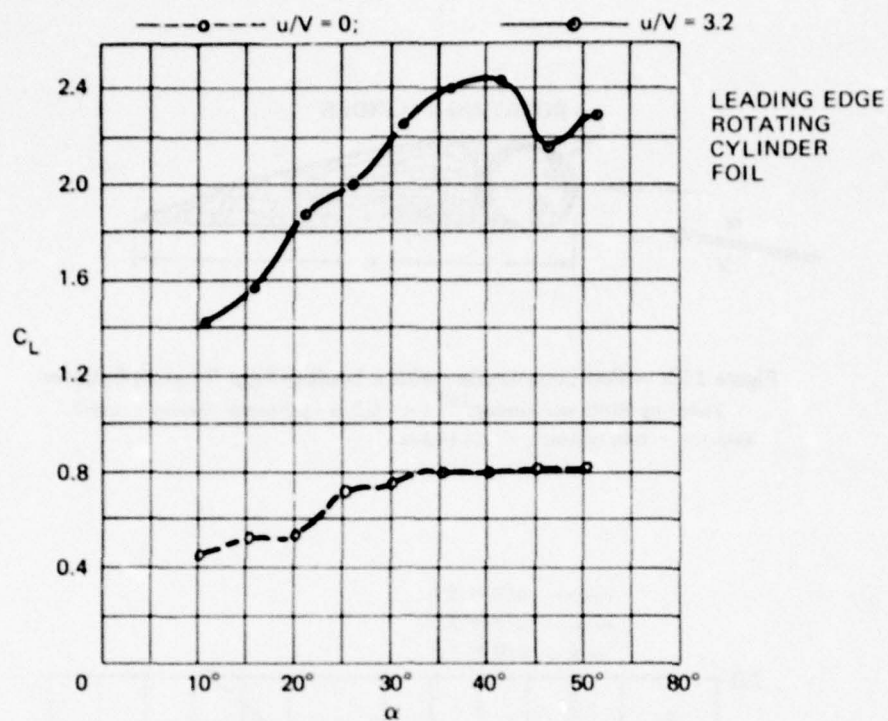


Figure 151 — Variation of Lift Coefficient versus α

Foil of Figure 150a for zero cylinder rotation and $u/V = 3.2$,
Wolff and Koning.¹⁰⁷

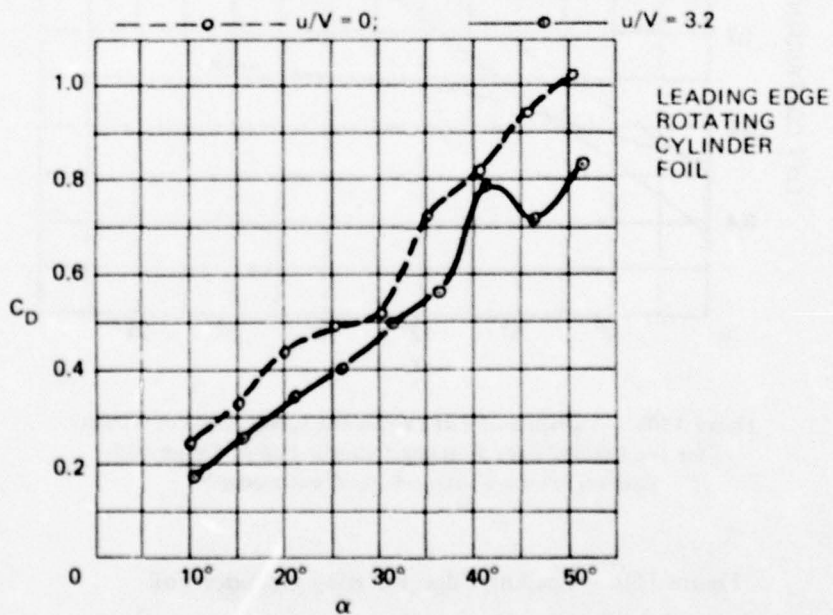


Figure 152 — Variation of Drag Coefficient versus α

Corresponds to Figure 151 for zero cylinder rotation
and $u/V = 3.2$.¹⁰⁷

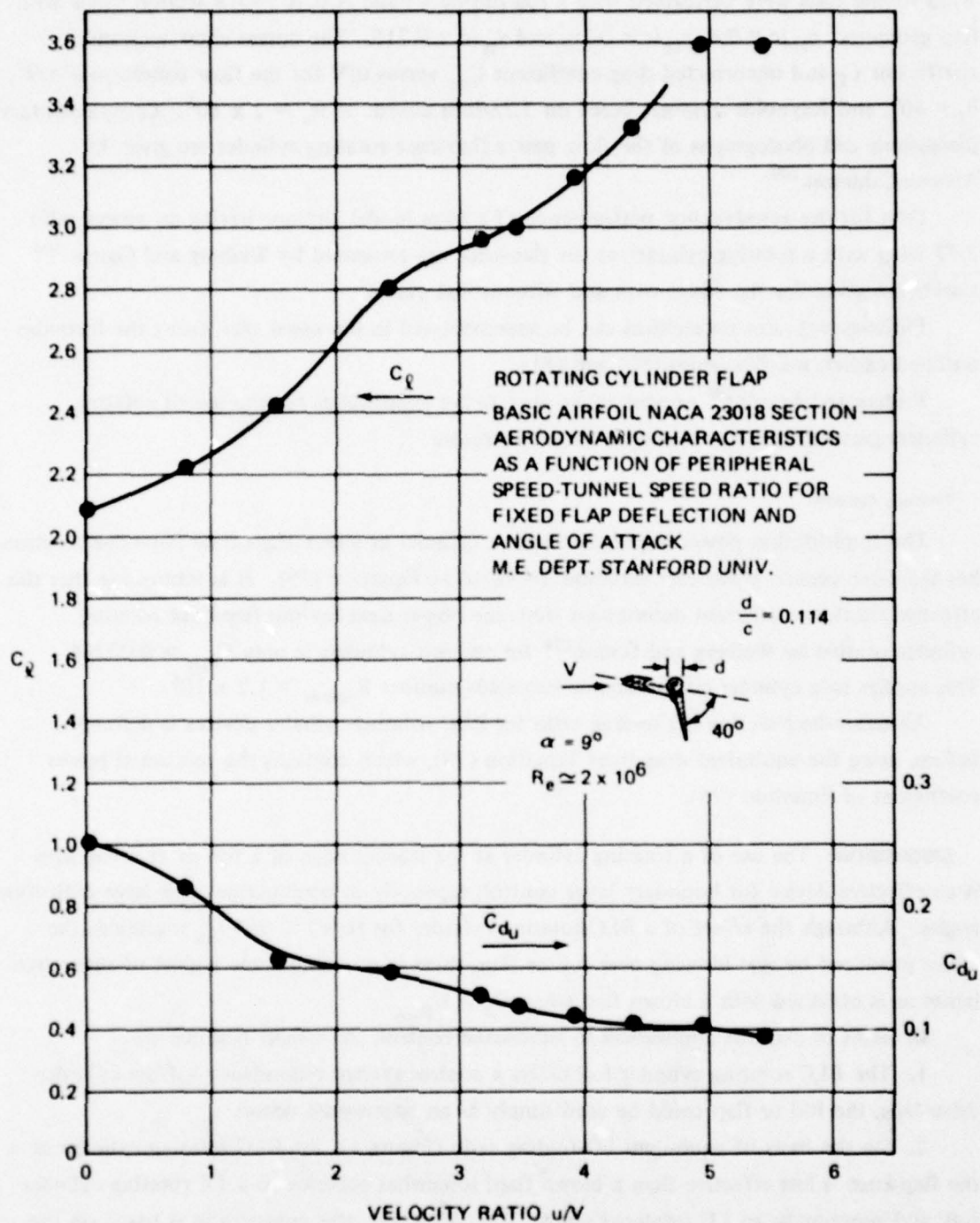


Figure 153 – Variation of Section Lift and Uncorrected Drag Coefficients versus Velocity Ratio for the Rotating Cylinder Flap

Alvarez-Calderon and Arnold.¹⁰⁸

Alvarez-Calderon and Arnold¹⁰⁸. The foil-cylinder-flap arrangement is shown in Figure 148a. Wind tunnel tests were performed with a foil having a basic NACA 23018 section shape with flap geometry: $c_{f1}/c = 0.4$, $c_{f2}/c = 0.16$, and $l_H/c = 0.715$. The curves show section-lift coefficient C_L and uncorrected drag coefficient C_{du} versus u/V for the flow condition $\alpha = 9^\circ$, $\delta_f = 40^\circ$, and Reynolds number, based on 3.28-foot chord, of $R_e \approx 2 \times 10^6$. Complementary discussions and photographs of the flow past a flap-knee rotating cylinder are given by Alvarez-Calderon.¹⁰⁹

Data for the aerodynamic performance of a large model airplane having an aspect ratio 3.57 wing with a rotating cylinder at the flap-knee are presented by Weiberg and Gamse.¹⁰⁴ Curves are given for the wings with and without end plates.

Finite-aspect-ratio corrections can be approximated in the usual way, using the formulas outlined earlier; see Equations (80) and (81).

Foshag and Boshler⁹⁸ present other provocative possibilities for the use of rotating cylinders gleaned from the extensive patent literature.

Powering Estimate

The fluid-friction power required to spin a cylinder at either the LE or flap-knee location has the same general parameter variation displayed in Equation (75). It is interesting that the effective friction coefficient determined from the power data for the flap-knee rotating cylinder studied by Weiberg and Gamse¹⁰⁴ for smooth cylinders is only $C_{F_{eff}} \approx 0.00266$. This applies to a cylinder-circumference Reynolds number $R_{circum} \approx 1.2 \times 10^6$.

An equivalent section lift-to-drag ratio for BLC rotating-cylinder devices is defined as before, using the equivalent drag from Equation (78), which contains the rotational power coefficient of Equation (76).

DISCUSSION: The use of a rotating cylinder at the leading edge of a foil or at a flap knee is an effective device for boundary layer control, especially in conjunction with large deflection angles. Although the effect of a BLC rotating cylinder for $(u/V) \leq (u/V)_{crit}$ resembles the effect produced by slot blowing over foil or flap, there is no comparable regime of supercirculation as is obtained with a blown flap when $C_\mu > C_{\mu_{crit}}$.

In terms of possible application to submarine control, the salient features are:

1. The BLC rotating cylinder foil offers a control system redundancy—if the cylinder drive fails, the foil or flap could be used simply as an unpowered device.
2. On the basis of equivalent lift-to-drag ratio (Figure 1), the BLC rotating cylinder at the flap-knee is less effective than a blown flap; somewhat superior to a TE rotating cylinder foil; and superior to an LE rotating cylinder foil. However, this comparison is based on the meager data available and will probably need revision as more data are generated. Note in Figure 1 that the various rotating cylinder devices are compared in their appropriate modes:

the CC device at $\alpha = 0$, and the two BLC devices at large foil incidence and/or large flap angle.

3. Compared to the CC rotating cylinder device, the BLC devices should have lower drag penalties at $C_L = 0$ because of their sharp trailing edges.

4. The BLC rotating-cylinder devices require large power at high speeds, power $\propto V^3$ at constant u/V . The same is true of course for the CC device. Therefore, the best regime of operation for these devices would be at low speed, leaving high-speed control forces to be generated by simple foil or flap deflection.

5. Marine fouling would probably be less of a problem with rotating cylinders than with slot-blowing or suction devices.

6. Reversing the foil or flap deflection in order to reverse the lift-force direction would require stopping and reversing the cylinder. This would require extra machinery and versatility.

7. Other problems areas include noise, vibration, and cavitation.

NAME: Rotating Foils and Flaps.

DESCRIPTION AND FORCE ESTIMATES: A rotating foil lifting device is similar to rotating circular cylinders used for circulation control, and, of course, the cylinder can be thought of as a special case of a rotating foil in which the rotating foil chord and foil thickness are the same. Therefore, this discussion begins with the characteristics of an isolated rotating foil.

FORCE ESTIMATES

Figure 154a is a sketch of an isolated rotating foil. Data obtained by Küchemann⁹⁹ and reviewed by Neumark¹⁰⁶ are reproduced in Figures 154b and 154c for the lift versus velocity ratio and lift versus drag curves, respectively. These curves are for both rotating cylinders and biconvex foils, having various aspect ratios and end-disk arrangements. The following features of rotating foils are evident.

1. The lift curve slope $\Delta C_L / \Delta \frac{u}{V}$ in the range $u/V < 1$ is considerably larger for the biconvex rotating foil than for the rotating cylinder.

2. The drag coefficient is very large—often nearly twice the lift coefficient—for all cases when $u/V \neq 0$.

3. The ultimate $C_{L_{\max}}$ is larger for a rotating cylinder than for a rotating foil. The rotating foil is a much more efficient inducer of circulation at low u/V values, compared with the circular cylinder. More important is the fact that the foil will autorotate at some $u/V < 1$ and, hence, will produce lift augmentation with no direct power expenditure. The penalty of course is a tremendous drag coefficient. Although the drag coefficient of a rotating foil is comparable to or larger than that of a cylinder, the foil can be held fixed ($u/V = 0$) with the flap chord parallel to the free stream, so that it has a relatively small drag coefficient, no larger than an ordinary foil at $C_L = 0$.

A rotating foil can be used together with a fixed foil, in which case the combination is called a rotating-flap airfoil; see Figure 155. An inviscid analysis of the rotating flap airfoil is presented by Neumark¹⁰⁶. The results are restricted to cases where: $t/c \ll 1$, ℓ is comparable to $d/2$, the circulation induced by the flap rotation is $\Gamma \sim u$, and the incidence angle of the foil is small. Figure 155 indicates the notation. The assumption that $\Gamma \sim u$ is in accordance with the experimental data of Figure 154b for free-rotating flaps, where it is seen that $C_L \propto u/V$ up to a maximum value, and $\Gamma \sim u$ also implies no interference between the airfoil and the rotating flap.

Under the previously described restrictions, Neumark¹⁰⁶ obtained an approximate result for the two-dimensional, lift-coefficient increment

$$\Delta C_L \approx \sqrt{\frac{d^2}{c^2} + \frac{2d}{c(1+\epsilon)}} \cos \frac{\beta}{2} \cdot \left(\frac{u}{V}\right) \quad (85)$$

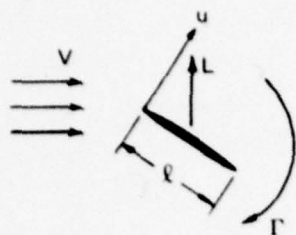


Figure 154a – Isolated Rotating Foil in a Uniform Stream V

Figure 154b – Variation of Lift Coefficient C_L versus Velocity Ratio u/V for Several Rotating Foil and Rotating Circular Cylinder Arrangements
Neumark¹⁰⁶; data from Kuchemann⁹⁹

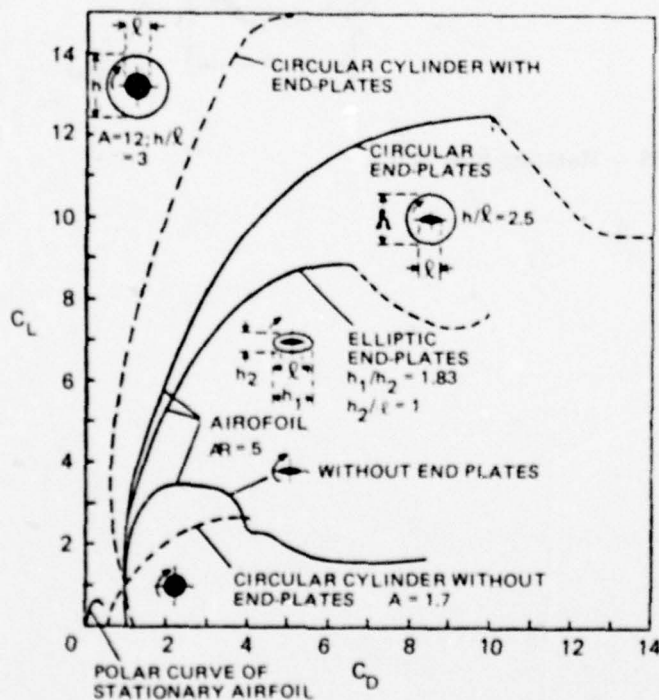
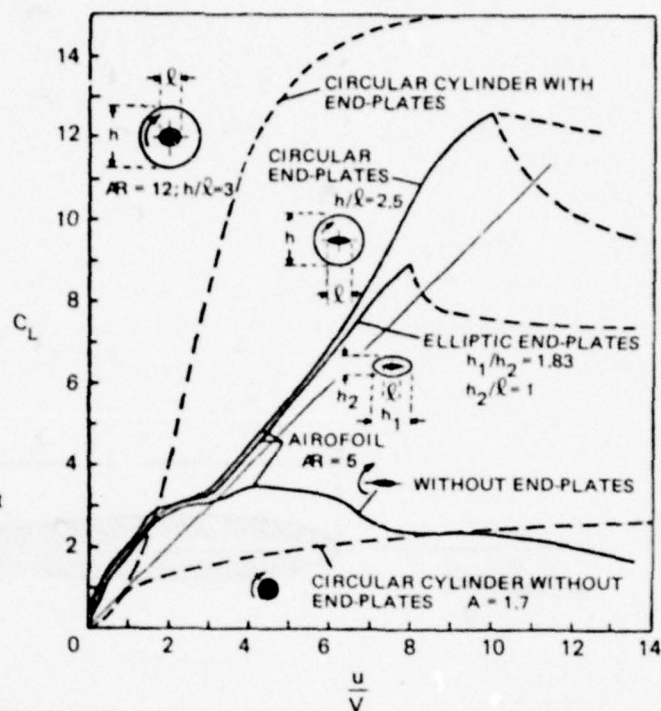


Figure 154c – Polar Curves of C_L versus C_D for Several Rotating Foil and Rotating Cylinder Arrangements
Neumark¹⁰⁶; data from Kuchemann⁹⁹

Figure 154 – Rotating Foils

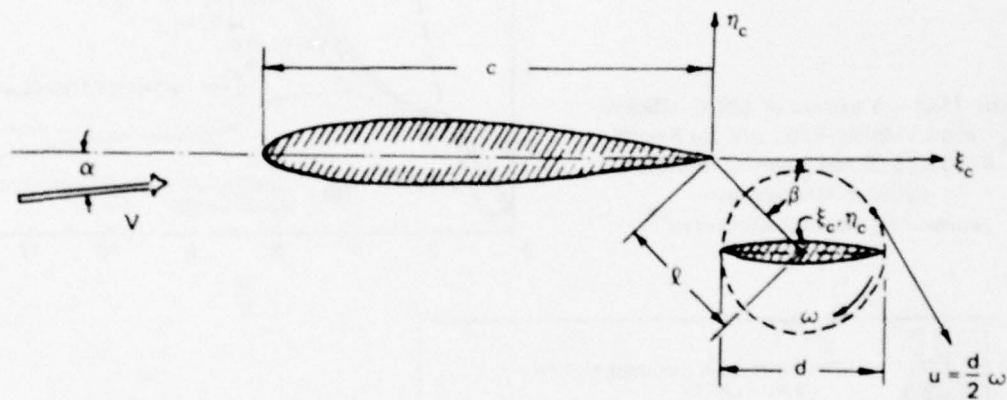


Figure 155 - Rotating-Flap Airfoil

where $\epsilon = 2\ell/d - 1$ so that

$$\ell = \frac{1}{2} (1 + \epsilon) d \quad (86)$$

To the approximation considered, the lift increment is the same, regardless of whether the flap is above or below the chord line of the foil. That is, the lift increment is an even function of β . Also the lift increment is increased as β is decreased and as the gap ($= \epsilon d/2$) between the leading edge of the rotating flap and the trailing edge of the airfoil is decreased.

Some experimental data from Küchemann for the performance of a rotating-flap airfoil are shown in Figure 156, reproduced from Neumark.¹⁰⁶ These data apply to the lift on an aspect ratio 2.67, rectangular planform wing-flap combination, fitted with elliptical end plates, where both wing and flap have an NACA 23015 section shape, and where the flap chord length is $0.25c$. The curves show the maximum attainable lift coefficient $C_{L_{\max}}$, with respect to angle of attack, plotted versus velocity ratio for three configurations. Note that for the flap in position 2, for example, a value $C_{L_{\max}} \approx 2.4$ is obtained at $u/V \approx 0.7$. At this condition, the flap autorotates and thus has no augmentation power requirement, aside from the power required to overcome the increased drag.

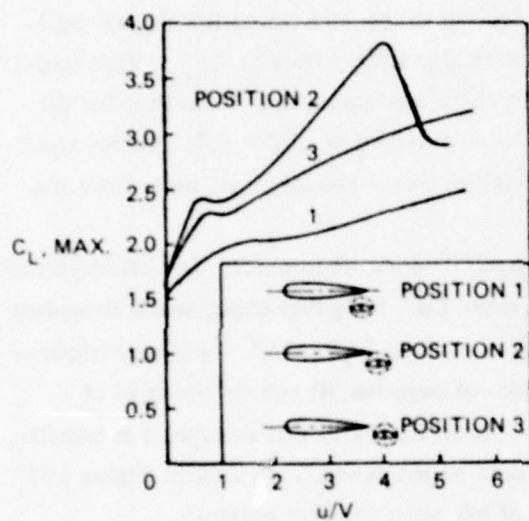
Figures 157 and 158, reproduced from Crabtree,¹¹⁰ show, respectively, the lift-incidence and the lift-drag polar curves for the same aspect ratio 2.67, wing-flap combination described previously, with the rotating flap in position 2. Note that in Figure 157, the large variations of C_L at fixed angle of attack and substantial values of negative lift can be obtained at positive angle of attack by making $u/V < 0$. This means that with this scheme, it is possible to achieve the desirable property of "lift independent of incidence." As seen in Figure 158, the drag coefficient C_D is very large at all values of lift when the flap rotates.

When the flap is held fixed in place ($\beta = 0^\circ$ and 45°), the drag coefficients are considerably smaller and are roughly comparable to those of ordinary foil-flap arrangements.

Several other proposed configurations for the use of rotating flaps and imbedded rotors for augmenting circulation and/or BLC on foils are reviewed by Foshag and Boshler.⁹⁸

POWERING REQUIREMENT

As for rotating cylinders, the power required to rotate a flap, excluding bearing-friction power, is proportional to rpm^3 ; this is evident from the fact that the power coefficient K_{P_R} given in Figure 159 is essentially a constant for $u/V > 2$. Here, the flap rotational power coefficient K_{P_R} , based on the planform area of the rotating member and the peripheral velocity, is defined as



POSITION	ξ_c	η_c
1	- 0.13	- 0.18
2	+ 0.05	- 0.13
3	+ 0.13	- 0.10

HERE $d = c_f$

Figure 156 - Variation of $C_{L, max}$ versus Velocity Ratio u/V for Aspect Ratio 2.67 Rotating-Flap Wing

Tested by Küchemann⁹⁹; foil and flap have the same section, NACA 23015, $AR = 2.67$, and $c_f/c = 0.25$. Position 1 lies on the locus of theoretically best positions for a rotating flap; see Crabtree.¹¹⁰

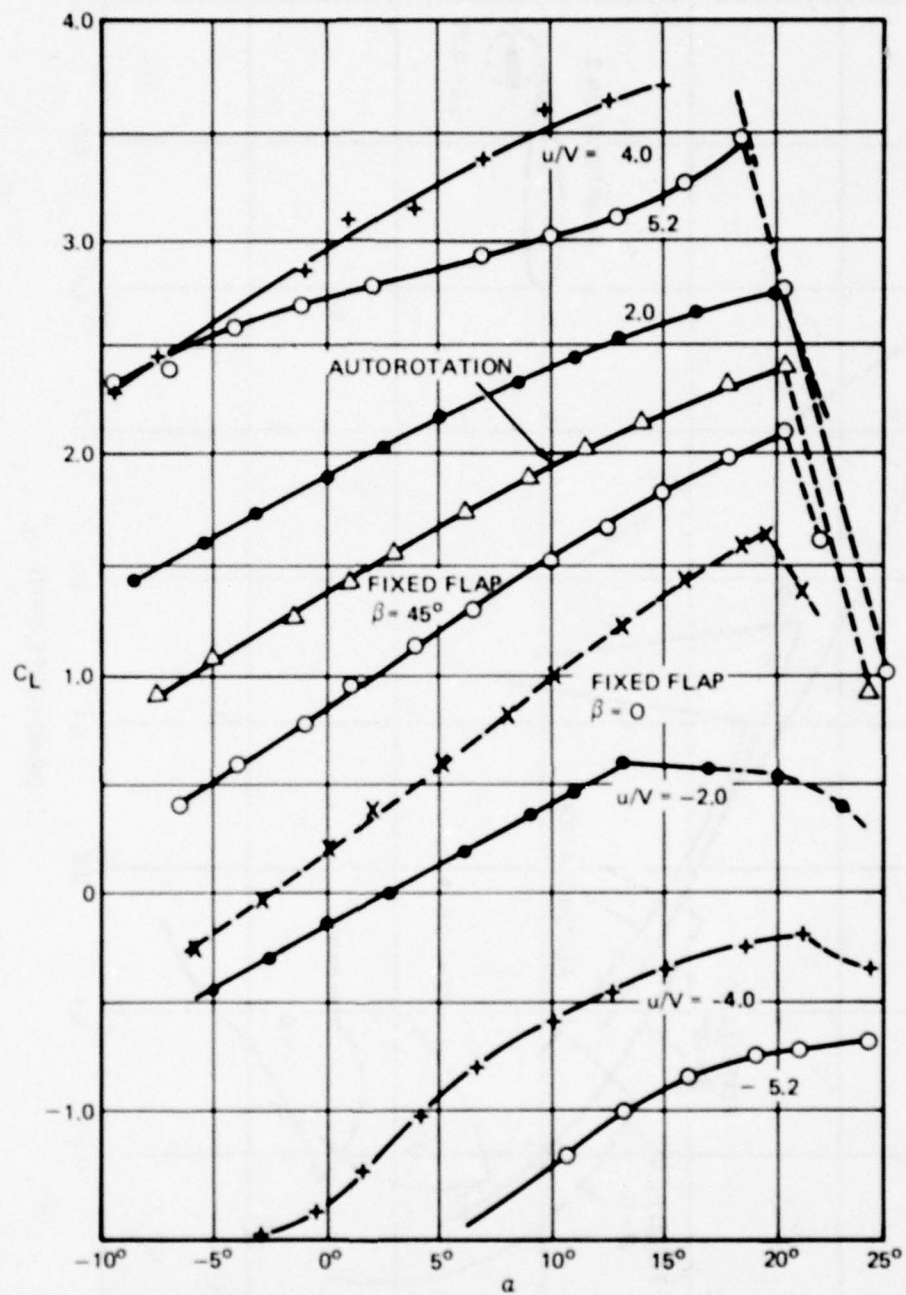


Figure 157 - Variation of Lift Coefficient C_L versus α for the Aspect Ratio 2.67
 Rotating Flap Wing of Figure 156
 Contours of u/V and β . Position 2, Crabtree.¹¹⁰

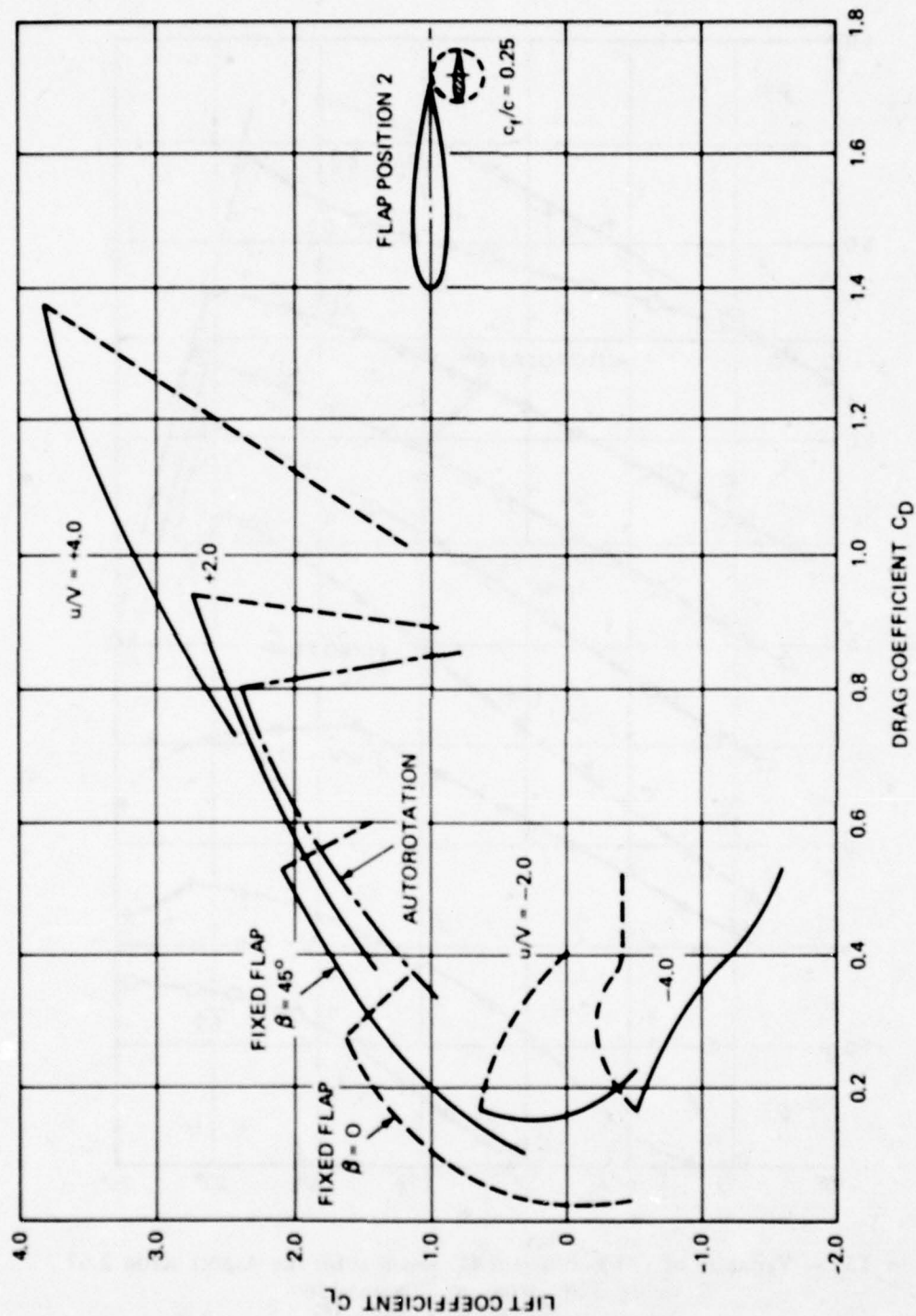


Figure 158 - Polar Curves of C_L versus C_D for Aspect Ratio 2.67 Rotating Flap Wing of Figure 156

Contours of u/V and β , Position 2, Crabtree, 110

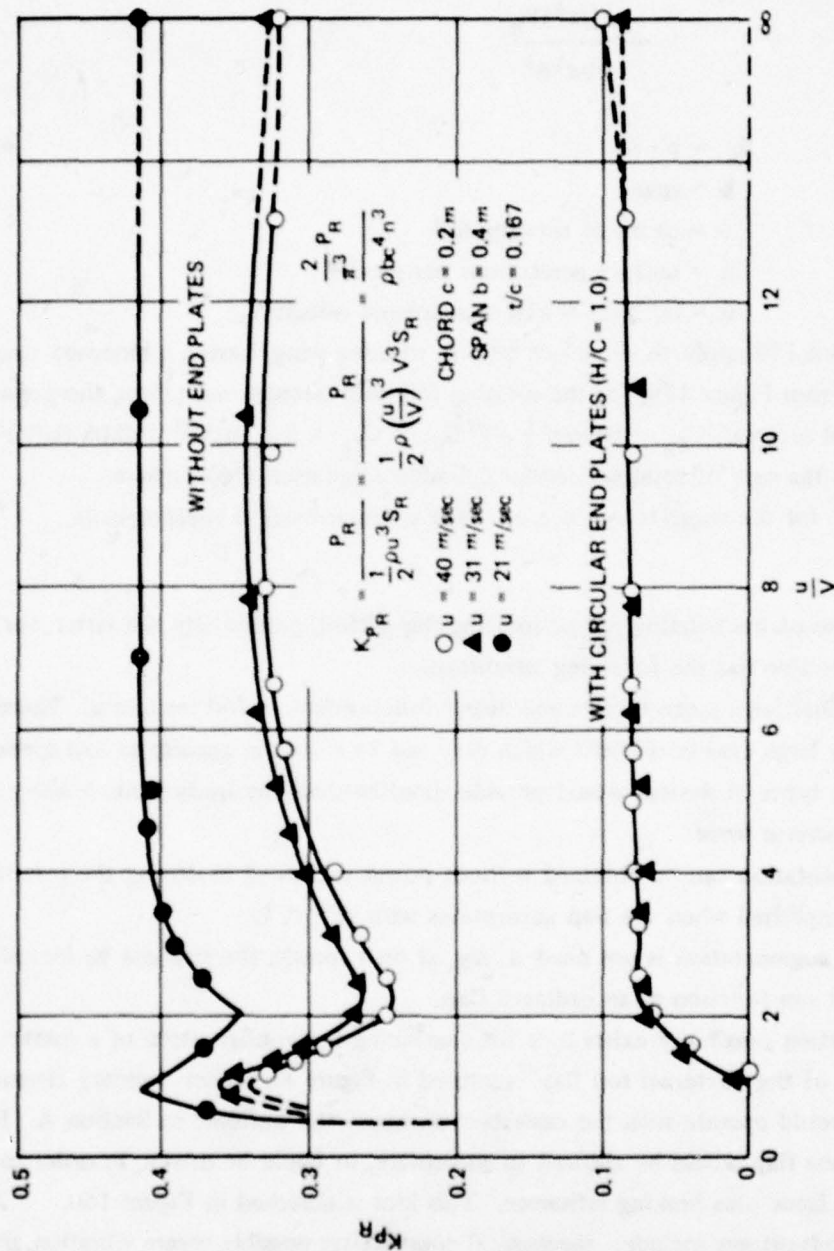


Figure 159 - Variation of Power Coefficient K_{PR} versus u/V for an Aspect Ratio 2 Rotating Wing. Biconvex, Circular Arc Section Shape, $t/c = 0.167$
 Crabtree, 111 data from Kuchemann, 95

$$\begin{aligned}
 K_{P_R} &= \frac{P_R}{\frac{1}{2} \rho u^3 S_R} = \frac{P_R}{\frac{1}{2} \rho \left(\frac{u}{V}\right)^3 S_R V^3} \\
 &= \frac{(2/\pi^3) P_R}{\rho b c^4 n^3}
 \end{aligned} \tag{87}$$

where

$$S_R = b \cdot c$$

$$b = \text{span}$$

$$c = \text{chord of rotating foil}$$

$$n = \omega/2\pi = \text{revolutions per second}$$

$$u = (c/2) \cdot \omega = \pi c n = \text{peripheral velocity.}$$

The curves in Figure 159 apply to an aspect ratio 2, rotating wing, having a biconvex circular arc foil section. From Figure 159, for the rotating foil with circular end plates, the power coefficient, defined as usual, $C_{P_R} = \text{Power} / \frac{1}{2} \rho V^3 S_R$, is $C_{P_R} = K_{P_R} (u/V)^3 \approx 0.08 (u/V)^3$. Compare this with the case of rotating circular cylinders (Equation (76)), where $C_{P_r} \approx 0.022 (u/V)^3$ for the suggested choice of rough cylinder-friction coefficient in Equation (77).

DISCUSSION: Use of the rotating foil or rotating flap airfoil, particularly the latter, for control-force production has the following advantages.

1. High lift coefficients can be attained nearly independent of foil incidence. There is a corresponding very large drag coefficient which may not be a serious penalty at low speeds. Actuation of these types of devices would provide simultaneously hydrodynamic *braking* as well as a large transverse force.
2. Lift augmentation can be obtained without power expended in driving the rotating flap. This is accomplished when the flap autorotates with $u/V < 1$.
3. When lift augmentation is not needed, say, at high speeds, the flap can be locked into a position where it can function as an ordinary flap.
4. An interesting possibility exists here for combining the configuration of a rotating-flap foil with that of the "external foil flap" pictured in Figure 8. Under ordinary circumstances, the flap would operate with the desirable characteristics outlined in Section A. In an emergency, the same flap would be allowed to autorotate, or could be driven, in order to generate a control force plus braking influence. This idea is sketched in Figure 160.

The main disadvantages include: mechanical complexity; possible severe vibration and noise problems; and possibly cavitation, if large u/V values are used.

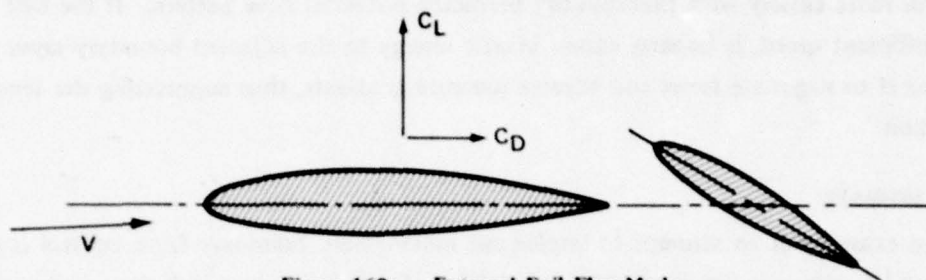


Figure 160a - External Foil Flap Mode

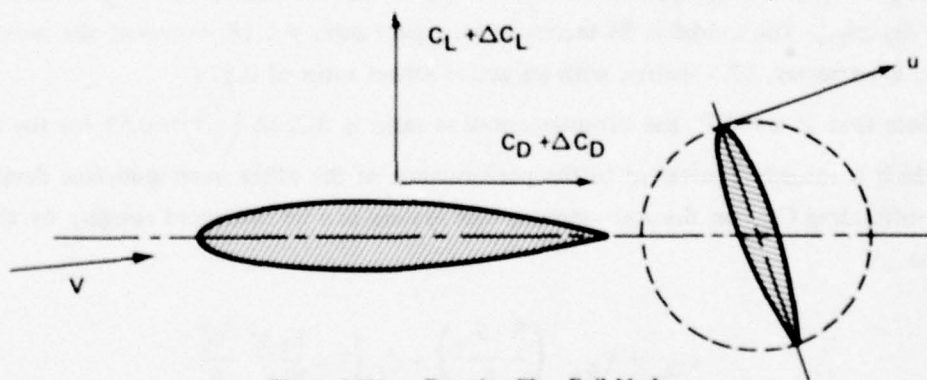


Figure 160b - Rotating-Flap Foil Mode

Figure 160 - A Possible Combination of External Foil Flap and Rotating-Flap Foil for an Emergency High-Lift and Braking-Drag Device

NAME: Moving Belts.

DESCRIPTION AND FORCE ESTIMATES: A moving belt may be used to replace the upper or suction side of a lifting foil. If the direction of the motion of the belt is such that its exposed part moves in the same direction as the free stream, there will be some reduction in skin friction locally; however, more importantly, the moving surface helps force the streamlines to conform more closely with theoretically predicted potential flow pattern. If the belt moves with sufficient speed, it imparts excess kinetic energy to the adjacent boundary layer flow, enabling it to negotiate turns and adverse pressure gradients, thus suppressing the tendency for separation.

FORCE ESTIMATE

An example of an attempt to implement moving-belt, boundary layer control is presented by Bond,¹¹¹ who also has provided a helpful list of references that includes some pertinent U.S. patents. Figure 161b, reproduced from Reference 111, shows the variation of lift coefficient versus angle of attack for a 30.5-inch-chord NACA 66₄A421 foil section, equipped with a moving belt stretching over the forward 85 percent of the chord; see Figure 161a. Data are included for the cases with the belt moving and with the belt held stationary as well as for both flapped and unflapped configurations. The moving-skin curves apply to the case of $V_b/V_o \approx 1$, where V_b is the absolute velocity of the belt surface, and V_o is the free stream velocity. The model is 36 inches wide, aspect ratio = 1.18; however, the moving-belt portion is narrower, 17.5 inches, with an active aspect ratio of 0.574.

Note that at $\alpha = 20^\circ$, the lift-augmentation ratio is $\Delta C_L / \Delta \left(\frac{V_b}{V_o} \right) \approx 0.55$ for the unflapped foil, which is roughly equivalent to the performance of the other moving-surface devices.

Profile drag C_{D_p} on the foil-moving-belt system can be estimated roughly by the formula

$$C_{D_p} = C_{D_{p_o}} \left(\frac{S - S_{b_e}}{S} \right) + C_f \left(1 - \frac{V_b}{V_o} \right)^2 \frac{S_{b_e}}{S} \quad (88)$$

where $C_{D_{p_o}}$ = profile drag of foil section shape, based on planform area S

S_{b_e} = surface area of belt exposed to the free stream

C_f = friction drag coefficient appropriate for belt-length Reynolds number.

Corrections on lift and drag for finite-aspect-ratio effects can be approximated in the usual way using Equations (80) and (81).

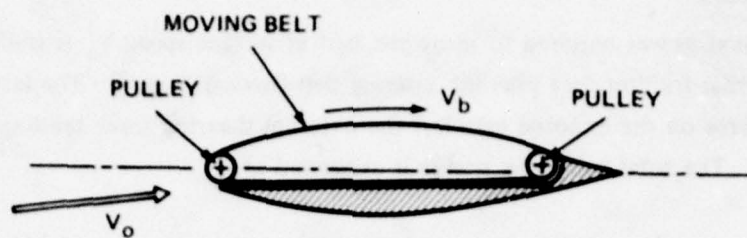


Figure 161a - Moving-Belt Foil, BLC Mode

V_b = surface velocity of belt.

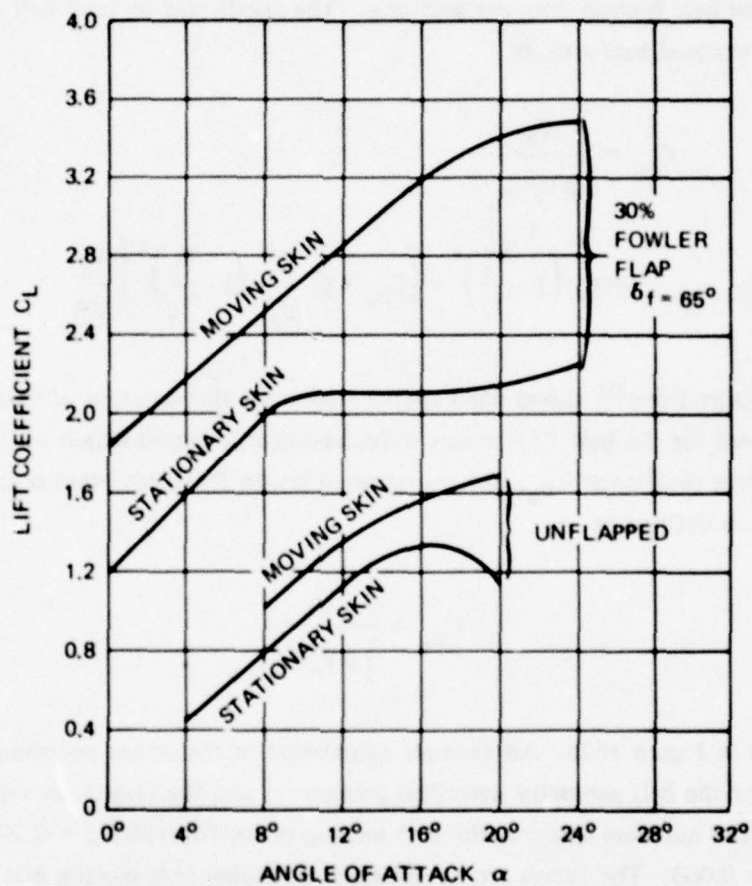


Figure 161b - Variation of Lift Coefficient versus Angle of Attack for a NACA 66₄A421 Basic Foil Shape with a Moving Belt Extending over the Forward 85-Percent Chord Length

Here $V_b/V_o \approx 1.0$, Bond.¹¹¹

Figure 161 - Moving-Belt Foil

POWER REQUIREMENTS

The total fluid power required to move the belt at surface speed V_b is the sum of the part due to external friction drag plus the internal belt-friction drag.¹¹¹ The latter is estimated as the friction force on the exposed area less the external shearing force tending to autorotate the moving belt. The total belt drive power is expressed as

$$P_B = \frac{1}{2} \rho C_f (V_o - V_b)^2 S_{b_e} + V_b [D'_b - \frac{1}{2} \rho C_f (V_o - V_b)^2] S_{b_e} \quad (89)$$

where D'_b is the belt friction drag per unit area. The coefficient of total belt drive power, based on the exposed belt area, is

$$\begin{aligned} C_{PB} &= \frac{P_B}{\frac{1}{2} \rho V_o^3 S_{b_e}} \\ &= C_f \left(1 - \frac{V_b}{V_o}\right)^2 + \left[C_{D_b} + C_f \frac{V_o^2}{V_b^2} \left(1 - \frac{V_b}{V_o}\right)^2 \right] \frac{V_b^3}{V_o^3} \end{aligned} \quad (90)$$

Figure 162a, from Bond¹¹¹ shows wind tunnel results for the variation of total belt drag D_b versus belt speed for the belt 17.5 inches wide, having an exposed length of 25.92 inches. The belt friction-drag coefficient C_{D_b} , (for the exposed-length Reynolds number $0.93 \times 10^6 < R_b < 1.6 \times 10^6$), is defined as

$$C_{D_b} = \frac{D_b}{\frac{1}{2} \rho V_b^2 S_{b_e}} \quad (91)$$

and is plotted in Figure 162b. An example calculation of the power-per-unit-area is presented by Bond¹¹¹ for the belt geometry described previously, and the results are reproduced in Figure 163. The numbers apply to the belt moving in *air*, for which $\rho = 0.00238$ slug/ft³, and with $C_f = 0.003$. The curves are not directly applicable to a moving belt in water but are included here because they show that a *minimum* of total belt power lies near the condition of autorotation. Note that the autorotation occurs in the range from $V_b/V_o \approx 0.24$ to $V_b/V_o \approx 0.27$. For the case of $V_o = 200$ ft/sec, the power coefficient at the minimum condition is found to be approximately $C_{PB} \approx 0.114 (V_b/V_o)^3$, which is higher than the rotational power coefficients of $0.022(u/V)^3$ and $0.08(u/V)^3$ for a rotating circular cylinder and a rotating foil, respectively.

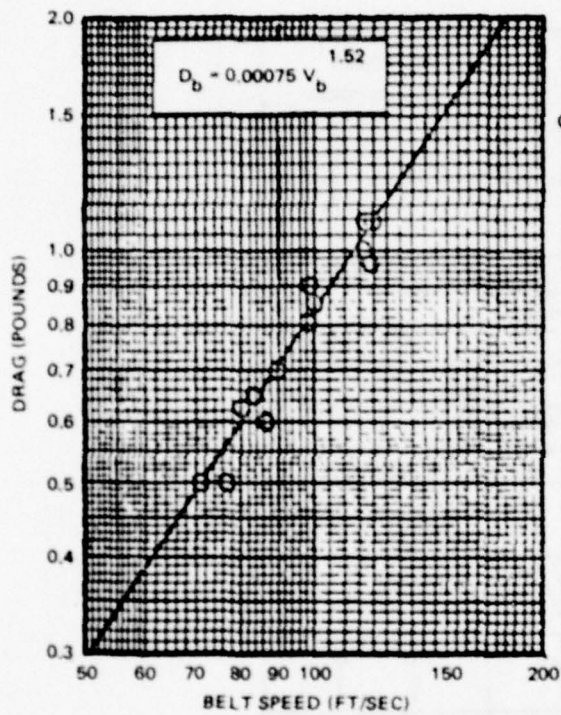


Figure 162a – Belt Drag versus Surface Speed V_b
 For a Mylar belt 17.5 inches wide, exposed length
 ≈ 25.9 inches, in air, Bond,¹¹¹

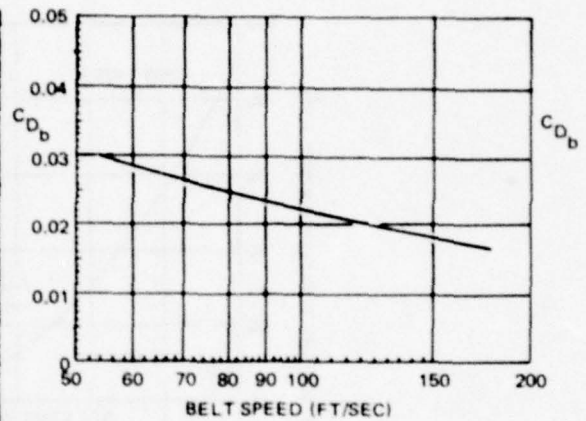


Figure 162b – Coefficient of Belt Drag, Based on
 Exposed Belt Area, for Data of Figure 162a

Figure 162 – Moving-Belt Drag Data

DISCUSSION: Although a moving-belt system is shown to be effective for boundary-layer-control – lift augmentation, the mechanical complexity, and foil section structural problems would be acute. For a large span belt there would be serious problems with belt “tracking” and slipping on the pulleys. The power requirements appear to be considerably higher than for either the rotating cylinder or the rotating foil devices. This is because of the large surface area of a belt, compared with that of a rotating cylinder moving with the same $u = V_b$.

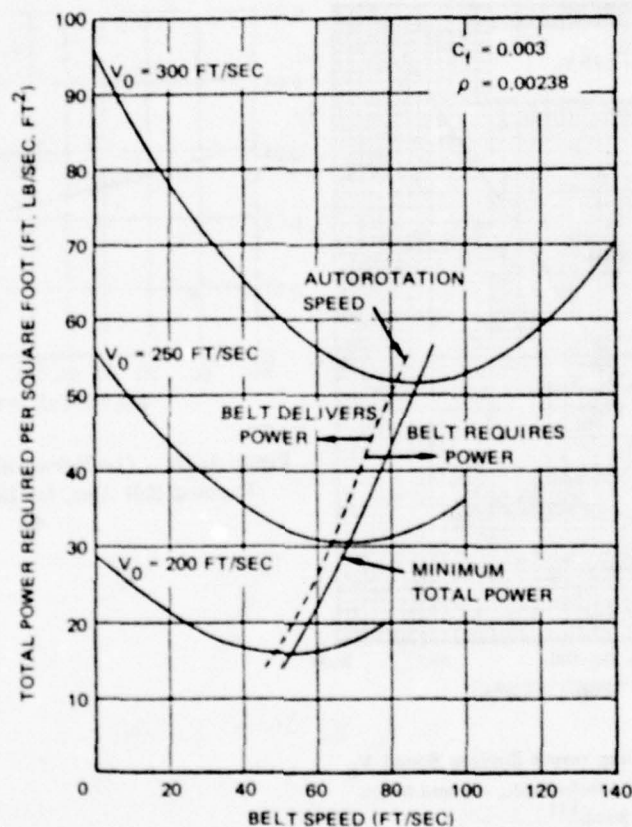


Figure 163 – Variation of Total-Belt-Drag-per-Unit-Area versus Surface Speed

Calculated by Bond¹¹¹ for a belt in air; applies to the belt configuration described in Figure 161.

NAME: Swimming Plates.

DESCRIPTION AND FORCE ESTIMATES: Thrusting swimming propulsion by a thin platelike surface immersed in water can be accomplished, for example, either by propagating a transverse sinusoidal wave motion down the length of a thin flexible foil or by the oscillatory pitching and heaving motions of a rigid plate. While many kinds of swimming or flapping motions are commonly observed in nature for propulsion and maneuvering of fishes, cetaceans, birds, etc., there are no known *practical* applications of mechanical swimming plate devices. Nevertheless, there exist reliable two-dimensional theories for estimating swimming thrust and power, and the predicted ideal efficiencies are attractive enough that these types of force producers cannot be entirely ignored. A comprehensive review of two-dimensional, swimming-propulsion theory is presented, for example, by Wu¹¹² who also provides an extensive reference list.

The present outline explains briefly how the results of the linear theories can be used to predict the performance of a thrusting lifting surface, for transverse-force production.

FLEXIBLE PLATE SWIMMING

A schematic of a two-dimensional, waving flexible plate aligned with the free stream of speed U is shown in Figure 164, reproduced from Wu.¹¹³ The sinusoidal wave motion of the plate has a phase speed c ; circulatory frequency ω ; and dimensionless wave number $k = \pi L/\lambda$, based on half-chord, for the wave contour having a wave length λ passing along the plate of length L . The phase speed must be $c > U$ in order to produce a positive thrust. Integration of the time-dependent pressure forces over the length of the plate furnishes estimates of the instantaneous thrust T , lift L_f , kinetic energy left in the wake E_w , and the total power input $P = TU + E_w$. The time average over the period $\tau = 2\pi/\omega$ gives the physically interesting quantities \bar{T} , \bar{E}_w , and \bar{P} . The time-averaged lift force is zero. Then, the average propulsion efficiency for producing useful thrust is defined as

$$\eta = U\bar{T}/\bar{P} \quad (92)$$

where $\bar{P} = \bar{T}U + \bar{E}_w$.

Force Estimates

Several cases are included here for flexible plate thrust, generated by different traveling wave contours in a stream of constant speed U . A thrust coefficient based on the time-averaged thrust is defined as

$$K_{\bar{T}} = \frac{\bar{T}}{\pi \frac{1}{2} \rho U^2 L} \quad (93)$$

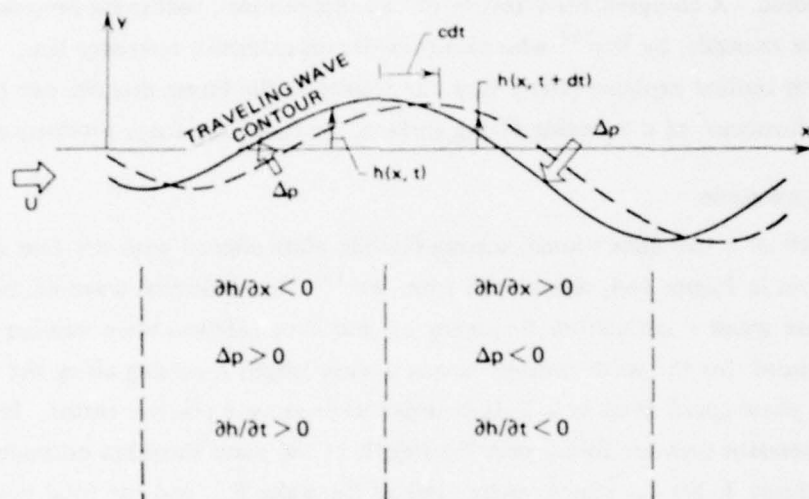


Figure 164 – Fluid Pressure Jumps, Arising on a Waving Flexible Plate Moving at a Speed U through a Fluid

The traveling wave contour speed $c \geq U$. Wu;¹¹³

where L is the plate length. Note that the usual definition of two-dimensional thrust coefficient would be

$$C_T = \frac{\bar{T}}{\frac{1}{2} \rho U^2 L} = \pi K_{\bar{T}} \quad (94)$$

Based on the theory developed by Wu,¹¹⁴ Figures 165a and 165b show the variation of the thrust coefficient $K_{\bar{T}}$ plotted versus the reduced frequency parameter

$$\sigma = \frac{\omega(L/2)}{U} = \pi \frac{L}{\lambda} \frac{c}{U} \quad (95)$$

for two simple wave contours. These curves apply to the case when the plate length contains one wavelength, i.e., $k = \pi$, $\sigma = \pi \frac{c}{U}$. Figure 165a shows the performance of a constant amplitude traveling wave, and Figure 165b is for a linearly increasing amplitude wave. Sketches of the chordwise contours are included. The experimental points were obtained in a water tunnel by Kelly,¹¹⁵ using a flexible hydrofoil actuated by seven pairs of rods which govern the chordwise amplitude profile. The theoretical result¹¹⁴ that the thrust $C_T \geq 0$, as $\sigma \geq k$, or as $c \geq U$, is roughly verified.

Results of another version of this same type of flexible plate propulsion (Figure 166a) are shown in Figure 166b, reproduced from Szeles.¹¹⁶ In this case the leading edge of a flexible plate of length L immersed in water is held fixed and clamped. The fluid is streaming by with velocity U . At a distance x_0 measured from the leading edge, the plate is forced to oscillate transversely by a force $F_1(t)$ with frequency ω . The resulting propagating-wave motion along the plate produces a net thrust. The curves in Figure 166b apply to a 10-foot long, 0.4-inch thick, steel plate in water, excited at $x_0/L = 0.25$.

Thrusting Lifting Surface

From the linear theory, there is *no* steady-state lift developed by an undulating flexible plate having a centerline aligned with the free stream; however, a resultant lift force can be generated by supposing the plate has a drooped stationary position, angle of attack plus camber, about which the wave motion occurs. Figure 167 is a schematic representation of this idea. The resolution of the actual fluid motion past a drooped, swimming flexible plate into the components indicated is a consequence of the linear theory. The thrust component of the resultant force is given by \bar{T} from swimming-propulsion theory, and the time-averaged two-dimensional lift obtained from thin airfoil theory is

$$\bar{L}_t = a_0(\alpha_0 + 2f/L) \frac{1}{2} \rho U^2 L \quad (96)$$

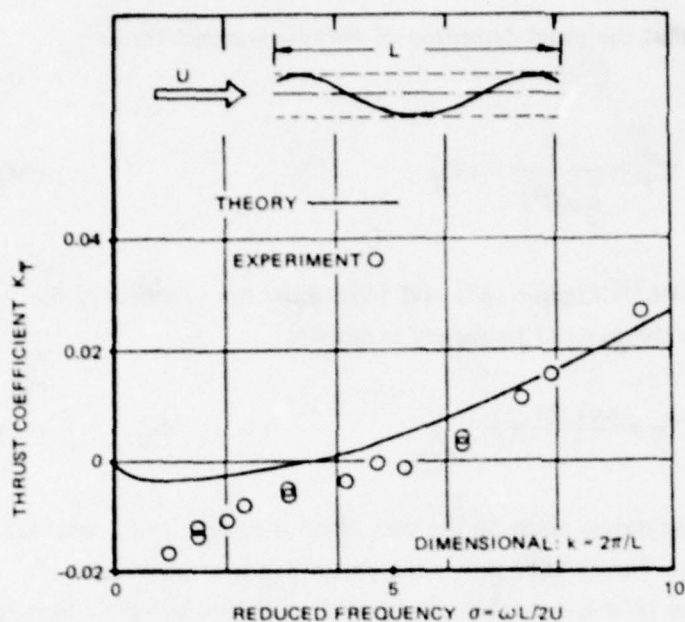


Figure 165a - For Flexible Plate, Constant-Amplitude Wave Contour; Nondimensional $k = \pi$
Kelly¹¹⁵

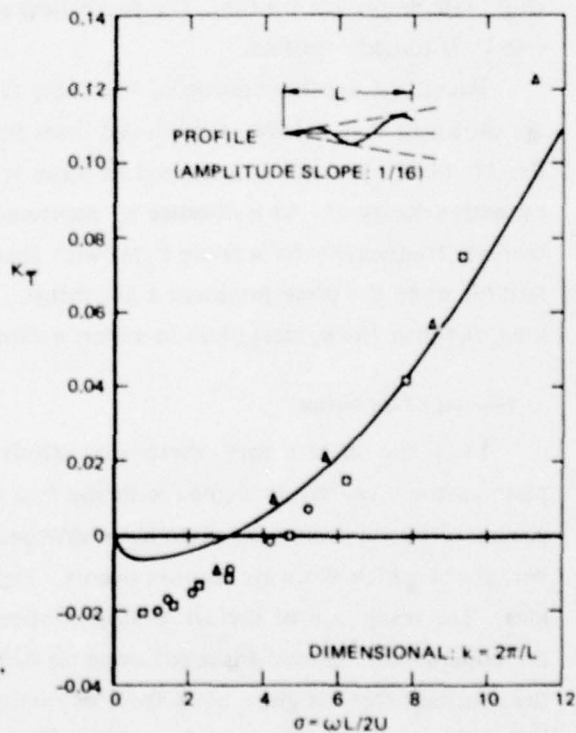


Figure 165b - For Flexible Plate, Linearly Increasing, Amplitude-Wave Contour; Nondimensional $k = \pi$
Wu¹¹²

Figure 165 - Variations of Swimming Thrust Coefficients K_T versus Reduced Frequency σ

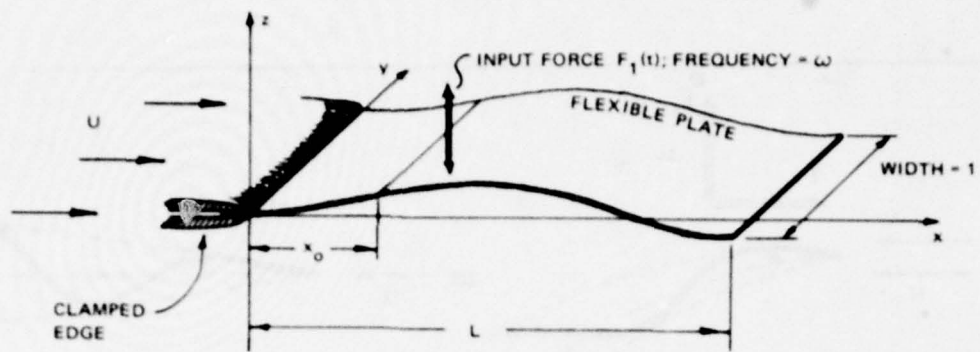


Figure 166a – Forced Harmonic Wave Motion on a Flexible Plate Propeller
Szeles¹¹⁶

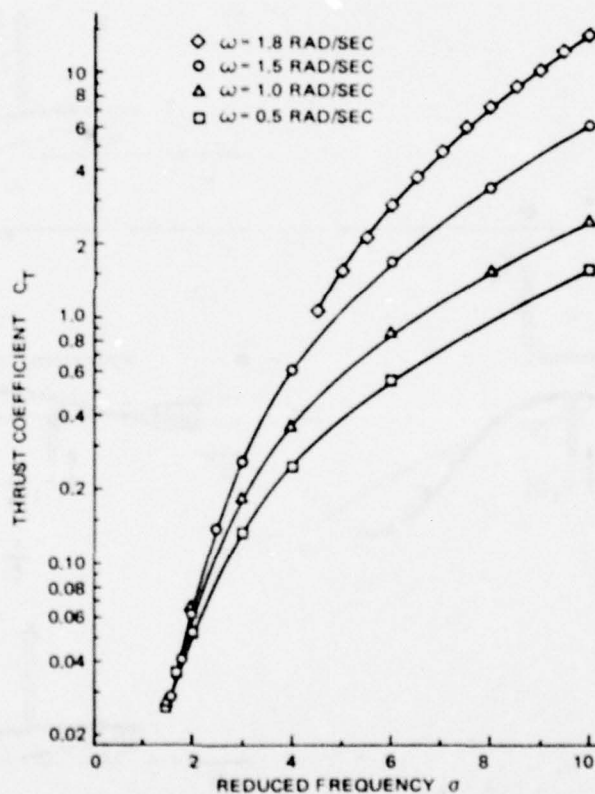


Figure 166b – Variation of Swimming Thrust Coefficient C_T versus
Reduced Frequency σ for Forced Undulating Flexible Plate of
Figure 166a

Szeles¹¹⁶

Figure 166 – Swimming Flexible Plate Studies

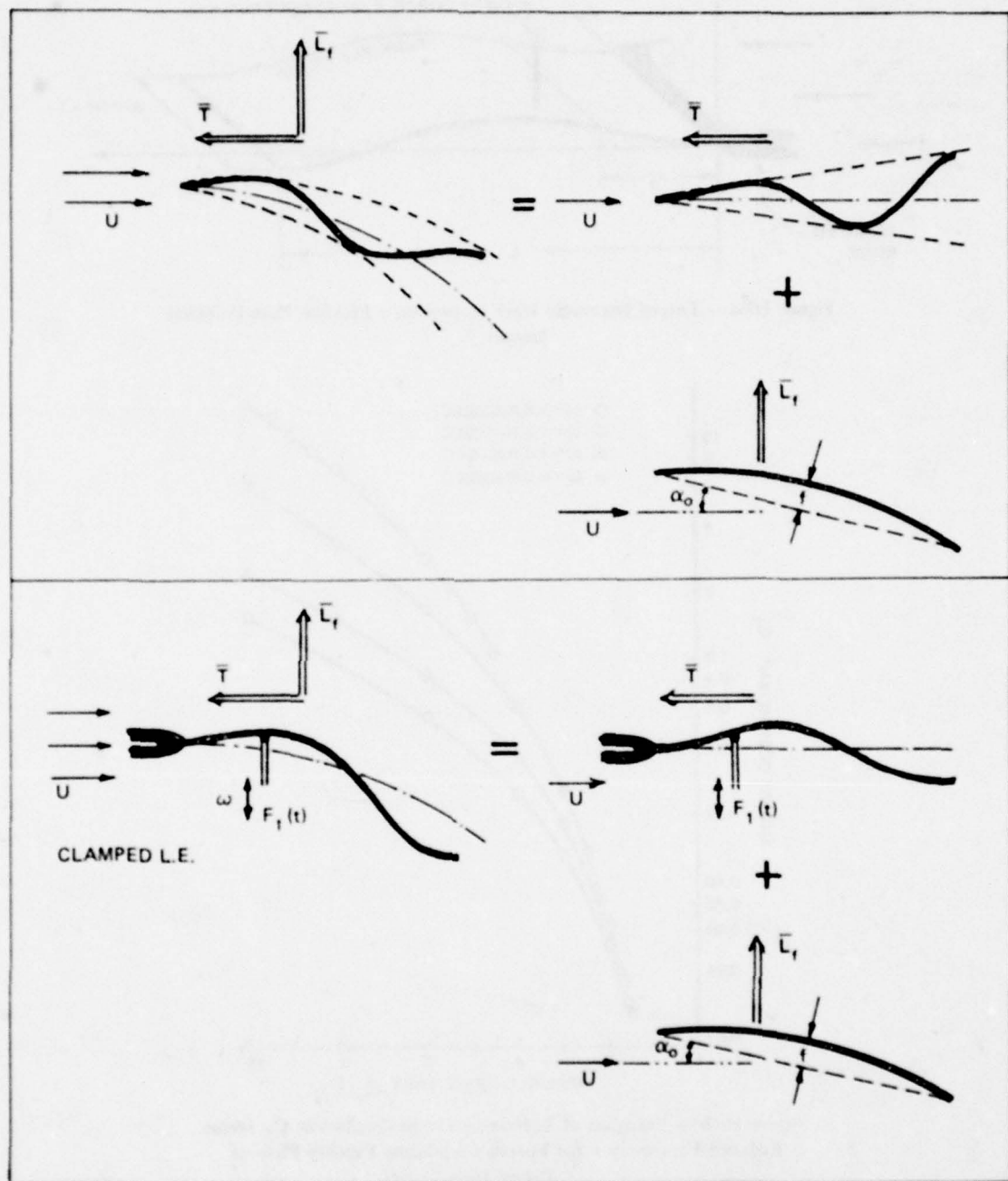


Figure 167 – Conceptual Flow Decomposition, Linearized, for Swimming, Flexible Plate Lifting Foils

\bar{T} and \bar{L}_f are time-averaged thrust and lift, respectively; the latter is due to angle of attack and camber only.

where a_0 = flat-plate, section-lift-curve slope = $2\pi \text{ rad}^{-1}$
 f = camber displacement
 α_0 = angle of attack.

Power Estimates

The power required to maintain a given wave contour, sweeping periodically down a flexible plate, has also been determined in the linear theory and is usually presented in terms of a power coefficient

$$C_P = \frac{\bar{P}}{\frac{1}{2} \rho U^3 L} \quad (97)$$

so that the propulsion efficiency of Equation (92) is simply

$$\eta = \frac{C_T}{C_P} \quad (98)$$

Figures 168a and 168b show the theoretical swimming-thrust efficiency η plotted versus reduced frequency σ , corresponding to the wave profiles of Figures 165a and 165b, respectively. Figure 169 is a plot of efficiency η for the forced flexible plate of Figure 166.

To the linear theory approximation, the same ideal input-power estimates apply to the configurations of Figure 167.

RIGID-PLATE SWIMMING

Swimming thrust can be produced by pitching and heaving lateral displacements of a rigid plate immersed in a stream of speed U . These motions are sketched in Figure 170. Analyses of the hydrodynamic thrust performance produced by these types of movements are presented, for example, by Lighthill¹¹⁷ and by Wu.¹¹⁸

Force and Power Estimates

Consider first some results from the work of Lighthill¹¹⁷ on the combined pitching and heaving movements described by the equation for lateral displacement.

$$y_p(x, t) = [h_0 - i\alpha(x - b)] e^{i\omega t}, \quad (-a < x < a) \quad (99)$$

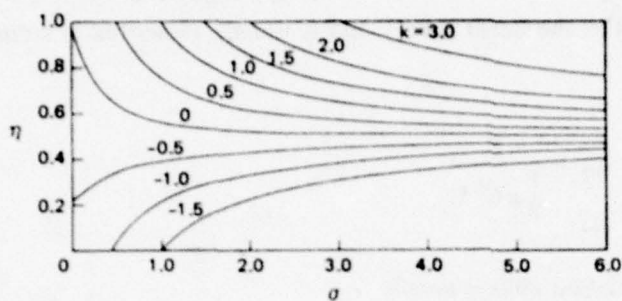


Figure 168a - Constant Amplitude Contour
Wu¹¹⁴

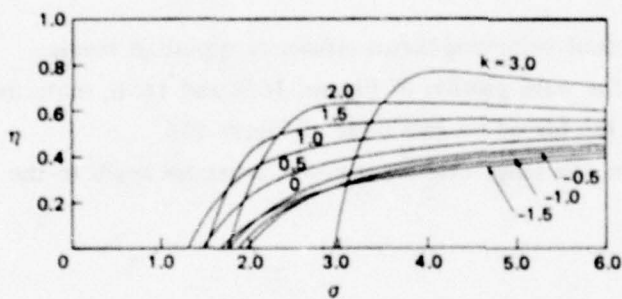


Figure 168b - Linearly Increasing Amplitude Contour
Wu¹¹⁴

Figure 168 - Traveling Wave Propulsion

Variation of thrust efficiency η versus reduced frequency of σ with contours of nondimensional

Wave number $k = \pi L / \lambda$.

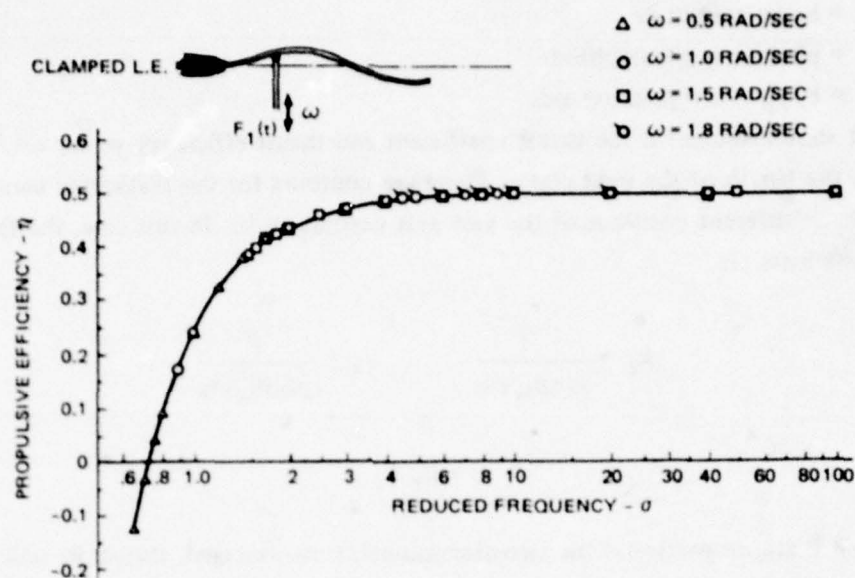


Figure 169 - Forced Harmonic Wave, Flexible Plate Propulsion

Variation of thrust efficiency η versus σ , at several forcing frequencies; corresponds to Figure 166. This curve applies to 10 foot long, 0.4 in thick steel plate in water, $x_0/L = 0.25$; Sizeless. 116

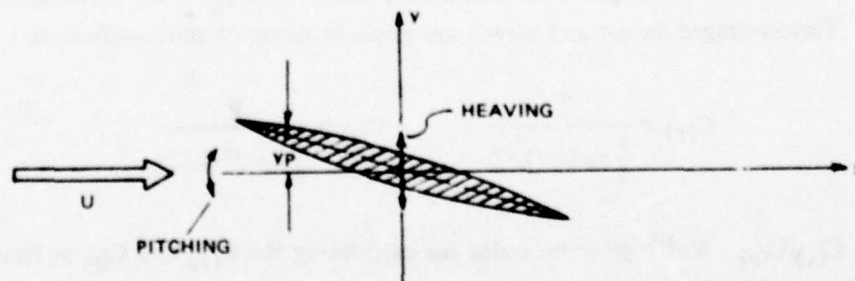


Figure 170 - Rigid-Plate Swimming, Produced by Harmonic Pitching and Heaving Motions

where $a = L/2 = \text{half chord}$

$\omega = \text{circular frequency of the oscillating motion}$

$h_o = \text{heave amplitude}$

$\alpha = \text{pitching-angle amplitude}$

$x = b, y_p = 0 = \text{pitching axis}$

Figure 171 shows results for the thrust coefficient and thrust efficiency versus $\omega L/U (= 2\sigma)$, where L is the length of the rigid plate. There are contours for the feathering parameter $\theta = U\alpha/\omega h_o$. Different positions of the yaw axis depend on b . In this case, the thrust and power coefficients are

$$k_T = \frac{\bar{T}}{\rho(\omega h_o)^2 a} \quad k_P = \frac{\bar{P}}{\rho(\omega h_o)^3 a} \quad (100)$$

so that

$$\eta = k_T/k_P$$

where \bar{T} and \bar{P} are, respectively, the two-dimensional, time-averaged, thrust-per-unit span and power-per-unit span.

Wu¹¹⁸ presents some results for the hydrodynamic thrust and propulsion efficiency for pure heaving and pure pitching. In complex form, the equation of nondimensional lateral displacement studied by Wu is

$$y_p(x, t) = \left[\frac{1}{2} \xi_o + (\xi_1 + i \xi_2) x \right] e^{i\omega t} \quad (|x| \leq 1) \quad (101)$$

where $\xi_o/2$ is the nondimensional heave amplitude, and $\sqrt{\xi_1^2 + \xi_2^2}$ is the pitching angle amplitude. Time-averaged thrust and power are given in terms of the coefficients

$$C_{(T)} = \frac{\bar{T}}{\frac{1}{4} \pi \rho U^2 (L/2)} \quad C_{(P)} = \frac{\bar{P}}{\frac{1}{4} \pi \rho U^3 (L/2)} \quad (102)$$

so that $\eta = C_{(T)}/C_{(P)}$. Wu¹¹⁸ gives formulas for calculating the $C_{(T)}$ and $C_{(P)}$ as functions of σ for pure heave ($\xi_1 = \xi_2 = 0$) and for pure pitching ($\xi_o = \xi_2 = 0$). Figure 172 shows curves of the ideal efficiencies η_h (heave) and η_p (pitch) plotted versus σ . Note that for pure pitching, there is a certain value of $\sigma = \sigma_o = 1.781$ below which $C_{(T)} < 0$.

Wu¹¹⁸ also treats the important problem of the optimum combination of pitching and heaving movements.

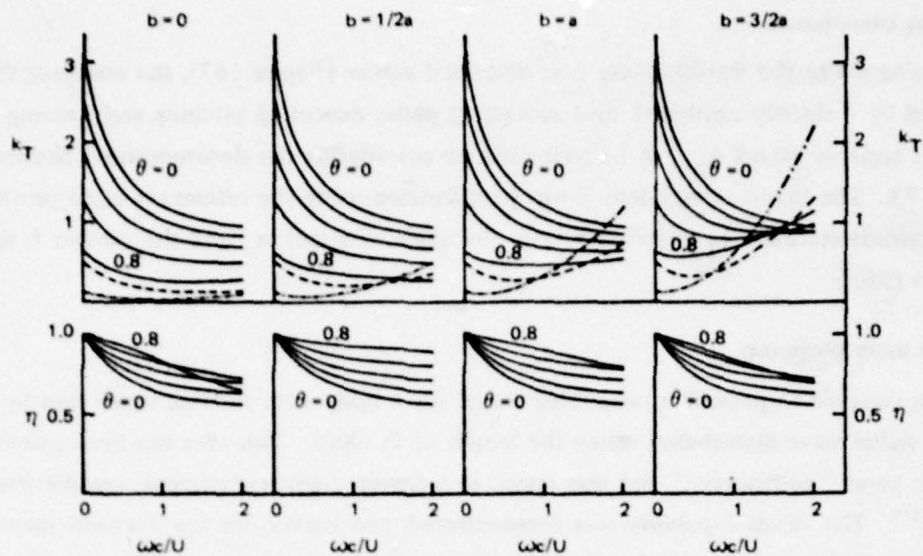


Figure 171 — Thrust Coefficient k_T and Efficiency η , Predicted by Two-Dimensional Airfoil Theory

For values 0, 0.2, 0.4, 0.6, and 0.8 of a feathering parameter $\theta = U\alpha/\omega h$, plotted as a function of $\omega c/U$, which is 2σ , for different positions $x = b$ of the yaw axis, namely half-chord $b = 0$, three-quarter-chord $b = 1/2a$, trailing-edge $b = a$, and a position five-quarters-chord, $b = 3/2a$, beyond the trailing edge; ----, part of k_T for $\theta = 0.6$, predicted as coming from leading-edge suction; - · - · - , same for $\theta = 0.8$; Lighthill.¹¹⁷

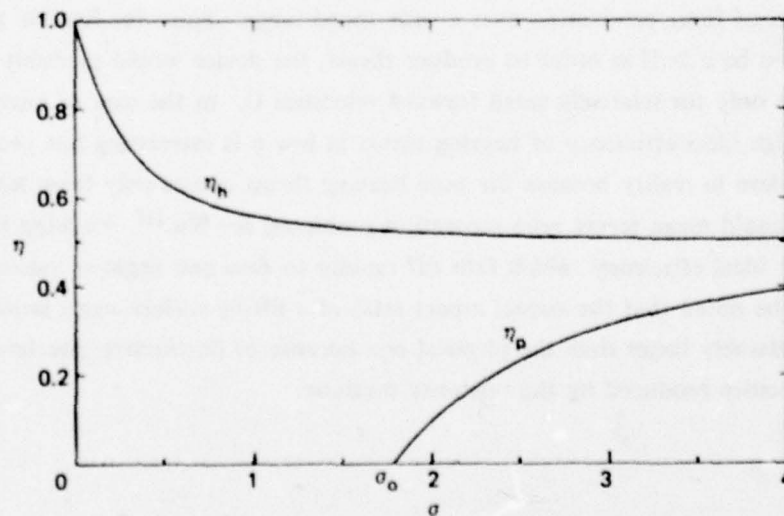


Figure 172 — Variation of Separate Ideal Thrust Efficiencies η_h , Heave Only, and η_p , Pitch Only, versus σ for Rigid-Plate Propulsion

w_u^{18}

Thrusting Lifting Surface

Analogous to the flexible plate case described earlier (Figure 167), the resultant force generated by a slightly cambered rigid swimming plate, executing pitching and heaving motions about an angle of attack α_0 , can be estimated by considering the decomposition shown in Figure 173. The thrust component \bar{T} can be estimated using the references cited previously, and the steady-state lift \bar{L}_T arises only from the angle of attack α_0 and the camber f ; see Equation (96).

FLEXIBLE BODY SWIMMING

It is possible to provide a propulsive thrust for a body with flexible outer skin by propagating a radial wave disturbance down the length of the hull. This idea has been proposed, given the name "dermadrive," and was tested in a towing basin experiment, see Alberty and Jacquet.¹¹⁹ The thrust capability was demonstrated, just barely, for low forward speeds. To provide lateral forces for control, a nonradially symmetric waveform would have to be used. The expense and complexity of such a system would be staggering and of doubtful propulsion effectiveness.

DISCUSSION: Although it appears that a "swimming lifting surface" (Figure 167 and 173) could conceivably function as indicated, using either flexible plates or rigid foils, there are several important disadvantages. The mechanical complexity and the structural, noise, and vibration problems would be severe, considering the magnitude of control forces needed and the requirement of force production over a wide speed range. Since for flexible plates, the wave speed must be $c > U$ in order to produce thrust, the device would probably be mechanically realizable only for relatively small forward velocities U . In the case of heaving and pitching, the high ideal efficiency of heaving thrust at low σ is interesting but probably difficult to achieve in reality because the pure heaving thrust comes only from leading-edge suction which could mean severe nose separation problems; see Wu.¹¹⁸ Pitching thrust has generally lower ideal efficiency, which falls off rapidly to zero and negative values for small σ .

It should be noted that the virtual aspect ratio of a lifting surface using swimming thrust *might* be considerably larger than the physical one because of destructive interference of the downwash velocities produced by the unsteady motions.

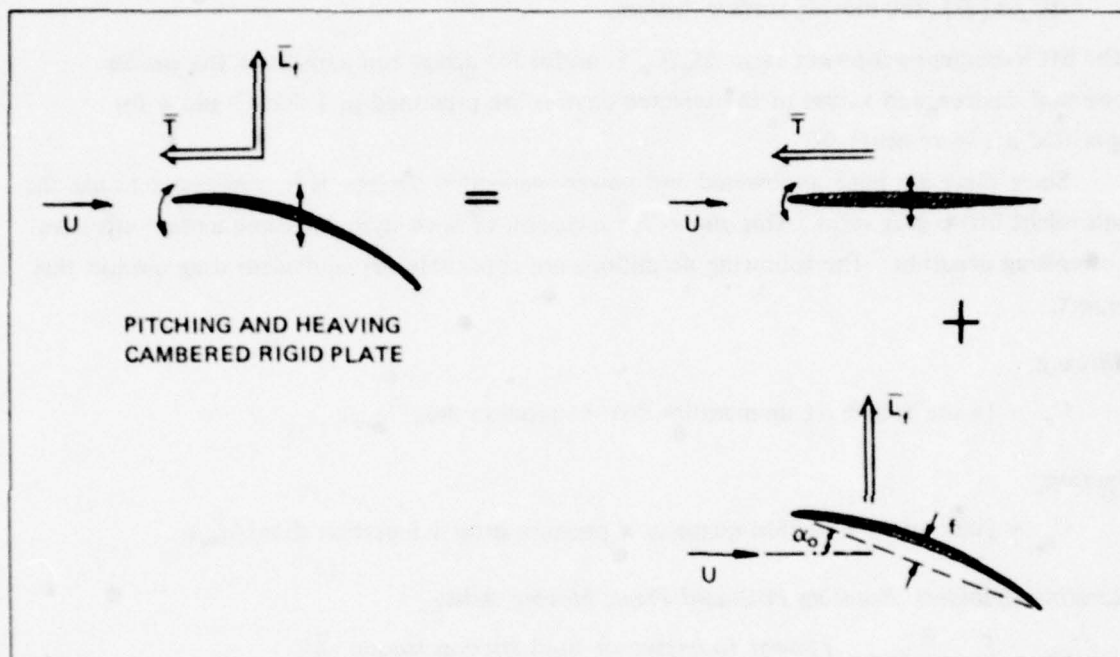


Figure 173 – Conceptual Flow Decomposition, Linearized, for Swimming, Oscillating, Rigid-Plate Lifting Foil

\bar{T} and \bar{L} are time-averaged *thrust* and *lift*, respectively; the latter is due to angle of attack and camber of the mean position only.

SUMMARY FOR CHAPTER 1

It is useful to have some sort of universal quantitative comparison between the hydrodynamic performance of the various types of lifting devices discussed in Chapter 1. Throughout the previous subsections, comparative powered-lift performance is discussed in terms of the augmentation ratios:

$$\begin{aligned}\Delta C_l / \Delta C_{\mu} & \quad \text{for blowing concepts} \\ \Delta C_l / \Delta C_Q & \quad \text{for suction concepts} \\ \Delta C_l / \Delta \left(\frac{u}{V} \right) & \quad \text{for moving surface devices.}\end{aligned}$$

The lift increment-per-power ratio $\Delta C_l / C_p$ is useful for direct comparison of the similar powered devices, and values of the selected devices are presented in Tables 3 and 4 for specified lift increments ΔC_l .

Since there are both unpowered and power-augmented devices, it is convenient to use the equivalent lift-to-drag ratio. This allows for inclusion of *both* hydrodynamic and an effective power-drag penalties. The following definitions are applicable for equivalent drag used in this report.

Blowing:

$$C_{d_e} = [\text{wake drag} + \text{jet momentum flux} + \text{ingestion drag}] / q_{\infty} c$$

Suction:

$$C_{d_e} = [\text{wake drag} + \text{suction quantity} \times \text{pressure drop} + \text{ingestion drag}] / q_{\infty} c$$

Rotating Cylinders; Rotating Foils and Flaps; Moving Belts:

$$C_{d_e} = \left[\text{wake drag} + \left(\frac{\text{power to overcome fluid friction torque}}{\text{free stream velocity}} \right) \right] / q_{\infty} c \quad (103)$$

where wake drag is the measured momentum deficit drag in the wake, with the powered device turned on. For an unpowered device, the wake drag is simply the section-profile drag.

Experimental data for 16 different lift-producing concepts have been analyzed and reduced to the common form of values of equivalent two-dimensional lift-to-drag C_l / C_{d_e} , corresponding to values of section-lift coefficient C_l . Whenever good two-dimensional data are not available, the results of tests with a finite-aspect-ratio lifting surface are extrapolated to $AR = \infty$ by use of the estimating formulas discussed in the various subsections of Chapter 1. The results are given in Figure 174. Table 7 is a list of the devices represented in Figure 174, including the principal geometric features of each device and the source of the data.

TABLE 7 - GEOMETRY AND REFERENCES FOR DATA ABOUT
CIRCULATORY LIFT DEVICES PLOTTED IN FIGURE 174

Item	Geometry, Test Parameters, Comments	Reference
① NACA 66015 Foil Simple Incidence Lift	$0^\circ \leq \alpha \leq 12^\circ$, Smooth Finish	Abbot and Doenhoff ⁵
② Plain Flapped NACA 23012 Foil	$c_f/c \approx 0.2$; Flap Deflected Optimum Amount at Each C_l	Abbot and Doenhoff ⁵
② Slotted Flapped NACA 23012 Foil	$c_f/c \approx 0.2566$, $0 < \delta_f < 40^\circ$	Abbot and Doenhoff ⁵
③ Double-Slotted Flapped Foil with Kruger Slat	NACA 64A210 Foil, $c_f/c \approx 0.35$, $\delta_f = 37.5^\circ$	Mavriplis ¹³
④ _a Blown TE Flap	RAE 102 Cambered Foil, $t/c = 13\%$, $\delta_R = 20^\circ$, $c_{fR}/c = 0.25$, $C_\mu = 0.017$, $0 < \alpha \leq 15^\circ$	Lawford and Foster ³²
④ _b	Same Foil as 4a, $\alpha = 0^\circ$, $\delta_R = 20^\circ$, $0.017 \leq C_\mu \leq 0.047$	Lawford and Foster ³²
⑤ _a Jet Flap	Elliptical Section Shape, $t/c = 16\%$, $\delta_J = 90^\circ$, $\alpha = -0.15^\circ$, $c_f/c = 0$, $0.02 \leq C_\mu \leq 0.2$	Franklin and Bailey ⁴¹ and N.A. Dimmock (1957)
⑤ _b	Elliptical Section Shape, $t/c = 12.5\%$, $\delta_J = 31.3^\circ$, $\alpha = 0^\circ$, $c_f/c = 0$, $0.0169 \leq C_\mu \leq 3.19$. Equivalent 2D Results Extrapolated from Finite-Aspect-Ratio Data.	Williams and Alexander ⁴⁸
⑥ _a Circulation Control Foil; Tangential Jet Blowing	Rounded Ellipse Section Shape, $t/c = 20\%$, Uncambered, $\alpha = 0^\circ$	Englar and Williams (NSRDC Tech Note AL-200 (1971))
⑥ _b	Rounded Ellipse, $t/c = 20\%$, Uncambered, $\alpha = 5^\circ$	Englar and Williams (NSRDC Tech Note AL-200 (1971))
⑥ _c	Rounded Ellipse, $t/c = 20\%$, Cambered 5%, $\alpha = 0^\circ$	Williams and Howe (NSRDC Tech Note AL-176 (1970))
⑥ _d	Rounded Ellipse, $t/c = 15\%$, Uncambered, $\alpha = 0^\circ$	Englar (NSRDC Tech Note AL-211 (1971))

TABLE 7 - Continued

Item	Geometry, Test Parameters, Comments	Reference
⑥ _e Circulation Control Foil; Tangential Jet Blowing	50% Thick Ellipse, Curve Represents Maximum Envelope; Two Slots at $x/c = 0.886$ and 0.985 .	Englar and Williams (NSRDC Tech Note AL-200 (1971))
⑦ Blowing-Stabilized Trapped Vortex Foil	$t/c = 11\%$, $\delta_R = 15^\circ$, $\delta_N = 30^\circ$, $c_{fR}/c = 0.275$, $c_{fN}/c = 0.25$, $C_{\mu R} = 0.069$, $C_{\mu N} = 0.175$.	Krall and Haight ⁷⁰
⑧ Spanwise Blowing	NACA 65A006 Section $\alpha = 0^\circ$, $\delta_f = 40^\circ$; Equivalent 2D Results Extrapolated from Finite-Aspect-Ratio Data.	Dixon ⁷⁷
⑨ Slot Suction at Flap Knee	NACA 66 ₄ A421 Section $c_f/c = 0.168$, $\delta_f = 30^\circ$, $C_Q = 0.0351$, $C_\mu = 0.328$, $-6^\circ < \alpha < 14^\circ$.	Arnold ⁸⁶
⑩ Trailing Edge Slot Suction Foil	NACA 23015 Section $\alpha = 5^\circ$, $0 \leq C_Q \leq 0.04 \Rightarrow 0 \leq C_\mu \leq 0.143$.	Hazen, et al. ⁹¹
⑪ Thwaites Flap	All Porous Cylinder, $d = 3''$, Splitter-Plate Angle = 30° , $\bar{U}/d = 0.167$, $R_e = 4.23 \times 10^4$, $0.073 \leq C_Q \leq 0.194$.	Pankhurst and Thwaites ⁸⁵
⑫ Trailing Edge Rotating Cylinder Foil	$t/c = 18.2\%$, $d/c = 0.136$, $\alpha = 0^\circ$, $0.374 \leq u/V \leq 1.4$, Knurled Cylinder Data; Power Data from Test Results, Equivalent 2D Results Extrapolated from Finite-Aspect-Ratio Data.	Brooks ¹⁰³
⑬ Rotating Cylinder at Flap Knee	NACA 23018 Section $\alpha = 9^\circ$, $\delta_f = 40^\circ$, $c_f/c = 0.4$, $1 \leq u/V \leq 5.5$, Power Data Used Here Are Taken from Reference 108, Probably Too Low.	Alvarez-Calderon and Arnold ¹⁰⁸

TABLE 7 - Continued

Item	Geometry, Test Parameters, Comments	Reference
(14) Leading Edge Rotating Cylinder Foil	$t/c = 20\%$, $\alpha = 40^\circ$, $d/c = 0.2$, $u/V = 0$ and 3.2 assumed $C_F = 0.007$; Equivalent 2D Results Extrapolated from Finite-Aspect-Ratio Data; Only 2 Points Calculated for $\alpha = 40^\circ$.	Wolff and Koning ¹⁰⁷
(15) Rotating-Flap Airfoil	NACA 23015 Section, $c_f/c = 0.25$, $d/c = 0.1143$, Driven Flap at $u/V = 4.0$, $-7^\circ \leq \alpha \leq 15^\circ$, $K_{PR} = 0.08$; Equivalent 2D Results Extrapolated from Finite-Aspect-Ratio Data.	Crabtree ¹¹⁰
(16) Isolated Rotating Cylinder	$1 \leq u/V \leq 8$, Assumed $C_F = 0.0064$.	Swanson ⁴

Although Figure 174 does not contain a performance curve for every device discussed in Chapter 1, it does present representative performance for all the general types. These curves may be thought of as illustrating the magnitude of useful force obtainable divided by what must be paid (drag + power) plotted versus the level of useful force achieved.

Some general remarks should be made about use and interpretation of the curves of Figure 174.

1. The plot for each device may not necessarily represent the optimum operational point on the $C_L - C_{d_e}$ curve. However, whenever possible the best data available were used. For some devices there were very few test results in existence. A distinct effort was made to pick data that showed a lifting concept at the highest lift and reasonable drag. Also, care was taken to compare various devices in their proper regimes of angle of attack and/or flap angle, e.g., BLC devices for large α and δ_f , and CC concepts for α small.
2. Although a comparison of the two-dimensional performance of the various devices does put them on a more or less equal footing, the numerical values of usable lift coefficient are too high by a factor of ~ 4 , since typical control surfaces of interest have aspect ratios near $AR = 1$.
3. One is tempted to concentrate strictly on those devices with a high equivalent lift-to-drag ratio. However, as is pointed out in the Summary and Conclusions portion of this report (Table 2), there are certain concepts that feature other desirable characteristics that may or may not be measureable with numbers. These include: the large augmentation effectiveness

($\Delta C_l/C_p$) of LE and TE rotating-cylinder devices; the simplicity of spanwise blowing; the possible emergency effectiveness of rotating flap foil, etc. These features are brought out whenever possible in the separate discussions of each concept, and should be weighed carefully in assessing the curves of Figure 174.

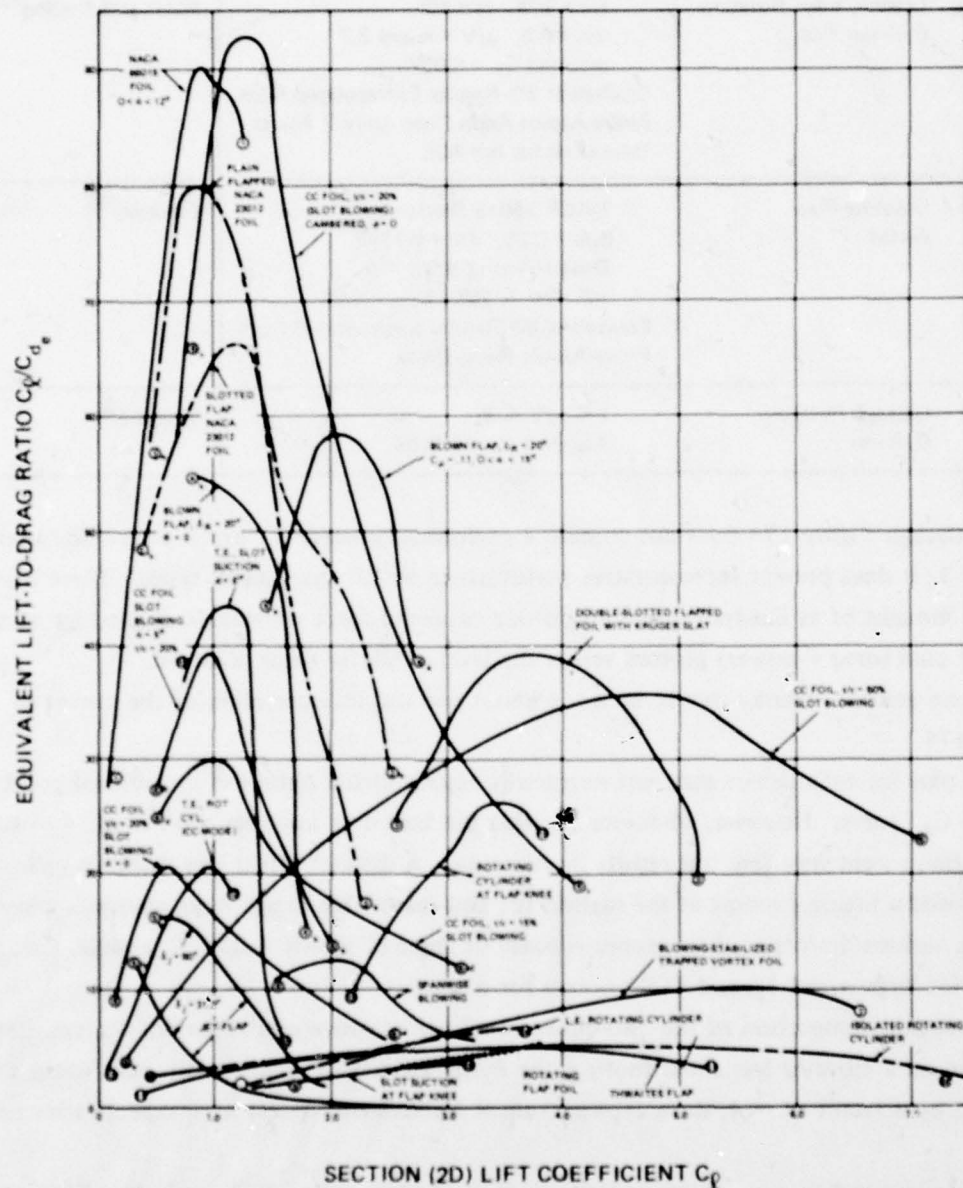


Figure 174 — Hydrodynamic Efficiency C_l/C_{d_e} versus Section-Lift Coefficient C_l for 16 Representative Circulatory Lift-Producing or Lift-Augmenting Schemes

See Table 7 for particulars of geometry and references

CHAPTER 2. REACTION DEVICES

This chapter is concerned with propulsors that derive their force(s) from reaction to an accelerated stream of water. It does not include all types of propulsion concepts, however. Only those devices are candidates in this category that produce lateral forces for horizontal and vertical control purposes either by their fixed direction, orientability, or some special geometry.

Auxiliary thrusters and jets of the fixed-duct and trainable variety are discussed in Section A. Many types of propeller-, impeller-, and pump-driven devices are included. Main propulsion schemes, capable of producing lateral forces, are discussed in Section B.

SECTION A THRUSTERS AND JETS

The fluid-reaction devices discussed in this section are to be thought of as strictly *auxiliary* and therefore separate from the main propulser. The two subsections are:

- (1) Tunnel Thrusters (Fixed Ducts) and
- (2) Directional Thrusters.

Tunnel Thrusters, Fixed Ducts

All of the devices in this category are characterized by a housing or duct having a fixed orientation with respect to the main hull.

NAME: Propeller-Driven Lateral Tunnel Thruster.

DEFINITION AND OPERATION: The ducted lateral thruster is by now a common fixed-direction auxilliary force producer, used extensively on surface ships for slow-speed maneuvering. An interesting discussion of model tests and full scale design considerations for surface ship applications of tunnel thrusters is presented by Pehrsson.¹²⁰ This type of device has also been installed on the submersible Deep Submergence Research Vehicle (DSRV) in pairs for vertical and horizontal lateral movement at both fore and aft positions, Young.¹²¹ The thruster consists basically of a tube, usually circular in cross section, that runs transversely through the hull. A stream of water is induced to flow through the tube. A propeller (or propellers) located within the tube provides the prime thrusting action. The resultant lateral thrust on the hull is developed from the effects of the jetlike flow.

Several different propeller schemes for lateral tunnel thrusters are shown in Figure 175, reproduced from Hawkins.¹²² Figure 176 shows the location of the thruster tubes on DSRV.

FORCE ESTIMATES

Lateral Thrust

A momentum analysis of the flow produced by an actuator disk within a lateral thruster duct has been performed by English.¹²³ Figure 177 shows the geometry and notation. For a wall-sided hull section, the total lateral force T exerted on the body consists of three parts:

$$T = \left[\begin{array}{c} \text{left side} \\ \text{hull force} \end{array} \right] + \left[\begin{array}{c} \text{actuator force} \end{array} \right] + \left[\begin{array}{c} \text{right side} \\ \text{hull force} \end{array} \right] \quad (104)$$

$$T = \frac{1}{2} \rho A_1 V_1^2 + \frac{1}{2} \rho A_1 V_J^2 - \frac{1}{2} \rho A_1 V_1^2 \left(1 - \frac{A_1}{A_J} \right)^2 \quad (105)$$

This emphasizes that the total thrust force depends as much on the suction force exerted by the sinklike flow at the left side of the hull as it does on the pressure rise across the actuator. Therefore the shape of the tube walls is important for good inlet-flow behavior. This problem is discussed by English.¹²⁴ Note that diffusion of the flow from area A_1 to A_J gives a theoretical improvement of the total force. However, the constant area or straight-tube geometry is the most common type.

With $V_J A_J = V_1 A_1$ the total lateral force of Equation (105) is also expressed as

$$T = \rho A_1 V_1^2 \left(\frac{A_1}{A_J} \right) = \rho A_J V_J^2 \quad (106)$$

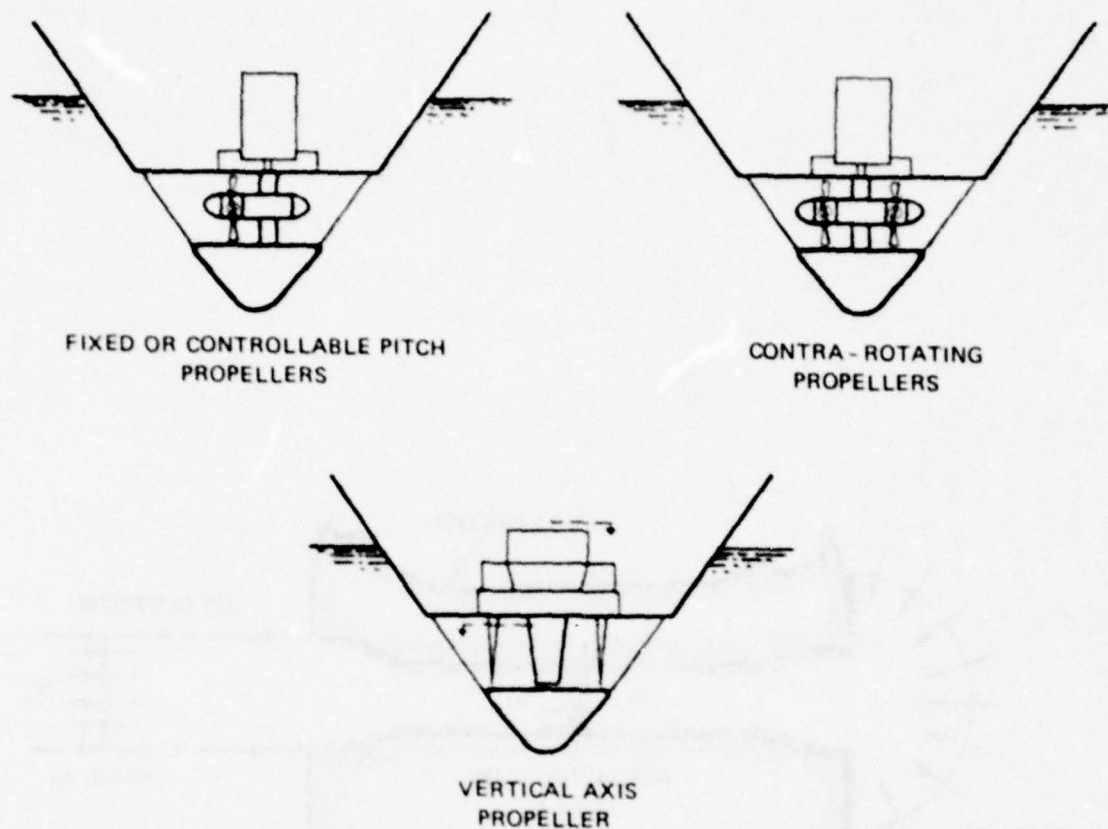


Figure 175 - Some Propeller-Driven Tunnel Thrusters
Hawkins et al.¹²²

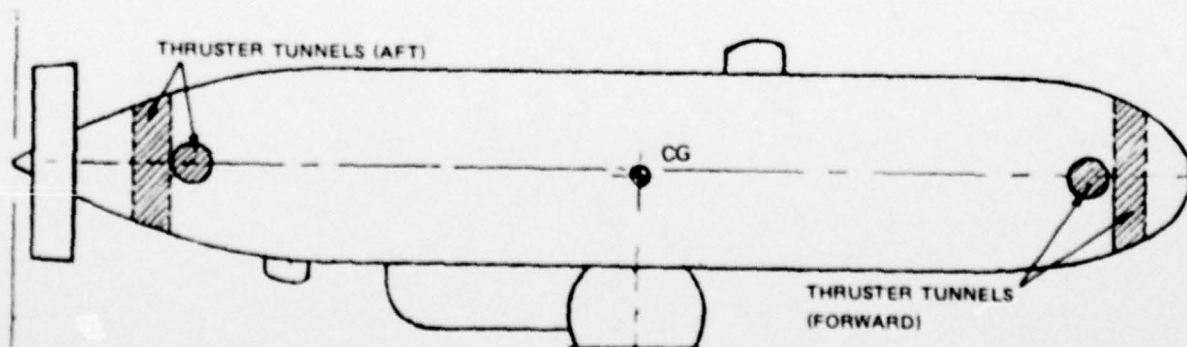


Figure 176 - Lateral Tunnel Thrusters on the Deep-Submergence Rescue Vehicle

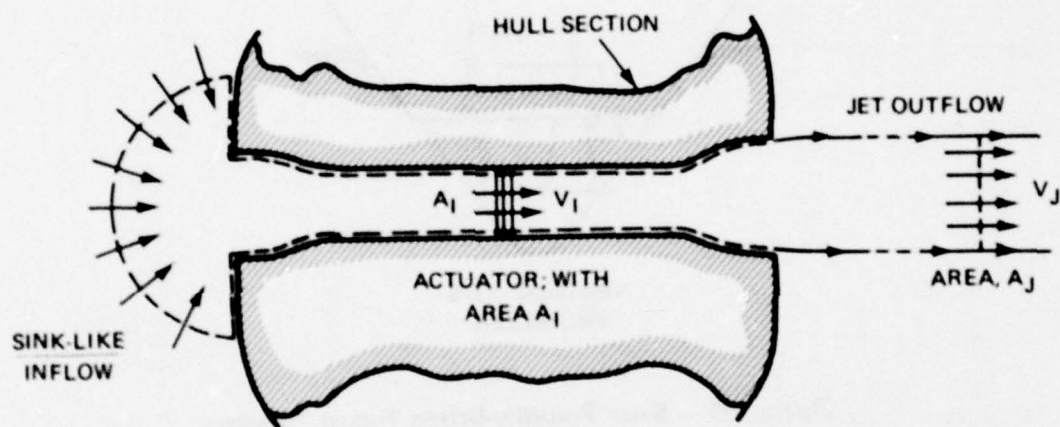


Figure 177 – Idealized Hull Section and Propeller-Driven Lateral Tunnel Thruster

which permits an estimate of the jet velocity required to produce the total thrust T

$$V_j = \sqrt{T/\rho A_j} \quad (107)$$

The force estimate mentioned previously is the static value, i.e., zero forward vehicle speed and no lateral motion. Unfortunately, when the ship is underway, the resultant side force exerted by the operation of the thruster is seriously degraded. Loss of both body force and body moment is due to interaction of the thruster jet flow and the mainstream. Chislett and Bjorheden¹²⁵ have suggested that the way to view this interaction is to assume that the thruster produces the same thrust at all forward speeds. Then changes in the body side force and moment arise because of suction forces exerted on the hull when the deflected thruster jet is bent over alongside the hull. Figure 178, reproduced from Chislett and Bjorheden,¹²⁵ shows the jet deflection by the free stream at various speed ranges. Figure 179 shows how the force and moment coefficients vary with the speed ratio U_∞/V_j for the DSRV.¹²⁶ Feldman¹²⁷ has presented a detailed description of the performance of both fore and aft located thrusters for the DSRV body with pairs of thruster tunnels canted at 45° to the horizontal (Scheme A).

Hawkins et al.¹²² gives some purely empirical estimates of bow thruster side force, based on experimental performance. Norrby¹²⁸ discusses the effectiveness of a bow thruster for maneuvering a ship underway.

Taniguchi et al.¹²⁹ has presented perhaps the most comprehensive systematic study to date on the thrust performance of the isolated tunnel thruster by considering variations of many properties of the propeller and tunnel geometry. The very essential problem of the longitudinal location of the tunnel along the hull is as yet unexplored in a definitive experimental program.

A procedure for the preliminary design of the tunnel thrusters on DSRV is outlined in a report by Lockheed Missiles and Space Co.¹³⁰

Drag

The tunnel duct openings in the hull are a source of increased drag. For a carefully faired opening, Stuntz and Taylor¹³¹ found that an average drag coefficient could be estimated with $C_D = 0.07$, where

$$C_D = \frac{D_{\text{duct}}}{\frac{1}{2} \rho A U_\infty^2} \quad (108)$$

D_{duct} = drag added by duct opening of cross sectional area A .

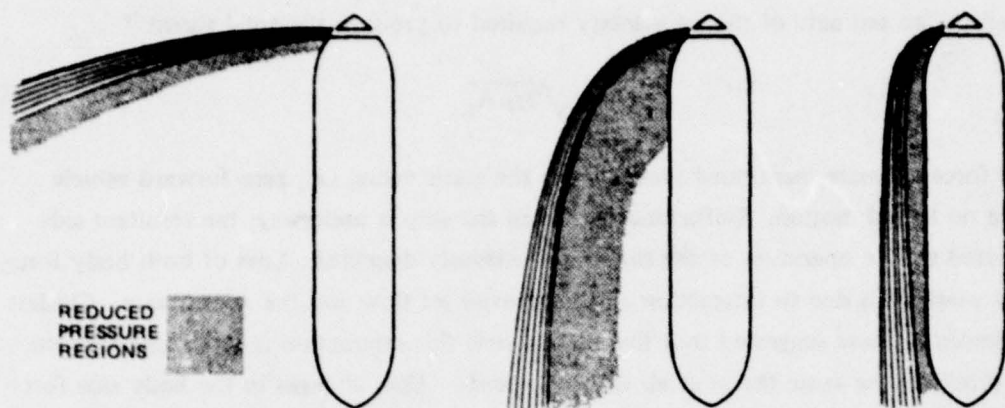


Figure 178a - Very Low Speed Ahead, Large Moment

Figure 178b - Intermediate Speed Ahead, Small Moment

Figure 178c - High Speed Ahead, Small Moment

Figure 178 - Jet Deflections at Very Low, Intermediate, and High Forward Speed

Chislett and Bjorheden.¹²⁵

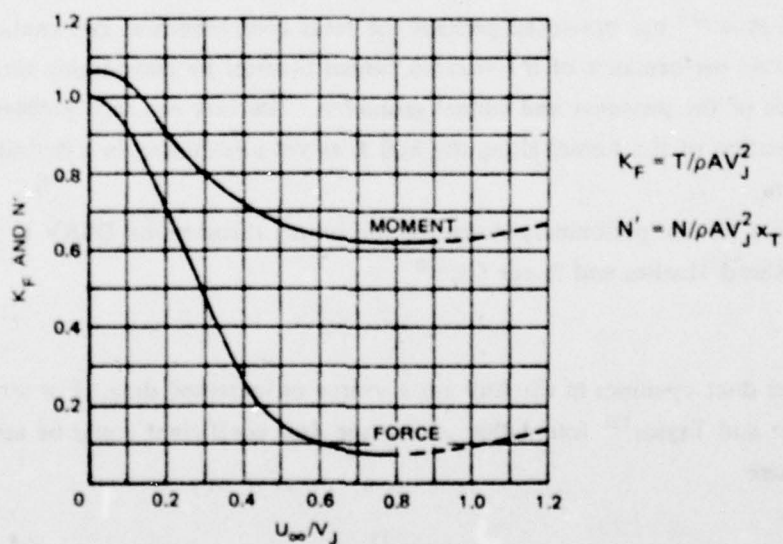


Figure 179 - Variation of Body Side-Force and Body Moment with Velocity Ratio for the Deep-Submergence Rescue Vessel with a Tunnel Bow Thruster

Here A = duct cross section area; N = body moment; x_T = characteristic distance from duct to center of gravity, Beveridge.¹²⁶

The fairings of the tunnel lip are important for good inlet and jet outlet characteristics as well as for reasonable drag values. Stuntz and Taylor,¹³¹ Taylor,¹³² and Taniguchi et al.¹²⁹ have discussed the problem of lip fairings. Beveridge¹²⁶ has provided a summary of some of the useful results.

POWER REQUIREMENTS: THRUST-POWER COEFFICIENTS

The ideal power required to deliver the total body thrust T for the tunnel thruster is

$$P_i = \frac{1}{2} \rho A_1 V_j^2 V_i = \frac{1}{2} T V_j \quad (109)$$

or

$$P_i = \frac{T^{3/2}}{2 \sqrt{\rho A_j}} \quad (110)$$

The actual power required to produce the thrust T is not accurately predicted by this estimate because of viscous losses, inlet losses, diffusion losses in the induced jet flow downstream of the propeller hub, rotation of the jet flow, and propeller losses.

It is the usual practice to rate a static thrusting device such as the tunnel thruster by means of a figure of merit. In the marine thruster field, there are two commonly used figures of merit which are essentially thrust-to-power coefficients. The static merit coefficient is

$$C = \frac{T^{3/2}}{P \sqrt{\rho A}} \quad (111)$$

and the Bendemann static thrust factor is

$$\zeta = \frac{T}{P^{2/3} D^{2/3} \sqrt{\rho \pi/2}} \quad (112)$$

where D = duct diameter

P = power supplied to the propeller shaft

T = total thrust on body

A = propeller disk area (A_1).

Then, for convenient comparison

$$C = \sqrt{2} \zeta^{3/2} \quad (113)$$

For an ideal unducted, unshrouded propeller, the ratio $A_j/A_1 = 1/2$, so that the theoretically maximum attainable values are $C_{\max} = \sqrt{2}$ and $\xi_{\max} = 1.0$.

For tunnel-ducted propellers with no flow diffusion ($A_1 = A_j$), the ideal maximum values are

$$\begin{aligned} C_{\max} &= 2.0 \\ \xi_{\max} &= 2^{1/3} \end{aligned} \quad (114)$$

These coefficients are very useful because they contain the essential information – thrust delivered, power required, actuator area – about the performance of the device. Actual values of C determined by experiment range typically from 1.5 to 0.55. For example, a value of $C = 1.46$ for the DSRV bow thruster is reported by Beveridge.¹²⁶

Note that the definition of the static merit coefficient C can be rewritten to give the thrust-to-power ratio as a function of C , and the power-to-area- ratio

$$\left(\frac{T}{P}\right) = \frac{C^{2/3}}{\rho^{1/3}} \left(\frac{1}{P/A}\right)^{1/3} \quad (115)$$

Hawkins¹³³ has presented a plot of T/P versus P/A for a variety of auxilliary force producers, including tunnel thrusters and other devices discussed in other subsections. This plot is reproduced in Figure 180, with the actual data points shown in Figure 181.

PROPELLERS

A detailed description of the correct propeller geometry for operation in tunnel thruster ducts is beyond the scope of this report. It should be noted, however, that a variety of propeller types have been used for experiments or in actual installations. Taniguchi et al.¹²⁹ presents rather complete data about propeller designs that are capable of producing C values around 1.0. Beveridge¹²⁶ gives some general hints and observations. The articles, for example, by Van Manen¹³⁴ and by Van Manen and Oosterveld¹³⁵ are useful for choosing reasonable ducted propeller geometries. Vertical axis propeller tunnel thrusters are advertised by American Shipbuilding Co.¹³⁶ and Pacific Car and Foundry¹³⁷ and are discussed by English.¹²⁴

DISCUSSION: At its present level of development, the lateral tunnel thruster is severely limited by the degradation of its thrust force with increasing vehicle forward speed. Also, the usual fixed tunnel through the hull represents a loss of considerable internal volume, and large exit holes could generate undesirable drag and noise increase at high speeds. Nevertheless, the maneuvering possibilities of strong lateral thrusters are appealing. Thrust-augmentation techniques could improve the thrust performance, and closures could be used to cover the holes.

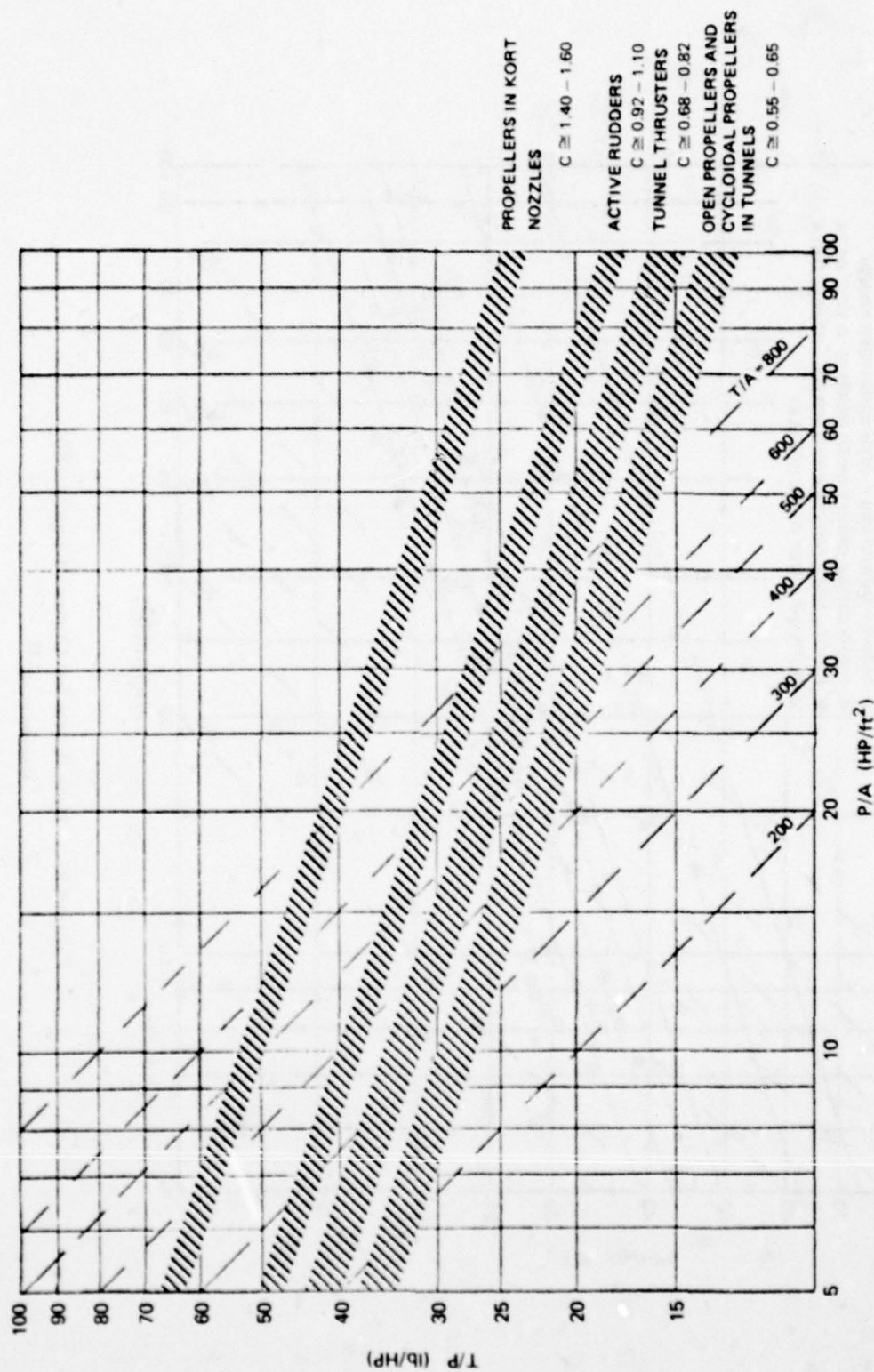


Figure 180 - Curves of Thrust/Power Ratio versus Power/Area Ratio with Contours of Static Merit Coefficient C

Hawkins 133

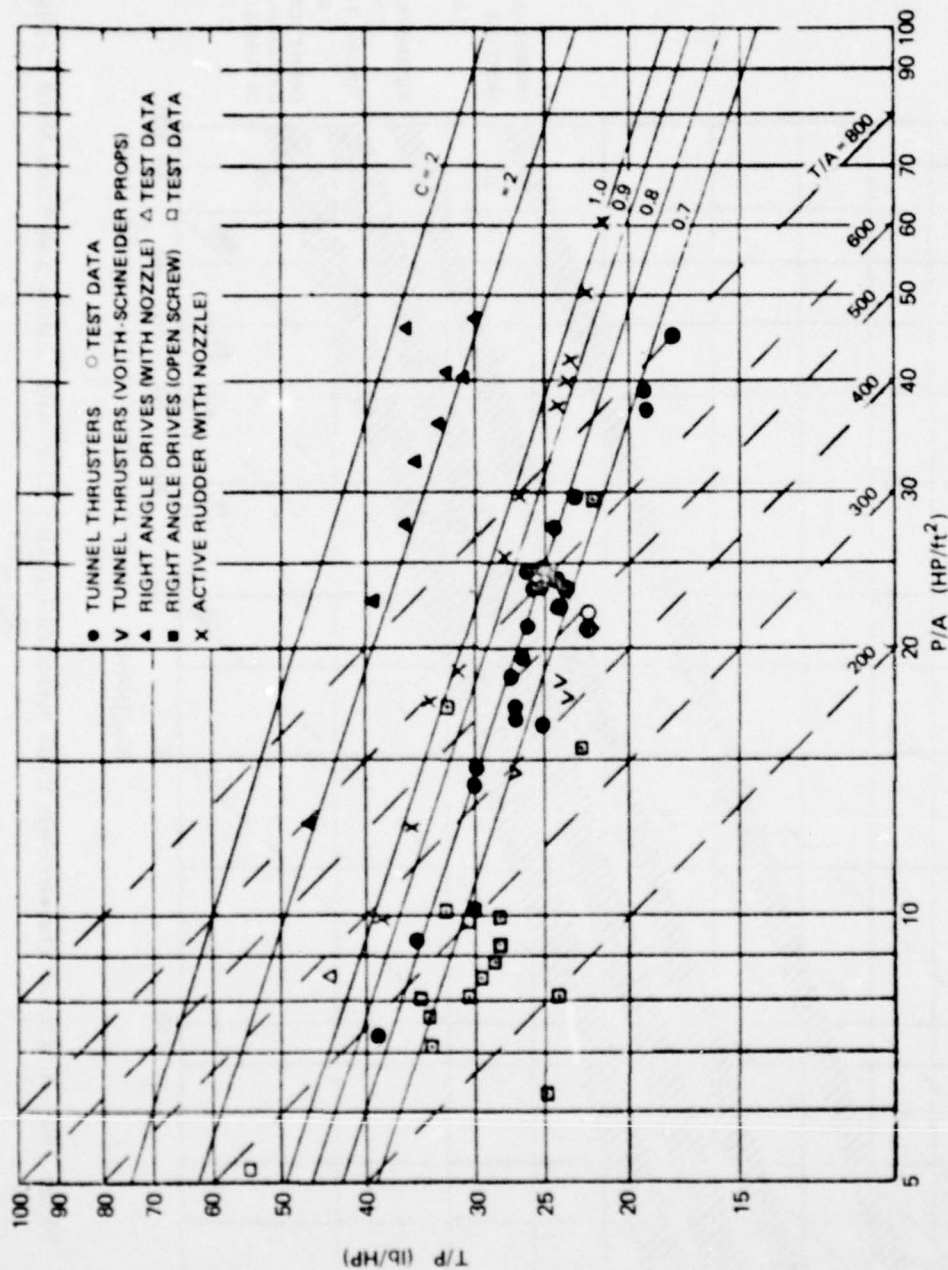


Figure 181 - Data Points for Curves of Figure 180

Hawkins et al.¹²²

NAME: Ejector Lateral Tunnel Thruster.

DEFINITION AND OPERATION: An ejector lateral thruster is similar to the propeller-driven tunnel thruster described previously. However, in this case, the primary thruster is a jet of water issued out of a nozzle positioned within the tunnel. The location of the nozzle and the shape of the tube walls are such that the primary jet induces a strong secondary flow at the inlet side of the nozzle by the viscous and turbulent entrainment of the surrounding fluid. The resulting jet flow gives an augmented thrust over the original jet-reaction thrust. Hence the device resembles a jet pump operating against a zero head.

Several possible arrangements for ejector tunnel thrusters are shown in the sketches of Figures 182 and 183, reproduced from Witte¹³⁸ and from Van Manen et al.¹³⁹

FORCE AND POWER ESTIMATES

Plain Nozzles

A simple, plain nozzle system is described by Witte¹³⁸ as a base level of performance to which an ejector-augmentation system can be compared. The geometry and notation are shown in Figure 184. The pressure drops across the tube and in the nozzle, respectively, are given by

$$\Delta p_t = \xi_t \frac{1}{2} \rho V_t^2 \quad (116)$$

$$\Delta p_n = (\alpha_R^2 - 1)(1 + \xi_n) \frac{1}{2} \rho V_t^2 \quad (117)$$

where $\alpha_R = A_t/A_n$ and ξ_t, ξ_n are the loss coefficients for the nozzle and tube, respectively. The total pressure across the pump is

$$\rho g \cdot \Delta H_p = \Delta p_t + \Delta p_n + \frac{1}{2} \rho V_t^2 \quad (118)$$

and so the pump power is

$$P_p = \rho g(\Delta H_p)Q \quad (119)$$

where $Q = \text{flow rate} = V_t A_t$. The thrust delivered by the simple nozzle is

$$T = \rho Q V_1 \quad (120)$$

where $V_1 = V_t \alpha_R$.

The static merit coefficient is defined as usual by

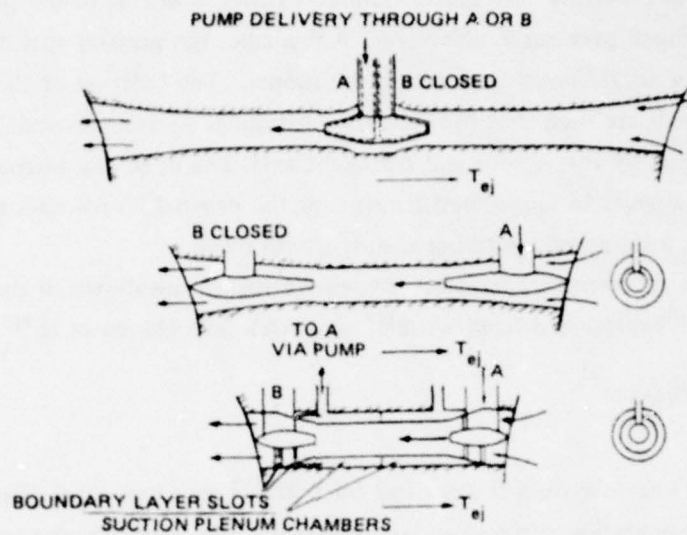


Figure 182 – Two-Directional Ejector Thruster Designs

Witte¹³⁸

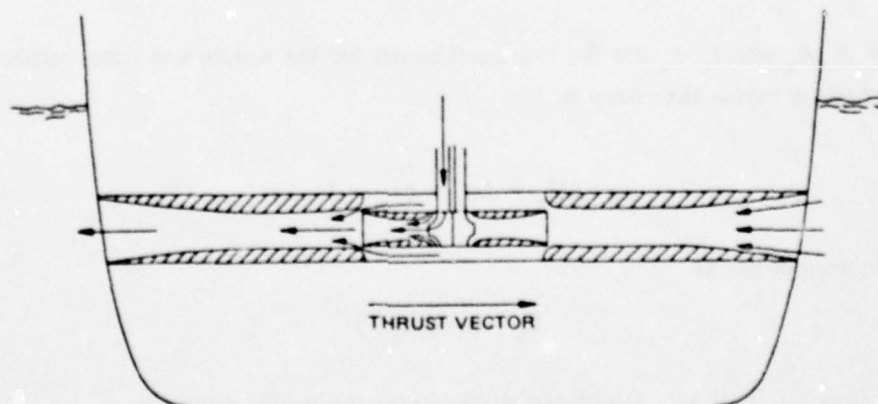


Figure 183 – Arrangement of Two-Stage Ejector System

van Manen et al.¹³⁹

AD-A078 423

DAVID W TAYLOR NAVAL SHIP RESEARCH AND DEVELOPMENT CE--ETC F/G 20/4
AN INVENTORY OF SOME FORCE PRODUCERS FOR USE IN MARINE VEHICLE --ETC(U)
NOV 79 M B WILSON , C V KERCZEK
DTNSRDC-79/097

UNCLASSIFIED

NL

4 OF 5
AD-
A 078423



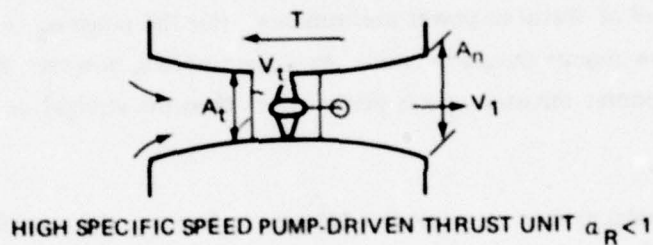
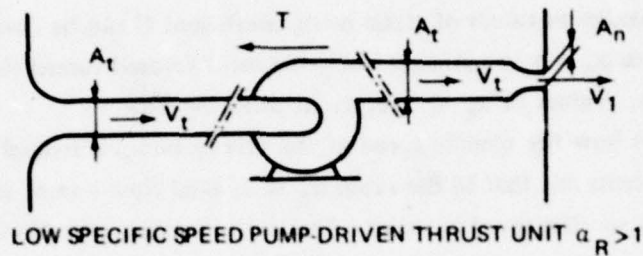


Figure 184 – Low and High Specific Speed Pump-Driven Thruster Units

α_R = area ratio = A_t/A_n . A nondimensional definition of pump specific speed is

$$n_s = \frac{2 \pi^{1/2} Q^{1/2}}{(2 \Delta P_p / \rho)^{1/4} n_p}$$

where n_p = pump revolutions per second

$\Delta P_p = \rho g \Delta H_p$ = total pressure across the pump

Witte, 138

$$C = \frac{T^{3/2}}{P_p (\rho A_t)^{1/2}} \quad (121)$$

Figure 185 shows a plot of C versus α_R for the plain-jetting nozzle, for various tube-loss coefficients ξ_t and the nozzle-loss coefficient $\xi_n = 0$. Witte¹³⁸ shows that the locus of maximum C values is given by

$$C = \frac{3}{2} \left(\frac{1}{1 + \xi_n} \right) \frac{1}{\sqrt{\alpha_R}} \quad (122)$$

and this line is also shown in Figure 185.

The highest maximum values of static merit coefficient C can be obtained when $\alpha_R < 1.0$. Of course $\alpha_R = 1$ is a straight duct, the most favored tunnel thruster because of its simple construction. Values of $\alpha_R < 1$ represent diffusing flow.

Witte¹³⁸ shows how the specific speed of the driving pump is related to the area ratio $\alpha_R = A_t/A_n$. He points out that in the range $\alpha_R \leq 1$, axial flow pumps are appropriate because of the high specific speed required. This is the familiar propeller-in-tunnel thruster discussed earlier, and it is seen that this type of thruster, interpreted as a nozzle, has an inherently high level of thrust-to-power performance. For the range $\alpha_R > 1$, converging flow, radial or mixed-flow pumps should be used. As a plain nozzle, however, the converging jet has an inherently poorer thrust-to-power performance than the straight or diffusing nozzle.

Ejector Augmentation

The ejector-augmentation principle can be used to improve the overall performance of a converging jet. This is appealing because the low specific speed pumps appropriate to the $\alpha_R > 1$ nozzles are cheaper and require less space than typical high specific speed pumps.¹³⁸

Figure 186 shows an ejector tunnel-thruster geometry analyzed by Witte. A converging nozzle of area A_t to A_n (with $\alpha_R > 1$) is placed within a straight mixing chamber of area A_3 , which is long enough to permit complete mixing. A diffusing length may also be used which brings the ultimate tunnel exit area to A_4 . In Figure 187, the final thrust-to-power performance curves of the ejector tunnel thruster at optimum configuration are plotted as graphs of static merit coefficient C versus α_R . The parameters β and ξ_{ej} are defined as

$$\begin{aligned} \beta &= A_3/A_t \\ \xi_{ej} &= W/\frac{1}{2} \rho V_3^2 A_3 \end{aligned} \quad (123)$$

where V_3 = the average velocity in A_3 at the end of the mixed section, and W = total friction-loss force in the ejector system. Details concerning the ejector-flow analysis and results of experimental determination of the loss factor ξ_{ej} can be found in Witte.¹³⁸

One of the important results found by Witte is that the performance of an ejector tunnel thruster, based on the figure of merit coefficient C , is somewhere between that of a conventional, screw-propeller-driven tunnel thruster and a plain, convergent-nozzle system driven by radial pumps.

Work about optimizing general ejector design is presented by Payne,⁶¹ along with an extensive bibliography and historical review of the subject.

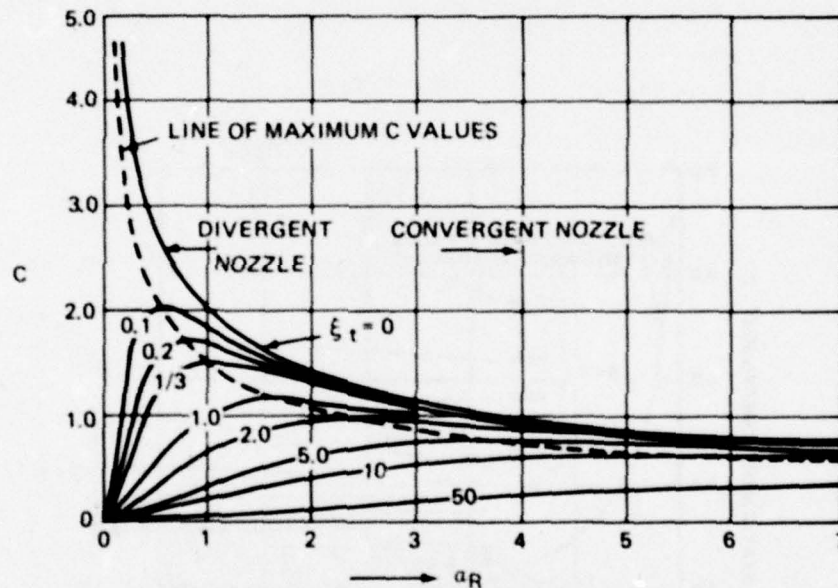


Figure 185 - Plot of C versus a_R , Contours of ξ_t , for Plain Nozzles in Figure 184

$$\xi_n = 0, C = T^{3/2} / P_p \sqrt{\rho A_t}, P_p = \text{pump power}, a_R = A_t / A_n; \text{Witte.}^{138}$$

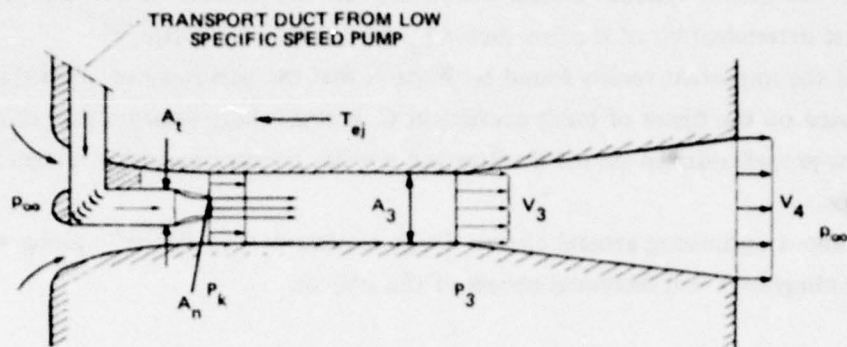


Figure 186 – Ejector Thruster

Witte¹³⁸

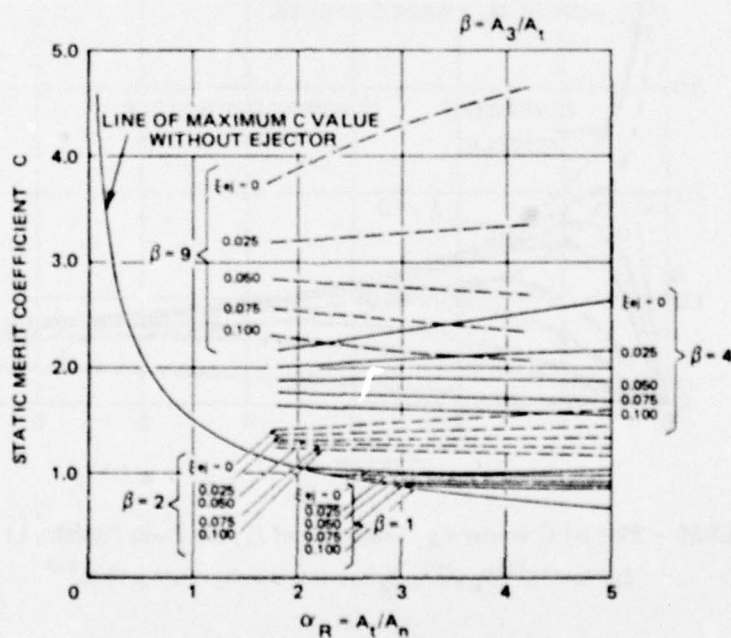


Figure 187 – Optimum C -Values versus α_R for the Ejector System, Compared with Maximum C -Values for Plain Nozzles

Witte¹³⁸

NAME: Ejector Lateral Tunnel Thruster with Jet-Flap Diffusion

DEFINITION AND OPERATION: Flow diffusion at the outlet end of any type of tunnel thruster can improve its thrust performance considerably; see English¹²³ or Beveridge.¹²⁶

A possible alternative to a rigid-wall tunnel diffuser is an angled-jet sheet, or "jet-flap diffuser." This has been suggested as an attractive means of boosting the static and low-speed performance of ducted fans or ejector augmentors for V/STOL aircraft; see Morel and Lissaman.⁶⁵ Its use on a lateral tunnel thruster would be a novel application of the concept. The principle of jet-flap diffusion is mentioned earlier in this work in connection with the jet-flap diffuser augmentor wing; see Figure 73.

For the tunnel thruster, the angled-jet sheet would be issued circumferentially out of a slot around the tunnel exit. This peripheral jet would induce the uniform tunnel flow to expand to a wider uniform cylindrical flow, thus achieving the desired pressure recovery. The diffuser shape could be tailored by modulating the slot-jet momentum and slot-jet angle.

The presence of the vertical walls at the exit of a tunnel thruster is known to create a problem. If any part of the tunnel exit flow clings to the hull surface instead of peeling off and joining the ultimate jet flow, the momentum thrust of that portion will be at a 90° angle to the intended thrust direction. This diverted flow will reduce the thruster effectiveness. Small steps inside the tunnel can improve the flow separation; see Stuntz.¹³¹ With the jet-flap diffuser, it is probably necessary to extend the lips of the nozzle out from the hull to allow for a clean separation and definition of the final exhaust jet boundary.

Possible configurations of the concept are shown in Figure 188.

FORCE AND POWER ESTIMATES

As with any tunnel thruster, the effectiveness is degraded by forward speed of the hull. The present estimates apply only to the speed range $0 < U_\infty/V_j < 0.2$, where V_j is the final expanded-jet velocity exhausted by the thruster. Beyond this speed, the interaction of the bent over jet and the hull cannot be ignored, and the general performance will fall off significantly.

The estimates included here are taken directly from an article by Morel and Lissaman.⁶⁵ The results reported in that paper actually pertain to the ideal static thrust of jet-flap diffusers on both ducted propellers and ejector augmentors. However, it is assumed that these results give relative thrust values that apply to tunnel thrusters as well. Also, only the estimate for the ejector system is included herein.

Figure 189c shows the geometry and notation for an axisymmetric ejector system with diffusion by an angled jet sheet. Consider separately the thrust of the components of this system. For the simple free nozzle (Figure 189a), the idealized thrust and power are

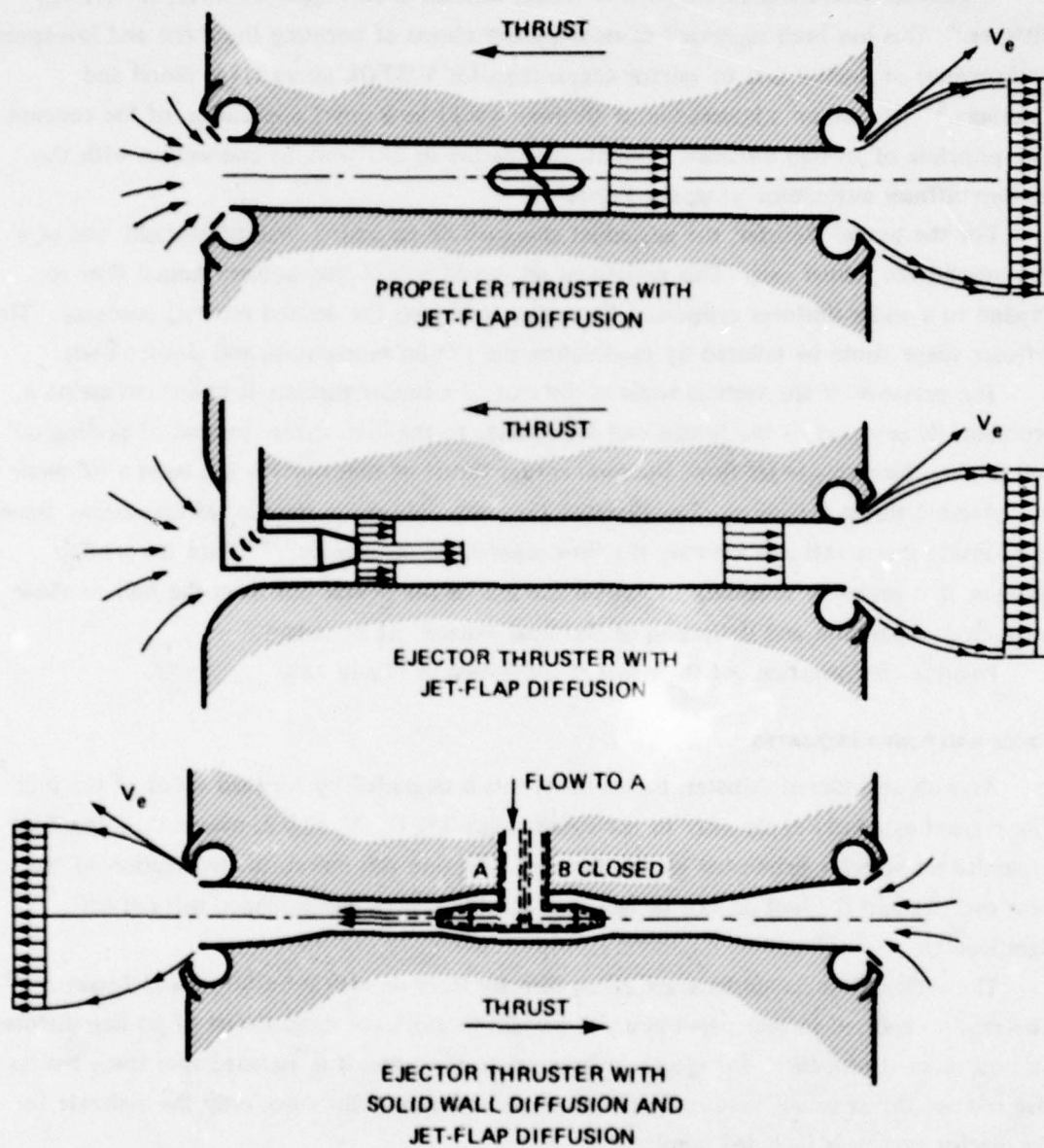


Figure 188 – Possible Thruster Systems Augmented by Jet-Flap Diffusion

Idea proposed by M.B. Wilson

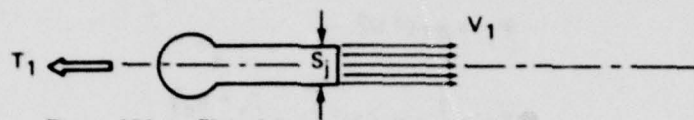


Figure 189a - Plain Jet

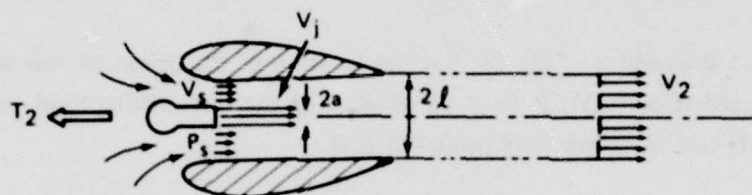


Figure 189b - Ejector

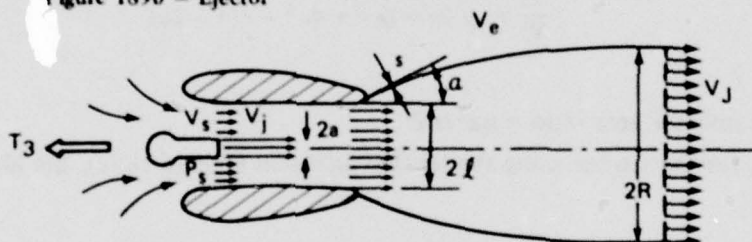


Figure 189c - Ejector with Jet-Flap Diffusion

Figure 189 - Plain Jet, an Ejector, and an Ejector with Jet-Flap Diffusion

Morel and Lissaman.⁶⁵

$$T_1 = \rho S_j V_1^2 \quad (124)$$

$$P_1 = \frac{1}{2} \rho S_j V_1^2 \quad (125)$$

where S_j = exit area of the jet, and V_1 = uniform jet-exit velocity. For an ejector (Figure 189b), the thrust and power are

$$T_2 = \rho \pi \ell^2 V_2^2 \quad (126)$$

$$P_2 = \frac{1}{2} \rho \pi a^2 V_j^3 \left[1 + \frac{p_s - p_o}{V_j^2} \right] \quad (127)$$

where p_s = static pressure of the fluid at the location of the prime jet exit where there is a uniform induced velocity V_s , p_o = static pressure of the surrounding fluid, so that $(p_s - p_o) = -\frac{1}{2} \rho V_s^2$. It can be shown (McCormick³) that

$$\frac{V_2}{V_j} = \sqrt{2\epsilon - 6\epsilon^3 + 4\epsilon^4} - \epsilon(1 - 2\epsilon) \quad (128)$$

where ϵ = augmentor area ratio = $\pi a^2 / \pi \ell^2$.

Finally, for the ejector using the jet-flap diffusion (Figure 189c), the idealized thrust and power are

$$T_3 = \rho \pi R^2 V_j^2 + 2\pi \rho s \ell V_e^2 \quad (129)$$

$$P_3 = \frac{1}{2} \rho \pi a^2 V_j^3 \left[1 + \frac{p_s - p_o}{V_j^2} \right] + \frac{1}{2} \rho (2\pi \ell s) V_e^3 \quad (130)$$

where R = ultimate radius of the cylindrical jet

V_j = ultimate uniform jet velocity

V_e = fluid velocity of the jet sheet issued out of the slot of width s and perimeter length $2\pi \ell$.

The details can be found in Morel and Lissaman⁶⁵ or Morel.¹⁴⁰

An example of the expected thrust improvement is given in Figure 190, where the following definitions are needed

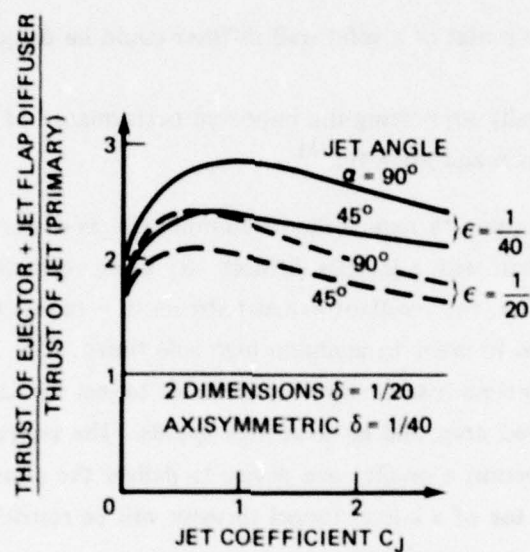


Figure 190 – Thrust Comparison of an Ejector with Jet-Flap Diffusion with a Plain Jet at *Fixed Total Power*

ξ = ejector-area ratio = $\pi \alpha^2 / \pi \ell^2$; Morel and Lissaman.⁶⁵

$$C_J = \frac{2\pi\rho s\ell V_e^2}{\frac{1}{2}\rho\pi a^2 V_j^2} = \text{external jet momentum coefficient}$$

$$\epsilon = a^2/\ell^2 = \text{ejector parameter}$$

$$\delta = \frac{s}{\ell/4} = \text{external jet ratio (for axisymmetric case).}$$

It is seen that for an augmentor with $\epsilon = 1/40$, and a jet-sheet angle of $\alpha = 45^\circ$, an ideal thrust augmentation of 2.4 over the primary jet thrust is obtained. This occurs at a maximum in the curve at $C_J \approx 0.9$.

A jet-flap diffuser at the outlet of a solid wall diffuser could be designed to reach even better thruster performance.

Experimental data generally supporting the improved performance of a jet-flapped ejector are presented by Alperin and Marlotte.¹⁴¹

DISCUSSION: It may be possible to reduce the deleterious effects of forward vehicle speed, a cross flow at the thruster exit, with a jet-flap diffuser. By using controllable jet-flap angles and variable jet-momentum flux, the resultant exhaust stream of a tunnel thruster could possibly be directed as desired in order to maintain high side thrust. For application to submarines, the same disadvantages listed earlier for ordinary tunnel thrusters apply here as well: too much space, increased drag, and noise at high speeds. The improved performance of an augmented thruster may permit a smaller size device to deliver the same lateral force. However, it appears that any use of a lateral tunnel thruster will be restricted to specialized vehicles that must have good maneuvering at very slow speeds.

NAME: Impeller-in-Wing.

DEFINITION AND OPERATION: The impeller-in-wing configuration, or fan-in-wing, is another type of force producer concept being explored for use on V/STOL aircraft. It consists of a propeller submerged in the plane of a lifting surface. For example, see Figure 191. The lift on the wing and impeller combination is composed of direct propeller thrust, aerodynamic lift on the wing, and induced lift caused by the interaction of the impeller discharge with the free stream.

The action of the propeller produces a circular jet directed at an angle to the free-stream direction. This jet is turned eventually in the downstream direction, and the resulting asymmetric flow pattern gives rise to an increased lift due to induced circulation about the wing. Figure 192 shows a schematic of the resultant wing and impeller flow. Goldsmith and Hickey¹⁴² have presented a simplified theory to describe the various aspects of the interference between wing and impeller. In their interpretation, the part of the wing area upstream of the duct opening (area S_1 of Figure 192) experiences an increase in lift that can be estimated by an idealized jet-flap analysis. The appropriate momentum coefficient C_{μ} in this case depends on the propeller thrust T (i.e., $C_{\mu} = T/q_{\infty} S_1$). The jet exit angle δ_j depends on the angle β (Figure 192) which can be controlled by exit louvers.

Unfortunately, there is no firm theoretical basis for predicting the lift on that part of the wing area S_3 aft of the propeller duct where the flow is separated over the lower surface. Also, the complex interrelationships between wing planform geometry, the number of fans, fan location, and fan-area ratio are not predicted well by existing theories. Hickey and Cook¹⁴³ discuss the simple theoretical estimates as they are presently developed.

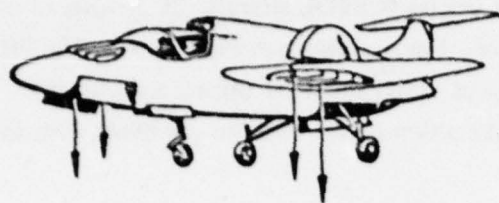
A large amount of experimental data on the aerodynamics of fan-in-body and jet-in-wing arrangements is discussed by Williams.¹⁴⁴

LIFT AND DRAG FORCE ESTIMATES

Extensive wind tunnel testing of different fan-in-wing arrangements provides a basis for estimating the forces. For example, Hickey and Cook have presented a summary of data from several test series. Some of these results have been reproduced to illustrate the important trends.

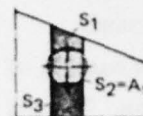
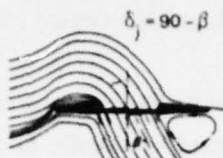
The table of Figure 193 gives the geometrical variations considered. In the plot of Figure 193, the variation is shown of L/T_s versus the speed ratio V/V_j , where L = total lift of the wing-fan combination, T_s = fan thrust when $V = 0$, V = free stream velocity, V_j = velocity of the fan exhaust, α = wing angle of attack, and β = exit louver angle measured from the vertical.

The lift increment exerted on the wing and fan combination due to the fan operation is denoted ΔL_1 . Plots of $\Delta L_1/T_s$ are given in Figures 194 and 195 to point out, respectively,



FAN-IN-WING
VTOL AIRCRAFT
RYAN XV-5A

THE FLOW FIELD
WITH FAN OPERATING



AREAS FOR INDUCED
LIFT CALCULATION

Figure 191 – Fan-in-Wing Vertical
Takeoff and Landing Aircraft,
Ryan XV-5A

Figure 192 – Definition of Flow Field and
Terms Used for Induced Lift Computation

A_f = area of fan

LARGE-SCALE MODEL GEOMETRY									
MODEL	TYPE	WING EXPOSED AREA	WING CHORD INCHES	TAPER	$\frac{b}{c}$	$\frac{D}{c}$	$\frac{x}{c}$	$\frac{D}{b}$	REFERENCE
1	FAN-IN-FUSELAGE	5	27	5	0.86	5.52	147	25	1.2
2	FAN-IN-WING	5.5	40	5	0.86	4.28	200	300	3
3	FAN-IN-WING	5.11	40.00	52	1.47	48	549	4.3	4
4	FAN-IN-WING, 1 FAN UP FAN-IN-WING, 2 FAN UP FAN-IN-WING, 3 FAN UP FAN-IN-WING, 4 FAN UP	5.45	20	47	1.1	5.95	150	24	
5	FAN-IN-WING	7.7	52.4	0	0	5.95	163	4.3	
6	1 FAN IN WING, 1 FAN DOWN IN WING, 2 FAN UP FAN-IN-WING, 2 FAN FORWARD	FLYING DOWN FORWARD	30	5	0.77	7.96	164	266	5.4
7	VTOL, LONG LIFT FAN INCLINING, LARGE FAN	5.4	10	5	0.5	—	—	—	5.4

D = FAN DIAMETER
C = LOCAL WING CHORD
b = HALF SPAN OF WING
x = DIST. FROM L.E. OF WING
TO FAN RADIUS

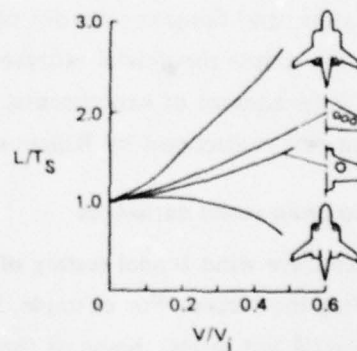


Figure 193 – Variation of Lift with
Velocity Ratio for Several Fan-in
Wing Models, Flaps Up

$\alpha = 0$, $\beta = 0$; β = angle of exit louvers from
vertical; Hickey and Cook¹⁴³

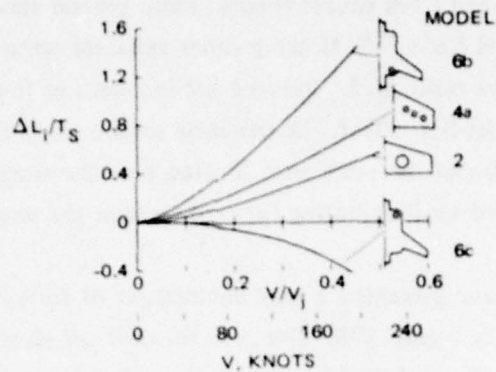


Figure 194 – Induced Lift with Different Lift-Fan Arrangements
 $\delta_f = 0$ degrees, $\beta = 0$ degrees.¹⁴³

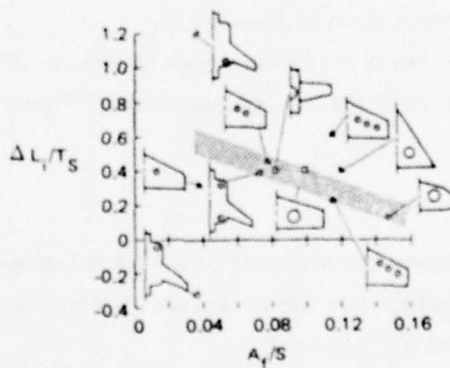


Figure 195 – Influence of Fan-to-Wing Area Ratio on Induced Lift
 $V/V_j = 0.4$, flaps up, $\beta = 0$.¹⁴³

the influence of different fan arrangements and the effect of fan-to-wing ratio. Figure 196 shows the effect of fan chordwise position on $(\Delta L_i/T_s)(A_f/S)$, that is, with the area-ratio influence removed.

From these test data and from simple theory, some general statements can be made about induced lift; see Hickey and Cook.¹⁴³ Holding other variables constant, the $\Delta L_i/T_s$ is inversely proportional to the fan area ratio A_f/S . Induced lift increases as fans are moved aft along the chord because of a better jet-flap effect. Distributing several small fans spanwise improves the induced lift over a single fan of the same area, located near the wing root. Maximum induced lift would likely be achieved by distributing fans spanwise at the wing trailing edge; see Figure 194.

Hickey and Ellis¹⁴⁵ have presented a very detailed set of tests on one particular fan-in-wing configuration shown in Figure 198. For zero forward speed, static case, it was found that the thrust coefficient ($K_T = T/\rho n^2 D^4$) on the propeller alone was $K_T = 0.3$, and on the propeller-in-wing configuration, it was $K_T = 0.5$.

Then for nonzero forward speed, the curves in Figure 199a show the influence of propeller loading $C_F = T/q_\infty S$ upon the lift increase ΔC_L . Here, the definition of lift increment is

$$\Delta C_L = C_L(n) - C_L(n=0) \quad (131)$$

where n = propeller revolutions per second.

These curves illustrate that the lift of the wing and fan combination is about 2.5 times the thrust of the fan for the configuration of Figure 198.

Incremental drag due to fan operation is shown in Figure 197 for several fan arrangements of Figure 196; and in Figure 199b for the configuration of Figure 198 tested by Hickey and Ellis.¹⁴⁵

POWERING ESTIMATE

As an example of the power requirements of a typical fan-in-wing arrangement, the data of Hickey and Ellis¹⁴⁵ are useful. For the static case ($V = 0$), the static power coefficient is found to be $K_p = 0.59$, where $K_p = P/\rho n^3 D^5$.

Now the static merit coefficient $C = T^{3/2}/P\sqrt{\rho A_f}$ can be rewritten in terms of the propeller coefficients

$$C = \frac{2}{\sqrt{\pi}} \frac{K_T^{3/2}}{K_p} \quad (132)$$

So, for this wing and fan arrangement, with $K_T = 0.5$, the static thrust-to-power performance is

$$C = 0.672 \quad (133)$$

which is relatively poor, compared with ducted propellers and the better tunnel thrusters. McCormick³ makes a comparison between the fan-in-wing and the tilt-wing concepts. On the basis of lift-to-static lift, the fan-in-wing arrangement is poorer.

DISCUSSION: For application to submarine control, the candidate control surface for impeller-in-wing arrangements might be the horizontal stern planes and the sail planes. Although the thrust-to-power performance would be poorer than for tilt-wing designs, the impeller-in-wing would have the advantage of being slightly less vulnerable to damage since the propeller, typically, is imbedded within the wing planform. Noise would be a problem, as would the complication of shafting, gears, and linkages needed to drive and control the propeller.

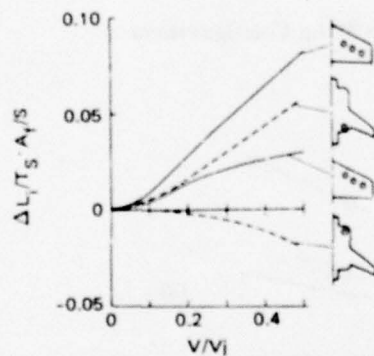


Figure 196 – Influence of Fan Chordwise Position on Induced Lift
Flaps up, $\beta = 0$ degrees.¹⁴³

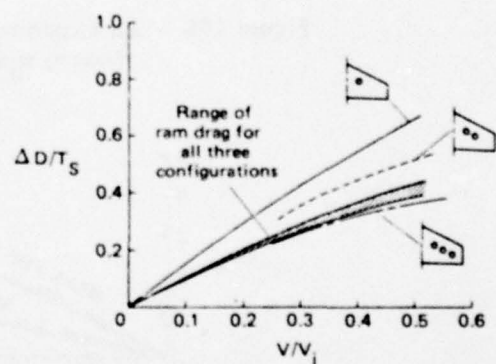


Figure 197 – Effect of Spanwise Fan Distribution on Drag Due to Fan Operation

$\alpha = 0$ degree
 $\alpha = 0$ degrees, $\beta = 0$ degrees.¹⁴³

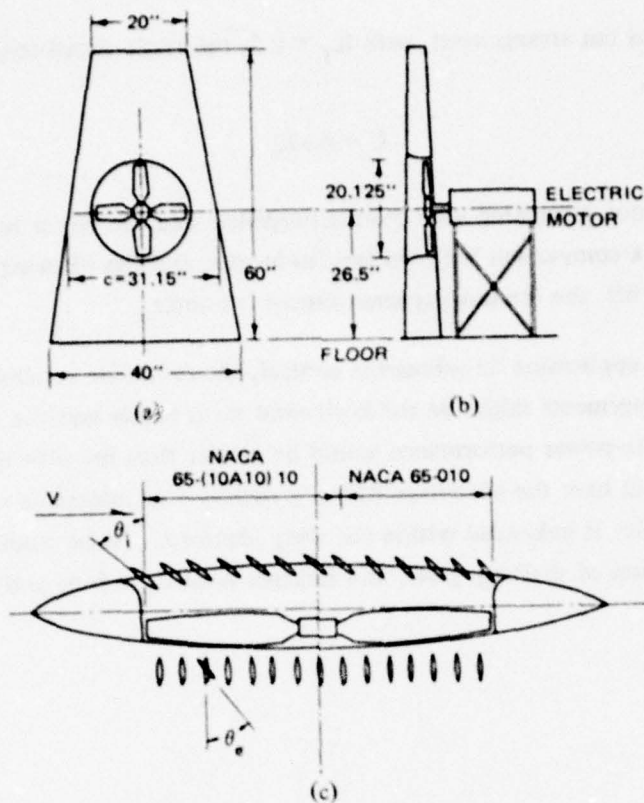


Figure 198 – An Experimental Fan-in-Wing Configuration
Tested by Hickey and Ellis.¹⁴⁵

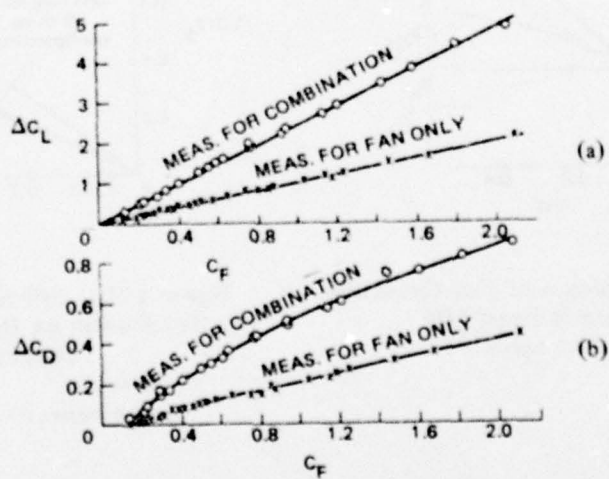


Figure 199 – Incremental Lift and Drag Coefficients versus Propeller Loading, for the Fan-in-Wing Scheme of Figure 198
 $C_L = \text{lift}/q S$, $C_F = T/q S$, $C_D = \text{drag}/q S$, $S = \text{total wing area}$.

Directional Thrusters

The devices discussed in this subsection are auxiliary propulsors which are intended for *steerable* operation. These are distinguished from the main propulsors in that their function would be *strictly for producing maneuvering forces*.

NAME: Directional Propeller Devices.

DEFINITION AND OPERATION: A directional propeller is referred to here as a small trainable thruster, mounted, for example, on a fixed or retractable rotatable strut or on swivels at the tips of a lifting surface. The thrust line can be directed as desired by angle changes.

These types of devices have seen more extensive application on aircraft than in the marine field. In the particular case of V/STOL aircraft, there is an amazing and bewildering variety of proposed configurations. For example, Figure 200 shows a picture outline of VTOL arrangements, many of which employ free or ducted propellers that swivel, tilt, or rotate. An overview of the aerodynamics problems involved with these aircraft is presented by Poisson-Quinton.¹⁴⁶ A deeper treatment of some of the special problems of the propeller-driven types of V/STOL is given by Stepniewski.¹⁴⁷ The McCormick textbook³ also presents a quantitative discussion of the aerodynamic aspects of V/STOL aircraft.

For marine vehicles, trainable propellers have been used for low speed maneuvering of deep-diving submersibles such as the ALVIN (Mavor et al.¹⁴⁸); for the close-quarters control of surface ships in harbors; or for dynamic positioning of ships in a seaway; see Dewhurst¹⁴⁹ and Graham et al.¹⁵⁰ Two arrangements of shipboard trainable propeller thrusters are pictured in Figure 201.

A brief review of marine propeller propulsors is presented by Thurston and Amsler¹⁵¹ with emphasis on uncommon ducted propellers.

FREE PROPELLERS

Thrust and Power Estimate

Some crude estimates of propeller performance are provided by the momentum theory and an actuator-disk model of propeller operation. For example, von Mises¹⁵² has presented an elegant outline of the elementary theory. Quick estimates can be made of the ideal limits and for simple relationships between thrust, power required, size, and speed of advance.

The connection between thrust and ideal power is given by the ideal efficiency of a propeller with diameter D

$$\eta_i = TV_\infty/P_i = C_T/C_{P_i} \quad (134)$$


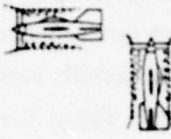
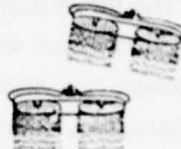
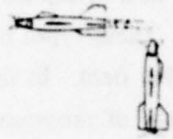
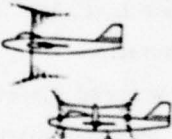
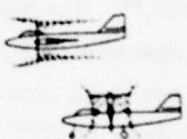
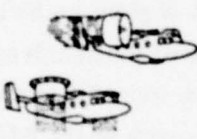
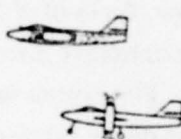
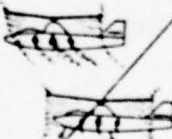
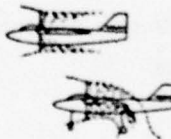

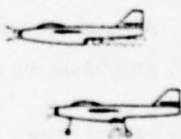
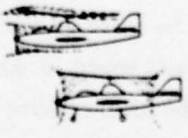

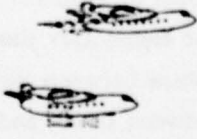
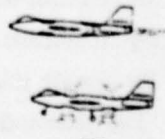
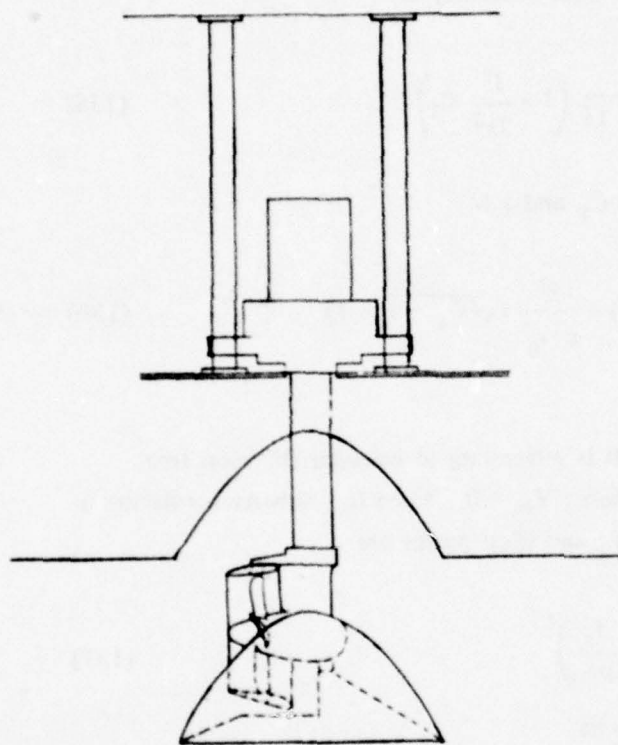
METHODS TO PERFORM THE TRANSITION	TYPES OF LIFT GENERATORS (HOVERING)			
	ROTORS	FREE PROPELLERS	DUCTED FANS	TURBO- JETS
AIRCRAFT TILTING	 <p>A1 Helicopter</p>	 <p>B1 (US: Convair XFV 1, Lockheed XFV 1)</p>	 <p>C1 (US: Flying Jeeps)</p>	 <p>D1 (US: Ryan X 13) (F.: Coleoptere)</p>
THRUST TILTING	 <p>A2 (US: Bell XV 3, Kaman K16)</p>	 <p>B2 (US: Vertol VZ-2, Hiller X 18, Vought XC 142, Curtiss X 19) (Can.: CL-84)</p>	 <p>C2 (US: Doak VZ 4, Bell X 22) (F.: N-500)</p>	 <p>D2 (US: Bell A.T.V.) (All.: VJ 101 C)</p>
THRUST DEFLECTION	 <p>A3</p>	 <p>B3 (US: Ryan VZ 3, Fairchild VZ 5) (F.: Breguet 941-STOL)</p>	 <p>C3 (US: Adam project)</p>	 <p>D3 (US: Bell X 14, Lockheed XV 4 A) (GB: Hawker 1127)</p>
SEPARATE PROPULSIONS	 <p>A4 (US: McDonnell XV 1, Lockheed AH-56A) (GB: Rotodyne)</p>	 <p>B4</p>	 <p>C4 (US: Ryan XV 5-A)</p>	 <p>D4 (GB: Short SC 1) (F.: Balzac, Mirage III V) (All.: Do-31E)</p>

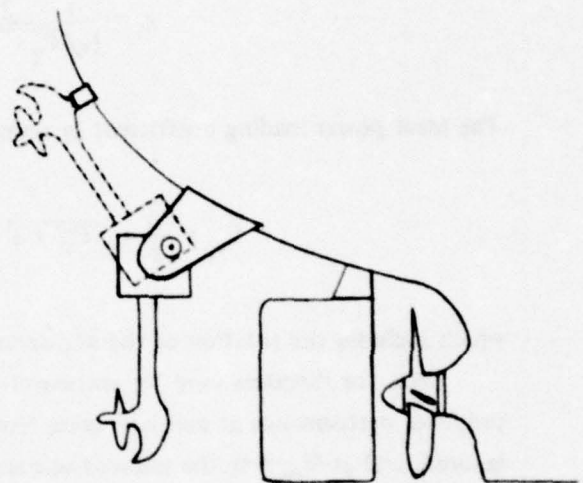
Figure 200 – Vertical Takeoff and Landing Morphology

After Campbell, J. P., "Vertical Take-Off and Landing Aircraft,"

McMillan, N.Y. 1962



RIGHT ANGLE DRIVE
VERTICALLY RETRACTABLE



RIGHT ANGLE DRIVE
FIXED OR RETRACTABLE

Figure 201 — Trainable Propeller Thrusters
Hawkins et al.¹²²

where $C_T = T / \frac{1}{2} \rho V_\infty^2 A_0$ = thrust-loading coefficient

$C_{P_i} = P_i / \frac{1}{2} \rho V_\infty^3 A_0$ = ideal power-loading coefficient

$A_0 = \pi D^2 / 4$ = disc area

J = advance ratio V_∞ / nD .

The propeller frequency is $n = \omega / 2\pi$ revolutions per second. If the rotational velocity of the slipstream is included, an approximation to the ideal efficiency is¹⁵²

$$\eta_i = \frac{2}{[\sqrt{C_T + 1} + 1]} \left(1 - \frac{J^2}{2\pi^2} C_T \right) \quad (135)$$

The ideal power-loading coefficient in terms of C_T and J is

$$C_{P_i} = \frac{C_T}{2} (\sqrt{C_T + 1} + 1) + \frac{J^2}{\pi^2 \eta_i^2} (\sqrt{C_T + 1} - 1) \quad (136)$$

which includes the rotation of the slipstream.

Now, for thrusters used for maneuvering, it is interesting to consider the ideal free-propeller performance at and near *static* conditions: $V_\infty = 0$. When the slipstream rotation is ignored, and at $V_\infty = 0$, the induced-velocity u_{1_0} and ideal power are

$$u_{1_0} = \left(\frac{T_0}{2\rho A_0} \right)^{1/2} \quad (137)$$

$$P_i = \frac{T_0^{3/2}}{\sqrt{2\rho A_0}} \quad (138)$$

for the static or bollard thrust T_0 .

Note that this would give the ideal static merit coefficient $C_i = T_0^{3/2} / P_i \sqrt{\rho A_0} = \sqrt{2}$; see Equation (111).

If the power absorbed by the propeller is kept constant for speeds ranging from $V_\infty = 0$ to some nonzero value, the resulting thrust delivered can be determined by equating the expressions for power at static and ahead conditions. McCormick³ gives a curve, reproduced in Figure 202, for the decreasing available thrust for the same diameter propeller as the forward speed is increased. This approximation ignores the slipstream rotation.

Unfortunately the ideal estimates of power are poor and should be viewed only as an indicator of the limiting level of performance.

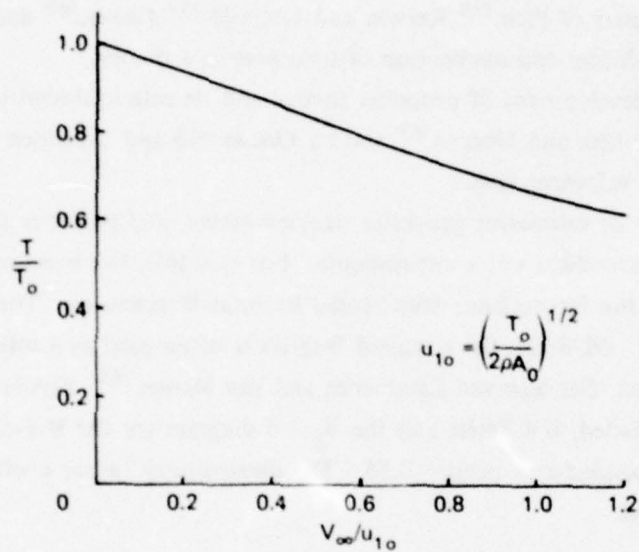


Figure 202 – Variation of Available Thrust with Forward Speed at Constant Power
Result from elementary, actuator disk theory, McCormick.³

While the simple momentum theory provides crude estimates of the overall relationships between thrust, power, and gross size, it does not give information about the connection between propeller geometry and thrust and torque. It does not provide details of the induced-velocity field. Many of these important detailed features are determined from a lifting-line theory as presented, for example, by Betz,¹⁵³ Goldstein,¹⁵⁴ and Lerbs¹⁵⁵ and then exploited for design, for example, by Eckhardt and Morgan.¹⁵⁶ The classical vortex-system representation has also been explored by Hough and Ordway,¹⁵⁷ and the results are identified with the infinite-blade-number or actuator-disk solution.

Lifting-surface theory permits even greater detailed investigations. In particular, the chordwise distribution of lift for the typical wide blade marine propeller can be determined. For example, the papers of Pien,¹⁵⁸ Kerwin and Leopold,¹⁵⁹ Cheng,¹⁶⁰ and of Morgan et al.¹⁶¹ pertain to the formulation and application of lifting-surface theory.

The historical development of propeller theory and its role in design is reviewed in two interesting papers by Cox and Morgan¹⁶² and by Oosterveld and Oossanen.¹⁶³ Both these works give extensive reference lists.

A practical way of estimating propeller size, geometry, and power is to use the cross-plotted results of methodical series experiments. For example, the most extensive series has been carried out by the Netherlands Ship Model Basin at Wageningen. The results are presented by Troost.¹⁶⁴ Of these, the so-called B-series is often used as a reference for good standard performance. See also van Lammeren and van Manen.¹⁶⁵ Figure 203 shows a sketch of the four-bladed, B 4 Series and the $B_p - \delta$ diagram for the B 4-55 series propellers — four blades with expanded-area ratio = 0.55. The dimensional Taylor coefficients B_p and δ are defined as follows

$$B_p = \text{power coefficient} = \frac{NP_D^{1/2}}{V_A^{5/2}}$$

$$\delta = \text{diameter coefficient} = \frac{ND}{V_A} \quad (139)$$

where N = revolutions/minute

P_D = delivered horsepower at the propeller

V_A = speed of advance in knots

D = propeller diameter in feet.

Familiar nondimensional thrust, power, and torque coefficients are defined

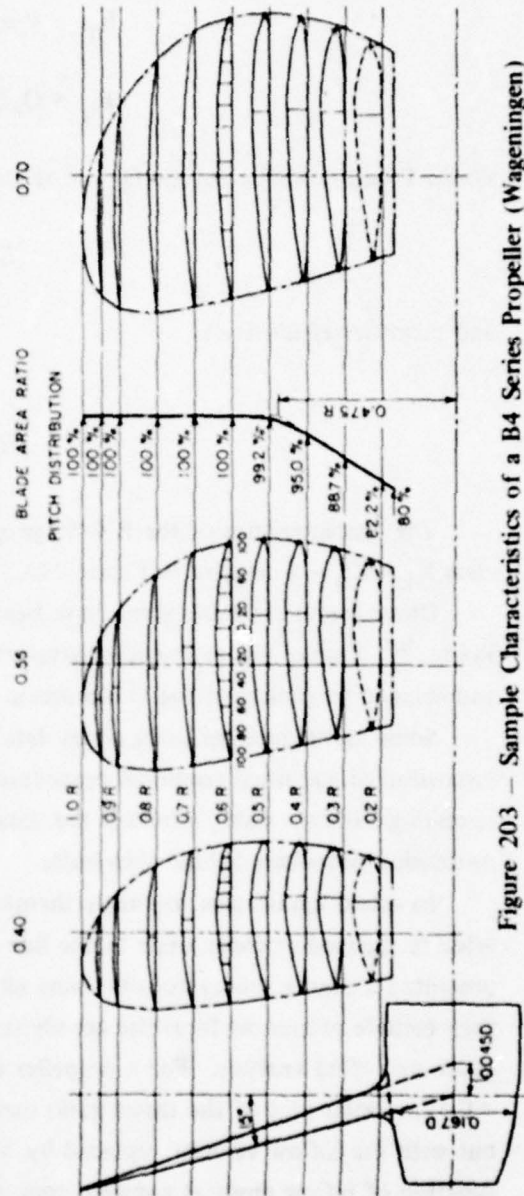
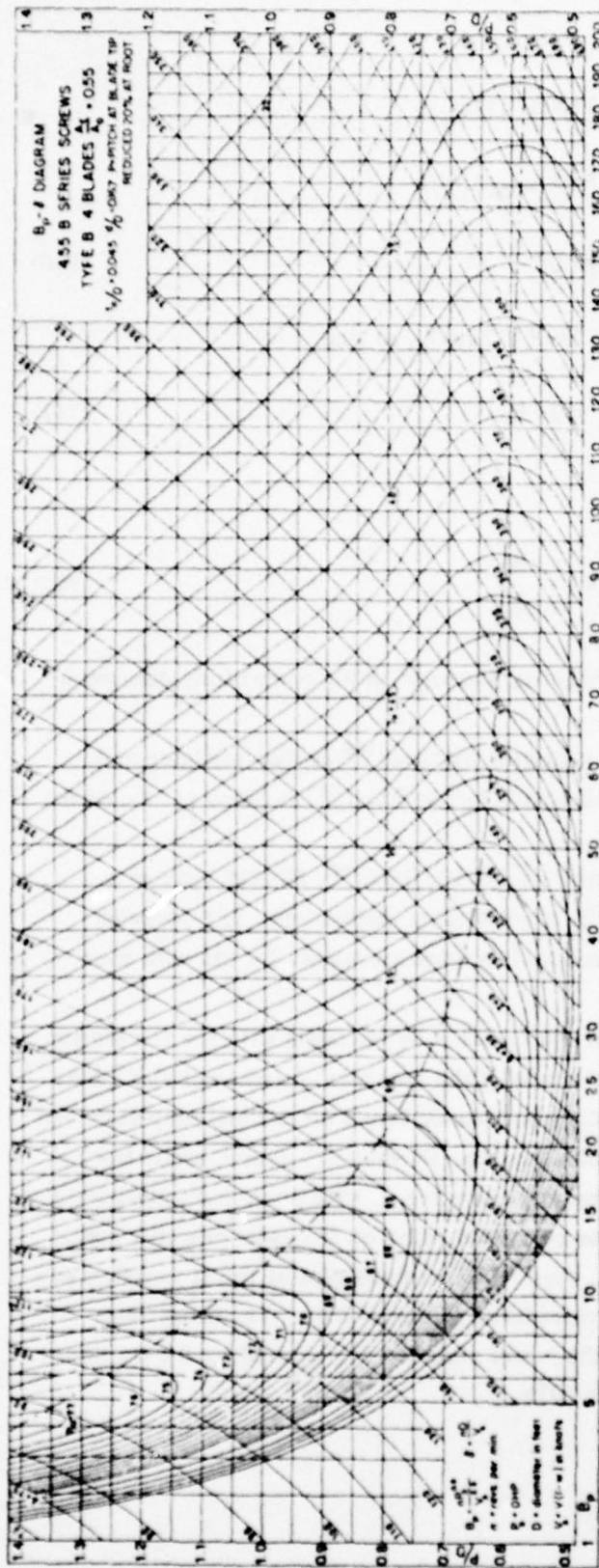


Figure 203 - Sample Characteristics of a B4 Series Propeller (Wageningen)

$$K_T = T/\rho n^2 D^4 = \pi J^2 C_T/8$$

$$K_P = P/\rho n^3 D^5 = \pi J^2 C_P/8$$

$$K_Q = Q_P/\rho n^2 D^5 \quad (140)$$

Power P and propeller torque Q_P are related by $P = 2\pi n Q_P$, so that

$$K_P = 2\pi K_Q \quad (141)$$

and propeller efficiency is

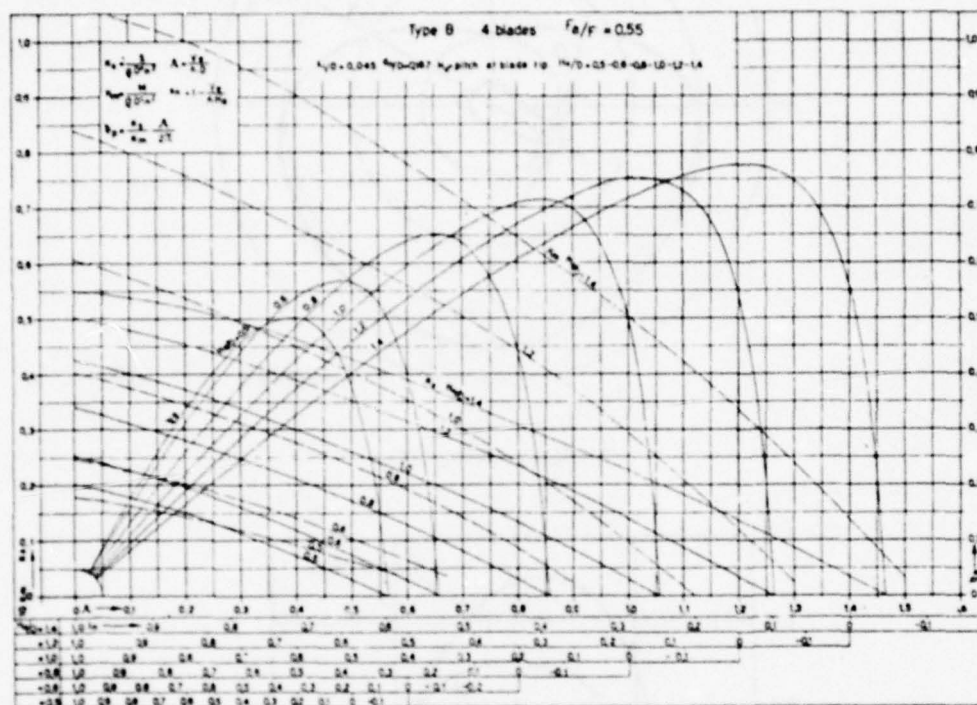
$$\eta_P = \frac{J}{2\pi} \frac{K_T}{K_Q} \quad (142)$$

The characteristics of the B 4-55 propeller are presented in the form of the dimensionless $K_T - K_Q - J$ diagram in Figure 204.

Other useful propeller series have been presented by Gawn¹⁶⁶ and by Lindgren and Bjärne.¹⁶⁷ One of the right-angle thrusters discussed by Dewhurst,¹⁴⁹ is based on one of the wide-bladed propellers of the Gawn series.

Some techniques for using series data are outlined by Todd.¹⁶⁸ He also includes a discussion of the usual empirical procedure for predicting the performance of a propeller operating within a wake, although the data referred to there are mainly for use with main propulsion propellers behind ship hulls.

In actual application, trainable thrusters will typically be operating with the free-stream velocity inclined at some angle to the line of thrust of the propeller. Laschka et al.¹⁶⁹ have presented a simple theory for obtaining all the aerodynamic forces on inclined propellers, and they include references from the aerodynamic literature. Dewhurst¹⁴⁹ shows results from a much-simplified analysis. For a propeller from the Gawn series, with pitch-to-diameter ratio = 0.57, a polar plot of the thrust ratio can be calculated based on the usual propeller curves but with the inflow velocity replaced by $V_\infty \cos \theta$. The resulting plot of thrust variation as a function of inflow angle at constant rpm is reproduced in Figure 205a. The thrust ratio increases as the angle increases but so does the power absorbed as indicated by the constant rpm curve of Q/Q_0 versus θ shown in Figure 205b.



NOTATION:

PRESENT

WAGENINGEN

K_T

K_S

K_Q

K_M

J

Λ

η_p

η_p

A_E/A_0

= EXPANDED AREA RATIO =

F_a/F

Figure 204 - Results of Open Water Tests on Four-Bladed Propellers of the B 4-55 Type

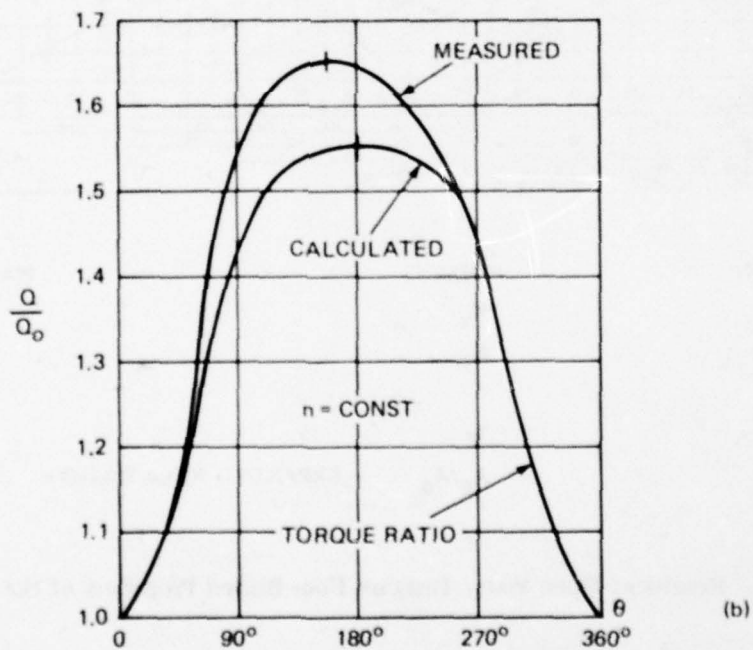
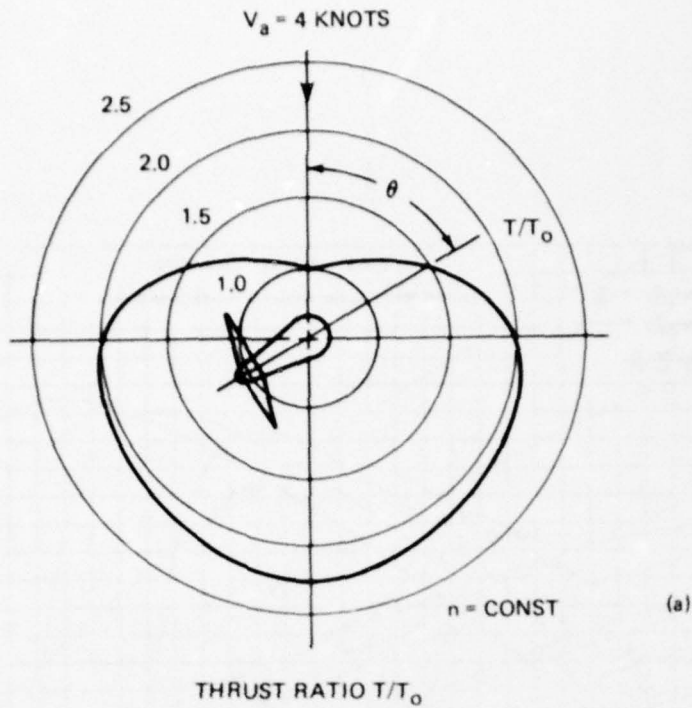


Figure 205 — Example Performance of a Right-Angle Thruster as a Function of Inclination Angle to Free-Stream

Determined by replacing inflow velocity by $V \cos \theta$. Data for these curves are based on a Gawn series propeller, Dewhurst.¹⁴⁹

DUCTED PROPELLERS

Thrust and Power Estimate

If a propeller is encased in a shroud, the flow through the duct can markedly affect the performance of the propeller and nozzle combination. The shroud shape controls both the distribution of velocity through the duct and the pressure at the propeller disk. This is shown in the sketches of Figure 206a, where a schematic comparison is made between the idealized pressure distributions through an open propeller disk of area A and the pressure distributions through ducted propellers whose disk area is $S = A + \Delta A$. The presence of the shroud also allows a larger loading on the blades toward the tips.

For a flow-decelerating nozzle, or pumpjet, $\Delta A > 0$, and there is a pressure rise in front of the actuator disk. This may be useful for inhibiting screw cavitation. The induced circulation about the nozzle (Figure 206b) creates a negative thrust on the duct.

For a flow-accelerating duct, Kort nozzle, the $\Delta A < 0$, and there is an augmented decrease in the pressure in front of the disk. In this case, the induced circulation on the nozzle creates a positive thrust on the duct, and the overall efficiency of this configuration is improved. In general it may be stated that for low-speed, high-thrust-loading applications, the accelerating nozzle is appropriate.

For axial inflow into a ducted propeller, the momentum theory and actuator-disk model again provide some rough estimates of performance. For example, the pertinent discussion by van Manen and Oosterveld¹³⁵ is useful.

Thrust and ideal power are connected by the ideal efficiency

$$\eta_i = \frac{C_T}{C_{P_i}} = \frac{2}{[1 + \sqrt{1 + \tau C_T}]} \quad (143)$$

and the ideal power-loading coefficient is

$$C_{P_i} = \frac{C_T}{2} (1 + \sqrt{1 + \tau C_T}) \quad (144)$$

The ratio τ is defined as

$$\tau = \frac{T_P}{T_P + T_N} = \frac{T_P}{T} \quad (145)$$

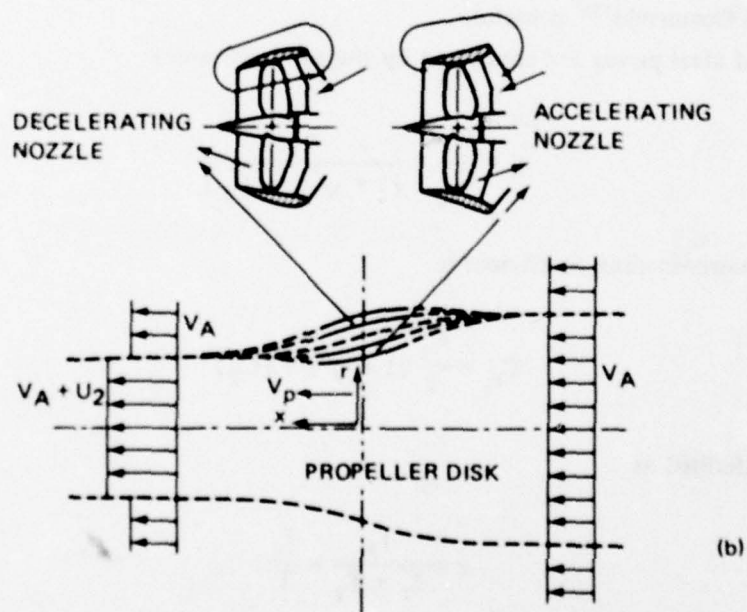
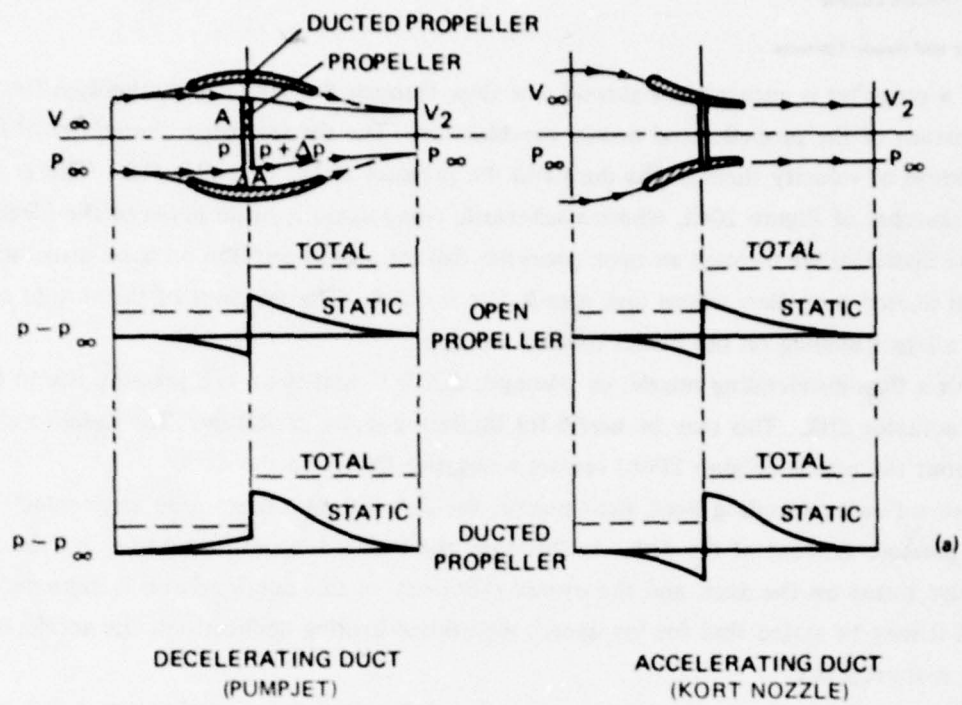


Figure 206 – General Form of Streamlines Enforced by Different Nozzle Types

and is an important parameter of ducted-propeller performance; C_T and C_{p_i} are defined as before. The total thrust is made up of thrust on the propeller plus thrust on the nozzle:

$$T = T_P + T_N.$$

Comparing the ducted propeller η_i with the ideal efficiency of the free propeller at the same C_T , we see that by carrying more thrust on the nozzle $\tau < 1$, the overall efficiency can be improved. Or, to deliver the same thrust, a ducted propeller requires a smaller diameter than a free propeller.

The benefit of the duct is obviously degraded by viscous drag on the nozzle. This degradation is worse at higher forward speeds. Van Manen and Oosterveld¹³⁵ have provided an estimate of the effect of duct drag upon the ideal efficiency. A nozzle-efficiency factor is defined as

$$\eta_{f_N} = \frac{T - D_N}{T} = 1 - \frac{4\epsilon}{D} \frac{C_{D_N}}{C_T} \quad (146)$$

where ϵ = nozzle length in axial direction, and $D_N = C_{D_N} \frac{1}{2} \rho V_\infty^2 \pi D \epsilon$ is the nozzle drag estimated by empirical means. The open water efficiency of the ducted propeller is then $\eta = \eta_i \cdot \eta_{f_N}$. Note that $\eta_{f_N} \rightarrow 1.0$ when the $D_N \rightarrow 0$. Figure 207 gives the estimated η_{f_N} as a function of the thrust loading C_T . In Figure 208, the overall efficiency is plotted against C_T , showing curves for an open propeller and for ducted propellers with and without nozzle-friction drag included. The graph shows that ducted propellers lead to higher efficiencies than free propellers for the heavier thrust loadings — here, for $C_T > 1$.

Another limiting factor of ducted-propeller performance is flow separation on the inner face of the nozzle. This may occur either from too great an acceleration of the flow into the propeller or from too rapid a diffusion of the slipstream downstream of the propeller. Lazareff¹⁷⁰ discusses several aspects of the performance effects when separation occurs on shrouded propellers.

It is possible to envision a form of ducted propeller employed routinely for forward propulsion that could also generate a substantial side force for lateral control. Such a concept has been proposed and analyzed to some extent by Gordon and Tarpgaard.¹⁷¹ The idea is to use a nonsymmetric propeller shroud that develops a force perpendicular to the propeller axis under the action of propeller stream flow. Gordon and Tarpgaard¹⁷¹ have carried out an analysis of a *semicircular* shroud using lifting line theory. They also performed open water model propeller experiments with a 6.2-inch-diameter, three-bladed propeller operating within an 180°-arc duct and found, for example, that at a forward thrust coefficient of $C_T = 5$, the measured side-to-forward thrust ratio is about 0.216 for the particular choice of duct geometry. To operate such a ducted propeller in the straight ahead condition, the shroud would have to be rotated about the propeller axis so that the side thrust would be aimed either vertically

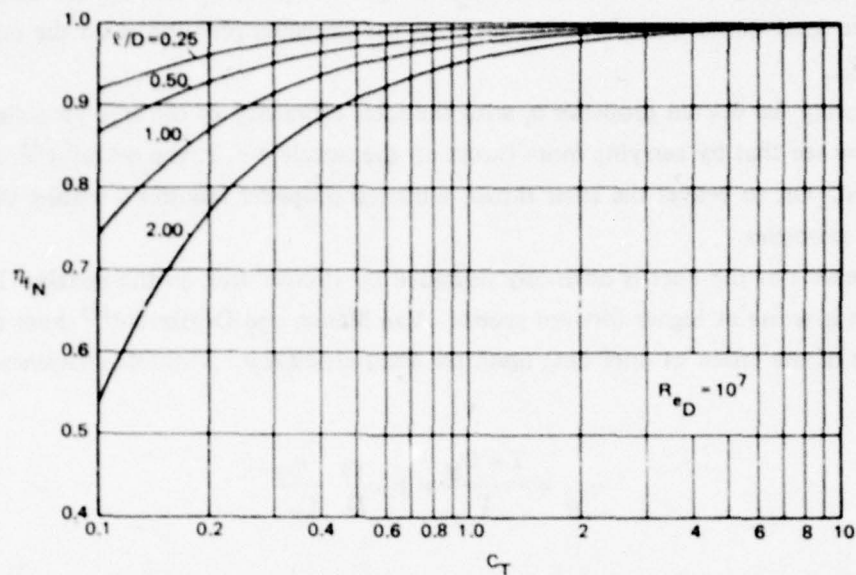


Figure 207 – Efficiency Factor Due to Frictional Nozzle Drag as a Function of C_T and l/D

here, D = Diameter, van Manen and Oosterveld.¹³⁵

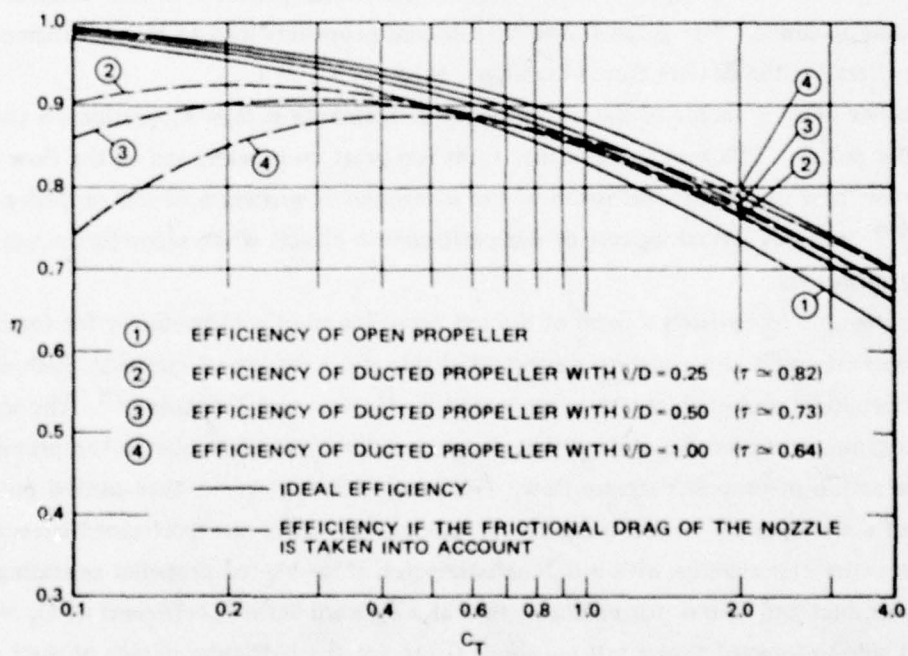


Figure 208 – Optimum Ideal Efficiency and Efficiency Losses Due to Frictional Nozzle Drag of a Ducted-Propeller System

here, D = Diameter, van Manen and Oosterveld.¹³⁵

upward or downward.

For a ducted propeller to be operated as a trainable thruster, the static performance is important for maneuvering. In this case, it is interesting to include the effect of flow diffusion created by the shroud shape. Lazareff¹⁷⁰ present a useful discussion of the ideal static thruster. Figure 209 gives the geometry and notation. If the diffusion parameter is defined by

$$\sigma = S_4/S_1 \quad (147)$$

then the total thrust T and ideal power P_i are connected by

$$T = (\rho \sigma S_1)^{1/3} (2 P_i)^{2/3} \quad (148)$$

Then, the thrust-to-area and thrust-to-power ratios are

$$T/S_1 = (\rho \sigma)^{1/3} (2 P_i/S_1)^{2/3} \quad (149)$$

$$T/P_i = (2 \rho \sigma)^{1/3} \left(\frac{2}{T/S_1} \right)^{1/2} \quad (150)$$

Note that the ideal static merit coefficient is a function of the diffusion parameter

$$C_i = T^{3/2}/P_i \sqrt{\rho S_1} = 2 \sigma^{1/2} \quad (151)$$

Thus, there is much to be gained from diffusion. With no diffusion $\sigma = 1$, the static thrust effectiveness is $\sqrt{2}$ times that of a free propeller, ignoring, of course the viscous drag on the shroud.

Lazareff¹⁷⁰ has mentioned an experimental result with a shrouded propeller using diffusion, where a remarkable static merit coefficient of $C = 2.34$ was achieved. No details are given about the amount of diffusion, geometry, etc.

To obtain the detailed flow features such as the induced velocity field and the influence of blade geometry and duct geometry, more complete theories of screw propellers and ring wings must be brought to bear. The review articles of Burnell and Sacks¹⁷² and Weissinger and Maass¹⁷³ provide a historical view and the status of the use of theory for predicting performance of shrouded propellers. Morgan and Caster¹⁷⁴ present a recent comparison between theory and experiment.

As in free propellers, the use of *methodical series* experiments is very useful for ducted-propeller design. For example, series test results for the Wageningen B-series propellers

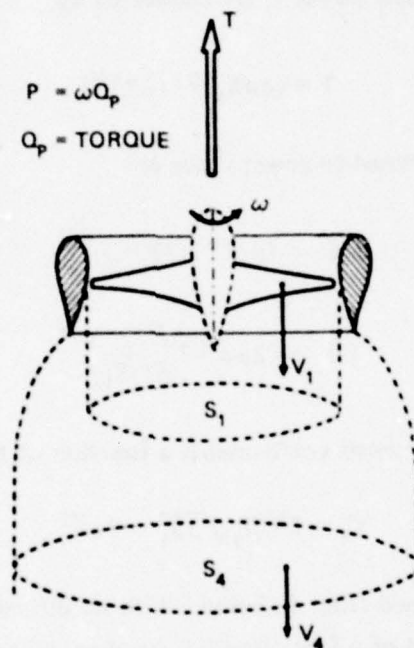


Figure 209 – Ducted Propeller with a Diffusing Shroud;
Notation for Static Thrusting

operated in several different nozzle designs are presented by van Manen.^{175, 176} Ducted propellers with Kaplan-type blade shapes (K-series) are presented by van Manen and Superina,¹⁷⁷ and an improved shape, the Ka-series, is discussed by van Manen.¹³⁴

Figure 210, reproduced from Strom-Tejsen's discussion of Reference 135, shows some results for the measured efficiency η and thrust ratio τ for the B 4-55 propeller in several nozzle shapes. The curve of η for the B 4-55 screw as a free propeller illustrates the benefit of the duct for $C_T > 1.0 - 2.0$.

Typical results for the open water performance of the Wageningen Ka-series ducted screws are shown in Figure 211, reproduced from van Manen and Oosterveld.¹³⁵ Similar test results are given in Oosterveld¹⁷⁸ and in Oosterveld and van Oosanen¹⁶³ for several other types of ducted propeller shapes.

Lewis¹⁷⁹ has presented an interesting technique for predicting the off-design performance of a flow-accelerating nozzle given three values of initial data at one central design point: the thrust coefficient C_T , the thrust ratio τ , and the advance coefficient J .

Steering and Control

The performance of a ducted propeller at an angle of incidence is of interest for maneuvering. In the case of the shrouded screw, the forces are dependent on the interacting effects of the propeller and the ring wing. Lazareff¹⁸⁰ has discussed some aspects of this problem.

There are data available for the performance of Kort-nozzled propellers at nonzero steering angles. For example, Hawkins et al.¹²² present some results obtained from experiments performed at the University of Michigan. Figure 212 is a sketch showing the notation used here. The ducted propeller model was based on the Wageningen Ka 4-55 series propeller in a slightly altered Wageningen Nozzle 18. Curves of K_X , K_Y , etc., versus inflow angle θ are reproduced in Figure 213. The force and torque coefficients here are defined as usual.

$$\begin{aligned} K_X &= F_X / \rho n^2 D^4 \\ K_Y &= F_Y / \rho n^2 D^4 \\ K_Q &= Q / \rho n^2 D^5 \end{aligned} \quad (152)$$

where D = propeller, Q = propeller torque, and F_X and F_Y are defined in Figure 212.

The thrust of a ducted propeller may also be directed by means of rudders. Several configurations designed for pushboats are shown in Figure 214, reproduced from Oosterveld.¹⁷⁸

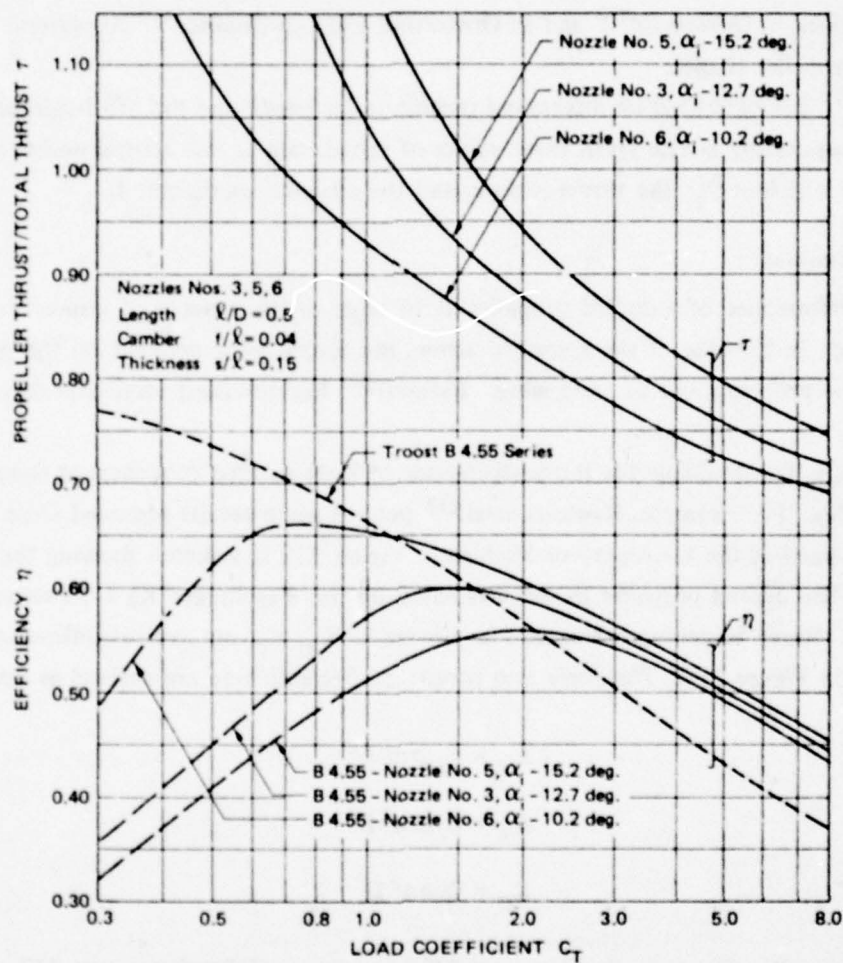
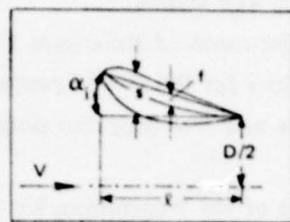
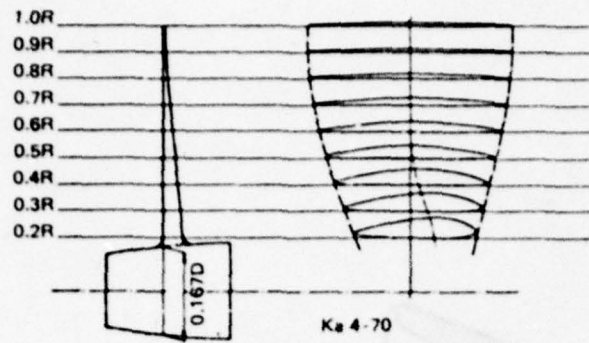


Figure 210 — Sample Data for Wageningen B 4-55 Propeller as a Ducted Screw and as an Open Screw

Strom-Tejzen's discussion of Reference 135.



PARTICULARS OF Ka 4-70 SCREW SERIES

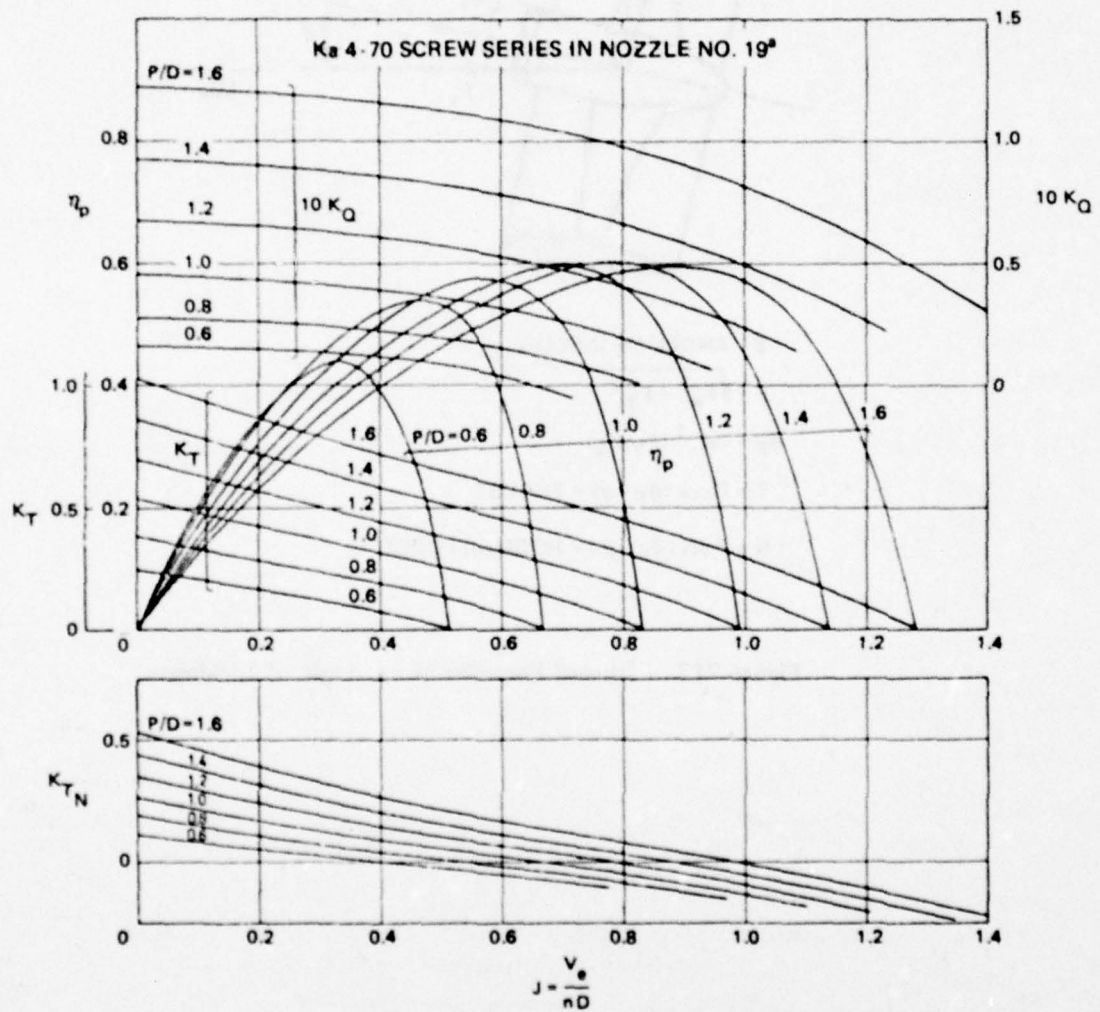
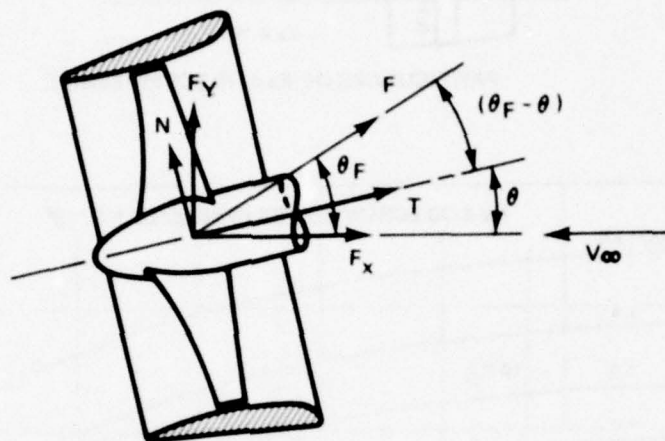


Figure 211 - Results of Open-Water Tests with Ka 4-70 Screw Series in Nozzle 19a
van Manen and Oosterveld.¹³⁵



θ = ANGLE OF INFLOW

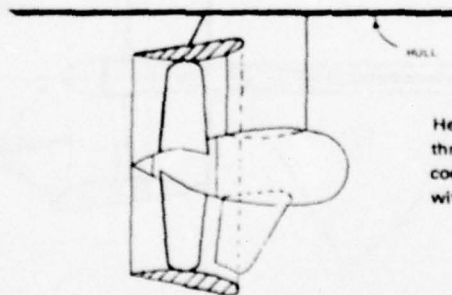
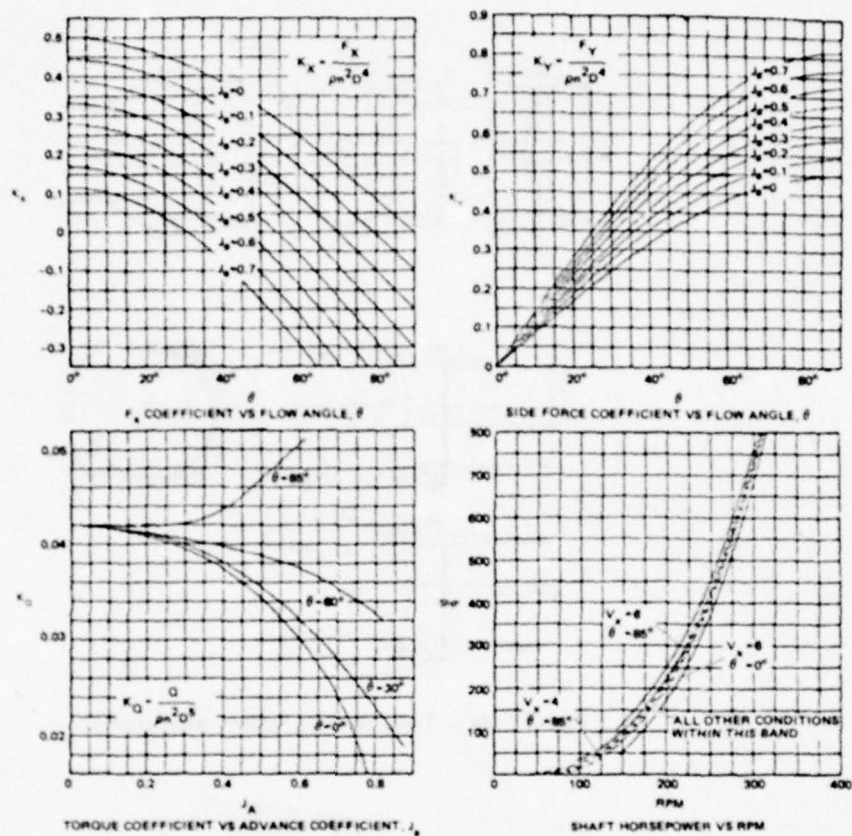
$$F = \sqrt{F_x^2 + F_y^2}$$

$$\theta_F = \tan^{-1} (F_y/F_x)$$

$$T = F \cos (\theta_F - \theta) = \text{THRUST}$$

$$N = F \sin (\theta_F - \theta) = \text{NORMAL FORCE}$$

Figure 212 — Ducted Propeller at an Angle of Incidence



Here, K_X and K_Y are the thrust and side force coefficients, respectively; with θ = steering angle.

Figure 213 - Ducted Propeller Performance at Various Incidence Angles

Hawkins et al. 122

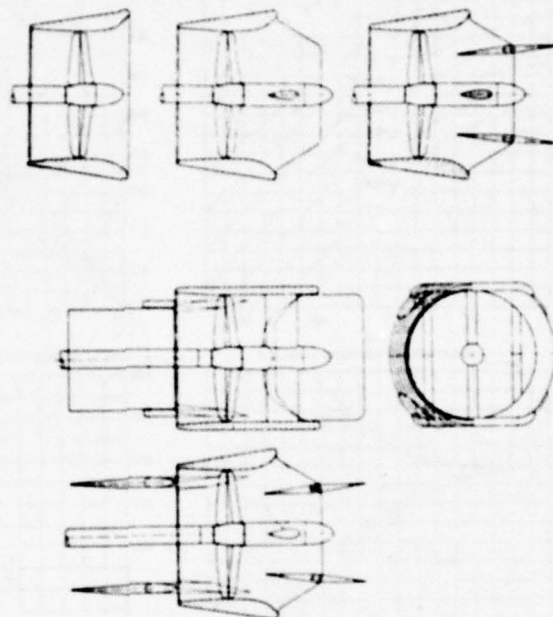


Figure 214a - Twin Steering-Rudder Arrangement

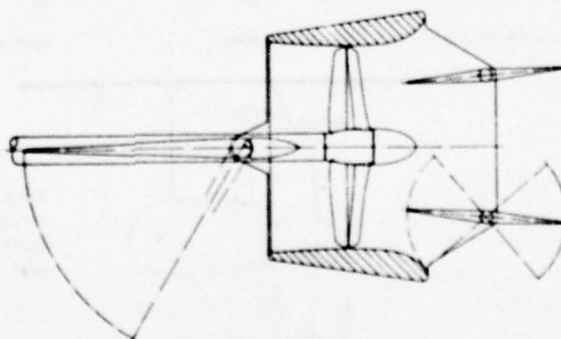


Figure 214b - Single-Rudder Arrangement for Pushboats

Figure 214 - Ducted Propeller Configurations with Rudders

Oosterveld¹⁷⁸

RING PROPELLER AND RELATED DEVICES

Several other devices similar to ducted propellers have been suggested for applications requiring large thrust loadings and low forward speeds.

For example, Oosterveld¹⁷⁸ discusses experiments performed with ringpropellers, ringpropellers in nozzles, and multiple nozzle-ringpropeller systems. These devices are shown in Figure 215. The ringpropeller features a ring fitted to the propeller blade tips which rotates *with* the propeller. The ringpropeller may also be operated within a shroud by providing a slot to accommodate the ring. The multiple nozzle arrangement in Figure 216 has the forward ring fixed with adjustable stator blades. Then, the after ring is attached to the blade tips and rotates with the screw.

Oosterveld¹⁷⁸ presents numerous diagrams of open water performance of these various devices. From these, it is concluded that the ringpropeller systems have lower open-water efficiency than do conventional ducted propellers. This is due mainly to the frictional drag on the rotating ring.

One interesting comparison of all three arrangements is given in Figure 217 for static thrusting conditions. The efficiency factor η_d is the static merit coefficient C

$$\eta_d = \frac{K_T^{3/2}}{\pi^{3/2} K_Q} = C \quad (153)$$

The figure shows the superior performance of the conventional ducted propeller Ka 4-70 in Nozzle 19A.

AUGMENTED DUCTED PROPELLER

Flow diffusion within the shroud increases the static thrust performance of a ducted propeller; see Figure 209. A jet-flap diffuser appears to be even more promising. It consists of an angled peripheral jet sheet blowing at the trailing edge of the duct. It can provide a rapid and efficient expansion of the propeller slipstream to a slower speed exhaust flow; see Figure 218b.

Morel and Lissaman⁶⁵ have presented static thrust comparisons between conventional thrusters and the same devices with jet-flap diffusers. For the conventional ducted propeller with effectively no diffusion or contraction of the slipstream, the thrust and power are

$$T_d = \rho S V_2^2 \quad (154)$$

$$P_d = \frac{1}{2} \rho S V_2^3 \quad (155)$$

where $S = \pi D^2/4$, D = propeller diameter, V_2 = uniform duct-exhaust velocity.

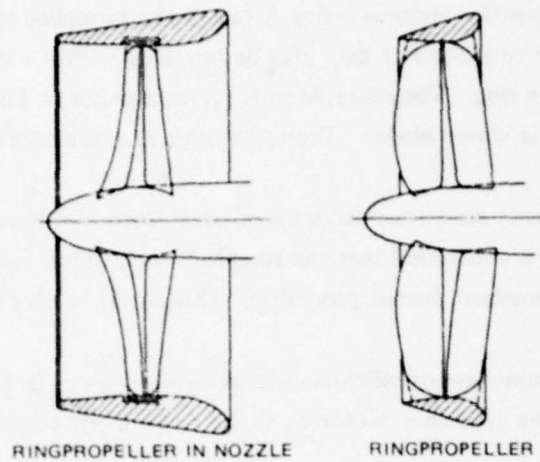


Figure 215 - Ringpropellers
Oosterveld¹⁷⁸

MULTIPLE NOZZLE-
RING PROPELLER ARRANGEMENT

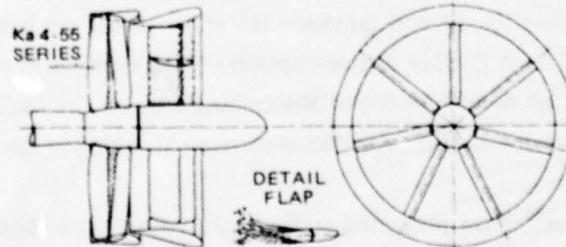


Figure 216 - Particulars of Multiple Nozzle-
Ringpropeller System
Oosterveld¹⁷⁸

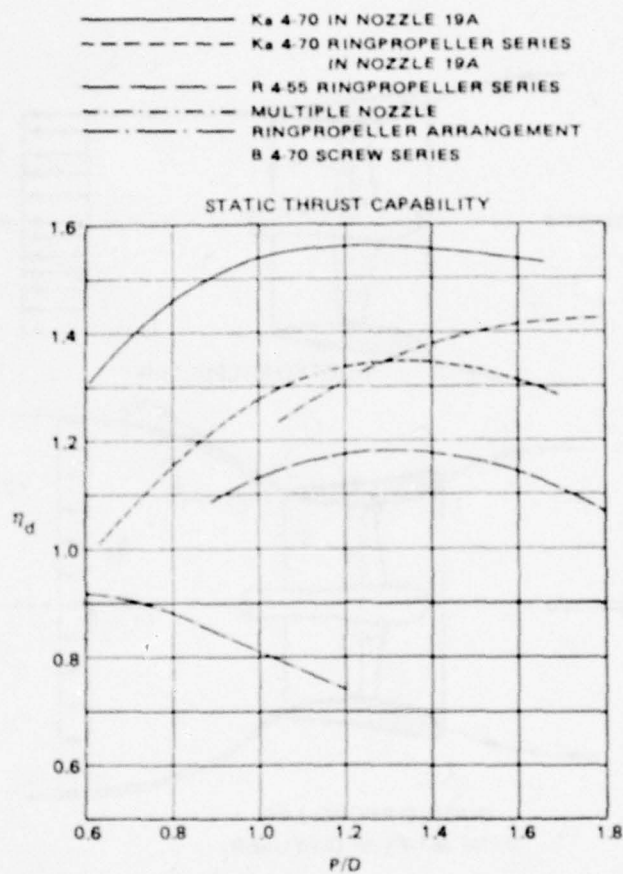


Figure 217 - Efficiency Factor η_d of B 4-70
Screw Series, Ka 4-70 Screw Series in
Nozzle 19A, and Different
Ringpropeller Series
Oosterveld¹⁷⁸

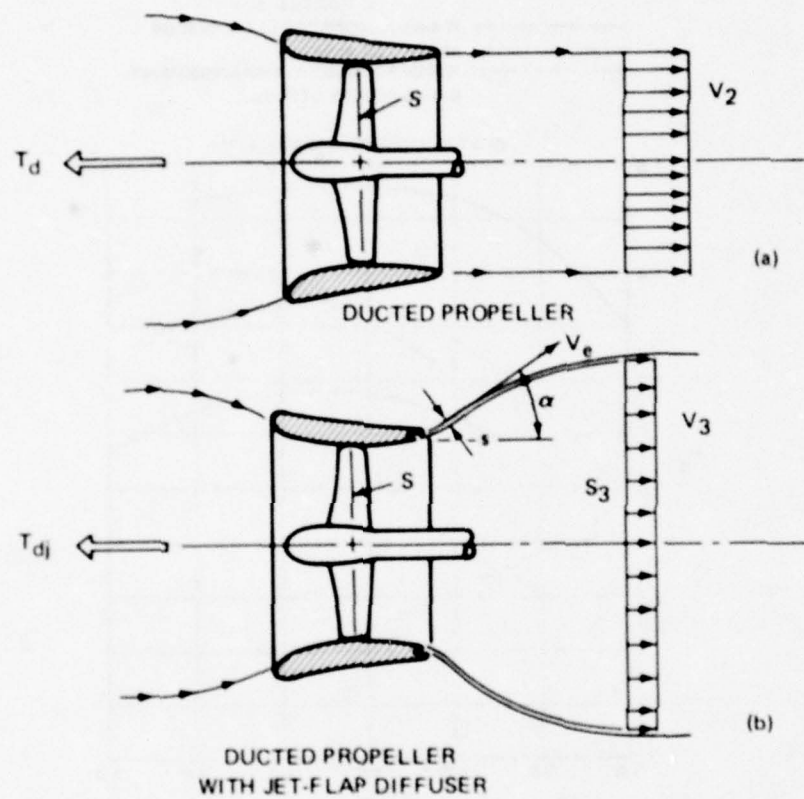


Figure 218 — Comparison between a Regular Ducted Propeller and One with Jet-Flap Diffusion

Morel and Lissaman.⁶⁵

For the ducted propeller with jet-flap diffusion, the idealized thrust and power are

$$T_{d_j} = \rho S V_3^2 (\sigma + C_J/2) \quad (156)$$

$$P_{d_j} = \frac{1}{2} \rho S V_3^3 \left(\sigma + \frac{C_J}{2} \frac{V_e}{V_3} \right) \quad (157)$$

where σ = diffusion parameter = S_3/S

V_e = jet exit velocity

C_J = external jet momentum coefficient

$$= \frac{2\pi s(D/2)\rho V_e^2}{\frac{1}{2}\rho\pi(D/2)^2 V_3^2} = \frac{8s}{D} \left(\frac{V_e}{V_3} \right)^2$$

s = thickness of jet sheet at exit of duct.

Note that the ideal static merit coefficient is

$$C = \frac{T_{d_j}^{3/2}}{P_{d_j} \sqrt{\rho S}} = 2\sigma^{1/2} \frac{(1 + C_J/2\sigma)^{3/2}}{\left(1 + \frac{C_J}{2\sigma} \frac{V_e}{V_3}\right)} \quad (158)$$

Lazareff¹⁸⁰ has tested the arrangement pictured in Figure 219. This is a "blown duct"; with slot-blowing — boundary layer control on the inner face of the duct and also on the rear part of the propeller hub. At the same power absorbed, the ratio of the blown-duct thrust performance to the unblown thrust was found to be ~ 1.18 . This order of magnitude increase is also predicted by the simple analysis of the jet-flap diffuser of Morel and Lissaman.⁶⁵

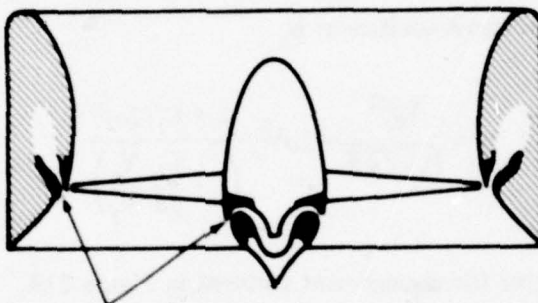
Note that the configuration of Figure 219 is not a true jet-flap diffuser. The jet sheet should be issued at the duct exit and at an angle to the centerline. Actual data for a jet-flap diffuser used on an ejector is presented, for example, by Alperin and Marlotte.¹⁴¹

ACTIVE RUDDER

The active rudder is a well-known marine application of directional ducted propeller. It consists of a small shrouded screw operating at the trailing edge of a ship rudder. Figure 220 is a schematic of a typical installation on a surface ship.

Brief discussions of some of the hydrodynamic characteristics of these devices are presented for example by Minsaas¹⁸¹ and Hawkins et al.¹²² The latter reference gives a simple example based on the thrust characteristics of a standard series ducted propeller.

As indicated in the sketch of Figure 221, the effect of the ducted propeller is to direct the flow parallel to the rudder centerline. Thus the inflow to the ducted propeller is at an



BLOWING SLOTS FOR BLC

Figure 219 — Blown-Duct Shrouded Propeller

Tested by Lazareff.¹⁸⁰

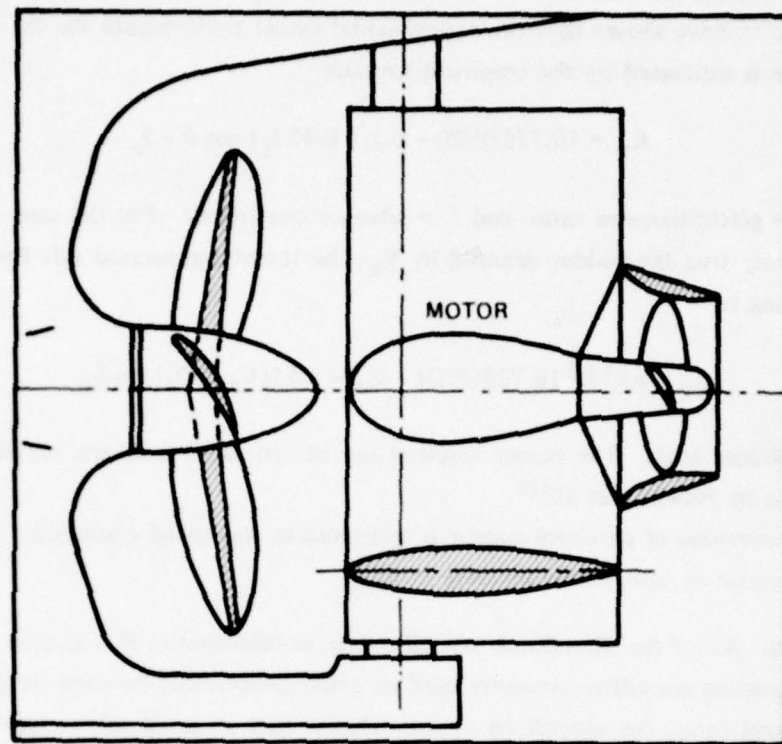


Figure 220 – Arrangement of Conventional Powered Rudder behind the Screw of a Surface Ship

Minnaas 181

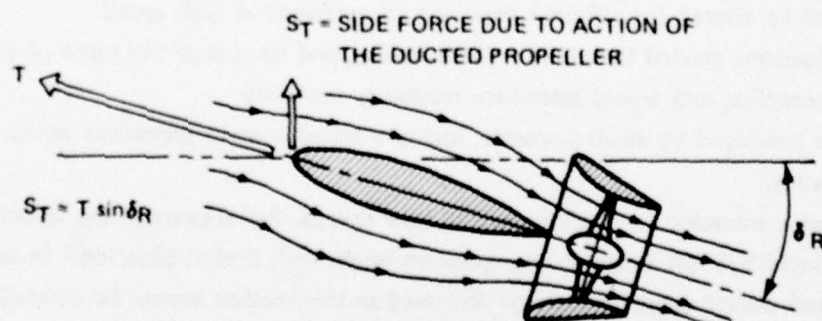


Figure 221 – Flow and Geometry of the Active Rudder

angle $\theta = 0$. It is possible to estimate the steering force S_T provided by the ducted screw. Hawkins et al.¹²² have shown that the experimental thrust performance for the Wageningen Ka 4-55 screw is estimated by the empirical formula

$$K_T = [0.725(P/D) - 0.2 + 0.45 J_a] \cos \theta - J_a \quad (159)$$

where (P/D) = pitch/diameter ratio, and J_a = advance coefficient. For the case of $\theta = 0$ and with the velocity past the rudder denoted by V_R , the thruster-generated side force available for maneuvering is

$$S_T = \rho n^2 D^4 [0.725(P/D) - 0.2 - 0.55(V_R/nD)] \sin \delta_R \quad (160)$$

where δ_R = rudder angle. The power required can be estimated from the curves for K_Q versus J_a curves given by Hawkins et al.¹²²

The effectiveness of an active rudder is restricted to low-speed operation. At high speeds the duct can cause an undesirable increase in drag.

DISCUSSION: All of the directional propeller devices discussed in this section about directional thrusters are either presently used or could conceivably be used for producing auxiliary control forces for specialized marine vehicles such as small submersibles, drill rigs, harbor craft, etc. A small retractable, directional, ducted propeller is an eminently practical device as a slow-speed-propulsion unit for a submarine. However, for submarines as they are presently configured, these devices are not as suitable for *control* purposes as are the general class of lifting surfaces discussed in Chapter 1. The reasons for this are:

1. Although the devices would be extremely effective at slow speed, say, for hovering near the surface in a heavy seaway, their drag at high speeds would be high, unless the pitch of the blades could be altered for efficient thrusting (propulsion) at high speed.
2. The mechanisms needed to orient a tilt-duct, say, and to change the pitch of the blades would be complex, and would introduce reliability problems.
3. The noise produced by small-diameter, highly pitched control propellers would probably be excessive.

For a submarine intended to operate *only* at slow speeds, the arguments are no longer applicable, and simple V/STOL-inspired arrangements might well find application. In such a case, the augmented ducted-propeller devices discussed in this section should be carefully explored because of their potentially superior hydrodynamic performance. Also, blowing flow control on the propeller blades could be used to alter the effective blade pitch by simple valving instead of a complex mechanism.

Unless there is some special reason for moving a submarine *sideways* at zero or low speed, directional propeller device cannot compete with a flapped- or lift-augmented lifting surface for producing a lateral control force over a range of speeds and with minimum mechanical complexity.

NAME: Directional Plain Waterjet.

DEFINITION AND OPERATION: The trainable waterjet is another form of a reaction thruster analogous to the directional propeller discussed in the previous paragraphs. In fact, the ducted propeller could be thought of as an axial flow pump particularly suited to a large flow rate and a relatively low pump head.

The most compact steerable waterjet consists of a short tube with an inlet, internal ducting leading to an appropriate type of pump, and a jet discharge nozzle aligned with the inlet. Such a nacellelike jet can be mounted on a fixed or retractable strut, or on hinges at the tip ends of a lifting surface.

Here, the plain waterjet refers to the simplest form of the device. It uses water as the working fluid and features no special augmentation schemes to improve the thrust performance. Several augmentation concepts are discussed in separate subsections.

Figure 222 shows an aligned nacellelike waterjet configuration intended for use as a propulsor on a high-speed hydrofoil boat.¹⁸² It has a centrifugal pump, for the large head required at high speed, and very short stretches of internal ducting.

Another compact configuration is the S-type jet propulsor shown in Figure 223.¹⁸³ In this case, the vectoring of the exhaust jet is accomplished with a swiveling steering conduit and vanes. Although the bends in the internal ducting tend to increase the internal head loss, this arrangement would not require a Z-drive transmission from the prime mover to the pump.

The references by Brandau,¹⁸⁴ Kruppa et al.,¹⁸⁵ and Kulikov et al.¹⁸⁶ are examples of useful surveys of the waterjet technology and of the critical problem areas. Each of these contain long lists of source material.

THRUST AND POWER ESTIMATES

Estimates of jet performance are provided by the use of the momentum theory and by including some form of assumed system losses. Figure 224 is a sketch of an idealized waterjet and the variation of the specific energy through the system. By using the notation given, the thrust delivered and fluid power absorbed are expressed by

$$T = \rho Q(V_j - V_o) \quad (161)$$

$$P_f = \frac{1}{2} \rho Q(V_j^2 - V_o^2) + \rho g Q \cdot H_L \quad (162)$$

where V_o = uniform inflow velocity, V_j = jet velocity, Q = volume flow rate through the system, and H_L = total system internal head loss due to inlet, diffusion, ducting, and nozzle losses — measured in units of *length*.

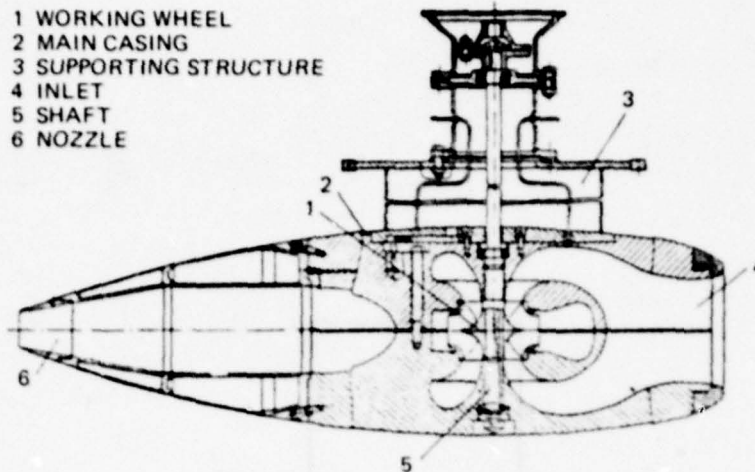


Figure 222 - A Waterjet Propulsion Unit Having a Centrifugal Pump

Bashun et al.¹⁸²

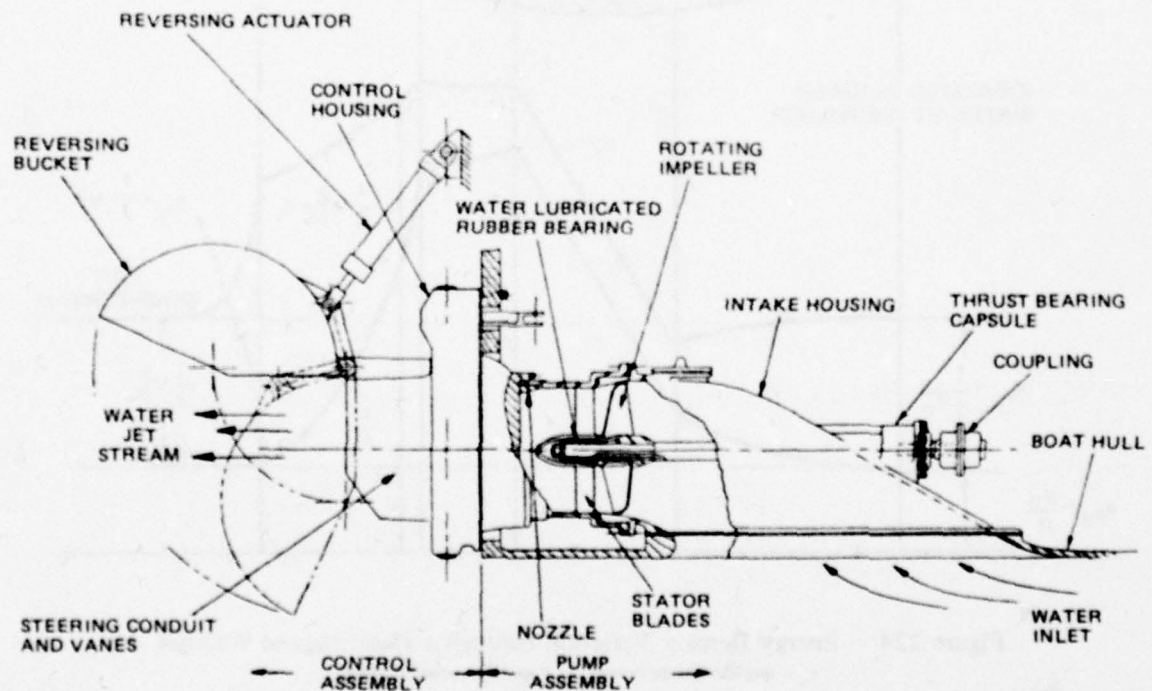


Figure 223 - Cross Sectional View of Flush-Mounted Waterjet

Delao¹⁸³

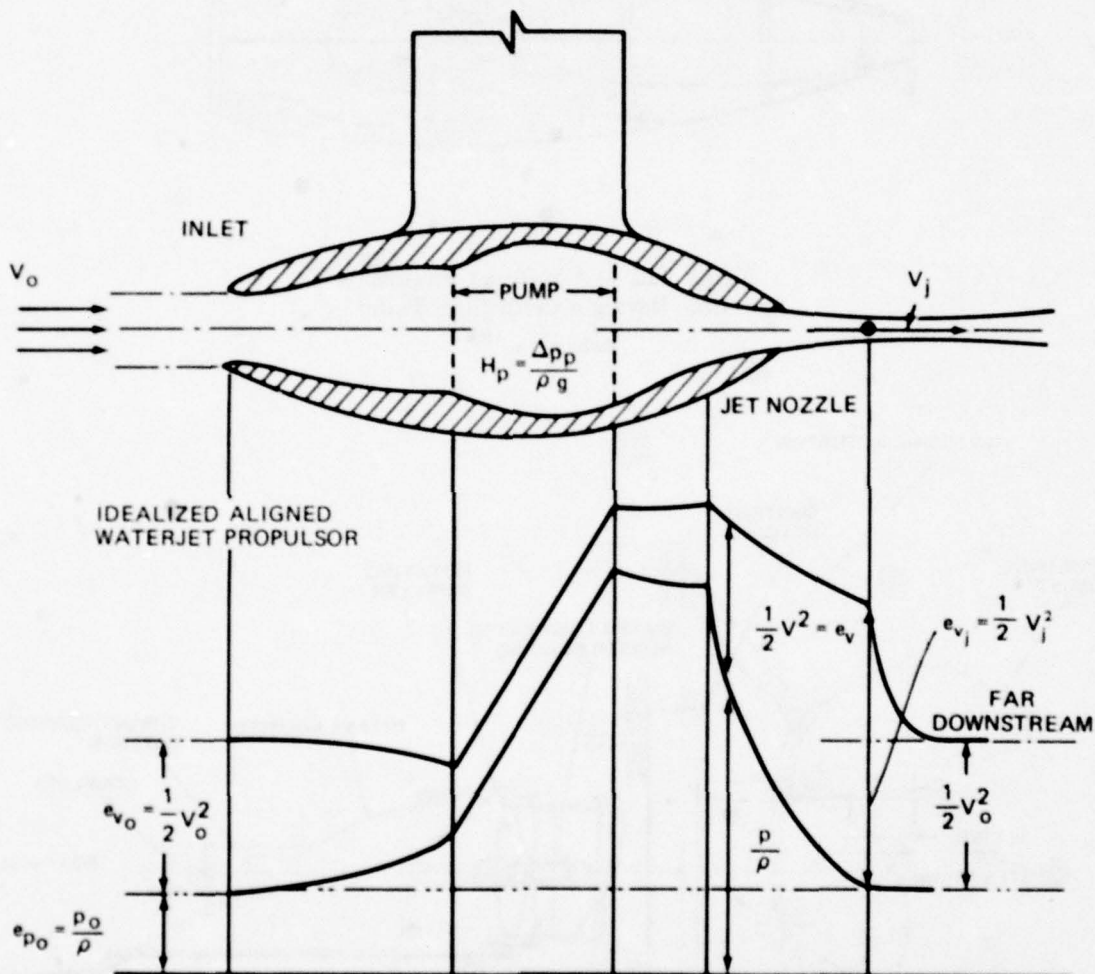


Figure 224 – Energy Density Variation through a Plain Aligned Waterjet
 e_v = specific kinetic energy, e_p = specific pressure energy

If the head-loss term is neglected, the ideal, or Froude, jet efficiency $\eta_j = T \cdot V_o / P_f$ is simply

$$\eta_j = 2/(1 + V_j/V_o) \quad (163)$$

This formula is impossibly inaccurate but it does establish an ideal upper limit to η_j as a function of the ratio $k = V_j/V_o$. The thrust equation is correct, of course, and Figure 225 shows curves of the thrust-to-area ratio $T/\rho A_j$ plotted on a graph of V_j versus V_o . The dotted lines are contours of the ideal efficiency η_j .

Now, the real jet-system propulsive efficiency is defined by Brandau¹⁸⁴ to be $\eta_{jpr} = \eta_j \cdot \eta_{system}$ and is expressed as

$$\eta_{jpr} = \frac{TV_o}{P_f} = \frac{2(k-1)}{k^2 + 2gH_L/V_o^2 - 1} \quad (164)$$

There are various ways of representing the overall head loss H_L as proposed by several authors. For example, three different expressions are included here with the corresponding coefficient form of the losses

Levy¹⁸⁸: $H_L = K_L V_j^2/2g$ (defines K_L)

$$\eta_{jpr} = \frac{2(k-1)}{[k^2(1 + K_L) - 1]} \quad (165)$$

Johnson¹⁸⁹: $H_L = K V_o^2/2g$ (defines K)

$$\eta_{jpr} = \frac{2(k-1)}{[k^2 - 1 + K]} \quad (166)$$

Kruppa, et al.¹⁸⁵: $H_L = \xi' V_o^2/2g + \xi_j V_j^2/2g$

$$\eta_{jpr} = \frac{2(k-1)}{k^2(1 + \xi_j) - 1 + \xi'} \quad (167)$$

In the last case, the nozzle loss ξ_j is isolated from the total of the other internal losses ξ' and is referred separately to the jet velocity head. This third form of H_L by Kruppa et al.¹⁸⁵ is particularly well suited to finding the best operating jet velocity ratio.

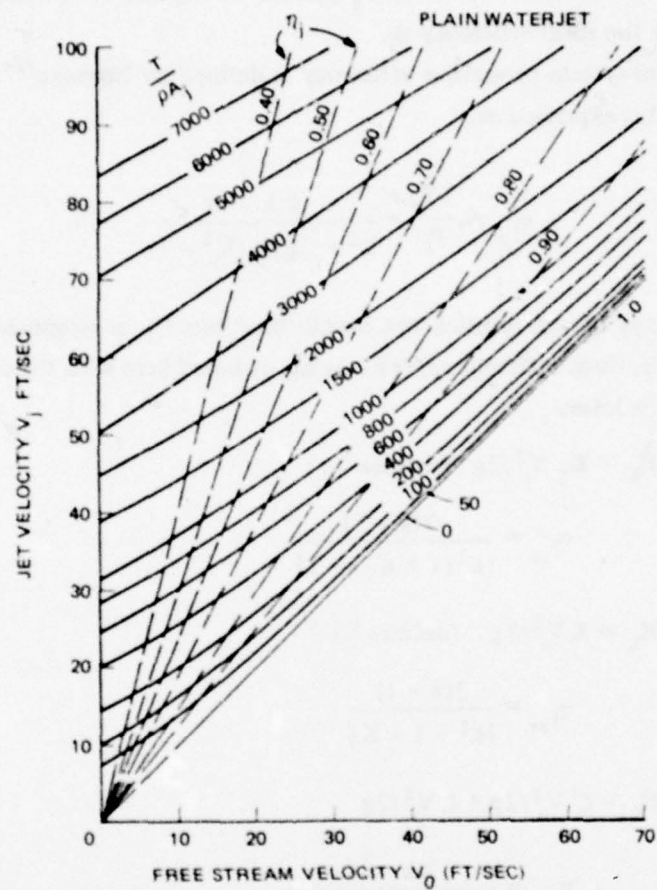


Figure 225 - Contours of $T/\rho A_j$ versus V_j and V_0
for Plain Waterjet

Kim¹⁸⁷

In Figure 226, the efficiency η_{jpr} is plotted versus k for various constant values of the total loss coefficient $K = H_L / (V_o^2 / 2g)$. This plot shows the marked effect losses have on the more accurate estimate of jet efficiency, especially in the range of low forward speeds.

OPTIMUM VELOCITY RATIO

With reasonable values of loss coefficients, it is possible to choose the value of $k = V_j / V_o$ for maximum jet-system efficiency. For purposes of comparison Table 8 summarizes three of the published procedures for determining (V_j / V_o) .

TABLE 8 – COMPARISON OF LOSS COEFFICIENT

Modified from Kruppa, et al.

Source	Definition of Overall Head Loss H_L	Assumptions
Levy	$K_L V_j^2 / 2g$	$k^2 \xi' = \text{const}, \quad \xi_j = \text{const}$
Johnson (1964)	$K V_o^2 / 2g$	$\xi' = \text{const}, \quad k^2 \xi_j = \text{const}$
Kruppa et al. (1968)	$\xi' V_o^2 / 2g + \xi_j V_j^2 / 2g$	$\xi' = \text{const}, \quad \xi_j = \text{const}$
Note: $\xi' = \text{sum of internal loss coefficients, except jet nozzle.}$ $\xi_j = \text{jet nozzle loss coefficient.}$ $k = (V_j / V_o).$		

For example, the result obtained by Kruppa et al.¹⁸⁵ for the optimum value of $\mu = k^{-1}$ is

$$\mu_{\text{opt}} = \left(\frac{V_o}{V_j} \right)_{\text{opt}} = \frac{1 + \xi_j}{1 + \xi'} \left[1 - \sqrt{1 - \frac{1 - \xi'}{1 + \xi_j}} \right] \quad (168)$$

when the inflow velocity V_o is uniform

Clearly, this result for μ_{opt} is only as good as the accuracy of the loss coefficients ξ' and ξ_j . It is possible to estimate these from the geometry of the system. For example, Kim¹⁸⁷ has presented a useful discussion of loss predictions for the various components of a waterjet layout.

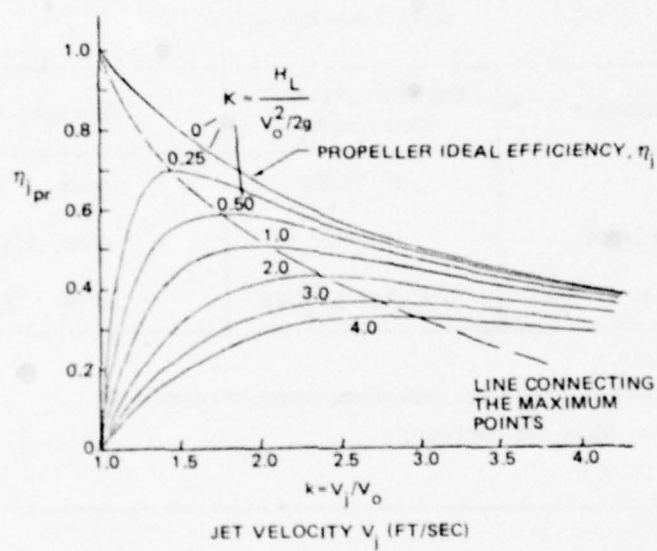


Figure 226 – Jet Efficiency versus Jet-Velocity Ratio for Various Nondimensional Loss
Kim¹⁸⁷

FLOW RATE AND HEAD

If the optimum velocity ratio $k_{opt} = 1/\mu_{opt}$ is known for a given system, then the required pump-design parameters, flow rate Q and head H , are determined from the thrust required and the forward speed. When the inflow is a uniform velocity V_o ,

$$Q = T/\rho V_o (k_{opt} - 1) \quad (169)$$

$$H = \frac{V_o^2}{2g} [k_{opt}(1 + \zeta_j) - 1 + \zeta'] \quad (170)$$

Note that the pumping capacity varies as V_o^{-1} , and the required head varies as V_o^2 .

Selection of the proper pump is based on the relative magnitudes of flow rate Q and head H as measured by the specific speed

$$n_s = n \frac{Q^{1/2}}{(gH)^{3/4}} \quad (171)$$

where n = pump rotational speed. In general, large values of n_s require axial-flow pump designs to achieve the best pump efficiency; low values of n_s require radial or centrifugal pumps. Intermediate values of n_s require mixed-flow pump types.

Discussions of the pertinent details of pump type and specific speed are given for example in Stepanoff,¹⁹⁰ Wislicenus,¹⁹¹ Johnson,¹⁸⁹ Kruppa et al.,¹⁸⁵ and Witte.¹³⁸

The recent work by Wislicenus¹⁹¹ is an extended treatment of the details of the design of plain waterjet systems. The problem areas outlined previously, plus many others, are discussed in depth there. A fascinating survey that covers plain waterjets as well as a great variety of related propulsion schemes and augmented waterjets is presented by Schuster et al.¹⁹²

STATIC PERFORMANCE

In the present context, the most interesting modes of jet operation are the static and near-static conditions. For this regime, the analysis of static thruster performance by Witte¹³⁸ is applicable. Consider the sketches of aligned jet propulsors in Figure 227. These are operating statically, that is, with the forward velocity $V_o = 0$. With the notation indicated in the figure, the pressure increase across the pump for either device is

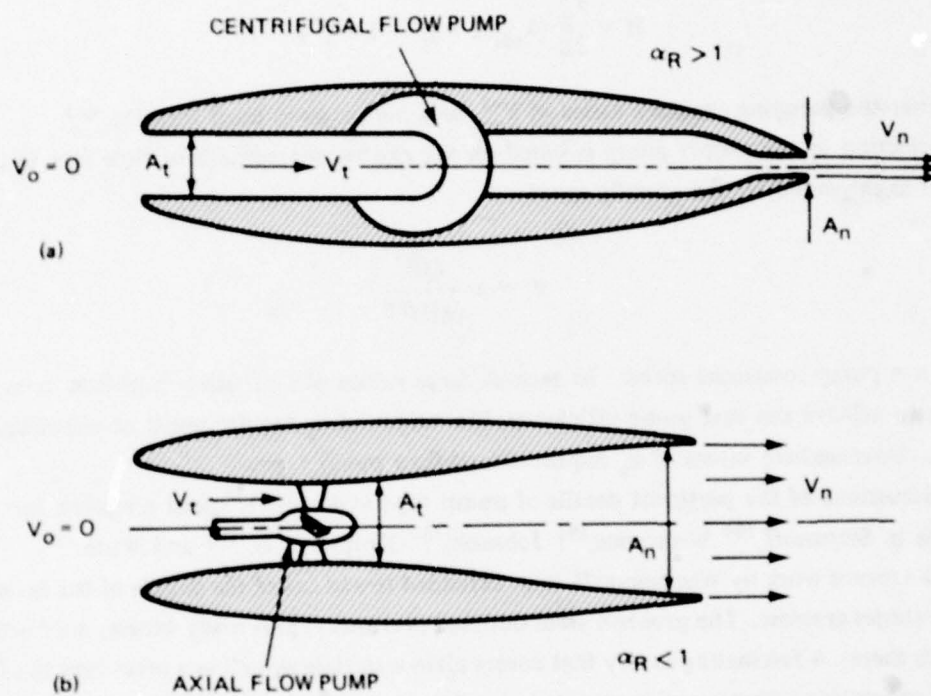


Figure 227 – Aligned Waterjet Propulsors in Static Operation

$$\alpha_R = \text{area ratio} = A_t / A_n$$

$$\rho g \cdot \Delta H = \rho g H_L + \frac{1}{2} \rho V_t^2 \quad (172)$$

$$\rho g H_L = \Delta p_L = (\alpha_R^2 - 1)(1 + \xi_n) \frac{1}{2} \rho V_t^2 + \xi_t \frac{1}{2} \rho V_t^2 \quad (173)$$

where ξ_n, ξ_t are the loss coefficients of the nozzle and tube, respectively, and α_R = area ratio = A_t/A_n .

The thrust developed and fluid power are

$$T = \rho (V_t A_t) V_t \cdot \alpha_R, \quad P_f = \rho g (\Delta H) A_t V_t \quad (174)$$

Then the static merit coefficient is a function of the area ratio α_R

$$C = \frac{T^{3/2}}{P_f \sqrt{\rho A_t}} = \frac{2 \alpha_R^{3/2}}{[(\alpha_R^2 - 1)(1 + \xi_n) + \xi_t + 1]} \quad (175)$$

This function is plotted in Figure 185 for $\xi_n = 0$, and it shows that the best *static* thrust per unit power can be obtained with diffusing tube nozzles ($\alpha_R < 1$), rather than accelerating tube nozzles ($\alpha_R > 1$).

Witte¹³⁸ shows that the specific speed n_s is also a simple function of α_R

$$n_s = n \cdot (\text{const}) \cdot \frac{A_t^{1/2}}{V_t} \left\{ \frac{1}{[(\alpha_R^2 - 1)(1 + \xi_n) + \xi_t + 1]^{3/4}} \right\} \quad (176)$$

If a diffusing tube nozzle ($\alpha_R < 1$) is chosen to obtain a large static thrust-to-power ratio, then this demands a large specific speed n_s . Large values of n_s require axial flow pumps as pictured in Figure 227b. An accelerating tube nozzle ($\alpha_R > 1$) is consistent with centrifugal pumps (Figure 227a) but the static thrust-to-power ratio that can be achieved is inferior to the case of $\alpha_R < 1$.

DISCUSSION: It may be concluded that the best form of *plain* waterjet propulsor for static and low-speed operation is one with an axial flow pump. The Kort nozzle-ducted propeller is an excellent choice for such a "pump"; hence, the conclusions relating to the application of directional propellers apply here directly.

NAME: Directional Augmented Waterjets.

DEFINITION AND OPERATION: This section is devoted to a number of propulsor concepts that are related to the basic simple waterjet. These devices each involve special features intended to *augment* the thrust performance of the waterjet, given a diameter and power available. The subcategories included here are:

1. Ejector and Jet-Flap Diffuser Ejector
2. Bypass Systems
3. Two-Phase Hydropropulsers
4. Psuedoblade Propeller

EJECTOR AND JET-FLAP DIFFUSER EJECTOR

The low-specific-speed, centrifugal-pump system is not the best choice for the plain waterjet operation at zero and low forward speeds. However, as is pointed out by Witte,¹³⁸ centrifugal pumps tend to be more compact and less expensive than axial flow pumps. It is therefore worthwhile considering techniques of augmenting the performance of a converging-nozzle, low n_s system.

Using the converging-nozzle jet as the primary thruster, the ejector or the ejector with jet-flap diffusion are two devices that are adaptable to the waterjet geometry and are known to give thrust augmentation. The thrust and power performance of these concepts are discussed elsewhere; see Figure 189 and Equations (124) through (130). Figure 228 reproduced from Morel and Lissaman,⁶⁵ illustrates the ideal relative thrust values obtainable with these thruster concepts at the same total power consumed.

Experimental support for the ejector concept can be found, for example, in Fancher¹⁹³ and in several references cited by McCormick.³ Fancher¹⁹³ also discusses some features of a "hypermixing" nozzle that improves the mixing process between the primary jet and the entrained flow; see Figure 229. Use of this special nozzle allows an improved thrust augmentation for a solid-wall diffuser as well.

Experimental evidence for the ejector with jet-flap diffusion can be found in Alperin and Marlotte.¹⁴¹ The greatest appeal of the jet-flap diffuser is the possibility it provides for reducing the bulk, especially the length, of a diffusing ejector.

BYPASS SYSTEMS

Another approach to the problem of augmenting the thrust of a plain jet issued out of a converging nozzle is the use of bypass systems. These are combinations of fan and jet, and two types are shown in Figure 230.

Using the notation in the figure, the thrust of the plain jet is $T_t = \dot{m}_t V_j$, where \dot{m}_t = mass flow rate through the jet. If the exhaust velocity at the exit of the turbine V_{jte} is



Figure 228a - Plain Converging Jet

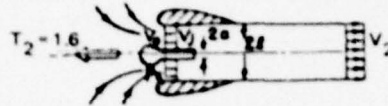


Figure 228b - Constant-Area-Mixing-Duct Ejector

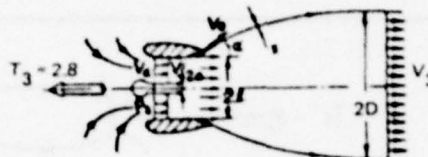


Figure 228c - Ejector with Jet-Flap Diffuser

Figure 228 - Comparison of Relative Thrust Values at Constant Power

Morel and Lissaman.⁶⁵

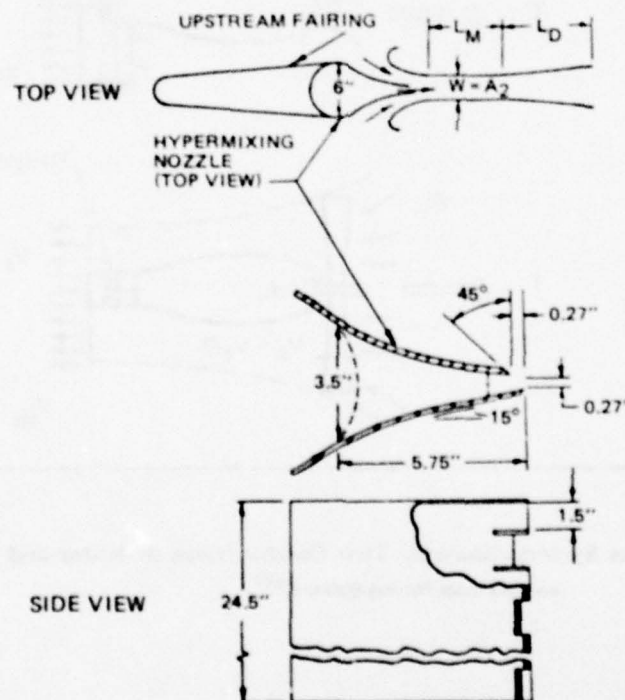


Figure 229 - Ejector Cross Section and Details of Hypermixing Nozzle

Fancher¹⁹³

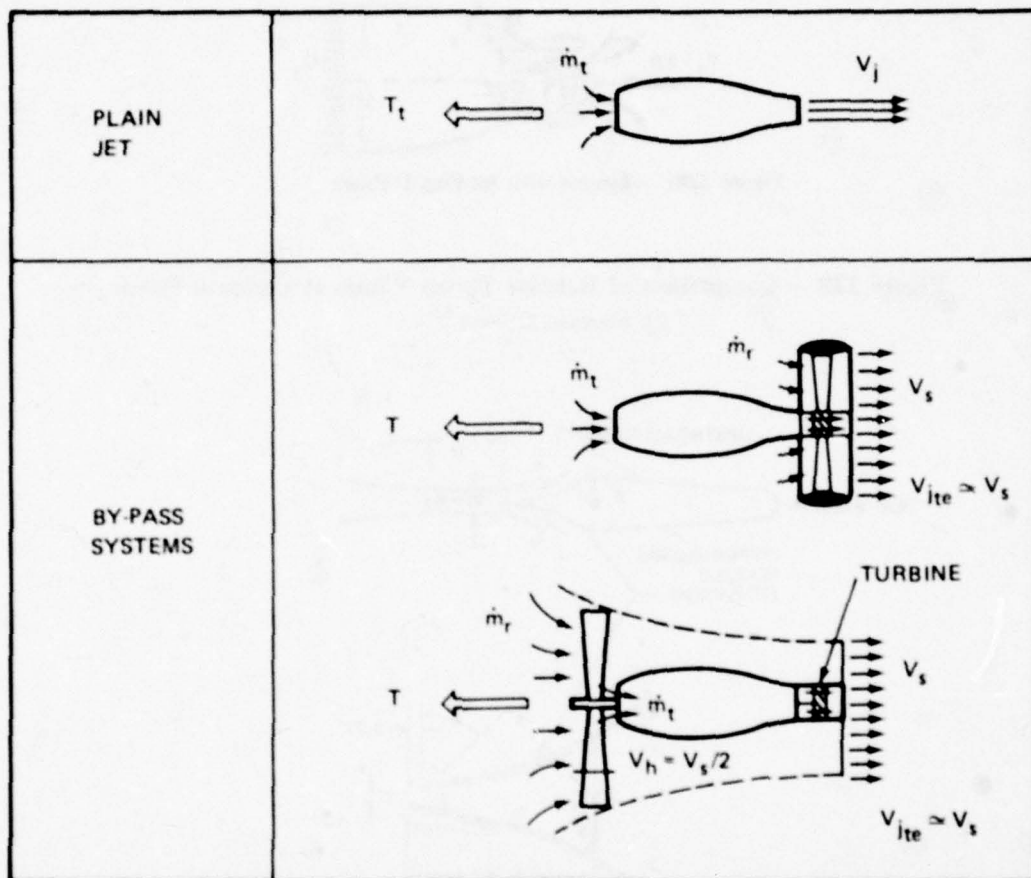


Figure 230 – Bypass Systems Showing Two Combinations of Rotor and Jet

Adopted from Poisson-Quinton.¹⁴⁶

equal to the slipstream velocity V_s , the thrust of the bypass devices is

$$T = (\dot{m}_t + \dot{m}_r) V_s \quad (177)$$

where \dot{m}_r = mass flow rate through the rotor of ducted fan. Then, the thrust augmentation ratio is

$$\frac{T}{T_t} = \left(1 + \frac{\dot{m}_r}{\dot{m}_t} \right) \frac{V_s}{V_j} \quad (178)$$

where the bypass ratio is

$$\frac{\dot{m}_r}{\dot{m}_t} = \eta_t \cdot \eta_a \cdot \left[\left(\frac{V_j}{V_s} \right)^2 - 1 \right] \quad (179)$$

with η_t = power-turbine efficiency and η_a = bypass hydrodynamic efficiency. These concepts work extremely well in air; however, in water the cumulative efficiency involving turbine, rotor, and mixing losses would probably be poor. A free or ducted propeller alone would have a superior efficiency.

TWO-PHASE HYDROPROPULSORS

The basic idea behind the operation of all two-phase hydropropulsors can be outlined as follows: water enters the inlet of the jet and is diffused to increase its static pressure. A larger pressure head may be supplied by a pump. Following this pressure increase, a gas is introduced into the water stream in such a way that good mechanical mixing occurs. What should result is a frothy mixture of small, evenly distributed bubbles. Differences in the various types of multiphase propulsors have to do with the type of gas, its temperature, and the method of introducing the gas. If the gas is hot, then even though good mechanical mixing of the bubbles is still necessary, good thermal mixing is undesirable because the large heat capacity of water can quickly cool the gas temperature and create large thermal energy losses.

After leaving the mixing section, the low-density, high-pressure froth is accelerated in a nozzle; then it is expanded to the ambient pressure. The expansion of the lower density and compressible mixture occurs under the action of a negative pressure gradient to produce an exhaust velocity that is sufficiently higher than the inflow velocity to create a thrust. Another way to state this is that the expanding gas bubbles of the mixture do work on the water, imparting additional momentum to the stream, to help expel it from the nozzle.

The whole process resembles a turbojet engine in air, where the low-density compressible mixture is formed by high-temperature combustion. In an air jet engine, the fuel mass-flow

rate adds significantly to the thrust; whereas, in a water and gas mixture, the mass flow rate of the water is considerably more important.

Pallabazzer¹⁹⁴ has presented a survey of some of these propulsor types and a discussion of the performance of different forms of waterjets.

The most informative article on two-phase hydrothrusters is the review paper by Muench and Garrett¹⁹⁵ which also gives some general results for the mist-jet concept, or water-augmented air jet. The latter has been proposed for high-speed, surface-ship propulsion.

Several variations on the main theme of two-phase thruster are mentioned as follows, along with sample references. However, only one of the propulsors is singled out here for a brief outline of its thrust performance results.

Air-Augmented Waterjet

In the case of an air-augmented hydrojet, the injected gas is high-pressure air, not necessarily heated; this air is introduced through slots into the mixing chamber of the waterjet. There are two basic types: pump-driven jet and ram jet; see Figure 231.

Pump-Driven, Air-Augmented Waterjet. An analysis of the thrust of an air-augmented waterjet is given by Amos et al.¹⁹⁶ The basic geometry of an aligned waterjet with air injection is shown in Figure 232. Using conservation equations of mass, momentum, and energy and with a separated-flow – two-phase analysis of the bubble mixture within the nozzle, some performance curves have been generated. The total thrust of the augmented waterjet is

$$T = \dot{m}_w (U_e - U_\infty) + \dot{m}_g V_e + A_e (p_e - p_\infty) \quad (180)$$

where \dot{m}_w = mass flow rate of water
 \dot{m}_g = mass flow rate of air
 U_e, U_∞ = water velocities at the nozzle exit and ambient
 V_e = air-bubble velocity at nozzle exit
 A_e = exit area
 p_e, p_∞ = exit and ambient pressures, respectively.

Figure 233 shows the thrust augmentation ratio versus the pressure ratio of pump outlet to ambient.

Figures 234 and 235 show, respectively, the variation of thrust-augmentation ratio versus the mass-flow ratio ν and versus the temperature ratio of injection air to water. The latter plot indicates the weak effect of elevated air temperatures on the thrust performance.

An interesting variation of this device would be an air-augmented turbojet. A turbine positioned in the exhaust could help drive the inlet pump. This is shown in Figure 236.

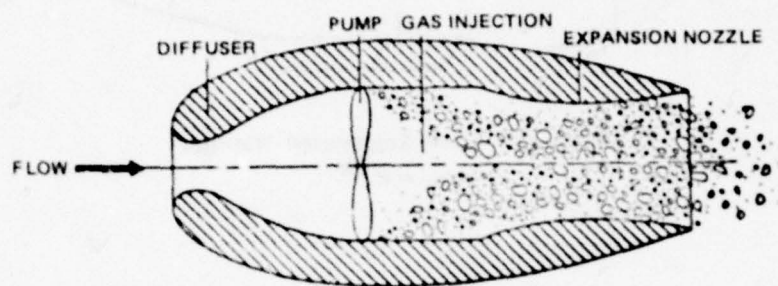


Figure 231a - Gas Boost of a Waterjet or Propjet

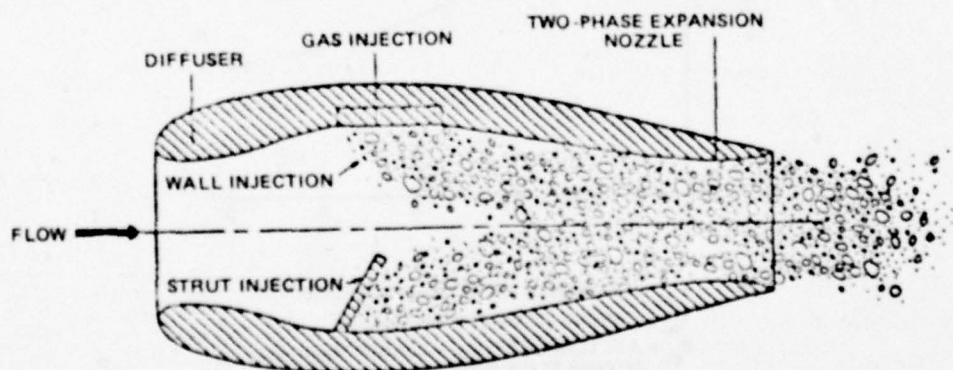


Figure 231b - Hydramjet

Figure 231 - Two Basic Types of Air-Augmented Waterjet Thrusters
Muench and Garret, 195

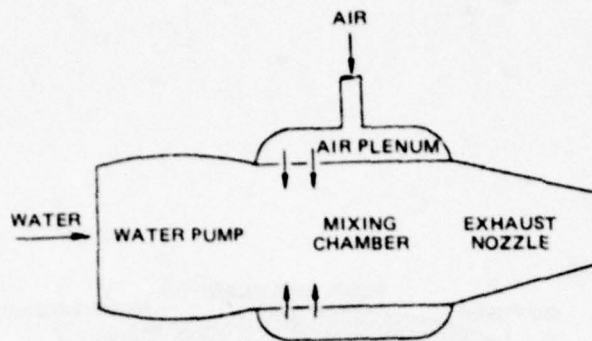


Figure 232 – Air-Augmented Waterjet
Amos et al.¹⁹⁶

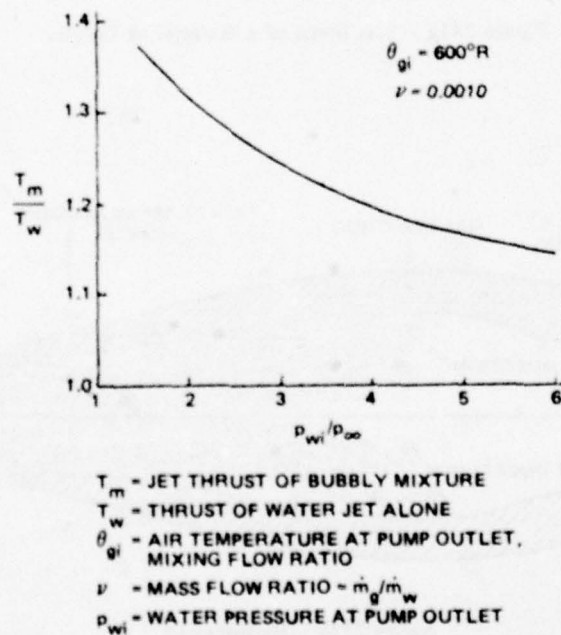


Figure 233 – Variation of Thrust Augmentation with Pump-Outlet Pressure
Amos et al.¹⁹⁶

AIR-AUGMENTED WATER JET

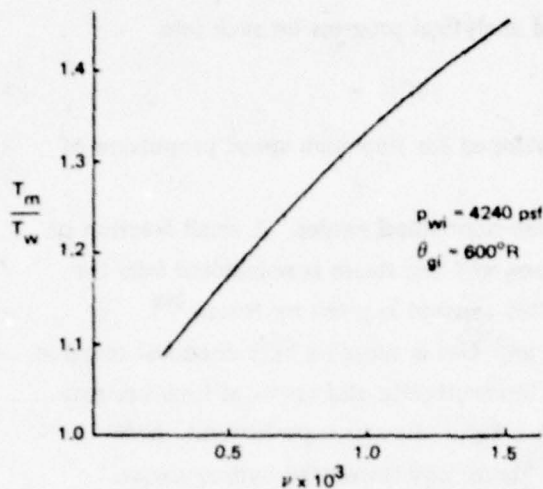


Figure 234 - Variation of Thrust Augmentation with Mass Flow Ratio
Amos et al.¹⁹⁶

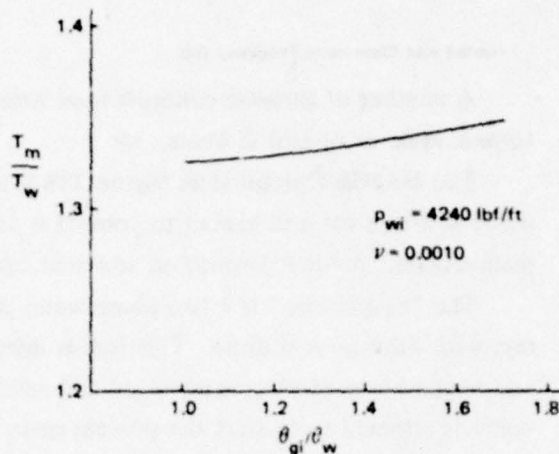


Figure 235 - Variation of Thrust Augmentation with Air Injection Temperature
Amos et al.¹⁹⁶

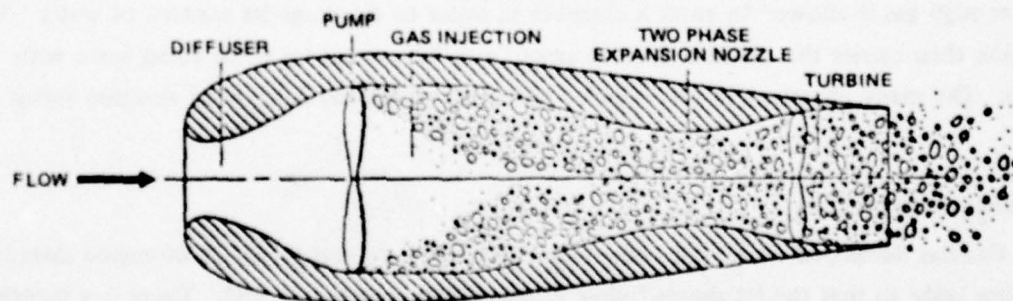


Figure 236 - Hydroturbojet
Sketch from Muench and Garret.¹⁹⁵

Air-Augmented Ramjet. The ramjet version of the air-augmented hydrojet has no pump but depends on diffusion alone to recover sufficient pressure for its operation. Muench and Garrett¹⁹⁵ relate an interesting history of this concept. Figure 237 shows a sketch of a ramjet configuration developed at Netherlands Ship Model Basin. Oosterveld and van Oossanen¹⁹⁷ have given a recent survey of the experimental and analytical progress on such jets.

Heated and Chemically Produced Gas

A number of thruster concepts have been developed for very high speed propulsion of torpedoes or of hydrofoil boats.

The MARJET pictured in Figure 238 is a steam-augmented ramjet. A small fraction of water is drawn off and heated to convert it to steam, and the steam is re-injected into the main stream. A brief description and analysis of this concept is given by Rosen.¹⁹⁸

The "hydropulse" is a two-phase water pulse jet. Gas is supplied by a chemical reaction, say, with lithium or sodium. This fuel is injected intermittently and reacts at high pressure and temperature, producing much gas and steam. A tubeful of water is pushed out. New water is rammed in to start the process again.¹⁹⁹ Figure 239 shows the hydropulsejet.

Another type of hydramjet is the "hydroduct"; see Gongwer.¹⁹⁹ A heat source such as a nongassing propellant causes the water to flash to steam at ram pressure. Turbulators make a good mixture of steam and water, which is then exhausted via the nozzle. A hydro-turbojet version has also been tried, where a turbine in the exhaust drives a pump that is used to help force water into the combustion chamber. Molten lithium is one type of fuel that has been tested. Use of lithium and sodium as hydrofuels are discussed by White.²⁰⁰

A related concept is the "aerohydrorotor" (Figure 240) where the ram-filled expansion tubes consist of small chambers in a rotating cylinder tailpiece arranged behind a gas source. Just enough gas is allowed to enter a chamber in order to discharge its content of water. The rotation then carries the chamber around away from the gas source to be filled again with water. The many chambers in the cylinder permit a continuous delivery of reaction thrust force.

PSUEDOBLADE PROPELLER

Foa has developed an ejector consisting of primary jets that issue out of angled slots in a rotating body so that the jet sheets follow a helical path; see Figure 241. There is a thrust-augmentation effect caused by the unsteady entrainment of a secondary inflow into the duct by some amount of viscous mixing; also, the jet sheets tend to sweep fluid through the mixing duct mechanically as blades would do. Figure 242 from Foa²⁰¹ shows the orientation of the angled slots. Plots of predicted thrust augmentation are plotted against the area ratio A_2/A_1 , with contours of β_{1i} in Figure 243. The notation is identified in the figure.

The Foa paper²⁰¹ is a timely survey of the results available, and it provides a substantial reference list.

DISCUSSION: With regard to the possible application of any of the waterjet propulsors to submarine control, say, as a tilt-jet device, most of the same remarks concerning directional propellers apply here as well.

1. At high speeds, the production of lateral control forces by a laterally directed jet stream is poor and grows steadily worse as the forward speed increases.
2. The mechanisms needed for a tilting or swiveling waterjet would be complex.
3. Comparing the static or nearly static performance of propellers with that of waterjets (Figure 185) indicates quite clearly the superiority of the axial flow type of 'pump' device, i.e., a ducted propeller. This general conclusion applies to the augmented waterjet devices as well, with the possible exception of the augmented ejector.

Aside from being capable of moving a submarine hull sideways at zero or low speed, an arrangement of orientable waterjets could not duplicate the directness and simplicity of a deflectable lifting surface for producing a lateral control force.

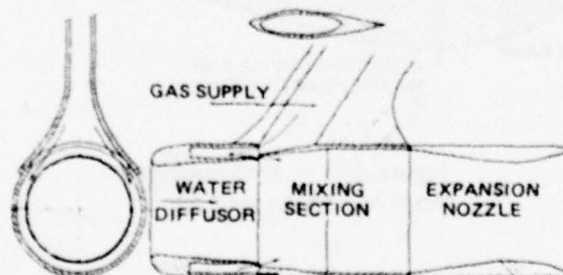


Figure 237 - Principal Parts of a Water-Ramjet

Similar configurations have been widely investigated at NSMB, Oosterveld and van Oossanen.¹⁶³

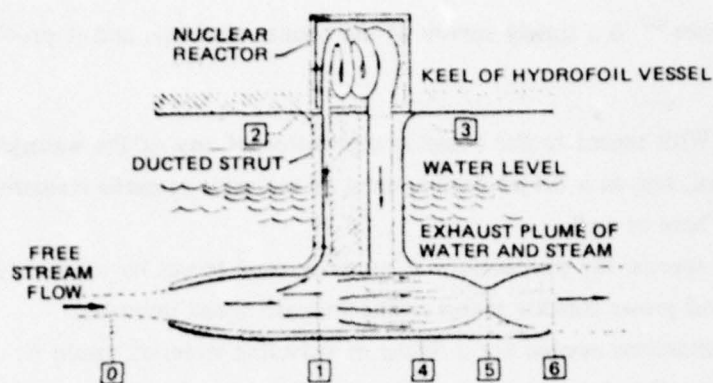


Figure 238 - Nuclear Powered Water-Ramjet Adapted to a Hydrofoil Vessel

Rosen¹⁹⁸

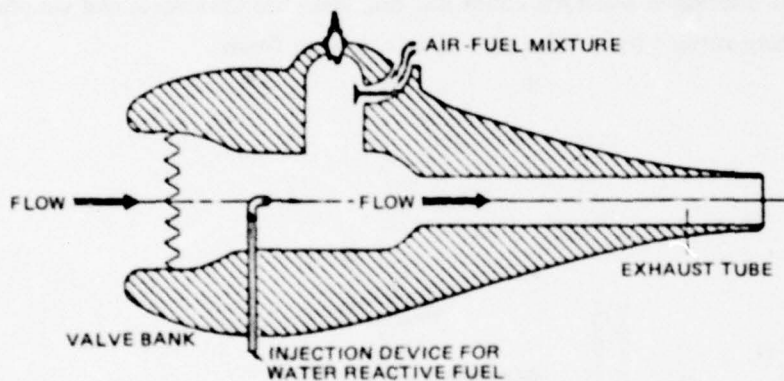


Figure 239 - Hydropulsejet

Sketch from Muench and Garret.¹⁹⁵

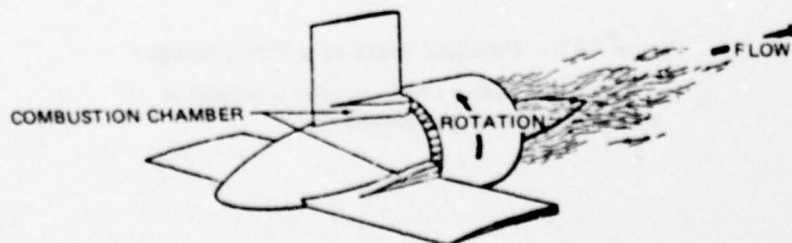
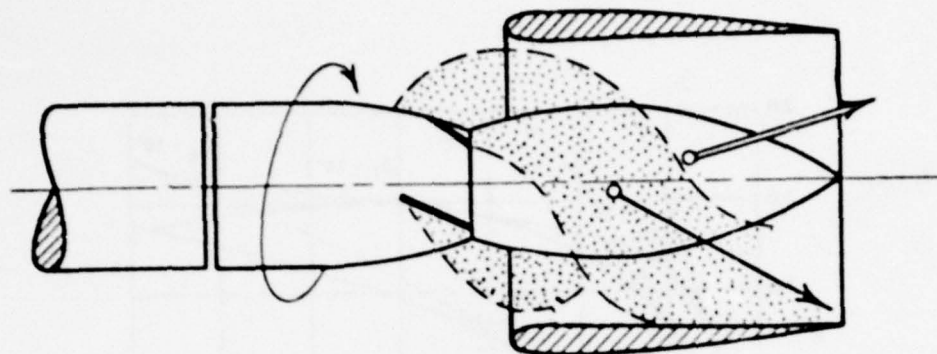


Figure 240 - Aerohydrotor Propulsion Concept

Sketch from Muench and Garret.¹⁹⁵



JETS ROTATING THROUGH A DUCT

Figure 241 - Principle of the Foa Crypto-Steady Flow Eductor

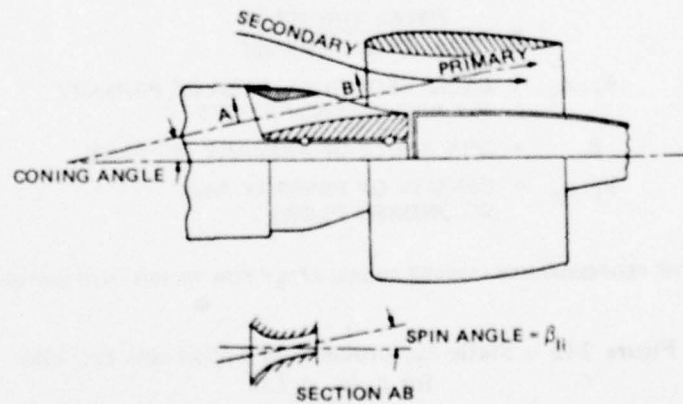
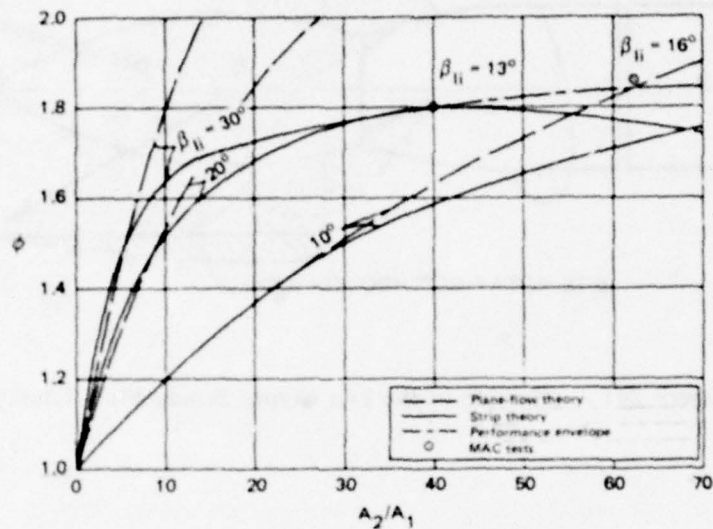


Figure 242 - Bladeless Propeller
Foa²⁰¹



ϕ = THRUST AUGMENTATION
 $= \frac{\text{TOTAL THRUST}}{\text{PRIMARY JET THRUST}}$

A_1, A_2 = CROSS SECTIONAL AREA OF PRIMARY JET AND SECONDARY JET

β_{li} = SPIN ANGLE OF PRIMARY JET SLOT

ρ_1, ρ_2 = DENSITY OF PRIMARY AND SECONDARY FLOWS

THE PERFORMANCE CURVES COULD APPLY FOR WATER INTO WATER

Figure 243 - Static Performance of a Bladeless Propeller
 for $\rho_2/\rho_1 = 1.0$
 Foa²⁰¹

NAME: Vortex Propeller.

DEFINITION AND OPERATION: The vortex propeller is a disk-shaped, impeller-pump, propulsion device, consisting of a multibladed rotor that turns inside a specially shaped housing. It is capable of producing a thrust force in any selected direction in the plane of the rotor, accompanied by a lift force along the axis of rotor rotation. A sketch of this device is shown in Figure 244, reproduced from Taggart,²⁰² who presents a discussion of this concept in conjunction with the maneuvering and propulsion of supertankers.

In Figure 244, the flow through the housing (Figure 244b) is from right to left and downward into the plane of the paper. The thrust force in this case is toward the right, and the lift force is upward out of the plane of the paper. The housing consists of upper and lower chambers divided by a separation plate having the same thickness as the rotor-hydrofoil lift elements. Flow passes through the device along a vortical path: in through the suction chamber, open to surrounding fluid only on the right; down; and out through the discharge chamber, open to the surrounding fluid only to the left.

The proportion of lift to thrust is determined by the rotor-blade configurations, and the direction of the thrust is determined by the housing arrangements and the alignment of the suction and discharge openings. According to the description given by Taggart,²⁰² typical thickness-to-diameter ratios of the pill-like housing would be 1:5 or 1:4. Figure 245 shows sketches reproduced from Taggart²⁰² showing how a group of four of these vortex propellers could be used to propel and maneuver a tanker ship.

DISCUSSION: For possible application to submarine control, it is conceivable that small, thin versions of these thrust-and-lift units could be mounted vertically either at the tips of submarine stern-control planes or as retractable devices near the bow of a submarine. In such arrangements, the thrust force of the vortex propeller would be acting in the longitudinal plane, pitch and heave control, while the propeller "lift" force acting at a right angle to the plane of the rotor could be used for lateral control, for yaw and sway. Use of the propeller forces would probably be restricted to low-speed operation. Quantitative performance data are not available at this time; however, it would appear that because of the rather short internal fluid path, the losses would be relatively low, and the efficiency of the vortex propeller might be better than an ordinary converging-nozzle waterjet.

Problem areas would include: noise, extra complications of the machinery for powering and control, and loss of thrust effectiveness in the transverse direction as the forward speed increases.

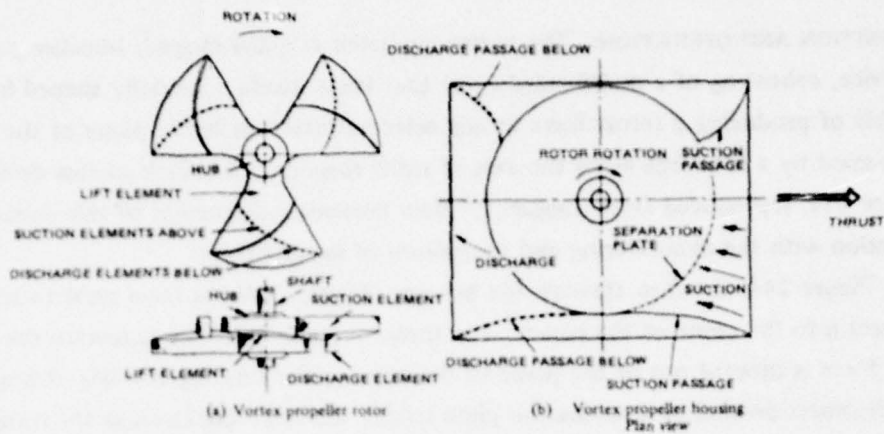


Figure 244a - Vortex Propeller Rotor

Figure 244b - Vortex Propeller Housing Plan View

Figure 244 - Vortex Propeller
Taggart²⁰²

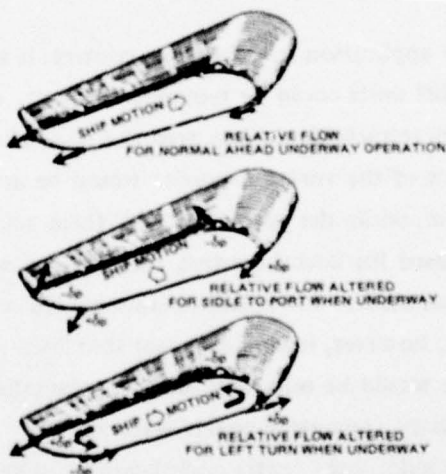


Figure 245 - Various Combinations of Thrust Vector Directions for Maneuvering, Using Four Vortex Propellers Mounted on Hull of a Surface Ship
Taggart²⁰²

SECTION B MAIN PROPELLERS

In this section the following are considered:

1. Vertical Axis or Cycloidal Propellers
2. Controllable Pitch Propellers
3. Propellers with Flow Controls

Here we consider a twofold purpose of the main propulsion system. The first is, of course, to provide the propulsive force for forward motion. The second is the possible use of the main propulsive unit for control purposes also. Present submarines use the main propulsive unit strictly for producing longitudinal thrust, e.g., control in only this single degree of freedom. The propulsive device is usually a single standard screw propeller of large diameter with respect to its hub diameter. Typically the propeller is of fixed pitch, though controllable pitch has also been considered.

The discussion here is centered around using fixed propellers of different types that can achieve force variations in any direction by certain variations in *blade* motion. The word *fixed*, mentioned previously means that the unit is fixed in location and orientation as compared to *steerable* propellers, jets, etc., discussed in Section A. We will consider only units whose function is also to provide the main motive thrust for the submarine. These will usually be restricted in number to one or two units. We will not consider auxiliary devices used for steering but not for main motive thrust. Neither are systems of *many* small units, each individually controllable, considered. Though such systems are possible, they are clearly unsuitable for large submarines because of mechanical complexity and of low efficiency at cruise and at high speed.

Because the devices considered here must be used for main-propulsion purposes, two points must be kept in mind: (1) The efficiency at cruising must be at least comparable to present day single-screw submarines, which is quite good; however, enough thrust must be produced at given engine power so as not to unduly degrade high-speed capability. (2) At low speed, all power must not be sapped just to provide forward speed; hence, sufficient power should be available to produce necessary control forces.

Johnson and Barr²⁰³ have considered various propulsive devices which may be used for both propulsion and maneuvering control. They emphasized *low speed* operation for small deep-diving submarines and were concerned with weight, size, and attainable control forces. Therefore, some of their work is directly pertinent to the present survey. They present a plot showing optimum thrust efficiency of four types of propulsion systems which is of considerable interest. Figure 246 reproduced from Reference 203 shows the approximate efficiencies η versus power parameter K that are attainable for the following types of propellers: standard free, Kort nozzle, Haselton, and vertical axis. We will be mainly interested in the vertical axis and Haselton propellers. It is immediately evident that a substantial price in efficiency must

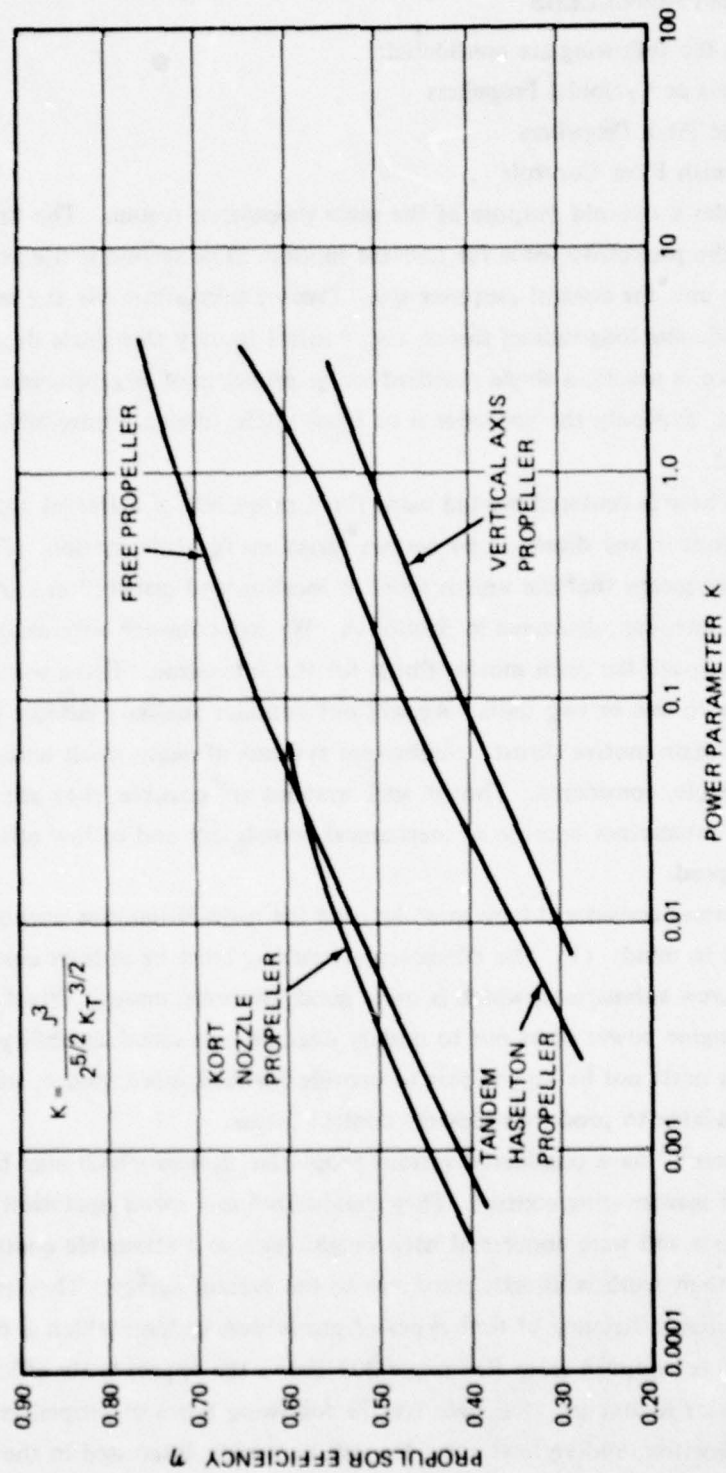


Figure 246 — Optimum Propulsor Efficiencies as a Function of Power Parameter K
Johnson and Barr, 203

be paid to obtain the control capability of these propellers. Other disadvantages will be detailed later.

In Figure 246, the power parameter is

$$K = \frac{J^3}{2^{5/2} K_T^{3/2}} \quad (181)$$

where $J = V/n D$

V = forward speed

n = revolutions per second of the propeller

D = diameter of the propeller

$K_T = T/\rho n^2 D^4$ where T = thrust in pounds produced by the propeller, and ρ = density of the fluid medium.

The propeller efficiency is

$$\eta = \frac{TV}{2\pi nQ} \quad (182)$$

where Q is the torque supplied to the propeller.

NAME: Vertical Axis or Cycloidal Propellers

DESCRIPTION AND FORCE ESTIMATES: The vertical axis or cycloidal propeller derives its name from the fact that the propeller blades are normal to the plane of rotation, and this plane is parallel to the free stream. The name "cycloidal" refers to the blade path under condition of zero slip. These propellers are usually mounted in flat sides or on the bottom of a hull surface whose plane is parallel to the free stream.

Figure 247 shows a view of a vertical axis propeller looking down on the propeller plane or disk; S_c is called the steering center and is positioned so that the blades have motion that keeps their chord normal to the line joining S_c with a fixed point of the blade. These propellers produce forces only in the plane of the disk; so, if control is to be achieved in all six degrees of freedom, at least two of these propellers must be used having disks that are at right angles. In a possible application to a submarine, a group of vertical axis propellers could be used as a main propulsor, as an auxiliary control device, or both. As conceptual examples, Figures 248a and 248b show arrangements of cycloidal propellers, where, for instance, the two horizontal propellers could be used strictly as pitch control-force producers for maneuvering in the vertical plane. Of course, they could also provide horizontal thrust force for propulsion.

Figure 249 shows the two types of cycloidal blade motion, neglecting changes in blade angle relative to the propeller disk. The relevant kinematic parameters of the cycloidal propeller are:

P = propeller pitch = V/n = ratio of forward velocity at zero slip condition, to the rate of rotation. Geometrically, the propeller pitch is $P = 2\pi XR$, where X is the distance from the center of rotation to the steering center as a fraction of the disk radius R .

$P/D = X\pi$ = nondimensional pitch ratio.

J = advance ratio = $\pi V_o / \omega R = V_o / nD$, where $n = \omega / 2\pi$ and V_o is the free stream velocity.

ϕ = steering angle, defined as the angle between the right hand normal to the direction of V_o and the line joining the center of rotation with the steering center; see Figure 247.

The steering angle ϕ controls the direction of the resultant force produced by the propeller relative to the direction of propeller advance. The magnitude and direction of the resultant force depends in a complicated way upon the three parameters described previously.

Ficken and Dickerson²⁰⁴ present extensive data on the forces produced by a vertical axis propeller as a function of $P/\pi D$, J , and ϕ . To provide some idea of the magnitude and character of the forces produced, some sample data from Reference 204 are reproduced here. Figures 250 through 252 show the variations of efficiency η , thrust coefficient K_T , and torque coefficient K_Q for a six-bladed, 9-inch-diameter propeller. These performance coefficients are defined as follows

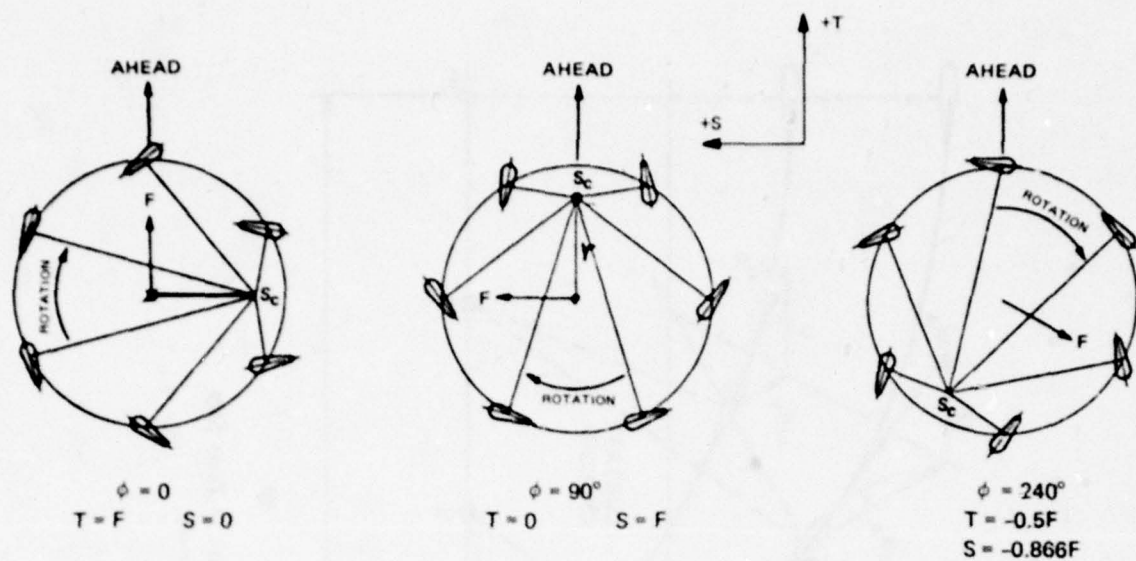


Figure 247 — Six-Bladed Vertical Axis Propeller
 Ficken and Dickerson 204

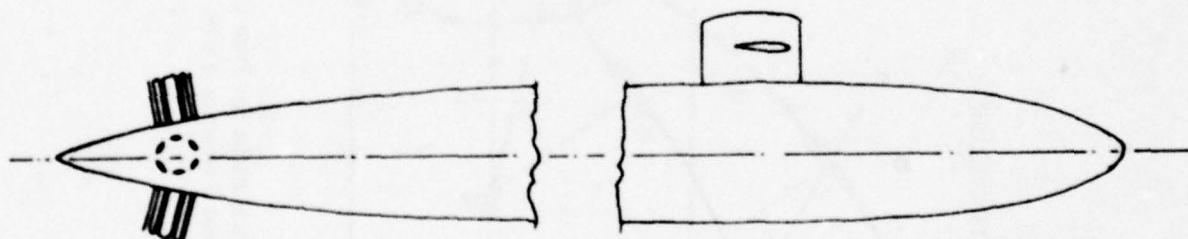


Figure 248a — Criciform Arrangement of Four Cycloidal Propellers for Control in Both Vertical and Horizontal Planes, Plus Thrust

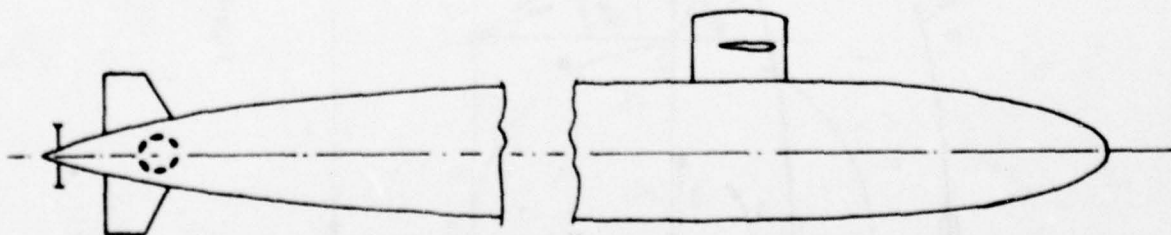


Figure 248b — Pair of Cycloidal Propellers for Pitch Control and Thrusting

Figure 248 — Possible Applications of Vertical Axis Propellers for Submarine Control

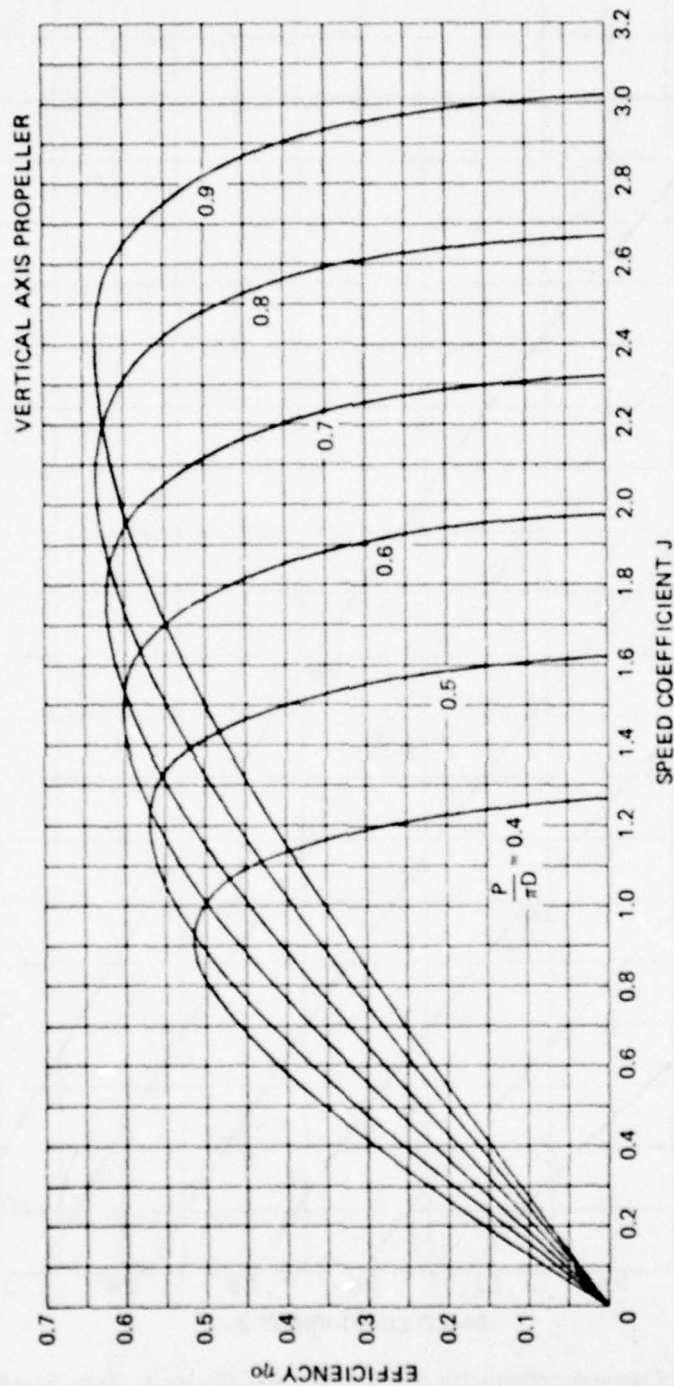


Figure 250 — Propeller Efficiencies with Six Rectangular Blades at Zero Steering Angle
Ficken and Dickerson,²⁰⁴

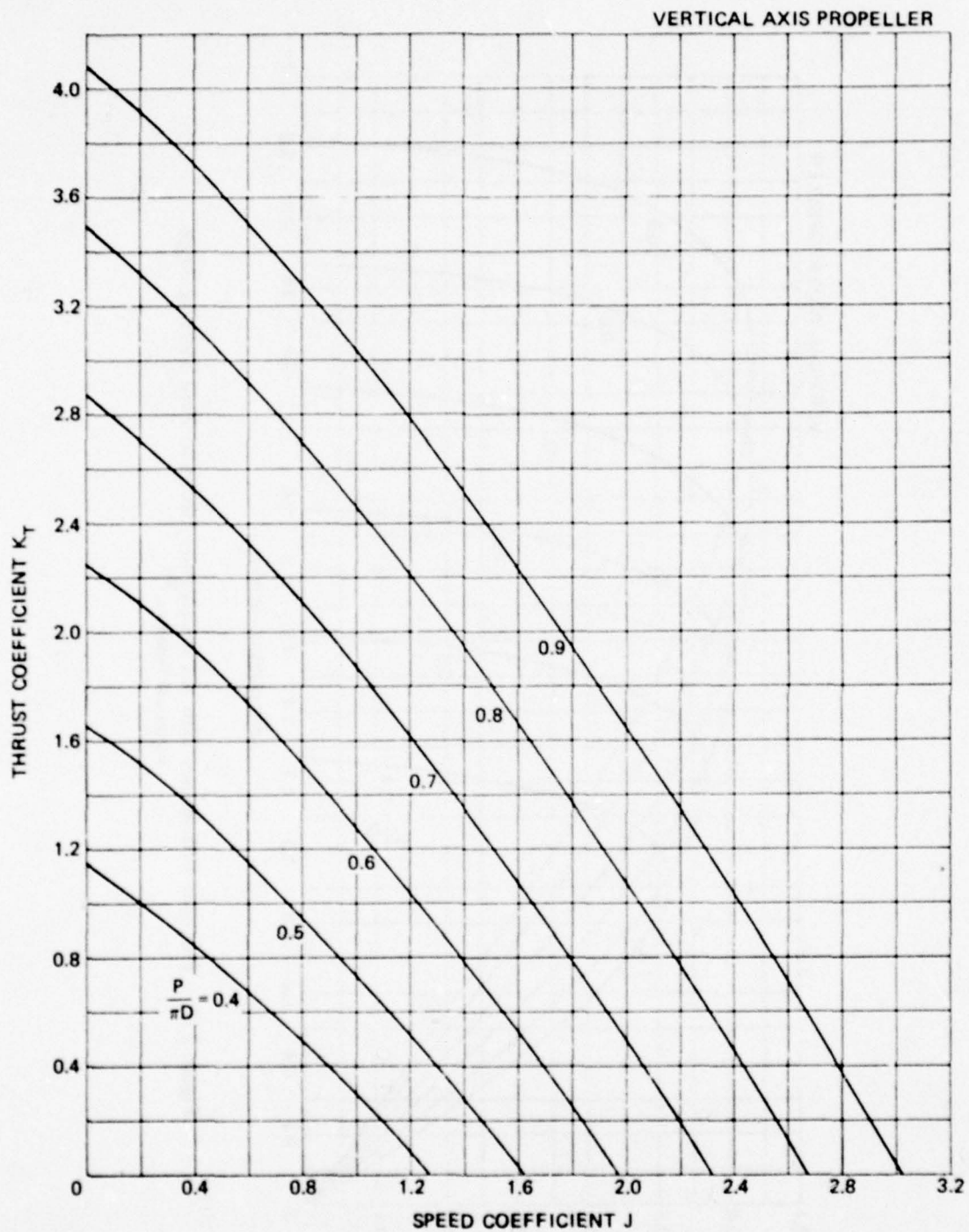


Figure 251 – Thrust Characteristics with Six Rectangular Blades at Zero Steering Angle

Ficken and Dickerson,²⁰⁴

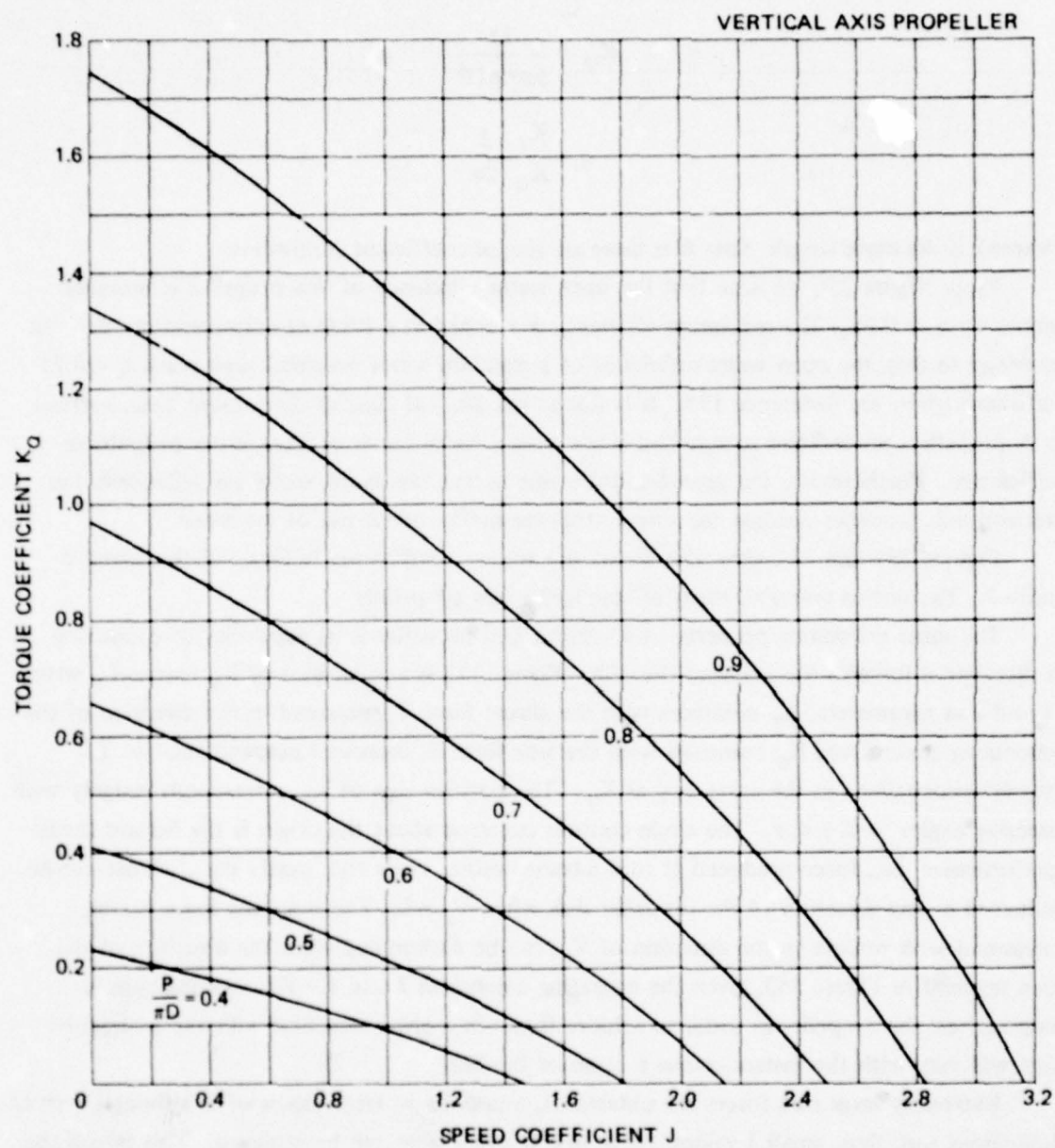


Figure 252 - Torque Characteristics with Six Rectangular Blades at Zero Steering Angle
Ficken and Dickerson.²⁰⁴

$$K_T = \frac{T}{\rho n^2 b D^3}$$

$$K_Q = \frac{Q}{\rho n^2 b D^4}$$

$$\eta = \frac{K_T}{K_Q} \frac{J}{2\pi}$$

where b is the blade length. Note that these are special coefficient definitions.

From Figure 250 we note that the open water efficiency of this propeller is bounded above by $\eta \cong 0.65$. The maximum efficiency is reached at a $P/\pi D$ of approximately 0.9. In contrast to this, the open water efficiency of a standard screw propeller may reach $\eta = 0.75$ or even higher; see Reference 173. It is fair to say that, at least at the present time, vertical axis propellers are inferior to standard screw propellers in terms of open water propulsion efficiency. Furthermore, the propeller-hull combination favors the screw propeller over the vertical axis propeller because the screw propeller makes better use of the wake.

Figures 251 and 252 show the thrust and torque coefficients in terms of the advance ratio J . The curves resemble those of standard screw propellers.

The most interesting property of a vertical axis propeller is its capability of producing a directional force in the plane of the disk. Figure 253 is a polar plot of K_S versus K_T with ϕ and J as parameters; K_T coincides with the thrust force T , measured in the direction of the oncoming stream, and K_S coincides with the side force S , measured perpendicular to T — nondimensionalized in the same way as K_T . The positive sign of K_S corresponds roughly with steering angles $0 \leq \phi < \pi$. The circle contour centered about the origin is the bollard thrust performance, i.e., force produced at zero advance ratio. Note that nearly equal thrust can be achieved in any direction of the propeller disk when $V_o = 0$. The resultant force vector, measured with respect to the direction of V_o , can be determined from the direction of the line segment in Figure 253, given the operating conditions J and ϕ . The steering angle ϕ imposed on the propeller in order to achieve thrust in a given direction with the hull centerline will vary with the instantaneous motion of the hull.

Extremely large side forces are obtainable, especially at large values of J ; although even at low speed and, thus, small J values, fairly sizable side forces can be achieved. This means that these propellers are capable of providing good maneuvering characteristics through a large speed range, a fact that has been recognized for some time.

Other experimental data for cycloidal propellers are provided, for example, by van Manen.²⁰⁵ Mendenhall and Spangler²⁰⁶ present some interesting insight about the operation of these propellers with their analysis.

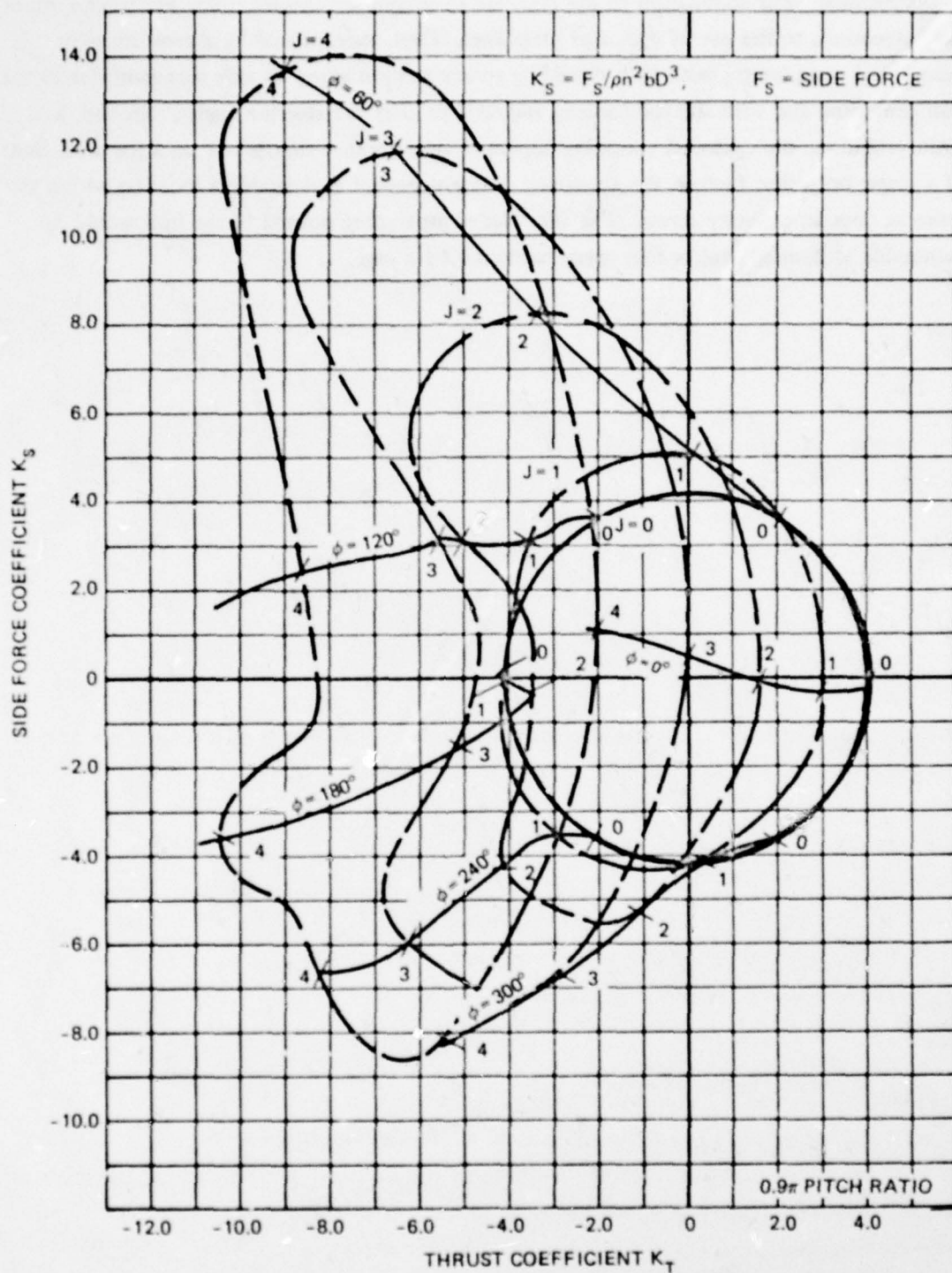


Figure 253 – Full Circle Polar Diagram for Vertical Axis Propeller

Ficken and Dickenson,²⁰⁴

DISCUSSION: For application to the problem of submarine control, there are several important objections to the use of cycloidal propellers. First, there would be a problem with mechanical complexity, both with providing rotary motion along an axis perpendicular to the hull centerline and with the mechanisms required to alter the steering angles. Second, as a main propulsor, the cycloidal propeller displays a performance that is not on a par with that of a screw propeller; further, the geometry does not permit as desirable a location within the wake as does an ordinary screw. The slim blades protruding normal to the hull would be vulnerable to damage, unless they were protected by a cage.

NAME: Controllable Pitch Propellers

DESCRIPTION AND FORCE ESTIMATES: Two distinct types of controllable pitch propellers will be discussed: (1) the Haselton propeller system, and (2) ordinary controllable pitch screws with rake.

Very Large Hub, Haselton, Propellers. The very large hub or Haselton propeller for a submarine consists of small blades arranged around the periphery of a large hub. The propellers may be placed at convenient axial positions along the submarine, each one with a hub diameter equal to the submarine diameter at that position. Large hub propellers typically have hub-to-propeller diameter ratios from 0.5 to 0.9; whereas, for ordinary screw propellers, this ratio is much smaller. A sketch of the Haselton configuration is shown in Figure 254. The principle feature of the individual large hub propeller is that there is sufficient space for mechanisms to provide both collective and cyclic pitch control for the blades spaced around the circumference of the hub. By various combinations of blade-pitch angles, lateral forces as well as a longitudinal thrust force can be generated. An extensive experimental and theoretical investigation of the Haselton propeller configuration is given for example in Reference 207. Further experimental data obtained for a particular large-hub arrangement are presented by Joosen et al.²⁰⁸ These data form the basis for the present outline. The geometry and dimensions of the model tested in Reference 208 are given in the caption of Figure 254. Test results in Reference 208 pertain to a single Haselton propeller with or without a shroud, and in either the fore or the aft location. No experiments were made with the tandem arrangement, both fore and aft propellers operating together.

LONGITUDINAL THRUST PERFORMANCE

Using collective pitch only, the large hub propeller produces an axial thrust. Figure 255 shows the typical variation of thrust and torque coefficients and efficiency versus advance ratio Λ , for a front-mounted shrouded propeller from Reference 207. The usual propeller coefficient definitions apply in this case:

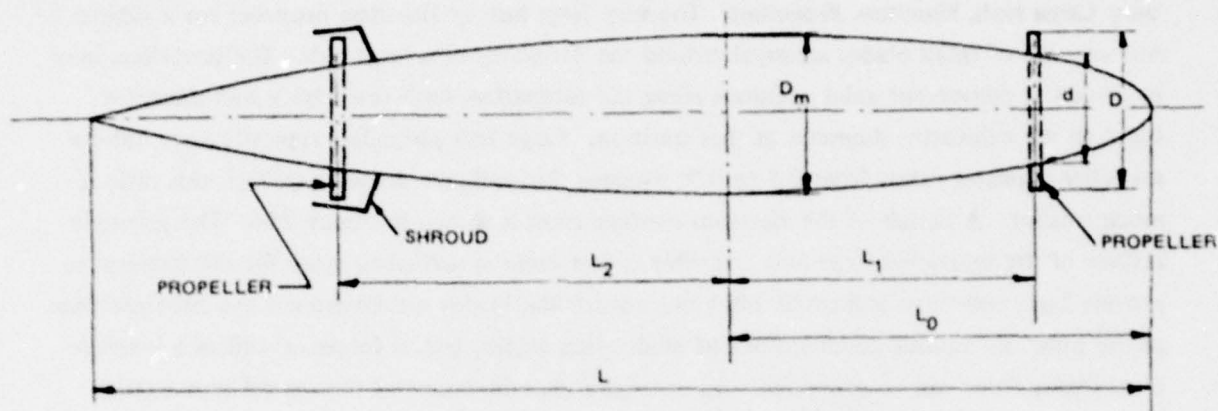
$$K_T = T/\rho n^2 D^4$$

$$K_Q = Q/\rho n^2 D^5$$

$$\eta = \Lambda K_T / 2\pi K_Q$$

$$\Lambda = V/nD$$

where the thrust and torque are denoted by T and Q , respectively. Further details showing the differences between the performance of front and rear mounted propellers and discussions about the effects of the shrouds at various advance ratios can be found in Reference 208.



PROPELLERS		HULL
BLADE SPAN	$b = 0.045\text{m}$	$L = 4.10\text{m}$
BLADE CHORD	$c = 0.225\text{m}$	$D_m = 0.60\text{m}$
NO. OF BLADES	$N = 12$	$L_0 = 1.78\text{m}$
BLADE DIAMETER	$D = 0.49\text{m}$	$L_1 = 1.32\text{m}$
HUB DIAMETER	$d = 0.4\text{m}$	$L_2 = 1.32\text{m}$
BLADE PROFILE	NACA 0016	$D = 0.49\text{m}$
		$d = 0.40\text{m}$

SHROUD

SHROUD LENGTH $l = 0.09\text{m}$

PERCENT SHROUD IN FRONT OF PROPELLER DISK = 60

PROFILE FOR THICKNESS: NACA 0007

Figure 254 — Haselton Configuration, Tandem Very Large Hub Propellers

NSMB Model Particulars, Joosen et al.²⁰⁸

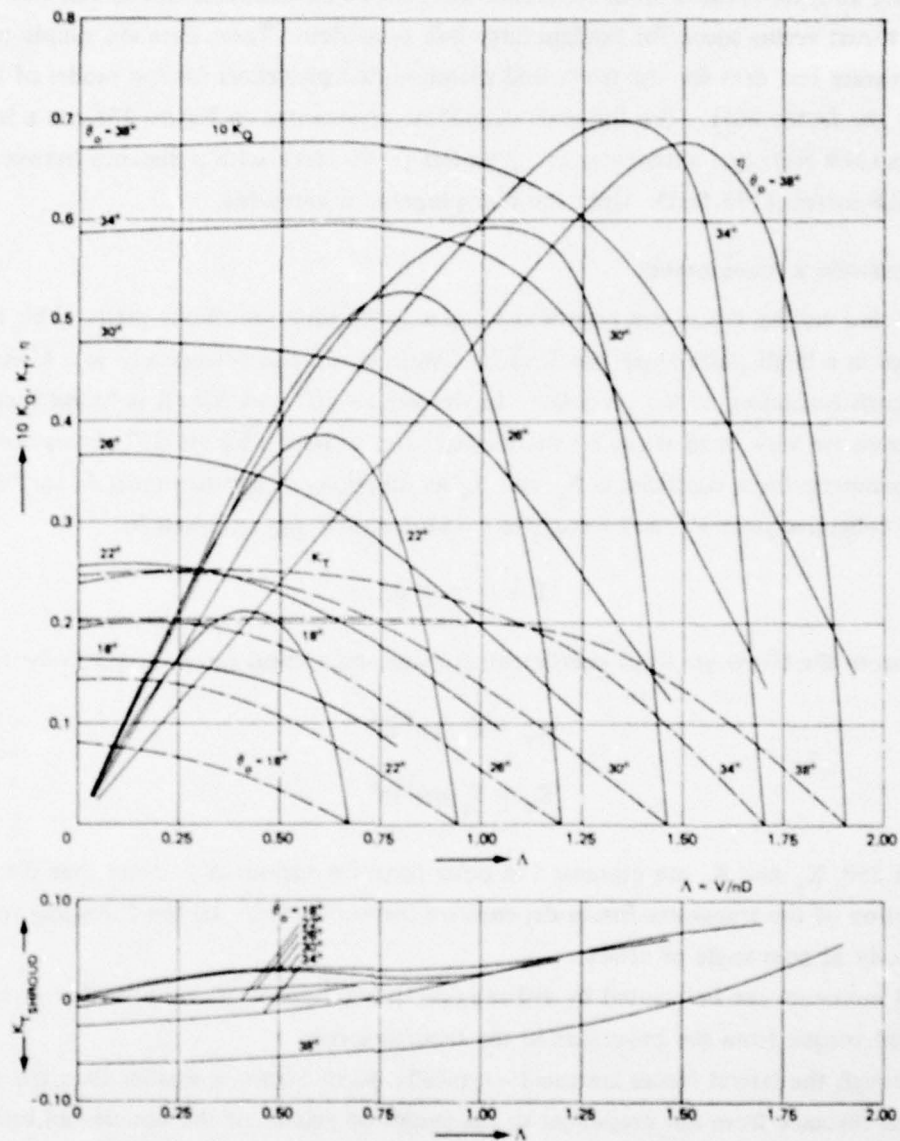


Figure 255 – Thrust and Torque Coefficients and Efficiency versus Λ for a Front-Mounted Shrouded Very Large Hub Propeller with Collective Pitch Angle θ_0 as a Parameter

Jensen et al.²⁰⁸

As seen in Figure 255, the maximum efficiency obtained with the tested large hub propeller is about 70 percent, which is lower but comparable to the open water maximum values of ordinary screw propellers.

Figure 256, reproduced from Reference 207, shows an extrapolation to full size of the available thrust versus speed for tandem large hub propellers. These data are simple summations of the separate test data for the front- and rear-mounted propellers for the model of Figure 254, scaled by the factor 20:1. The full-scale submarine represented in Figure 256 has a length of 82 meters (269 feet) and a diameter of 12 meters (~ 40 feet), with a distance between propellers of 52.8 meters (173 feet). Only the rear propeller is shrouded.

TRANSVERSE-FORCE PERFORMANCE

Side and vertical forces are produced using a *cyclic* variation of the pitch. This refers to the change in a blade-pitch angle which varies continuously and periodically as a blade sweeps through each revolution of the propeller. In References 207 and 208, it is found that the lateral forces are very small taken by themselves. For example, Figure 257 shows sample data for the transverse-force coefficients K_y and K_z as functions of advance ratio Λ , for typical values of collective pitch θ_0 , and for cyclic circumferential angle φ given by

$$\theta = \theta_0 + \theta_1 \sin \varphi$$

Definitions of the transverse force coefficients for side and vertical forces, respectively, are

$$K_y = F_y / \rho n^2 D^4$$

$$K_z = F_z / \rho n^2 D^4$$

In Figure 258, K_y and K_z are presented in polar form for various Λ 's. Note that the magnitude and direction of the transverse forces depends on forward speed. All the foregoing results are for the body at zero angle of attack.

Roll moments can be created by either cyclic pitch control of one propeller or by the unbalanced torque from the propellers in the tandem setup.

Although the lateral forces are small – typically 40 or 50 times smaller than the thrust force – the distance from the propellers to the center of gravity of the vehicle can be made large on an elongated body so that substantial pitch and yaw moments can be achieved on the body.

POWER REQUIREMENTS

Information about the power required to create transverse forces by cyclic pitch control will be presented indirectly as sample plots of the changes in axial thrust and torque versus Λ

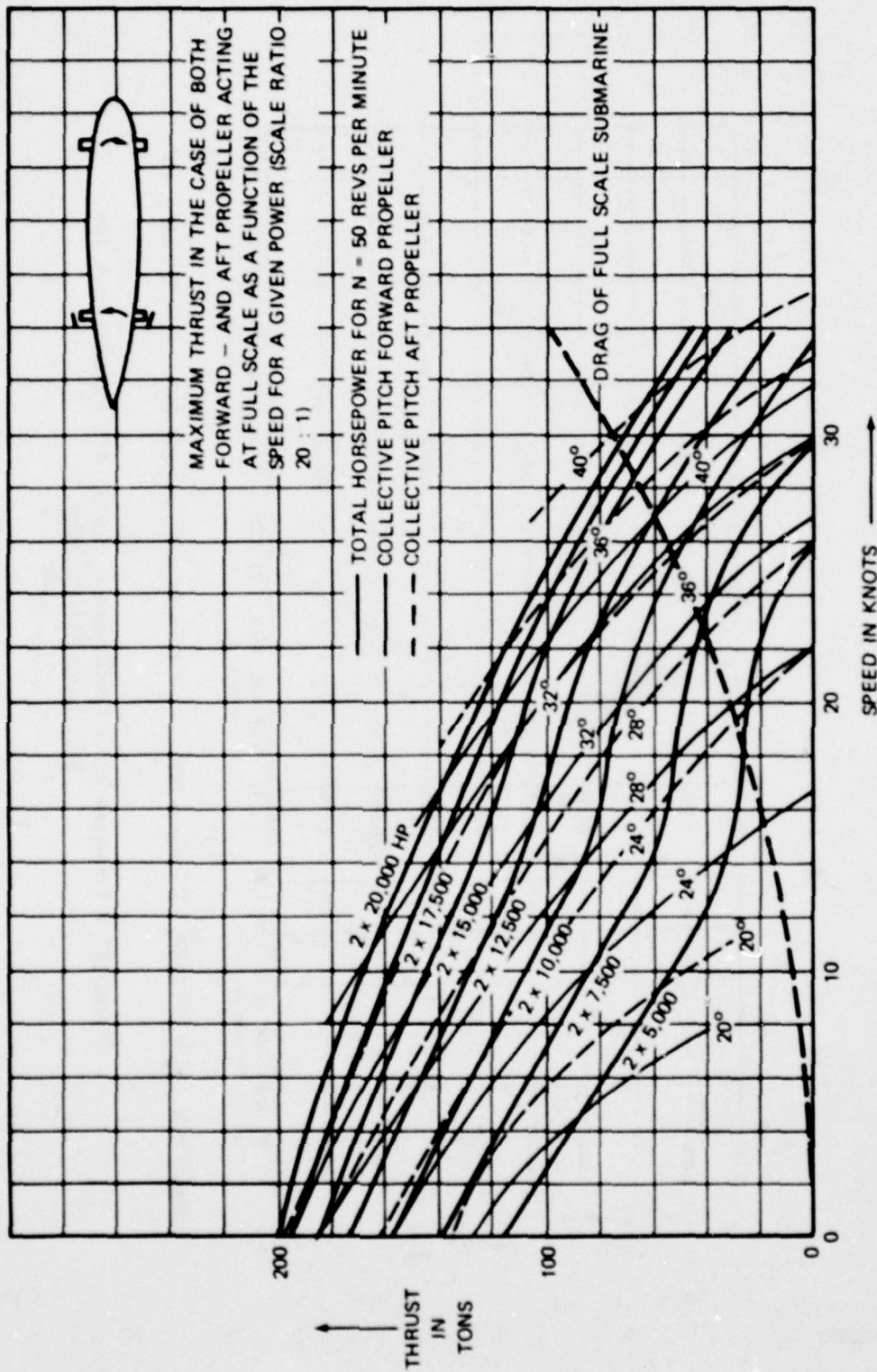


Figure 256 - Extrapolated Thrust Performance of Tandem Very Large Hub Propellers on a Body 269 Feet Long and 40 Feet in Diameter

Reference 207

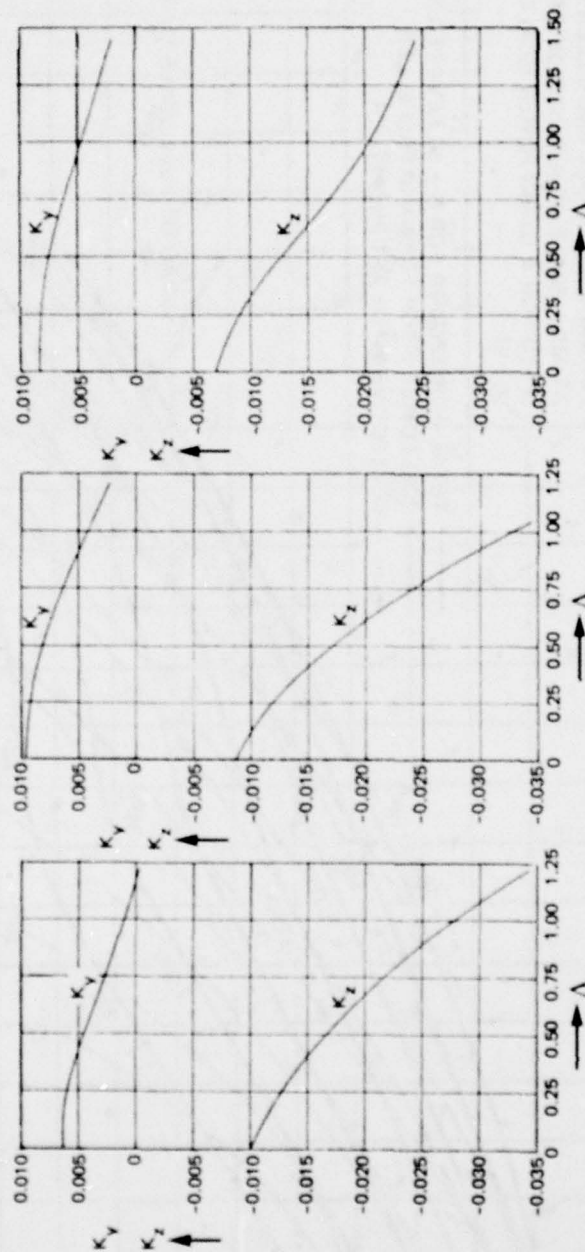


Figure 257a - $\theta_0 = 22^\circ$; and $\theta_1 = 8^\circ$ Figure 257b - $\theta_0 = 26^\circ$; and $\theta_1 = 8^\circ$ Figure 257c - $\theta_0 = 30^\circ$; and $\theta_1 = 8^\circ$

Transverse Force Coefficients K_y and K_z as a Function of Λ , for
Very Large Hub Propeller

Jensen et al. 208

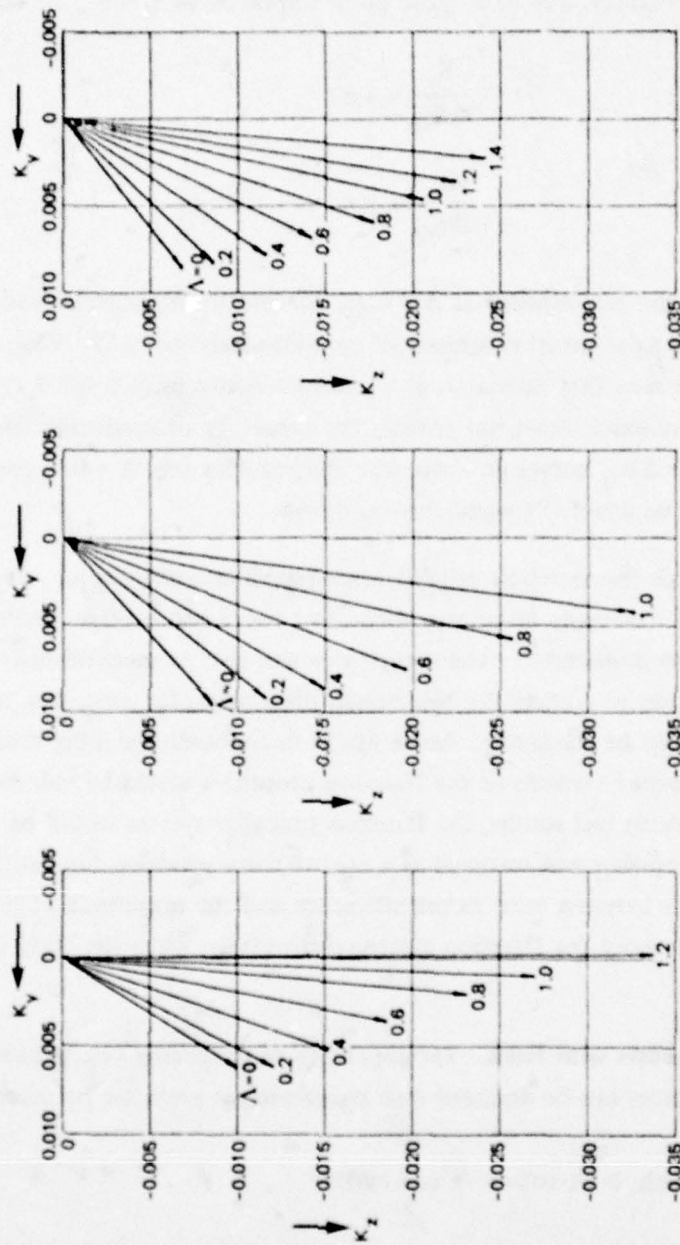


Figure 258a - $\theta_0 \approx 22^\circ$; and $\theta_i = 8^\circ$ Figure 258b - $\theta_0 = 26^\circ$; and $\theta_i = 8^\circ$ Figure 258c - $\theta_0 \approx 30^\circ$; and $\theta_i = 8^\circ$

Figure 258 - Vectorial Representation of Transverse Force Developed by Very Large Hub Propeller

Joosen et al. 208

with contours of the collective pitch angle θ_o . Figures 259 show a sample of such data, which indicate that the imposition of cyclic pitch is usually accompanied by a decrease in K_T and an increase in K_Q . Using the data from Figures 257 and 259 for $\theta_o = 26^\circ$, representative performance ratios of force-to-power, due to a cyclic pitch amplitude of $\theta_i = 8^\circ$, are found to be

$$\frac{K_y}{\Delta K_Q} = 1.62$$

$$\frac{|K_z|}{\Delta K_Q} = 0.6$$

These ratios pertain to the performance at $\Lambda = 0.75$, for which the propeller with $\theta_o = 26^\circ$ experiences a maximum axial thrust efficiency of approximately $\eta = 0.53$. From the other data included, it can be seen that operation at a larger collective pitch angle θ_o tends to increase the efficiency of axial thrust but reduces the capability of producing transverse forces. Note, however, that the ΔK_Q curves do cross zero at approximately $\Lambda = 0.9$; presumably, an optimum system could be directed toward this condition.

DISCUSSION: Although the Haselton variable pitch propeller configuration offers the possibility of producing simultaneously propulsive thrust and transverse control forces, the system taken as a whole appears undesirable. The complexity and cost of mechanisms needed to drive the hub rotation and to control the blade-pitch programming for propellers the size of a submarine diameter would be staggering. Noise would undoubtedly be a big problem with a device so large. Unshrouded versions of the Haselton propellers would be vulnerable to damage. Based on available test results, the Haselton propeller system would be relatively inefficient as a main propulsor and marginal as a control-force producer because of the apparent contrary trends between axial thrust efficiency and the magnitude of transverse forces. Little is known about the Haselton system performance when the body is inclined to the flow.

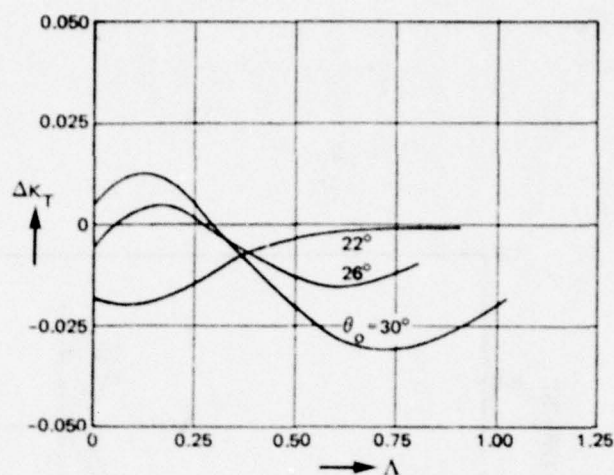
Controllable Pitch Propellers with Rake. The capability of producing simultaneously axial thrust and transverse forces can be designed into a single-screw propeller by incorporating the following features

1. Controllable pitch, both collective and cyclic
2. Raked blades
3. Moderate hub-to-diameter ratio.

Raked blades are necessary to achieve sufficient magnitude of the side forces; see Figure 260 for typical curves of side force-to-thrust ratio, obtained using simple helicopter theory. The moderate sized hub must be big enough to house the blade pitch mechanism while being

Figure 259a - Additional Thrust Coefficient ΔK_T Due to Cyclic Pitch for $\theta_i = 8^\circ$ as a Function of θ_0 and Λ for Very Large Hub Propeller

Reference 208



Λ = ADVANCE COEFFICIENT
 θ_0 = COLLECTIVE PITCH
 θ_i = CYCLIC PITCH AMPLITUDE

Figure 259b - Additional Torque Coefficient ΔK_Q Due to Cyclic Pitch for $\theta_i = 8^\circ$ as a Function of θ_0 and Λ for Very Large Hub Propeller

Reference 208

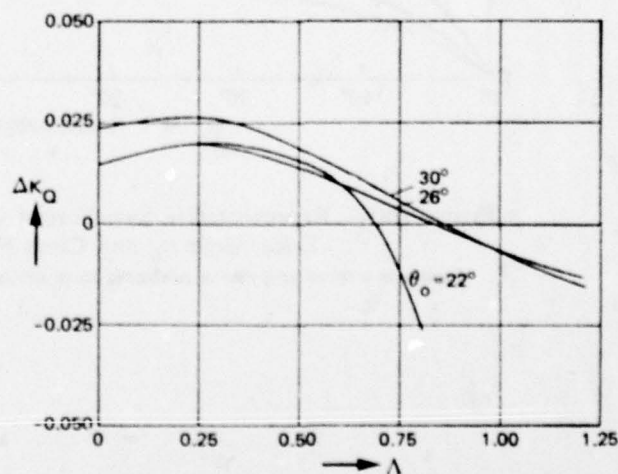


Figure 259 - Additional Thrust and Torque Due to Cyclic Pitch for Very Large Hub Propeller

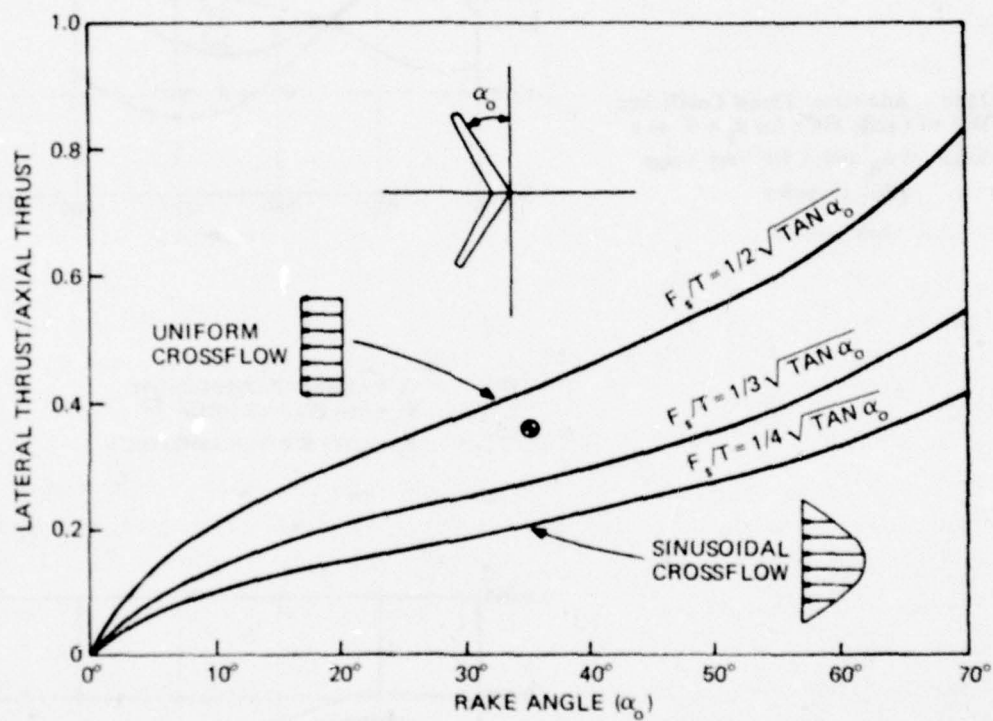


Figure 260 – Representative Side-Force-to-Thrust Ratios as Function of Rake Angle α_0 and Cross Flow Condition

Applies to a raked propeller as calculated from simple helicopter theory, Peach.²⁰⁹

small enough to avoid a penalty in efficiency, characteristic of large hub propellers.

Rake has the effect of decreasing the axial thrust force by a factor proportional to $\cos \alpha_o$, where α_o is the rake angle; see Figure 260. Hence for rake angles between, say, 25° and 40° , the reduction in thrust, compared with zero rake, would be in the range from 10 to 20 percent, which is a large degradation.

Figure 261, reproduced from Peach,²⁰⁹ shows an example of a raked, controllable pitch propeller having three blades, diameter of 5.5 feet, and rake angle α_o of 39 degrees.

FORCE AND POWER ESTIMATE

Denny²¹⁰ has provided some experimental data concerning performance of a six-bladed unraked propeller having a hub-to-diameter ratio of 0.5. The thrust, torque, and efficiency were inferred from measurements of thrust and spindle moment on a single blade. The blade was rectangular in shape with no camber or twist. Figure 262 shows the thrust and torque coefficients for the propeller versus advance coefficient J for various blade pitch angles θ . Figure 263 shows the propeller efficiency η as a function of J for several pitch angles. For comparison, Figure 263 also shows a performance curve²¹⁰ for a propeller having blades that were conventionally shaped, which was designed for high cruising speed efficiency using a lifting surface design program. The rectangular blade propeller has a rather poor thrust performance; however, the results are interesting because from the single-blade data, estimates were made of the side-force performance of the complete six-bladed propeller at various cyclic pitch and blade-rake angles. Figure 264 shows the variation of the side-force coefficient K_{Fs} versus the cyclic pitch angle amplitude at zero advance at several rake angles. For a cyclic pitch amplitude of 15° , a blade rake of 35° is needed for K_{Fs} to be 1/10 of the magnitude of K_T .

Some information is available concerning the static thrust and power performance of the three-bladed, 39° raked VARIVEC propeller of Figure 261. Peach²⁰⁹ indicates that at 8 horsepower, the 5.5 foot diameter propeller delivers 755 pounds static axial thrust at θ_o (collective pitch) = 27.5° , and 275 pounds static transverse force at θ_i (cyclic pitch amplitude) = 27.5° . This means the thrust and side force "static merit coefficients" (Equation (111)) are

$$C_{\text{thrust}} = T_{\text{thrust}}^{3/2} / P \sqrt{\rho A} = 0.694$$

$$C_{\text{side force}} = F_s^{3/2} / P \sqrt{\rho A} = 0.153$$

Recall that for an unducted, unshrouded propeller the ideal maximum static merit coefficient is $C_{\text{max}} = \sqrt{2}$; there is a substantial loss of thrust effectiveness here, probably due to rake.

Optimization of a raked, cyclic pitch propeller would involve numerous parameters, including the shape of the body on which the propeller is mounted and, at best, would be a

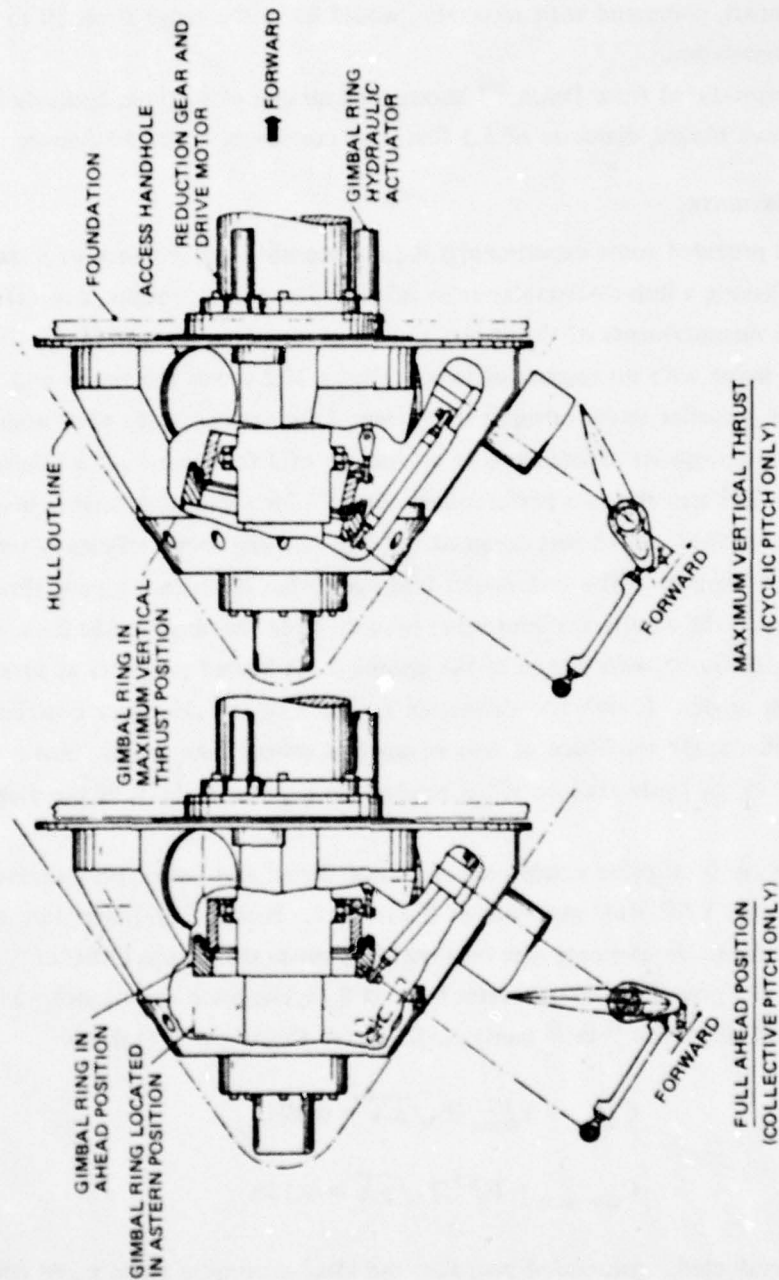


Figure 261 - Three-Bladed, 39-Degree, Raked Controllable Pitch Propeller, VARIVEC
Peach 209

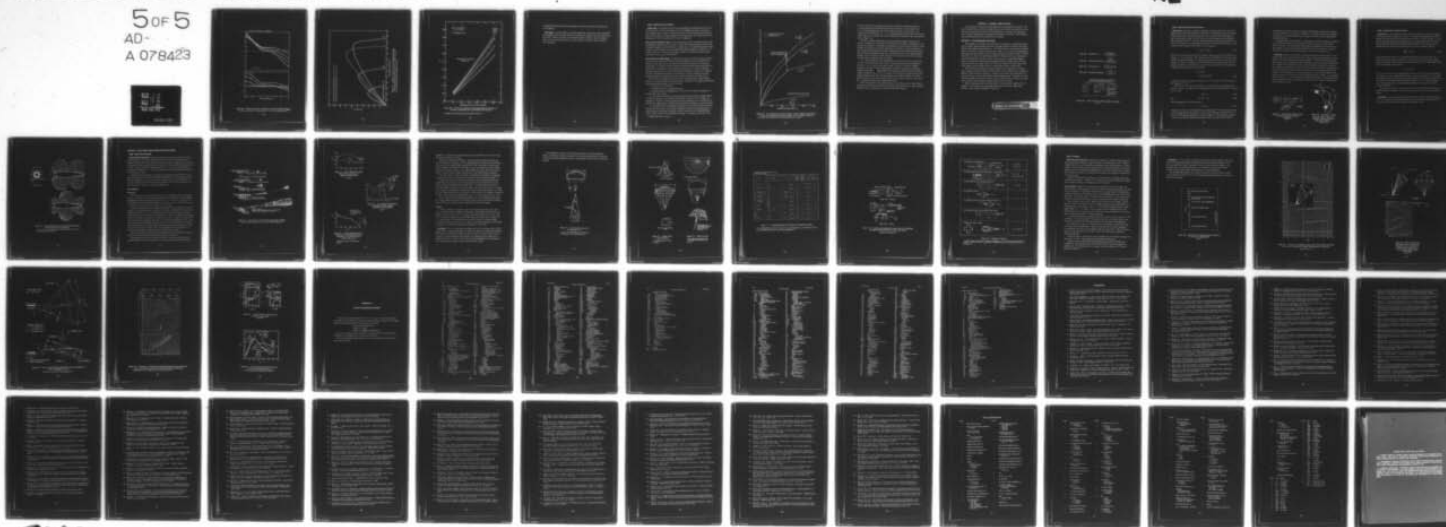
AD-A078 423

DAVID W TAYLOR NAVAL SHIP RESEARCH AND DEVELOPMENT CE--ETC F/G 20/4
AN INVENTORY OF SOME FORCE PRODUCERS FOR USE IN MARINE VEHICLE --ETC(U)
NOV 79 M B WILSON , C V KERCZEK
DTNSRDC-79/097

UNCLASSIFIED

5 OF 5
AD-
A 078423

NL



END
1-80

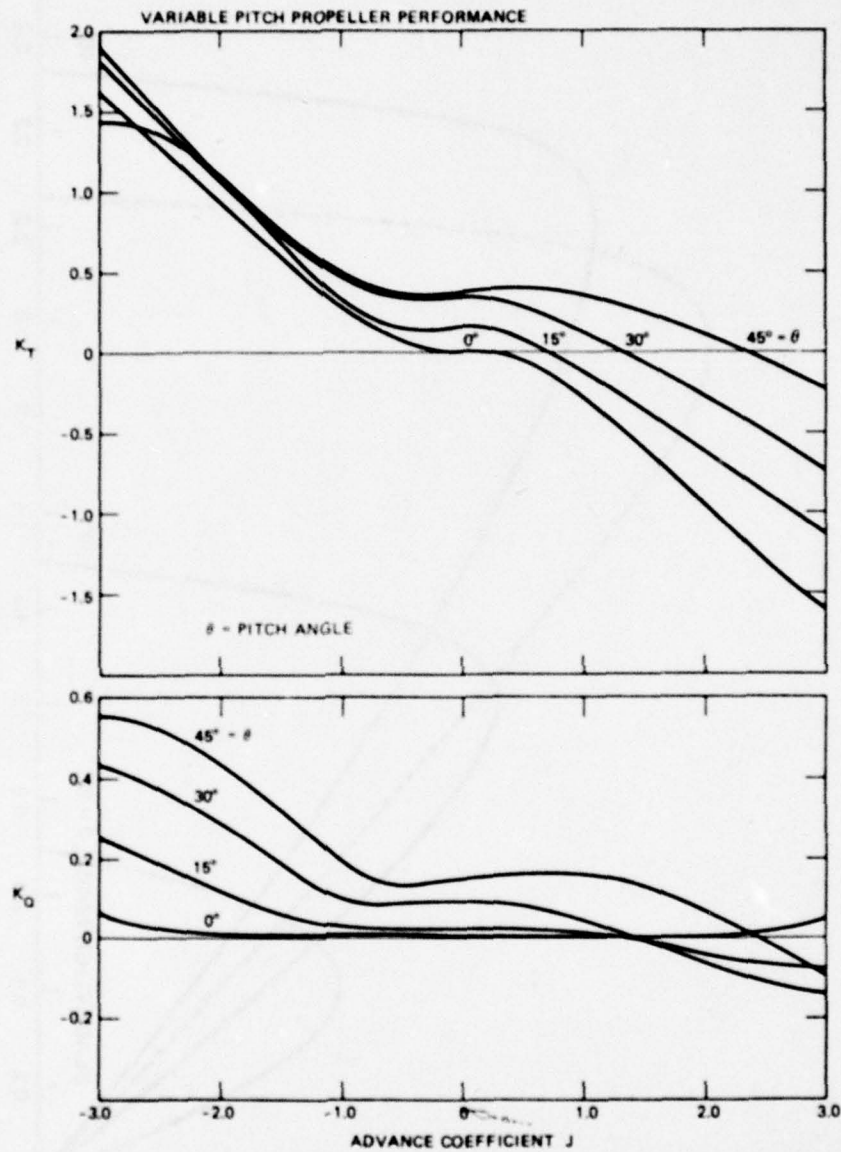


Figure 262 – Thrust and Torque Coefficients for Entire Six-Bladed Propeller
Deduced from measurements on a single blade, at $\theta = 0, 15, 30$, and 45 degrees, Denny.²¹⁰

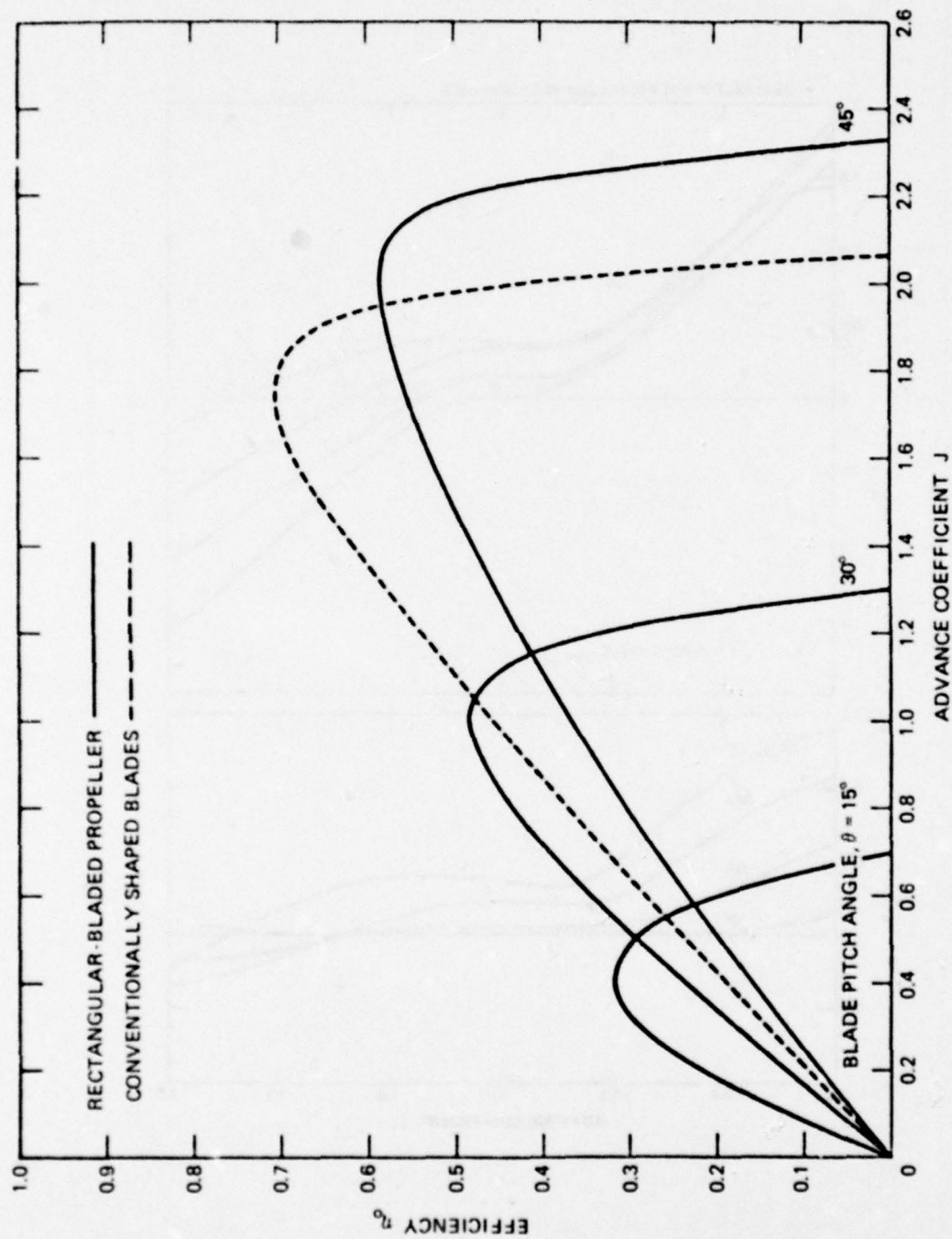


Figure 263 — Efficiency Curves for Entire Six-Bladed Propeller
Curves for propeller with rectangular blades at $\beta = 15, 30$, and 45 degrees; and
with conventionally shaped blades at design pitch, Denny.²¹⁰

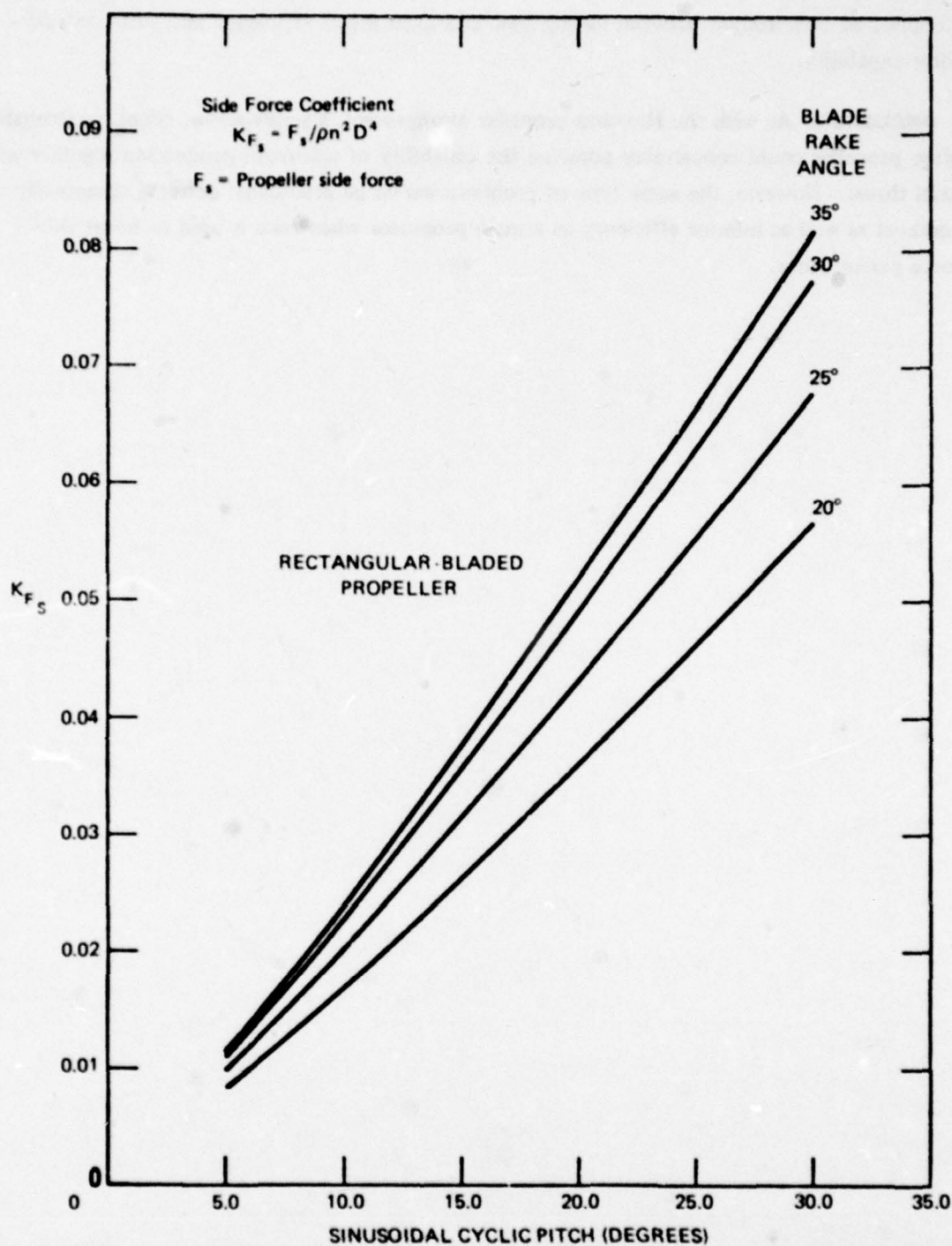
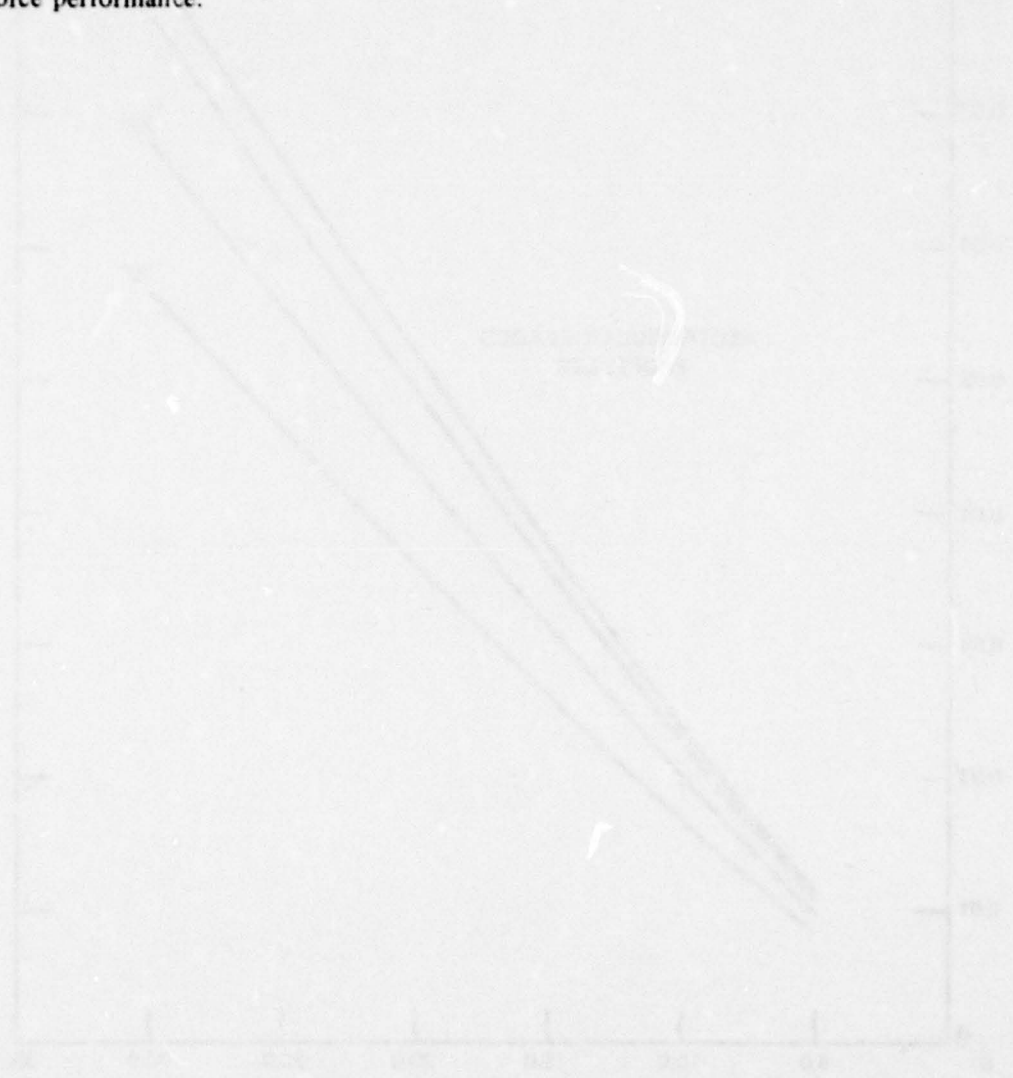


Figure 264 – Side-Force Coefficients for Rectangular-Bladed Propeller as a Function of Blade Rake and Cyclic Pitch at Zero Advance

This applies to six-bladed-propeller predictions obtained by Denny.²¹⁰

complicated compromise between having adequate axial thrust efficiency and sufficient side-force capability.

DISCUSSION: As with the Haselton propeller arrangement, a single screw, raked, controllable pitch propeller could conceivably combine the capability of side-force production together with axial thrust. However, the same type of problems would be attendant: extreme complexity and cost as well as inferior efficiency as a main propulsor when rake is used to boost side-force performance.



NAME: Propellers with Flow Control

DESCRIPTION: Conceptually there exist several possibilities for producing transverse forces by the use of flow control on the blades or duct of a propeller system that is operated as a main propulsion device. There are no known test data or theoretical estimates for the performance of these schemes on water propellers for this purpose; thus, only word descriptions are included here. These are supposed to be provocative suggestions.

Flow Control on Shrouds or Ducts. If the main-propulsion screw is a ducted propeller, various lift-augmenting schemes discussed in Chapter 1 Section B about blowing and/or suction could be applied to segments of the periphery of a propeller duct. The resultant thrust of the system could be skewed at an angle to the centerline, thus producing a transverse control force. An example of this type of concept already noted in Chapter 1 is pictured in Figure 80, reproduced from the U.S. patent of Oosterveld.⁶⁹

Flow Control on Propeller Blades. The whole host of flow-control ideas discussed in Chapter 1 Section B could conceivably be applied to the individual blades on a main propeller for the purpose of *cyclic pitch control*. Of course the field of likely candidates can be narrowed considerably. For example, as discussed earlier, slot-blowing techniques generally appear to be better suited to applications in water than do the suction concepts. Overall, the best slot-blowing concepts seem to have better hydrodynamic performance, see Figure 174. Moreover, the marine fouling problem is liable to be more serious for suction schemes than for slot blowing, especially for arrangements requiring continuous operation of the flow control.

Many of the slot-blowing schemes are used with a mechanical flap. Flapped propeller blades are conceptually possible, but entail avoidable complications. This eliminates all schemes employing mechanical changes in camber and leaves:

1. Jet flap, with no control flap
2. Circulation control by tangential jet blowing
3. Spanwise blowing as lift-augmenting concepts that are reasonable for application to propeller cyclic pitch control.

(1) The jet flap has already been explored somewhat for the purpose of augmenting the axial thrust performance of an ordinary screw propeller; see Hunt et al.²¹¹ and Lasky and Cumming.²¹² However, no known research data exist concerning the use of a jet flap for the selective cyclic augmentation of blade lift that would effectively produce cyclic pitch variation.

(2) Circulation control by tangential slot blowing is a more effective scheme for producing lift than is the jet flap. There are many indications of this fact in earlier discussions. A typical example of the inherent superiority of the CC concept over the jet-flap lift-performance is shown in Figure 265, reproduced from Englar.* For small C_{μ} values ($C_{\mu} < 0.10$)

*NSRDC Technical Note AL-308(1973).

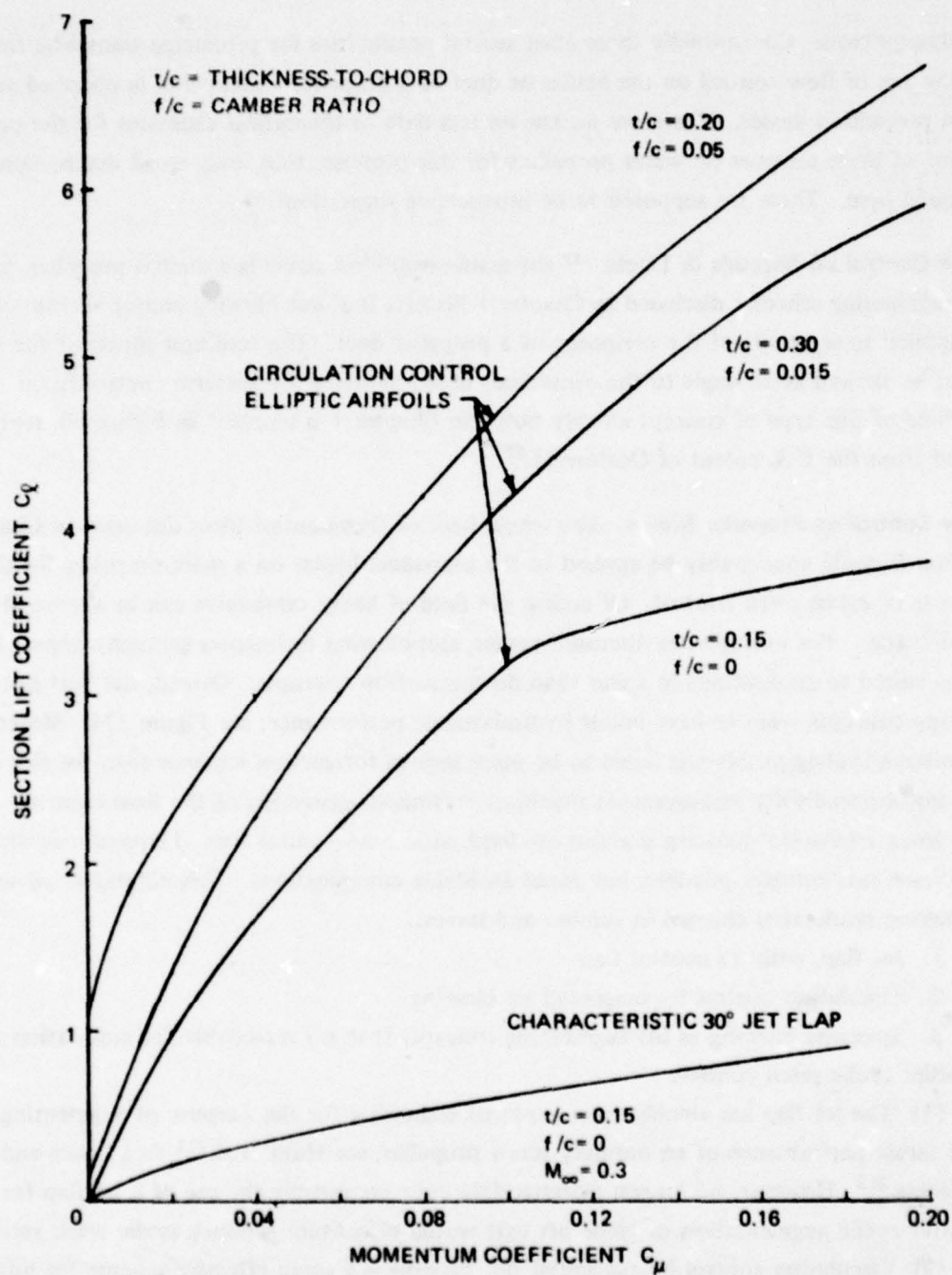


Figure 265 – Two-Dimensional Lift Characteristics of Blown Elliptic Airfoil Shapes

This shows typical lift-augmentation superiority of circulation control by tangential jet blowing over pure jet flap, when comparing only these two flapless high-lift foils, R.J. Englar.

the 15-percent-thick CC foil displays more than six times the lift increment realized by a 15-percent-thick jet flap foil with the same amount of blowing. At zero incidence, and $C_{\mu} = 1.0$, the lift-augmentation ratio of the 15-percent-thick CC foil is $\Delta C_l / \Delta C_{\mu} = 22.5$, compared with the jet-flap value of ~ 5.3 . A similar comparison between these concepts over a wide range of C_l is revealed in the curves of equivalent lift-to-drag ratio versus lift coefficient shown in Figure 174.

The CC by tangential jet-blowing concept has already been widely explored for the purpose of collective and cyclic pitch control of helicopter rotor blades; see Wilkerson et al.²¹³ and the cited references. Conceptually, the application of this flow-control technique to water propellers shows promise and could be explored for the purpose of side-force production as well as other possible performance benefits. Problems areas with the typically bluff, trailing-edge foil shapes will include cavitation, noise, and drag if the foils are ever operated without blowing. Also, the typically low-aspect-ratio water screw blades may suffer more deleterious end-effects than do large-aspect-ratio rotor blades.

(3) A third flapless form of lift augmentation is spanwise blowing. This technique has the virtue of being extremely simple; however, it displays relatively poor lift augmentation, $\Delta C_l / \Delta C_{\mu} \approx 3$ to 5; it also requires large foil angle of attack to be effective. (Spanwise blowing at a flap knee requires a large flap angle.) It might be interesting to consider the spanwise blowing idea on propeller blades for the *off-design* condition in which the blades see a large flow angle of attack. As for cyclic pitch control to achieve propeller side forces, the spanwise blowing concept does not look appealing. One important question, for example, is the time required for the effect to build up when the jet is turned on and vice versa. Cyclic pitch control would require a fast responding flow effect.

Even if flow-control concepts could be used for cyclic pitch control, it is likely that the transverse forces would be too small to be interesting, unless blade rake were used. Unfortunately blade rake is accompanied by a decrease in axial thrust efficiency.

CHAPTER 3. EXTERNAL FORCE DEVICES

A few examples of external force-producing concepts are discussed in this chapter. The word "external" refers to the fact that these devices act on the fluid some distance away from the body or control surface as well as on the fluid adjacent to the body. The distinction is more a matter of emphasis than a fundamental hydrodynamic characteristic. Electromagnetic devices and deployable drag- and lift-producers are included.

SECTION A ELECTROMAGNETIC DEVICES

Electromagnetic force-producers are operated by the principle that a conducting medium, such as seawater, passing through static electric and magnetic fields or through a time-varying magnetic field experiences the Lorentz force. The fluid body force can be used for propulsion thrust or conceivably to produce transverse forces as well. As far as is known, electromagnetic thrusting has been discussed only in terms of ship or submarine propulsion; see Way²¹⁴ and the references cited. Figure 266, reproduced from Way,²¹⁴ indicates the variety of schemes that have been considered for propulsion. There are two main types: internal electromagnetic pumps, using either the simple crossed-field arrangement shown in Figure 266a or the linear induction setup shown in Figure 266b. The external flow approach may also employ either crossed fields as shown in Figure 266c or a varying magnetic field as in Figure 266d.

The internal duct systems are essentially waterjets that are "pumped" by the Lorentz force. Examples of both the induction method and the crossed field method are presented by Phillips²¹⁵ and by Doragh,²¹⁶ respectively. In general these internal duct systems suffer the same low efficiency as do the other waterjet schemes discussed earlier. Nevertheless, it is easy at least to visualize how the exit jet stream from such a device could be turned by, say, guide vanes or flaps in order to produce transverse control forces on the body.

With the external systems, on the other hand, it is possible to use a small body force, applied to a large volume of the surrounding water, with the result that a higher ideal efficiency can be achieved; see Phillips²¹⁵ and Way.²¹⁴

PRECEDING PAGE BLANK-NOT FILMED

Figure 266a - Internal Flow, d-c



Figure 266b - Internal Flow, Induction

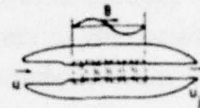


Figure 266c - External Flow, d-c

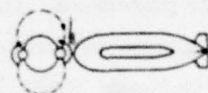


Figure 266d - External Flow, Induction



Advantages and disadvantages of different methods of electromagnetic propulsion

Method	Advantages	Disadvantages
Internal, d.c.	Compact; slight external field	Low ϵ ; larger power plant
Internal, a.c.	Compact; no electrodes	Low ϵ ; nonsuperconducting magnet
External, d.c.	Good ϵ ; low flow disturbance	Spreading magnetic fields
External, a.c.	No electrodes	Low ϵ ; nonsuperconducting magnet; spreading magnetic fields

Figure 266 - Various Methods of Electromagnetic Propulsion
Way²¹⁴

NAME: External Flow, Static Field Thruster

DESCRIPTION: Using direct currents, static magnetic and electric fields are set up between magnetic coils and electrodes, respectively. When these "crossed fields" interact with seawater streaming past the hull, a spatially varying body force is exerted on the fluid throughout a large external volume of water. Figure 267 shows a six-pole arrangement of the propulsion concept discussed by Way.²¹⁴ The active field region extends along the parallel length of the body over which there is an average fluid-velocity field, \vec{V} . Extending into the fluid is a region in which a current density per unit volume \vec{j} is set up, given by

$$\vec{j} = \sigma(\vec{E} + \vec{V} \times \vec{B}) \quad (183)$$

where \vec{E} is the electric field vector, \vec{B} is the magnetic induction, and σ is the conductivity of seawater, $\sigma \approx 4 - 4.5$ mho/meter. The orientation of the \vec{E} and \vec{B} fields as well as the current density \vec{j} are sketched in Figure 268. There, the fluid-flow direction is into the plane of the drawing. The effect of creating the crossed \vec{E} and \vec{B} fields is to generate an eddy current \vec{j} acting circumferentially. The body force created by the interaction of the eddy current with the \vec{B} field is the Lorentz force per unit volume.

$$\begin{aligned} \vec{f} &= \vec{j} \times \vec{B} \\ &= \sigma[\vec{E} \times \vec{B} - B^2 \vec{V}] \end{aligned} \quad (184)$$

so that part of the force is directed in the direction of $-\vec{V}$, and part of the force depends on the orientation of $\vec{E} \times \vec{B}$.

In Figure 267, of course, the \vec{E} and \vec{B} are set up specifically for thrusting in the *axial* direction. In such a case, the ratio of the magnitudes of the static fields \vec{E} and \vec{B} is a constant, say, n , so that

$$VB = nE \quad (185)$$

$$\text{with} \quad \vec{V} \times \vec{B} = -n\vec{E} \quad (186)$$

then the magnitude of the current density is

$$j = \sigma E(1 - n) \quad (187)$$

Details on the thrust force and the efficiency are given by Way.²¹⁴ To give some idea of the size of the fields required for propulsion, a result from the Way paper is quoted here. For a body of 25,850 long tons displacement, 496 feet in length, 56.7 feet in diameter, moving at 15 knots, and having an estimated drag coefficient based on wetted surface of 0.00156,

the drag is about 69,500 pounds, and the required critical magnetic induction field strength is computed by Way²¹⁴ to be $7 \text{ Wb/m}^2 = 7000 \text{ gauss}$. The propulsive efficiency is alledged to be 81 percent. The current required from one anode is 22,100 A, and the voltage between electrodes is 490 volts.

For application for the production of control forces, it is possible to imagine orientations of \vec{E} and \vec{B} so that Lorenz force components $\sigma \vec{E} \times \vec{B}$ are *transverse* to the free stream direction. Note that this would require entirely different arrangements of the same type of large magnetic conductors and electrodes displayed in the sketch of Figure 267. Separate groups of these elements would be needed for both vertical and horizontal forces.

DISCUSSION: Based on the properties of the propulsion system described by Way,²¹⁴ some general remarks can be made about this class of devices. Superconducting magnets would be needed to support the anticipated intensities of the \vec{B} field. There would be numerous problems with the power and geometry of the refrigeration system for the magnet, with handling the circulation of liquid helium, and with the structural support system of the coils which must withstand very large forces. All this would be very expensive and bulky. The spreading of the external magnetic field away from the body would pose a serious detection threat for a submarine. In an arrangement for producing transverse forces, the inherent bulkiness of the magnet and electrodes would prevent their being easily movable or orientable. The magnitude of the vertical force, say, could be altered by changing field strengths in the appropriate group of magnet/electrode elements. Taken altogether, this class of force producer is highly unsuitable for submarine control.

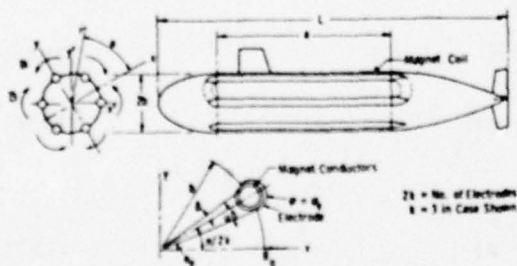


Figure 267 - Six-Pole Static Field External Flow Electromagnetic Propulsion Arrangement
Way²¹⁴

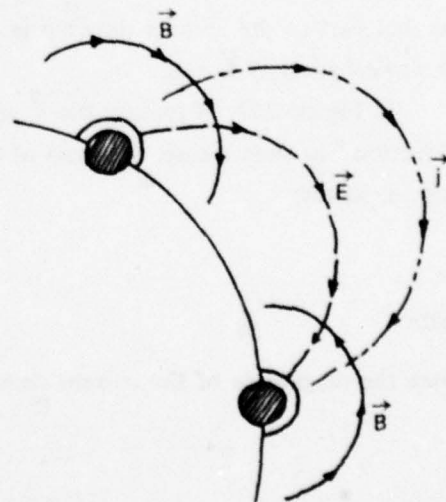


Figure 268 - Orientation of Static \vec{E} and \vec{B} Fields for One Pair of Magnetic Conductor/Electrode Coils used in Scheme of Figure 267

NAME: External Flow, Induction Thruster

DESCRIPTION: In the induction method of external electromagnetic propulsion, a magnetic field with an intensity proportional to $\sin k(z - ct)$ is created by energizing outward facing magnetic coils successively down the length of the hull, where z is in the axial direction. The time-varying radially directed magnetic field induces a circumferential electric field, and the resulting eddy-current density is also directed circumferentially. If \vec{B} is the time varying magnetic field, the induced electric field is given by a form of the Maxwell equation

$$\frac{\partial \vec{B}}{\partial t} = - \nabla \times \vec{E} \quad (188)$$

Figure 269 shows the variation of the magnetic field during one-fourth of a cycle. The magnetic wave speed c must be larger than V , the water speed. No electrodes are needed in this case because the \vec{E} field is created by the time-changing \vec{B} field. The longitudinal Lorentz force per unit volume is estimated by

$$f \sim \sigma(c - V)B^2$$

since $c - V$ is the velocity of the magnetic field relative to the water. Details concerning the force estimates and the resulting propulsive efficiency are given in Phillips.²¹⁵ As an example from Phillips, a submarine going 15 knots, having a length of 656 feet and a diameter of 32.8 feet, with an estimated drag coefficient based on wetted surface of ~ 0.001 has a drag of about 25,800 pounds. With a magnetic induction amplitude of 2500 gauss, it achieves a propulsive efficiency ≈ 0.3 .

As in the previous case, to produce transverse forces, entirely different orientations and separate groups of the magnetic coils must be used. In this case, of course, no electrodes are needed.

DISCUSSION: The same remarks presented earlier for the static field thruster apply here as well. If anything, the induction scheme appears to be less efficient as a propulsion device; in any case, this scheme is plainly unsuitable for submarine control.

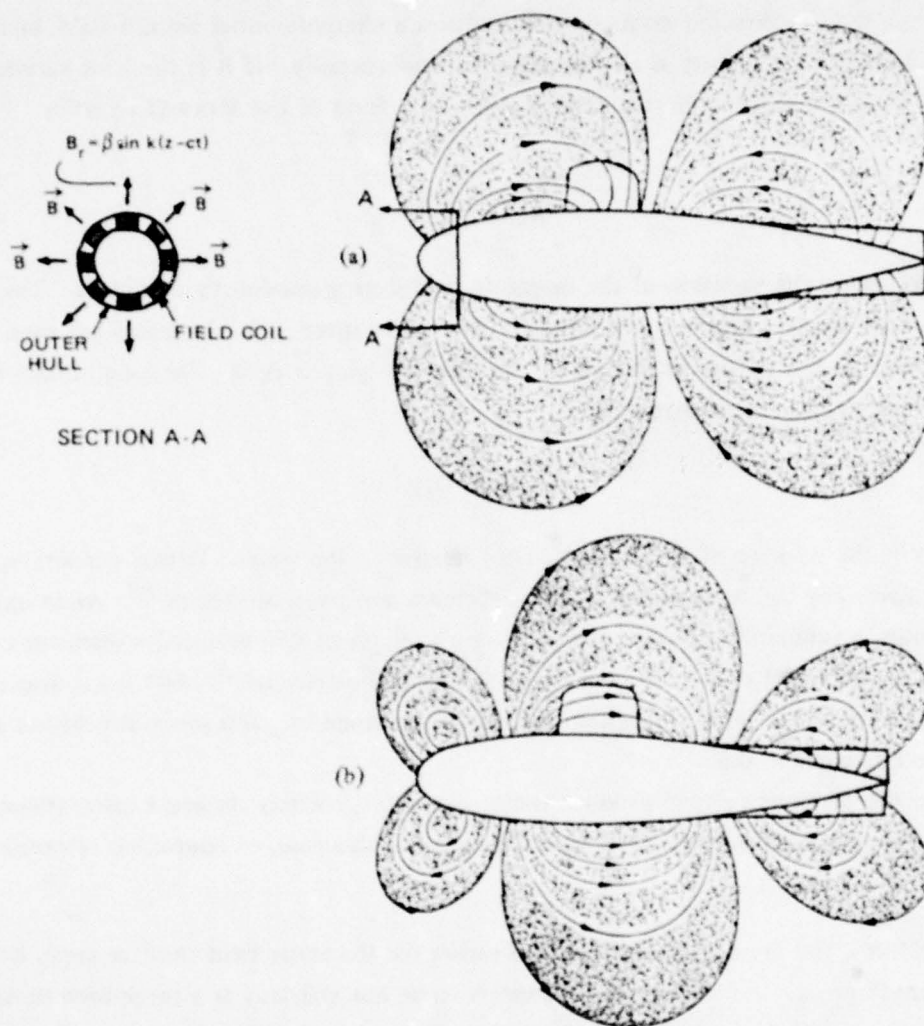


Figure 269 – Field Configurations for an External Field Induction Propulsion System for a Submarine

Field sweeps aft along hull, configuration (b) being approximately one-fourth cycle after (a); reproduced from Phillips.²¹⁵

SECTION B DEPLOYABLE DRAG PRODUCERS AND GLIDERS

NAME: Parachutes and Drogues

DEFINITION AND OPERATION: Parachutes and drogues are drag-producing devices, usually consisting of fabric, or some sort of flexible material, which when fully deployed form a canopy or baglike shape; they are attached to the load by means of rigging lines. Such devices are folded into compact packages that can be popped open when a large restraining drag force is required. Figure 270 shows a familiar application to the recovery of an airborne object, reproduced from Reference 217. In general, parachutes are used to decelerate and/or stabilize a body moving in a fluid.

Extensive technical discussions of parachutes—their design and their application in the aeronautical field—are found in the USAF Parachute Handbook²¹⁷ as well as in the books by Brown²¹⁸ and Hoerner.¹⁴ The research articles by Whicker et al.²¹⁹ and by Heinrich²²⁰ are also useful. Waters and Gale²²¹ have presented information about the use of parachutes in both air and water and how to compare their performance.

Force Estimate.

PARACHUTES

The basic shape of a simple parachute canopy may be regarded as close to a hemisphere. Figure 271, from Hoerner,¹⁴ shows that an impervious cuplike drag shape closely resembling a hemisphere will give the maximum drag coefficient $C_{Dp} = 1.4$, where C_{Dp} is based on the projected area S_p . Very often drag coefficients of parachutes are given in terms of the total canopy area S_o and are denoted C_{Do} . Then $C_{Do} = (S_p/S_o)C_{Dp}$.

Parachute design depends on considerably more than just the drag coefficient. Figure 272 indicates that a hemispherical shell at an angle to the inflow can develop a lift. Thus a simple hemispherical canopy can reach an equilibrium situation by gliding at some angle *different* from the dragline direction. However, this gliding mode is usually overwhelmed by oscillations in which the resultant aerodynamic force rotates and can cause a pendulum or rocking motion of the load as well as causing the entire chute to "cone" about the drag-direction axis. Some experimental data about hemispherical parachutes are given by Scher and Gale.²²² A totally stable canopy would be one having neither pendulum oscillations nor coning motions. However, the usual term "stable canopy" refers to a configuration where the oscillations are confined to small angular excursions and are not objectionable or dangerous.

Porosity of the fabric can help to reduce the large oscillations of an impervious canopy; however, it also reduces the drag coefficient of the shape; see Figure 273.

Other important factors are the strength of the fabric, the opening shock factor, the opening reliability, and velocity limitations. These are all discussed in the USAF Parachute

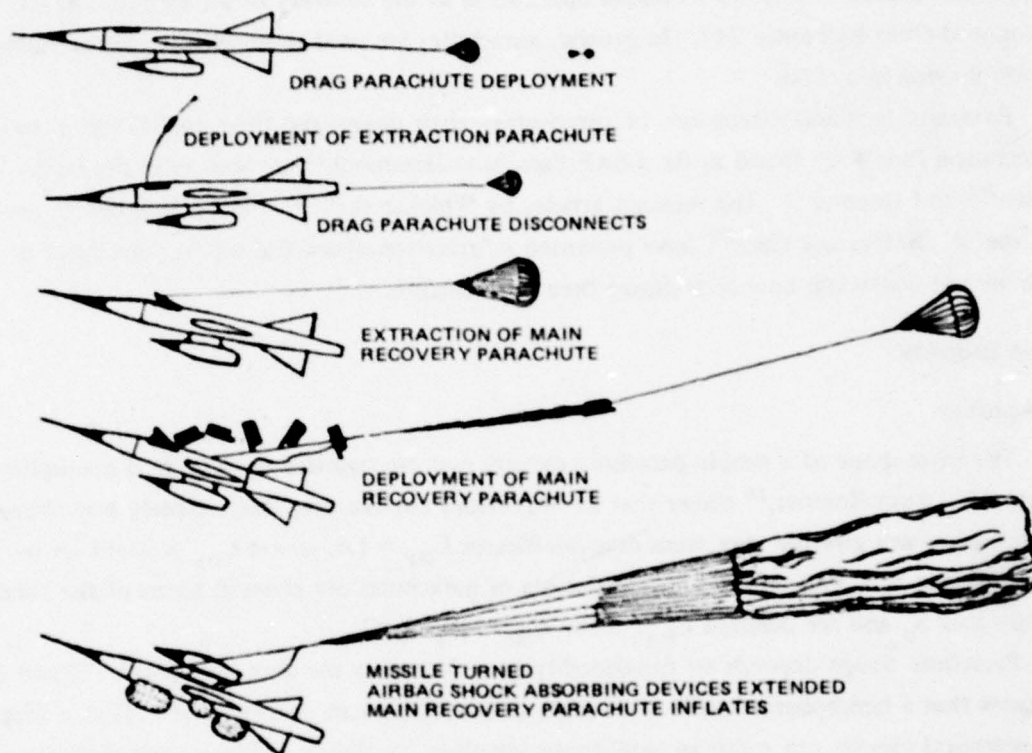


Figure 270 – Classic Recovery System Using a Deployable Parachute
Functional sequence for retrieving a rocket or drone; USAF Parachute Handbook.²¹⁷

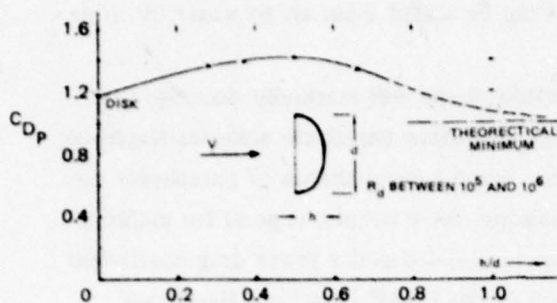


Figure 271 – Drag Coefficients of Sheet-Metal Caps as a Function of Height-to-Diameter Ratio

Hoerner¹⁴

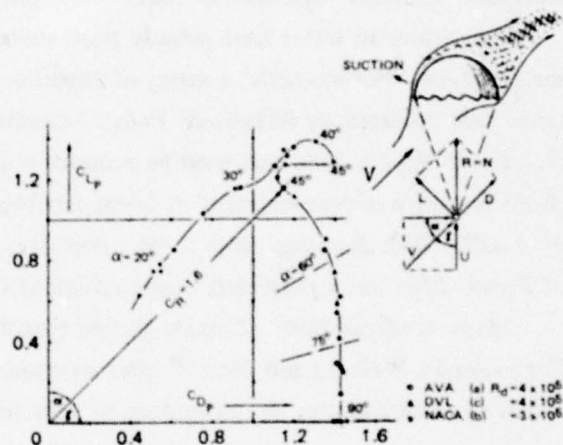


Figure 272 – Aerodynamic Characteristics of Hemispherical Shells, Rigidly Suspended in Wind Tunnels

Hoerner¹⁴

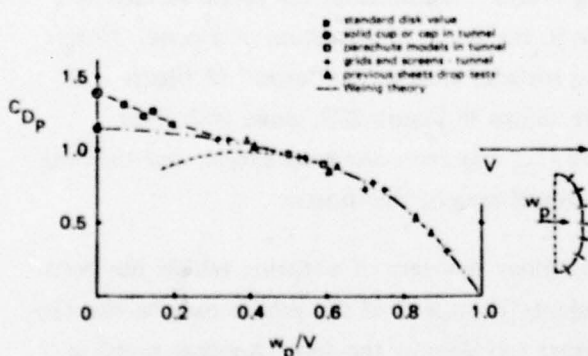


Figure 273 – Drag Coefficient, Based on Frontal Area, of Pervious Sheets and Parachutes, as a Function of the Velocity Ratio w_p/V

Defined for maximum cross sectional area,
Hoerner.¹⁴

Handbook.²¹⁷ In general, the velocity limitations can be scaled from air to water by using the dynamic pressure $q_{\infty} = \frac{1}{2} \rho U_{\infty}^2$.

Shape is very important for stability. A beretlike shape will markedly decrease the typical oscillations of a parachute. The so-called guide-surface parachute achieves this shape and is known to have good stability characteristics. Some typical shapes of parachutes are shown in Figures 274 through 276. The ribbon canopy, for example, is good for stability because of its porosity; however, it has a higher opening speed and a lower drag coefficient. Details of these canopies and many others are given in the USAF Parachute Handbook.

The table in Figure 277 gives a summary of the important characteristics of parachute canopies. Intricate variations of many other parachute types are discussed by Brown.²¹⁸

Parachutes in water have already been successfully used in braking experiments with surface ships. For example, a series of experiments with models, small ships, and a huge tanker are reported by Mitsubishi Heavy Industries.²²³ The 10-foot-diameter parachute pictured in Figure 278a was used to produce a drag of 30 long tons at 16 knots. A multiple chute system was demonstrated as being capable of reducing the stopping distance of a tanker by a half. With discharge slots to give porosity, and thus stability, the hemispherical parachute of Figure 278a has a projected drag coefficient $C_{Dp} = 1.18$, which means that $C_{Do} \approx 0.59$.

Many configurations of stable gliding parachutes have been investigated experimentally. For example, Weiberg and Mort²²⁴ present wind tunnel data about several different arrangements of slotted chutes and groupings of parachutes that resemble parawings.

DROGUES

A drogue is similar to a parachute, being a fabric drag-producing surface that can be used to slow down and/or to stabilize a moving body. Traditionally, the fabric surface of a drogue is a surface of revolution.²¹⁸ It is often in the shape of a frustum of a cone. However, now the term includes other types of drag surfaces such as the "cross" of Figure 279.

Some examples of several drogue types are shown in Figure 279, along with their characteristic drag coefficient C_{Do} or C_{Dx} . The C_{Do} has been discussed earlier, and the drag coefficient C_{Dx} is based on maximum cross sectional area of the drogue.

DISCUSSION: The use of a parachute for emergency recovery of a marine vehicle has been suggested before. Several disadvantages are evident: The speed of the vehicle may be inappropriate for use of a parachute of a given size, either too slow or too fast. Another problem would be to provide deterioration-proof storage of the parachute plus its ejection device. Deployment would be at most a one-shot affair at some unspecified time in the lifetime of the submarine, and the storage volume would be difficult to justify.

It is interesting to speculate on the possible effectiveness of a *buoyant* parachute balloon, into which air or some other gas may be injected upon deployment. The inflation by the gas would hasten deployment and also would augment the force exerted by the drag producer.

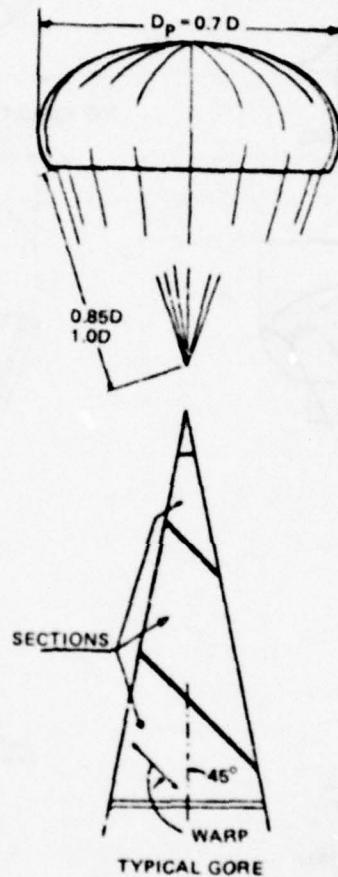


Figure 274 – Flat Circular Canopy with Its Triangular Gore

A gore is a fabric panel making up a pie slice of the entire parachute, USAF Parachute Handbook.²¹⁷

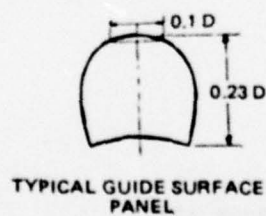
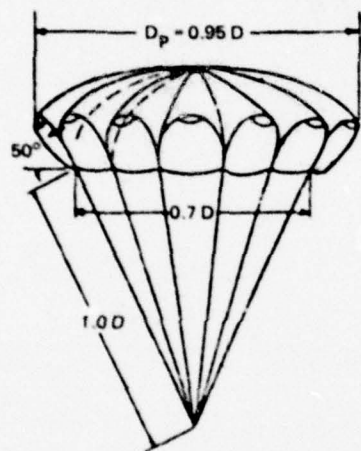
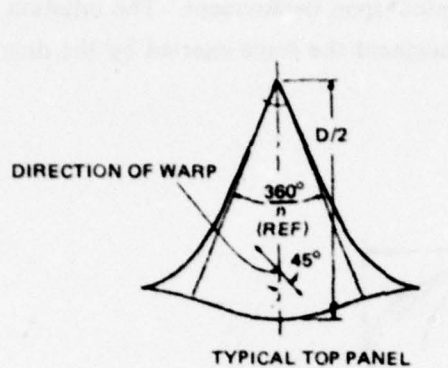
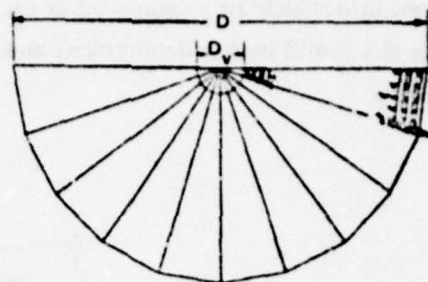


Figure 275 – Ribless Guide Surface Canopy

This parachute design can be made very stable.²¹⁷



TYP INFLATED PROFILE

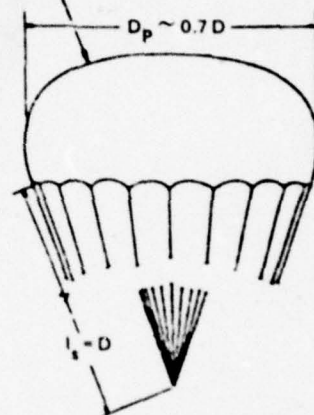


Figure 276 – Ribbon Canopy

Flat circular shape is composed of concentric ribbons and supported by radial ribbons.²¹⁷

AVERAGE PERFORMANCE CHARACTERISTICS
OF PARACHUTE CANOPIES




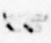














CANOPY TYPE		CONSTRUCTED SHAPE		DIAMETER RATIOS		DRAG COEFFICIENT		OPENING SHOCK FACTOR (INFINITE MASS)	STABILITY	
		PLAN VIEW	PROFILE VIEW	D_p/D	D_o/D	RANGE	AVERAGE (PRELIM. DESIGN)		REMARKS	AVG. ANGLE OF OSCILL.
SOLID TEXTILE	FLAT CIRCULAR			0.70	1.000	C_{D_o} 0.65-0.90	C_{D_o}	> 2.0	UNSTABLE	$\pm 30^\circ$
	EXTENDING SKIRT			~ 0.76	1.24	C_{D_o} 0.65-0.85	C_{D_o} 0.70	~ 1.8	UNSTABLE	$\pm 20^\circ$
	GUIDE SURFACE (STABILIZATION)			~ 1.7	1.60 FOR 10 GORES	C_D 0.8-1.0	C_D 0.85	~ 1.1	STABLE	$\pm 1^\circ$
	GUIDE SURFACE (RIBLESS)			~ 0.95	1.51 FOR 10 GORES	C_D 0.75-0.85	C_D 0.80	1.1-1.3	STABLE	$\pm 1^\circ$
	GUIDE SURFACE (PERSONNEL)			~ 0.73	1.15	C_{D_o} 0.68-0.80	C_{D_o} 0.72	~ 1.2	STABLE	$\pm 7^\circ$
	ROTAFOIL			0.91	0.95	C_{D_o} 0.63-0.90	C_{D_o} 0.78	~ 1.06	STABLE	$\pm 8^\circ$
	SHAPE (CONICAL)			~ 0.70	1.08	C_{D_o} 0.68-0.95	C_{D_o} 0.80	~ 1.8	UNSTABLE	$\pm 20^\circ$
RIBBON	FIST			0.67	1.000	C_{D_o} 0.45-0.55	C_{D_o} 0.50	~ 1.05	STABLE	$\pm 3^\circ$
	RING SLOT			0.70	1.000	C_{D_o} 0.45-0.65	C_{D_o} 0.55	~ 1.05	STABLE	$\pm 7^\circ$

Figure 277 - Average Performance Characteristics of Parachute Canopies

D_o = nominal inflated canopy diameter = $(4S_o/\pi)^{1/2}$, D_p = projected diameter, S_o = total fabric area of canopy,
 C_{D_o} = drag coefficient based on area S_o , USAF Parachute Handbook.²¹⁷

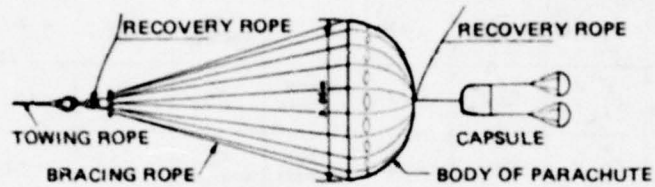


Figure 278a - Parachute

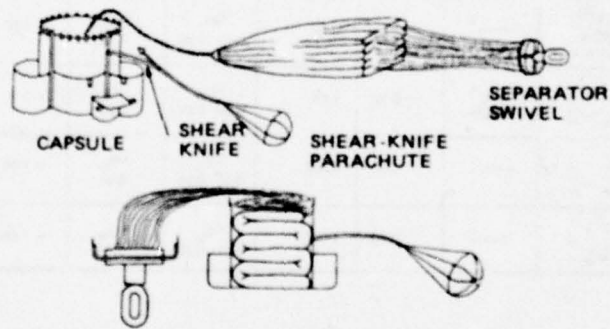


Figure 278b - Capsule

Figure 278 - Parachute and Deployment System Used for a Full-Scale, Emergency-Braking Experiment with a Large Tanker

Mitsubishi Heavy Industries, ²²³

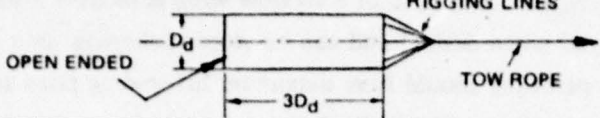
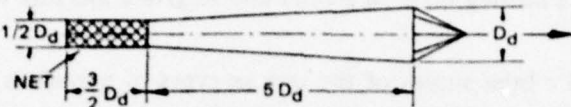
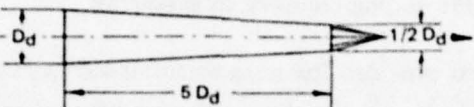
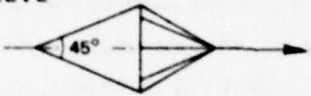
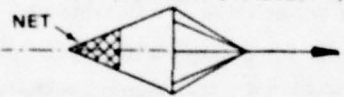
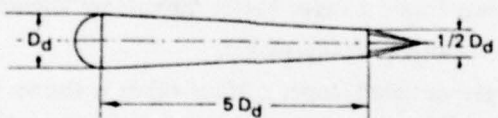
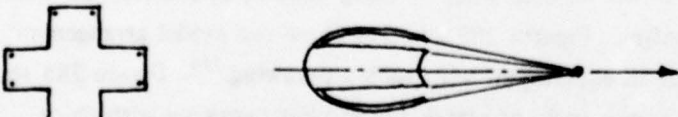
<p>(a) PARALLEL SIDED SLEEVE</p> 	$C_{D_x} \approx 0.42$ $C_{D_0} \approx 0.033$
<p>(b) OPEN-ENDED SLEEVE, WITHOUT NET (c) WITH NET</p> 	<p>(b) $C_{D_x} \approx 0.8$ (c) $C_{D_x} \approx 0.82 - 0.88$</p>
<p>(d) LOW DRAG SLEEVE, CLOSED REAR END</p> 	$C_{D_x} \approx 0.32$
<p>(e) CONICAL SLEEVE</p> 	
<p>(f) CONICAL SLEEVE, WITH NET (BETTER STABILITY)</p> 	
<p>(g) LOW DRAG SLEEVE WITH SHAPED REAR END</p> 	
<p>CROSS WITH EQUAL ARMS</p> 	$C_{D_0} \sim 0.55 - 0.86$

Figure 279 - Examples of Drogues

In general, drogues are much easier to manufacture than parachutes. The cross chute is more properly a form of parachute. It can be made to have a C_{D_0} larger than a hemisphere canopy. Items (a) through (g) are reproduced from Brown.²¹⁸

NAME: Parawings

DEFINITION AND OPERATION: Parawing is the name given to families of flexible wings that have been developed primarily by NASA. The idea of a flexible wing is to have a foldable winglike device that can be deployed when desired and can be stored otherwise in a compact package. Unlike a parachute, the parawing should have maximum lift-to-drag ratio and good stability and control characteristics in gliding flight. Such devices could be used in an emergency situation to decelerate a moving body in a fluid and to give a measure of maneuvering control for recovery.

Rogallo²²⁵ has presented a brief survey of the various types of parawings and the gross aerodynamic performance. Campbell,²²⁶ for example, has discussed the application of deployable parawings specifically for the gliding recovery of spacecraft.

Force Estimates. Rogallo²²⁵ has provided the wing-performance spectrum of Figure 280 which shows how increasing rigidity increases the maximum lift-to-drag achievable with a wide variety of wing types. It should be remembered that for strength reasons, all flexible wings are inherently limited in their ultimate aspect ratio, whereas rigid wings can be built with very large values. The $(L/D)_{\max}$ values in this figure reflect this difference, in part, and represent extremes. Typical values of $(L/D)_{\max}$ are more modest than those indicated in Figure 280.

Three examples are given here of wings from the flexible end of the rigidity spectrum. Figure 281 shows the lift, drag, and L/D for a single-keel, all-flexible parawing attached to a small lifting body. The $(L/D)_{\max}$ is about 2.5. By separating the rigging attachment points, a slightly higher L/D can be achieved. Also, providing a greater longitudinal spread of the attachment points on the body was found to give better directional alignment of the body in flight; see Bugg and Sleeman²²⁷ for other arrangements.

A twin-keel parawing with ram-inflated upper surface tubes is shown in Figure 282. This presentation of data from Fournier²²⁸ illustrates another point about flexible wings; maneuvering forces are obtained by differential lengthening and shortening of the rigging lines.

More rigidity can be built into a flexible wing by using inflated cylindrical tubes along the keel and along the leading edges. Figures 283 and 284 show the model arrangement, force definitions, and data, from an experiment with such a parawing.²²⁹ Figure 285 shows a collection of aerodynamic data versus angle of attack for another parawing with thick, rounded leading edges.

Figure 286 shows a comparison of L/D for cylindrical and conical shaped parawings with aspect ratios 2.8 and 6. These wings have rigid streamlined leading edges.

There are numerous NASA publications describing a great variety of flexible wing configurations. Some general theoretical work about the shape and structural aspects of parawings has also been published; see for example, the work by Nielsen et al.²³⁰ and by Spangler and Nielsen.²³¹

DISCUSSION: For use in water, the all-flexible parawing with inflated cylindrical tubes along the keel and leading edges (Figures 283 through 285) may be especially interesting. If these tubes were made large enough, considerable *buoyancy* could be provided in addition to the hydrodynamic forces on the parawing shape. In an emergency situation such a buoyant-parawing could be inflated rapidly, using high-pressure air upon deployment.

The principle disadvantages of an emergency parawing are the same as with a parachute. Another problem area would be how to control simply the gliding performance of a parawing from inside a submarine.

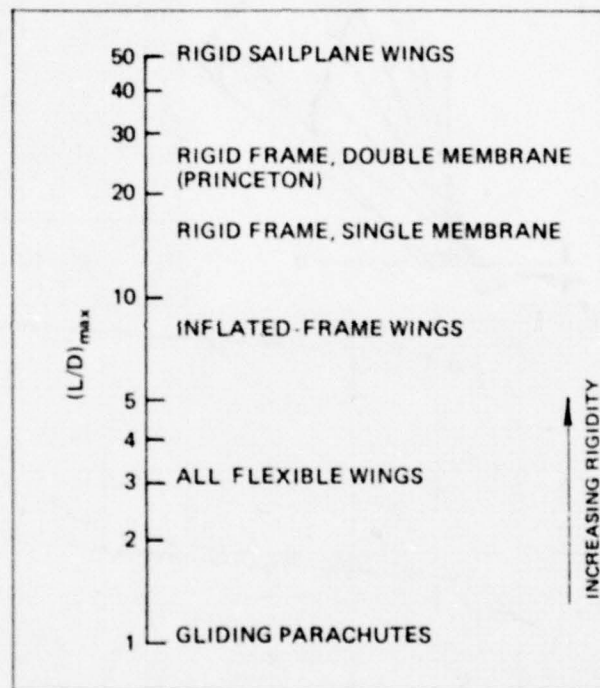


Figure 280 - Maximum Lift-to-Drag Performance Spectrum as a Function of Wing Rigidity

Rogallo²²⁵

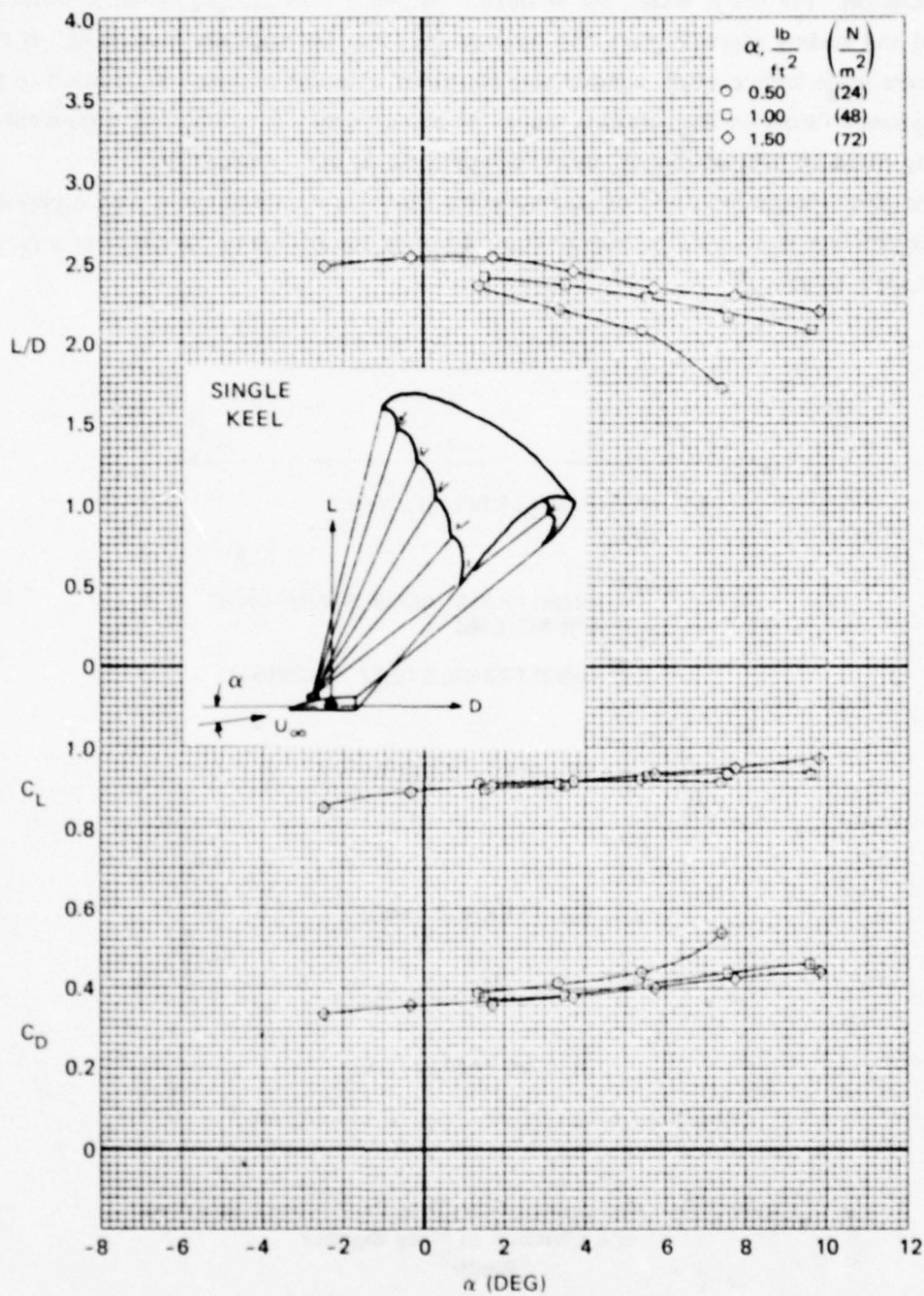


Figure 281 — Variation of Longitudinal Aerodynamic Characteristics with Angle of Attack for a Single-Keel Flexible Wing Supporting a Lifting Body

Bugg and Sleeman,²²⁷

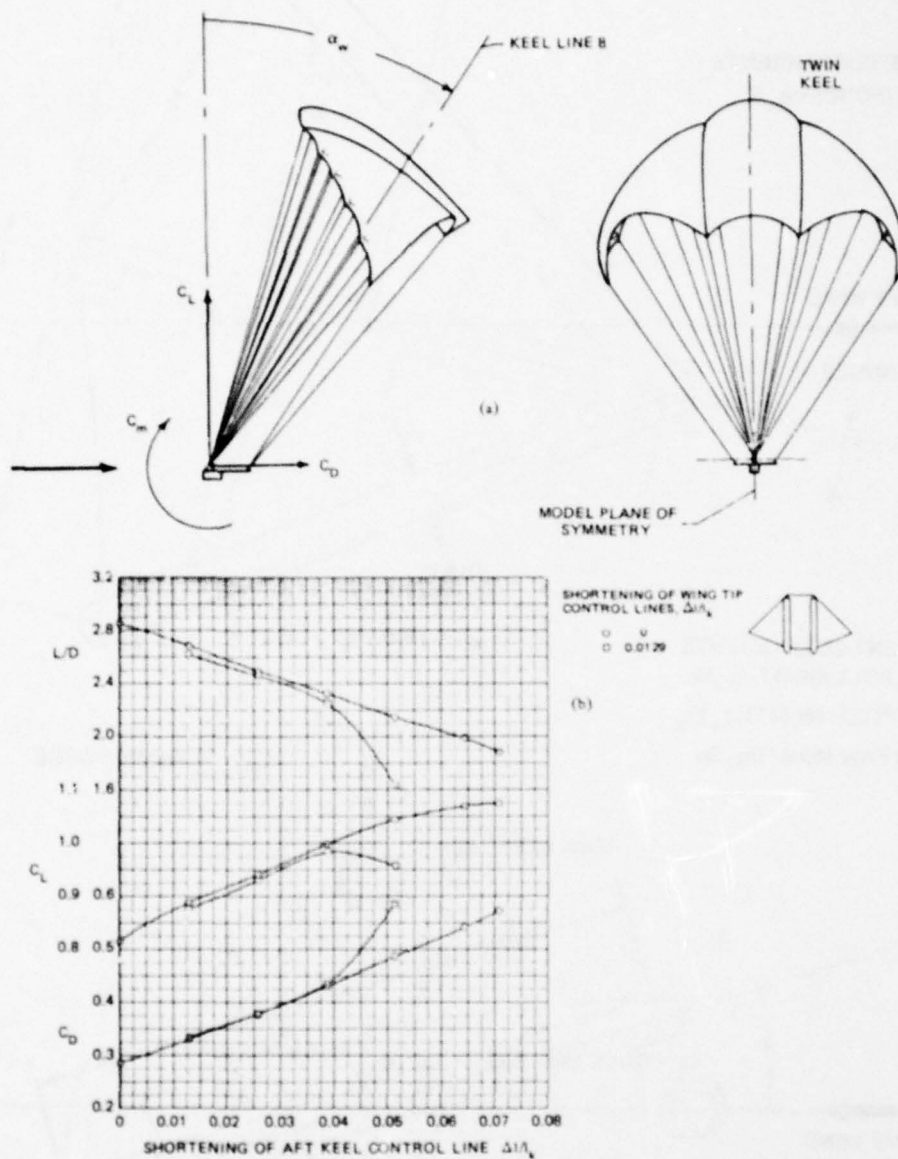


Figure 282 — Effect of Control Line Shortening on Some Aerodynamic Characteristics of a Twin-Keel, All Flexible, Tension-Structure Parawing with Ram-Inflated Upper Surface Tubes

Fournier²²⁸

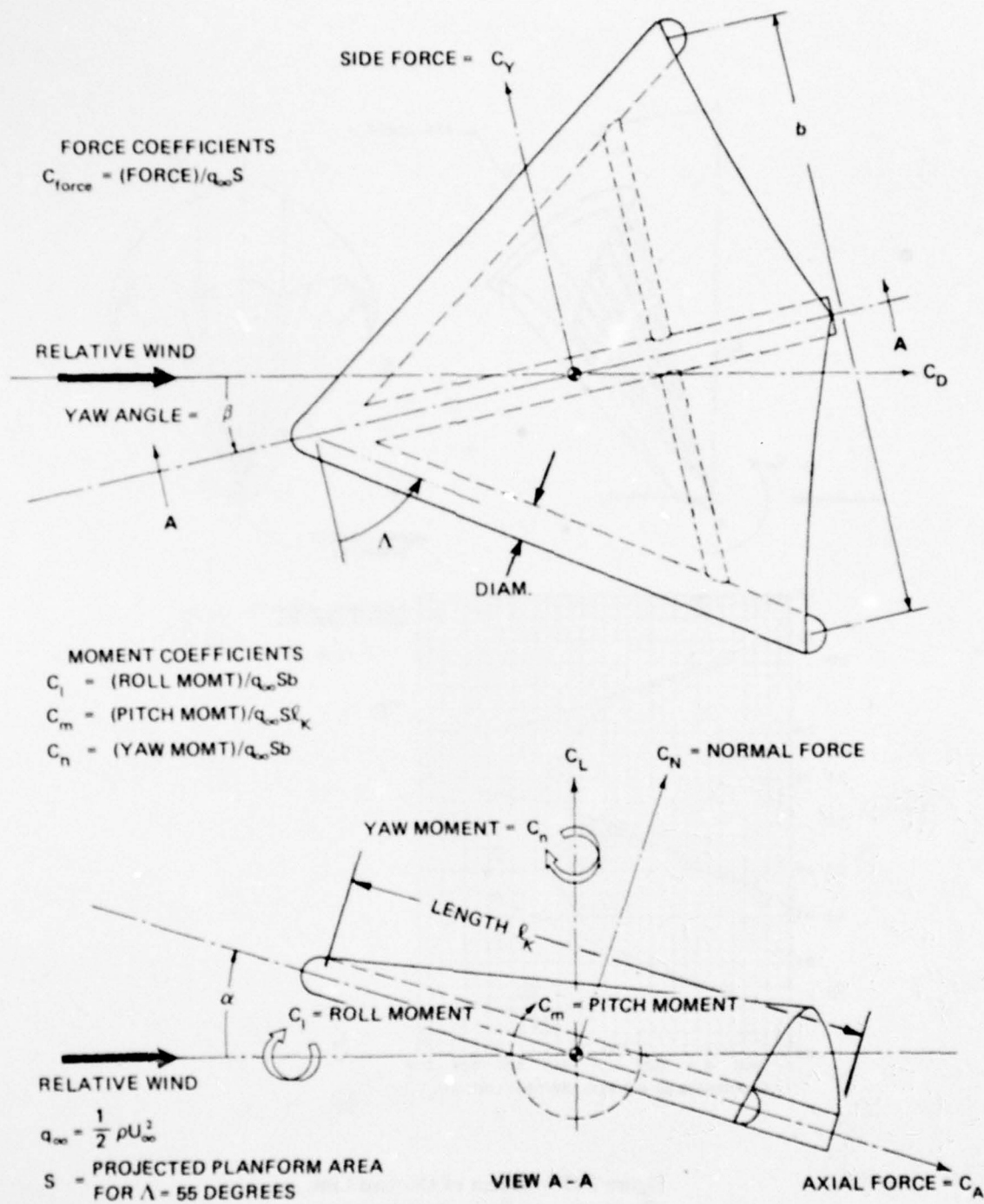


Figure 283 – System of Axes and Positive Directions of Forces and Moments
 Used in Presentation of Data

Model tested by Croom et al.,²²⁹ has diam/length = 0.07

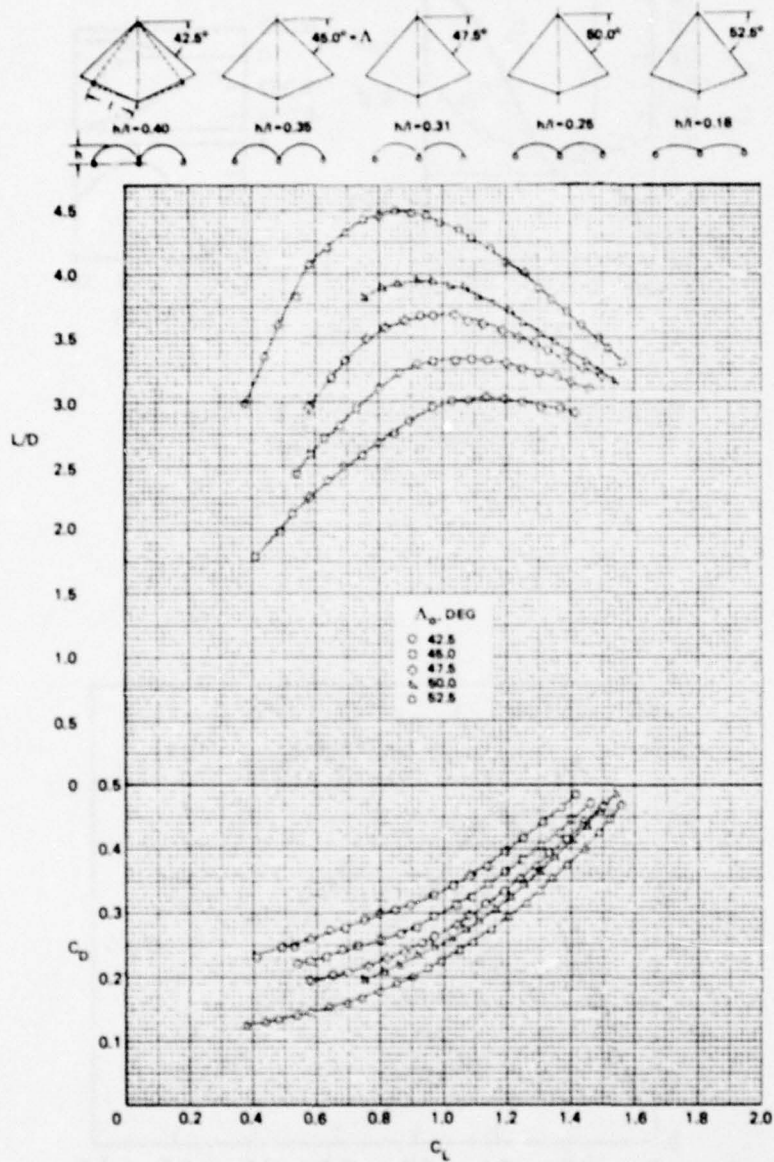


Figure 284 – Performance of Parawing with Inflated Cylindrical Tubes (Figure 283)

Effect of canopy flat-pattern sweep on variation with lift coefficients of drag coefficients and lift-drag ratios of the $\Lambda = 55$ degrees wing; $q = 20 \text{ N/m}^2$; Croom et al.²²⁹

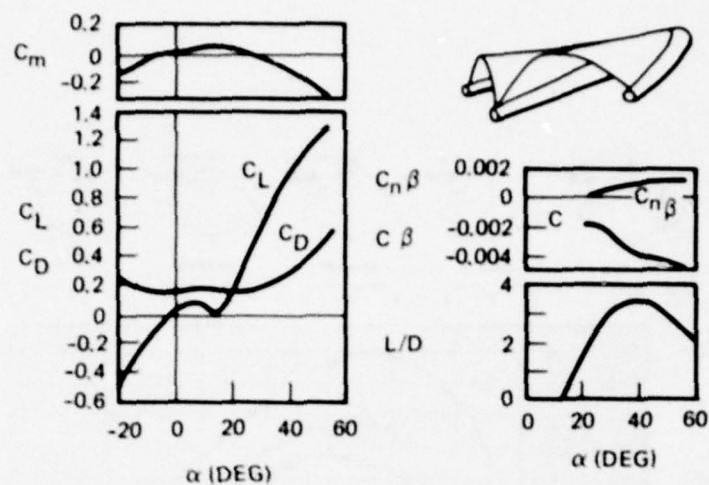


Figure 285 — Aerodynamics of a Parawing with Rounded Leading Edges
Campbell²²⁶

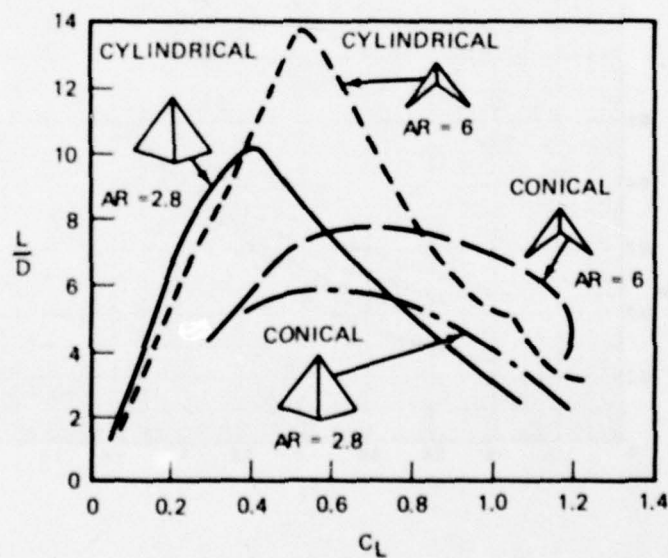


Figure 286 — Lift-to-Drag Values for Parawings with Conical and Cylindrical Surfaces
These have rigid, streamlined leading edges; Campbell²²⁶

APPENDIX B

PATENT CATEGORIES SEARCHED

As part of the research performed for this survey, a search of patents was made that covered the pertinent subclasses of three major patent categories as listed in the "U.S. Patent Office Manual of Classification." The three classes searched were:

CLASS 244, AERONAUTICS

CLASS 114, SHIPS

CLASS 115, MARINE PROPULSION

Lists of the subclasses of these main classes are reproduced here from the Manual of Classification. The starred items (*) received special attention.

The search provided a background matrix of ideas and breadth to the review of the open technical literature.

17.13 . . Automatic or condition responsive control

- 390

AIRCRAFT POWER PLANTS		93	Stabilizing weights
54	Mounting	94	Ballast storage and release
55	Arrangement	95	Ballast making
56	Tilting	96	Airship control
57	Radiator arrangement	97	Buoyancy varying
58	Auxiliary	98	Gas bag inflation
59	High altitude	99	Gas release
60	Transmission of power	100 R	LANDING GEAR
61	Power plant using airship gas as fuel	100 C	Endless track
62	AIRCRAFT PROPULSION	100 A	Inflatable
63	Launching	101	Amphibian
64	Manual	102 R	Retractable
65	Screw	102 A	Interconnected elements
66	Tilting	102 SL	Strut locks
67	Body encircling	102 SS	Strut shortening
68	Elongated	103 R	Wheel
69	Contra-propeller arrangements	103 S	Prerotation
70	Paddle wheel	103 W	Cross wind gear
71	Reciprocating propeller	104 R	Resiliently mounted
72	Beating wing	104 CS	Coil spring
73 R	Fluid	104 FP	Fluid pressure
73 B	Vacuum induced by radial flow	104 LS	Leaf spring
73 C	Radial outward and downward flow	105	Water landing
74	Explosive jet	106	Flying boat
• 75 R	AIRCRAFT CONTROL	107	Emergency
75 A	Flutter prevention	108	Skids
• 76 R	Automatic	109	Tail supports
76 A	Motor torque control of flaps or tabs	• 110 R	RETARDING AND RESTRAINING DEVICES
76 B	Velocity operated devices	110 A	Brake
76 C	Gust compensators	110 B	Thrust reversers
76 J	Steerable jets	110 C	Cable or net support
77 R	Electric	• 110 D	Aerodynamic braking
77 A	Glide path control	110 E	Landing platforms
77 B	Course finding and computing	110 F	Snarres
77 C	Radio control	110 G	Arresting hoods
77 D	Altitude, speed and angle of attack control	110 H	Friction brakes
77 E	Bank control	111	Wheel brake arrangement
77 F	Trim control	112	Water brake arrangement
77 G	Acceleration responsive	• 113	Aerodynamic retarders
77 M	Monitor	114 R	LANDING FIELD ARRANGEMENT
77 V	Over-ride of automatic by human	114 B	Blast deflectors
77 SE	Selective engagement	115	Mooring devices
77 S	Softener	116	Movable
77 DZ	Dead zone	117 R	AIRCRAFT STRUCTURE
77 SS	Space ships	117 A	Skin cooling
78	Fluid	118 R	Special passenger and cargo accommodations
79	Gyroscope actuated	118 P	Passenger
80	Gravity actuated	119	Fuselage and body construction
81	Operated by landing	120	Sectional
82	Vane operated	121	Shields and other protective devices
• 83 R	Pilot operated	122 R	Seats and safety belts
83 A	Locking devices	122 A	Ejection seats
83 B	3-way steering, single control	122 AB	Catapult and rocket combined
83 C	Plural surface by single control	122 AC	Catapult
83 D	Feel	122 AD	Rocket
83 E	Electrical pick-up	122 AE	Automatic sequence
83 F	Controllers	122 AF	Canopy release
83 G	Control systems	122 AG	Restraint positioning and protective devices
83 H	Variable	122 AH	Seat separation
83 K	Cable	122 B	Safety belts
83 J	Linkage	123	Airfoil construction
84	Dual	124	Sectional
85	Hydraulic	125	Airship hull construction
86	Rudder bars and pedals	126	Airship skin construction
87	Rudders and empennage	127	Airship load attachment
88	Rudders universally mounted	128	Airship gas cell construction and arrangement
89	Elevators both front and rear	129 R	Details
• 90 R	Ailerons and other roll control devices	129 D	Door
• 90 A	Roll control spoilers	129 H	Hand hole covers
• 90 B	Balanced air pressure	129 S	Steps
91	Vertical fins	129 W	Windows
• 92	Stabilizing propellers		

AIRCRAFT STRUCTURE

- . Details
 - 129 FP . . . Fire prevention devices
 - 130 . . . Aerodynamic resistance reducing
 - 131 . . . Joints and connections
 - 132 . . . Skin fastening devices
 - 133 . . . Materials of construction
 - 134 R . . . Ice prevention
 - 134 A . . . Flexible surfaces
 - 134 B . . . Heating fluid in airfoil
 - 134 C . . . Deicing fluid on airfoil exterior
 - 134 D . . . Electric
 - 134 E . . . Nature of surface
 - 134 F . . . Initiators and indicators
 - 135 R . . . Fuel supply
 - 135 A . . . Aircraft refueling
 - 135 B . . . Flexible containers
 - 135 C . . . Fuel balancing systems
 - 136 . . . Material discharging and diffusing
 - 137 R . . . Passenger and cargo loading and discharging
 - 137 P . . . Passenger
- 138 R SAFETY LOWERING DEVICES
 - 138 A . . . Rotating vanes
 - 139 . . . Entire aircraft
 - 140 . . . Passenger compartment
 - 141 . . . Seat
 - 142 . . . Parachutes
 - 143 . . . Garment attached
 - 144 . . . Aircraft element convertible to parachute
 - 145 . . . Canopy construction
 - 146 . . . Inflated bracing
 - 147 . . . Storage and release
 - 148 . . . Packs
 - 149 . . . Opening devices
 - 150 . . . Timing mechanism
 - 151 R . . . Harness
 - 151 A . . . Parachute harness connection
 - 151 B . . . Parachute load releasing
 - 152 . . . Control devices
 - 153 R KITES
 - 153 A . . . Rotating
 - 154 . . . Airplane type
 - 155 R . . . Accessories
 - 155 A . . . Kite controls
- DIGESTS
 - DIG. 1 . . . Flex wing
 - DIG. 2 . . . Inflatable evacuation slides

Original Classification 1905

5R	MISCELLANEOUS	44	VESEL RAISING AND DOCKING
0.5BD	.. Floating boat dock	45	.. Floating dry docks
0.5F	.. Float structures	46	.. Sectional
0.5T	.. Floating storage tanks	47	.. End gates
0.5D	.. Drilling	48	.. Elevators
0.5A	.. Fishing vessels	49	.. Camels, caissons, and pontoons
0.5RC	.. Surface cleaning vessels and garbage, sewage and refuse handling	50	.. Submerged
1	WARSHIPS	51	.. Hoisting
2	.. Rams	52	.. Air tanks
3	.. Battering	53	.. Camels, caissons, and pontoons
4	.. Floating batteries	54	.. Inflatable bags
5	.. Turret	55	.. Sand and mud loosening
6	.. Combined elevating and rotary	56	FORM
7	.. Elevating	57	.. Screw-propeller type
8	.. Rotary	58	.. Paddle wheelers
9	.. Armored	59	.. Spindle
10	.. Deflectors	60	.. Canal and ferry boats
11	.. Belting and plating	61	.. Divided hull
12	.. Compound	62	.. Concave bottom
13	.. Buffers	63	.. Flat bottom
14	.. Screens and shields	65 R	BUILDING
15	.. Concealment	65 A	.. Concrete ships
16 R	SUBMARINE VESSELS	66	.. Observation boats
16 A	.. Underwater swimming vehicles	66.5R	.. Hydroplane boats
16 B	.. Conning tower	66.5F	.. Pontoons
16 C	.. Periscope	66.5H	.. Hydrofoils
16 D	.. Ventilation	66.5P	.. Planing members
16 E	.. Ballasting	66.5S	.. Stepped bottom
16 F	.. Diving planes	67 R	.. Antifriction surfaces
16 G	.. Power plants	67 A	.. Air and oil films
17	.. Torpedo boats	68	.. Insubmersible vessels
16.4	.. Life and vessel saving devices	69	.. Linings and fillings
16.5	.. Buoys	70	.. Canal and ferry boats
16.6	.. Escapes	71	.. Cabins
16.7	.. Boats and buoys	72	.. Freighters
16.8	.. Salvage	73	.. Bulk cargo
18	TORPEDO BOATS	74 R	.. Liquid
19	.. Spar	74 T	.. Floating tank
20 R	TORPEDOES	74 A	.. Double hull or insulated tank
20 A	.. Power plants	75	.. Antishifting devices
20 B	.. Net cutting	76	.. Ceilings and floors
21 R	.. External control	77 R	.. Sectional
21 W	.. Remote controlled	77 A	.. Horizontal sections
21 A	.. Homing-all kinds	78	.. Bulkhead and compartment
22	.. Separable sections	79 R	.. Iron
23	.. Steering mechanism	79 W	.. Welded joint
24	.. Gyroscope	80	.. Corrugated
25	.. Depth regulation	81	.. Tubular
26	SCOWS	82	.. Wood
27	.. Dumping and unloading	83	.. Bracing and staying
28	.. Sectional	84	.. Sheathing and planking
29	.. Hinged	85	.. Decks
30	.. Separable	86	.. Calking and seaming
31	.. Platform	87	.. Knees
32	.. Tilting	88	.. Joints
33	.. Carriers	89	SPARS
34	.. Conveyors	90	.. Masts and masting
35	.. Side doors	91	.. Swinging
36	.. Bottom doors	92	.. Cross and trestle trees
37	.. Flooding gates	93	.. Coats, shields, and steps
38	.. Turnover	94	.. Heads and irons
39	SAILBOATS	95	.. Yards
40	ICE BREAKERS	96	.. Trusses and parrels
41	.. Rams	97	.. Gaffs, booms, etc.
42	.. Cutters	98	.. Pivoted
43	ICE BOATS	99	.. Crotches and supports
43.5R	MOTHER SHIPS, FLOATING LANDING PLATFORMS AND HARBORS	100	.. Spar irons
43.5VC	.. Vessel carrier	101	.. Fair leaders and checks
43.5AC	.. Aircraft carrier	102	SAILS AND RIGGING
		103	.. Sails
		104	.. Reefing and furling
		105	.. Fore-and-aft sails

	SAILS AND RIGGING	169	. . . Post bearings and heads
	. Sails	170	. . . Brakes
	. . . Reefing and furling	171	. . . Hydraulic
	. . . Fore-and-aft sails	172	. . . Locks
106	. . . Rolling	173	PORTS
107	. . . Rolling	174	. Stoppers
108	. . . Fastening devices	175	. . . Gun port
109	. Rigging screws and stretchers	176	. . . Hinged
111	. Running rigging	177	. . . Light and air
112	. Mast travelers	178	. . . Hinged covers
113	. Hoops and connections	179	HAWSE PIPES
114	. Cringles and hanks	180	. Stoppers and covers
115	. Clews	181	. Friction rollers
116	BULKHEADS AND DOORS	182	SCUPPERS
117	. Doors	183 R	BILGE DISCHARGE
118	. . . Automatic	183 A	. . . Wave motion
119	. . . Sliding	184	. . . Ejectors
120	. . . Sliding	185	. . . Ships motion
• 121	BALLASTING	186	. . . Ash
• 122	. Antirolling	187	SMOKESTACKS
123	. Floats	188	FURNITURE
124	. Shifting weights	189	. Cabins and staterooms
• 125	. Water tanks	190	. Life-preserver racks
126	. Fins and boards	191	. Self-leveling
127	CENTERBOARDS	192	. . . Berths
128	. Steering	193	. . . Single pivot
129	. Multiple	194	. . . Chairs
130	. Vertical drop and pivoted swing	195	. . . Tables
131	. . . Sectional		VALVES
132	. Pivoted	197	. . . Boat plugs
133	. . . Sectional	198	. . . Sea cocks
134	. . . Fan	199	CABLE STOPPERS
135	. . . Lateral	200	. Chain
136	. . . Lateral swing	201 R	HATCHES AND COVERS
137	. . . Lateral tilt	201 A	. . . Inflatable gaskets
138	. Vertical drop	202	. Sliding
139	. . . Sectional	203	. . . With fasteners
140	KEELS	204	TRAVELERS
141	. Vertical adjustment	205	. Tension relievers
142	. Bilge	206 R	ANCHORS
143	. Rocking	206 A	. . . Explosive
• 144 R	STEERING MECHANISM	207	. Fluke
144 RE	. . . Electrical	208 R	. . . Pivoted
144 A	. . . Remote control steering excluding manual operation	208 A	. . . Spring release
144 B	. . . Dynamic anchor	209	. . . Drags or sea anchors
144 C	. . . Wind vane operated	210	ANCHOR TRIPPERS
• 145 R	. Speed retarders	211	VENTILATION
145 A	. . . Trolling plates	212	. Valves
146	. Auxiliary	213	TENSION RELIEVERS
147	. Paddles and wheels	214	. Fluid
148	. Channels	215	. Cable
149	. Keel	216	. Couplers
• 150	. Fluid pressure	217	. . . Safety release
151	. . . Jet	218	BITTS, CLEATS, AND PIN RAILS
152	. Fins	219	FENDERS
153	. Foot	220	. Roller
154	. Wheel-shaft gearing	221 R	IMPLEMENTS
155	. . . Screw	221 A	. . . Underwater cutting
156	. . . Intermediate gear	222	. . . Hull cleaning
157	. . . Right and left	223	. Riggins
158	. . . Intermediate gear	224	. . . Calking, paying, etc.
159	. . . Segmental rack	227	LEAK STOPPERS
160	. Wheel and drum	228	. Interior
161	. . . Intermediate gear	229	. . . Aprons, mats, etc.
• 162	. Rudders	230	MOORING DEVICES
163	. . . Multiple	231	. Ferry slip
164	. . . Auxiliary	232	OIL DISTRIBUTERS
165	. . . Hanging and shipping	233	. Ship structure
166	. . . Tubular	234	. . . Drags and floats
167	. . . Sectional	235 R	TOWING
168	. . . Jury	235 WS	. . . Water skis
		235 A	. . . Tow coupling
		235 B	. . . Submerged body towing
		235 F	. . . Cable fairing

Original Classification 1905

5R	MISCELLANEOUS	63	CHAIN PROPELLER
5A	.. Automobile driven boats	64	.. Steering and adjustable
5B	.. Motor mounts and plural prime movers	66	CRANK PADDLE
5E	.. Exhaust	67	.. Steering and adjustable
5HC	.. Heating- cooling	17	PORTABLE PROPELLERS (E. G., OUT-BOARD TYPE)
5S	.. Seals	18 R	.. Steering
1R	LAND AND WATER BOATS	18 E Electrical
1A	.. Fully retractable wheels	18 A Auxiliary
1B	.. Amphibious bridges and ferries	18 B Rudders fixed to outboard aft of screw
1C	.. Air propelled boats	28 R	OSCILLATING PROPELLERS
2	.. Pedomotors	28 A	.. Full wave impeller
3	WIND MOTORS	29	.. Steering
4	WAVE PROPULSION	30	.. Reversing
5	.. Oscillating weight	31	RECIPROCATING PROPELLERS
6	TOWING	32	.. Steering
6.1	.. With body harness, handhold or remote control for tow unit	33	.. Reversing
7	.. Cable systems		
8	.. Track systems		
9	.. Ground wheels or poles		
70	SELF-PROPELLED OCCUPANT SUPPORTING SURFBOARD OR SKI TYPE		
11	JET		
12 R	.. Steering		
12 A Outboard jet		
13	.. Explosive		
14	.. Hydraulic		
15	.. Pneumatic drive		
16	.. Wheel drive		
19	BUOYANT PROPELLER		
20	.. Rotary hull		
21	MANUAL POWER		
22	.. Catamaran		
22.1	.. With body harness		
22.2	.. Water immersed operator		
22.3	.. Water immersed operator		
23	.. Paddle wheel		
24	.. Screw		
24.1	.. Operator supported type impeller (e. g., oar, scull, etc.)		
24.2	.. Articulated oar shaft (e. g., bow facing rower type, etc.)		
24.3 Motion transfer through gearing or flexible member		
24.4	.. Adjustable impeller support		
24.5	.. Medial fixed-pivot gunwale fulcrum		
24.6 Closed oar lock or secure connection		
25	MARINE PEDOMOTORS		
26	.. Catamaran		
26.1	.. With body harness		
26.3	.. Water immersed operator		
27	.. Bicycle propelled		
34 R	SCREW PROPELLER		
34 A	.. Hydraulic propulsion system		
34 B	.. Peripheral mechanical drive		
34 C	.. Contra-Propeller		
35	.. Steering		
37	.. Multiple screw		
38	.. Side		
39	.. Channel or way		
40	.. Self-clearing		
41 R	.. Depth regulation		
41 HT Hydraulic tilt-up		
42	.. Casing or shield		
43	.. Propeller-shaft brakes		
49	PADDLE WHEEL		
50	.. Steering		
52	.. Horizontal or inclined		
53	.. Channel or way		
54	.. Depth regulation		

REFERENCES

1. Cone, C.D., Jr., "A Theoretical Investigation of Vortex Sheet Deformation Behind a Highly Loaded Wing and Its Effect on Lift," National Aeronautics and Space Administration TN D-657 (1961).
2. Sato, M. and K. Matsuoka, "A Study on the Limit of Circulatory Lift on Wings with Finite Span," Bulletin of University of Osaka Prefecture, A 15, pp. 25-34 (1966).
3. McCormick, B., Jr., "Aerodynamics of V/STOL Flight," Academic Press, New York (1967).
4. Swanson, W.M., "The Magnus Effect: A Summary of Investigations to Date," Journal of Basic Engineering, American Society of Mechanical Engineers, Series D (1961).
5. Abbot, I.H. and A.E. Doenhoff, "Theory of Wing Sections," Dover Publications Inc., New York (1959).
6. Young, A.D., "The Aerodynamic Characteristics of Flaps," British Aeronautical Research Council R & M 2622 (1953).
7. Kuhlman, W.H., "The Douglas Double-Slotted Flap," Chapter in Boundary Layer and Flow Control, Edited by G.V. Lachman, Pergamon Press, New York, Vol. 1 (1961).
8. Martin, M., "The Stability Derivatives of a Hydrofoil Boat - Part I," Hydronautics, Inc. TR 001-10(1) (1963).
9. Whicker, L.F. and L.F. Fehlner, "Free Stream Characteristics of a Family of Low Aspect Ratio Control Surfaces," David Taylor Model Basin Report 933 (1958).
10. Mandel, P., "Ship Maneuvering and Control," Chapter 8 in Principles of Naval Architecture, Society of Naval Architects and Marine Engineers, New York (1967).
11. Kerwin, J.E. et al., "An Experimental Study of a Series of Flapped Rudders," Journal of Ship Research, Vol. 16, No. 4 (1972).
12. Callaghan, J.G. and T.D. Beatty, "A Theoretical Method for the Analysis and Design of Multielement Airfoils," Journal of Aircraft, Vol. 9, No. 12 (Sep 1972).
13. Mavriplis, F., "Aerodynamic Research on High Lift Systems," Canadian Aeronautical and Space Journal (May 1971).
14. Hoerner, S.F., "Fluid-Dynamic Drag," Published by Author, New Jersey (1965).
15. Woods, L.C., "Theory of Aerofoil Spoilers," British Aeronautical Research Council R & M 2969 (1953).
16. Brown, G.P. and G.V. Parkinson, "A Linearized Potential Flow Theory for Airfoils with Spoilers," Journal of Fluid Mechanics, Vol. 57, p. 695 (1973).
17. Soderberg, L.R., "Aircraft Control Means," U.S. Patent 3, 125, 313 (17 Mar 1964).
18. Ringleb, F.O., "Separation Control by Trapped Vortices," Chapter in Boundary Layer and Flow Control, Edited by G.V. Lachman, Pergamon Press, New York, Vol. 1 (1961).
19. Hurley, D.G., "The Use of Boundary Layer Control to Establish Free Streamline Flows," Chapter in Boundary Layer and Flow Control, Edited by G.V. Lachman, Pergamon Press, New York, Vol. 1 (1961).

20. Poisson-Quinton, P. and L. Lepage, "French Research on Control of Boundary Layer and Circulation," Chapter in Boundary Layer and Flow Control, Edited by G.V. Lachman, Pergamon Press, New York, Vol. 1 (1961).
21. Korbacher, G.K. and K. Sridhar, "A Review of the Jet Flap," University of Toronto Institute of Aerophysics Review 14 (1960).
22. Dike, D.J. et al., "A Study of the Low Speed Aerodynamic Characteristics of High-Lift Flow Controlled Profiles and Wings," Princeton University Report 349 (1958).
23. Lopez, M.L. et al., "A Theoretical Method for Calculating the Aerodynamic Characteristics of Arbitrary Jet-Flapped Wings," Douglas Aircraft Co. Report MDCJ5519 (1973)
24. Williams, J. and S.F.J. Butler, "Aerodynamic Aspects of Boundary Layer Control for High Lift at Low Speeds," Journal of the Royal Aeronautical Society, Vol. 67, No. 628, pp. 201-223 (1963).
25. Thomas, F., "Boundary Layer and Circulation Control for STOL Aircraft," Paper F in "The Aerodynamics of V/STOL Aircraft," AGARDograph 126 (1968).
26. Attinello, J.S., "Design and Engineering Features of Flap Blowing Installations," Chapter in Boundary Layer and Flow Control, Edited by G.V. Lachman, Pergamon Press, New York, Vol. 1 (1961)
27. Thomas, F., "Untersuchungen uber die Erhohung des Auftriebes von Tagflugeln mittels Grenzschichtbeeinflussung durch Aufblasen," Zeitschrift fuer Flugwissenschaften, Vol. 10, pp. 46-65 (1962).
28. Hay, A.J. and W.J. Egginton, "An Exact Theory of a Thin Aerofoil with Large Flap Deflection," Journal of the Royal Aeronautical Society, Vol. 60, p. 753 (1956).
29. Williams, J., "An Analysis of Aerodynamic Data on Blowing Over Trailing Edge Flaps for Increasing Lift," British Aeronautical Research Council CP 209 (1955).
30. Riebe, J.M., "A Correlation of Two-Dimensional Data on Lift Coefficient Available with Blowing-, Suction-, Slotted-, and Plain-Flap High-Lift Devices," National Advisory Committee for Aeronautics (NACA) RM L55D29a (1955).
31. Dods, J.B. and E.C. Watson, "The Effects of Blowing over Various Trailing-Edge Flaps on an NACA 0006 Airfoil Section, Comparisons with Various Types of Flaps on Other Airfoil Sections, and an Analysis of Flow and Power Relationships for Blowing Systems," National Advisory Committee for Aeronautics (NACA) RM A56C01 (1956).
32. Lawford, J.A. and D.N. Foster, "Low-Speed Wind-Tunnel Tests on a Wing Section with Plain Leading- and Trailing-Edge Flaps Having Boundary-Layer Control by Blowing," British Aeronautical Research Council R & M 3639 (1970).
33. Spence, D.A., "The Lift Coefficient of a Thin, Jet-Flapped Wing," Proceedings of the Royal Society, Series A, Vol. 238, pp. 46-68 (1956).
34. Spence, D.A., "The Lift on a Thin Aerofoil with a Jet-Augmented Flap," Aeronautical Quarterly, Vol. 9, pp. 287-299 (1958).
35. Williams, J. et al., "The Aerodynamics of Jet Flaps," British Aeronautical Research Council R & M 3304 (1963).
36. Maskell, E.C. and D.A. Spence, "A Theory of the Jet Flap in Three Dimensions," Proceedings of the Royal Society, Series A, Vol. 251, p. 407 (1959).

37. Williams, J., "British Research on Boundary-Layer Control for High Lift by Blowing," *Zeitschrift fuer Flugwissenschaften*, Vol. 6, pp. 143-150 (1958).
38. Thomas, F., "Boundary Layer Control for Increasing Lift by Blowing," *American Institute of Aeronautics and Astronautics Journal*, Vol. 3, pp. 967-968 (1965).
39. Lissaman, P.B.S., "Analysis of High-Aspect-Ratio Jet-Flap Wings of Arbitrary Geometry," *National Aeronautics and Space Administration CR-2179* (1973).
40. Smith, A.M.O. and J.A. Thelander, "The Power Profile. A New Type of Airfoil," *Douglas Aircraft Co. Report MDC J6236* (1974).
41. Franklin, R.E. and A.B. Bailey, "Preliminary Experiments on a Jet-Flap Hydrofoil," *University of Oxford Engineering Laboratory Report 1067/73* (1973).
42. Kerney, K.P., "A Theory of the High-Aspect-Ratio Jet Flap," *American Institute of Aeronautics and Astronautics Journal*, Vol. 9, No. 3, pp. 431-435 (1971).
43. Tokuda, N., "An Asymptotic Theory of the Jet Flap in Three Dimensions," *Journal of Fluid Mechanics*, Vol. 46, Part 4, pp. 705-726 (1971).
44. Lopez, M.L. and C.C. Shen, "Recent Developments in Jet Flap Theory and its Application to STOL Aerodynamic Analysis," *American Institute of Aeronautics and Astronautics Paper 71-578* (1971).
45. Erickson, J.C., Jr., and A.L. Kaskel, "Theoretical Solutions and Numerical Results for Low-Aspect-Ratio Rectangular Jet-Flap Control Surfaces," *Therm Advanced Research, Inc. TR 6603* (1966).
46. Kaplan, P. and A.F. Lehman, "An Experimental and Analytical Study of Jet Flap Hydrodynamics for Application to Submarine Control Surfaces," *Oceanics, Inc. Technical Report 67-41* (1967).
47. Verhagen, J.H.G., "Boundary Layer Control on a Ship's Rudder," *Netherlands Ship Research Center TNO Report 1355* (1970).
48. Williams, J. and A.J. Alexander, "Some Exploratory Three-Dimensional Jet-Flap Experiments," *Aeronautical Quarterly*, Vol. 8, pp. 21-30 (1957).
49. English, J.W. et al., "Some Maneuvering Devices for Use at Zero and Low Ship Speed," *British National Physical Laboratory Ship Report 163* (1972).
50. Kaplan, P. and T.R. Goodman, "Use of Jet-Flapped Hydrofoils as Ship Antipitching Fins," *Journal of Aircraft*, Vol. 4, No. 2, pp. 165-173 (1967).
51. Das, A., "Theoretical and Experimental Testing on Jet Flap Wings, Part I - Testing of a Rectangular Wing at Various Aspect Ratios," *National Aeronautics and Space Administration Translation TT F-13, 715* (1971).
52. Das, A., "Theoretische und Experimentelle Untersuchungen an Tragflugeln endlicher Spannweite mit Strahlklappen," *Deutsche Forschungsanstalt fuer Luft-und Raumfahrt FB 64-40* (1964).
53. Das, A., "Lifting Surface Theory for Wings with Jet Flaps," *National Research Council of Canada Translation TT 1122* (1964).

54. Lowry, J.G. and R.D. Vogler, "Wind-Tunnel Investigation at Low Speeds to Determine the Effect of Aspect Ratio and End Plates on a Rectangular Wing with Jet Flaps Deflected 85°," National Advisory Committee for Aeronautics (NACA) TN 3863 (1956).
55. Kind, R.J. and D.J. Maull, "An Experimental Investigation of a Low-Speed Circulation-Controlled Aerofoil," *Aeronautical Quarterly*, Vol. 19, pp. 170-182 (1968).
56. Dunham, J., "A Theory of Circulation Control by Slot-Blowing Applied to a Circular Cylinder," *Journal of Fluid Mechanics*, Vol. 33, pt. 3, pp. 495-514 (1968).
57. Williams, R.M., "Some Research on Rotor Circulation Control," Contribution to Third Cornell Aeronautical Laboratory/U.S. Army Aviation Material Laboratories Symposium on Aerodynamics of Rotary Wing and V/STOL Aircraft, Vol. 11 (1969).
58. Williams, R.M. and E.O. Rogers, "Design Considerations of Circulation Control Rotors," Paper presented at 28th Annual National Forum of the American Helicopter Society (May 1971).
59. Osborn, A.R. and J.M. Kettly, "Wind Tunnel Tests on a 20% Ellipse with Tangential Slot Blowing," British National Gas Turbine Establishment NT 593, Peystock (1966).
60. Cheeseman, I.C. and A.R. Seed, "The Application of Circulation Control by Blowing to Helicopter Rotors," *Journal of the Royal Aeronautical Society*, Vol. 71, No. 679, pp. 451-467 (1967).
61. Payne, P.R., "Steady-State Thrust Augmentors and Jet Pumps," U.S. Army Aviation Material Laboratories Technical Report 66-18, Fort Eustis, Va. (1966).
62. Quigley, H.C. and R.F. Vomaske, "Preliminary Results of Flight Tests of the Augmentor-Wing Jet STOL Research Aircraft," National Aeronautics and Space Administration SP-320 (1972).
63. Woolard, H.W., "Thin-Airfoil Theory of an Ejector-Flapped Wing Section," American Institute of Aeronautics and Astronautics Paper 74-187, Washington, D.C. (1974).
64. Koenig, D.G. and V.R. Corsiglia, "Aerodynamic Characteristics of a Large-Scale Model with an Unswept Wing and Augmented Jet Flap," National Aeronautics and Space Administration TN D-4610 (1968).
65. Morel, J-P. and P.B.S. Lissaman, "The Jet Flap Diffuser: A New Thrust Augmenting Device," American Institute of Aeronautics and Astronautics Paper 69-777 (1969).
66. Harris, G., "Aerodynamic Vehicle," U.S. Patent 3,664,611 (1972).
67. Malavard, L. et al., "Jet-Induced Circulation Control," *Aero Digest*, Parts 1, 2, and 3 (Sep-Nov 1956).
68. Wagner, F.G., "Design and Engineering Features for Flap Suction and Combined Blowing Suction," Chapter in *Boundary Layer and Flow Control*, Edited by G.V. Lachman, Pergamon Press, New York, Vol. 1 (1961).
69. Oosterveld, M.W.C., "Nozzle for Ships Propeller with Water Ejection Along the Trailing Edge of the Nozzle," U.S. Patent 3,675,424 (1972).
70. Krall, K.M. and C.H. Haight, "Wind Tunnel Tests of a Trapped Vortex-High Lift Airfoil," Advanced Technology Center, Inc. Report B-94300/3TR-10 (1973).
71. Küchemann, D. et al., "Aircraft," U.S. Patent 3,090,584 (1963).

72. Saunders, W.S., "*Beating Jet-Wing Aircraft*," U.S. Patent 3,168,997 (1965).
73. Goodmanson, L.T. and L.B. Gratzner, "*Recent Advances in Aerodynamics for Transport Aircraft - Part One*," *Astronautics and Aeronautics*, (Dec 1973).
74. Phelps, A.E., "*Aerodynamics of the Upper Surface Blown Flap*," National Aeronautics and Space Administration SP-320 (1972).
75. Cornish, J.J., "*Method and Apparatus for Modifying Airfoil Fluid Flow*," U.S. Patent 3,480,234 (1969).
76. Dixon, C.J., "*Lift Augmentation by Lateral Blowing Over a Lifting Surface*," American Institute of Aeronautics and Astronautics Paper 69-193 (1969).
77. Dixon, C.J., "*Analysis of Experimental Force Data for Lift Augmentation by Spanwise Blowing over Trailing Edge Flaps and Aircraft Control Surfaces*," Lockheed-Georgia Co. Naval Air Systems Command Final Report ER-11190 (1971).
78. von Schertel, H., "*Supramar's PT 150-DC*," *Hovering Craft and Hydrofoil*, Vol. 6, No. 9, p. 25 (1967).
79. Smith, K.E., "*Method and Apparatus for Steering Underwater Bodies*," U.S. Patent 3,096,739 (1963).
80. Lang, T. and D. Daybell, "*Water Tunnel Tests of Three Vented Hydrofoils in Two-Dimensional Flow*," *Journal of Ship Research*, pp. 1-15 (1961).
81. Acosta, A.J. and R.B. Wade, "*Selectively Ventilated Ring Wing Hydrofoils*," California Institute of Technology, Division of Engineering and Applied Science Report E-138.2 (1967).
82. Acosta, A.J. et al., "*Measurements on Fully Wetted and Ventilated Ring Wing Hydrofoils*," California Institute of Technology, Division of Engineering and Applied Science Report E-138.1 (1965).
83. Sweeney, T.E., "*Preliminary Full-Scale Measurements of Jet Spoiler Performance on the L-21 Airplane*," Princeton University Report 304 (1955).
84. Ringleb, F.O., "*Investigations of Suction Flaps*," Naval Aircraft Factory, Philadelphia, Pa., Princeton University Report 304 (1955).
85. Pankhurst, R.C. and B. Thwaites, "*Experiments on the Flow Past a Porous Circular Cylinder Fitted with a Thwaites Flap*," British Aeronautical Research Council R & M 2787 (1950).
86. Arnold, K.O., "*Untersuchungen uber die Auftriebserholung eines Klappenflu gels durch Schlitzabsaugung*," *Zeitschrift fuer Flugwissenschaften*, Vol. 15, No. 2, pp. 37-56 (1967).
87. Preston, J.H. et al., "*The Theoretical Estimation of Power Requirements for Slot-Suction Aerofoils, with Numerical Results for Two Thick Griffith-Type Sections*," British Aeronautical Research Council R & M 2577 (1953).
88. Thwaites, B., "*Incompressible Aerodynamics*," Oxford University Press (1960).
89. Goldstein, S., "*Low-Drag and Suction Aerofoils*," *Journal of Aeronautical Science*, Vol. 15, p. 189 (1948).

90. Williams, J., "A Brief History of British Research on Boundary Layer Control for High Lift," Chapter in Boundary Layer and Flow Control, Edited by G.V. Lachman, Pergamon Press, New York, Vol. 1 (1961).
91. Hazen, D.C. et al., "Circulation Control by Means of Trailing Edge Suction," Princeton University Report 239 (1953).
92. Glauert, M.B. et al., "Wind-Tunnel Tests on a Thick Suction Aerofoil with a Single Slot," British Aeronautical Research Council R & M 2646 (1952).
93. Gibson, C.H., "Oceanic Turbulence Measurements," American Institute of Aeronautics and Astronautics Paper 74-64, Washington, D.C. (1974).
94. Weiburg, J.A. et al., "Large-Scale Wing Tunnel Tests of an Airplane Model with an Unswept, Aspect-Ratio-10 Wing, Two Propellers, and Area-Suction Flaps," National Advisory Committee for Aeronautics (NACA) TN 4365 (1958).
95. Thwaites, B., "The Production of Lift Independently of Incidence - the Thwaites Flap," British Aeronautical Research Council R & M 2611 (1947).
96. Thwaites, B., "On the Design of Aerofoils for which the Lift is Independent of the Incidence," British Aeronautical Research Council R & M 2612 (1947).
97. Hazen, D.C. and F.O. Ringleb, "Boundary Layer Control System," U.S. Patent 2,894,703 (1959).
98. Foshag, W.F. and G.D. Boshler, "Review and Preliminary Evaluation of Lifting Horizontal-Axis Rotating-Wing Aeronautical Systems (HARWAS)," Aerophysics Co. U.S. Army Aviation Materiel Laboratories Technical Report 69-13 (1969).
99. Küchemann, D., "Auftrieb und Widerstands eines rotierenden Flügels," Deutsche Luftfahrtforschung, Forschungsbericht 1651, Gottingen (1942).
100. Mangler, W., "The Lift Distribution of Wings with End Plates," National Advisory Committee for Aeronautics (NACA) TM 856 (1938).
101. Thom, A., "Air Torque on a Cylinder Rotating in an Air Stream," British Aeronautical Research Council R & M 1520 (1932).
102. Steele, B.N. and M.H. Harding, "The Application of Rotating Cylinders to Ship Maneuvering," British National Physical Laboratory Ship Report 148, Great Britain (1970).
103. Brooks, J.D., "The Effect of a Rotating Cylinder at the Leading and Trailing Edge of a Hydrofoil," Bureau of Naval Weapons Report 8042 (Naval Ordnance Test Station TP 3036) Naval Ordnance Test Station, China Lake, Calif. (Apr 1963).
104. Weiberg, J.A. and B. Gamse, "Large-Scale Wind-Tunnel Tests of an Airplane Model with Two Propellers and Rotating Cylinder Flaps," National Aeronautics and Space Administration TN D-4489 (1968).
105. Lockwood, V.E. and L.W. McKinney, "Effect of Reynolds Number on the Force and Pressure Distribution Characteristics of a Two-Dimensional Lifting Circular Cylinder," National Aeronautics and Space Administration Technical Note D-455 (1960).
106. Neumark, S., "Rotating Aerofoils and Flaps," Journal of the Royal Aeronautical Society, Vol. 67, pp. 47-63 (1963).

107. Wolff, E.B. and C. Koning, "Tests for Determining the Effect of a Rotating Cylinder Fitted into the Leading Edge of an Airplane Wing," Translation, National Advisory Committee for Aeronautics (NACA) TM No. 354 (1962).
108. Alvarez-Calderon, A. and F.R. Arnold, "A Study of the Aerodynamic Characteristics of a High-Lift Device Based on a Rotating Cylinder and Flap," Stanford University, Department of Mechanical Engineering Technical Report RCF-1 (1961).
109. Alvarez-Calderon, A., "Rotating Cylinder Flaps for V/STOL Aircraft," Aircraft Engineering, Vol. 36, p. 304 (1964).
110. Crabtree, L.F., "The Rotating Flap as a High-Lift Device," British Aeronautical Research Council CP 480 (1960).
111. Bond, W.H., "Moving Skin Boundary Layer Control," Presented to Canadian Aeronautics and Space Institute/American Institute of Aeronautics and Astronautics Meeting on the Prospects for Improvement in Efficiency in Flight, AIAA Paper 70-881, Toronto, Canada (1970).
112. Wu, T. Y-t, "Hydromechanics of Swimming of Fishes and Cetaceans," Chapter in Advances in Applied Mechanics, Vol. 11, Academic Press, New York (1971).
113. Wu, T. Y-t, "Hydromechanics of Swimming Propulsion: Part 1, Swimming of a Two-Dimensional Flexible Plate at Variable Forward Speeds in an Inviscid Fluid," Journal of Fluid Mechanics, Vol. 46, Part 2, pp. 337-355 (1971).
114. Wu, T. Y-t, "Swimming of a Waving Plate," Journal of Fluid Mechanics, Vol. 10, Part 3, pp. 321-344 (1961).
115. Kelly, H.R., "Fish Propulsion Hydrodynamics," Contribution to Developments in Mechanics, Edited by Lay and Malvern, Vol. 1, Plenum Press, New York (1961).
116. Szeless, A.G., "Undulating Plate Type Propeller: the Two-Dimensional Ideal Case," Journal of Ship Research, Vol. 13, No. 3, pp. 171-177 (1969).
117. Lighthill, M.J., "Aquatic Animal Propulsion of High Hydromechanical Efficiency," Journal of Fluid Mechanics, Vol. 44, Part 2, pp. 265-301 (1970).
118. Wu, T. Y-t, "Hydromechanics of Swimming Propulsion: Part 2, Some Optimum Shape Problems," Journal of Fluid Mechanics, Vol. 46, Part 2, pp. 521-544 (1971).
119. Alberty, H.F. and E.K. Jacquet, "Dermadrive," University of Michigan Department of Naval Architecture and Marine Engineering Report 094 (1970).
120. Pehrsson, L., "Model Tests with Bow-Jet (Bow-Steering) Screw Propellers," David Taylor Model Basin Report 1461 (Oct 1960).
121. Young, D.B., "Model Investigation of the Stability and Control Characteristics of the Contract Design for the Deep Submergence Rescue Vehicle (DSRV)," NSRDC Report 3030 (1969).
122. Hawkins, S. et al., "The Use of Maneuvering Propulsion Devices on Merchant Ships," Robert Taggart, Inc. Report RT-8518 (1965).
123. English, J.W., "Further Considerations in the Design of Lateral Thrust Units," International Shipbuilding Progress, Vol. 13, No. 137, pp. 14-28 (1960).

124. English, J.W., "The Design and Performance of Lateral Thrust Units for Ships," Royal Institution of Naval Architects, Vol. 105, No. 3, pp. 251-278 (1963).
125. Chislett, M.S. and O. Bjorheden, "Influence of Ship Speed on the Effectiveness of a Lateral-Thrust Unit," Hydro- and Aerodynamic Laboratory (Denmark) Report Hy-8 (1966).
126. Beveridge, J., "Design and Performance of Bow Thrusters," Marine Technology, Vol. 9, No. 4 (Oct 1972).
127. Feldman, J.P., "Model Investigation of Stability and Control Characteristics of a Preliminary Design for the Deep Submergence Rescue Vehicle (DSRV Scheme A)," David Taylor Model Basin Report 2249 (1966).
128. Norrby, R., "The Effectiveness of a Bow Thruster at Low and Medium Ships Speeds," International Shipbuilding Progress, Vol. 14, No. 156, pp. 315-318 (1967).
129. Taniguchi, K. et al., "Investigations Into the Fundamental Characteristics and Operating Performances of Side Thruster," Mitsubishi Technical Bulletin No. 35 (1966).
130. Lockheed Missiles and Space Company, "Deep Submergence Rescue Vehicle, Propulsion and Maneuvering System Evaluation, Final Report," RV-R-0024 (Oct 1966).
131. Stuntz, G.R. and R.J. Taylor, "Some Aspects of Bow-Thruster Design," Society of Naval Architects and Marine Engineers Transactions, Vol. 72 (1964).
132. Taylor, R.T., "Experimental Investigation of the Effects of Some Shroud Design Variables on the Static Thrust Characteristics of a Small-Scale Shrouded Propeller Submerged in a Wing," National Advisory Committee for Aeronautics (NACA) TN 4126 (1958).
133. Hawkins, S., "The Use of Maneuvering Propulsion Devices on Merchant Ships," Paper presented at Chesapeake Section of Society of Naval Architects and Marine Engineers (1965).
134. Van Manen, J.D., "Effect of Radial Load Distribution on the Performance of Shrouded Propellers," International Shipbuilding Progress, Vol. 9, No. 93 (1962).
135. Van Manen, J.D. and M.W.C. Oosterveld, "Analysis of Ducted-Propeller Design," Society of Naval Architects and Marine Engineers Transactions, Vol. 74 (1966).
136. American Shipbuilding Company, "AMTHRUST Bow Tunnel," Brochure (1964).
137. Pacific Car and Foundry, "Voith-Schneider Bow Thruster" (1964).
138. Witte, J.H., "The Pump-Driven Lateral-Thrust Unit with Ejector Augmentation," Marine Technology, pp. 291-302 (Jul 1969).
139. Van Manen, J.D. et al., "Research on the Maneuverability and Propulsion of Very Large Tankers," Sixth Office of Naval Research Symposium, ARC-136, pp. 239-275 (1966).
140. Morel, J.-P., "Theoretical Solutions for the Jet Flap Diffuser," Ph. D. Thesis, California Institute of Technology (May 1969).
141. Alperin, M. and G.L. Marlotte, "A Jet Flap Diffuser Ejector," Flight Dynamics Research Corporation Technical Report AFFDL-TR-71-66 (1971).
142. Goldsmith, R.H. and D.H. Hickey, "Characteristics of Lifting-Fan V/STOL Aircraft," Astronautics and Aeronautics Engineering, pp. 70-77 (1963).

143. Hickey, P.H. and W.L. Cook, "*Aerodynamics of V/STOL Aircraft Powered by Lift Fans*," Paper 15 in Fluid Dynamics of Rotor and Fan Supported Aircraft at Subsonic Speeds, Advisory Group for Aerospace Research and Development CP 22 (1967).
144. Williams, J., "*Turbo-Jet/Turbo-Fan Aircraft*," Paper E in The Aerodynamics of Vertical/Short Take-Off and Landing Aircraft, AGARDograph 126 (1968).
145. Hickey, D.H. and D.R. Ellis, "*Wind-Tunnel Tests of a Semispan Wing with a Fan Rotating in the Plane of the Wing*," National Aeronautics and Space Administration TN D-88 (1959).
146. Poisson-Quinton, P., "*Introduction to V/STOL Aircraft Concepts and Categories*," Paper A in the Aerodynamics of Vertical/Short Take-Off and Landing Aircraft, AGARDograph 126 (1968).
147. Stepniewski, W.Z., "*Basic Aerodynamics of Convertible Rotor/Propeller Aircraft*," Paper C in the Aerodynamics of Vertical/Short Take-Off and Landing Aircraft, AGARDograph 126 (1968).
148. Mavor, J.W. et al., "*Alvin, 6000-Ft Submergence Research Vehicle*," Society of Naval Architects and Marine Engineers Transactions, Vol. 74 (1966).
149. Dewhurst, P.K., "*Experience in the Control of Ships by Right Angle Drive Thrusters*," Naval Engineers Journal, pp. 33-47 (Aug 1970).
150. Graham, J.R. et al., "*Design and Construction of the Dynamically Positioned Glomar Challenger*," Marine Technology, Vol. 7, No. 2 (Apr 1970).
151. Thurston, S. and R.C. Amsler, "*Review of Marine Propellers and Ducted Propeller Propulsive Devices*," Journal of Aircraft, Vol. 3, No. 3, pp. 255-261 (1966).
152. Von Mises, R., "*Theory of Flight*," Dover Publications, New York (1965).
153. Betz, A., "*Schraubenpropeller mit geringsten Energieverlust*," Aus den Nachrichten der Gesellschaft der Wissenschaften zu Gottingen, Mathematisch-Physikalische Klasse, Vol. 2, pp. 193-217 (1919).
154. Goldstein, S., "*On the Vortex Theory of Screw Propellers*," Proceedings of the Royal Society, Series A, Vol. 63, pp. 440-465 (1929).
155. Lerbs, H.W., "*Moderately Loaded Propellers with Finite Number of Blades and an Arbitrary Distribution of Circulation*," Society of Naval Architects and Marine Engineers Transactions, Vol. 60, pp. 73-117 (1952).
156. Eckhardt, M.K. and W.B. Morgan, "*A Propeller Design Method*," Society of Naval Architects and Marine Engineers Transactions, Vol. 63, pp. 325-374 (1955).
157. Hough, G.R. and D.E. Ordway, "*The Generalized Actuator Disc*," Chapter in Developments in Theoretical and Applied Mechanics, Vol. 11, Pergamon Press, pp. 317-336 (1965).
158. Pien, P.C., "*The Calculation of Marine Propellers Based on Lifting-Surface Theory*," Journal of Ship Research, Vol. 5, No. 2, pp. 1-14 (1961).
159. Kerwin, J.E. and R. Leopold, "*A Design Theory for Subcavitating Propellers*," Society of Naval Architects and Marine Engineers Transactions, Vol. 72, pp. 294-335 (1964).

160. Cheng, H.M., "*Hydrodynamic Aspects of Propeller Design Based on Lifting Surface Theory, Parts 1 and 2*," David Taylor Model Basin Reports 1802 and 1803 (1964 and 1965).
161. Morgan, W.B. et al., "Propeller Lifting-Surface Corrections," Society of Naval Architects and Marine Engineers Transactions, Vol. 76, pp. 309-347 (1968).
162. Cox, G.G. and Wm. B. Morgan, "*The Use of Theory in Propeller Design*," Marine Technology, Vol. 9, No. 4, pp. 419-429 (1972).
163. Oosterveld, M.W.C. and P. van Oossanen, "*Recent Developments in Marine Propeller Hydrodynamics*," International Jubilee Meeting on the Occasion of the 40th Anniversary of the Netherlands Ship Model Basin (30 Aug - 1 Sep 1972).
164. Troost, L., "*Open Water Test Series with Modern Propellers*," Part 1 North-East Coast Institute of Engineers and Shipbuilders (NECI), Part 2 NECI, Part 3 NECI (1937 - 38, 1939 - 40, 1950 - 51).
165. van Lammeren, W.P.A. et al., "*The Wageningen B-Screw Series*," Society of Naval Architects and Marine Engineers Transactions, Vol. 77, pp. 269-317 (1969).
166. Gawn, R.W.L., "*Results of Experiments on Model Screw Propellers with Wide Blades*," Transactions of the Institution of Naval Architects (1937).
167. Lindgren, H. and E. Bjarne, "*The SSPA Standard Propeller Family Open-Water Characteristics*," Swedish State Shipbuilding Experimental Tank Publication 60 (1967).
168. Todd, F.H., "*Resistance and Propulsion*," Chapter 7 in Principles of Naval Architecture, Society of Naval Architects and Marine Engineers, New York (1967).
169. Laschka, B. et al., "*A Contribution on the Determination of Overall Forces of Inclined Propellers*," Paper 7 in Advisory Group for Aerospace Research and Development CP 22 (1967).
170. Lazareff, M., "*Aerodynamics of Shrouded Propellers*," Paper D in The Aerodynamics of Vertical/Short Take-Off and Landing Aircraft, AGARDograph 126 (1968).
171. Gordon, S.J. and P.T. Tarpgaard, "*Utilization of Propeller Shrouds as Steering Devices*," Marine Technology, Vol. 5, No. 3 (Jul 1968).
172. Burnell, J.A. and A.H. Sacks, "*Ducted Propellers - A Critical Review of the State of the Art*," Progress in Aeronautical Sciences, Vol. 3, Pergamon Press, New York, pp. 82-135 (1960).
173. Weissinger, J. and D. Maass, "*Theory of the Ducted Propeller - A Review*," Seventh Office of Naval Research Symposium on Naval Hydrodynamics, Rome, pp. 1209-1264 (1968).
174. Morgan, Wm. B. and E.B. Caster, "*Comparison of Theory and Experiment on Ducted Propellers*," Seventh Office of Naval Research Symposium on Naval Hydrodynamics, Rome, pp. 1311-1349 (1968).
175. van Manen, J.D., "*Open-Water Test Series with Propellers in Nozzles*," International Shipbuilding Progress, Vol. 1, No. 3 (1954).
176. van Manen, J.D., "*Recent Research on Propellers in Nozzles*," International Shipbuilding Progress, Vol. 4, No. 36 (1957).

177. van Manen, J.D. and A. Superina, "The Design of Screw Propellers in Nozzles," International Shipbuilding Progress, Vol. 6, No. 55 (1959).
178. Oosterveld, M.W.C., "Ducted Propeller Systems Suitable for Tugs and Pushboats," International Shipbuilding Progress, Vol. 19, No. 219, pp. 351-371 (1972).
179. Lewis, R.I., "A Theory for Prediction of the Off-Design Performance of Kort Nozzle Ducted Propellers," International Shipbuilding Progress, Vol. 20, No. 224, pp. 122-129 (1973).
180. Lazareff, M., "Controle de Diffusion aval sur Helice Carenee," Paper 11 in Advisory Group for Aerospace Research and Development CP 22 (1967).
181. Minsaas, K.J., "Baugpropeller og Aktivror," Norwegian Skipsmodelltankens Report 81 (1965).
182. Bashun, V.D. et al., "A Water-Jet Propulsion Unit for Hydrofoil Vessels," Hovering Craft and Hydrofoil, Vol. 11, No. 11, pp. 20-22 (1972).
183. Delao, M., "Some Experimental Results of Tests of a Low-Speed Waterjet Propulsion System," Journal of Hydronautics, Vol. 1, No. 2, pp. 97-101 (1967).
184. Brandau, J., "Performance of Waterjet Propulsion Systems - A Review of the State-of-the-Art," Journal of Hydronautics, Vol. 2, No. 2, pp. 61-73 (1968).
185. Kruppa, C. et al., "Wasserstrahlantriebe fur Hochgeschwindigkeitsfahrzeuge," Jahrbuch der Schiffbautechnischen Gesellschaft, Vol. 62, pp. 228-258 (1968).
186. Kulikov, S.V. and M.F. Khramkin, "Waterjet Propulsion Systems - Theory and Design," Translation Leningrad Shipbuilding Publishing House (1970).
187. Kim, H.C., "Hydrodynamic Aspects of Internal Pump-Jet Propulsion," Marine Technology, Vol. 3, pp. 80-98 (1966).
188. Levy, J., "The Design of Waterjet Propulsion Systems for Hydrofoil Craft," Marine Technology, Vol. 2 (1965).
189. Johnson, V.E., Jr., "Water-Jet Propulsion for High-Speed Hydrofoil," American Institute of Aeronautics and Astronautics Paper 64-306 (1964).
190. Stepanoff, A.J., "Centrifugal and Axial Flow Pumps," John Wiley and Sons, Inc., New York (1948).
191. Wislicenus, G.F., "Hydrodynamic Design Principles of Pumps and Ducting for Waterjet Propulsion," NSRDC Report 3990 (1973).
192. Schuster, S. et al., "On Certain Problems of Water Jet Propulsion," David Taylor Model Basin Translation 306 (1962).
193. Fancher, R.B., "Low-Area Ratio, Thrust-Augmenting Ejectors," Journal of Aircraft, Vol. 9, No. 3, pp. 243-248 (1972).
194. Pallabazzer, R., "Design Analysis of Gas-Turbine Powerplants for Two-Phase Hydropropulsion," Seventh Office of Naval Research Symposium on Naval Hydrodynamics, Rome (1968).
195. Muench, R.K. and J.H. Garrett, "A Review of Two-Phase Marine Propulsion," American Institute of Aeronautics and Astronautics Paper 72-589 (1972).

196. Amos, R.G. et al., "*Thrust of an Air-Augmented Waterjet*," Journal of Hydronautics, Vol. 7, No. 2, pp. 64-71 (1973).
197. Oosterveld, M.W.C. and P. van Oossanen, "*Ship Research Activities in the Netherlands*," International Shipbuilding Progress, Vol. 19, No. 215, pp. 213-246 (1972).
198. Rosen, G., "*Design of a Nuclear-Powered Water Ramjet*," American Rocket Society Journal, pp. 1403-1404 (Sep 1962).
199. Gongwer, C., "*Some Aspects of Underwater Jet-Propulsion Systems*," American Rocket Society Journal, pp. 1148-1151 (Dec 1960).
200. White, W.D., "*Lithium and Sodium as Water-Reactive Fuels for Torpedo Propulsion*," Chapter in Underwater Missile Propulsion, Edited by L. Greiner, Compass Publishers, Arlington, Va. (1967).
201. Foa, J.V., "*The Bladeless Propeller*," Seventh Office of Naval Research Symposium on Naval Hydrodynamics, Rome (1968).
202. Taggart, R., "*A New Approach to Supertanker Design*," Ocean Industry Magazine, pp. 21-25 (Mar 1974).
203. Johnson, V.E. and E.E. Barr, "*Propulsion of Deep Diving Submarines*," Hydronautics Inc., Paper presented at American Society of Mechanical Engineers Underwater Technology Conference, New London, Conn. (5-7 May 1965).
204. Ficken, N.L. and M.C. Dickerson, "*Experimental Performance and Steering Characteristics of Cycloidal Propellers*," NSRDC Report 2983 (1969).
205. Van Manen, J.D., "*Results of Systematic Tests with Vertical Axis Propellers*," International Shipbuilding Progress, p. 383 (1966).
206. Mendenhall, M.R. and S.B. Spangler, "*Theoretical Analysis of Cycloidal Propellers*," Nielsen Engineering and Research, Inc. Technical Report 53 (Jun 1973).
207. Netherlands Ship Model Basin, "*Final Report and Supplements 1-4 of Experimental and Theoretical Research on the Hydrodynamic Characteristics of Large Hub to Diameter Ratio Propellers*," Office of Naval Research Report on Contract N 26558-3463, Wageningen, Netherlands (Apr 1961).
208. Joosen, W.P.A. et al., "*Large Hub-to-Diameter Ratio Propellers with Programmed Blade Control*," International Shipbuilding Progress, Vol. 10, No. 101 (1963).
209. Peach, R.W., "*Propulsion Control by VARIVEC Propeller*," Third Ship Control Symposium, England (1972).
210. Denny, S.B., "*Measurement of Forces and Spindle Moments on Individual Blades of a Large-Hubbed Propeller*," NSRDC Report 3252 (1969).
211. Hunt, R.R. et al., "*Performance Characteristics of a Jet Flap Propeller*," NSRDC Report 2936 (1968).
212. Lasky, M.P. and R.A. Cumming, "*Further Studies of the Performance of a Jet Flap Propeller*," NSRDC Report 3331 (1971).
213. Wilkerson, J.B. et al., "*The Application of Circulation Control Aerodynamics to a Helicopter Rotor Model*," 29th Annual National Forum of the American Helicopter Society, Washington, D.C. (May 1973).

214. Way, S., "Electromagnetic Propulsion for Cargo Submarines," *Journal of Hydronautics*, Vol. 2, No. 2 (1968).
215. Phillips, O.M., "The Prospect for Magnetohydrodynamic Ship Propulsion," *Journal of Ship Research*, Vol. 5, No. 1, pp. 43-51 (1962).
216. Doragh, R.A., "Magnetohydrodynamic Ship Propulsion Using Superconducting Magnets," *Society of Naval Architects and Marine Engineers Transactions* (1963).
217. Wright Air Development Center, "United States Air Force Parachute Handbook," Wright-Patterson Air Force Base, Ohio, Wright Air Development Center Technical Report 55-265 (1965).
218. Brown, W.D., "Parachutes," Sir Isaac Pitman and Sons, Ltd., London (1951).
219. Whicker, L.F. et al., "Stability, Strength, and Opening Characteristics of Parachutes in Water," David Taylor Model Basin Report 1169 (1957).
220. Heinrich, H., "Development of Parachutes for Bombs, Mines, and Torpedoes," David Taylor Model Basin Translation 215 (1949).
221. Waters, M.H.L. and G.G. Gale, "A Comparison of the Performance of Small Parachutes in Air and Water," Royal Aircraft Establishment Technical Note Mechanical Engineering 319 (1960).
222. Sher, S.H. and L.J. Gale, "Wind-Tunnel Investigation of the Opening Characteristics, Drag, and Stability of Several Hemispherical Parachutes," National Advisory Committee for Aeronautics TN 1869 (1949).
223. Mitsubishi Heavy Industries, Ltd., "Underwater Parachutes for Emergency Halts," *Japan Shipbuilding and Marine Engineering*, Vol. 6, No. 1, pp. 22-24 (1971).
224. Weiberg, J.A. and K.W. Mort, "Wind-Tunnel Tests of a Series of Parachutes Designed for Controllable Gliding Flight," National Aeronautics and Space Administration TND-3960 (1967).
225. Rogallo, F., "Flexible Wings," *Aeronautics and Astronautics*, pp. 50-54 (Aug 1968).
226. Campbell, J.P., "Low-Speed Aerodynamic Research Related to the Landing of Space Vehicles," *Aerodynamics of Space Vehicles*, National Aeronautics and Space Administration SP-23, pp. 11-22 (1962).
227. Bugg, F.M. and W.C. Sleeman, Jr., "Low-Speed Tests of an All-Flexible Parawing for Landing a Lifting-Body Spacecraft," National Aeronautics and Space Administration TN D-4010 (1967).
228. Fournier, P.G., "Low-Speed Wind-Tunnel Investigation of All-Flexible Twin-Keel Tension-Structure Parawings," National Aeronautics and Space Administration TN D-5956 (1970).
229. Croom, D.R. et al., "Effects of Canopy Shape on Low-Speed Aerodynamic Characteristics of a 55° Swept Parawing with Large-Diameter Leading Edges," National Aeronautics and Space Administration TN D-2551 (1964).
230. Nielsen, J.N. et al., "An Exploratory Aerodynamic and Structural Investigation of All-Flexible Parawings," National Aeronautics and Space Administration CR-1674 (1970).
231. Spangler, S.B. and J.N. Nielsen, "Theoretical Investigation of the Aerodynamic Characteristics of All-Flexible Parawings," *Astronautics and Aeronautics* (Apr 1972).

INITIAL DISTRIBUTION

Copies		Copies	
1	DOD, ARPA/P. Selwyn		NAVSEASYSKOM (Continued)
1	US Army Aviation R&D COMMAND/ L.E. Olson		1 SEA 63R/Peirce
1	US Army Trans R&D Marine Trans Div		1 SEA 083
2	CNR		1 PMS 393
	1 Code 211/Whitehead		1 PMS 396
	1 Code 438/Cooper	1	NAVSEC NORFOLK VA/ Code 6660.03, Blount
1	CNRBRO BOSTON MA	1	NAVFACENGCOM/Code 032C
1	CNRBRO NEW YORK NY	3	CBC PORT HUENEME CA (CEL)
1	CNRBRO PASADENA CA		2 L-44/Ward, Meggitt
1	CNRBRO SAN FRANCISCO CA		1 Lib
1	CHNAVMAT/Code 08T23	1	NAVSHIPYD BREMERTON WA
1	NRL/Lib	1	NAVSHIPYD CHARLESTON SC/Lib
1	NORDA	1	NAVSHIPYD LONG BEACH CA/Lib
4	USNA	1	NAVSHIPYD PEARL HARBOR HI/ Code 202.32
	1 Tech Lib	1	NAVSHIPYD PHILADELPHIA PA/Lib
	1 Nav Sys Eng Dept	1	NAVSHIPYD PORTSMOUTH NH/Lib
	1 B. Johnson	1	NAVSHIPYD PORTSMOUTH VA/Lib
	1 N. Salvesen	2	NAVSHIPYD VALLEJO CA
2	NAVPGSCOL		1 Lib
	1 Lib		1 Code 250
	1 T. Sarpkaya	12	DDC
1	NAVAIRDEVGEN	1	AFFOL/FYS, J. Olsen
3	NAVOCEANSYSCEN	1	AFOSR/NAM
	1 Lib	1	US COAST GUARD ACADEMY/Lib
	1 G. Donahue	1	US COAST GUARD NAVAL ENGINEERING/ H. Chatterton
	1 M. Reischman		
1	NAVCOASTSYSCEN/Code 712, D. Humphreys	1	DOT/Lib, TAD-491.I
1	NAVSWC DAHLGREN VA/Lib	1	Library of Congress/Sci & Tech
1	NAVSWC SILVER SPRING MD/Lib	2	MMA
1	NUSC NEW LONDON CT/Lib		1 Capt McCready
12	NAVSEASYSKOM		1 Lib
	1 SEA 0322	1	NASA HQ/Lib
	1 SEA 033	1	NASA Ames Res Center/G. Chapman
	1 SEA 312/Kennell		
	1 SEA 32R2/Sejd		
	2 SEA 3213/Cauldwell, Keane		
	2 SEA 513		

Copies

- 2 NASA Langley Res Center
1 D. Bobbit
1 R. Whitcomb
- 2 National Bureau of Standards
1 Lib
1 G. Kulin
- 2 National Science Foundation
1 Eng Lib
1 G. Lea
- 1 U of Bridgeport/E. Uram
- 4 U of Cal/Dept Naval Arch, Berkeley
1 Lib
1 J. Paulling
1 W. Webster
1 J. Wehausen
- 2 U of Cal, San Diego
1 A.T. Ellis
1 Scripps Inst Lib
- 2 CIT
1 Aero Lib
1 A.J. Acosta
- 1 Catholic U of Amer/Civil
& Mech Eng
- 1 City College, Wave Hill/Pierson
- 1 Colorado State U/Eng Res Cen
- 1 U of Conn/Scottron
- 1 Cornell U/Shen
- 2 Florida Atlantic U
1 Tech Lib
1 S. Dunne
- 2 Harvard U
1 G. Carrier
1 Gordon McKay Lib
- 1 U of Hawaii/Bretschneider
- 1 U of Illinois/J. Robertson
- 4 U of Iowa
1 Lib
1 J. Kennedy
1 L. Landweber
1 V.C. Patel
- 1 Johns Hopkins U/S. Corrin
- 1 Kansas State U/Nesmith
- 1 U of Kansas/Civil Eng Lib

Copies

- 1 Lehigh U/Fritz Eng Lab Lib
- 3 U of Maryland
1 Eng Lib
1 F. Buckley, Dept Mech Eng
1 A. Platkin, Dept Aero Eng
- 5 MIT
1 Lib
1 M. Abkowitz
1 P. Leehey
1 P. Mandel
1 J.N. Newman
- 4 U of Minn/St. Anthony Falls
1 Lib
1 R. Arndt
1 Silberman
1 Song
- 4 U of Mich/NAME
1 Lib
1 Couch
1 Hammitt
1 F. Ogilvie
- 2 U of Notre Dame
1 Eng Lib
1 A. Szewczyk
- 2 New York U/Courant Inst
1 A. Peters
1 J. Stoker
- 3 Ohio State U
1 Eng Lib
1 R.J. Freuler
1 J. Lee
- 3 Penn State U
1 ARL Lib
1 R.E. Henderson
1 B.R. Parkin
- 1 Princeton U/Mellor
- 2 U of Rhode Island
1 T. Kowalski
1 F.M. White
- 5 SIT
1 Lib
1 Breslin
1 P.W. Brown
1 Savitsky
1 Tsakonas
- 1 U of Texas/Arl Lib
- 2 Texas A&M U
1 Eng Lib
1 L.A. Carlson

Copies

1 Utah State U/Jeppson

2 Southwest Res Inst
1 Applied Mech Rev
1 Abramson

2 Stanford U
1 S.J. Kline, Dept Mech Eng
1 R. Street, Dept Civil Eng

1 Stanford Res Inst/Lib

1 U of Washington/Arl Tech Lib

1 U of Wisconsin
T/Bratanow, College of Eng

3 VPI
1 H.L. Moses, Dept Mech Eng
1 W.S. Saric, Dept of Eng,
Science & Mechs
1 J. Schetz, Dept Aero & Ocean
Eng

3 Webb Inst
1 Lib
1 Lewis
1 Ward

1 Woods Hole/Ocean Eng

1 Worcester PI/Tech Lib

1 SNAME/Tech Lib

1 Beech Aircraft Corp,
Wichita, Kansas/Shand Naik

1 Bethlehem Steel/New York/Lib

1 Bethlehem Steel/Sparrows Point

2 The Boeing Co., Seattle, WA
1 G. Brune
1 P. Ruppert

1 Bolt, Beranek & Newman/Lib

1 CADCOM
107 Ridgely Avenue
Annapolis, MD 21401

1 DCW Industries, Inc./D.C. Wilcox

1 Designers & Planners, Inc.
2341 Jefferson-Davis Hghwy
Arlington, VA 22202

1 Exxon Math & System, Inc.

1 Exxon, NY/Design Div, Tank Dept

Copies

1 Flow Res Co., Kent, WA
E.M. Murman

1 Friede and Goldman, LTD
Suite 1414, 225 Barronette St.
New Orleans, LA 70112

1 General Dynamics, EB/Boatwright

1 Gibbs & Cox/Tech Info

1 L.R. Glosten & Assoc., Inc.
610 Colman Building
811 First Avenue
Seattle, WA 98104

1 Gruman Aerospace Co., NY
G. Volpe

2 J.J. Henry Co., Inc.
1 Two World Trade Center
Suite 9528
New York, NY 10048
1 Washington, DC

5 Hydronautics
1 Lib
1 A. Goodman
1 C.C. Hsu
1 V. Johnson
1 E. Miller

1 Lockheed, Sunnyvale/Waid

1 Alan C. McClure Assoc., Inc.
2600 South Gessner, Suite 504
Houston, TX 77063

2 McDonnell Douglas, Long Beach
1 T. Cebeci
1 J. Hess

1 McDonnell Douglas, St Louis, MO/
R. James

1 John J. McMullen Assoc., Inc.
One World Trade Center
Suite 3000
New York, NY 10048

1 Newport News Shipbuilding/Lib

1 Nickum & Spaulding Assoc., Inc.
811 First Avenue
Seattle, WA 98104

1 Nielsen Eng & Res

1 Oceanics

1 Dynamics Technology, Inc./D.R.S. Ko

Copies		Copies	Code	Name
3	Rand Corp	1	154	M. Ochi
	1 J. Aroesty	1	1544	R. Boswell
	1 C. Gazley	1	1544	R. Cumming
	1 E.R. Van Driest	1	1548	R. Folb
1	Rockwell International/B. Ujihara	1	1548	J. Pattison
		1	1548	P. Rispin
2	M. Rosenblatt & Son, Inc.	1	1552	T. Huang
	1 350 Broadway	1	1552	J. McCarthy
	New York, NY	5	1552	C. von Kerczek
	1 2341 Jefferson-Davis Hghwy	1	1556	P. Besch
	Arlington, VA 22202	1	1556	G. Santore
1	SAI, Inc., San Diego, CA/	1	1556	W. Souders
	B. Chapman	1	156	G. Hagen
1	George G. Sharp, Inc.,	1	1562	M. Martin
	Arlington, VA	1	1564	J. Feldman
1	Sperry Rand/Tech Lib	1	1568	E. Baitis
		1	1572	G. Wachnik
1	Sun Shipbuilding/Chief Naval Arch	1	1572	J. Fein
		1	1572	D. Moran
1	Robert Taggart	1	1572	E. Zarnick
		1	1576	W. Smith
1	Tracor	1	16	H. Chaplin
1	Vought Corp.	1	1606	S. de los Santos
	Advanced Tech Center/	1	1606	R. Williams
	C.S. Wells	1	1615	R. Furey
2	Westinghouse Electric	1	1619	K. Reader
	1 Gulino	1	1630	A. Ford
	1 M.S. Macovsky	1	1660	R. Englar
		1	2704	D. Gregory
		1	2731	E. Petrisko
		1	2732	D. Laster
		10	5211.1	Reports Distribution
		1	522.1	Unclassified Lib (C)
		1	522.2	Unclassified Lib (A)

CENTER DISTRIBUTION

Copies	Code	Name
1	11	W. Ellsworth
1	117	S. Hawkins
1	117	D. Jewell
1	117	J. Luckart
1	117	R. Stevens
1	15	W. Morgan
1	1504	V. Monacella
1	1507	D. Cieslowski
1	1508	F. Peterson
1	152	G. Cox
1	1521	P. Pien
1	1524	W. Day
1	1524	W. Lin
1	1524	Y. Shen
1	1532	G. Dobay
5	1532	M. Wilson
1	1536	R. Stenson

DTNSRDC ISSUES THREE TYPES OF REPORTS

1. DTNSRDC REPORTS, A FORMAL SERIES, CONTAIN INFORMATION OF PERMANENT TECHNICAL VALUE. THEY CARRY A CONSECUTIVE NUMERICAL IDENTIFICATION REGARDLESS OF THEIR CLASSIFICATION OR THE ORIGINATING DEPARTMENT.

2. DEPARTMENTAL REPORTS, A SEMIFORMAL SERIES, CONTAIN INFORMATION OF A PRELIMINARY, TEMPORARY, OR PROPRIETARY NATURE OR OF LIMITED INTEREST OR SIGNIFICANCE. THEY CARRY A DEPARTMENTAL ALPHANUMERICAL IDENTIFICATION.

3. TECHNICAL MEMORANDA, AN INFORMAL SERIES, CONTAIN TECHNICAL DOCUMENTATION OF LIMITED USE AND INTEREST. THEY ARE PRIMARILY WORKING PAPERS INTENDED FOR INTERNAL USE. THEY CARRY AN IDENTIFYING NUMBER WHICH INDICATES THEIR TYPE AND THE NUMERICAL CODE OF THE ORIGINATING DEPARTMENT. ANY DISTRIBUTION OUTSIDE DTNSRDC MUST BE APPROVED BY THE HEAD OF THE ORIGINATING DEPARTMENT ON A CASE-BY-CASE BASIS.